

0115

## REPORT DOCUMENTATION PAGE

Public reporting burden for this collection of information is estimated to average 1 hour per response, including the time for reviewing instructions, searching existing data sources, gathering the data needed, and completing and reviewing the collection of information. Send comments regarding this burden estimate or any other aspect of this collection of information, including suggestions for reducing this burden, to Washington Headquarters Services, Directorate for Information Operations and Reports, 1215 Jefferson Davis Highway, Suite 1204, Arlington, VA 22202-4302, and to the Office of Management and Budget, Paperwork Reduction Project (0704-0188), Washington, DC 20503

1. AGENCY USE ONLY (Leave blank)	2. REPORT DATE 3/06/02	3. REPORT TYPE AND DATES COVERED Final 11/15/97-3/6/02	
4. TITLE AND SUBTITLE  Investigation of Non-Equilibrium Plasmas		5. FUNDING NUMBERS  \$359,969 AFOSR \$190,793 UAH Cost Share	
6. AUTHORS  Clark W. Hawk		8. PERFORMING ORGANIZATION REPORT NUMBER	
7. PERFORMING ORGANIZATION NAME(S) AND ADDRESS(ES) University of Alabama/ Huntsville Propulsion Research Center 5000 Technology Dr. Huntsville, AL 35899			
9. SPONSORING/MONITORING AGENCY NAME(S) AND ADDRESS(ES) USAF/AFRL AF Office of Scientific Research 801 N. Randolph St. Rm. 732 Arlington, VA 22203-1977			
11. SUPPLEMENTARY NOTES			
12a. DISTRIBUTION/AVAILABILITY STATEMENT  Approved for Public Release		AIR FORCE OFFICE OF SCIENTIFIC RESEARCH (AFOSR) NOTICE OF TRANSMITTAL DTC. THIS TECHNICAL REPORT HAS BEEN REVIEWED AND IS APPROVED FOR PUBLIC RELEASE LAW AFR 100-12. DISTRIBUTION IS UNLIMITED.	
13. ABSTRACT (Maximum 200 words) The research program investigated non-equilibrium plasmas with a variety of simple gases for the purpose of obtaining experimental data that can be used to anchor analytical models of flowing plasmas suitable for various electric propulsion devices. A microwave plasma generator (MPG) operating at 2.45GHz and 3kW was the initial source of the plasmas. The working fluids included: argon, helium, nitrogen, carbon dioxide, and water vapor. The research also included investigation of several MHD devices placed at the outlet of the MPG to accelerate the plasmas to velocities of interest for propulsion so that the plasma plume data could be obtained in representative environments. Diagnostic methods included Langmuir probes and a Rayleigh scattering technique. The latter experienced poor signal to noise ratios that are believed to be a result of the small vacuum bell jar in which the experiments were conducted. Electron densities and other key parameters are presented for the range of working fluids and acceleration devices.			
14. SUBJECT TERMS  Plasmas, magnetohydrodynamics, (MHD), MHD accelerators		15. NUMBER OF PAGES	
		16. PRICE CODE	
17. SECURITY CLASSIFICATION OF REPORT  Unclassified	18. SECURITY CLASSIFICATION OF THIS PAGE  Unclassified	19. SECURITY CLASSIFICATION OF ABSTRACT  Unclassified	20. LIMITATION OF ABSTRACT  None

20020402 067

Research Administration



MAR 20 2002

Huntsville, Alabama 35899  
Phone: (256) 824-6000  
Fax: (256) 824-6677

March 11, 2002

AFOSR/PKC  
ATTN: Ms. Wendy M. Veon  
801 N. Randolph Street, Room 732  
Arlington, VA 22203-1977

RE: Grant # F49620-98-1-0083

Dear Ms. Veon:

Please find enclosed one (1) copy of the Final Technical Report for the above referenced grant entitled, "Investigation of Non-Equilibrium Plasmas," in accordance with your email dated March 11, 2002. Upon notification of Dr. Mitat Birkan's acceptance, this office will distribute two (2) copies of the report to DTIC as required.

Should you have any questions, please contact me at (256) 824-2659.

Sincerely,

A handwritten signature in cursive script that reads "Patricia J. Vail".

Patricia J. Vail  
Contract Administrator

Enc.



the data unacceptable with any degree of accuracy. An iodine cell has been constructed to help isolate the signal but has yet to be evaluated.

The emphasis of the research turned toward increasing the electron density above that achieved with the microwave plasma source solely. This was intended to create a plasma flow more suitable for propulsion purposes. A DC glow discharge ionization device (GDID) consisting of a cylindrical, open-ended anode and an inner coaxial cathode provided an order of magnitude better electron density with an order of magnitude less power input.

Research has continued with emphasis upon MHD accelerators. Both Faraday type crossed-field and a Hall current accelerator have been built. Each is installed in line with the MPG. Testing with the Faraday type crossed-field accelerator is complete and data are in analysis. Testing of the Hall current accelerator is underway at UAH expense. The results of these experiments will be provided upon their completion.

The following technical papers, reports, dissertations and theses have been produced as a direct result of this research and are appended to this final report.

1. Jones, Jonathan. E., "*An Assessment of microwave Generated Plasma for Use in Magnetohydrodynamic Accelerators*", Ph.D. Dissertation, University of Alabama in Huntsville, MAE Department, April 2000
2. Culley, Matthew J., "*Development and Study of a Rayleigh Scattering Technique for Microwave Plasma Measurements Taken in a Vacuum*", Master's Thesis, University of Alabama in Huntsville, MAE Department, August 1999
3. Deaconu, Stelu, "*Experimental Study of Plasma Energization at Magnetic Neutral Points*", Ph.D. Dissertation, University of Alabama in Huntsville, MAE Department, March 2002.
4. Li, Zhongmin, "*MHD Accelerator Technology research at the UAH Propulsion research Center*", Interim report, March 2002
5. Jonathan E. Jones, and Clark W. Hawk, "*Electrical Transport Properties of Pulsed Microwave Plasmas*", Interim Report, August 1998
6. Zhongmin Li, Clark W. Hawk, and Jonathan E. Jones, "*Experimental Investigation of MHD Plasma Accelerators for In-Space Propulsion Application*", Pennsylvania State University Propulsion Engineering Research Center 13<sup>th</sup> Annual Symposium on Propulsion, 22-23 October 2001, Huntsville, AL
7. Zhongmin Li, Clark W. Hawk, and Jonathan E. Jones, "*Experimental Study of Crossed-Field MHD Accelerator Coupling with Microwave Plasma*", AIAA Paper 2001-3495, 37<sup>th</sup> AIAA/ASME/SAE/ASEE Joint Propulsion Conference & Exhibit, 7-11 July 2001, Salt Lake City, UT
8. Stelu Deaconu, Clark W. Hawk, "*Evaluation of the Ionization Performance of a Stable DC Glow-Discharge in Flowing Plasmas*", AIAA Paper 2000-3757, 36<sup>th</sup> AIAA/ASME/SAE/ASEE Joint Propulsion Conference & Exhibit, 17-19 July 2000, Huntsville, AL

9. Zhongmin Li, Jonathan E. Jones, Clark W. Hawk, "*Experimental Study of Microwave Plasma MHD Accelerators*", AIAA Paper 2000-3882, 36<sup>th</sup> AIAA/ASME/SAE/ASEE Joint Propulsion Conference & Exhibit, 17-19 July 2000, Huntsville, AL
10. M. J. Culley, J. E. Jones, and C.W. Hawk, "*Rayleigh Doppler Velocimetry Measurements of a Microwave Thruster*", AIAA Paper 99-3717, 30th Plasmadynamics and Lasers Conference, 28 June – 1 July, 1999, Norfolk, VA
11. Stelu Deaconu, J. E. Jones, and C. W. Hawk, "*Diagnostics of Electric Properties of Flowing Microwave Plasmas for MHD Applications*" AIAA Paper 99-2715, 35<sup>th</sup> AIAA/ASME/SAE/ASEE Joint Propulsion Conference & Exhibit, 20-24 June, Los Angeles, CA

## ABSTRACT

School of Graduate Studies  
The University of Alabama in Huntsville

Degree: Doctor of Philosophy

College/Department: Engineering/Mechanical  
and Aerospace Engineering

Name of Candidate: Jonathan E. Jones

Title: An Assessment of Microwave Generated Plasmas for Use in Magnetohydrodynamic Accelerators

The initial mass of a spacecraft in low earth orbit may be reduced by over 50% when conventional chemical upperstages are replaced by a magnetohydrodynamic (MHD) system. In order for these gains to be realized, both low specific mass power plants and high efficiency MHD accelerators are required. This dissertation focuses on the latter requirement: high efficiency MHD accelerators.

To assess the benefits of a microwave plasma generator (MPG), detailed measurements of electron temperature and density at the exit of an MPG were obtained. A quadruple Langmuir probe was used to measure electron temperature and density. Measurements of gas temperature and pressure were obtained with thermocouples and Pitot tubes, respectively. A time of flight velocity technique was used to measure the velocity of the flow. These measurements allowed for the calculation of flow conductivity, thus MHD accelerator efficiency.

The experimental setup consisted of a TM<sub>011</sub> microwave resonant cavity, operating at 2.45 GHz, connected to a vacuum chamber. Tests were conducted with three conductive graphite nozzles with expansion ratios of 7.11, 26.21, and 64. One insulative boron nitrate nozzle was also tested. Finally, tests were conducted without a nozzle on the MPG. This allowed the MPG to operate at lower pressures ( $< 0.1$  atm) where the lower collision frequency resulted in enhanced non-equilibrium conditions. Argon, helium, nitrogen, carbon dioxide, and

water vapor were all successfully tested as working fluids. For the majority of the tests, the microwave power was held constant at 3 kW.

The results showed that an electron temperature an order of magnitude higher than the gas temperature can be obtained in both diatomic and monatomic gases. For the monatomic gases argon and helium, electron densities slightly higher than the critical plasma density for 2.45 GHz microwaves ( $10^{17}$  e/m<sup>3</sup>) were obtained. For diatomic and polyatomic molecules, electron densities were one to two orders of magnitude below the critical density correlating with the higher electron to neutral collision cross sections, as well as, large electron energy loss factors for diatomic and polyatomic gases.

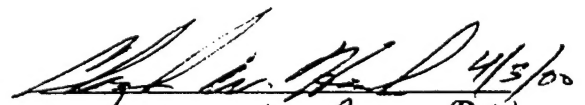

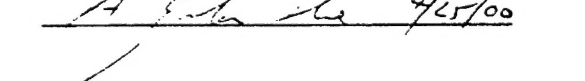
Based on the experimentally measured conductivity, ideal cross field MHD and Hall channel accelerator efficiencies were calculated. Efficiencies for helium and argon were 10.5% and 19.6%, respectively. All diatomic and polyatomic gases tested resulted in MHD efficiencies less than 1%; efficiencies greater than 30% are needed for competitive performance. This leads to the conclusion that microwave resonant cavities cannot be used as the sole source of ionization for MHD accelerators; however, the high electron temperatures obtained suggest the possibility of driving the non-equilibrium ionization to acceptable levels within the MHD channel itself. In addition, the gas temperatures were well below the temperatures required for thermal ionization; therefore, heat transfer to the walls and thermal losses at the accelerator exit should be reduced proportionally. This work presents for the first time experimental measurements that can be used to design a prototype MHD channel to test these hypotheses.

Abstract Approval:

Committee Chair

Department Chair

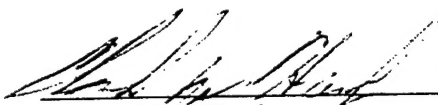
Graduate Dean

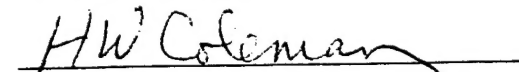
  
  


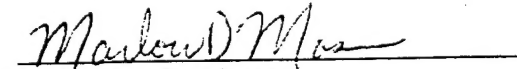
## DISSERTATION APPROVAL FORM

Submitted by Jonathan E. Jones, in partial fulfillment of the requirements for the degree of Doctor of Philosophy in Mechanical and Aerospace Engineering.

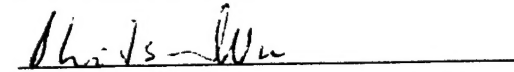
Accepted on behalf of the Faculty of the School of Graduate Studies by the dissertation committee:

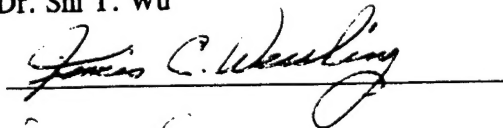
 4/13/00 Committee Chair  
Dr. Clark W. Hawk (Date)


  
Dr. Hugh W. Coleman


  
Dr. Marlow D. Moser

  
Dr. Richard H. Comfort

  
Dr. Shi T. Wu

 Department Chair

 College Dean

 Graduate Dean

## ABSTRACT

School of Graduate Studies  
The University of Alabama in Huntsville

Degree: Doctor of Philosophy

College/Department: Engineering/Mechanical  
and Aerospace Engineering

Name of Candidate: Jonathan E. Jones

Title: An Assessment of Microwave Generated Plasmas for Use in Magnetohydrodynamic Accelerators

The initial mass of a spacecraft in low earth orbit may be reduced by over 50% when conventional chemical upperstages are replaced by a magnetohydrodynamic (MHD) system. In order for these gains to be realized, both low specific mass power plants and high efficiency MHD accelerators are required. This dissertation focuses on the latter requirement: high efficiency MHD accelerators.

To assess the benefits of a microwave plasma generator (MPG), detailed measurements of electron temperature and density at the exit of an MPG were obtained. A quadrupole Langmuir probe was used to measure electron temperature and density. Measurements of gas temperature and pressure were obtained with thermocouples and Pitot tubes, respectively. A time of flight velocity technique was used to measure the velocity of the flow. These measurements allowed for the calculation of flow conductivity, thus MHD accelerator efficiency.

The experimental setup consisted of a TM<sub>011</sub> microwave resonant cavity, operating at 2.45 GHz, connected to a vacuum chamber. Tests were conducted with three conductive graphite nozzles with expansion ratios of 7.11, 26.21, and 64. One insulative boron nitrate nozzle was also tested. Finally, tests were conducted without a nozzle on the MPG. This allowed the MPG to operate at lower pressures ( $< 0.1$  atm) where the lower collision frequency resulted in enhanced non-equilibrium conditions. Argon, helium, nitrogen, carbon dioxide, and

water vapor were all successfully tested as working fluids. For the majority of the tests, the microwave power was held constant at 3 kW.

The results showed that an electron temperature an order of magnitude higher than the gas temperature can be obtained in both diatomic and monatomic gases. For the monatomic gases argon and helium, electron densities slightly higher than the critical plasma density for 2.45 GHz microwaves ( $10^{17}$  e/m<sup>3</sup>) were obtained. For diatomic and polyatomic molecules, electron densities were one to two orders of magnitude below the critical density correlating with the higher electron to neutral collision cross sections, as well as, large electron energy loss factors for diatomic and polyatomic gases.

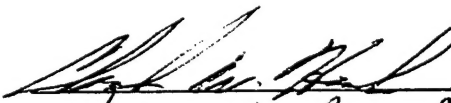
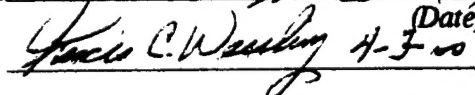

Based on the experimentally measured conductivity, ideal cross field MHD and Hall channel accelerator efficiencies were calculated. Efficiencies for helium and argon were 10.5% and 19.6%, respectively. All diatomic and polyatomic gases tested resulted in MHD efficiencies less than 1%; efficiencies greater than 30% are needed for competitive performance. This leads to the conclusion that microwave resonant cavities cannot be used as the sole source of ionization for MHD accelerators; however, the high electron temperatures obtained suggest the possibility of driving the non-equilibrium ionization to acceptable levels within the MHD channel itself. In addition, the gas temperatures were well below the temperatures required for thermal ionization; therefore, heat transfer to the walls and thermal losses at the accelerator exit should be reduced proportionally. This work presents for the first time experimental measurements that can be used to design a prototype MHD channel to test these hypotheses.

Abstract Approval:

Committee Chair

Department Chair

Graduate Dean

 4/5/00  
(Date)  
 4-5-00  
 4/5/00

**AN ASSESSMENT OF MICROWAVE GENERATED PLASMAS FOR USE IN  
MAGNETOHYDRODYNAMIC ACCELERATORS**

by

**JONATHAN E. JONES**

**A DISSERTATION**

Submitted in partial fulfillment of the requirements  
for the degree of Doctor of Philosophy in  
The Department of Mechanical and Aerospace Engineering  
of  
The School of Graduate Studies  
of  
The University of Alabama in Huntsville

**HUNTSVILLE, ALABAMA**

**2000**

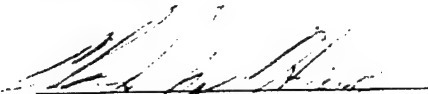


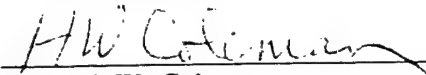
**Copyright by**  
**Jonathan E. Jones**  
**All Rights Reserved**  
**2000**

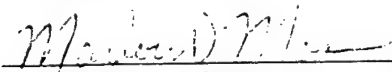
## DISSERTATION APPROVAL FORM

Submitted by Jonathan E. Jones, in partial fulfillment of the requirements for the degree of Doctor of Philosophy in Mechanical and Aerospace Engineering.

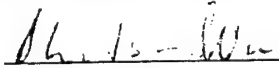
Accepted on behalf of the Faculty of the School of Graduate Studies by the dissertation committee:

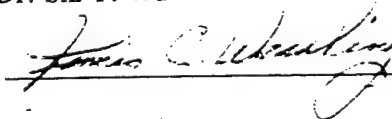
 4/15/10 Committee Chair  
Dr. Clark W. Hawk (Date)

  
Dr. Hugh W. Coleman

  
Dr. Marlow D. Moser

  
Dr. Richard H. Comfort

  
Dr. Shi T. Wu

  
Department Chair

  
College Dean

  
Graduate Dean

## ABSTRACT

School of Graduate Studies  
The University of Alabama in Huntsville

Degree: Doctor of Philosophy

College/Department: Engineering/Mechanical  
and Aerospace Engineering

Name of Candidate: Jonathan E. Jones

Title: An Assessment of Microwave Generated Plasmas for Use in Magnetohydrodynamic Accelerators

The initial mass of a spacecraft in low earth orbit may be reduced by over 50% when conventional chemical upperstages are replaced by a magnetohydrodynamic (MHD) system. In order for these gains to be realized, both low specific mass power plants and high efficiency MHD accelerators are required. This dissertation focuses on the latter requirement: high efficiency MHD accelerators.

To assess the benefits of a microwave plasma generator (MPG), detailed measurements of electron temperature and density at the exit of an MPG were obtained. A quadruple Langmuir probe was used to measure electron temperature and density. Measurements of gas temperature and pressure were obtained with thermocouples and Pitot tubes, respectively. A time of flight velocity technique was used to measure the velocity of the flow. These measurements allowed for the calculation of flow conductivity, thus MHD accelerator efficiency.

The experimental setup consisted of a  $TM_{011}$  microwave resonant cavity, operating at 2.45 GHz, connected to a vacuum chamber. Tests were conducted with three conductive graphite nozzles with expansion ratios of 7.11, 26.21, and 64. One insulative boron nitrate nozzle was also tested. Finally, tests were conducted without a nozzle on the MPG. This allowed the MPG to operate at lower pressures ( $< 0.1$  atm) where the lower collision frequency resulted in enhanced non-equilibrium conditions. Argon, helium, nitrogen, carbon dioxide, and

water vapor were all successfully tested as working fluids. For the majority of the tests, the microwave power was held constant at 3 kW.

The results showed that an electron temperature an order of magnitude higher than the gas temperature can be obtained in both diatomic and monatomic gases. For the monatomic gases argon and helium, electron densities slightly higher than the critical plasma density for 2.45 GHz microwaves ( $10^{17}$  e/m<sup>3</sup>) were obtained. For diatomic and polyatomic molecules, electron densities were one to two orders of magnitude below the critical density correlating with the higher electron to neutral collision cross sections, as well as, large electron energy loss factors for diatomic and polyatomic gases.


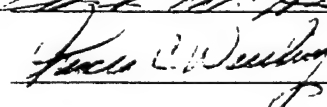

Based on the experimentally measured conductivity, ideal cross field MHD and Hall channel accelerator efficiencies were calculated. Efficiencies for helium and argon were 10.5% and 19.6%, respectively. All diatomic and polyatomic gases tested resulted in MHD efficiencies less than 1%; efficiencies greater than 30% are needed for competitive performance. This leads to the conclusion that microwave resonant cavities cannot be used as the sole source of ionization for MHD accelerators; however, the high electron temperatures obtained suggest the possibility of driving the non-equilibrium ionization to acceptable levels within the MHD channel itself. In addition, the gas temperatures were well below the temperatures required for thermal ionization; therefore, heat transfer to the walls and thermal losses at the accelerator exit should be reduced proportionally. This work presents for the first time experimental measurements that can be used to design a prototype MHD channel to test these hypotheses.

Abstract Approval:

Committee Chair

Department Chair

Graduate Dean

 4/5/00  
(Date)  
 4-5-00  
 4/5/00

## ACKNOWLEDGEMENTS

As I close the formal student chapter of my life, many feelings of gratitude and appreciation are present. It is hard to know where to start as I look back over the many people who have had a positive impact on my education and life. I have been blessed to be surrounded with people who believe in me and in my dreams. The most important person being my father, who married my beautiful, intelligent, and creative mother. Together they have supported me and my eleven brothers and sisters in all of our endeavors. Their support for each of us has welded us together as a family, and each of us draws from the well of strength that comes from our family. No greater education can be received than the education we received as we worked beside our parents on the family ranch in Wyoming.

Such a big part of my education took place during the long, cold Wyoming winters that I must express appreciation for the many teachers, coaches, and friends who touched my life in Sublette County School District No. 9. I will always be well pleased to know that I am a Big Piney Puncher.

My life was changed forever at Brigham Young University when I met and married Laura Jean Meyer. Laura's sacrifice, support, and uplifting encouragement have been constant. She has become a part of my dreams and has never doubted my ability to succeed. Our three children, Katrina, Joseph, and Shadrach, that have been born during my graduate studies provide reason, comic relief, frustration, and joy to the pursuit of our dreams.

Many Professors and fellow students have made an impact. Dr. J. Ward Moody helped me win my first proposal. Dr. Steven E. Jones and Dr. Lee D. Hansen introduced me to research and helped me publish my first paper. Dr. Frank J. Redd raised my excitement for aerospace and desire to be a rocket scientist. Dr. R. Rees Fullmer introduced me to dynamics

and controls and made me realize that I really didn't want to control rockets; I just wanted to make them go.

The students that worked with me in the Advanced Propulsion Laboratory deserve special recognition. Eric Tuck wired, plumped, debugged, and reworked three or four vacuum systems as I struggled to determine the system that would work. In addition, he built numerous probes and diagnostic devices as we learned the art of plasma diagnostics. Matthew Culley rebuilt and improved many of the systems in the laboratory. He enabled us to see Rayleigh scattering for the first time at UAH. Finally, Doug Parkinson designed the stepper motor system and steam delivery system that enabled us to obtain the electron temperature and density profiles presented in Chapter 5. I also appreciate the helpful discussions and support from Stelu Deaconu, David Wagner, Mary Breeden, Gary Hicks, Joseph Bonometti, and the rest of the "Old Guys."

I especially appreciate the help and guidance of Jim Sanders. As a volunteer at the Propulsion Research, he chose to give a little back. He always took the time to review proposals and papers. Even when he disagreed, he found ways to build me up and encouraged me in all my endeavors. He did not serve officially on any committees, but his counsel and support did not go unnoticed. Thanks Jim.

The staff of the Propulsion Research Center was always accommodating and understanding. Linda Marion and her assistants were always ready and willing to help with travel, purchases, proposals, parties, and meetings.

Those who served on my committee willingly offered advice and criticism. In addition to the members of my committee, Dr. Jim Chapman from UTSI and Whitt Brantley from NASA Marshall deserve special recognition for the guidance that they rendered to this work.

Finally, I must thank Dr. Clark W. Hawk. No one in my life, except my father, has ever built me up and helped me to accomplish more than Dr. Hawk. His enthusiasm and

genuine care are traits I would like to emulate. He was always mindful of us as students and strove to provide resources for us academically, technically, and financially. I will always be grateful for the atmosphere that he established within the Propulsion Research Center. There were times when Alabama was a long way from Wyoming, and the PRC family was very comforting. He always had time to listen and discuss things with me, whether it was the inconsistencies in electron temperature measurements or the purchasing of a house. Thanks Dr. Hawk, because of you, I am a "Rocket Scientist."

# TABLE OF CONTENTS

	Page
List of Figures.....	xii
List of Tables.....	xv
List of Symbols.....	xvi
Chapter	
1. INTRODUCTION.....	1
1.1 Motivation and Objectives.....	1
1.2 Previous MHD Work.....	4
1.3 Microwave Resonant Cavity Development.....	10
1.4 Uniqueness of Approach.....	11
2. IONIZATION AND CONDUCTION in MHD INTERACTIONS.....	12
2.1 Non-equilibrium Ionization.....	12
2.2 Electrical Conductivity.....	16
2.3 Similarity Parameters for MHD Flows.....	18
2.4 Generalized Ohm's Law.....	20
2.5 Efficiency of MHD Accelerators.....	21
3. EXPERIMENTAL SETUP.....	25
3.1 Microwave Plasma Generator.....	25
3.2 Vacuum System.....	27
3.3 Propellant Feed System.....	28
3.3.1 Steam Feed System.....	28
3.4 Pitot Tubes and Thermocouples.....	30



3.5 Langmuir Probes .....	31
3.6 Data Acquisition.....	32
4. DIAGNOSTIC TECHNIQUES FOR FLOWING PLASMAS .....	33
4.1 Diagnostics in Weakly Ionized Plasma.....	33
4.2 Intrusive Techniques.....	33
4.2.1 Langmuir Probes .....	34
4.2.2 Quadruple Langmuir Probes .....	36
4.2.3 Thermocouples.....	38
4.2.4 Pitot Tubes.....	41
4.2.5 Power Ripple Time of Flight Velocimetry.....	42
4.3 Rayleigh Scattering .....	46
5. EXPERIMENTAL RESULTS .....	49
5.1 Approach .....	49
5.2 Nozzle Tests .....	51
5.2.1 Large Nozzle .....	51
5.2.2 Medium Nozzle .....	55
5.2.3 Boron Nitride Nozzle .....	59
5.3 Open Cavity Tests .....	61
5.3.1 Radial Profiles .....	71
5.3.2 Axial Profiles .....	72
6. DISCUSSION OF RESULTS .....	76
6.1 Non-equilibrium Ionization.....	76
6.2 MHD Efficiency.....	79
6.3 Benefits to MHD Devices .....	82
7. CONCLUSIONS AND RECOMMENDATIONS.....	83

7.1 Conclusions .....	83
7.2 Recommendations .....	85
APPENDIX .....	86
Formulation of Optimization Equation and Assumptions .....	87
LEO to GEO Orbit Transfer .....	92
WORKS CITED .....	101
REFERENCES .....	107

## LIST OF FIGURES

Figure	Page
1.1 MHD augmented propulsion system.....	4
1.2 Cross-field MHD channel.....	5
1.3 Losses in an MHD accelerator.....	6
1.4 Diagram of Demetriade's MGD driver.....	8
2.1 Energy loss factor, $\delta'$ , for various gases.....	14
2.2 Collision cross section for some atoms and molecules.....	17
2.3 MHD efficiency comparison for Hall and Faraday channels.....	23
2.4 Thrust density versus efficiency for Hall and Faraday channels.....	24
3.1 Microwave resonant cavity.....	25
3.2 Layout of microwave source, wave-guide, resonant cavity, and vacuum chamber.....	26
3.3 Schematic of the propellant feed system.....	28
3.4 Calibration curve for pressure fed steam system.....	29
3.5 Schematic of the steam delivery system.....	30
4.1 Domains of probe electrode performance.....	36
4.2 Quadruple Langmuir probe setup.....	37
4.3 Fluctuations in the microwave plasma emissions as a function of time.....	43
4.4 Emission ripple from two photodiodes located 3.5 inches apart.....	44
4.5 Positioning of electrostatic probes for time of flight velocity measurements.....	46
4.6 Rayleigh scatter Doppler velocimetry setup.....	47
4.7 Basic concept of the Rayleigh scattered diagnostic technique.....	47
5.1 Electron density profile for nitrogen with large nozzle.....	52

5.2	Electron temperature profile for nitrogen with large nozzle.....	53
5.3	Radial profile of nitrogen plume with graphite nozzle (expansion ratio = 7.11).....	54
5.4	Radial profile of nitrogen plume with graphite nozzle (expansion ratio = 7.11).....	55
5.5	Radial scan of electron temperature, 1.3 cm from the nozzle exit (expansion ratio = 26.21).....	56
5.6	Radial scan of electron density, 1.3 cm from the nozzle exit (expansion ratio = 26.21).....	57
5.7	Axial scan of electron temperature 1.3 to 14.5 cm from the nozzle (expansion ratio = 26.21).....	57
5.8	Axial scan of electron density 1.3 to 14.5 cm from the nozzle (expansion ratio = 26.21).....	58
5.9	Radial scan of electron temperature 14.5 cm from the nozzle (expansion ratio = 26.21).....	58
5.10	Radial scan of electron density 14.5 cm from the nozzle (expansion ratio = 26.21)....	59
5.11	Radial scan of electron temperature 1.3 cm from boron nitride nozzle.....	60
5.12	Radial scan of electron density 1.3 cm from boron nitride nozzle.....	60
5.13	Axial scan of electron density for the boron nitride nozzle.....	61
5.14	Electron density profile for carbon dioxide with no nozzle.....	63
5.15	Electron temperature profile for carbon dioxide with no nozzle.....	64
5.16	Electron density profile for helium with no nozzle.....	65
5.17	Electron temperature profile for helium with no nozzle.....	66
5.18	Electron density profile for argon with no nozzle.....	67
5.19	Electron temperature profile for argon with no nozzle.....	68
5.20	Electron density profile for nitrogen with no nozzle.....	69
5.21	Electron temperature profile for nitrogen with no nozzle.....	70
5.22	Radial electron temperature profiles at the exit for various gases.....	71
5.23	Radial electron density profiles at the exit for various gases.....	72

5.24	Axial scan of electron density for various gases.....	73
5.25	Axial scan of electron temperature for various gases.....	73
5.26	Axial gas temperature profiles.....	74
6.1	Power required to maintain a non-equilibrium electron temperature.....	78
6.2	Initial mass in low earth orbit, propellant mass, and power plant mass versus $I_{sp}$ for and accelerator efficiency of 16.7%.....	80
6.3	Initial mass versus trip time for an accelerator efficiency of 70%.....	81
A.1	The relationship between the initial mass, power plant mass, and propellant mass.....	88
A.2	Initial mass versus $I_{sp}$ of the augmented STR and the thrust of the STR only.....	93
A.3	Thrust of MHD augmented STR versus bus power.....	94
A.4	Specific Impulse of the MHD augmented STR versus bus power.....	94
A.5	Relationship between initial mass and trip time for several values of thrust.....	95
A.6	Initial mass versus trip time for optimum $I_{sp}$ conditions.....	97
A.7	Bus power versus trip time.....	98
A.8	Trip time versus initial mass for $\Delta v$ 's of 4.2, 6 and 8 km/sec.....	98
A.9	Initial mass versus trip time for a Mar's mission with a $\Delta v$ of 14.5 km/sec .....	99
A.10	Initial mass versus trip time for augmentation of a solar thermal steam rocket with an $I_{sp}$ of 300 sec and a futuristic 5 kg/kW specific power.....	100

## LIST OF TABLES

Table	Page
4.1 Rayleigh and Raman scattering cross sections.....	49
5.1 Test matrix for microwave resonant cavity plume evaluation.....	51
6.1 Cross-field and Hall accelerator efficiencies.....	79

## LIST OF SYMBOLS

<u>Symbol</u>	<u>Definition</u>
$B$	Magnetic field strength
$c_e$	Mean thermal speed of electrons
$C_p$	Specific heat at constant pressure
$E'$	Local electric field
$g_i$	Electronic partition function of ion
$g_o$	Electronic partition function of neutral gas
$h$	Planck's constant
$H_a$	Hartmann number
$I_p$	Magnetic interaction parameter
$I_{sp}$	Specific impulse
$J$	Current density
$K$	Thermal conductivity
$k_b$	Boltzmann's constant
$L$	Characteristic length, length of MHD channel
$M$	Mach number
$m_e$	Electron rest mass
$n_e$	Electron number density
$n_n$	Neutral gas number density
$n_s$	Number density of species $s$
$P_{requ}$	Power required to maintain non-equilibrium ionization ( $T_e > T_g$ )
$Q$	Average collision cross section

$Q_{es}$	Collision cross section for electrons with species s
$Q_{en}$	Average collision cross section for electrons with all neutral species
$Q_{el}$	Average collision cross section for electrons with ion I
$q_e$	Electron charge
$R_e$	Reynolds number
$R_m$	Magnetic Reynolds number
$S$	Magnetic force number
$T_e$	Electron temperature
$T_g$	Neutral gas temperature
$V$	Velocity
$W$	Kinetic energy transferred per collision

$\beta_0$	Hall constant ( $1/q_en_e$ )
$\delta$	Mean electron energy loss/collision
$\delta'$	Energy loss factor for inelastic collisions
$\varepsilon$	Ionization energy
$\varepsilon_0$	Permittivity of Free Space
$\gamma$	Ratio of specific heats
$\eta$	Efficiency, Viscosity
$\mu_0$	Permeability of Free Space
$\Lambda$	Ratio of Debye length to average impact parameter
$\rho$	Density



$\sigma$  Electrical conductivity

$\omega\tau$  Hall parameter

## **CHAPTER 1**

### **INTRODUCTION**

#### **1.1 Motivation and Objectives**

Magnetohydrodynamics has been studied for the past fifty years for power generation [Rosa, 1987; Bajovic, 1996], hypersonic wind tunnel [Baughman, et al., 1997; Crawford, et al. 1990], and propulsion applications [Demetriades, 1962; Litchford, et al., 1997]. This work focuses on non-equilibrium MHD accelerators for in-space propulsion applications. Non-equilibrium MHD accelerators utilize plasmas with electron temperatures much greater than the ion or neutral gas temperatures. The elevated electron temperature increases the free electron density and thus the conductivity of the plasma, improving the efficiency of the MHD accelerator [Macheret, et al., 1992].

Of particular interest was the use of water, carbon dioxide, or other non-conventional propellants as the working fluid for the MHD accelerator. Both water and carbon dioxide are plentiful throughout the solar system, enabling in-situ propellant utilization. However, because of the relatively large electron collision cross section and electron energy loss factors for water and carbon dioxide, it has been assumed previous to this work that non-equilibrium ionization would be unable to produce adequate conductivity for MHD acceleration [Sutton and Sherman, 1965].

However, a unique combination of microwave generated plasma and a low pressure ( $<10$  Torr) Hall channel MHD accelerator offers significant performance gains for MHD accelerators operating with water or carbon dioxide [Duclos, et al., 1965; Jones, et al., 1996]. This combination is enabled by preferentially adding energy to the electrons in the flow enhancing the conductivity of the working fluid [Macheret, et al., 1997]. One method to accomplish this is to excite the plasma with radio or microwave frequency radiation. By adding energy to the electrons, a non-equilibrium plasma can be created where the temperature of the electrons is higher than the temperature of the gas. The resulting free electron density can then be several orders of magnitude higher than electron densities at thermodynamic equilibrium. Thus, the operation of an MHD accelerator with non-equilibrium plasma can reduce thermal losses, extend electrode life, and improve overall efficiency [Agryopoulos, et al., 1967].

In traditional MHD devices, such as generators and hypersonic wind tunnels, non-equilibrium conditions are hard to maintain due to operation at pressures from 10 to 100 atm [Macheret, et al., 1997]. At these pressures collision rates are high, and a large amount of energy must be added to the flow to depart from equilibrium conditions. However, because in-space propulsion systems do not require operation at high pressures, the energy required to maintain non-equilibrium ionization is reduced; thus, it is advantageous to examine non-equilibrium ionization for in-space MHD accelerators.

The objectives of this work were to characterize the plumes of a 2.45 GHz microwave-generated plasma with various working fluids and assess the feasibility of coupling to a MHD accelerator taking advantage of the non-equilibrium plasma. This was accomplished by

1. Measuring electron density and electron temperature of the microwave generated plasma plumes to calculate conductivity and determine the extent of non-equilibrium ionization under selected microwave resonant cavity operating conditions.

2. Determining optimal operating regimes for driving a MHD accelerator through review of the literature, experimental measurements, and analysis.
3. Comparing predicted performance with reported experimental results for both MHD accelerators and alternate ionization sources to determine the net improvement offered by the addition of the microwave ionization source.

This work provides a guide to the design and testing of prototype MHD accelerators operating with non-conventional propellants at high degrees of non-equilibrium ionization, i.e., electron temperatures an order of magnitude greater than stream temperature.

A follow on to the prototype MHD accelerator could be used in a system in which plasma generated in a microwave resonant cavity and expanded through a thermodynamic nozzle would enter an MHD accelerator at pressures below 0.1 atm. The MHD accelerator, at these pressures, can then be used to increase the velocity or specific impulse ( $I_{sp}$ ) of the propellant to the optimal value. A system level study, included in the Appendix, shows optimal specific impulse for several missions as a function of MHD efficiency and electrical power plant specific mass (kW/kg). For example, the initial mass required in low earth orbit to transfer a 5,000-kg payload to geosynchronous orbit is reduced by over fifty percent for an optimized MHD system. A representation of a system using large solar concentrators to provide power is shown in Figure 1.1. In this system, electrical power to run the MHD system is provided by thermionic diodes or photovoltaics.

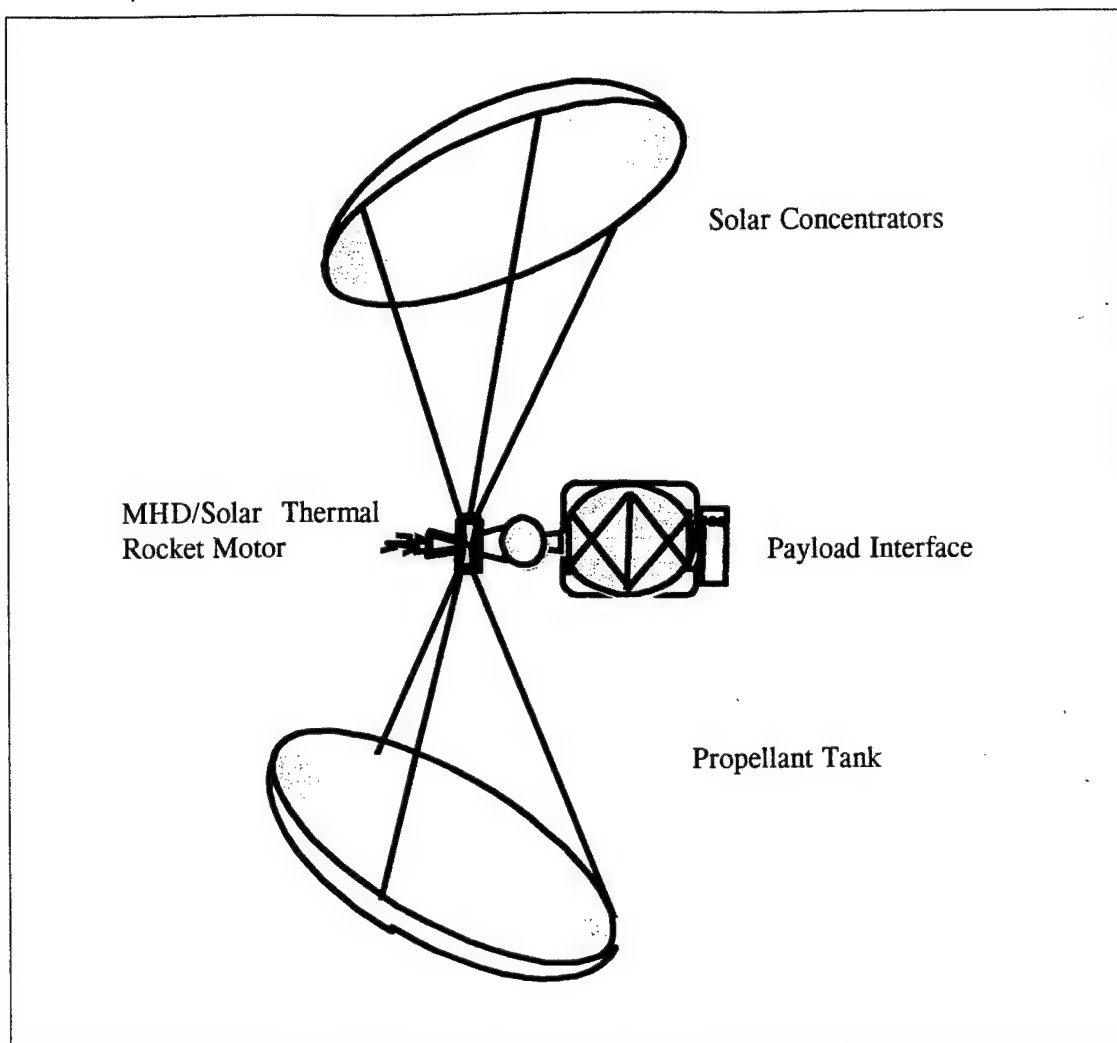


Figure 1.1. MHD augmented propulsion system.

## 1.2 Previous MHD Work

It is estimated that over 1,000 man-years have been spent towards the understanding and development of MHD systems [Demetriades, 1999]; thus, there exists an enormous amount of literature [Powers, et al., 1967; Agryopoulos, et al., 1974; Baughman, et al., 1997]. A large portion of the available literature focuses on the cross-field accelerator. Many useful insights can be gained from a review of this work even though the optimal pressure regimes for non-equilibrium operation favor a Hall channel configuration [Sutton and Sherman, 1965].

Figure 1.2 shows the orientation of the magnetic and electric fields for a single electrode, constant area cross-field channel. The Faraday configuration for the cross-field accelerator employs segmented electrodes to limit the Hall current. When the Hall parameter is in excess of 3, it is advantageous to use a Hall channel configuration [Klepeis and Rosa, 1965]. The Hall channel is segmented also, but the electric field is applied axially and the segmented electrode pairs are shorted so that the Hall current can flow across the channel.

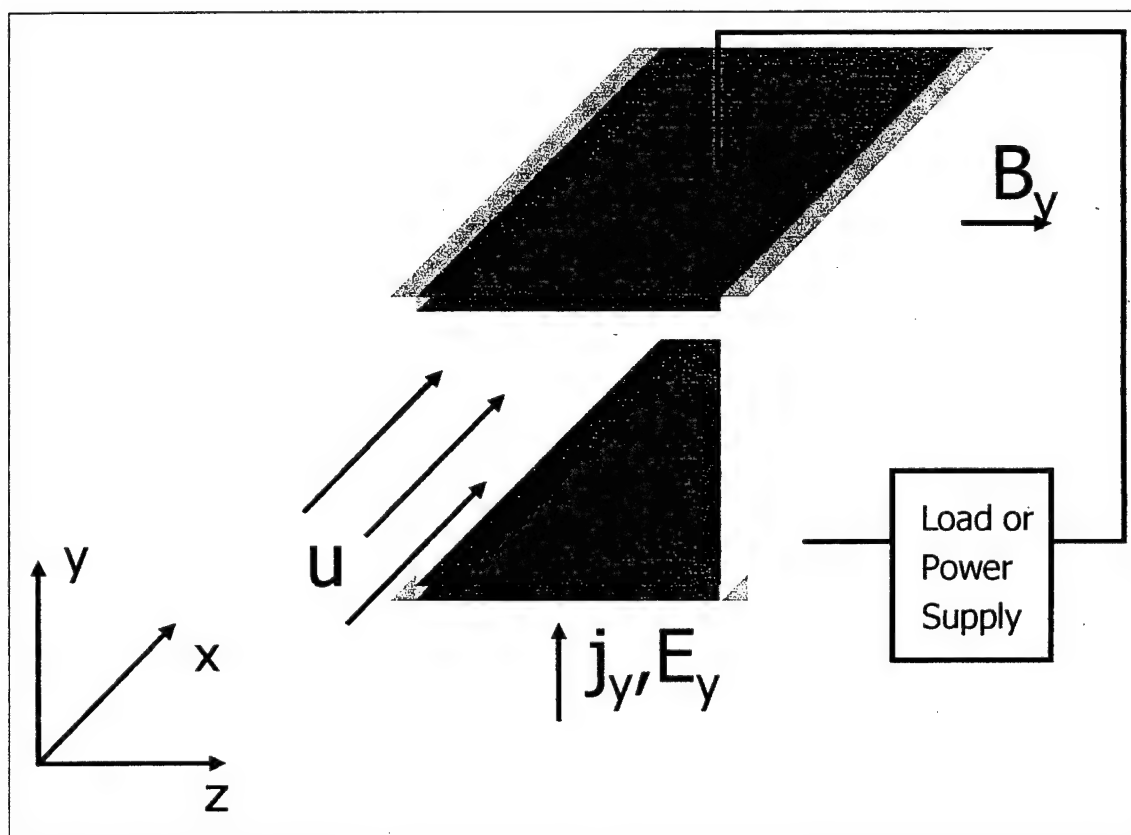


Figure 1.2. Cross-field MHD channel.

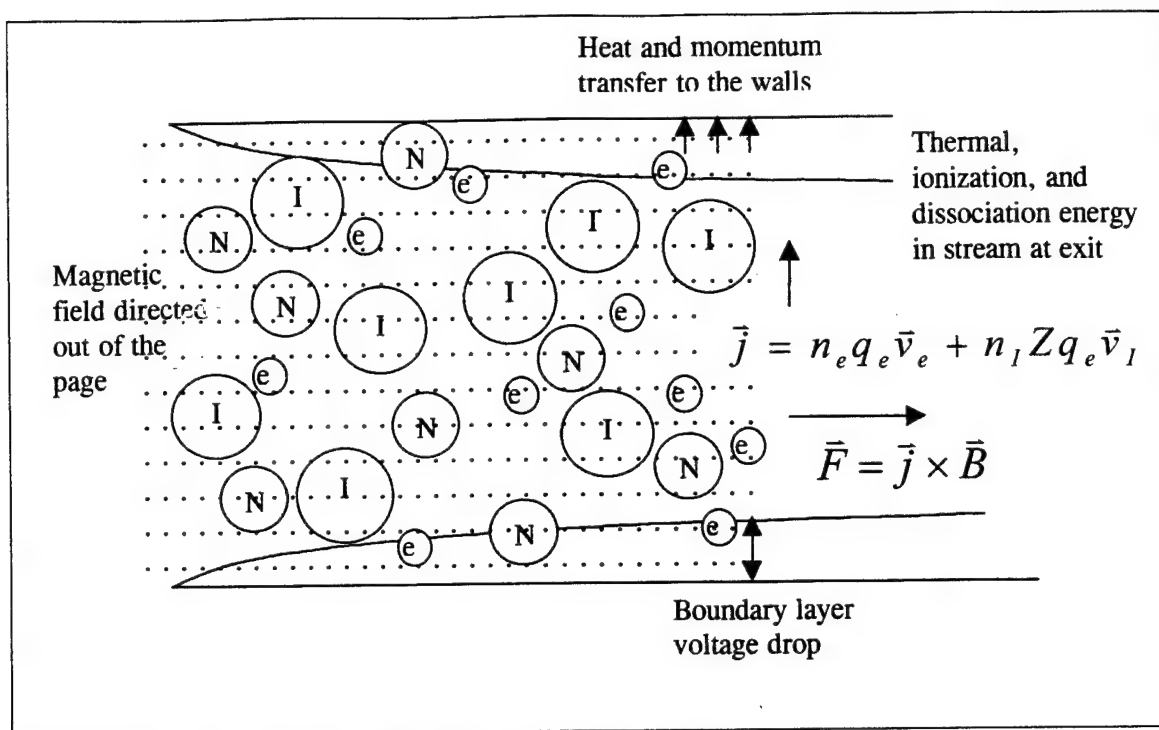


Figure 1.3. Losses in an MHD accelerator.

Figure 1.3 depicts the losses associated with MHD acceleration along with the participating species. Three species must be considered in the analysis of MHD flows: neutral atoms and molecules (N), ions (I), and electrons (e). These species interact with each other through collisional processes. When an electric field is applied, the electrons, due to their small mass, will move readily; thus, the current is primarily due to electron motion, and the Lorentz force acts upon the electrons to accelerate them.

The acceleration of the electrons causes a charge separation. The resulting electrical field accelerates the ions. In the absence of collisions, the ions and electrons accelerate through the neutral flow field. This condition has been termed ion slip. When the collision frequency between the ions and the neutrals is high, ion slip is negligible [Argyropoulos, et al., 1967].

The Generalized Ohm's Law gives the relationship between the current and the applied electric and magnetic fields. Electron collisions with neutrals and ions impede the flow of

current. In general, the collision cross section for electrons with ions is much larger than the collision cross section for electrons with neutrals. The collective effects of the electron collisions determine the conductivity of the plasma. Another useful parameter often used in the description of MHD accelerators is the magnetic interaction parameter,  $I_p$ , defined as the ratio of the Lorentz force or magnetic body force to the inertial forces acting on the plasma [Sutton and Sherman, 1965]. With this background, the pertinent experimental results can be reviewed.

Among the earliest experimental work is that of Carter and Wood [Wood, et al., 1961]. Nitrogen seeded with cesium was heated to a total temperature of 6,900 K and accelerated to Mach 2 before entering a 1-cm<sup>2</sup> channel. A 1.2 Tesla magnet provided the magnetic field to produce the Lorentz force accelerating the flow, confirming that MHD acceleration worked in a seeded plasma flow.

Hogan used a shock tube to demonstrate a two-fold increase in specific impulse [Hogan, 1964]. Pure argon was heated to 12,000 K in an 1.5 inch-diameter combustion driven shock tube. The flow entered the cross-field accelerator at a pressure of 1 atm and Mach = 2. With a 0.15 Tesla applied magnetic field, the specific impulse was increased from  $\approx 500$  sec at the inlet to  $\approx 1,000$  sec at the exit. Hogan estimated the efficiency of the accelerator to be  $\approx 50\%$ . The high temperatures produced high conductivity ( $\sigma = 4,500$  mhos/m); thus, a high magnet interaction parameter,  $I_p$ , was achieved. Electron heating or non-equilibrium conditions were minimal at the relatively high pressure of these experiments.

The most extensive work is that of Sterge Demetriades. He utilized the free jet from an arcjet in several cross-field magnetogasdynamic (MGD) accelerators [Demetriades, 1959, 1960, 1963, and 1966]. The terms magnetogasdynamic and engine were used in his work because gas provides a more general description than hydro, and experimental results showed that thrust



augmentation can be realized through an increase in thermodynamic pressure even when the flow is not accelerated.

A diagram of the experimental apparatus is shown in Figure 1.4. Experiments were performed with nitrogen, argon, air, and helium plasmas. Initial ionization was obtained with the arcjet without seeding the flow. He drew the following conclusions from his experience:

It was concluded that departure from thermal equilibrium ionization extends the desirable range of operation of MGD drivers (accelerator or engines) into regions which, hitherto, were considered prohibited, and alleviates thermal loss problems. "Cold" plasma operation of the MGD driver appears feasible and desirable. Electron temperatures an order of magnitude, or more, higher than the stream static temperature are to be expected, and the degree of ionization should be much higher than that indicated by equilibrium computations at stream temperature. The implications of the theoretical and experimental results are that magnetogasdynamic engines of high efficiency and long and stable engine life are possible. The same can be said of MHD power generators when the kinetic energy or enthalpy of the fluid is divorced from the ionizing energy, i.e., when the main thermal energy source is used to drive the fluid and an other-than-thermal source is used to produce the high degree of ionization. [Demetriades, 1960]

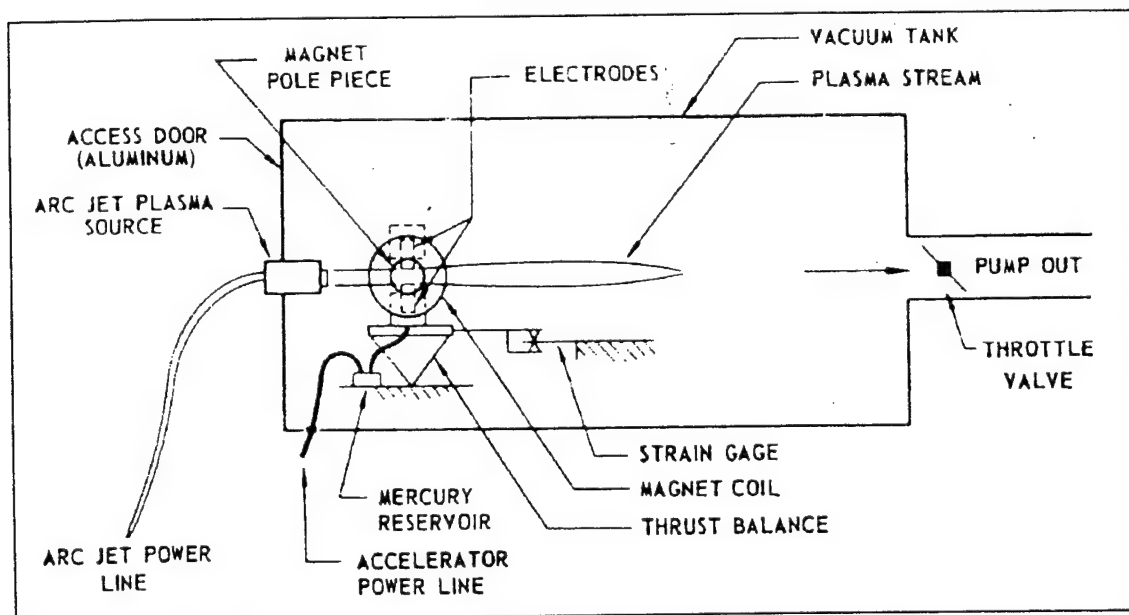


Figure 1.4. Diagram of Demetriade's MGD driver.

In addition to the general conclusion of the benefit of the non-equilibrium ionization, the following conclusions are directly applicable to this work.

1. Efficiencies greater than 40% at specific impulses up to 1,400 sec were demonstrated for operation with argon. Efficiencies for nitrogen and air were under 20%.
2. In a free jet, a conductive boundary layer extends beyond the viscous core of the plasma jet. This allows coupling of electric and magnetic fields without direct contact of the electrodes or insulating walls with the high momentum core flow. This substantially reduces viscous losses in the engine or accelerator. The high temperature electrons present in non-equilibrium plasma enhance this conductive boundary layer.
3. Large back-emf present for nitrogen and air plasmas at the entrance to MGD may be reduced by irradiating the plasma jet with microwaves [Sullivan, 1993], electron beams [Kerrebrock and Hoffman, 1964], neutron beams [Bittaker, 1998], or operating the arcjet at higher powers to increase the conductivity at the inlet.
4. Hall currents were substantially reduced and in some cases removed by staggering the electrodes, producing an axial electric field that opposed the Hall current [Rittenhouse, et al., 1967].
5. The idea that ion slip would limit the strength of magnetic induction that could be applied before performance dropped was shown to be false. Magnetic induction an order of magnitude higher than the calculated limit was applied before performance deteriorated. This may allow operation at lower pressures where non-equilibrium ionization is easier to maintain [Demetriades, 1963].
6. Electrode erosion due to oxidation was observed when operating with air. Active cooling of the electrodes is suggested as one method of reducing this problem. Operation at lower stream temperature will also aid this problem, but sufficient conductivity must be sustained [Demetriades, 1960].

Experimental work on MHD systems for in-space propulsion applications was very active from the late 1950's through the mid 1960's. Then the emphasis began to switch to accelerators for hypersonic testing and MHD power generation. From the mid 1960's through the early 1980's substantial progress was made in the development of 3D models and computational codes, which accurately predicted the performance of both MHD accelerators and generators [Demetriades, 1984].

The recent report, "Magnetohydrodynamic Accelerator Research Into Advanced Hypersonics," (MARIAH) outlines the progress in the field to date [Baughman, et al., 1997]. The proposal to use electron beams to sustain non-equilibrium ionization is of particular interest to this work. A review of technologies that may enhance the conductivity of the working fluid in accelerators is given. These technologies include electron beams, microwave sources, heavy charged particle beams, neutral particle beams, x-rays, gamma radiation, laser irradiation, and radio frequency sources. Analytical and computational studies have shown that low operating pressures ( $\sim 0.1$  atm) are critical for non-equilibrium enhanced conductivity to be beneficial.

### 1.3 Microwave Resonant Cavity Development

During the post-World War II years MacDonald and his colleagues measured breakdown fields for microwaves in air, hydrogen, nitrogen, and oxygen for pressures from 0.1 – 100 mm Hg. Minimal critical breakdown fields were obtained for each gas as a function of pressure [MacDonald, 1951].

Within the last ten years, researchers at the Pennsylvania State University have developed a resonant cavity microwave plasma generator [Sullivan, 1996], which may provide a suitable plasma source to drive an MHD accelerator. Their device is stable, electrodeless, and can be tuned to generate plasmas with a variety of propellants. The device is being

developed in hopes of providing a competitive alternative to arcjets for in-space propulsion. To date, work has focused on measuring the performance of the device as a thruster. Spectroscopic measurements of electron temperature have been made within the resonant cavity [Mueller, 1993]. In order to determine its suitability as a driver for an MHD system, the electrical transport properties in the plumes of the microwave plasma thruster needed to be evaluated.

#### 1.4 Uniqueness of Approach

A microwave plasma generator has never been used as the ionization driver for an MHD accelerator. The proposed system will operate at lower pressures than previous work to enhance non-equilibrium ionization and increase conductivity. While it is recognized that Hall currents and ion slip degrade MHD performance at low pressures, the literature reveals that electrode and channel configurations exist that will negate these effects. The characterization of the microwave source is the first step towards designing this MHD accelerator.

## CHAPTER 2

### IONIZATION AND CONDUCTION IN MHD INTERACTIONS

#### 2.1 Non-equilibrium Ionization

Two methods have been explored to obtain higher conductivities in MHD flows: seeding [Adamovich, et al., 1993, Bauman, et al., 1993] and non-equilibrium ionization [Macheret, et al., 1992; Harada and Tsunoda, 1998]. Seeded flows require the addition of low ionization potential elements such as potassium or cesium. Non-equilibrium ionization requires the addition of energy, which preferentially raises the temperature of the electrons relative to the gas temperature. The high-energy electrons in turn produce additional ionization events increasing the conductivity of the flow. We were interested in obtaining adequate conductivity through microwave excitation.

When the plasma is assumed to be in thermodynamic equilibrium at the gas or free-stream temperature, species concentrations can be obtained from thermodynamic equilibrium calculations. In the absence of a seedant, the concentration of different species was calculated to determine the species that may participate in the ionization process. Electron densities were also obtained from thermodynamic equilibrium calculations, but this did not include the effect of the applied fields, but was used to compare the conductivity of the microwave excited plasma to that of a plasma in thermodynamic equilibrium at the gas temperature.

In the presence of an external electric field, the electron temperature, rather than the gas temperature, characterizes the degree of ionization. The Saha equation can be used to determine the electron density as a function of electron temperature. Rosa, assuming quasi-neutrality, has rearranged the Saha equation. Solving for the electron density yields

$$n_e = f(T_e) \frac{\sqrt{1 + 4n_s / f(T_e)} - 1}{2}, \quad (2.1)$$

where  $n_s$  is the number density of the species participating in the ionization process,  $T_e$  is the electron temperature, and

$$f(T_e) = \frac{(2\pi m_e k_b T_e)^{3/2}}{h^3} \frac{2g_i}{g_0} \exp\left[-\frac{q_e \epsilon_i}{k_b T_e}\right], \quad (2.2)$$

where  $g_i$  and  $g_0$  are the internal partition functions of the ion and the neutral species,  $h$  is Planck's constant,  $k_b$  is Boltzmann's constant, and  $\epsilon_i$  is the ionization potential of the species [Rosa, 1987].

The electric field of the microwave accelerates the charged particles (electrons and ions) in the plasma increasing their kinetic energy. Electrons gain the majority of the kinetic energy because of their small mass compared to the mass of the ions. Energy is then transferred to the gas through electron collisions with the ions, atoms, and molecules in the flow. The fraction of excess kinetic energy transferred per collision is given by

$$W = \delta \frac{3}{2} k_b (T_e - T_g), \quad (2.3)$$

where  $\delta$  is the mean fractional energy lost per collision

$$\delta = \delta' \left[ \frac{2m_e}{m_g} \right] \quad (2.4)$$

and  $\delta'$  is the energy loss factor for inelastic collisions.

Electron collisions with monatomic species are generally elastic: the energy is transferred into translational energy of the heavy particle only and thus  $\delta' = 1$ . For this case, the energy loss per collision,  $\delta$ , is simply twice the mass ratio of the particles. Energy loss factors for diatomic and polyatomic molecules can be several orders of magnitude higher due to excitation of vibrational and rotational energy levels. Figure 2.1 shows the energy loss factor for several gases and molecules of interest. This explains, in part, the past assumption that the operation of a MHD device with non-conventional propellants such as carbon dioxide and water would be impractical.

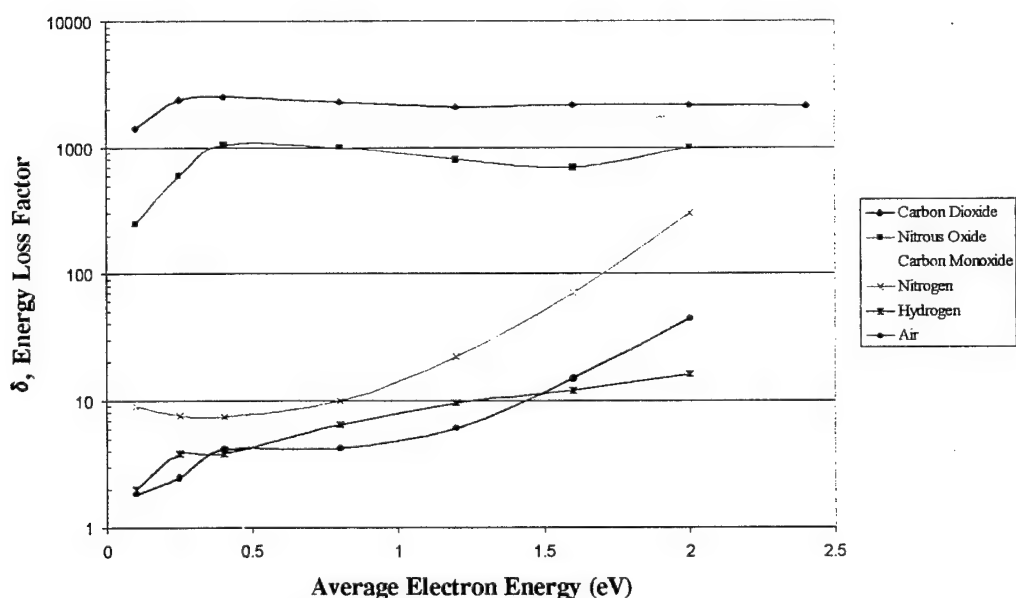


Figure 2.1. Energy loss factor,  $\delta'$ , for various gases [Massey and Craggs, 1959].

The power required to maintain a non-equilibrium ionization condition,  $T_e > T_g$ , can be approximated by

$$P_{requ} = n_s n_e Q c_e \delta \frac{3}{2} k_b (T_e - T_g), \quad (2.5)$$

where  $Q$  is the average collision cross section and  $c_e$  is the mean thermal speed of the electrons [Rosa, 1987; Sutton and Sherman, 1965].

This expression, as well as the assumption that  $n_e$  can be obtained by Equation 2.1, has been verified experimentally through the study of seeded gases used in MHD accelerators [Kerrebrock and Hoffman, 1964; Cool and Zukoski, 1966; Ben Daniel, 1962]. Data on the validity of Equation 2.5 for microwave excited plasmas is scarce. However,  $Q_{es}$ , and  $\delta$  are available in the literature and  $n_s$ ,  $n_e$ ,  $c_e$ ,  $T_e$ , and  $T_g$ , as well as the applied microwave power, can be obtained experimentally. Thus, Equation 2.1 can be verified directly, and the validity of Equation 2.5 can be inferred by assuming the efficiency with which the input microwave power adds energy to the electron ( $\eta_{ion} = P_{requ}/P_{input}$ ).

In conclusion, Equation 2.5 shows that the power required to maintain elevated electron temperature depends upon the number densities of the electrons and neutral gas, the collision cross section for electrons with neutrals and ions, and the energy loss factor. Therefore, the power required to maintain an elevated electron temperature in diatomic and polyatomic molecules is much higher than that for monatomic noble gases.



## 2.2 Electrical Conductivity

Sutton derives the scalar electrical conductivity of a mixture of gases in the absence of alternating electric fields and magnetic fields as shown in Equation 2.6 [Sutton and Sherman, 1965].

$$\epsilon_0 = \frac{n_e q_e^2}{m_e \langle c_e \rangle (n_n \langle Q_{en} \rangle + n_e Q_{el}^*)}, \quad (2.6)$$

where

$$Q_{en} = \sum_{s \neq e, l} \frac{n_s}{n_n} \langle Q_{es} \rangle, \quad (2.7)$$

and Rosa [1984] gives the mean electron speed by

$$c_e = \sqrt{\frac{8k_b T_e}{\pi m_e}}. \quad (2.8)$$

Rosa [1984] also gives the collision cross section for electrons with ions.

$$Q_{el}^* = 3.9 \left[ \frac{q_e^2}{8\pi\epsilon_0 k_b T_e} \right]^2 \ln \Lambda, \quad (2.9)$$

where

$$\Lambda = \frac{12\pi}{\sqrt{n_e}} \left[ \frac{\epsilon_0 k_b T}{q_e^2} \right]^{3/2}. \quad (2.10)$$

It is instructive after listing these equations to examine the physical picture. The conductivity of a plasma is the inverse of the plasma's resistance to the flow of electrical current. The diffusion of electrons is more rapid than the diffusion of ions; therefore, the number of free electrons and their mobility within the plasma determines the electrical conductivity of the flow. The mobility of the electrons is determined by the collision cross sections with the ions and neutral molecules or atoms in the flow. Collision cross sections for molecules and atoms are obtained mostly from experiments. If the electrons and atoms are viewed as hard spheres, the collision cross section is the cross-sectional area of the atom as seen by the electron.

Ion collision cross sections are much larger than neutral molecule or atomic cross sections. Thus, when the ionization fraction is large, the neutral particle collision term ( $n_n Q_{en}$ ) can be ignored. In weakly ionized plasma  $n_n Q_{en}$  is the same order of magnitude as  $n_e Q_{ei}$ , and both terms must be included. Collision cross section for atoms and molecules used in this work are given in Figure 2.2.

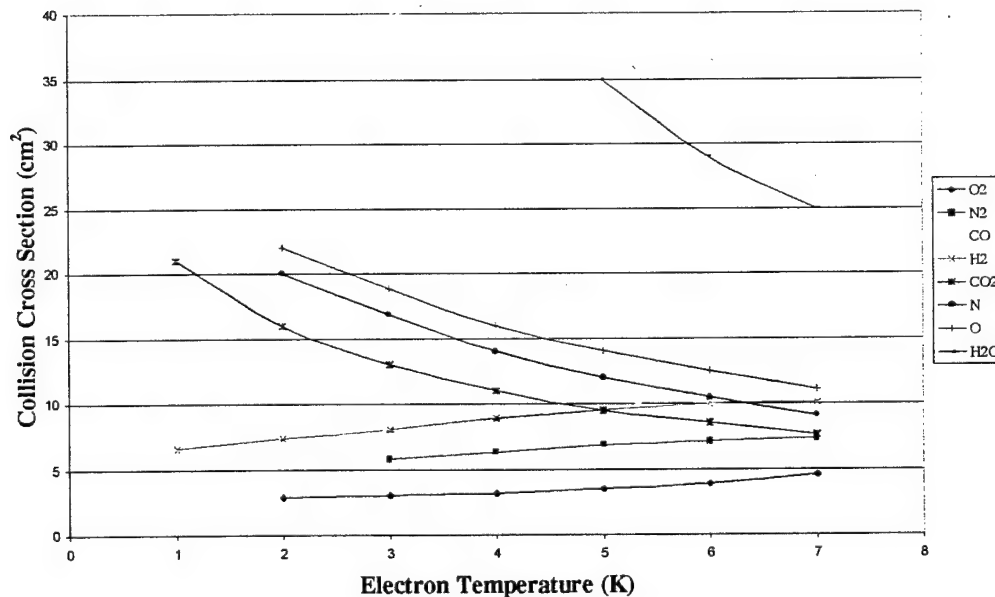


Figure 2.2. Collision cross section for some atoms and molecules [Sutton and Sherman, 1965].

The scalar conductivity is fundamental to the behavior of plasma in electric and magnetic fields; to maintain sufficient conductivity, the free electron density must be maintained, and collision cross sections must be minimized. Figure 2.2 shows that the collision cross section for water is a factor of 2 greater than the collision cross section for most other gases. One method of minimizing the collision cross section effects is to operate at lower pressure, decreasing the number density. However, this increases the Hall parameter and suggests the utilization of a Hall channel configuration.

### 2.3 Similarity Parameters for MHD Flows

It has been said that the “complexity of a physical problem is directly related to the number of dimensionless parameters that appear in it” [Sutton and Sherman, 1965]. This being the case, MHD theorists have guaranteed the difficulty of MHD problems by introducing a number of dimensionless parameters as well as retaining the conventional parameters. A review of these parameters sheds light on the importance of conductivity in MHD flows. The benefit of non-equilibrium ionization is apparent in this context.

The following dimensionless parameters will be discussed:

$$\text{Reynolds number: } R_e = \frac{\rho_0 V_0 L_0}{\eta_0} \quad (2.11)$$

$$\text{Magnetic Reynolds number: } R_m = \mu_0 \sigma_0 V_0 L_0 \quad (2.12)$$

$$\text{Mach number: } M_0 = \frac{V_0}{\sqrt{\gamma_0 R_0 T_0}} \quad (2.13)$$

$$\text{Hall parameter: } \omega\tau = \frac{q_e B_0}{m_e c_e \sum_{k,s} n_{k,s} Q_{k,s}} \quad (2.14)$$

$$\text{Magnetic Force number: } S = \frac{B_0^2}{\mu_0 \rho_0 V_0^2} \quad (2.15)$$

$$\text{Prandtl number: } P_R = \frac{C_{p0} \eta_0}{K_0} \quad (2.16)$$

The Reynolds number, Mach number, and Prandtl number are conventional parameters used in compressible flows. They are included in the description of MHD flows. Three new parameters have been introduced. The magnetic Reynolds number is a measure of how easily a magnetic field can penetrate a plasma or how easily a plasma slides through the magnetic field. When  $R_m$  is large, a small current will induce a large magnetic field. When the conductivity and velocity of the flow are high, the magnetic Reynolds number is high.

The magnetic force number is the ratio of the Lorentz force to the inertia force. The magnitude of the magnetic perturbations on the flow can be determined by the magnitude of  $S$ . Large values of  $S$  correspond to large perturbations. The final parameter is the Hall parameter, which determines the ratio of the Hall current to the current flowing parallel to the applied electric field. It can also be viewed as the ratio of the cyclotron frequency to the collision frequency.

In the attempt to achieve non-equilibrium ionization, it is desirable to lower the density of the plasma; this results in a higher conductivity, but the Hall parameter is also increased proportionally. Hall parameters greater than one result in a substantial fraction of the current flowing perpendicular to the applied electric field causing the plasma to accelerate into the walls of the channel. This has been observed experimentally by a deflection in the plume [Demetriades and Ziemer, 1962].

Two additional parameters are of interest,  $I_p$ , the magnetic interaction number, and  $H_a$ , the Hartman number. The magnetic interaction parameter is the ratio of the magnetic body force to the fluid inertia force. It is similar to  $S$ , except in this case the current is taken from

Ohm's law. Ohm's law can be given by  $j = \sigma(E + V \times B)$ , when the Hall effect and ion slip are negligible.

$$I_p = \frac{\sigma_0 B_0^2 L_0}{\rho_0 V_0} \quad (2.17)$$

The interaction parameter,  $I_p$ , tells how well the Lorentz force, due to an applied electric field, will accelerate or decelerate the flow for a given set of conditions. At first glance it appears that non-equilibrium ionization conditions are ideal for high MHD interaction. A lower density and higher conductivity both increase the magnetic interaction with the flow. However, it must be realized that Equation 2.17 was obtained by neglecting Hall effects and ion slip. This will be addressed in Section 2.4, but first the significance of Hartmann number will be discussed.

The Hartmann number is the ratio of the magnetic body force to the viscous forces in the flow. Its definition, as well as its relationship to other dimensionless parameters, is given in Equation 2.19.

$$\text{Hartmann number: } H_a^2 = \frac{\sigma_0 V_0 B_0^2}{\eta_0 V_0 / L_0^2} = \frac{\sigma_0 B_0^2 L_0^2}{\eta_0} = S R_e R_m \quad (2.18)$$

## 2.4 Generalized Ohm's Law

This section reviews the effects of ion slip and Hall current for low-pressure non-equilibrium flows. For a singly ionized plasma with only one ion species and one neutral species and for assumed weak ionization (ionization fraction  $< 1\%$ ), the Generalized Ohm's Law is given by [Kontaratos and Demetriades, 1963]

$$\bar{E} = \frac{1}{\sigma_0} \bar{J} + \chi (\bar{J} \times \bar{B}) - \psi (\bar{J} \times \bar{B}) \times \bar{B} \quad (2.19)$$

where  $\sigma_0$  is the scalar conductivity,  $\chi$  is the Hall coefficient (not to be confused with the Hall parameter), and  $\psi$  is the ion slip coefficient.  $\chi$  and  $\psi$  are given by Equations 2.20 and 2.21, respectively.

$$\chi = \frac{1}{n_e q_e} \quad (2.20)$$

$$\psi = 2(1 - \alpha)^2 \frac{\omega_i \tau_{is}}{n_e q_e B} \quad (2.21)$$

## 2.5 Efficiency of MHD Accelerators

The ideal efficiency for both Hall and Faraday channels is obtained by

$$\eta = \frac{\text{Push Work}}{\text{Input Power}} = \frac{\langle j_y u B_z \rangle}{\langle j_y E_y + j_x E_x \rangle}. \quad (2.22)$$

For the Hall accelerator the applied voltage is axial and it can be shown that the efficiency is

$$\eta = \frac{F_x u}{j_x E_x} = \frac{(\omega \tau)^2 K - 1}{(\omega \tau)^2 K(K + 1)}, \quad (2.23)$$

where the loading factor  $K$  is defined by

$$K = \frac{E_x}{(\omega \tau) \mu B_z}. \quad (2.24)$$

In a segmented Faraday accelerator, the voltage is applied across the channel and the efficiency is given by

$$\eta = \frac{\sigma u B_z}{j_y + \sigma u B_z} = \frac{1}{K_F}, \quad (2.25)$$

where the loading factor,  $K$  for the Faraday channel is equal to

$$K_F = \frac{E_y}{u B_z}. \quad (2.26)$$

Relationships for the ideal thrust efficiency for the cross-field (Faraday) and Hall current MHD accelerators are shown in Figure 2.3 as a function of loading factor. While the cross-field accelerator has been experimentally tested more thoroughly, the Hall current accelerator has comparable performance at the high values of Hall parameter measured in the plumes of the microwave plasma generator. In addition, the Hall current accelerator requires only a single power supply, substantially reducing the power conditioning equipment required for in space propulsion vehicles.

Figure 2.3 shows that the efficiency of Hall channels can be comparable to that of a Faraday channel for a Hall parameter greater than 2. The next question that must be asked is if the thrust of the Hall channel is competitive with that of a Faraday channel. The thrust for Hall and Faraday channels is given in Equations 2.27 and 2.28, respectively.

$$F_x = \frac{\sigma_0 u B_z^2}{1 + (\omega \tau)^2} [(\omega \tau)^2 K - 1] \quad (2.27)$$

$$F_x = \sigma_0 u B_z^2 [K_F - 1] \quad (2.28)$$

Figure 2.4 plots the thrust for the Hall and Faraday channels divided by  $\sigma_0 u B_z^2$ . For optimum loading the thrust of the Hall accelerator is always lower than that of the Faraday accelerator. However, the thrust increases and the efficiency drops off slowly as the loading factor is increased. As the Hall parameter is increased, the apparent disadvantage of the Hall channel is minimized.

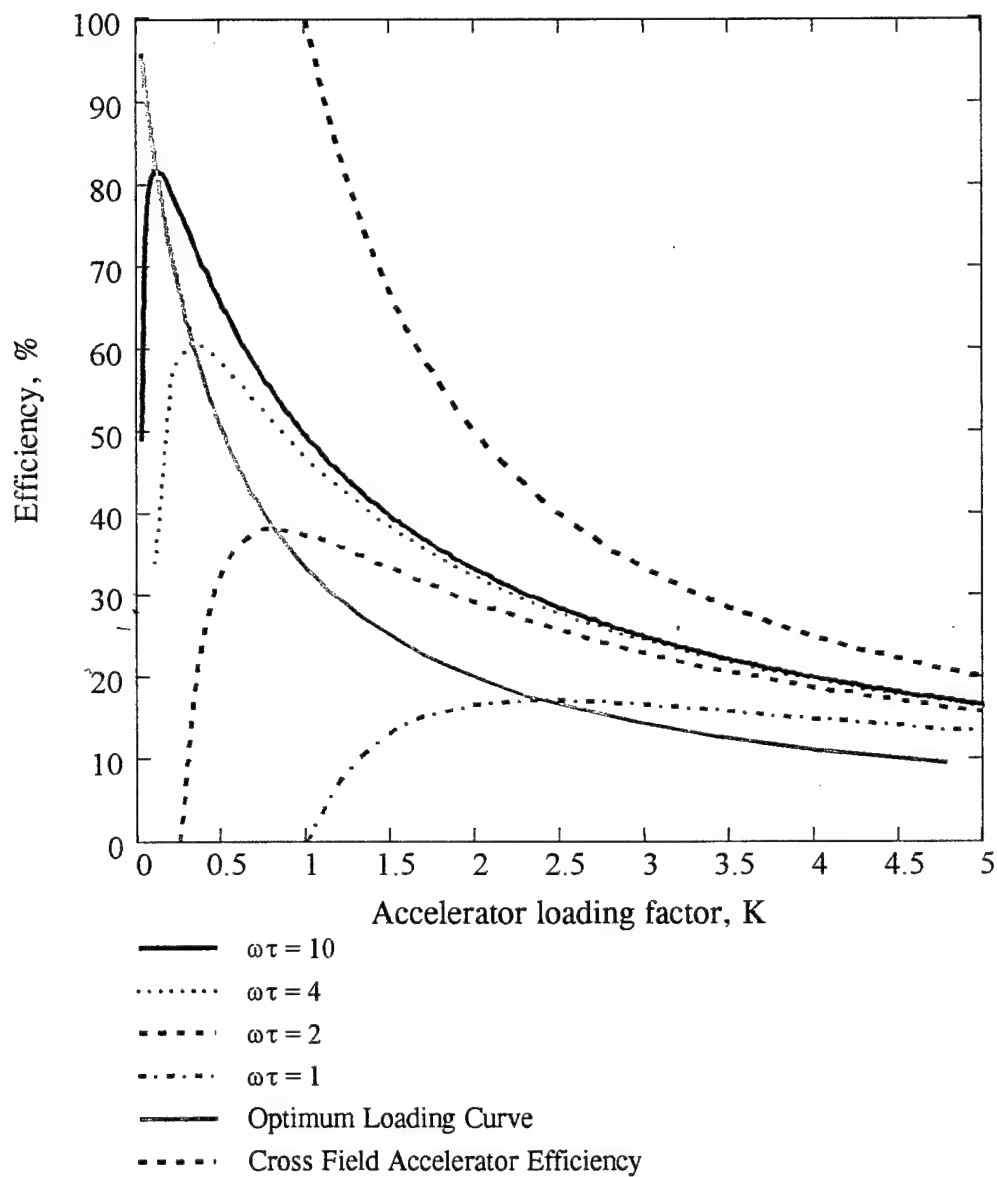


Figure 2.3. MHD efficiency comparison for Hall and Faraday channels.



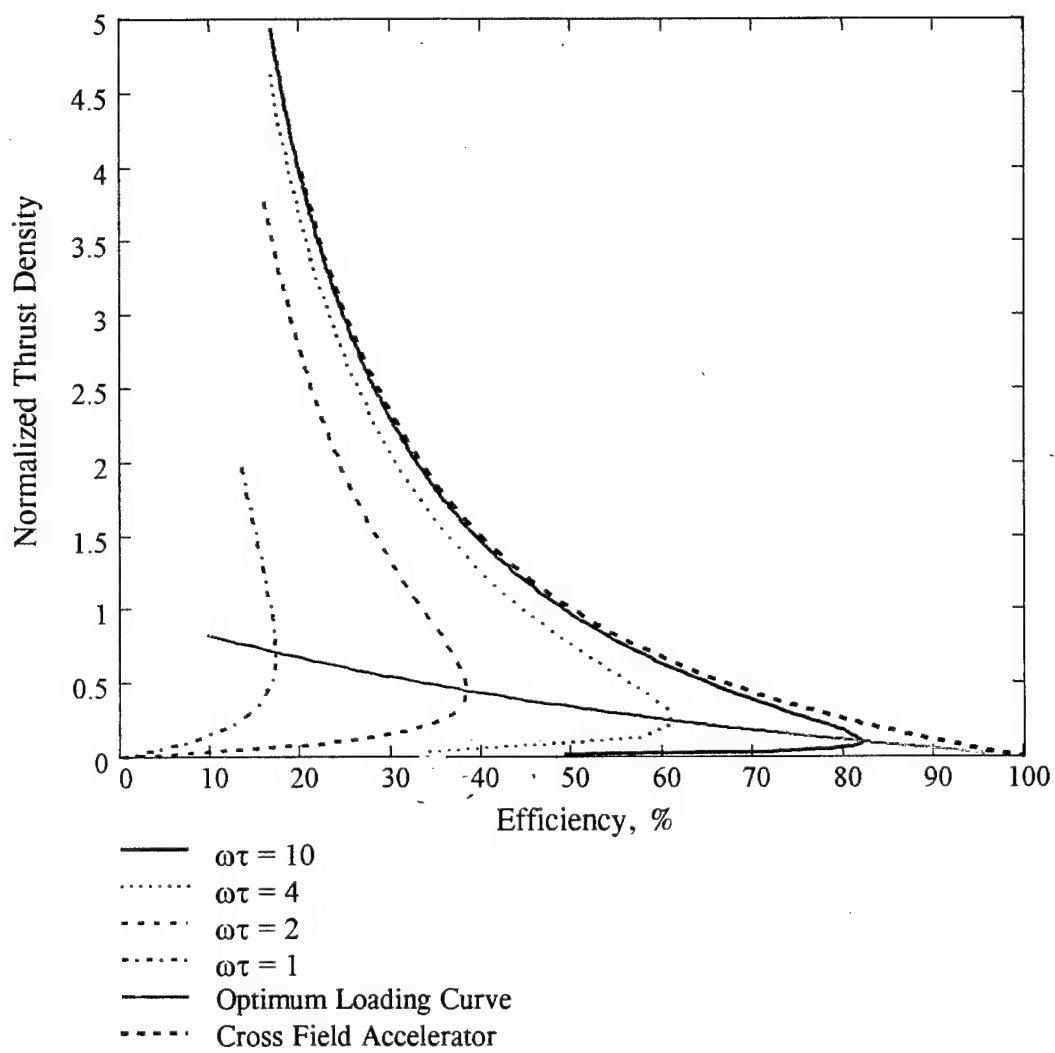


Figure 2.4. Thrust density versus efficiency for Hall and Faraday channels.

## CHAPTER 3

### EXPERIMENTAL SETUP

#### 3.1 Microwave Plasma Generator

The microwave plasma thruster is shown in Figure 3.1. The thruster was designed after the work of Sullivan and Micci at the Pennsylvania State University [Sullivan, 1996]. It consists of a 4-inch diameter by 8-inch long  $TM_{011}$  mode resonant cavity. A boron nitride diaphragm divides the cavity in half, lengthwise. Gas entered the aft end of the cavity through 3 tangential ports spaced equally around the circumference, 1-inch below the diaphragm. This injection scheme formed a vortex flow field that stabilized the plasma discharge. Propellant was heated in the plasma discharge and expanded through a converging-diverging nozzle. Propellant was heated in the plasma discharge and expanded through a converging-diverging nozzle.

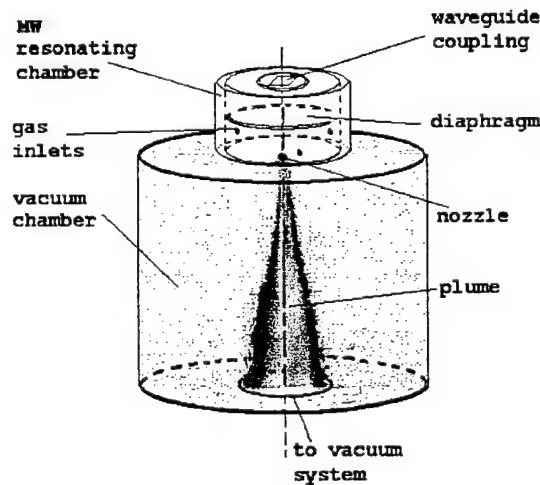


Figure 3.1. Microwave resonant cavity.

The resonant cavity was coupled with a Cober Electronics, 0-6 kW variable power microwave source. Several components of WR 284 wave-guide delivered the microwaves to the cavity. A four-stub tuner connected directly to the cavity was used to match the impedance of the source with the resonant cavity. A simple iris was required to couple the wave-guide to the cavity. The microwave generator, wave-guide, and resonant cavity were coupled to the vacuum chamber as shown in Figure 3.2. Two, one-foot, flexible wave-guide sections on either end of the ten-foot section of wave-guide allowed the top of the vacuum system to be removed without having to detach the microwave cavity from the top. This facilitated the many changes that had to be made within the vacuum chamber.

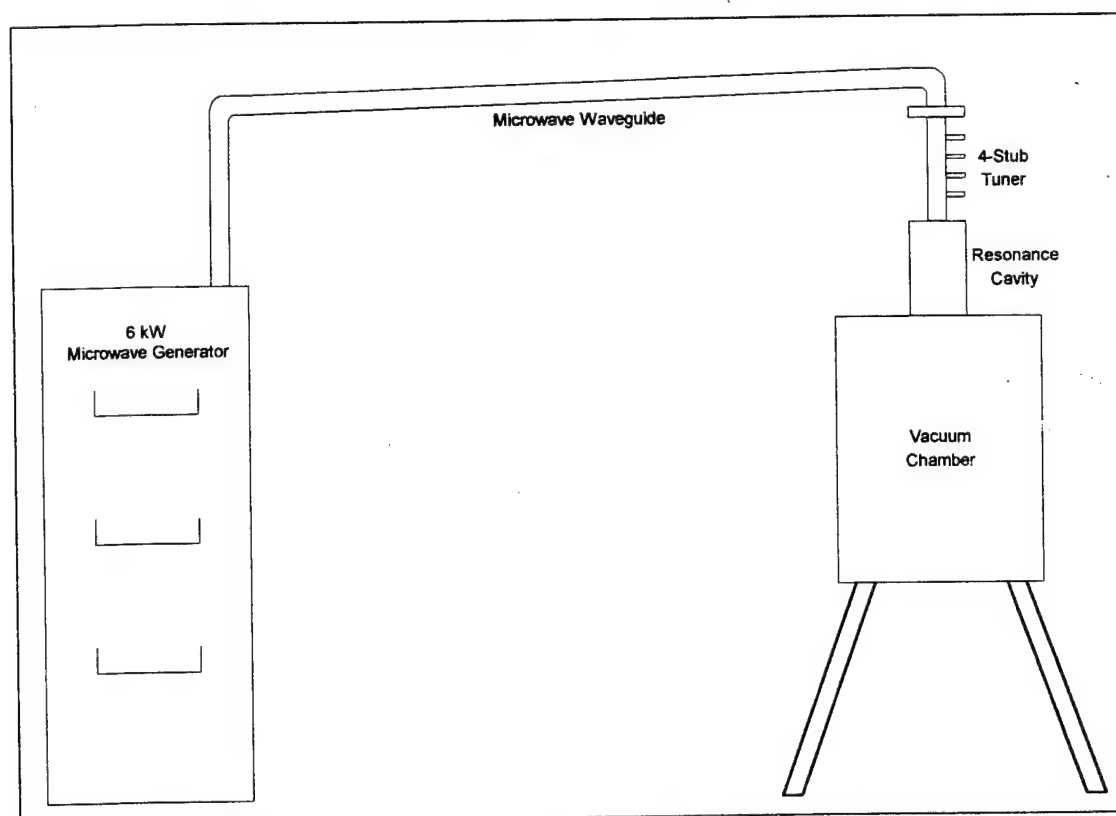


Figure 3.2. Layout of microwave source, wave-guide, resonant cavity, and vacuum chamber.

The microwave power could be controlled either locally or remotely with a 0 – 10 Volt analog signal. An analog output channel from a National Instruments E-Series board was used to control the forward power of the microwave source. Both forward power (power delivered to the microwave resonant cavity) and reflected power (power reflected back from the microwave resonant cavity) were available from the front panel meters and as analog outputs. The resonant cavity chamber pressure was measured with an Omega Model PX303-050A5V, 0 – 50 psia pressure transducer.

Several nozzles of various area ratios and materials were used. Three separate graphite nozzles with area ratios of 7.11, 26.21, and 64 were used. One boron nitride nozzle with an area ratio of 26.21 was used. The microwave cavity could also be operated without a nozzle. The chamber pressure within the microwave cavity was a function of the mass flow rate and the diameter of the nozzle throat. When no nozzle was present, chamber pressures were very low ( $< 5$  Torr).

### 3.2 Vacuum System

The vacuum system consisted of an 18-inch diameter by 24-inch length glass cylinder with 18-inch Varian port rings on the top and bottom. Twelve ports were available in both the top and the bottom port rings for optical and electrical feeds. The microwave cavity was mounted to the top of the tank with an aluminum adapter plate. The adapter plate was connected to a pulley system and hand crank, which was used to gain access to the chamber.

A Stokes, Model 412H-H, 300 CFM roughing pump provided base pressures down to 10 mTorr. Vacuum pressures between 0.5 – 2.0 Torr were maintained, while operating the microwave cavity. Vacuum pressure was measured with a Varian 801, thermocouple vacuum gauge with a range of 0 to 2,000 mTorr.

### 3.3 Propellant Feed System

A schematic of the propellant feed system is shown in Figure 3.3. All gases used in this study were supplied with standard K bottles. Regulators on the K bottles controlled the feed pressure between 5 and 50 psig. A series of filters removed all particulate greater than 0.2 microns from the flow. Volumetric flow rates were obtained with a 0 -120 scfh flow meter. The flow meter was calibrated for air, and corrections were made for other gases.

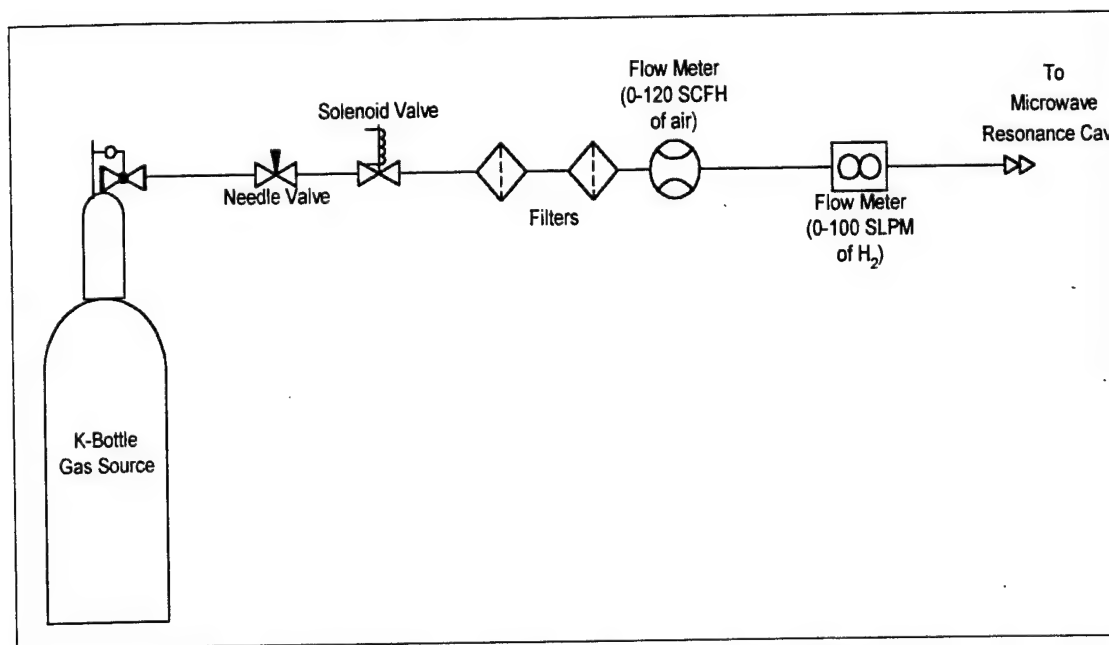


Figure 3.3. Schematic of the propellant feed system.

#### 3.3.1 Steam Feed System

A Presto GranPappy™ Deep Fryer provided the heat source for the steam generator. Fifty feet of ¼ inch copper tubing was coiled and submerged in 100% peanut oil. The temperature of the oil bath was maintained at 400°F by the GranPappy™ control system. A constant flow rate of water was pressure fed into the copper tubing. The pressure feed system consisted of a pressurized water reservoir and two feet of 0.02-inch ID stainless steel tubing.

The flow rate through the stainless steel tubing was proportional to the pressure in the reservoir. The mass flow rate through the stainless steel tube was calibrated by measuring the weight of water that flowed through the tube in a given time. The calibration curve obtained is shown in Figure 3.4.

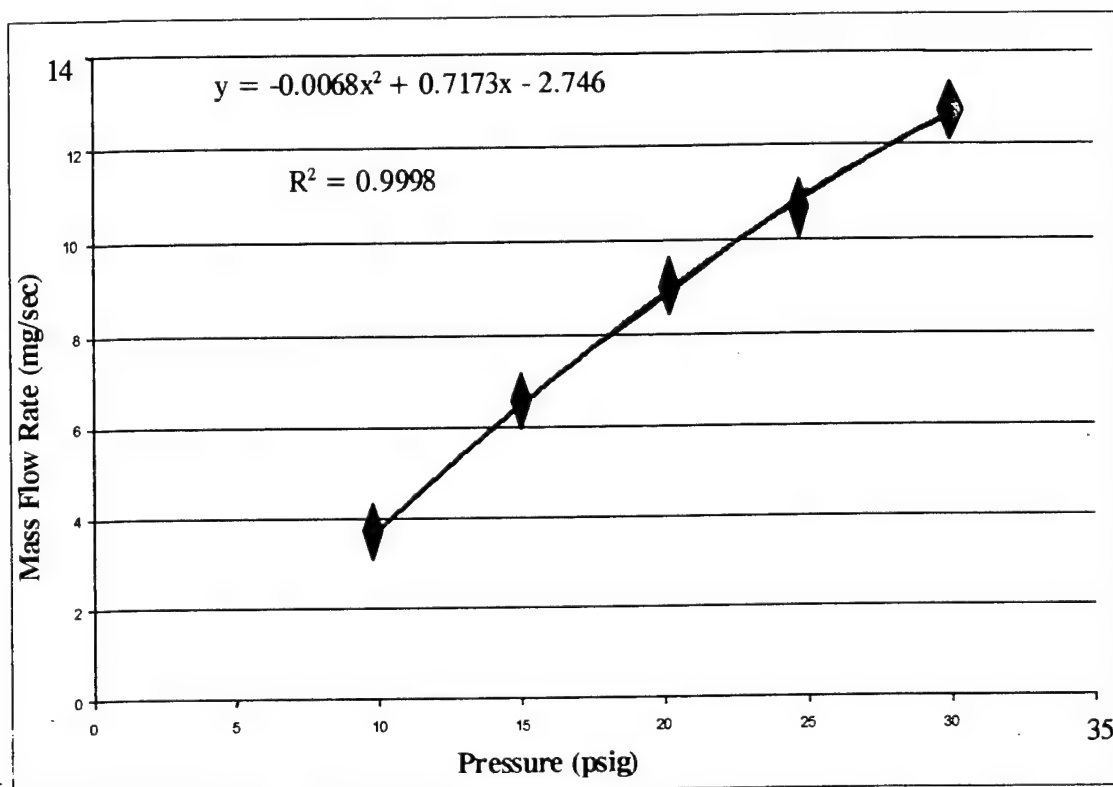


Figure 3.4. Calibration curve for pressure fed steam system.

Steam was fed to the microwave resonant cavity with a ¼-inch copper tube wrapped with heat tape. The steam delivery system including valves and pressure transducers is shown in Figure 3.5. During steady state operation the flow rate of steam was determined by the flow rate of water through the stainless steel tubing. The flow could also be metered with a metering valve, and the steam flow rate could be calculated from the pressure drop across the valves.

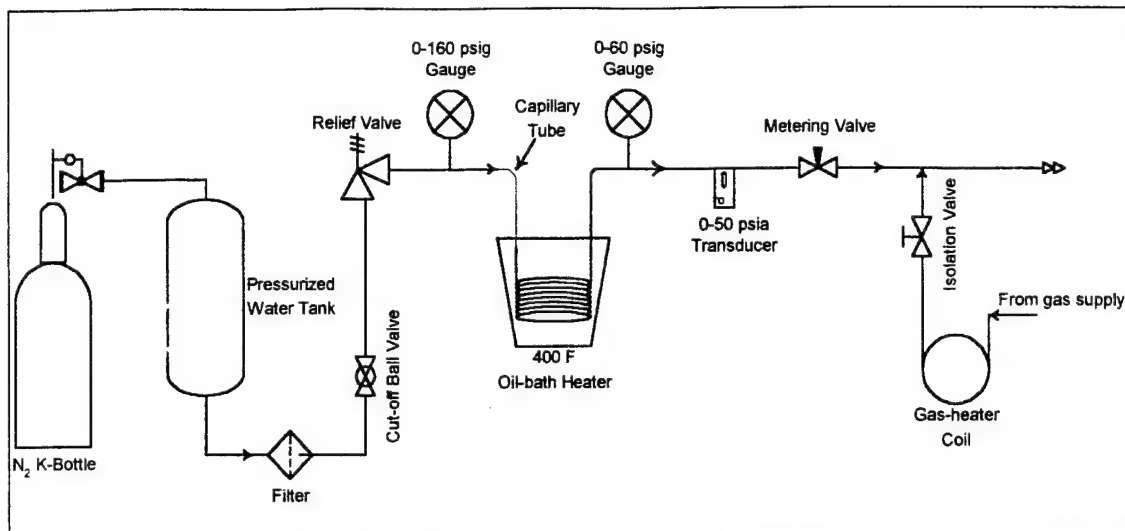


Figure 3.5. Schematic of the steam delivery system.

During startup the steam bypassed the microwave resonant cavity until a steady state flow condition was obtained. Nitrogen from the gas supply system was heated in a copper coil wrapped in high temperature heat tape to  $\approx 500^\circ\text{F}$ . The hot nitrogen served to preheat the lines and the microwave cavity. A discharge was initiated in the cavity with the gas and then the flow was slowly switched over to steam. This process provided a repeatable method for achieving microwave breakdown with steam.

### 3.4 Pitot Tubes and Thermocouples

Both C and K type thermocouples were used to measure the temperature of the flow. C type thermocouples can measure temperature up to 2300 K. For this reason C type thermocouples were chosen for the majority of the tests. Fast response times are desirable to capture transient behavior in the plume. However, very low mass thermocouples will burn up in the harsh environment of the plume; therefore, a compromise was made between the size of the thermocouple junction and the response time.

An exposed junction with a diameter of 0.027 inches was chosen. The thermocouple leads were insulated with alumina tubing that in turn was supported by a stainless steel tube. The leads were exposed 0.7 inches beyond the alumina tubing.

A Pitot-static tube was used to measure the Mach number of the flow. The O.D. of the tube was 0.1 inches, the i.D. of the stagnation port was 0.03 inches, and the static port was located 0.36 inches from the end of the tube. Two Omega Model PX303-015A5V, 0-15 psia, pressure transducers were used to measure the static and total pressures.

### 3.5 Langmuir Probes

Single, double, and quadruple Langmuir probes were constructed to measure electrical transport properties. Two percent thoriated tungsten wire was used for the electrodes for all the probes. One, two, and four hole alumina tubing was used to insulate the wire or probe electrodes. The alumina tubing was supported with stainless steel tubing that was connected to a shielded connecting block providing support for the probe. Several BNC connectors were attached to the shielded box to provide electrical connection for the probe circuitry.

For the single and double probes, a floating voltage ramp was required to produce the I-V characteristic from which the properties are determined. The probes for the quadruple probe were 0.032 inch O.D. by 0.18 inch long. Two twelve-volt batteries were used to supply power to the probe.

The data acquisition system and power supplies for the Langmuir probes were either electrically isolated from the plasma or allowed to float with the plasma. Because the data acquisition system had a common ground with the plasma, electrical isolation was required. A Dataforth<sup>TM</sup> SCM5B isolation module was purchased for this purpose.



### 3.6 Data Acquisition

Two data acquisition systems were utilized. Temperature data was primarily recorded using an Omega temperature measurement system. All other data was recorded using a National Instrument PCI-6071E 64-channel board. The PCI-6071E is capable of recording 1.25 MS/s. Labview<sup>™</sup> software was utilized to record and store all data.

## **CHAPTER 4**

### **DIAGNOSTIC TECHNIQUES FOR FLOWING PLASMAS**

#### **4.1 Diagnostics in Weakly Ionized Plasma**

Numerous plasma diagnostic techniques exist [Eckberth, 1988]. This review will focus on techniques suitable for measuring thermodynamic and electrical transport properties in sub-atmospheric pressure, weakly ionized plasmas. Both intrusive and non-intrusive techniques are considered. Generally, non-intrusive techniques provide more accurate results, but require more expensive equipment and more detailed experimental setups. The majority of the experimental work completed for this dissertation used intrusive techniques.

#### **4.2 Intrusive Techniques**

Intrusive techniques by definition affect the properties of the flow that is being measured. While attention to experimental detail and theoretical corrections can account for most errors introduced by the intrusion, calibration with more reliable non-intrusive techniques is often required for the most accurate results. Despite this, intrusive techniques are attractive because implementation of the technique is often straightforward and cost effective. Experimental data can be obtained quickly with probes, but the probes often require careful data reduction to account for the effects of the intrusion [Chen, 1984].

#### 4.2.1 Langmuir Probes

Langmuir probes provide a convenient method for the measurement of electron temperature and density. In addition, the quadruple probe technique recently used by Bufton and Burton can give the ratio of ion velocity to the mean speed of the flow [Bufton, 1996]. While more modern optical and microwave techniques offer non-intrusive measurement, Langmuir probes are inexpensive and can directly sense plasma particle fluxes by collecting charged particles (ions, electrons) while immersed in the plasma.

Irving Langmuir pioneered the use of Langmuir or electrostatic probes to measure plasma properties. His work focused on characterization of high temperature gases at very low pressures with minimal heat transfer to the probe [Langmuir and Mott-Smith, 1926]. The use of Langmuir probes has expanded and numerous probe configurations and data reduction techniques exist in the literature [Bufton, 1996]. The use of Langmuir probes requires a proper understanding of the plasma conditions that determine the appropriate operating regime for the probe. Before addressing specific probe techniques, the plasma parameters needed to characterize the plasma will be reviewed.

When an electrostatic probe is placed in a plasma, it creates a boundary in which plasma behaviors such as quasi-neutrality (the assumption that  $n_i = n_e$ ) do not hold [Aisenburg, 1963]. The Debye length,  $\lambda_D$ , is the length over which the plasma can feel local charge concentrations or external potentials. The Debye length is defined by Equation 4.1 as a function of the electron temperature and density. The electron temperature is used in the definition of  $\lambda_D$  because electrons are more mobile than the ions and generally do the shielding [Chen, 1984].

$$\lambda_D = \left( \frac{\epsilon_0 k T_e}{n_e e^2} \right)^{1/2} \quad (4.1)$$

The second parameter used to determine the operating regime for a probe is the mean free path between collisions. The mean free path,  $\lambda_{mfp}$ , is defined by

$$\lambda_{mfp} = \frac{1}{nQ}, \quad (4.2)$$

where  $n$  is the number density of the particles, and  $Q$  is the collision frequency of electrons with the particles [Chen, 1984]. Neutral particles, ions, and electrons exist, and the correct collision frequency and number density have to be used to calculate the mean free path for each species. This results in mean free paths for collisions of electrons with electrons, electrons with ions, and electrons with neutral particles. Mean free paths can also be computed for collisions between ions and ions, ions and neutrals, and neutrals and neutrals.

Figure 4.1 outlines the different modes of operation for Langmuir probes. The simplest evaluation can be made when the probe operates in the conventional Langmuir probe regime. For probes to operate in this regime, the sheath surrounding the probe must be thin compared to the probe radius ( $r_p/\lambda_D > 1$ ) and charged particles must not undergo collisions in the sheath ( $\lambda_{mfp}/\lambda_D > 1$ ). In addition, the ratio of the mean free path to the probe radius is important in determining the effect of collisions on the probe. When  $\lambda_{mfp}/r_p < 1$ , charged particles must diffuse to the sheath edge rather than arrive by free flight [Hutchinson, 1987]. For  $\lambda_{mfp}/r_p > 1$ , free molecular flow can be assumed, and particle collisions with the probe are negligible.

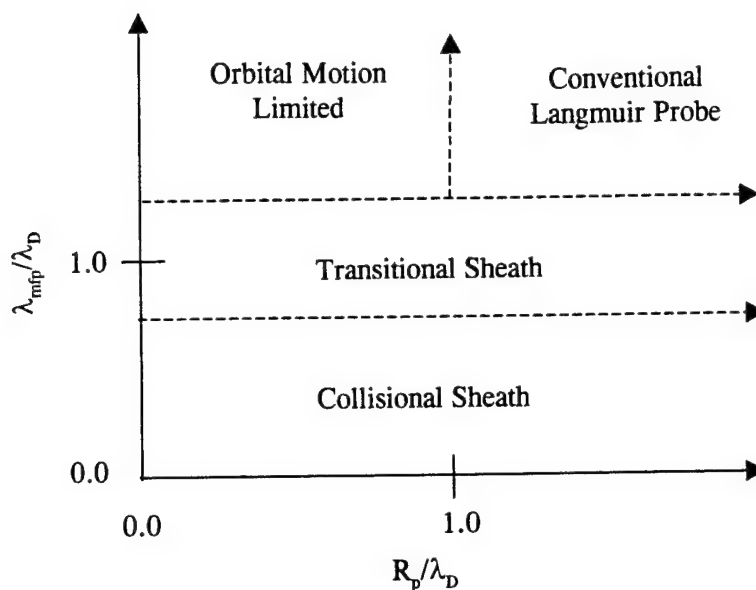


Figure 4.1. Domains of probe electrode performance [Chung, et al., 1975].

#### 4.2.2 Quadruple Langmuir Probes

Burton and Bufton have developed a four-probe measurement technique that allows the measurement of electron density and temperature, as well as the ratio of ion velocity to mean thermal speed [Burton, et al., 1994]. The four-probe configuration is shown in Figure 4.2. When coupled with the velocity and temperature measurements obtained from time of flight and thermocouple measurements, ion velocity can be approximated. The measurement of ion velocity at the exit plane will allow the approximation of ion slip and hall current in the MHD accelerator.

One advantage of the four-probe technique over single and double probe techniques is that the measurements are single point measurements and do not require the use of a voltage ramp. Two twelve-volt batteries were used in these experiments to supply a floating electric potential between probes 1 and 3, and probes 1 and 4. Probe 2 is allowed to float, and

measurements are made of the voltage between probe 1 and 2, and the current flow between probes 1 and 3, and probes 1 and 4.

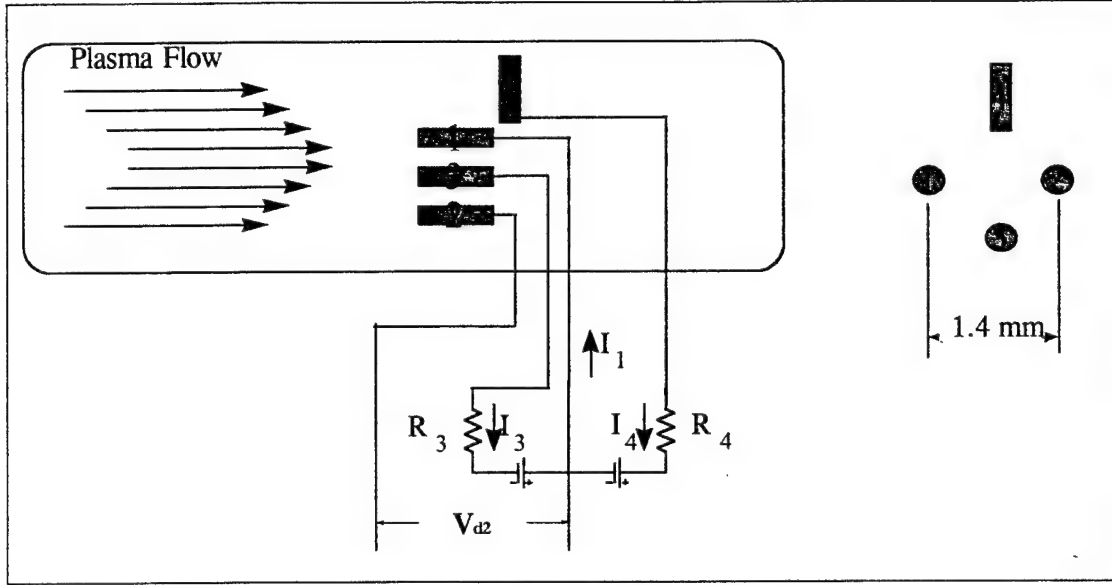


Figure 4.2. Quadruple Langmuir probe setup.

The derivation of the quadruple probe response is presented by [Bufton, 1996]. The electron temperature can be obtained from

$$1 = \frac{1 + \exp(\phi V_{d3}) - 2 \exp[\phi(V_{d3} - V_{d2})]}{(I_4 / I_3) \{ \exp[\phi(V_{d3} - V_{d2})] - 1 \}}. \quad (4.3)$$

The quantities  $V_{d2}$ ,  $I_3$ , and  $I_4$  are measured quantities, and  $V_{d3}$  is the battery voltage. The electron temperature is found by solving for  $\phi$  through iteration and noting that  $T_e = q_e/k_b\phi$ .

The electron density is given by Equation 4.4.

$$n_e = \frac{\kappa \left( \frac{I_3}{A_3} \right) \left( 1 + \frac{I_4}{I_3} \right) \exp\left(\frac{1}{2}\right) (m_{ion})^{1/2}}{q_e (k_b T_e)^{1/2} [\exp(\phi V_{d2}) - 1]} \quad (4.4)$$

### 4.2.3 Thermocouples

A thermocouple can be used to measure the gas temperature or the temperature of the neutral molecules and atoms in the flow. It is generally assumed that the ion temperature is equal to the gas temperature. Knowing the gas temperature and the electron temperature from the Langmuir probe measurements determines the degree of non-equilibrium ionization present in the plasma. Knowledge of the gas temperature allows an estimate of the ion velocity to be made by taking advantage of the measured ratio of ion velocity to mean thermal speed or temperature obtained with the quadrupole Langmuir probe.

Thermocouples in a flowing fluid or plasma can be treated much like a fin, allowing us to draw from the solutions and experience gained in fin design. Transient and steady state operating conditions, as well as the corrections for radiation losses can be treated in a straightforward manner. Viscous dissipation, conduction losses through the leads, and radiation heat transfer to the walls of the container must be considered. The use of small diameter thermocouple wire with long leads and appropriate insulation allows conduction losses to be neglected. In the high-speed flows expected in this study, viscous dissipation will play an important role. When conduction losses are neglected, the thermocouple will read the recovery temperature defined by

$$T_r = T_f \left( 1 + R \frac{k-1}{2} M^2 \right), \quad (4.5)$$

where  $R$  is the recovery factor,  $k$  is the ratio of specific heats  $c_p/c_v$ ,  $T_f$  is the true temperature of the fluid, and  $M$  is the Mach number. Moffat gives the recovery factor of  $0.86 \pm 0.09$  for wires parallel to the flow for gases whose Prandtl numbers are approximately 0.7 [Drake and Goldstein, 1970].

The radiation and convection heat loss from the thermocouple is given by

$$Q = hA_p(T_{surf} - T_r) + h_{rad}A_p(T_{surf} - T_w), \quad (4.6)$$

where  $A_p$  is the area of the thermocouple and exposed leads,  $h$  is the convective heat transfer coefficient, and  $h_{rad}$  is the radiation heat transfer coefficient as given in Equation 4.7.

$$h_{rad} = \frac{\varepsilon\sigma(T_{surf}^4 - T_w^4)}{T_{surf} - T_w}. \quad (4.7)$$

When conduction heat transfer at the thermocouple junction is negligible, the temperature that the thermocouple measures can be obtained by

$$T_{tc} = \frac{hT_r + h_{rad}T_w}{h + h_{rad}}. \quad (4.8)$$

Implementation of Equation 4.8 requires knowledge of both  $h_{rad}$  and  $h$ . The radiation heat transfer coefficient,  $h_{rad}$ , is temperature dependent and can be calculated using Equation 4.7 and assuming the  $T_{surf}$  is equal to  $T_{tc}$ . An estimate for the convective heat transfer coefficient can be obtained from the transient probe response.

A probe that experiences a change in temperature with time will obey the energy balance given in Equation 4.9. This formulation assumes negligible conduction to or from the sensor and neglects the effects of radiation.



$$Mc \frac{dT_{tc}}{dt} = hA_p (T_r - T_{tc}) \quad (4.9)$$

The solution to Equation 4.9 for a sudden change in temperature from  $T_0$  to  $T_f$  is

$$\frac{T_{tc} - T_r}{T_0 - T_r} = e^{\frac{-hA_p}{Mc} t} \quad (4.10)$$

Values for  $A_p$ ,  $M$ , and  $c$  are easily obtained. In Equation 4.10, the recovery temperature has been used as this is the final value the thermocouple will see. The value of  $h$  and  $T_r$  can be obtained using a least-squares curve fit. For the cases where radiation from the probe can be neglected, this provides a good estimate of the convective heat transfer coefficient. To account for the effect of radiation losses a more detailed calculation had to be developed. First Equation 4.9 was modified to include the effects of radiation.

$$Mc \frac{dT_{tc}}{dt} = hA_p (T_r - T_{tc}) - \epsilon \sigma (T_{tc}^4 - T_w^4) \quad (4.11)$$

The solution to Equation 4.11 was not readily available; however, it can be integrated numerically to obtain the temporal response to a sudden change in the fluid temperature. The following procedure was used to obtain an estimate of the heat transfer coefficient.

1. Estimates of the heat transfer coefficient and recovery temperature were obtained from a least squares curve fit of Equation 4.10.
2. The values of  $h$  and  $T_r$  obtained in Step 1 were used in the numerical integration of Equation 4.11.

3. The value of  $h$  was adjusted until the best fit to the experimental data was obtained.

Note the recovery temperature is given accurately by Step 2 because the least squares curve fit was performed on the experimental data that include radiation.

#### 4.2.4 Pitot Tubes

Pitot tubes were used to obtain pressure profiles in the plume. In addition, a total static pitot tube was used to obtain the local Mach number in the flow. Velocity profiles were obtained using the temperature measured with the thermocouple. Gamma or the ratio of specific heats was obtained assuming thermodynamic equilibrium at the measured temperature and pressure.

The ratio of static to total pressure for isentropic flow is given by

$$\frac{P_{0\infty}}{P_{\infty}} = \left( 1 + \frac{\gamma - 1}{\gamma} M_{\infty}^2 \right)^{\frac{\gamma}{\gamma - 1}}, \quad (4.12)$$

where the subscript,  $\infty$ , refers to free stream conditions. The flow in the plume is supersonic and thus a detached shock exists ahead of the Pitot tube. The flow behind the shock is subsonic. If the pitot tube opening is made much smaller than its outer diameter, the normal shock relation can be used to calculate the measured stagnation pressure. The stagnation pressure before the shock is the free-stream stagnation pressure used in Equation 4.12. The relationship between the stagnation pressure before and after the shock is

$$\frac{P_{0y}}{P_{0x}} = \left( \frac{2\gamma M_{\infty}^2 - (\gamma - 1)}{\gamma + 1} \right)^{\frac{\gamma}{\gamma - 1}} \left( \frac{(\gamma + 1) M_{\infty}^2}{2 + (\gamma - 1) M_{\infty}^2} \right)^{\frac{\gamma}{\gamma - 1}}, \quad (4.13)$$

where the subscripts  $x$  and  $y$  refer to conditions before (free-stream conditions) and after the shock, respectively. The measured free-stream stagnation and static pressures can then be related to the free stream Mach number by Equations 4.14 and 4.15.

$$\frac{p_{0Pilot}}{p_{\infty}} = \left( \frac{p_{0y}}{p_{0x}} \right) \left( \frac{p_{0\infty}}{p_{\infty x}} \right) \quad (4.14)$$

$$\frac{p_{0Pilot}}{p_{\infty}} = \frac{\left( \frac{(\gamma + 1) M_{\infty}^2}{2} \right)^{\gamma/(\gamma-1)}}{\left( \frac{2\gamma M_{\infty}^2}{\gamma + 1} - \frac{\gamma - 1}{\gamma + 1} \right)^{1/(\gamma-1)}} \quad (4.15)$$

#### 4.2.5 Power Ripple Time of Flight Velocimetry

The microwave resonance chamber was powered by a variable power (0 – 6 kW) microwave source. The microwave source had an associated power ripple of 5% at full power. In the experiments reported here, the power source was operated between 1 and 3 kW. Fluctuations of the measured emissions were as high as 15% of the DC or average emission. The emission from the resonant cavity measured with a photodiode is shown in Figure 4.3. Two frequencies dominated the signal, a 60 Hz signal with a large amplitude 360 Hz wave riding on it. The frequencies were consistent with the power ripple of the microwave source. In Figure 4.3, AC coupling was used on the digital oscilloscope so that only the power ripple was recorded.

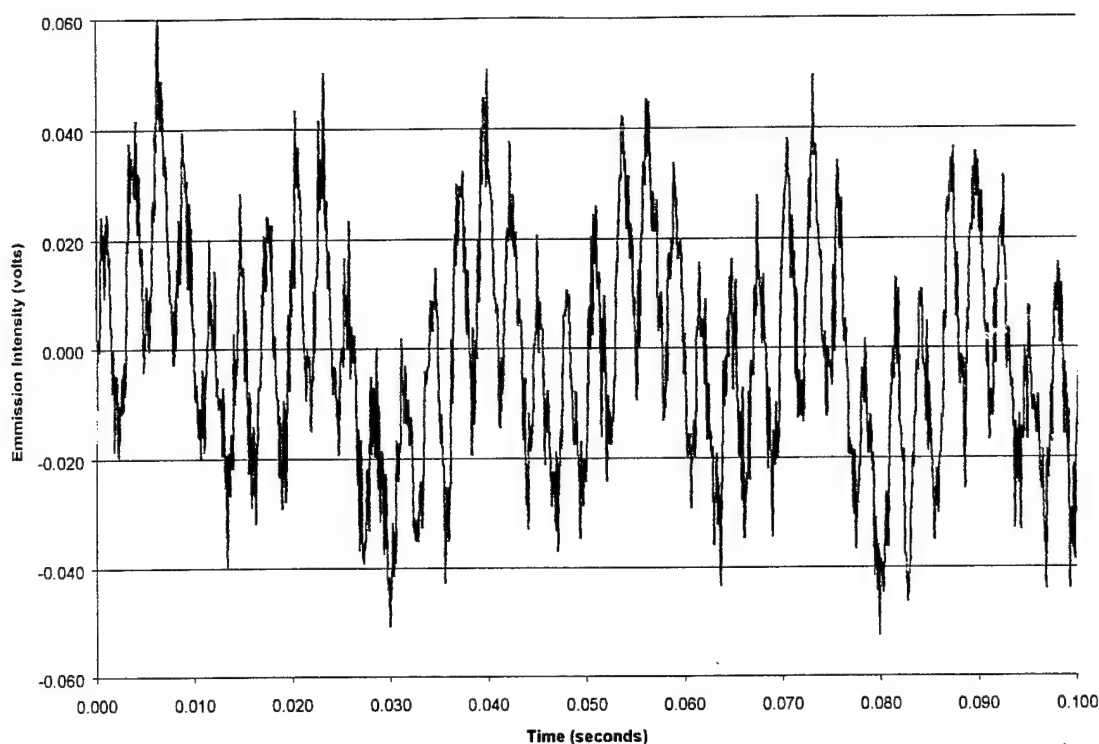


Figure 4.3. Fluctuations in the microwave plasma emissions as a function of time.

The fluctuations in the plasma emissions can be used to measure the velocity in the plume if two conditions are met. First, the fluctuations must travel with the flow. Second, the detectors must be sensitive enough to record the emissions from the relatively low intensity plume. The plasma emissions come from recombination of free electrons with ions and the subsequent decay of the excited ions. If the free electrons were to travel faster than the flow, then a space charge would build up, and the ions would be accelerated quickly to the speed of the electrons. So it is safe to assume that the ions and the electrons are travelling at the same speed. In the absence of electric and magnetic fields, the neutral and ion velocities should be very close because of collisional interactions. While the microwave field is present in the resonant chamber, it is blocked from the plume by the nozzle. The plasma is accelerated by

thermodynamic expansion through the nozzle, a highly collisional process, thus the ions and the neutral particles in the flow are travelling close to the same velocity.

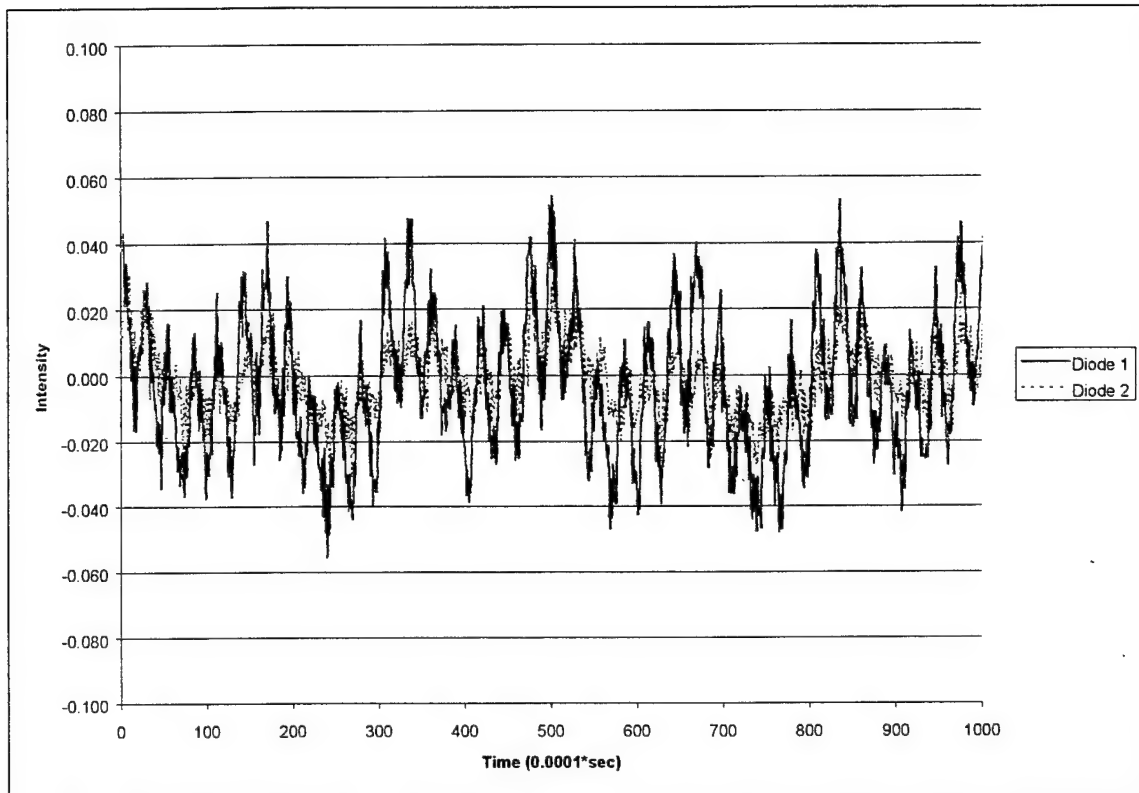


Figure 4.4. Emission ripple from two photodiodes located 3.5 inches apart.

The velocity of the flow can be determined from

$$V = \text{Distance between Detectors} / \text{Time Delay between the Signals.} \quad (4.16)$$

The distance between the detectors is a straightforward measurement; however, determining the phase or time delay between the two detectors requires additional effort. For a single frequency ripple, the time delay can be obtained by calculating the time it takes a single peak to go from one detector to the next. If multiple frequencies are present, then the cross

correlation between the signals must be utilized to calculate the phase delay. The cross correlation of two data series determines the phase shift required for the maximum correlation between the two signals. When noise is present in the signals, several cycles must be used to reduce the uncertainty in the measurement of the time delay. Simulations of the expected signals were used to determine the best data rate and number of cycles to use in the cross correlation. For the photodiode measurements shown in Figure 4.4, a sampling rate of 10,000 samples/sec was used.

The photodiode technique worked well for the brightest plumes. The brightest plumes came from low expansion ratio nozzles and plasma plumes that were not expanded through a nozzle but allowed to leave the resonant cavity through a one-inch hole. The plumes of most interest to this research were too dim to pick up the emission fluctuations with the diodes being used. Langmuir probe results showed that the power ripple caused a corresponding ripple in the electron density of the plasma. By placing two single electrostatic probes a distance,  $d$ , from each other along the centerline of the plume, the fluctuations in electron density can be used to measure the velocity of the flow. In using electrostatic probes to measure the velocity of the flow, care must be taken to minimize the effect of the wake of the upstream probe on the downstream probe. The configuration chosen for these tests is shown in Figure 4.5.

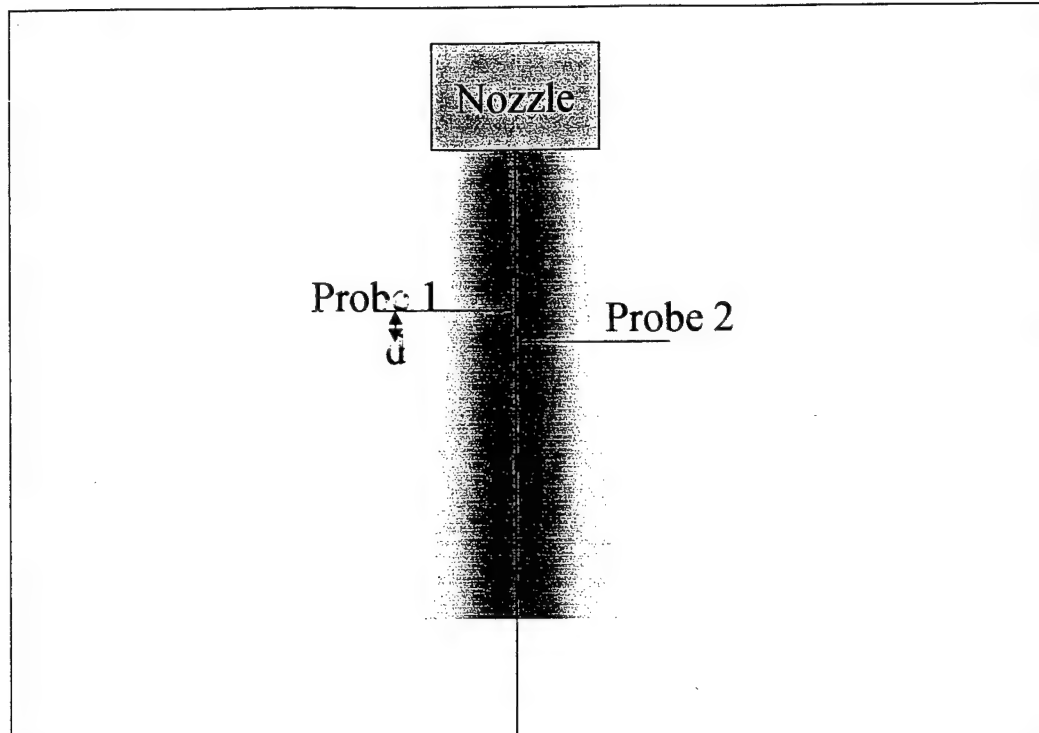


Figure 4.5. Positioning of electrostatic probes for time of flight velocity measurements.

### 4.3 Rayleigh Scattering

A pulsed laser Rayleigh scattering diagnostic technique has been developed to obtain planar velocity, density, and temperature of the scattering species. This technique utilizes a pulsed Nd:YAG to produce a laser sheet as shown in Figure 4.6. An iodine filter is capable of filtering all but the doppler-shifted component. When placed in front of an intensified CCD camera, planar velocity can be determined with a resolution near that of the intensified CCD camera. The velocity is determined by the magnitude of the doppler frequency shift; the temperature is proportional to the width of the doppler signal; and the density is obtained from the total scattered power or intensity of the signal as shown in Figure 4.7.

Table 4.1 lists differential Rayleigh and Raman cross sections for various species of interest for laser excitation at 532 nm. Both the Rayleigh and Raman cross sections are adequate for the proposed experimental equipment and techniques.

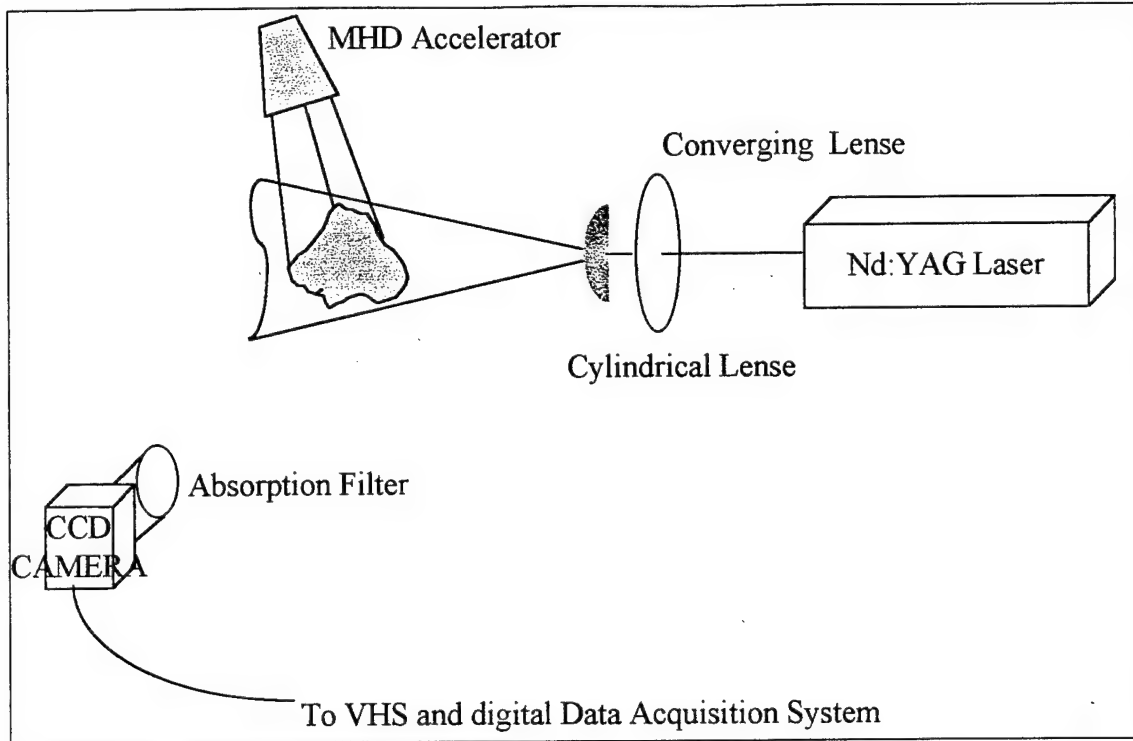


Figure 4.6. Rayleigh scatter Doppler velocimetry setup.

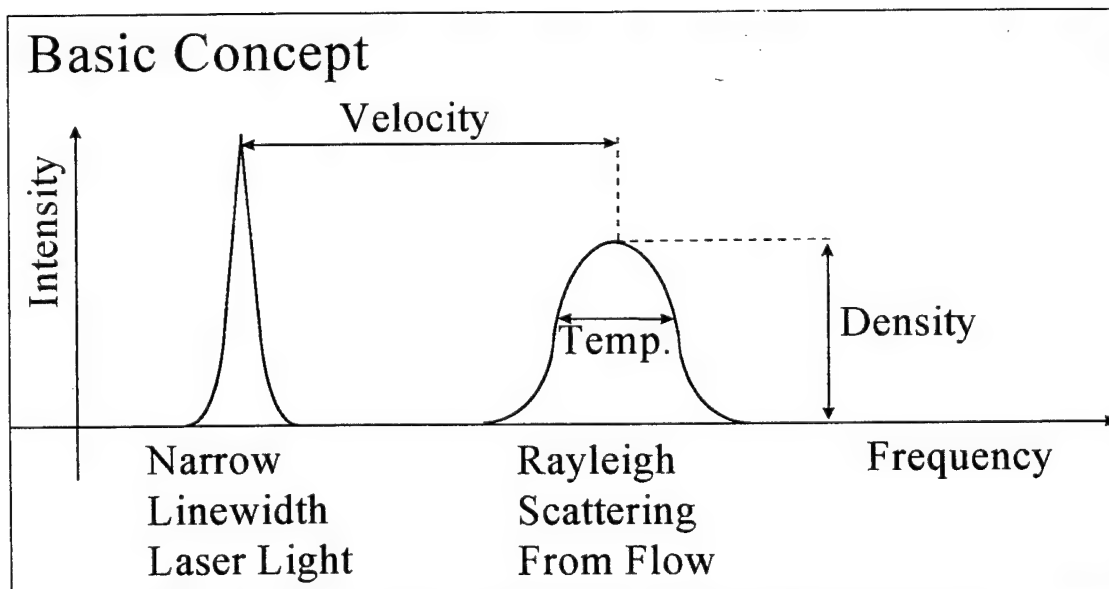


Figure 4.7. Basic concept of the Rayleigh scattered diagnostic technique.



Table 4.1. Rayleigh and Raman scattering cross sections [Eckbreth, et al., 1979].

Gas species	Rayleigh cross-section ( $\times 10^{28} \text{ cm}^2 \text{ ster}^{-1}$ )	Raman shift ( $\text{cm}^{-1}$ )	Raman cross-section ( $\times 10^{31} \text{ cm}^2 \text{ ster}^{-1}$ )
Hydrogen	1.1	4160	9.4
Methane	11.6	2915	26.0
		3017	17.0
Ethylene	25.5	3020	19.0
		1623	7.6
Oxygen	4.4	1556	4.7
Nitrogen	5.1	2331	3.7
Argon	4.7	—	—
Helium	0.1	—	—
Air	5.1	—	—
Freon 22	59.5	—	—
Water vapour	3.8	3657	9.0
Carbon dioxide	11.9	1388	6.0
		1285	4.5
Carbon monoxide	6.8	2145	4.8
Nitric oxide	5.2	1877	2.0

## CHAPTER 5

### EXPERIMENTAL RESULTS

#### 5.1 Approach

The objectives of this work were to characterize the plumes of a 2.45 GHz microwave-generated plasma with various working fluids and assess the feasibility of coupling to a MHD accelerator taking advantage of the non-equilibrium plasma. Three tasks were outlined in Section 1.1 to accomplish this. The first task was the focus of the experimental program.

1. Measuring electron density and electron temperature of the microwave generated plasma plumes to calculate conductivity and determine the extent of non-equilibrium ionization under selected microwave resonant cavity operating conditions.

To accomplish this experimental investigation, the tests outlined in Table 5.1 were conducted. The nozzle tests were conducted to determine the electron density and temperature at the exit for various expansion ratios. Three expansion ratios were tested. However, the flow rate for the small nozzle was so small that when Langmuir probe measurements were attempted, the signal was not large enough to record. A boron nitride nozzle was tested to determine the effect of a conductive (graphite) versus insulative (boron nitride) nozzle. For each test, the resonant cavity was tuned to minimize the reflected power by adjusting the four-stub tuner on the waveguide attached to the microwave resonant cavity.

Table 5.1. Test matrix for microwave resonant cavity plume evaluation.

Nozzle Tests	Throat Diameter (mm)	Exit Diameter (mm)	Area Ratio	Flow Rate for Nitrogen (mg/sec)	
Large Nozzle	3.81	10.16	7.11	72 & 155	
Medium Nozzle	1.98	10.16	26.21	135	
Small Nozzle	0.79	6.35	64	< 50	
Boron Nitride Nozzle	1.98	10.16	26.21	135	
Open Cavity Tests	Argon	Carbon Dioxide	Helium	Nitrogen	Steam
Vacuum Pressure (mTorr)	600	750	> 2000	1500	800
Flow Rate (mg/sec)	393	386	14	246	94.8
Resonant Cavity Pressure (mTorr)	4344	5689	2069	4654	2500- 5000

The open cavity tests were conducted with the nozzle removed from the microwave resonant cavity, allowing the flow to expand freely through a 1-inch diameter hole. Removing the nozzle allowed operation at lower pressures within the microwave resonant cavity. This low-pressure operation was experimentally determined to be the most stable regime for the gases of interest. Five gases were tested in the open cavity tests. The gases were chosen to cover a broad range of collision cross sections and electron energy loss factors. Argon and helium were chosen because they are monatomic gases with electron energy loss factors of one. Nitrogen was used in both the nozzle tests and the open cavity tests because it exhibited the most stable discharge behavior and represented a diatomic molecule with an average collision cross section and electron energy loss factor given in Tables 2.1 and 2.2. The final two gases,

carbon dioxide and steam, were chosen to determine what level of non-equilibrium ionization could be obtained in gases with large collision cross sections and electron energy loss factors.

## 5.2 Nozzle Tests

All of the nozzle tests were conducted with nitrogen as the propellant. Nitrogen exhibited stable discharge over a wide range of flow rates and resonant cavity operating pressures. Therefore, the effects of discharge instabilities within the microwave resonant cavity did not hamper the comparison between the different nozzle tests.

### 5.2.1 Large Nozzle

The large nozzle had an expansion ratio of 7.11. Flow rates of 72 and 155 mg/sec were used. Profiles of the electron density and temperature were obtained by scanning the quadrupole Langmuir probe through the plume starting 1 mm from the exit and repeating the measurement 10 times every 0.5 cm. Figures 5.1 and 5.2 show the electron density and temperature profiles, respectively. This test was conducted at a flow rate 155 mg/sec. During the test, supersonic shock diamonds were visible within the plume. The shock structure appears in both the electron density and temperature profiles. The visible shock structure was much sharper than the shock structure evident in Figure 5.2. This is most likely due to the diffusion of electrons across the shock.

Centerline velocity measurements were made for flow rates of 72 mg/sec and 155 mg/sec. Velocities of  $\approx 500$  m/sec and 1500 m/sec, respectively, were measured using the power ripple velocity technique with two 0.03-inch thoriated tungsten electrodes spaced 1-inch

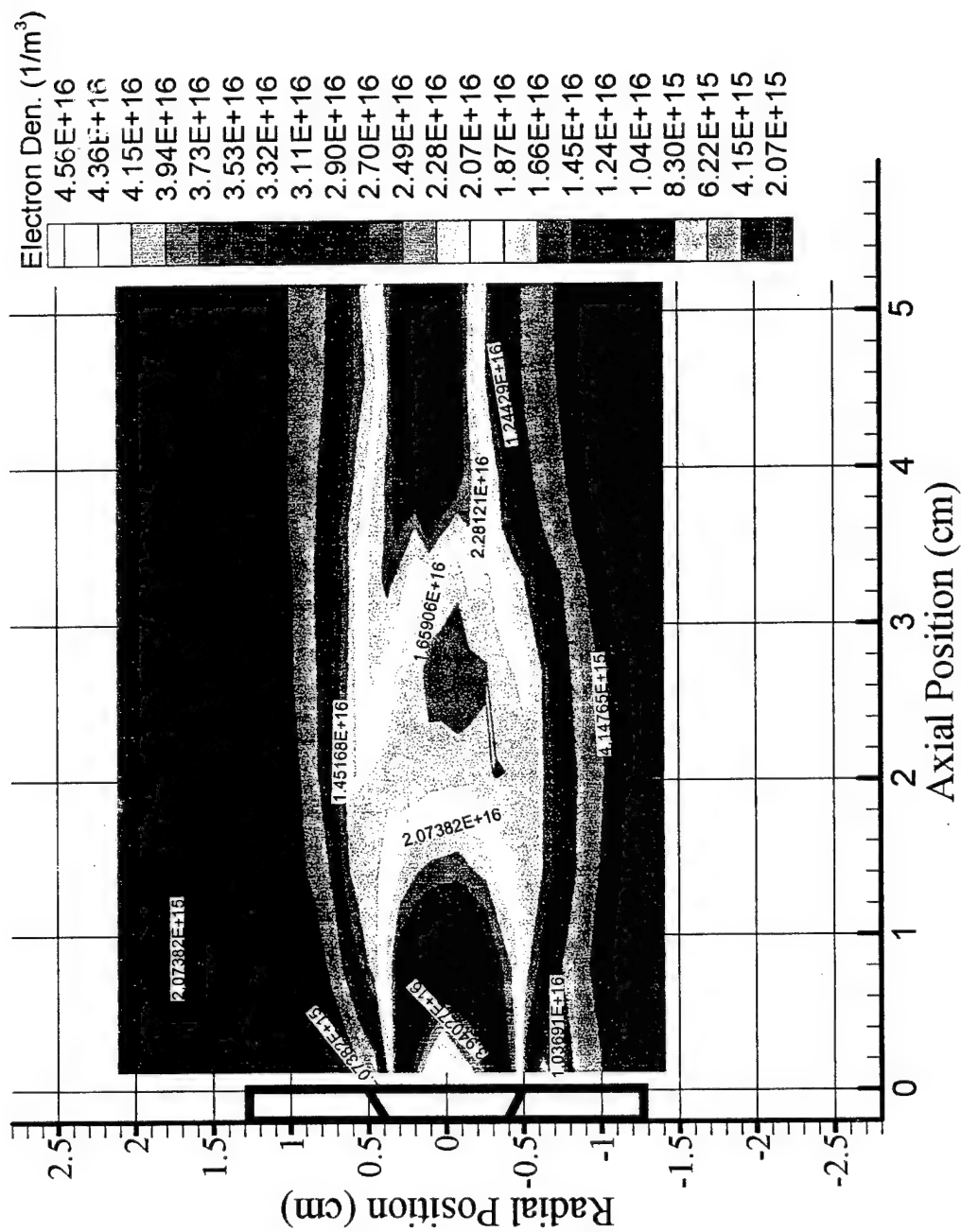


Figure 5.1.1. Electron density profile for nitrogen with large nozzle.

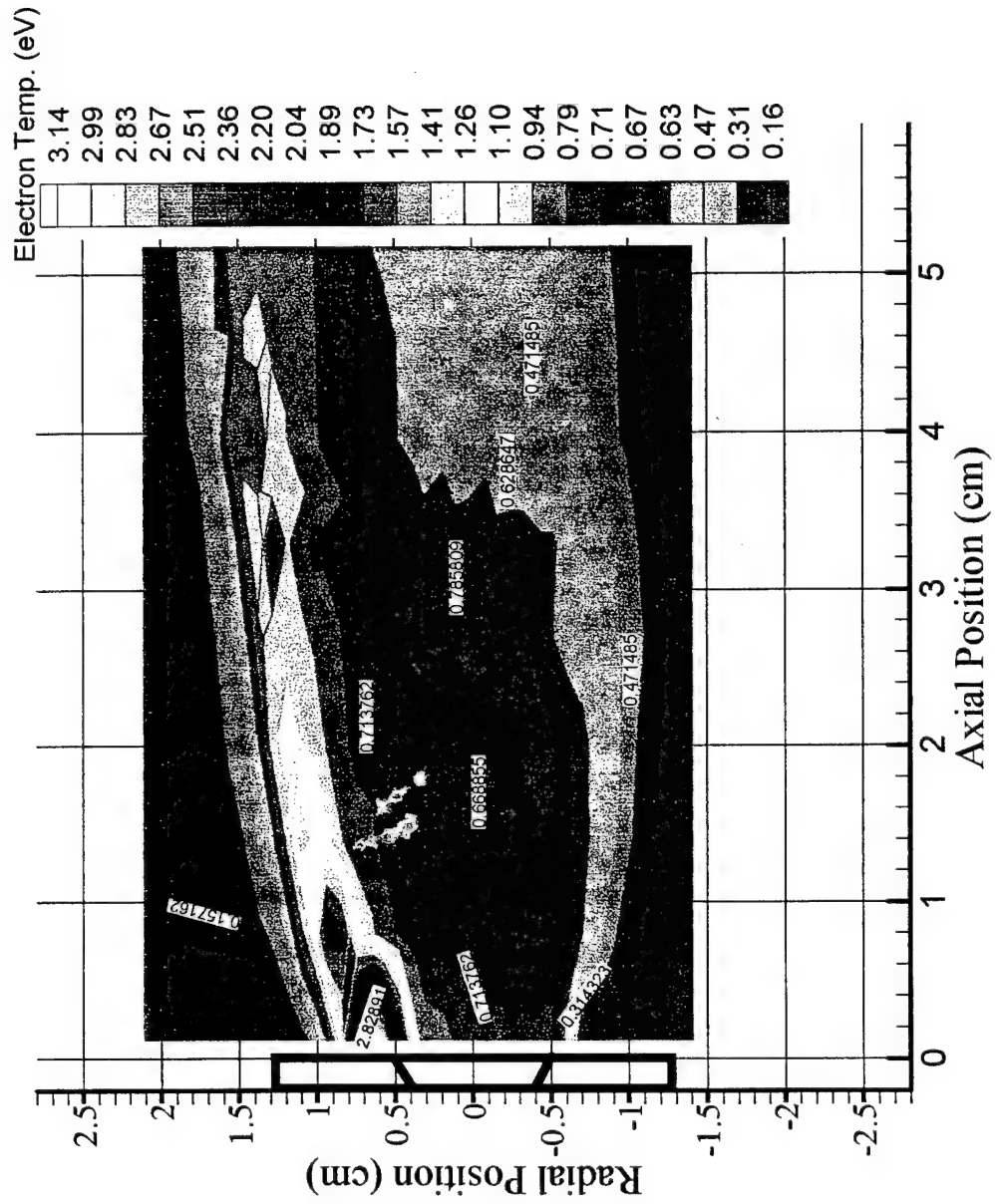


Figure 5.2. Electron temperature profile for nitrogen with large nozzle.

apart. Both positive and negative biases were used to verify that the ion current and electron current gave the same results. The analysis given in Section 4.2.2 used with thermocouple measurements gave plume temperatures on the order of 1500 K on the centerline at the exit to the microwave resonant cavity.

Radial profiles of electron density and temperature are shown in Figures 5.3 and 5.4, respectively, for a flow rate of 72 gm/sec. The measurements were made 1.3 cm from the nozzle exit. A peak electron density of  $2 \times 10^{16} \text{ e/m}^3$  was reached versus  $2.8 \times 10^{16} \text{ e/m}^3$  for the 155 mg/sec flow rate. The electron temperature had an average value of 0.6 eV and 0.67 eV in the center of the plume for the 72 and 155 mg/sec flow rates, respectively. The centerline of the plume is shown in each figure by the dark dash-dot line.

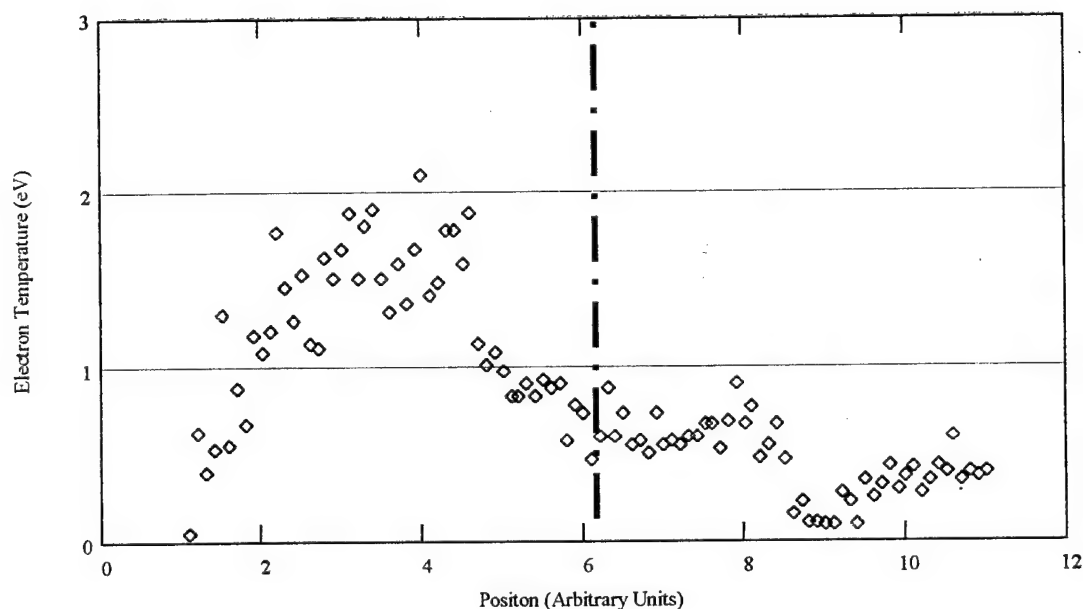


Figure 5.3. Radial profile of nitrogen plume with graphite nozzle (expansion ratio = 7.11).

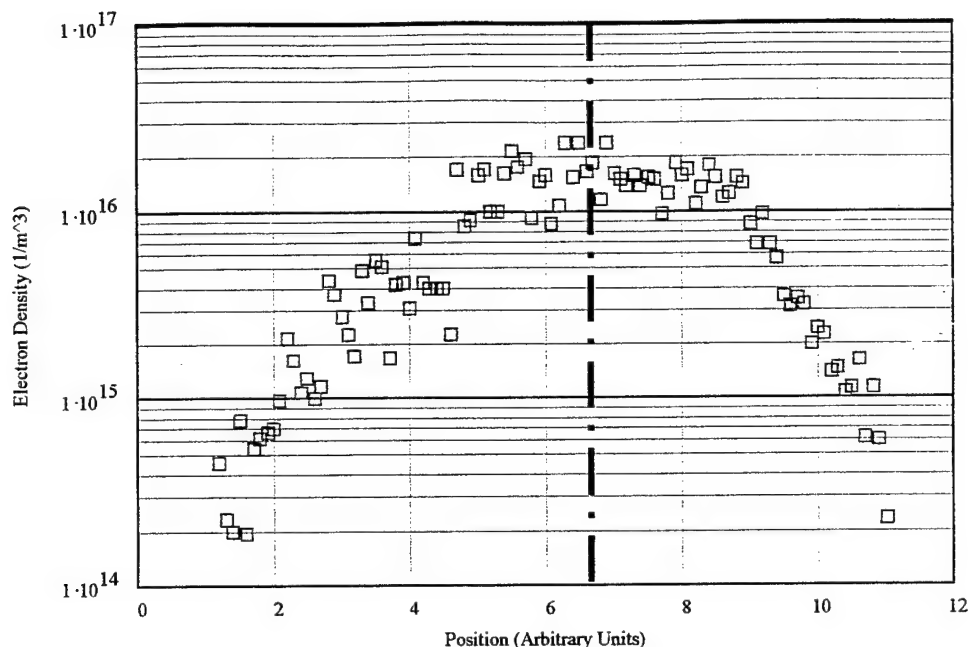


Figure 5.4. Radial profile of nitrogen plume with graphite nozzle (expansion ratio = 7.11).

On the left side of the plume an asymmetric peak of  $\cong 2$  eV in electron temperature was measured for both flow rates. Gradients in electron density can cause an asymmetric profile; however, they cannot account for a peak of this magnitude.

### 5.2.2 Medium Nozzle

The medium graphite nozzle had an expansion ratio of 26.21. A flow rate of 135g/sec was used for all the tests. The microwave resonant cavity chamber pressure was 8.2 psia, while the vacuum chamber pressure was 500 mTorr. Both axial and radial scans were taken. Figures 5.5 and 5.6 show radial scans of electron temperature and density 1.3 cm from the nozzle exit. The peak in electron density remains unchanged from the smaller area ratio nozzle. However, substantial reductions in the size of the peaks on the edge of the electron temperature profile are evident. Also the average electron temperature at the center of the plume increased to 0.9 eV.



Axial scans from 1.3 cm to 14.5 cm from the nozzle exit are shown in Figures 5.7 and 5.8. The shock structure in the plume is evident in the electron density plot. Three oblique shock waves were crossed, and the electron density increased behind each one. The electron density decreases from  $2 \times 10^{16} \text{ e/m}^3$  to  $8 \times 10^{15} \text{ e/m}^3$  along the radial scan. The radial profiles at 14.5 cm are shown in Figures 5.9 and 5.10. The profiles become broader, and the peak values decrease.

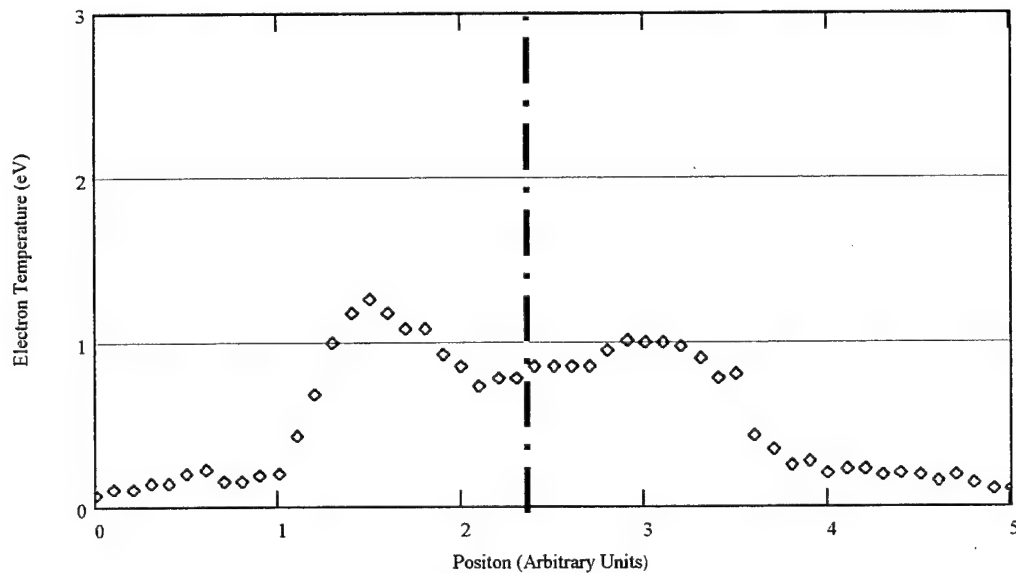


Figure 5.5. Radial scan of electron temperature, 1.3 cm from the nozzle exit (expansion ratio = 26.21).

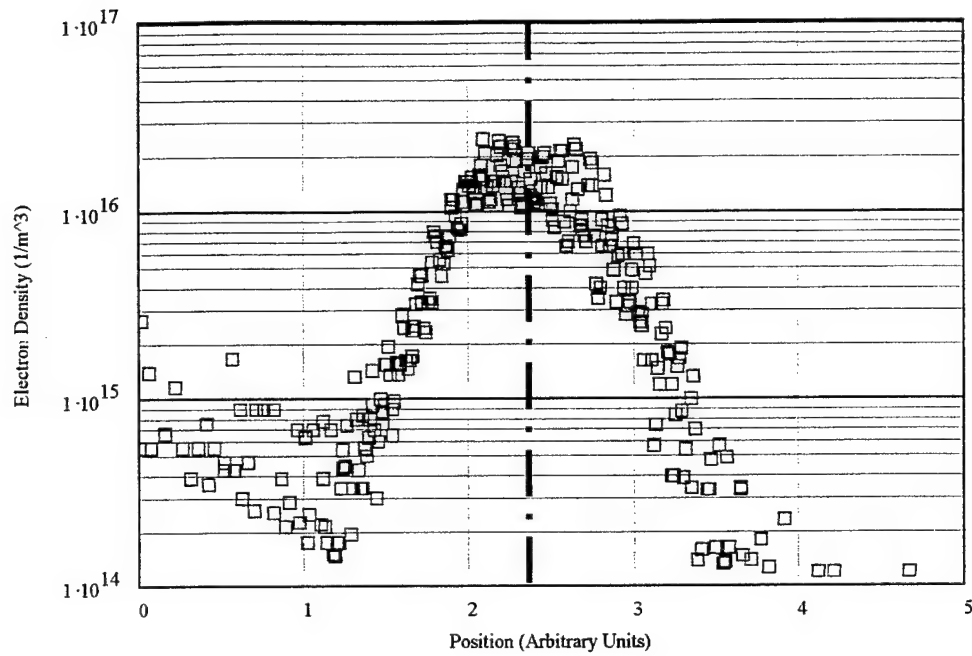


Figure 5.6. Radial scan of electron density, 1.3 cm from the nozzle exit (expansion ratio = 26.21).

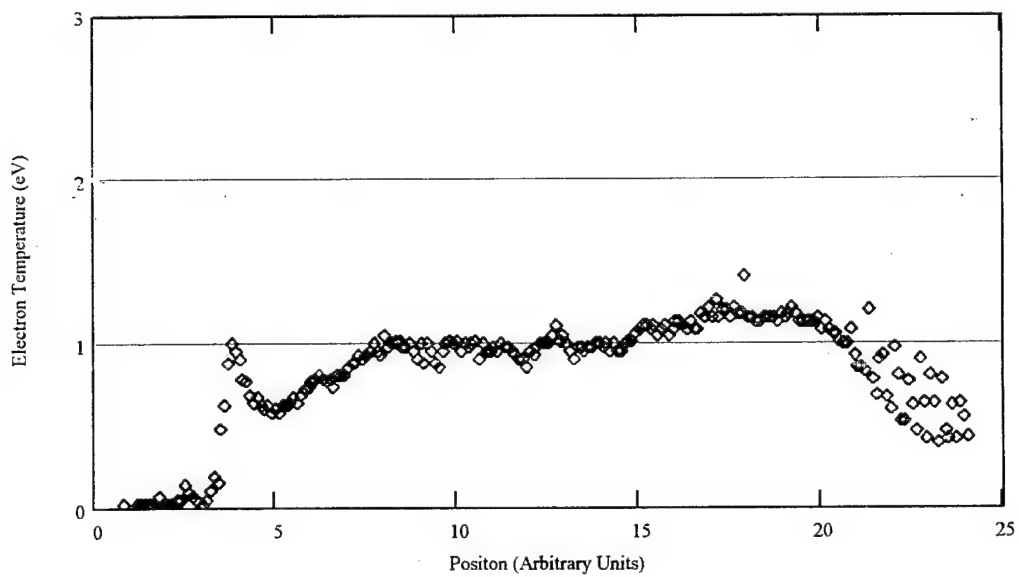


Figure 5.7. Axial scan of electron temperature 1.3 to 14.5 cm from the nozzle (expansion ratio = 26.21).

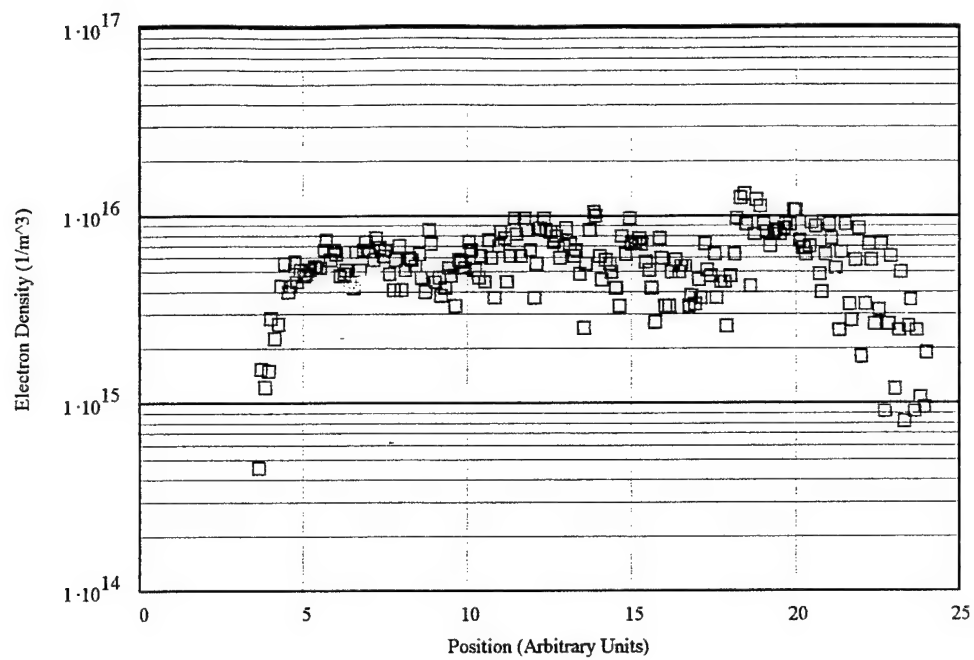


Figure 5.8. Axial scan of electron density 1.3 to 14.5 cm from the nozzle (expansion ratio = 26.21).

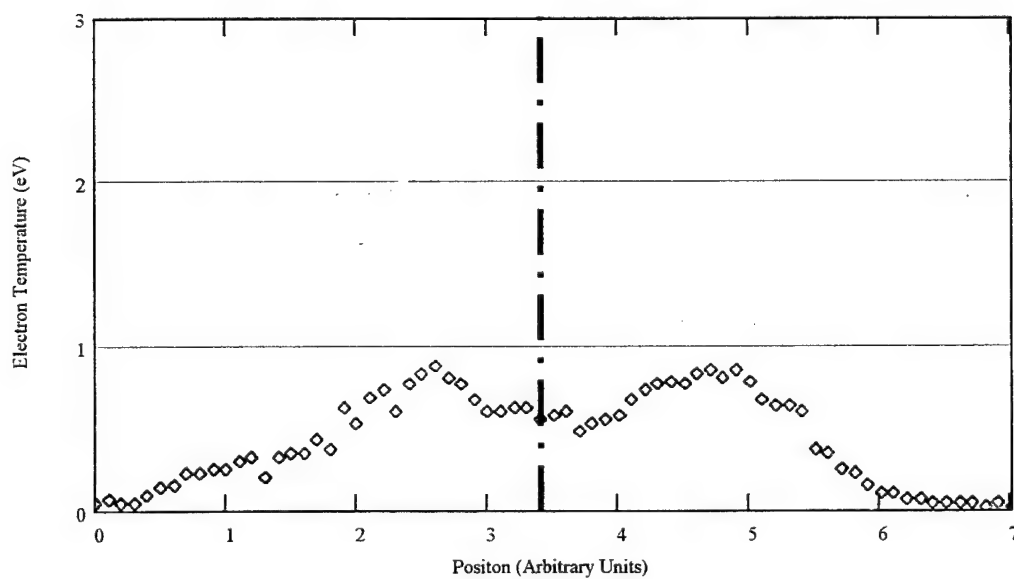


Figure 5.9. Radial scan of electron temperature 14.5 cm from the nozzle (expansion ratio = 26.21).

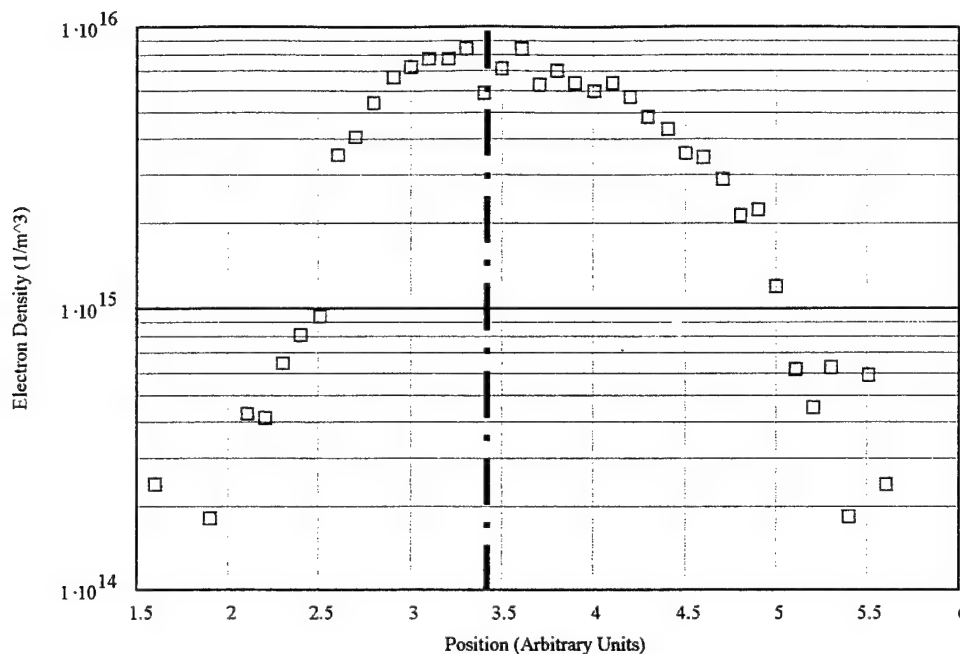


Figure 5.10. Radial scan of electron density 14.5 cm from the nozzle (expansion ratio = 26.21).

### 5.2.3 Boron Nitride Nozzle

A boron nitride nozzle identical to the medium graphite nozzle was also constructed. Boron nitride is an electrical insulator, and thus the affects of electrically isolating the nozzle from the resonant cavity were tested. The same flow rates and chamber pressure conditions used with the medium graphite nozzle were used for these tests. Radial scans of the electron density and temperature are shown in Figures 5.11 and 5.12.

The peaks on the edges of the electron temperature profiles reach 3 eV in Figure 5.9. These peaks are on the outer edges of the core flow of the plume. Electron temperatures of 3 eV were also measured in the open cavity tests. Corrections for gradients in electron density do not account for these large peaks. The centerline temperature remains close to 0.9 eV, the same value obtained with the medium graphite nozzle.

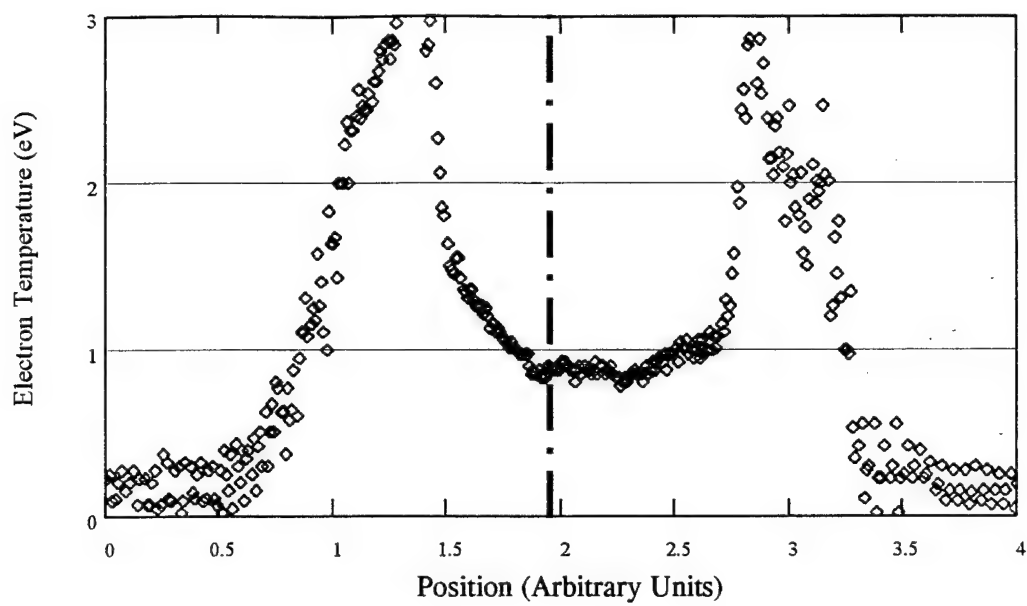


Figure 5.11. Radial scan of electron temperature 1.3 cm from boron nitride nozzle.

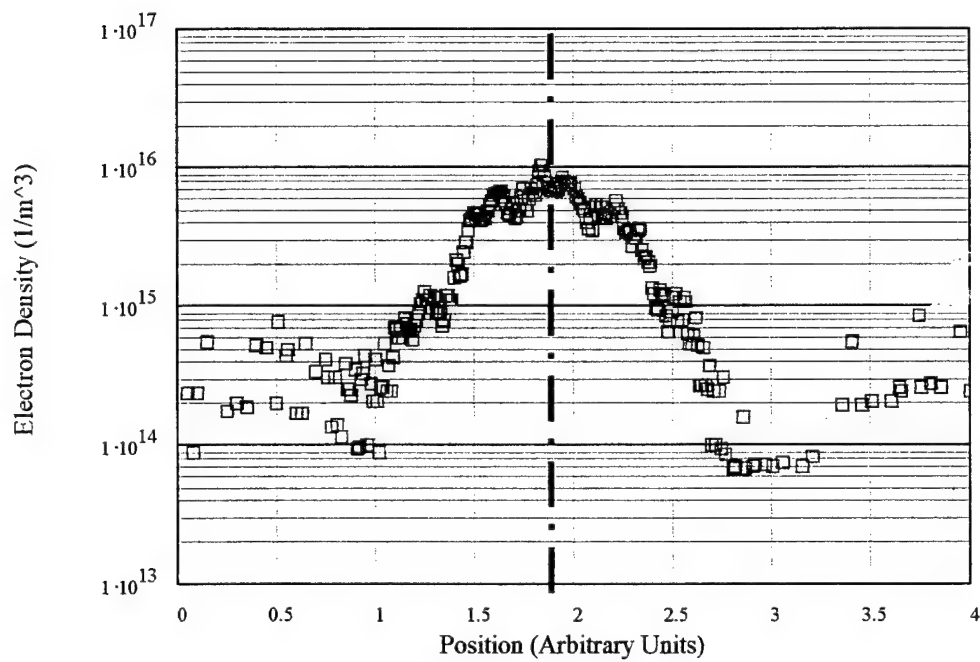


Figure 5.12. Radial scan of electron density 1.3 cm from boron nitride nozzle.

The microwave resonant chamber operating with a boron nitride nozzle was unstable. The fluctuations in electron density due to this instability are shown in Figure 5.13. The large fluctuations in electron density have a frequency of  $\cong 10$  Hz. This is far below the 60 and 360 Hz frequencies of the microwave power supply ripple. Also the amplitude of these fluctuations is an order of magnitude higher than the fluctuations due to the power ripple. The amplitude decreases with the distance from the cavity. The reason for this instability is not immediately obvious.

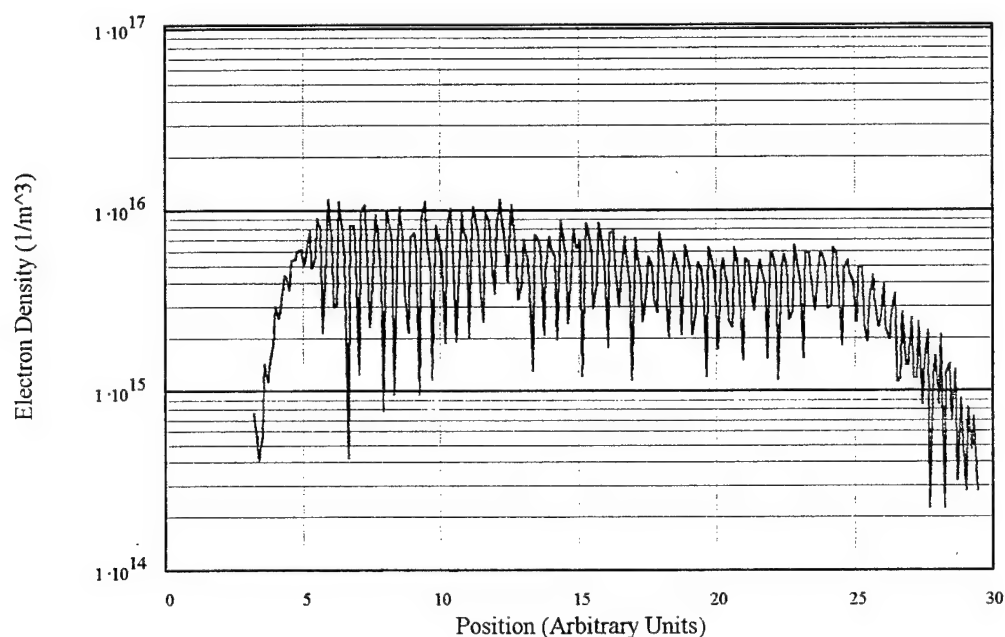


Figure 5.13. Axial scan of electron density for the boron nitride nozzle.

### 5.3 Open Cavity Tests

The nozzle was removed for the open cavity tests. This left a 1-inch diameter opening in the bottom of the resonant cavity. A microwave leak detector verified that the 1-inch hole was small enough to prevent microwave leaks into the lab.

Power ripple velocity measurements determined the velocity at the exit was less than 300 m/sec in the axial direction. No attempt was made to measure radial velocities. Resonant cavity and vacuum chamber pressures are given in Table 5.1. Because of the absence of the nozzle, the microwave resonant cavity operated much closer to the pressure of the vacuum chamber. Pitot tube measurements were not sensitive enough to measure the stagnation or static pressure in the plasma plumes; however, the pressures of the resonant cavity and the vacuum chamber bound the pressure in the plume.

Electron density and temperature profiles were measured for carbon dioxide, helium, argon and nitrogen. Electron density and temperature profiles are shown respectively in Figures 5.14 and 5.15 for carbon dioxide. Carbon dioxide was the only gas tested for which shocks were visible within the plume. These shock patterns are evident in the experimental data. The profiles for helium shown in Figures 5.16 and 5.17 show the most rapid decrease in both electron temperature and density. It is believed that the relatively high back pressure in the vacuum chamber is the cause of this rapid recombination. The back pressure is caused by the low molecular weight of helium, making it very difficult to pump.

A visible swirl existed in the flow at the exit due to the tangential injection and vortex stabilization within the cavity for both helium and argon. The swirl was not visible in any of the nozzle tests. This swirl is clearly displayed in the profiles for argon, Figure 5.18 and 5.19. The helium profiles also show evidence of the swirl.

Nitrogen was the most stable of all the gases tested in the open cavity tests. This is evident in the smooth profiles for nitrogen in Figures 5.20 and 5.21. Profiles for each gas were obtained by scanning the quadruple Langmuir probe through the plume starting 3 mm from the exit and repeating the measurement 10 times every 0.5 cm.





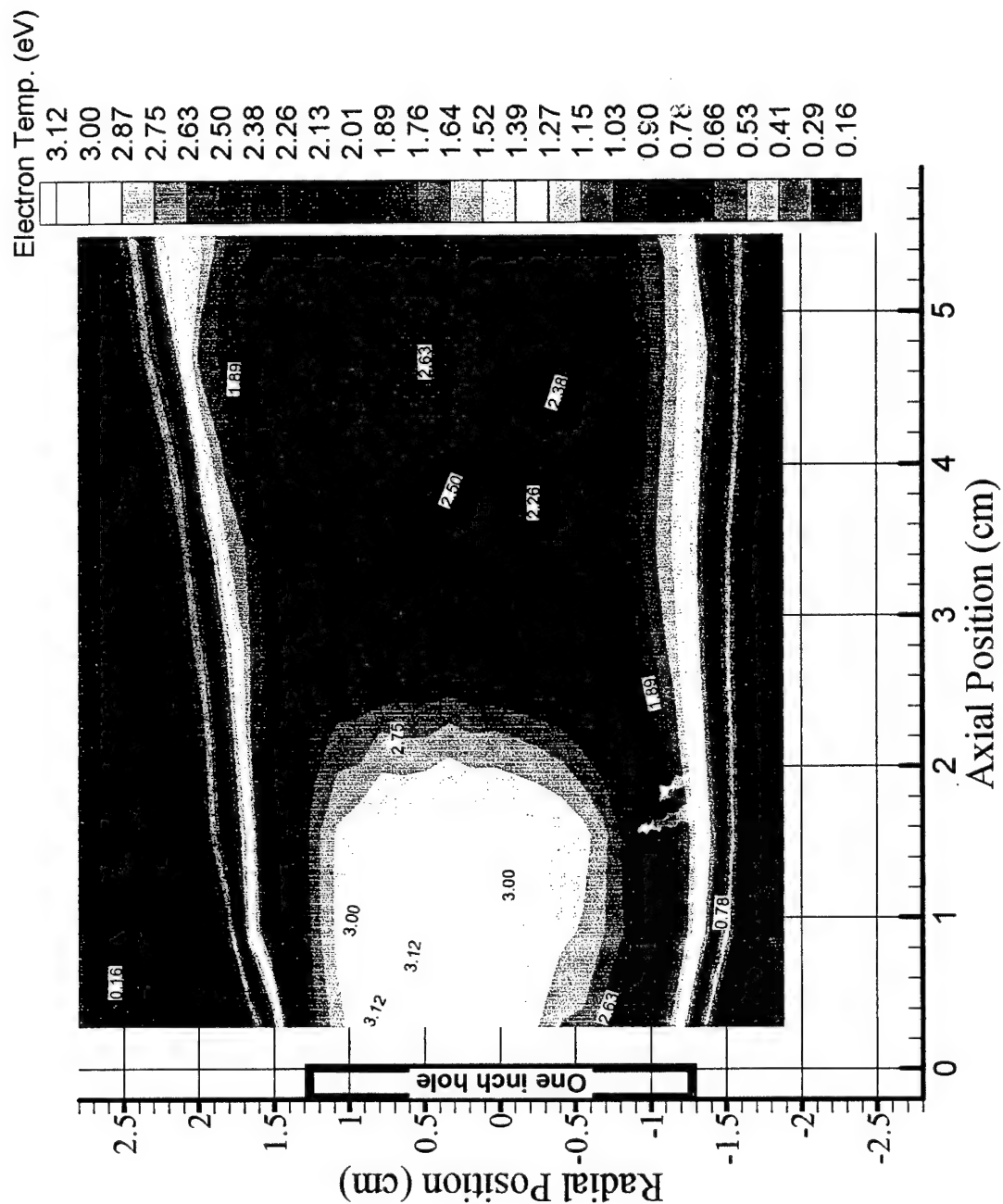


Figure 5.15. Electron temperature profiles for carbon dioxide with no nozzle.

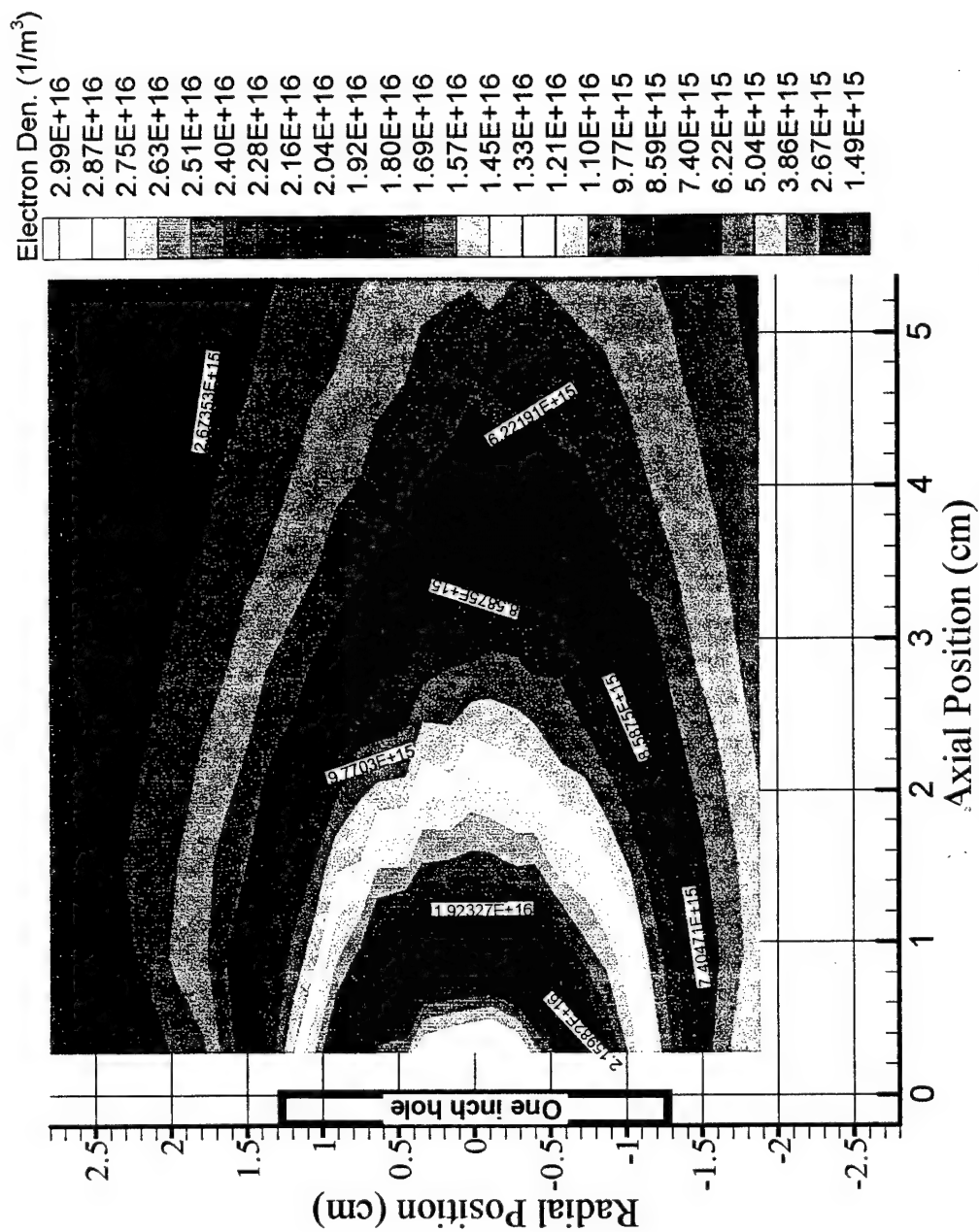


Figure 5.16. Electron density profile for helium with no nozzle.

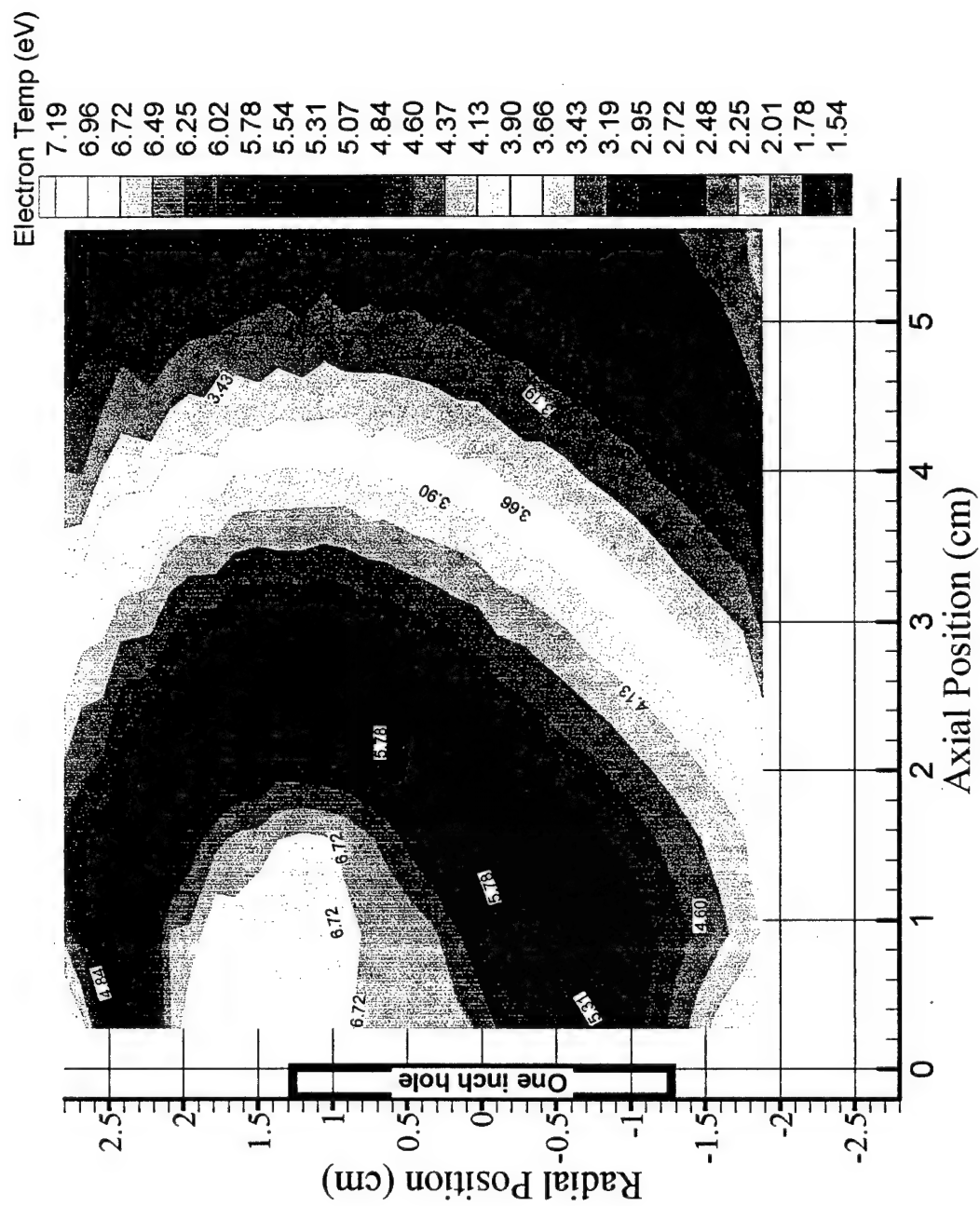


Figure 5.17. Electron temperature profile for helium with no nozzle.

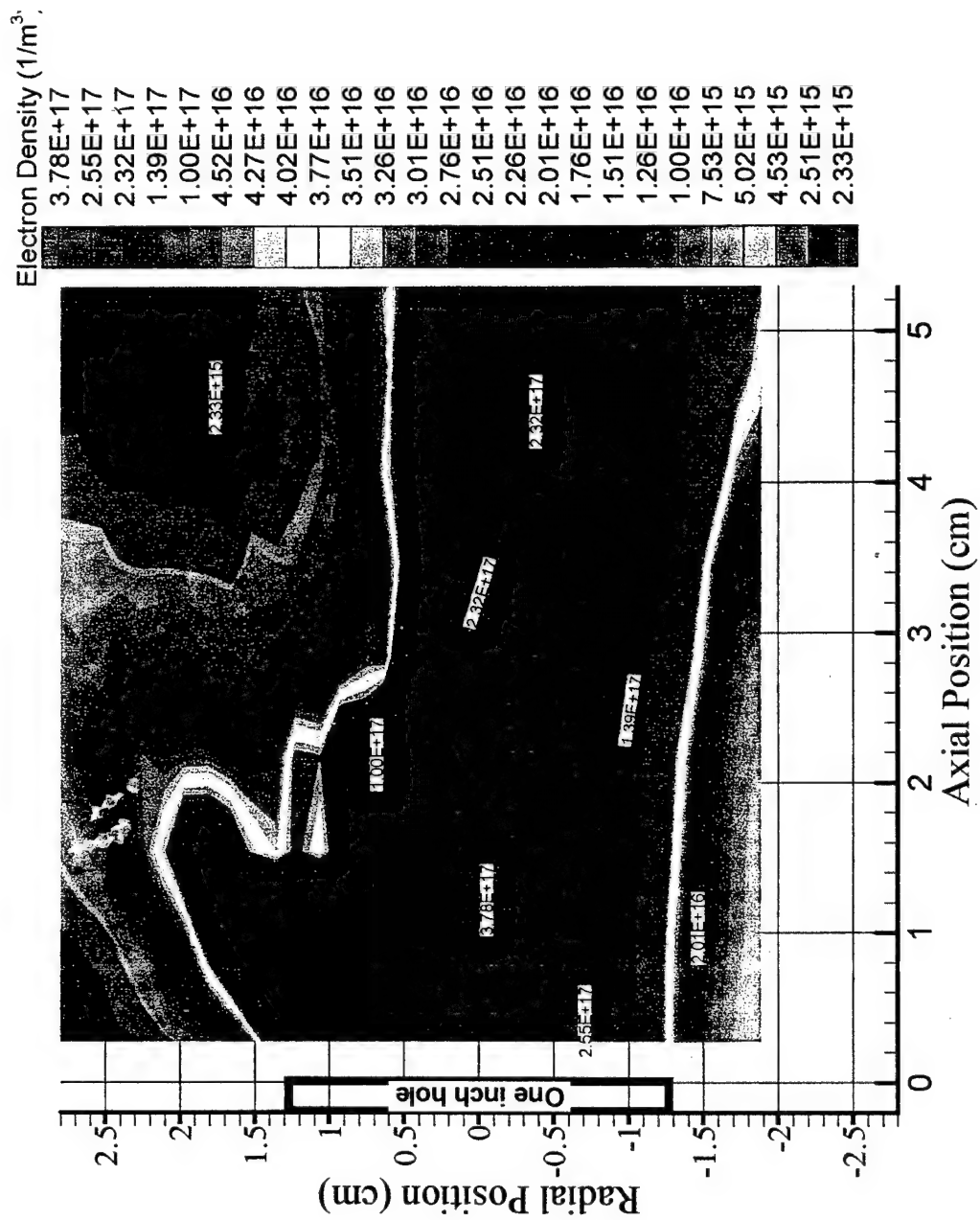


Figure 5.18. Electron density profile for argon with no nozzle.

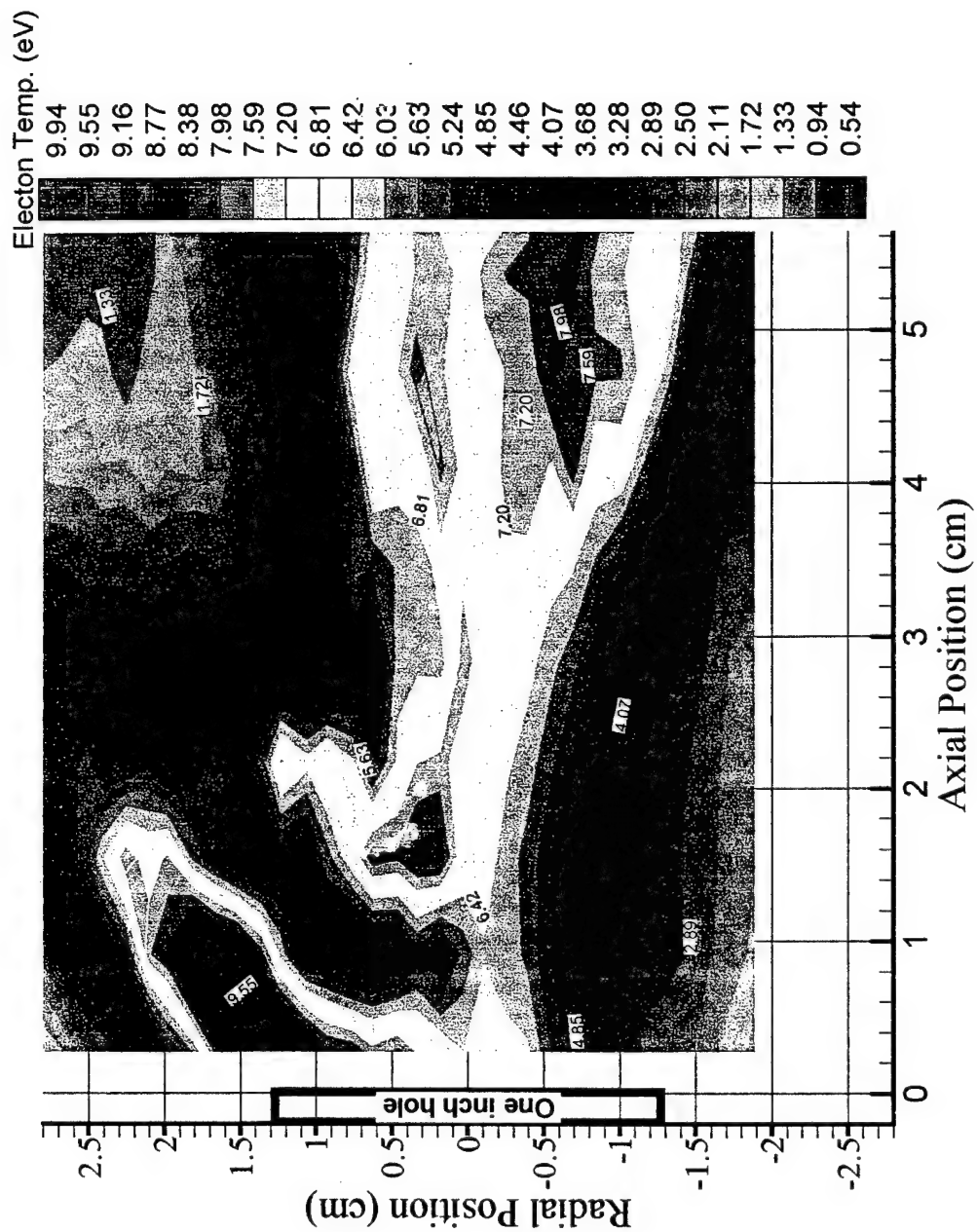


Figure 5.19. Electron temperature profile for argon with no nozzle.

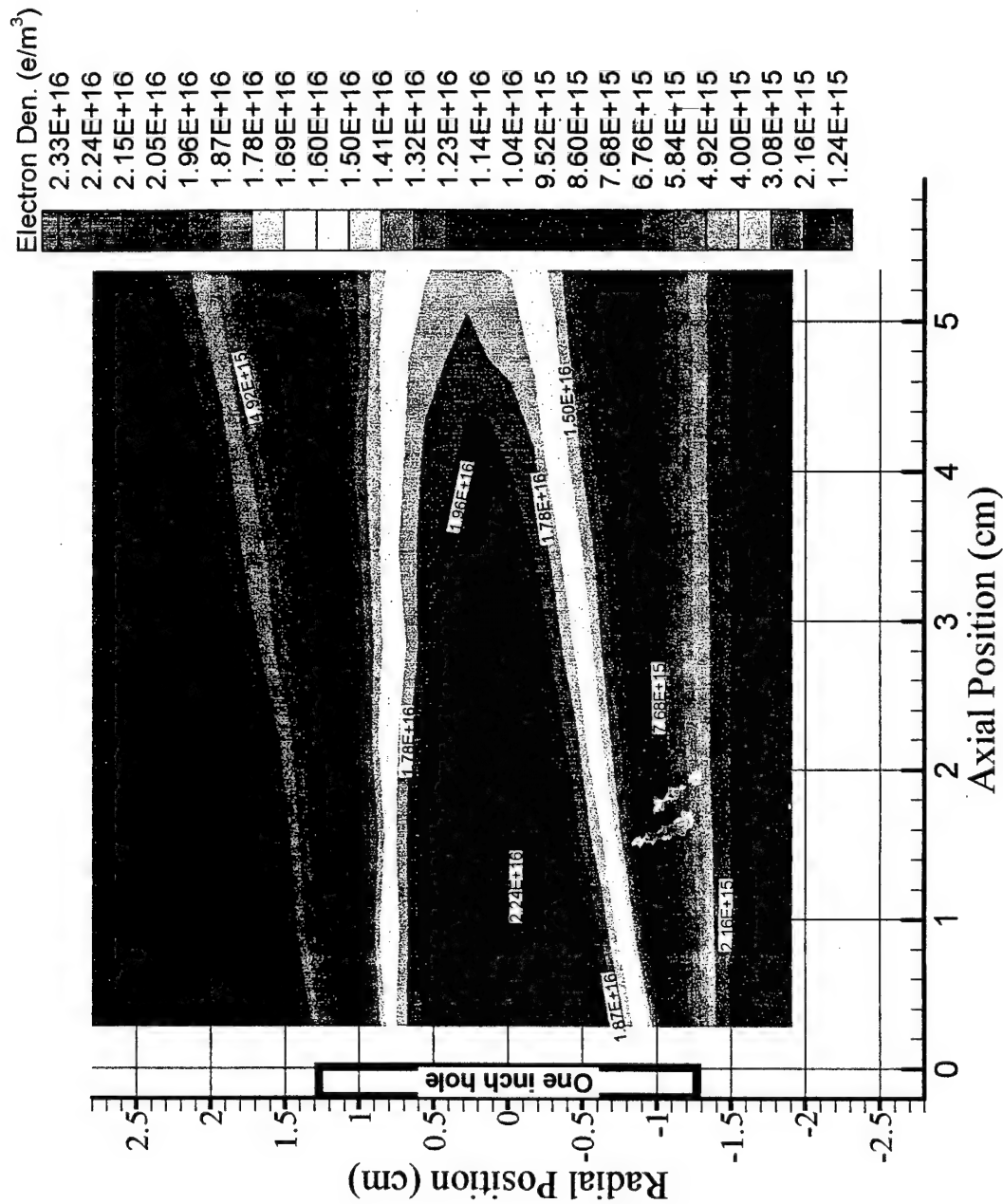


Figure 5.20. Electron density profile for nitrogen with no nozzle.

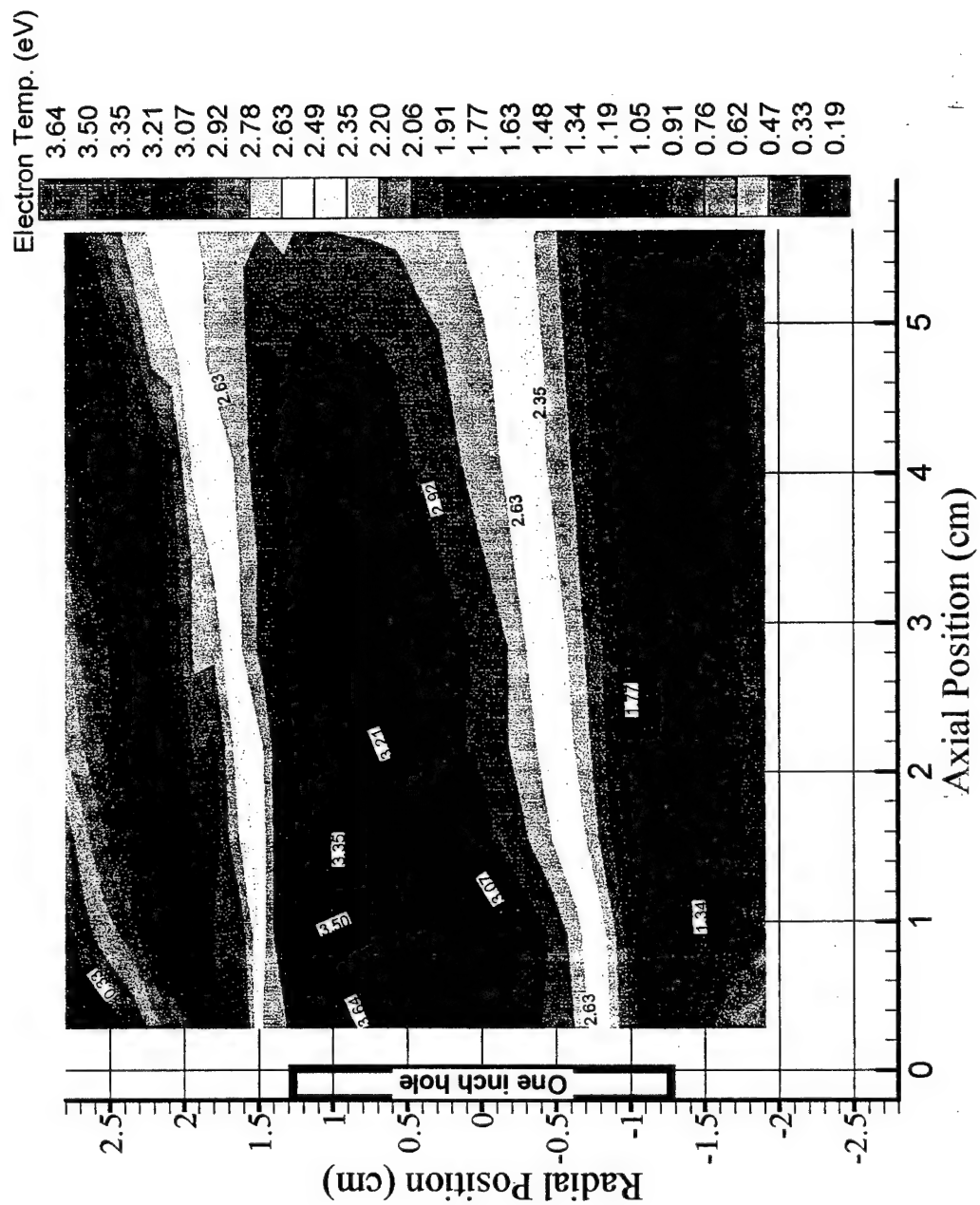


Figure 5.21. Electron temperature profile for nitrogen with no nozzle.

### 5.3.1 Radial Profiles

Radial profiles of electron density and temperature 3 mm from the exit of the microwave resonant cavity are compiled respectively in Figures 5.22 and 5.23 for carbon dioxide, nitrogen, helium and steam. Argon which has the lowest collision cross section and an electron energy loss factor of one reaches electron densities of  $3.5 \times 10^{17}$ . The magnitude of electron density for each gas decreases with increased collision cross section and energy loss factors.

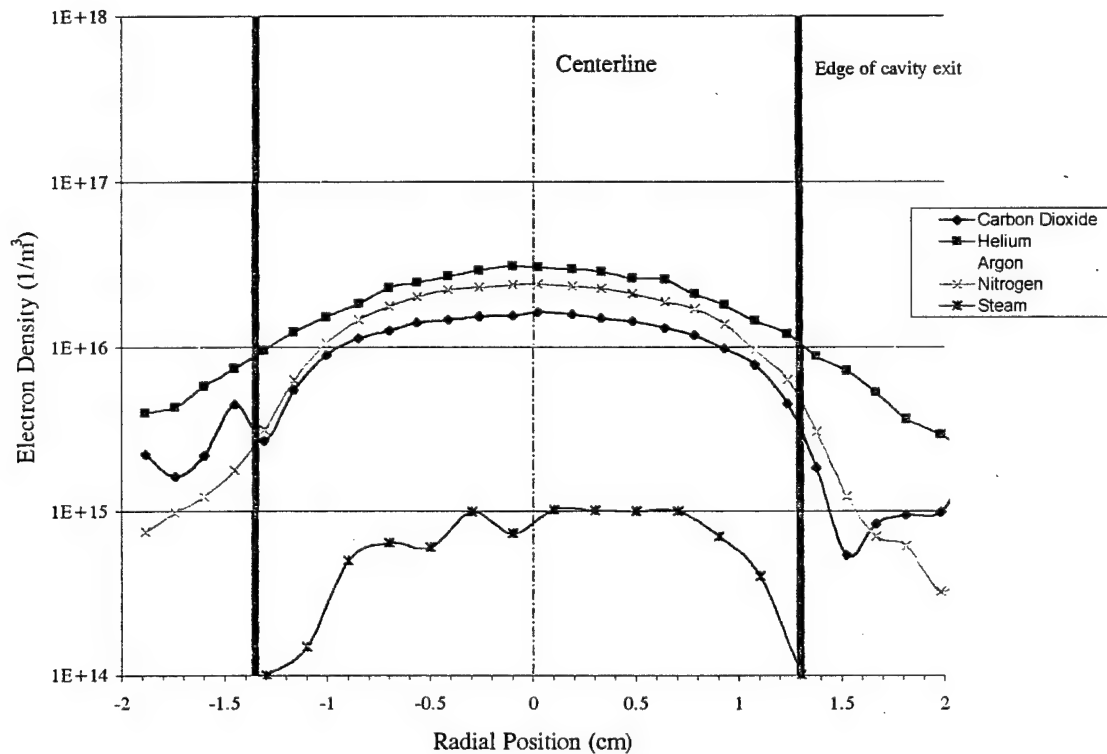


Figure 5.22. Radial electron temperature profiles at the exit for various gases.



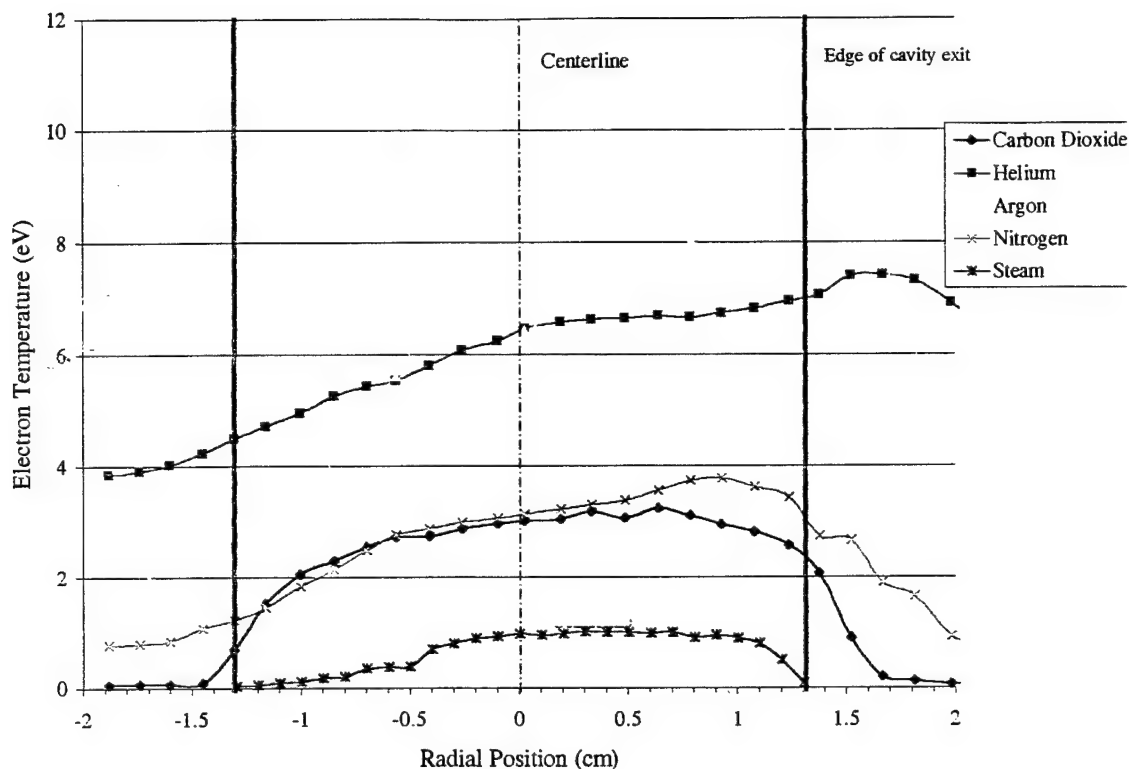


Figure 5.23. Radial electron density profiles at the exit for various gases.

### 5.3.2 Axial Profiles

Axial profiles of electron temperature and density are shown respectively in Figures 5.24 and 5.25 for argon, helium, carbon dioxide, nitrogen and steam. The axial profiles for the temperature of the gas are given in Figure 5.26. The electron temperature decreased as the probe was moved away from the exit of the cavity. The electron temperature for carbon dioxide and helium experienced the most rapid decrease. The decrease in electron temperature for carbon dioxide is due to its large electron loss factor ( $\delta = 2,000$ ), although the shocks present in the plume raise the electron temperature again. The decrease in electron temperature for helium is most likely due to the higher back pressure in the chamber when operating with helium. The higher back pressure caused the plume to break up sooner for helium than for other gases.

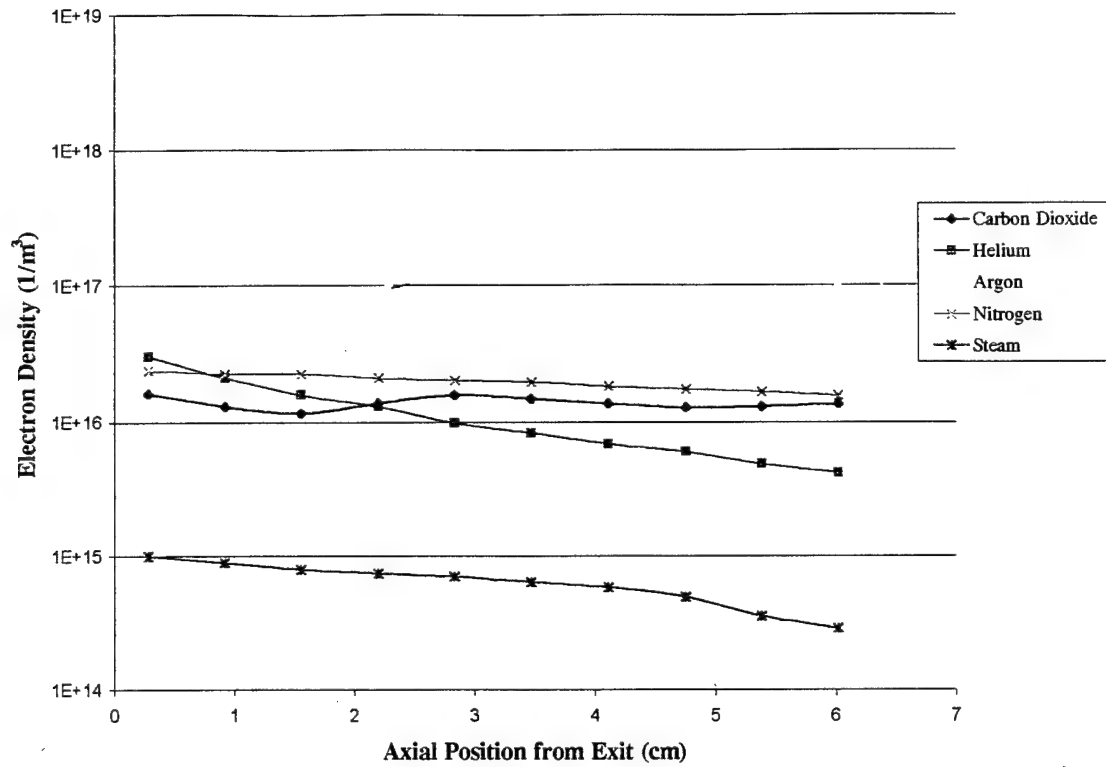


Figure 5.24. Axial scan of electron density for various gases.

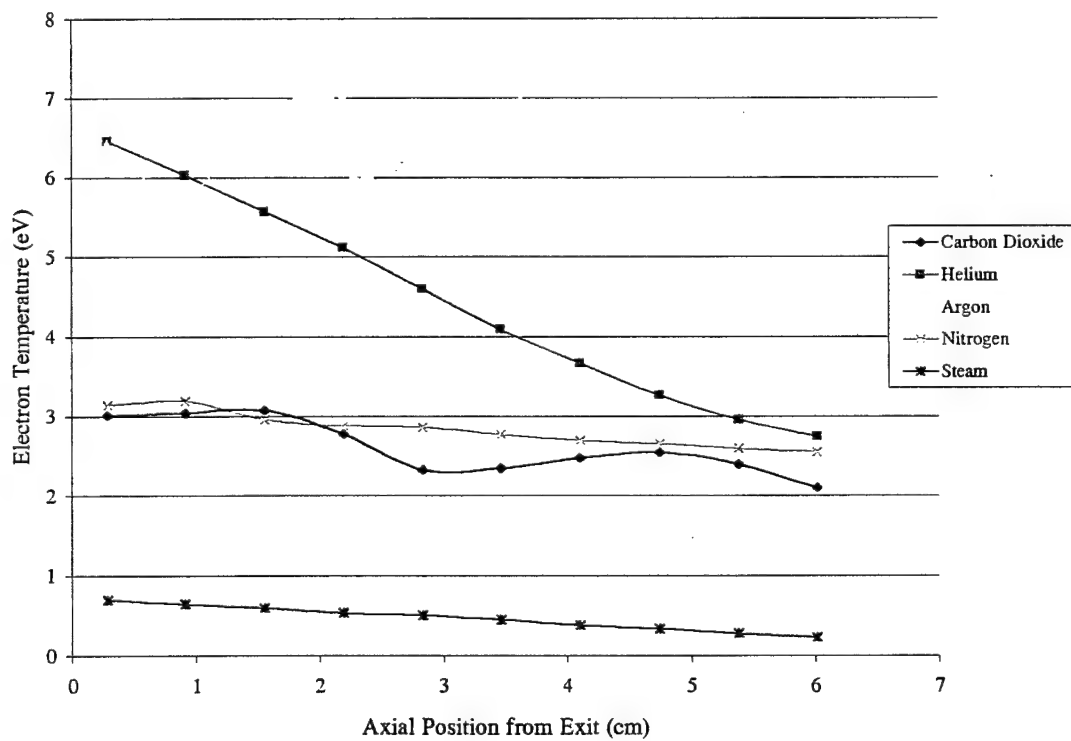


Figure 5.25. Axial scan of electron temperature for various gases.

The electron temperature for steam varied smoothly from 0.6 eV at the exit to 0.2 eV, 3 inches from the exit. The swirl in the flow for argon shows up clearly in the variation of electron temperature. The shocks in the carbon dioxide profile can be seen at approximately 1.5 cm and 5 cm from the exit. Notice that this shows up as peaks in the electron temperature profile and troughs in the electron density profile.

The electron density decreases rather slowly as you move axially away from the exit of the cavity. The electron density may be maintained by the high energy electrons within the plume. The electron density for helium decreases rapidly due to the higher back pressure. The increase in electron density in argon is due to the swirl in the flow as seen in Figure 5.18.

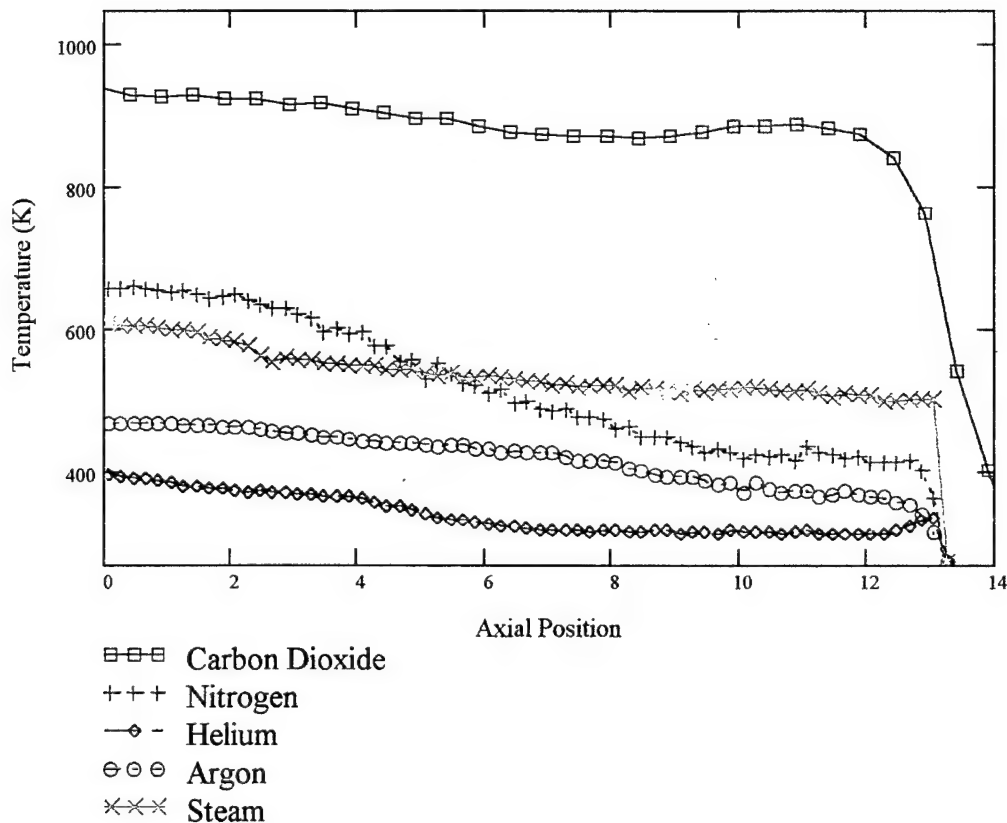


Figure 5.26. Axial gas temperature profiles.

The axial gas temperature scans shown in Figure 5.26 provide additional insight. The temperatures of carbon dioxide and steam decrease only slightly. The temperature of nitrogen decreases slowly for a short distance and then drops off rather quickly. These trends correlate with the electron loss factors which are a function of electron temperature. For carbon dioxide and steam, the electron loss factor is large and relatively constant. Thus, the energy stored in non-equilibrium ionization maintains the gas temperature through collisions with electrons.

## CHAPTER 6

### DISCUSSION OF RESULTS

#### 6.1 Non-equilibrium Ionization

Thermodynamic equilibrium calculations were performed at the gas temperatures measured in these experiments (500-1,500K). At these temperatures the number of free electrons is lower than the sensitivity of the thermodynamic equilibrium code, TEP<sup>TM</sup> (mole fractions less than  $10^{-6}$  are not reported), used to calculate equilibrium conditions. Gas stream temperatures greater than 2,000 K are needed to obtain significant ionization, unless the flow is seeded with an easily ionizable seed, such as cesium or potassium. Thus, the measured electron densities are almost entirely due to the microwave fields. The fact that electron densities over  $10^{17}$  e/m<sup>3</sup> were achieved at gas temperatures below 1,000 K is very promising for potential MHD applications.

In the past, arcjets have been utilized as ionization sources for MHD accelerators [Demetriades, 1960]. Recent measurements of electron temperature and density in low power arcjet plumes yielded electron densities over  $10^{18}$  e/m<sup>3</sup> with electron temperatures between 6,000 K and 8,000 K [Bufton, 1996]. However, the gas temperature in these plumes was 3,000-6,000 K; thus, the electron density was much closer to the equilibrium value expected at the gas temperature.

The lower gas temperatures obtained in the present study provide many benefits, but electron densities closer to that obtainable in arcjets are desirable. The critical electron density is defined as the density for which the plasma frequency is equal to the excitation frequency, 2.45 GHz for this study. The plasma frequency is given by

$$\omega_p = \sqrt{\frac{n_e q_e^2}{\epsilon_0 m_e}}. \quad (6.1)$$

Thus, the critical density for our experiments is  $n_{e,crit} = 7.45 \times 10^{16} \text{ e/m}^3$ . An electron density of  $3.8 \times 10^{17} \text{ e/m}^3$  was measured for argon at the exit of the microwave resonant cavity. Therefore, electron densities well over the critical plasma density and comparable to the densities reached in arcjets are achievable in monatomic gases through microwave excitation. The electron densities at the exit for nitrogen and carbon dioxide ( $4.6 \times 10^{16}$  and  $1.6 \times 10^{16} \text{ e/m}^3$ , respectively) are below the critical density. The electron density of steam ( $1 \times 10^{15} \text{ e/m}^3$ ) is well below the critical density.

Electron densities in Fabrey-Perot type pulsed microwave discharges have been measured as high as  $10^{22} \text{ e/m}^3$ , about four orders of magnitude above the critical density [Bohm, 1993]. Unfortunately, when the critical plasma frequency was reached in our resonant cavity, the plasma reflected the incident power. It may be possible however to operate a pulsed microwave discharge within the MHD channel to take advantage of the high electron densities recorded by Bohm.

The power required to maintain a non-equilibrium state can be calculated using Equation 2.5. This was calculated using the experimentally measured axial electron temperature and density profiles and the electron loss factors and collision cross section given in Figures 2.1 and 2.2, respectively. As expected, the power required to maintain the non-

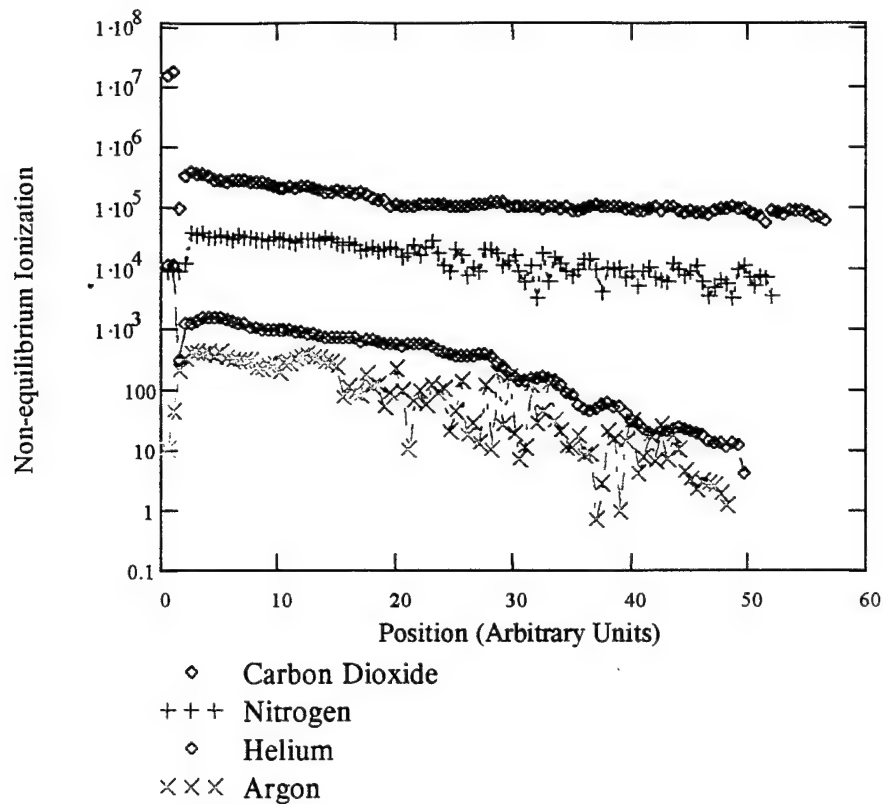


Figure 6.1. Power required to maintain a non-equilibrium electron temperature.

equilibrium conditions is greatest for carbon dioxide and lowest for argon as shown in Figure 6.1.

It was also of interest to determine if Saha's equation based on electron temperature could predict the electron density from the measured electron temperature. For the nozzle tests, Saha's equation predicted the right order of magnitude. However, for the open cavity test Saha's equation predicts electron densities several orders of magnitude higher than the measured densities near the exit to the cavity. The electron temperature in the open cavity tests is 1 to 2 eV higher than electron temperatures measured in the nozzle plumes. One reason for this may be the reduced chamber pressure in the open cavity tests. Local thermodynamic equilibrium may not be maintained at lower pressures. In fact, Schluter has reported that "for

pressures of about 100-2000 mTorr the approximation by Maxwellian electron distribution functions is certainly to be ruled out" [Schluter, 1993]. Our pressure regime is between 100-2000 mTorr and the condition of a Maxwellian distribution is required by Saha's equation. In order to account for the effects of Non-Maxwellian distributions, collisional-radiative models must be used along with self-consistent solutions of the Boltzmann equation [Schluter, 1993; Wu, 1968]. The focus of this work was experimental; therefore, this theoretical solution was not pursued.

## 6.2 MHD Efficiency

From the measured electron temperature and density, the conductivity of the plasma can be calculated using Equation 2.6. With the conductivity, the efficiency of a cross-field and Hall accelerator can be predicted. For an applied magnetic field of 0.5 Tesla and a current density of 5 amps/cm<sup>2</sup> the ideal efficiencies are given in Table 6.1.

Table 6.1. Cross-field and Hall accelerator efficiencies.

Gas	Q(10E-16 cm <sup>2</sup> )	$\sigma$ (mho/m)	$\omega\tau$	$\eta$	$\eta_{\text{Hall}}$
Argon	1	81	182	19.6	16.7
Helium	2	41	169	10.5	16.7
Nitrogen	7	1.2	51	0.35	16.7
Carbon Dioxide	10	0.82	43	0.25	16.7
Steam	30	0.03	35	0.08	16.7

The efficiencies for argon and helium may provide adequate performance, but the efficiencies for nitrogen, carbon dioxide, and steam are far too low. Also, limiting the current density to 5 amps/cm<sup>2</sup> may not allow the power densities required for space missions to be



accomplished. The Hall channel efficiencies look promising, but voltages in the 10 kV range must be applied.

Following the analysis outlined in the Appendix, the mass saving can be calculated assuming the efficiencies in Table 6.1 are reached. A solar steam rocket operating with a specific impulse of 300 sec and 1 N thrust will have an initial mass in low earth orbit (IMLEO) of 64 MT to deliver a 5 metric ton (MT) payload to geosynchronous (GEO) orbit. An MHD system can cut the IMLEO to 14.4 MT when operated at the optimum specific impulse for a specific mass of 19 kg/kW and an efficiency of 16.7%.

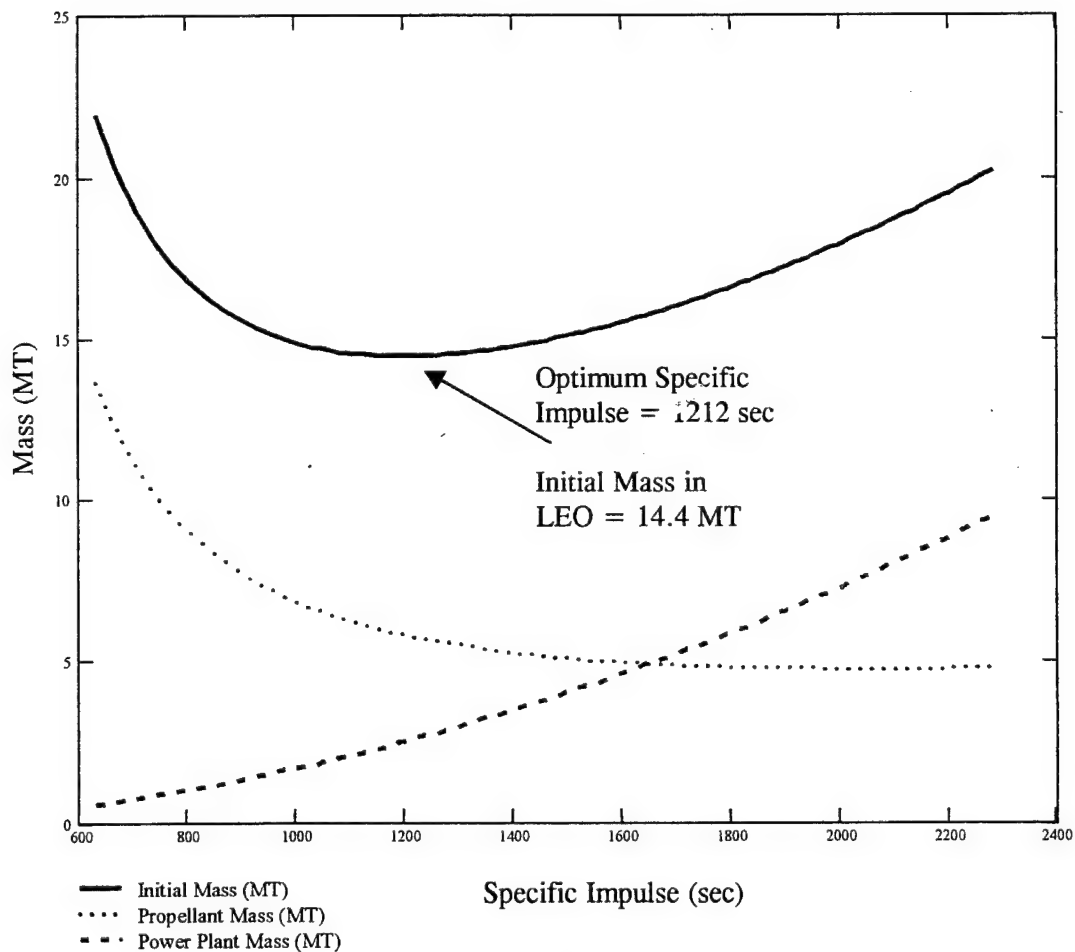


Figure 6.2. Initial mass in low earth orbit, propellant mass, and power plant mass versus  $I_{sp}$  for an accelerator efficiency of 16.7%.

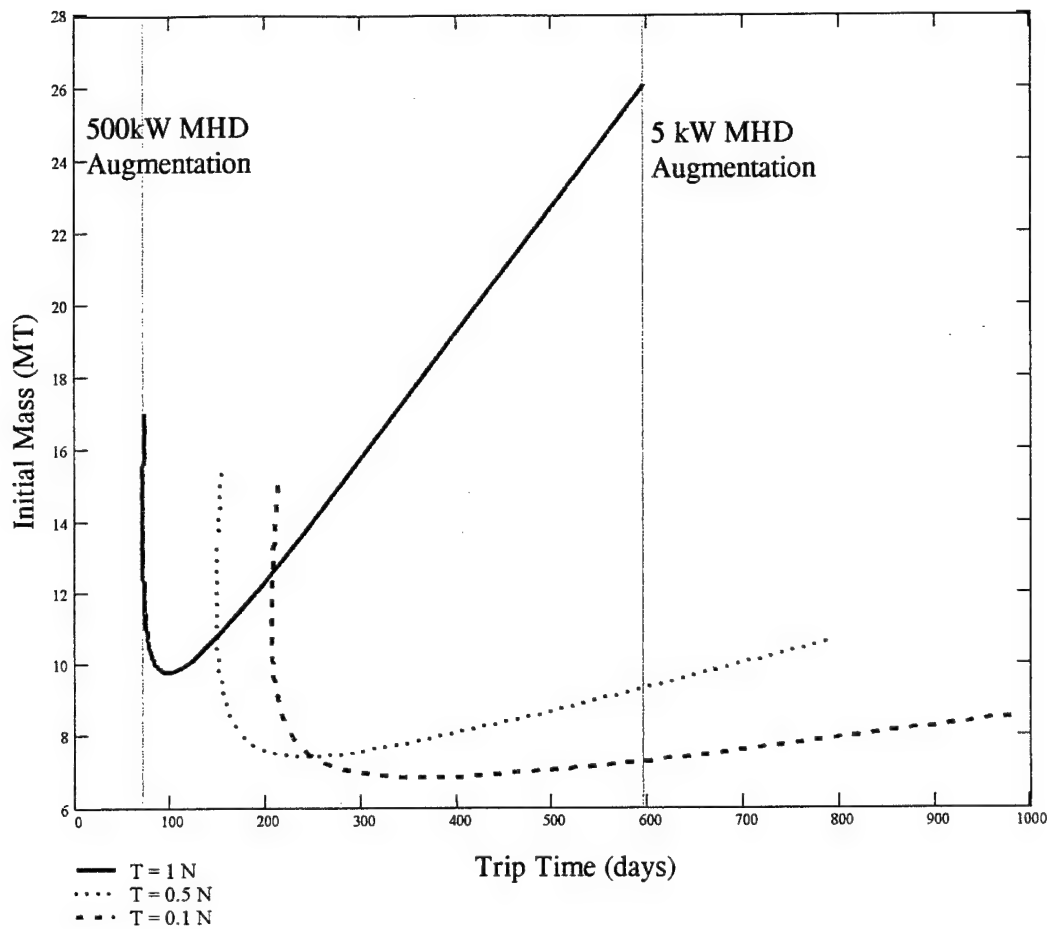


Figure 6.3. Initial mass versus trip time.

The trip time required when operating at the optimum specific impulse given in Figure 6.2 is over 200 days. This lengthy transfer time is not practical for most missions. It is desirable to cut the trip time below 100 days for a LEO to GEO transfer. This can be done in several ways. First, the energy used for the MHD accelerator can be used to heat a much higher mass flow rate thermally, thus a higher thrust can be obtained. If the thrust is increased to 100 N for the solar steam rocket, the trip time is reduced to 16.7 days, but recall the IMLEO is 64 MT. Second, the steam can be replaced with hydrogen, increasing the specific impulse to 860 sec, resulting in a trip time of 4 days. Third, an alternate microwave source, such as that

used by Bohm can be used to increase efficiency of the MHD accelerator. Figure 6.3 shows that trip times can be reduced to under 100 days, while the IMLEO is reduced to under 10 MT. For lower thrust levels even greater mass savings can be realized at the expense of increased trip times. An accelerator efficiency of 70% is used for all thrust levels reported in Figure 6.3.

### 6.3 Benefits to MHD Devices

The gas temperatures measured in the open cavity tests are a factor of 2 to 5 below typical operating temperatures for MHD devices. The ability to operate at low gas temperature may substantially reduce heat losses to the walls and electrode erosion.

Even though efficiencies for carbon dioxide and steam are low, no other ionization source can provide this level of conductivity in these propellants at this temperature. In fact, most ionization sources experience severe erosion due to oxidation when using steam. The addition of low ionization potential seed may improve the efficiency with steam and carbon dioxide to acceptable levels. The Hall channel offers the possibility of higher efficiencies if the applied voltage can be managed to limit instabilities and arcing.

The broad electron temperature profiles measured in the radial scans of both the nozzles and the open cavity tests indicated that high-energy electrons exist beyond the viscous core flow. Demetriades [1960] used this effect to pass current from MHD electrodes through the boundary layer without contacting the high momentum core. The presence of an electron boundary layer in the present tests suggests the same possibility for an accelerator coupled to the microwave resonant cavity.

## CHAPTER 7

### CONCLUSIONS AND RECOMMENDATIONS

#### 7.1 Conclusions

The objective of this work was accomplished by characterizing the plumes of a 2.45 GHz microwave generated plasma with various working fluids and under various operating conditions. The plume measurements were used to assess the feasibility of coupling a MHD accelerator to the microwave cavity. Magnetohydrodynamic accelerator efficiencies were calculated for two accelerator configurations based on the measured data.

Six major conclusions can be drawn from the experimental data:

1. Non-equilibrium plasmas with electron temperatures an order of magnitude higher than the gas temperature can be created with the microwave plasma generator.
2. The critical plasma density can be reached for monatomic propellants.
3. For diatomic and polyatomic molecules, the maximum electron density is an order of magnitude below the critical density.
4. High-energy electrons are present beyond the viscous core flow.
5. Hall parameters greater than 50 can be expected in an MHD channel coupled to the microwave cavity.

6. Measured gas temperatures below 1000 K were measured with electron densities greater than  $10^{15}$  e/m<sup>3</sup> even for the worst case of steam.

The implications of these conclusions will affect the design and development of a prototype MHD accelerator utilizing a microwave ionization source. At the outset of this work it was assumed that a segmented cross-field channel or Faraday MHD channel would be used. The fact that Hall parameters greater than 50 can be expected for all gases tested make this an impractical solution, because Faraday channels are designed to operate with Hall parameters less than 1. For the expected Hall parameters, efficiencies and thrust levels comparable to the Faraday channel can be achieved with a Hall channel configuration. This coupled with the fact that a Hall channel can be operated with a single power supply makes it the configuration of choice for this system.

No MHD accelerator has ever been operated at gas temperatures less than 1000 K. This should result in increased efficiency and extended electrode life. Boundary layer voltage drops and heat loss to the walls will be reduced.

Top-level systems analysis show that an MHD augmented system can reduce the IMLEO for a solar steam rocket by over 400%, if efficiencies calculated for the Hall channel can be achieved. For trip times to be reduced to acceptable levels, efficiencies approaching 70% need to be achieved. This may be possible if the current microwave resonant cavity is replaced with a Fabrey-Perot type resonator, which has demonstrated electron densities four orders of magnitude above the critical density. This possibility makes the pursuit of an MHD accelerator operating on steam available as waste water from the shuttle a competitive option for in-space propulsion systems.

## 7.2 Recommendations

Four areas of focus are of particular interest based on the results of this work.

1. Alternate microwave resonant cavity configurations should be implemented in both pulsed and steady state configurations and higher frequency microwave sources should be tested. This will raise the critical electron density and may allow operations at electron densities well above the critical density as reported in the literature.
2. Low ionization potential seed should be used with carbon dioxide and steam in an attempt to reach the critical density for a 2.45 GHz source. The addition of a seedant may increase the conductivity of the MHD accelerator to acceptable levels.
3. A Hall channel MHD accelerator should be coupled with the microwave plasma generator. Operation of an MHD accelerator with highly non-equilibrium propellants at low pressure will determine the extent of Hall current and ion slip. Actual operation of a Hall channel accelerator under these conditions has never been reported. The determination of efficiency and operating voltages are necessary to truly assess feasibility.
4. It is recognized that the diagnostic techniques used in these experiments were intrusive. A considerable amount of diagnostic equipment has been obtained for non-intrusive laser and microwave based diagnostics. The implementation of these techniques will provide more accurate measurements of thermodynamic and electrical transport properties.

## APPENDIX

This appendix presents a generic trade study for MHD augmented propulsion systems. No attempt is made to define a specific system. Masses for a solar thermal source of thermal energy and a nuclear electric power plant are used as examples. Optimum specific impulses are calculated for typical low earth orbit (LEO) to geosynchronous (GEO) transfers, as well as Mar's missions.

The trade study reveals a unique operating regime at lower thrust levels. Substantial mass savings are realized over conventional chemical, solar, and electrical propulsion concepts when MHD augmentation is used to obtain optimal  $I_{sp}$ . However, trip times for the most conservative estimates of power plant specific impulse and accelerator efficiency may be prohibitively long. Quasi-one-dimensional calculations show that a solar or nuclear thermal augmented system can provide competitive performance while utilizing a diverse range of propellants including water, which is available from the Space Shuttle, the Moon, asteroids, and various moons and planets within our solar system [Pryor, 1999]. The use of in-situ propellants will reduce costs of space operations as well as enable human exploration of our Solar System.

The following conclusions can be drawn from the results of the mission trade study:

- There exists a maximum thrust or mass flow rate above which MHD augmentation increases the initial mass in low earth orbit (LEO).

- Mass saving of over 50% can be realized for a unique combination of solar or nuclear/MHD systems.
- Trip times for systems utilizing current power supply technology may be prohibitively long. Theoretical predictions of MHD performance for in-space propulsion systems show that improved efficiencies can reduce trip times to acceptable levels.
- Long trip times indicative of low thrust systems can be shortened by an increase in the MHD accelerator efficiency or a decrease in the specific mass of the power supply and power processing unit.
- As for all propulsion concepts, missions with larger  $\Delta v$ 's benefit more from the increased specific impulse resulting from MHD augmentation.

#### Formulation of Optimization Equation and Assumptions

As with any electric propulsion system, MHD augmented systems have an optimal specific impulse. The optimum specific impulse is a result of the mass of the power supply increasing faster than the decrease of the propellant mass resulting from the increased specific impulse. Figure A.1 shows the relationship between the initial mass of a spacecraft, the power supply mass, and the mass of the propellant.



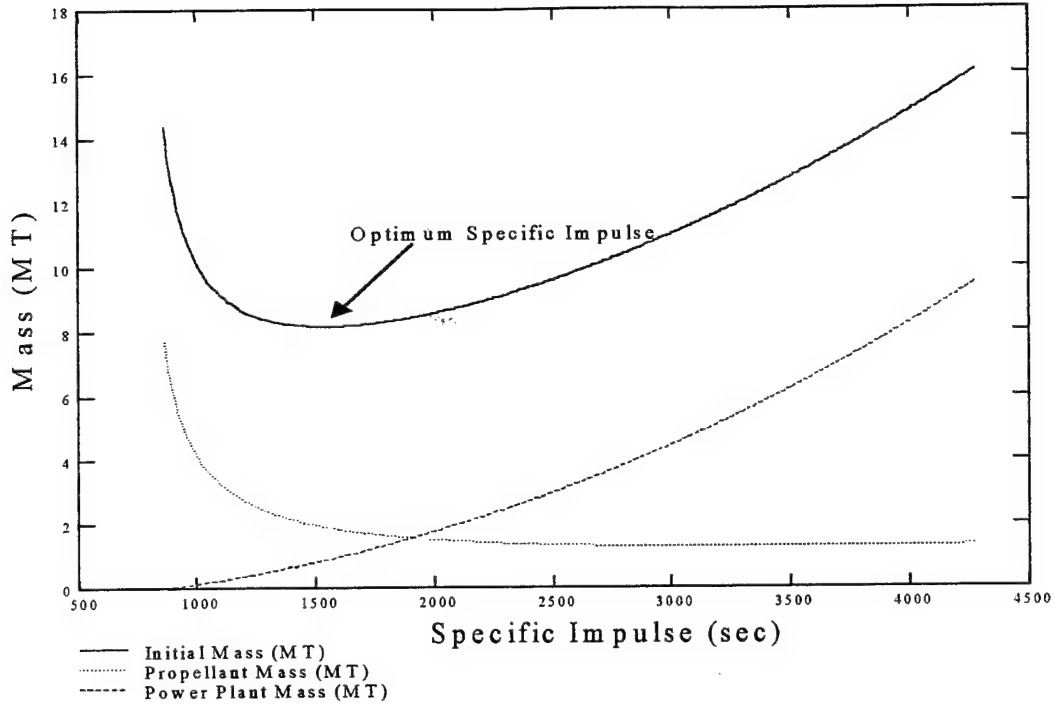


Figure A.1. The relationship between the initial mass, power plant mass, and propellant mass.

The kinetic power of the exhaust jet is given by

$$P_{jet} = \frac{1}{2} g T I_{sp}, \quad (A.1)$$

where  $T$  is the thrust of the rocket,  $g$  the acceleration of gravity at the earth's surface, and  $I_{sp}$  is the specific impulse of the rocket. The corresponding mass flow rate is then given by

$$\dot{m} = \frac{2P_{jet}}{(gI_{sp})^2}. \quad (A.2)$$

Keeping the mass flow rate constant, the jet power of the MHD system for a given bus power and efficiency of conversion ( $\eta$ ) of bus power to kinetic energy in the exhaust is determined by

$$P_{jet\_MHD} = P_{jet} + P_{bus} \eta . \quad (A.3)$$

Then the specific impulse of the MHD augmented system is simply

$$I_{sp\_MHD} = \frac{1}{g} \sqrt{\frac{2P_{jet}}{\dot{m}}} . \quad (A.4)$$

Likewise the thrust of the MHD augmented system is obtained by

$$T_{MHD} = \dot{m} g I_{sp\_MHD} . \quad (A.5)$$

With the thrust and specific impulse of the MHD augmented system defined as functions of the thrust and specific impulse of the unaugmented rocket, electrical bus power, and efficiency of the MHD system, the performance of the system can be examined. In order to do so, the mass of the propulsion system and the electrical power plant must be defined. The electrical power plant mass is simply

$$m_{elect} = \alpha P_{bus} , \quad (A.6)$$

where  $\alpha$  is the specific mass of the of the power system. In this study the mass of the power-processing unit has been included in  $\alpha$ . It was assumed that a SP-100 nuclear power system was available to deliver the electrical power. The specific mass of this system is 12 kg/kW. The specific mass of the power processing and conditioning system was set at 7 kg/kW, giving  $\alpha = 19$  kg/kW [Frisbee and Hoffman, 1993]. The effect of decreasing the specific mass of the power supply ( $\alpha$ ) will also be examined.

The mass of the solar thermal system can be broken up into two parts, the mass of the mirrors or concentrators and the mass of the thermal rocket engine. For a lightweight continuous thrust system the mass scaling is given by

$$m_{STR} = 0.125 T^{1.15}, \quad (A.7)$$

where the thrust,  $T$ , is in Newtons [Etheridge, 1979]. Marshall Space Flight Center has also used the following scaling for solar thermal systems, which utilize an energy storage and burn technique [Van Dyke, 1996].

$$m_{STR\_S} = 6.38 T, \quad (A.8)$$

The mass of the concentrator array can be expressed as

$$m_{array} = 6.34 T. \quad (A.9)$$

The dry mass of the vehicle can then be calculated as

$$m_{dry\_STR} = TF m_{prop} + m_{elect} + m_{STR} + m_{array}, \quad (A.10)$$

where  $TF$  is the tankage fraction for a given propellant. The mass of the vehicle at burnout is the sum of the payload mass plus the dry mass.

$$m_{b\_STR} = m_{dry\_STR} + m_{pl} \quad (A.11)$$

The process of determining the initial mass of the spacecraft and propulsion system involves an iterative procedure. First, the required mass of the propellant is estimated. Using this estimate, the initial mass can be calculated by the rocket equation.

$$m_0 = m_{b\_STR} \exp\left(\frac{\Delta v}{g I_{sp\_MHD}}\right) \quad (A.12)$$

A new value for the mass of the propellant can be obtained by subtracting the mass at burnout from the mass of the propellant. Mathcad™'s find function, which uses the Levenberg-Marquardt method, was used to converge on a final value for the mass of the propellant. This formulation lets us vary tankage fraction, bus power, specific power, payload mass,  $\Delta v$ ,  $I_{sp}$ , and MHD efficiency.

The mission  $\Delta v$  required for a given mission is a function of the initial thrust to mass ratio, and the number of burns in the case of multiple impulse burn trajectories. The gravity losses associated with very low thrust/to weight ratios can be substantial. The  $\Delta v$  required for a typical impulsive LEO-GEO transfer using a chemical upper stage is 4.2 km/sec, while the same mission utilizing a low thrust to weight ratio must have an effective  $\Delta v$  of over 5.9 km/sec [Spencer and Culp, 1995]. Other studies have shown that the losses due to low thrust to weight ratios may as much as double the required  $\Delta v$ , especially when large plane changes are required, such as LEO-GEO transfers with a 28.5° plane change. A  $\Delta v$  of 6 km/sec was used in this mission trade study for LEO – GEO transfers, which corresponds to a continuous spiral burn.

The ideal trip time required for the transfer is calculated by dividing the required mass of propellant by the mass flow rate.

$$t_{Transfer} = \frac{m_{prop}}{\dot{m}} \quad (A.13)$$

Calculating the transfer time in this manner assumes a continuous burn.

### LEO to GEO Orbit Transfer

The LEO to GEO orbit transfer mission defined for this study delivers a 5,000-kg payload from low earth orbit to geosynchronous orbit. Low thrust mission  $\Delta v$ 's are a function of the thrust to mass ratio of the vehicle. A mission  $\Delta v$  of 6 km/sec was used. Unless otherwise stated, the efficiency of the MHD system was conservatively set at 20%.

To determine how MHD augmentation affects the initial mass of the vehicle, the  $I_{sp}$  of the solar thermal rocket was fixed at 860 seconds and its thrust varied. This is equivalent to varying the mass flow rate of the solar thermal rocket. The variation of the initial mass as a function of the bus power or augmented  $I_{sp}$  is shown in Figure A.1 for an unaugmented thrust of 1, 5, and 10 Newtons. As we increase the thrust or mass flow rate, we quickly decrease the mass savings. Thus, there exists a maximum mass flow rate or thrust above which MHD augmentation will increase the initial mass required to deliver the payload to its desired orbit. For the current mission ( $\Delta v = 6$  km/sec,  $m_{payload} = 5000$  kg,  $\eta = 20\%$ ,  $\alpha = 19$  kg/kW), this maximum thrust is around 7.5 Newtons, which corresponds to a mass flow rate of 0.9 gm/sec. This maximum occurs because the power supply required to obtain a sufficient increase in the  $I_{sp}$  at larger mass flow rates is too large for the mass of propellant saved to compensate for its mass as shown in Figure A.1.

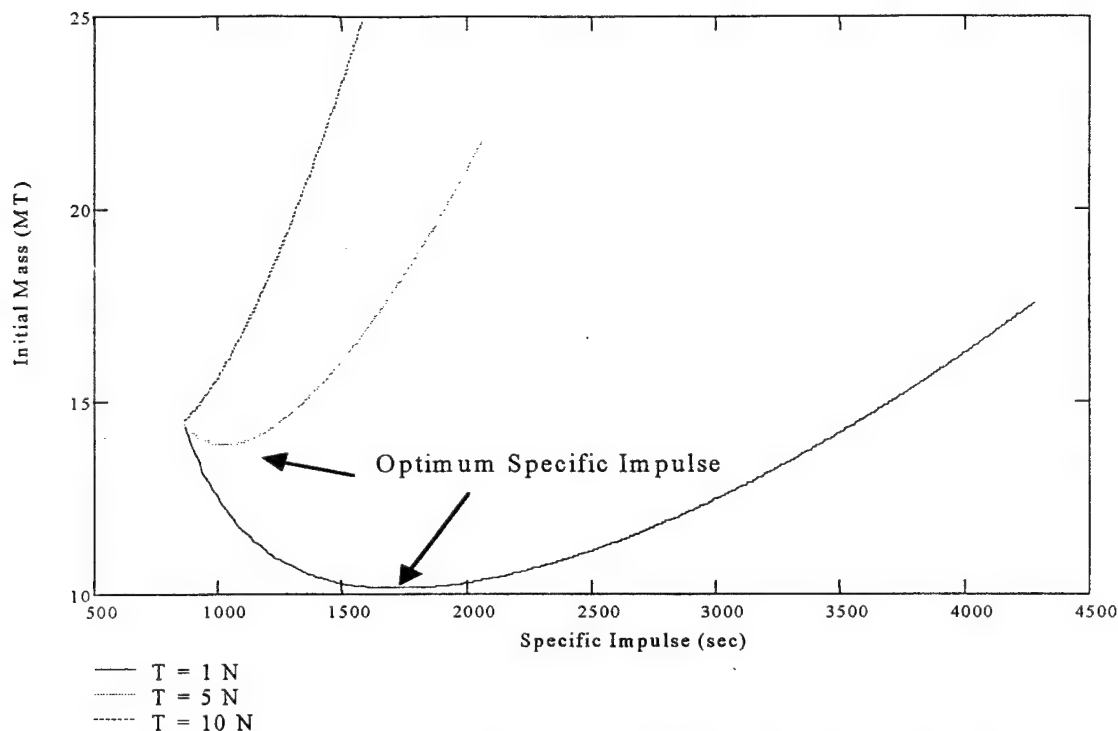


Figure A.2. Initial mass versus  $I_{sp}$  of the augmented STR and the thrust of the STR only.

Flow rates, smaller than the maximum possible flow rate, have an associated optimal  $I_{sp}$  or electrical bus power. Figure A.2 shows an optimal  $I_{sp}$  of 1700 sec for  $T_{STR} = 1$  Newton and 1030 sec for  $T_{STR} = 5$  Newtons. Note that there is no optimal  $I_{sp}$  for  $T_{STR} = 10$  Newtons because it is above the maximum thrust or flow rate. The decrease in initial mass due to MHD augmentation is 4.2 MT for the 1 Newton STR and 0.45 MT for the 5 Newton STR. The power required to achieve the optimal  $I_{sp}$  for the 1 Newton STR is found from Figure A.4 to be 62 kW, while the augmented thrust is increased to 2 Newtons as shown in Figure A.3.

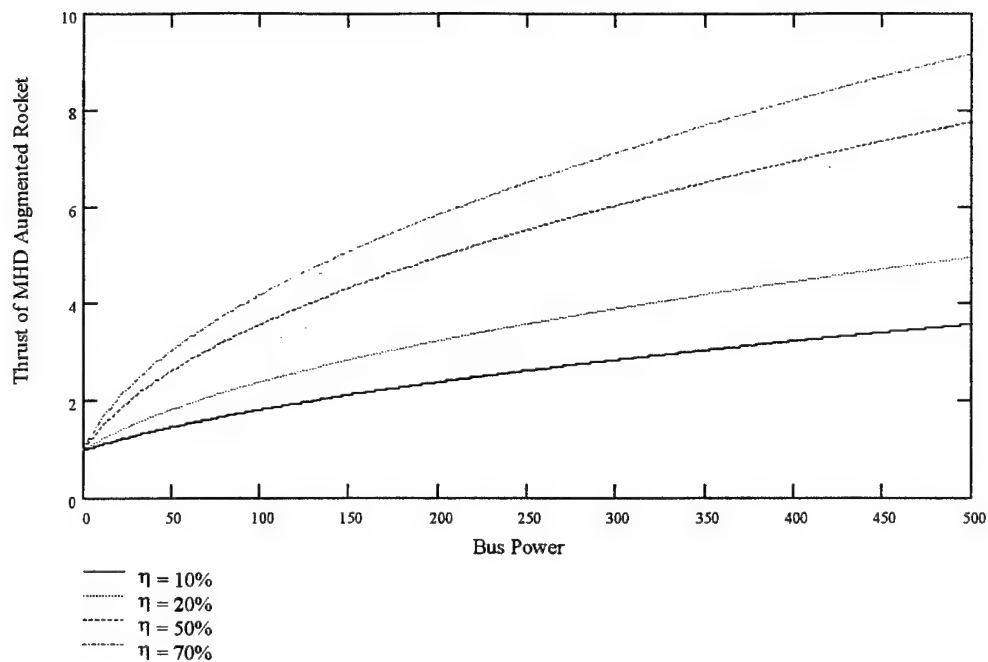


Figure A.3. Thrust of MHD augmented STR versus bus power.

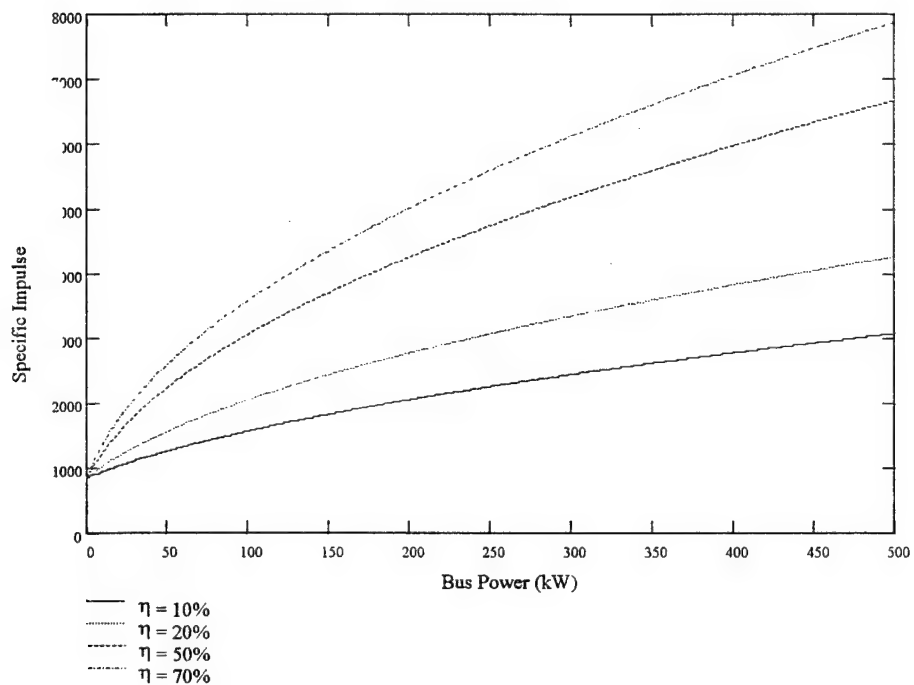


Figure A.4. Specific Impulse of the MHD augmented STR versus bus power.

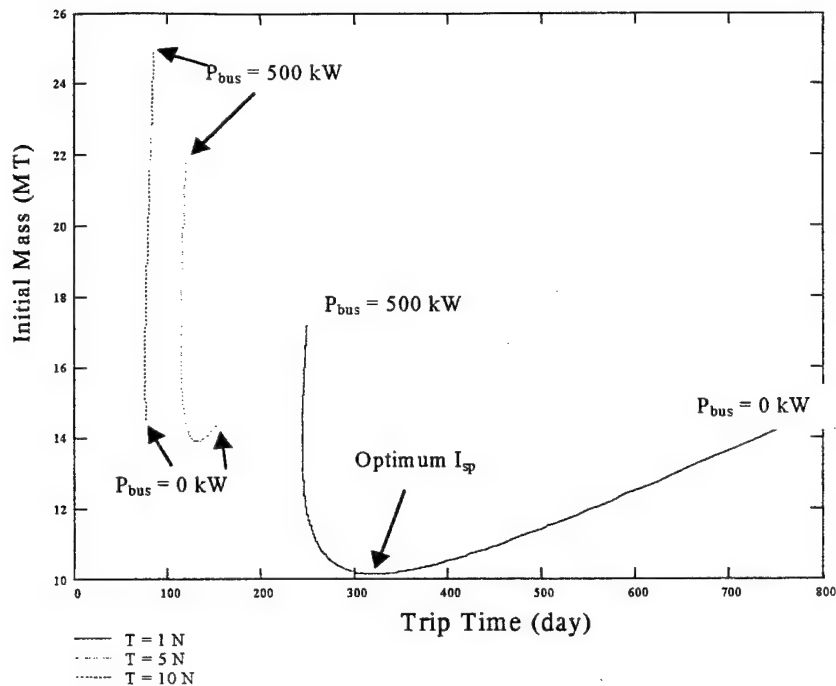


Figure A.5. Relationship between initial mass and trip time for several values of thrust.

Figure A.2 shows that a significant mass saving is realized through MHD augmentation; however, the trip time required to transfer the payload to geosynchronous may be impractical. Figure A.5 shows that the trip time for the 1 Newton augmented STR is 320 days at the optimum  $I_{sp}$ . While this cuts the transfer time by more than a factor of two from that of the unaugmented 1 Newton STR, it is still unreasonable for most missions. Increasing the bus power further will further decrease the trip time. However, if shorter trip times are desired, then we are much better off putting all of the power into thermal propulsion. If the 62 kW of electrical power required to reach the optimal  $I_{sp}$  were used in a STR, an achievable thrust of 50 Newtons would cut the transfer time to under 15 days. So the quick truth is that the battle between long trip times and optimal mass savings cannot be solved with MHD augmentation using current power supply technology.



An improvement in either the efficiency or power supply specific mass will result in reduction in both trip time and initial mass in LEO. Figure A.6 illustrates this for the efficiency of the MHD accelerator. Curves are shown for efficiencies of 20, 40 and 70%. Thrust of the STR is varied from a maximum of 26 Newtons to 1 Newton along each curve. The initial mass is plotted versus the trip time corresponding to the optimum  $I_{sp}$  for each value of thrust. As expected the trip time and initial mass decrease for all thrust values as the efficiency of the MHD accelerator is increased. The effect of the maximum thrust for effective augmentation can be seen in the rolling over of the curves for 20% and 40% efficiency. The maximum thrust for effective augmentation at 70% efficiency is around 26 Newtons; therefore, it does not roll over in Figure A.6. Finally, if an arbitrary limit of a 100 day trip time is imposed, the efficiency of the MHD augmentation must be greater than 20% to be beneficial. Thrust levels greater than 3 Newtons and 5 Newtons result in trip times less than 100 days for efficiencies of 70% and 40% respectively. The power required to achieve these trip times, while operating at optimal  $I_{sp}$ , is given in Figure A.7 as 62.4 kW and 67.7 kW for efficiencies of 70% and 40% respectively.

Magnetohydrodynamic augmentation benefits higher  $\Delta v$  missions more through increased saving in IMLEO. Figure A.8 shows the IMLEO versus trip time for  $\Delta v$  of 4.2, 6, and 8 km/sec. Finally, the IMLEO for a Mars mission with a  $\Delta v$  of 14.5 is given in Figure A.9 for efficiencies of 20, 40, and 70%.

The preceding analysis was conducted for augmentation of a solar thermal rocket operating with an  $I_{sp}$  of 860 sec. The benefit of MHD augmentation is even more dramatic for lower  $I_{sp}$  rockets. Figure A.10 shows what might be achievable in the future by augmentation of a steam rocket and utilization of advanced power supply technology.

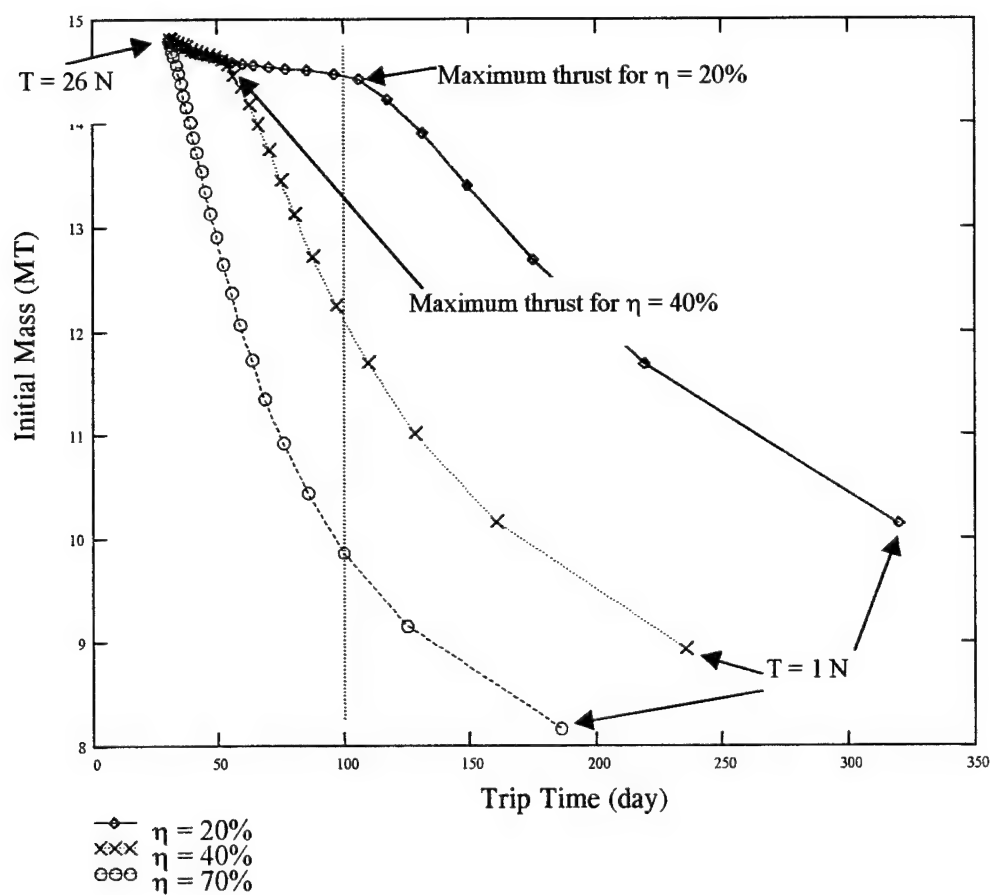


Figure A.6. Initial mass versus trip time for optimum  $I_{sp}$  conditions.

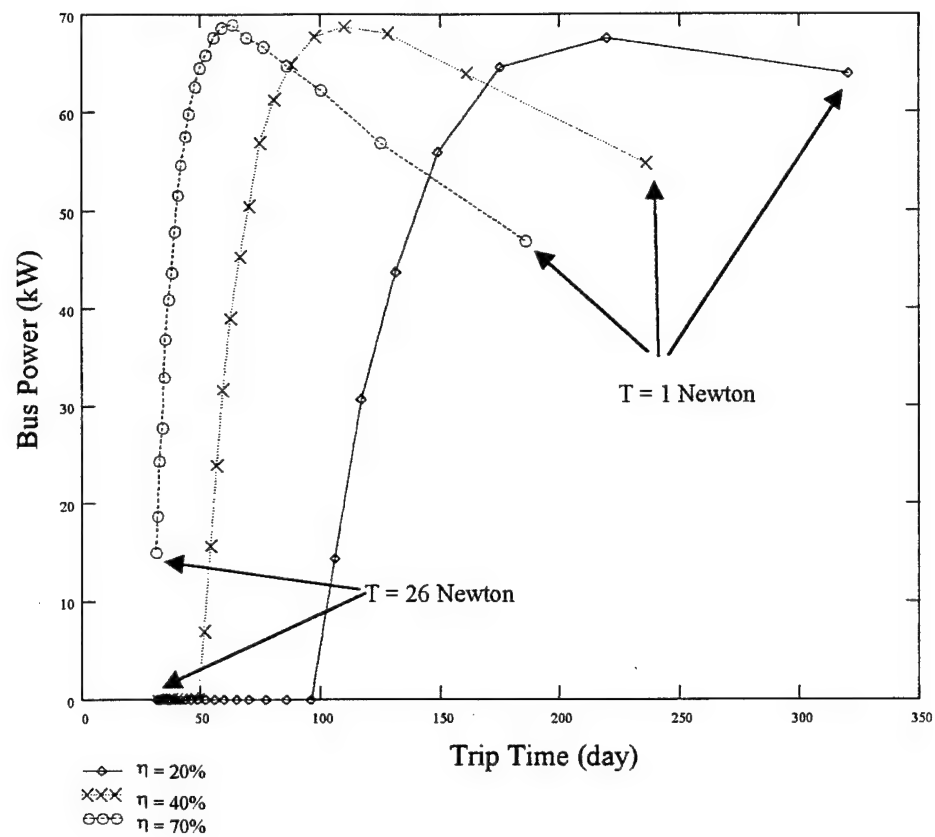
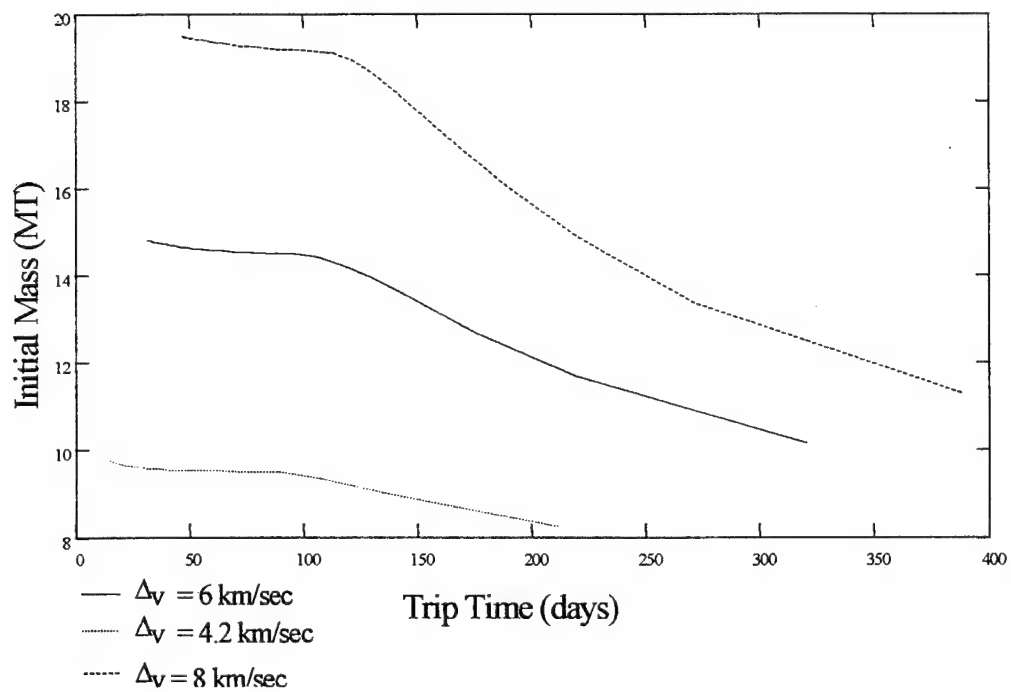


Figure A.7. Bus power versus trip time.

Figure A.8. Trip time vs. initial mass for  $\Delta v$ 's of 4.2, 6 and 8 km/sec.

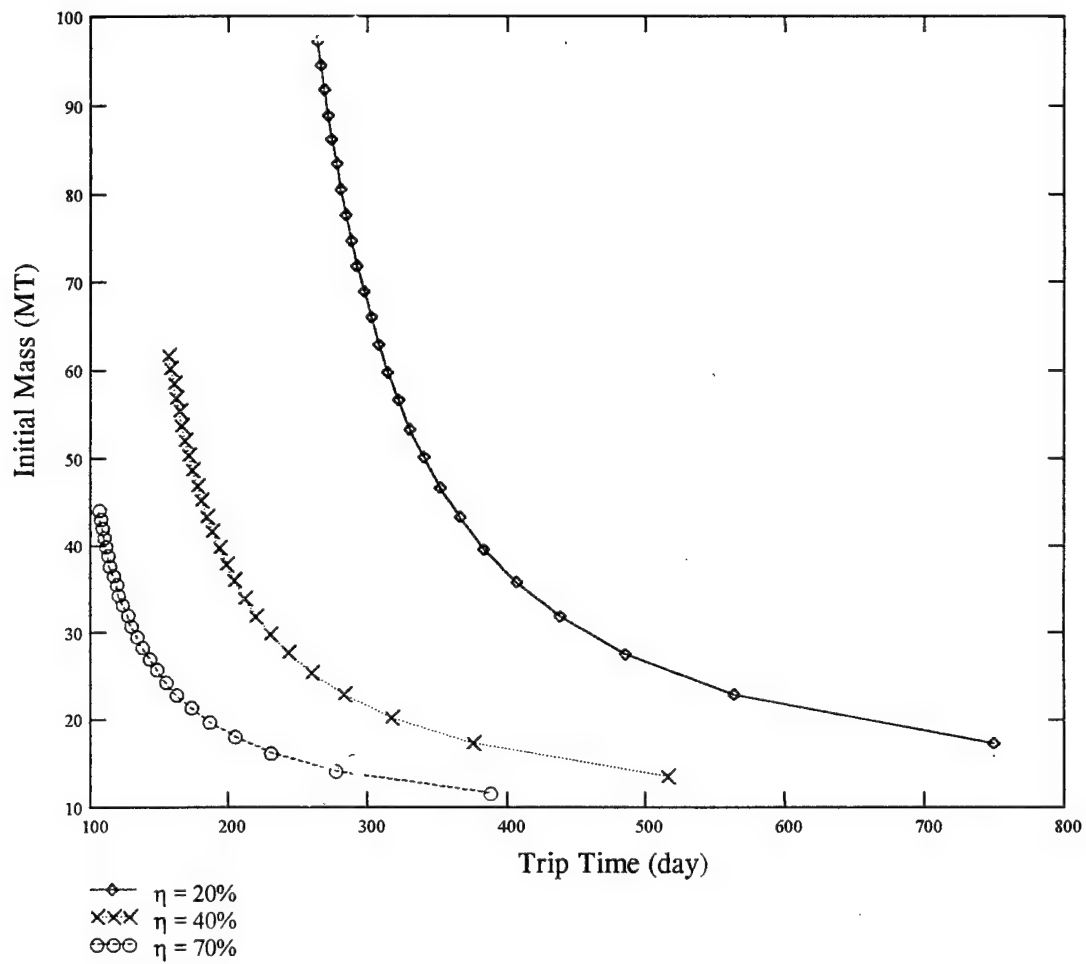


Figure A.9. Initial mass versus trip time for a Mars mission with a  $\Delta v$  of 14.5 km/sec.

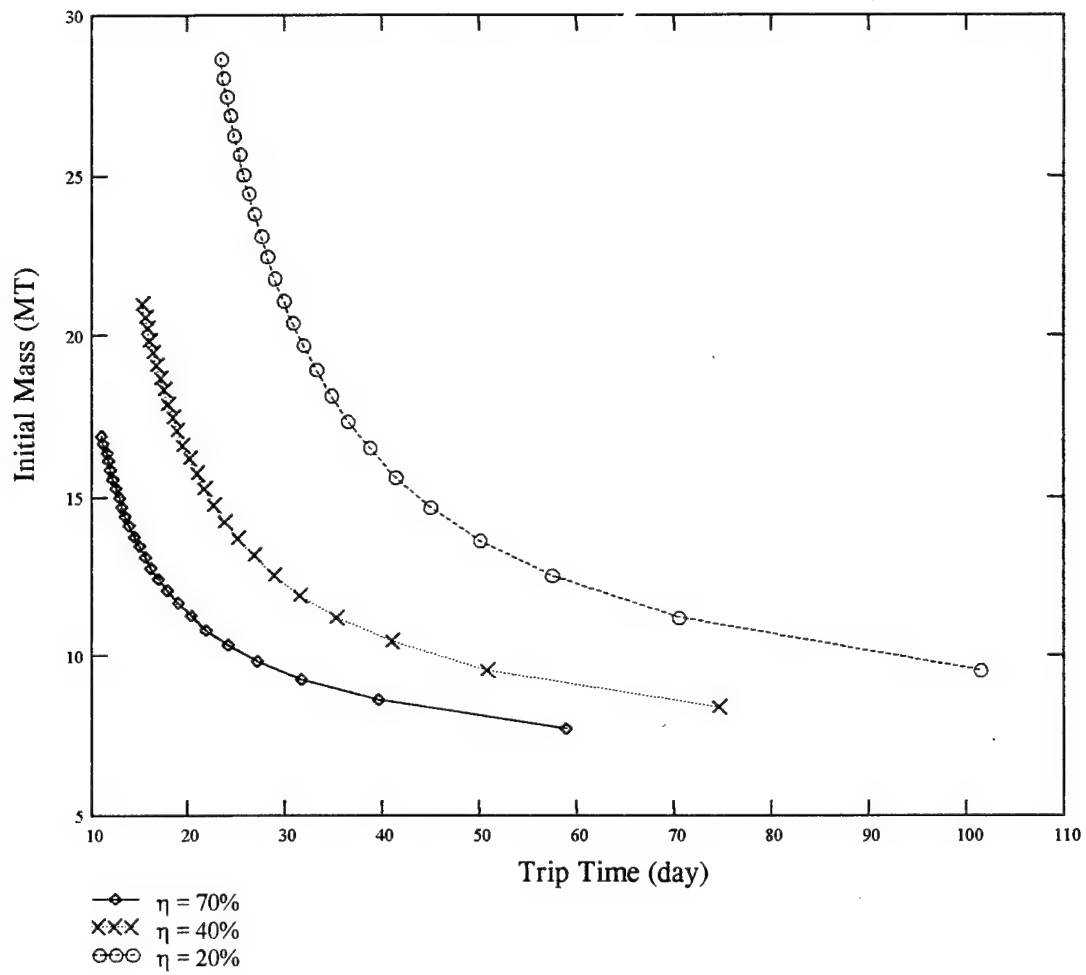


Figure A.10. Initial mass versus trip time for augmentation of a solar thermal steam rocket with an  $I_{sp}$  of 300 sec and a futuristic 5 kg/kW specific power.

## WORKS CITED

Argyropoulos, G. S., Demetriades, S. T., Doss, E. D., and Olivers, D. A., "Electron Nonequilibrium in Open-Cycle MHD Generators," *AIAA Journal*, Vol. 12, No. 5, May 1974, pp. 669-671.

Argyropoulos, G. S., Demetriades, S. T., and Kendig, A. P., "Current Distribution in Nonequilibrium JxB Devices," *Journal of Applied Physics*, Vol. 38, No. 13, Dec. 1967, pp. 5233-5239.

Adamovich, I. V., Rich, W. J., and Nelson, G. L., "Feasibility Study of MHD Acceleration of Unseeded and Seeded Air Flows," AIAA Paper 96-2347, July 1996.

Aisenburg, S., "Modern Probe Techniques for Plasma Diagnosis," 3<sup>rd</sup> Symposium on Engineering Aspects of Magnetohydrodynamics, 1963.

Bauman, L., Wang, W., Luthe, J., and Kumar, R. A., "Emission Absorption Measurements of Temperature and Seed Atom Density in High Speed Turbulent MHD Flows," AIAA Paper 93-3215, July 1993.

Baughman, J. A., Michelletti, D. A., Nelson, G. L., Simmons, G. A., "Magnetohydrodynamic Accelerator Research Into Advanced Hypersonics (MARIAH), Final Report," NASA/CR-97-206242, Oct. 1997.

Ben Daniel, D. J., "Theory of Nonthermal Ionization in Cesium Discharges," *The Physics of Fluids*, Vol. 5, April 1962, pp. 500-501.

Bohm, G., "Fabrey-Perot-Type Microwave Resonator," Published in Microwave Discharges: Fundamentals and Applications, Edited by C. M. Ferreira and M. Moisan, Plenum Press, New York, 1993.

Buften, S. A., "Exit Plane Plasma Measurements of a Low-Power Hydrazine Arcjet," Ph.D. Thesis, University of Illinois at Urbana-Champaign, 1996.

Chen, F. F., Plasma Physics and Controlled Fusion, Volume 1: Plasma Physics 2<sup>nd</sup> Edition, Plenum Press, New York, 1984.

Cool, T. A. and Zukoski, E. E., "Recombination, Ionization and Non-equilibrium Electrical Conductivity in Seeded Plasmas," *The Physics of Fluids*, Vol. 9, April 1966, pp. 780-796.

Craggs, J. D. and Massey, H. S. W., Hanbuch der Physik, Springer-Verlag OHG, 1959

Crawford, R. A., Chapman, J. N., and Rhodes, R. P., "Performance Potential and Technology Issues of MHD Augmented Hypersonic Simulation Facilities," AIAA Paper 90-1380, June 1990.

Demetriades, S. T., "Experimental Magnetogasdynamic Engine for Argon, Nitrogen, and Air," Technical Memorandum of the Astro Sciences Group, ASRL-TM-60-23, Nov. 1960.

Demetriades, S. T., "Experiments with a High Specific Impulse Crossed-field Accelerator," 3<sup>rd</sup> Symposium on Engineering Aspects of Magnetohydrodynamics, 1963.

Demetriades, S. T. and Argyropoulos, G. S., "Ohm's Law in Multicomponent Nonisothermal Plasmas with Temperature and Pressure Gradients," *The Physics of Fluids*, Vol. 9, No. 11, Nov. 1966, pp. 2136-2149.

Demetriades, S. T., "Orbital Propulsion System for Space Maneuvering (PROFAC)," *Astronautical Sciences Review*, Oct-Dec 1959.

Demetriades, S. T., "Plasma Propulsion, Part I," *Astronautics*, March 1962.

Demetriades, S. T., Private Communication, 1999.

Demetriades, S. T. and Ziemer, R. W., "Energy Transfer to Plasmas by Continuous Lorentz Forces," Magnetohydrodynamics (Proceedings of the 4<sup>th</sup> biennial Gas Dynamics Symposium, August 23-25, 1961), Edited by A. B. Cambel, T. P. Anderson and M. M. Slawsky, 1962.

Duclos, D. P., Wu, Y. C. L., Denison, M. R., and Ziemer, R. W. "Physical Property Distributions in a Low-Pressure Crossed-Field Accelerator," *AIAA Journal*, Vol. 3 No. 11, 1965.

Eckbreth, A. C., Laser Diagnostics for Combustion Temperature and Species, Abacus Press, Tunbridge, Wells, Kent, 1988.



Eckert, E. R. G. and Goldstein, R. J., Measurements in Heat Transfer, McGraw-Hill, New York, 1970.

Frisbee, R. and Hoffman, N., "SP-100 Nuclear Electric Propulsion for Mars Cargo Missions," JPL Internal Publication, JPL D-11012, Sept. 1993.

Harada, N. and Tsunoda, K., "Study of a Disk MHD Generator for Nonequilibrium Plasma Generator System," *Energy Conversion and Management*, Vol. 39, No. 5/6, pp. 493-503, 1998.

Hutchinson, I. H., Principles of Plasma Diagnostics, Cambridge University Press, Cambridge, 1987.

Kerrebrock, J. L. and Hoffman, M. A., "Nonequilibrium Ionization Due to Electron Heating: II Experiments," *AIAA Journal*, Vol. 2, 1964, pp. 1080-1087.

Jones, J. E., Hawk, C. W., and Chapman, J. N., "H2OTSTUF - A Magnetohydrodynamic/ Solar Thermal Water Rocket Feasibility Study," AIAA Paper 96-3213, 1996.

Klepeis, J. and Rosa, R., "Experimental Studies of Strong Hall Effects and  $V \times B$  Induced Ionization," *AIAA Journal*, Sept. 1965.

Langmuir, I. and Mott-Smith, H. M., "The Theory of Collectors in Gaseous Discharges," *Physical Review*, Vol. 28, 1926, pp. 727-763.

Litchford, R. J., Thompson, B. R., Lin, B.C., and Lineberry, J.T., "High-Temperature Current Layer MHD Power Extraction Experiments," AIAA Paper 97-2397, June 1997.

Macheret, S. O., Miles, R. B., and Nelson, G. L., "MHD Acceleration of Supersonic Air Flows Using Electron Beam – Enhanced Conductivity," AIAA Paper 98-2922, June 1992.

Mueller, J., "Performance Evaluation and Operating Characteristics of a Wave Guide Microwave Applicator for Space Propulsion Applications," Ph.D. Dissertation, The Pennsylvania State University, 1993.

Powers, W. L., Dicks, J. B., and Snyder, W. T., "A Graphical Presentation of Magnetogasdynamic Accelerator and Generator Performance Characteristics," *AIAA Journal*, Vol. 5, No. 12, 1967.

Pryor, W., "Solar System Resources," NASA/MSFC Summer Faculty Fellowship Final Report, 1999.

Rosa, R. J., Magnetohydrodynamic Energy Conversion, Hemisphere Publishing Corporation, New York, 1987.

Schluter, H., "Diagnostics of Microwave Discharges," Published in Microwave Discharges: Fundamentals and Applications, Edited by C. M. Ferreira and M. Moisan, Plenum Press, New York, 1993.

Sullivan, D. J., "Development and Performance Characterization of a Microwave Electrothermal Thruster Prototype," Ph.D. Dissertation, The Pennsylvania State University, 1995.

Sutton, G. W. and Sherman, A., Engineering Magnetohydrodynamics, McGraw-Hill, New York, 1965.

Wood, G. P., Carter, A. F., Sabol, A. P., and Weinstein, R. H., "Experiments in Steady State Crossed Field Acceleration of Plasmas," *The Physics of Fluids*, Vol. 4, 1961, pg. 652.

Van Dyke, M., "Beyond LEO Advanced Space Transportation Solar Thermal Upper Stage Study," Marshall Space Flight Center, 1996.

Wu, S. T., "Radiative Heat Flux for an Optically Thin Gas," *AIAA Journal*, Vol. 7, No. 4, April 1969.

## REFERENCES

Bajovic, V. S., "A Reliable Tool for the Design of Shape and Size of Faraday Segmented MHD Generator Channel," *Energy Conversion and Management*, Vol. 37, No. 12, 1996, pp. 1753-1764.

Bauman, L. and Zhong, L., "Monitoring MHD Boundary Layers using Emission Lineshapes Features," AIAA Paper 95-1968, June 1995.

Bergmann, V., Meier, W., Wolff, D., and Stricker, W., "Application of Spontaneous Raman Rayleigh Scattering and 2D LIF for the Characterization of a Turbulent CH<sub>4</sub>/H<sub>2</sub>/N<sub>2</sub> Jet Diffusion Flame," *Applied Physics B*, Vol. 66, No. 4, 1998, pp. 489-502.

Biondi, M. A., Sipler, D. P., Zipf, M. E., and Baumgardner, J. L., "All-Sky Doppler Interferometer for Thermospheric Dynamics Studies," *Applied Optics*, Vol. 34, No. 10, 1995, pp. 1646-1654.

Biturin, V. A., Bocharov, A. N., and Buznikov, A. E., "Numerical Study of Arcing Phenomena in MHD Channels," AIAA Paper 97-2399, June 1997.

Boley, C. D. and Yip, S., "Kinetic Theory of Time-Dependent Correlation Functions in a Binary Gas Mixture," *Physics of Fluids*, Vol. 15, No. 8, 1972, pp. 1433-1446.

Boley, C. D., Desai, R. C., and Tenti, G., "Kinetic Models and Brillouin Scattering in a Molecular Gas," *Canadian Journal of Physics*, Vol. 50, 1972, pp. 2158-2173.

Bréon, F., "Comment on Rayleigh-Scattering Calculations for the Terrestrial Atmosphere," *Applied Optics*, Vol. 37, No. 3, 1998, pp. 428-430.

Burton, R. L., Bufton, S. A., Tiliakos, N. T., and Krier, H., "Application of Multiple Electrostatic Probes to a Low Power Arcjet," *Journal of Propulsion and Power*, 1994.

Buuron, A. J. M., Dudeck, M., and Leprince, P., "Plasma Jets Departing from a Microwave Plasma Source," AIAA Paper 95-1958, June 1995.

Choi, S. H., Lee, J. H., and Tabibi, B. M., "Solar Thermal-Electric Propulsion for Upper-Stage Applications," AIAA Paper 95-2574, July 1995.

Choi, Y. S., Nguyen, D. X., Tabibi, B. M., and Lee, J. H., "Installation and Preliminary Operation of a Solar Thermal-Electric Propulsion System," AIAA Paper 96-2321, June 1996.

Chu, Benjamin, Laser Light Scattering, Academic Press, New York, 1974.

Dam, N. J., Rodenburg, M., Tolboom, R. A. L., Stoffels, G. G. M., Huisman-Kleinherenbrink, P. M., and Meulen, J. J., "Imaging of an Underexpanded Nozzle Flow by UV Laser Rayleigh Scattering," *Experiments in Fluids*, Vol. 24, No. 2, 1998, pp. 93-101.

de Groot, W. A. and Zupanc, F. J., "Laser Rayleigh and Raman Diagnostics for Small Hydrogen/Oxygen Rockets," *SPIE*, Vol. 1862, 1993, pp. 98-112.

Demtröder, W., Laser Spectroscopy: Basic Concepts and Instrumentation, Plenum Press, New York, 1981.

Eckbreth, A. C., Laser Diagnostics for Combustion Temperature and Species, Abacus Press, Tunbridge, Wells, Kent, 1988.

Elliot, G. S. and Samimy, M., "Rayleigh Scattering Technique for Simultaneous Measurements of Velocity and Thermodynamic Properties," *AIAA Journal*, Vol. 34, No. 11, 1996, pp. 2346-2352.

Forkey, J. N., Lempert, W. R., and Miles, R. B., "Accuracy Limits for Planar Measurements of Flow Field Velocity, Temperature and Pressure using Filtered Rayleigh Scattering," *Experiments in Fluids*, Vol. 24, No. 2, 1998, pp. 151-162.

Fredrickson, R. L. and Wu, J. C., "Effects of Hall Currents on the Performance of Crossed Field MHD Accelerators," 3<sup>rd</sup> Symposium on Engineering Aspects of Magnetohydrodynamics, 1963.

Gornall, W. S., "The World of Fabry-Perots, These Elegant Instruments are Versatile, High-Resolution Tunable Wavelength Filters," *Lasers & Applications*, July 1983, pp. 47-52.

Gornall, W. S., "Interferometry Determines Wavelengths Precisely," *Laser Focus World*, 1997, pp. 123-127.

Gourdine M. C., "Recent Advances in Magnetohydrodynamic Propulsion," *ARS Journal*, Dec. 1961.

Grinstead, J. H., Finkelstein, N. D., Miles, R. B., Lempert, W. R., and Lavid, M., "Doppler Velocimetry in a Supersonic Jet using Frequency-Modulated Filtered Light Scattering," AIAA Paper 97-0499, January, 1997.

Habiger, H. A., Auweter-Kurtz, M. K., and Helmut, L., "Investigation of Arc Jet Plumes with Fabry-Perot Interferometry," AIAA Paper, 1994.

Harada, S., Hoffmann, K. A., and Augustinus, J., "Development of a Modified Runge-Kutta Scheme with TVD Limiters for the Ideal Two-Dimensional MHD Equations," AIAA Paper 98-0981, January 1998.

Hariharan, P., Basics of Interferometry, Academic Press, New York, 1992.

Hernandez, G., Fabry-Perot Interferometers, Cambridge University Press, New York, 1986.

Hori, T., Bowden, D., Uchino, K., Muraoka, K., and Maeda, M., "Measurements of Electron Temperature, Electron Density, and Neutral Density in a Radio-Frequency Inductively Coupled Plasma," *Journal of Vacuum Science and Technology A*, Vol. 14, No. 1, 1996, pp. 144-151.

Kuninaka, H., Satori, S., and Horiuchi, Y., "Continuous Operation Test of Microwave Discharge Ion Thruster System," AIAA Paper 95-3070, July 1995.

Lempert, W. R., Wu, P. F., and Miles, R. B., "Filtered Rayleigh Scattering Measurements Using a MHz Rate Pulse-Burst Laser System," AIAA Paper 97-0500, January 1997.

Litchford, R. J., Thompson, B. R., Lin, B. C., and Lineberry, J. T., "Pulse Detonation MHD Experiment," AIAA 98-2918, June 1998.

Lock, J. A., Seasholtz, R. G., and John, W. T., "Rayleigh-Brillouin Scattering to Determine One-Dimensional Temperature and Number Density Profiles of a Gas Flow Field," *Applied Optics*, Vol. 31, No. 15, 1992, pp. 2839-2848.

Macheret, S. O., Miles, R. B., and Nelson, G. L., "Feasibility Study of a Hybrid MHD/Radiatively Driven Facility for Hypersonic Ground Testing," AIAA Paper 97-2429, June 1997.

McKenzie, R. L., "Measurement Capabilities of Planar Doppler Velocimetry using Pulsed Lasers," AIAA Paper 95-0297, January 1995.

McKenzie, R. L., "Planar Doppler Velocimetry Performance in Low-Speed Flows," AIAA Paper 97-0498, January 1997.



Miles, R. B., Lempert W. R., and Forkey, J., "Instantaneous Velocity Fields and Background Suppression by Filtered Rayleigh Scattering," AIAA 29<sup>th</sup> Aerospace Sciences Meeting, AIAA Paper 91-0357, 1991.

Miller, S. A. and Martinez-Sanchez, M., "Two-Fluid Nonequilibrium Simulation of Hydrogen Arcjet Thrusters," *Journal of Propulsion and Power*, Vol. 12, No. 1, 1996, pp. 112-119.

Monts, D. L., Qian, S., Cook, R. L., and Shepard, W. S., "Development of Laser Optogalvanic Spectroscopy as a Monitor of Alkali Seed in an MHD Environment," AIAA Paper 94-3905, August 1994.

Murphy, A. B. and Kovitya, P., "Mathematical Model and Laser-Scattering Temperature Measurements of a Direct-Current Plasma Torch Discharging into Air," *Journal of Applied Physics*, Vol. 73, No. 10, 1993, pp. 4759-4769.

Nakagawa, Y. and Wu, S. T., "On Multifluids Description of Shock Structure with Radiation," *Journal of Quantitative Spectroscopy and Radiation Heat Transfer*, Vol. 8, 1968, pp. 555-567.

Nakamura, H., Hirokawa, K., Okamura, T., and Shioda, S., "Nonequilibrium MHD Power Generation Experiments with a Shock-Tube Facility," AIAA Paper 97-2395, June 1997.

Nguyen, D.X., Nam, M.K., Tabibi, B.M., and Lee, J.H., "Performance of Thermal Plume in Solar Thermal-Electric Propulsion System," AIAA Paper 97-3207, July 1997.

Novikov, V., "Nonequilibrium Plasma Generation with Application of Self-Propagating High Temperature Synthesis (SHS)," AIAA Paper 97-2368, June 1997.

Ohler, S., Gilchrist, B., and Gallimore, A., "Non-Intrusive Plasma Diagnostics for Electric Propulsion Research," AIAA Paper 94-3297, June 1994.

Okinaka, N., Kikuchi, H., Misuhashi, K., Aoki, Y., and Kayukawa, N., "Measurement of Flow Velocity Distribution in Magnetohydrodynamic Channel Using Magnetic Resonance Imaging," AIAA 97-2369, 1997.

Ötügen, M. V., Kim, J., and Popović, S., "Nd:YAG Laser-Based Dual-Line Rayleigh Scattering System," *AIAA Journal*, Vol. 35, No. 5, 1997, pp. 776-781.

Ötügen, M. V., Annen, K. D., Seasholtz, R. G., "Gas Temperature Measurements Using a Dual-Line Detection Rayleigh Scattering Technique," *AIAA Journal*, Vol. 31, No. 11, 1993, pp. 2098-2104.

Panda, J. and Seasholtz, R. G., "Density Measurement in Underexpanded Supersonic Jets Using Rayleigh Scattering," AIAA Paper 98-0281, January 1998.

Primeau, G., "Magnetoaerodynamic(MAD) Propulsion for Exploration of Atmosphere-Bearing Planetary Bodies," AIAA Paper 98-3408, July 1998.

Rosa, R. J., "Magnetohydrodynamic Generators and Nuclear Propulsion," *ARS Journal*, Aug. 1962.

Schulz, R. J., Chapman, J. N., and Rhodes, R. P., "MHD Augmented Chemical Rocket Propulsion for Space Applications," AIAA Paper 92-3001, July 1992.

Schulz, R. J. and Chapman, J. N., "Optimum Performance of MHD-Augmented Chemical Rocket Thrusters for Space Propulsion Applications," 33<sup>rd</sup> SEAM Paper, June 1995.

Schwer, D. A., Venkateswaran, S., and Merkle, C. L., "Analysis of Microwave-Heated Rocket Engines for Space Propulsion," AIAA Paper 93-2105, June 1993.

Seasholtz, R. G., "Single-Shot Spectrally Resolved UV Rayleigh Scattering Measurements in High Speed Flow," NASA Technical Memorandum 107323, 1996.

Seasholtz, R. G., Buggele, A. E., and Reeder, M. F., "Flow Measurements Based on Rayleigh Scattering and Fabry-Perot Interferometer," *Optics and Lasers in Engineering*, Vol. 27, 1993, pp. 543-570.

Seasholtz, R. G., Zupanc, F. J., and Schneider, S. J., "Spectrally Resolved Rayleigh Scattering Diagnostic for Hydrogen-Oxygen Rocket Plume Studies," *Journal of Propulsion and Power*, Vol. 8, No. 5, 1992, pp. 935-942.

Sherman, A., "Theoretical Performance of a Crossed Field MHD Accelerator," *ARS Journal*, March 1962, pp. 414-420.

Smith, M.W. and Northam, G.B., "Application of Absorption Filter-Planar Doppler Velocimetry to Sonic and Supersonic Jets," AIAA Paper 95-0299, January 1995.

Snyder, S. C., Reynolds, L. D., Lassahn, G. D., Fincke, J. R., Shaw, C. B. Jr., and Kearney, R. J., "Determination of Gas-Temperature and Velocity Profiles in an Argon Thermal-Plasma Jet by Laser-Light Scattering," *Physical Review E*, Vol. 47, No. 3, 1993, pp. 1996-2005.

Suess, S. T., Wang, A.-H., Wu, S. T., Poletto, G., and McComas, D. J., "A Two-Fluid, MHD Coronal Model," *Journal of Geophysical Research*, Vol. 104, No. A3, March 1999, pp. 4697-4708.

Sugawara, A. and Yip, S., "Kinetic Model Analysis of Light Scattering by Molecular Gases," *The Physics of Fluids*, Vol. 10, No. 9, 1967, pp. 1911-1921.

Sullivan, D. J. and Micci, M. M., "Performance Testing and Exhaust Plume Characterization of the Microwave Arcjet Thruster," AIAA Paper 94-3127, June 1994.

Sullivan, D. J., Kline, J., Philippe, C., and Micci, M. M., "Current Status of the Microwave Arcjet Thruster," AIAA Paper 95-3065, July 1995.

Tabibi, B. M., Choi, S. H., and Lee, J. H., "Thermal-Electric Propulsion with Magnetoplasma-dynamic Acceleration," AIAA Paper 94-2468, June 1994.

Tenti, G., Boley, C. D., and Desai, R. C., "On the Kinetic Model Description of Rayleigh-Brillouin Scattering from Molecular Gases," *Canadian Journal of Physics*, Vol. 52, No. 4, 1974, pp. 285-290.

Usami, H., Aoki, Y., Okinaka, N., Kayukawa, N., and Okuo, T., "Y<sub>2</sub>O<sub>3</sub>-W Electrode for MHD Generator," AIAA Paper 97-2371, 1997.

Wei, T., Collins, L. R., and Phillips, J., "Measurement and Modeling of N-Atom Behavior in the Afterglow of a Microwave Plasma," *AIChE Journal*, Vol. 42, No. 5, 1996, pp. 1361-1370.

**DEVELOPMENT AND STUDY OF A RAYLEIGH SCATTERING TECHNIQUE  
FOR MICROWAVE PLASMA MEASUREMENTS TAKEN IN VACUUM**

**by**

**MATTHEW J. CULLEY**

**A THESIS**

**Submitted in partial fulfillment of the requirements  
for the degree of Master of Science in Engineering  
in The Department of Mechanical  
and Aerospace Engineering  
of  
The School of Graduate Studies  
of  
The University of Alabama in Huntsville**

**HUNTSVILLE, ALABAMA**

**1999**

**Copyright by**  
**Matthew James Culley**  
**All Rights Reserved**  
**1999**

## THESIS APPROVAL FORM

Submitted by Matthew J. Culley in partial fulfillment of the requirements for the degree of Master of Science in Engineering with a major in Mechanical Engineering.

Accepted on behalf of the Faculty of the School of Graduate Studies by the thesis committee:

Charles W. Runk 8/3/99 Committee Chair  
(Date)

HW Coleman 8/3/99

James C. Wenzel 8-3-99

James C. Wenzel 8-3-99 Department Chair

J. Cannon Runk 8/4/99 College Dean

A. Gabe Jha 8/10/99 Graduate Dean



## ABSTRACT


School of Graduate Studies  
The University of Alabama in Huntsville

Degree Master of Science in Engineering College/Dept. Engineering/Mechanical and  
Name of Candidate Matthew J. Culley Aerospace Engineering  
Title Development and Study of a Rayleigh Scattering Technique for Microwave Plasma  
Measurements Taken in Vacuum.

This work focuses on the study and development of a Rayleigh scattering technique to be used to measure velocity and temperature in the plume of a microwave plasma thruster. Tests were conducted from atmospheric pressure down to 1 torr. A detailed uncertainty analysis was conducted along with an extended analysis of the thermal drift of a Fabry-Perot interferometer. The uncertainty analysis run on a Rayleigh scattering code, for atmospheric pressure, zero velocity, and room temperature images, resulted in uncertainties that were  $\pm 38.8$  m/s for velocity and  $\pm 45.5$  K for temperature. The thermal drift was seen to be most stable using a commercially available thermal enclosure that provided a half-hour steady state window when set at 33°C. Rayleigh scattered light from an injection-seeded, frequency doubled Nd:YAG laser was analyzed using a planar mirror Fabry-Perot interferometer operating in the static imaging mode. Images were taken with an ICCD camera and digitally stored for later evaluation using a least squares curve fit. Preliminary data taken at 1 torr shows the Rayleigh signal dominated by scattered laser light coming from windows and metal surfaces. Methods of reducing this scatter along with the theory of Rayleigh scattering are discussed.

Abstract Approval:

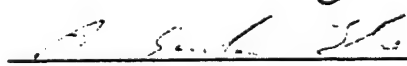
Committee Chair

 8/15/99  
(Date)

Department Chair

 8-3-99

Graduate Dean

 8/17/99

## ABSTRACT

School of Graduate Studies  
The University of Alabama in Huntsville


Degree Master of Science in Engineering College/Dept. Engineering/Mechanical and

Name of Candidate Matthew J. Culley Aerospace Engineering

Title Development and Study of a Rayleigh Scattering Technique for Microwave Plasma  
Measurements Taken in Vacuum.

This work focuses on the study and development of a Rayleigh scattering technique to be used to measure velocity and temperature in the plume of a microwave plasma thruster. Tests were conducted from atmospheric pressure down to 1 torr. A detailed uncertainty analysis was conducted along with an extended analysis of the thermal drift of a Fabry-Perot interferometer. The uncertainty analysis run on a Rayleigh scattering code, for atmospheric pressure, zero velocity, and room temperature images, resulted in uncertainties that were  $\pm 38.8$  m/s for velocity and  $\pm 45.5$  K for temperature. The thermal drift was seen to be most stable using a commercially available thermal enclosure that provided a half-hour steady state window when set at 33°C. Rayleigh scattered light from an injection-seeded, frequency doubled Nd:YAG laser was analyzed using a planar mirror Fabry-Perot interferometer operating in the static imaging mode. Images were taken with an ICCD camera and digitally stored for later evaluation using a least squares curve fit. Preliminary data taken at 1 torr shows the Rayleigh signal dominated by scattered laser light coming from windows and metal surfaces. Methods of reducing this scatter along with the theory of Rayleigh scattering are discussed.

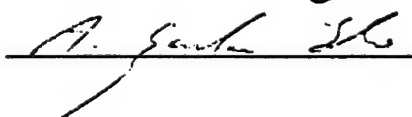
Abstract Approval: Committee Chair

 8/3/99  
(Date)

Department Chair

 8-3-99

Graduate Dean

 8/17/99

## ACKNOWLEDGEMENTS

This thesis is dedicated to my family whose words of encouragement and understanding go untold. I wish to thank my many professional colleagues and friends for their stimulating discussions on research topics and ideas. Hopefully, this research will encompass some of these discussions.

I would like to thank my advisor, Dr. Clark W. Hawk, for his invaluable guidance and support throughout the course of my research. I would also like to thank my other committee members, Dr. Hugh W. Coleman and Dr. Francis C. Wessling, for their helpful comments and overall expertise.

Special thanks need to be given for the invaluable time Dr. Richard G. Seasholtz, researcher at John H. Glenn Research Center, gave to me including the use of his Rayleigh scattering code and the many practical research tips he provided me. Also thanks must be given to Dr. Joseph N. Forkey along with Dr. G. Tenti for graciously allowing me to use their Fortran codes on an iodine absorption cell and kinetic theory respectively. Without them this research would not have been possible. Finally I wish to thank my co-researcher Jonathan Jones for the tremendous time he offered for my countless questions.

This research program was sponsored in part by NASA Marshall Space Flight Center and by the Air Force Office of Scientific Research under the grant number F49620-98-0-0083.

## TABLE OF CONTENTS

	Page
List of Figures .....	viii
List of Tables .....	x
List of Symbols .....	xi
 Chapter	
I. INTRODUCTION .....	1
A. Review of Existing Methods .....	1
B. Previous Work .....	3
C. Goals of This Thesis .....	4
II. RAYLEIGH SCATTERING THEORY .....	5
A. Laser .....	5
1. Laser Intensity .....	6
2. Quality Factor .....	6
3. Electromagnetic Waves .....	7
4. Polarization .....	7
B. Particle Scattering .....	8
1. Rayleigh Scattering Cross-Sections .....	8
C. Principles of Rayleigh Scattering .....	9
D. Fabry-Perot Interferometers .....	14
1. Fringe Pattern .....	17
E. Fortran Codes .....	19
1. Seasholtz Code .....	19
2. Tenti Model .....	20
3. Forkey Code .....	21
F. Iodine Absorption Filter .....	22

III.	EXPERIMENTAL SETUP .....	26
A.	Microwave Model .....	28
B.	Vacuum Chamber .....	28
1.	Optical Access .....	29
2.	Baffle System .....	29
C.	Scattered Light .....	30
1.	Stray Light Baffle System .....	30
2.	Background Light .....	31
D.	Mode Locking and Seeding .....	31
IV.	PROCEDURE .....	33
A.	Fortran Codes Developed .....	35
B.	Daily Burns .....	36
C.	System Check .....	36
D.	Data Acquisition .....	36
E.	Data Analysis .....	36
V.	RESULTS .....	37
A.	Thermal Drift .....	38
B.	Temperature Measurements .....	40
C.	Burleigh Thermal Isolation Box .....	41
D.	Uncertainty Analysis .....	44
E.	Uncertainty Percentage Contribution .....	49
VI.	CONCLUSIONS AND RECOMMENDATIONS .....	52
	APPENDIX A: USEFUL FORMULAS AND CONVERSIONS .....	55
	APPENDIX B: RAYLEIGH DIFFERENTIAL CROSS SECTION CALCULATION .....	59
	APPENDIX C: FORTRAN REMARKS .....	60
	REFERENCES .....	62
	BIBLIOGRAPHY .....	65

## LIST OF FIGURES

Figure	Page
1.1 Diagnostics Application Regimes .....	4
2.1 Vertically Polarized Electromagnetic Wave .....	7
2.2 Reference Laser Line and Rayleigh Scattered Spectrum .....	10
2.3 Solid Collection Angle Illustration .....	11
2.4 Interaction Wave Vector as Associated to Scattering Medium .....	13
2.5 Fabry-Perot Interferometer .....	15
2.6 Reference Image for Injection Seeded Nd: YAG Laser at 532 nm .....	17
2.7 One to One Correspondence of Measurement Region to CCD Array .....	18
2.8 Rayleigh Scattering Program Schematic .....	20
2.9 Rayleigh Scattering Spectra for Three Different Regimes .....	21
2.10 Iodine Absorption Cell .....	23
2.11 Iodine Absorption Spectrum for 200 mm Path Length; Pressure = 0.46 torr, Temperature = 303 K (calculated using code supplied by Forkey [30]) .....	24
2.12 Iodine Cell Effect on Rayleigh Scattering Spectrum .....	25
3.1 Optical Setup for Measuring Axial Properties .....	27
3.2 Vacuum Chamber and Resonant Cavity .....	29
3.3 Baffle System .....	30
3.4 Light Tight Cloth Assembly .....	31
4.1 Least Squares Fit to Reference Image .....	35
5.1 Reference Image for Injection Seeded Nd: YAG Laser at 532 nm .....	38
5.2 Rayleigh Scattered Image of Nitrogen at Atmospheric Temperature and Pressure ...	38
5.3 Thermal Drift of the Fabry-Perot Interferometer Over 3 Hours .....	40
5.4 Rayleigh Scatter Room Temperature Measurements .....	41
5.5 Low Setting Night Drift Test .....	42
5.6 High Setting Night Drift Test .....	43
5.7 Flowchart of Monte Carlo Simulation .....	47

5.8	Uncertainty Velocity Distribution .....	48
5.9	Uncertainty Temperature Distribution .....	48

## LIST OF TABLES

Table	Page
2.1 Rayleigh Scattering Differential Cross-Sections for Common Gases (@532 nm) ....	9
2.2 Photoelectron Calculations .....	12
5.1 Input Parameters with Associated Uncertainty .....	45
5.2 Final Reference Values .....	45
5.3 Velocity Uncertainty Data .....	48
5.4 Temperature Uncertainty Data .....	49
5.5 UPCs Calculated for Velocity Output .....	50
5.6 UPCs Calculated for Temperature Output .....	50



## LIST OF SYMBOLS

Symbol	Meaning	Units
$a$	Most probable molecular speed	m/s
$A_R$	Amplitude of the Rayleigh scattered signal	
$A_w$	Amplitude of the laser light scattered from walls and windows	
$B_q$	Broadband background light, detector dark current, and readout noise	
$c$	Speed of light	m/s
$c_s$	Speed of sound	m/s
$d$	Fabry-Perot mirror spacing	mm
$E$	Electric field	
$E_o$	Laser energy	J
$E_s$	Scattered energy	J
$f$	Frequency of scattered light	Hz
$f_o$	Frequency of incident light	Hz
$F$	Coefficient related to finesse	
FSR	Free Spectral Range	1/s
$h$	Planck's constant	J*s
$H$	Magnetic field	
$I_{FP}(\psi)$	Transmission function of Fabry-Perot	
$I_{I2}$	Transmission function of Iodine Cell	
$K$	Wave number	1/m
$\mathbf{K}$	Interaction wave vector	
$K$	Magnitude of wave vector	
$\mathbf{k}_o$	Incident wave vector	
$\mathbf{k}_s$	Scattered light wave vector	
$L_x$	Length along the beam of the scattering volume	
$m$	Molecular mass	kg
$n$	Number density	m <sup>-3</sup>
$N_E$	Effective finesse	
$N_R$	Number of detected photoelectrons collected by an optical system with solid collection angle $\Omega$	
$\langle N_{Dq} \rangle$	Expected number of detected photons for the qth pixel	
$P$	Gas pressure	atm
$Q$	Quality factor	
$r_n$	Fringe radii	
$R_L$	Molar refractivity	
$S(f)$	Normalized spectrum of Rayleigh scattered light	
$S_R$	Spectrum of Rayleigh scattered light	
$T$	Gas temperature	K
$u$	Mean gas velocity	m/s
$u_K$	Velocity component	
$x$	Optical frequency shift	
$x_o$	x coordinate of center of fringe pattern	pixel
$y$	Collision frequency	
$y_o$	y coordinate of center of fringe pattern	pixel

## Greek

$\gamma$	Ratio of specific heats	
$\epsilon$	Overall collection efficiency (including detector quantum efficiency and system losses)	
$\eta$	Shear viscosity	
$\theta_s$	Scattering angle	deg or rad
$\theta_r$	Angle between the ray and the optic axis	deg or rad
$\kappa$	Boltzmann's constant	J/K
$\lambda$	Wavelength	nm
$\lambda_0$	Incident wavelength	nm
$\Lambda_s$	Acoustic wavelength	
$\mu$	Index of refraction	
$\rho$	Molar density	mol/cm <sup>3</sup>
$d\sigma/d\Omega$	Rayleigh differential scattering cross-section	m <sup>2</sup> /sr
$\chi$	Angle between the electric field vector of the (linearly polarized) incident light and the direction of the scattered light.	
$\psi$	Phase change	
$\Omega$	Solid collection angle	sr

## Chapter I

### INTRODUCTION

The idea of utilizing the excess water that is dumped from each shuttle mission as a propellant source has not been thoroughly investigated. The use of this water as a propellant in an MHD accelerator has the potential to increase thruster efficiency as well as reduce thermal losses and electrode erosion. The focus of this research was to measure both thermodynamic and electrical transport properties in the plume of a microwave thruster in order to assess the feasibility of this option. This research specifically addresses the approach taken to measure thermodynamic properties for a thruster operating range of 1 atm down to 1 torr. The thermodynamic properties that may be obtained with Rayleigh scattering are velocity, temperature, and density. These properties will enable a determination of the behavior of the thruster system. This will help in the further design and development of the final steam propelled thruster to be used in space.

#### A. Review of Existing Methods

To date the majority of methods to measure the properties of flows can be placed under two categories, intrusive and nonintrusive. There are benefits and disadvantages to both methods and the choice is often project dependent. The need for techniques that can measure difficult to access regions of flow such as shock layers, boundary layers, non-equilibrium flows, and turbulence is becoming more apparent everyday.

Intrusive techniques often involve probes. These probes are normally a great deal cheaper to buy and operate than their respective nonintrusive counterparts. They are used very frequently to obtain properties such as temperature, velocity, and pressure. They are often used as a check for the nonintrusive techniques. However, laser methods today are being used

to measure complex flows that would either destroy a normal physical probe or possibly inhibit accurate data from being found.

There are many nonintrusive laser diagnostic techniques available today. Some of these are Rayleigh scattering, Raman scattering, Laser Induced Fluorescence (LIF), Laser Doppler Velocimetry (LDV), and Particle Image Velocimetry (PIV). Raman scattering provides information about the various functional groups in a molecule [1]. It has the advantage of being frequency shifted from the incident laser light; however, for low-density environments, the signal is an order of magnitude lower than the Rayleigh signal. The LIF method is an attractive option for measuring ion density, velocity, and temperature in low-density regimes but is dependent upon the material studied [2]. The LDV and PIV methods are both nonintrusive techniques used to measure velocity based on Mie scattering. Seeding of the flow is required for these methods. The size of the seed particle must be optimized to not only scatter enough detectable light for a clear signal but also be small enough to accurately follow the flow through high acceleration regions. Seeding involves a degree of intrusion that was not desired for this work. The technique that was chosen for this work was Rayleigh scattering. Rayleigh scattering is an elastic process where the internal energy of the scattering molecules is not changed, and is generally seen as the simplest molecular scattering technique. It was chosen due to its applicability to many different species of gases, along with its suitability over a large range of operating conditions. Rayleigh scattering requires no seeding of the flow. Another benefit unlike LIF and Raman scattering is that no specific laser frequency is required for the method.

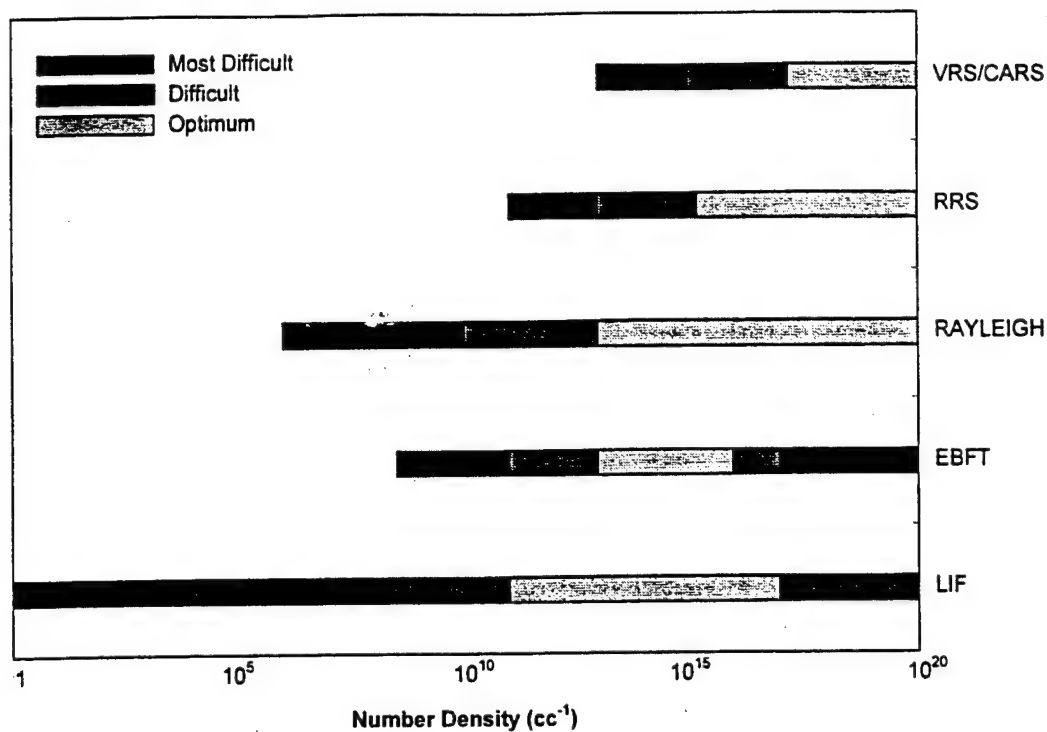
Laser techniques also have disadvantages. One such limitation is the need for optical access. The use of windows or fiber optics generally means that there will be losses involved with these elements. For low-density environments, compromises in either or both the space and time scales may be necessary to ensure adequate signal levels. Similar to probes, more than one technique may have to be used to measure several species and temperatures simultaneously. Rayleigh scattering suffers from Mie interferences and spuriously scattered laser light and can only be used in very clean, particle-free situations.

These optical techniques are not new: many of the methods were realized long ago. In the area of emission spectroscopy there was Swan's observations of  $C_2$  emissions from flames in 1857. Lord Rayleigh's research explained the blue color of the sky in 1871. Raman's scattering effect, which won him the Nobel Prize, was discovered in 1928. Developments from these discoveries have really only begun to surface in the last forty years though with the discovery of the first operative laser by Maiman in 1960. The laser now allows for a practical way to utilize these methods [3].

## B. Previous Work

The Rayleigh scattering technique has been implemented in many different situations. Its main usage to date has been in the study of jet plumes [4] and wind tunnel testing [5]. It has been utilized in nonequilibrium conditions [6], harsh environments [7], mixed flows [8], high speed flows [9], and low speed flows [10]. It has been studied in conjunction with codes like the JANNAF-TDK code [11]. The literature discussed assumptions that had to be made to apply the system to their respective project, such as isentropic flow. They also discuss different setup procedures that will enable the user to eliminate certain problems such as background light and scattered light. One such way of eliminating acoustic or vibrational noise is to use a fiber optic to guide the Rayleigh scattered light to another room, enabling the isolation of the system [10].

Lewis [12] showed the relative difficulties between five of the methods and the number density regimes where they are found to be optimum, Figure 1.1. The five methods he compares are vibrational Raman scattering (VRS), rotational Raman scattering (RRS), Rayleigh scattering, electron beam fluorescence technique (EBFT), and laser-induced fluorescence (LIF). At a pressure of 1 torr and a temperature of 300 K the ideal gas law gives a number density of  $3.2E16 \text{ cc}^{-1}$ , which puts the current work presented here in the optimum range for Rayleigh scattering according to Lewis's chart. At higher operating temperatures the number density decreases and the technique becomes more difficult.



**Figure 1.1 Diagnostics Application Regimes [12]**

### C. Goals of This Thesis

The primary goal of this thesis was to develop and study a Rayleigh scattering technique that could be used to measure microwave plasma plumes accurately. This thesis looks at Rayleigh scattering theory and atmospheric measurements that are used for verification of the technique, discusses the codes used for data reduction, presents Fabry-Perot drift tests, provides a detailed uncertainty analysis, and discusses the difficulties of getting to lower density regimes and the steps needed to get there.

## Chapter II

### RAYLEIGH SCATTERING THEORY

Rayleigh scattering, named after Third Baron Rayleigh, is the scattering of light caused by the interaction of an electric field with an atom or molecule. It is found that the scattered intensity is proportional to the square of the volume of the particle and proportional to  $1/\lambda^4$ .

Because the wavelength is much larger than the size of a molecule, a dipole moment is induced that oscillates and radiates at the frequency of the incident field. This is an elastic scattering process, where the internal energy of the molecule is not changed, so the frequency of the scattered light is equal to the frequency of the incident light altered only by the Doppler effect due to the motion of the molecules. This is sometimes referred to as coherent scattering since the scattered light is coherent with the incident light. When the entire medium is moving relative to a stationary observer, the Rayleigh line is not only broadened – its center is also shifted owing to this relative velocity. Because of the random spatial distribution of the molecules in a gas, the total intensity of the scattered light from a volume of gas is the sum of the intensities of the light scattered from the individual molecules. At low gas densities, molecular interactions are rare and the Rayleigh scattering spectrum is determined only by the molecular velocity distribution; for the usual Maxwellian velocity distribution the spectrum is, thus, a simple Gaussian. However, at higher gas density the molecular motions become correlated and the character of the spectrum changes. The spectrum can be analyzed by either considering the scattering from the individual molecules with proper accounting of the collective effects or by considering the scattering as being caused by fluctuations in the gas density. [13]

#### A. Laser

The laser's unique ability to output photons that are identical in phase, direction and amplitude make it an attractive research device for scientists to use. The coherence of light

from a laser both reduces the solid angle and the wavelength range of laser light. This allows for a very high amount of energy to be focused into a very small area. Lasers bring us as close to monochromatic light as physically possible today. When "monochromatic" is stated with respect to a laser, it generally means that the light is within a small band of wavelengths around a given wavelength.

### 1. Laser Intensity

In the visible spectrum, 400 to 700 nm, laser light is immediately recognizable to the unaided eye because of the phenomenon of speckle. Speckle is merely coherent light being scattered off a substance, typically dust, in all directions.

The Rayleigh scattering technique discussed in this paper utilized an injection seeded, frequency doubled trivalent Neodymium ions ( $\text{Nd}^{3+}$ ): Yttrium Aluminum Garnet ( $\text{Y}_3\text{Al}_5\text{O}_{12}$ ) laser. The acronym for which is Nd: YAG. The YAG operated at 1J in the 532nm range. Appropriate eye protection and beam dumps were used for safety reasons. This choice of laser represents a short wavelength and high pulse energy which is beneficial for Rayleigh scattering, as will be seen in later chapters. This type of pulse laser can provide instantaneous measurements at atmospheric conditions due to the high Rayleigh signal strength. It also has the benefit of virtually eliminating marker shot noise, which is the random noise that may appear in images that are not gated down. By incorporating a gated detector synchronized to the advance synchronized output of the laser, the broadband background light can be eliminated. A Helium Neon (or HeNe) laser operating at a wavelength of 543.5 nm was used in the alignment of optics and for drift tests.

### 2. Quality Factor

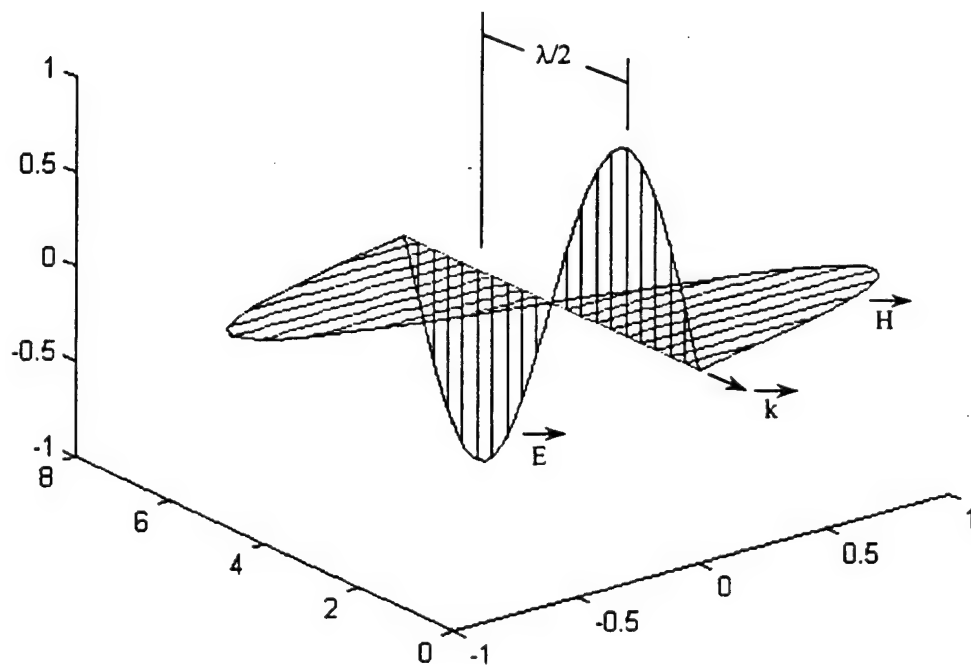
Quality factor switching, or Q-switching, is another feature in lasers today. It allows for roughly 10-ns duration pulses with energies on the order of 1J to be produced by a laser. Q-switching can be accomplished in a laser through the use of a Pockels cell, as is used in the Nd:YAG, which uses various polarizing and polarization rotating elements. It is through these polarizing elements that a large population inversion is created that can be quickly decreased.



A high voltage pulse sent to the Pockels crystal causes polarization rotation of the cavity radiation into a low loss mode and subsequent formation of the intense lasing pulse [14].

### 3. Electromagnetic Waves

It is important to understand that light is a transverse electromagnetic wave. The electric and magnetic fields are perpendicular to each other and to the propagation vector  $k$  (Figure 2.1). Both  $E$  and  $H$  oscillate in time and space. By understanding the composition of the laser beam along with the direction of propagation, the polarization of the beam can be described.



**Figure 2.1** Vertically Polarized Electromagnetic Wave

### 4. Polarization

Polarization is an important factor in Rayleigh scattering measurements. Having the electric field perpendicular to the viewing axis will produce the strongest signal. This is accomplished through the use of a half-wave plate along with the harmonic generator located

within the YAG itself. These devices allow the polarization to be rotated to the proper angle corresponding to this perpendicular requirement. Useful equations and conversions can be found in Appendix A.

## B. Particle Scattering

The primary reference for the following theory is Seasholtz [13].

### 1. Rayleigh Scattering Cross-Sections

The Rayleigh scattering method requires an understanding of how light interacts with a gas. The first equation used to describe this interaction is the Rayleigh differential scattering cross-section equation, shown below for scattering at  $90^\circ$ . It is seen that the equation is directly dependent on the index of refraction of the gas to be studied [3].

$$\left(\frac{d\sigma}{d\Omega}\right) = \frac{4\pi^2}{\lambda^4 n^2} (\mu - 1)^2 \quad (2.1)$$

This strong wavelength dependence enhances the scattering efficiency at shorter wavelengths. Therefore, operation of this technique in the ultraviolet regime leads to stronger scattering intensities and reduces stray light caused by the reflectivity of metals, but tends to have lower power levels, is more expensive, and is harder to operate [15,16]. This is why the second harmonic of the Nd:YAG was chosen for this work.

In 1836 Cauchy showed that in a region of normal dispersion, the variation of refractive index with wavelength for a given medium could be represented by an expression of the form

$$\mu = A + \frac{B}{\lambda^2} + \frac{C}{\lambda^4} + \dots \quad (2.2)$$

where A, B, and C, are constants characteristic of the medium concerned, and  $\lambda$  is usually the wavelength in a vacuum. These constants can be determined experimentally by measuring  $\mu$  for three values of  $\lambda$ . For many purposes it is sufficiently accurate to include the first two terms only [17].

Specific values of the Rayleigh differential cross-section can be calculated using published tables of the index of refraction for specific gases [18,19,20]. One way the tables present the data would be values of the molar refractivity,  $R_L$ , that assumes the form of the Lorenz-Lorentz equation shown below. The benefit of using this equation is the elimination of the density dependence of  $n$ .

$$R_L = \frac{n^2 - 1}{n^2 + 2} \cdot \frac{1}{\rho} \quad (2.3)$$

where  $n$  is the index of refraction and  $\rho$  is the molar density in mol/cm<sup>3</sup>, taken at the pressure and temperature at which  $n$  is measured. An example of how to extract the Rayleigh differential cross-section from these tables can be found in Appendix B. Rayleigh differential cross-sections for gases studied for this work are shown in Table 2.1.

**Table 2.1** Rayleigh Scattering Differential Cross-Sections for Common Gases (@532 nm)

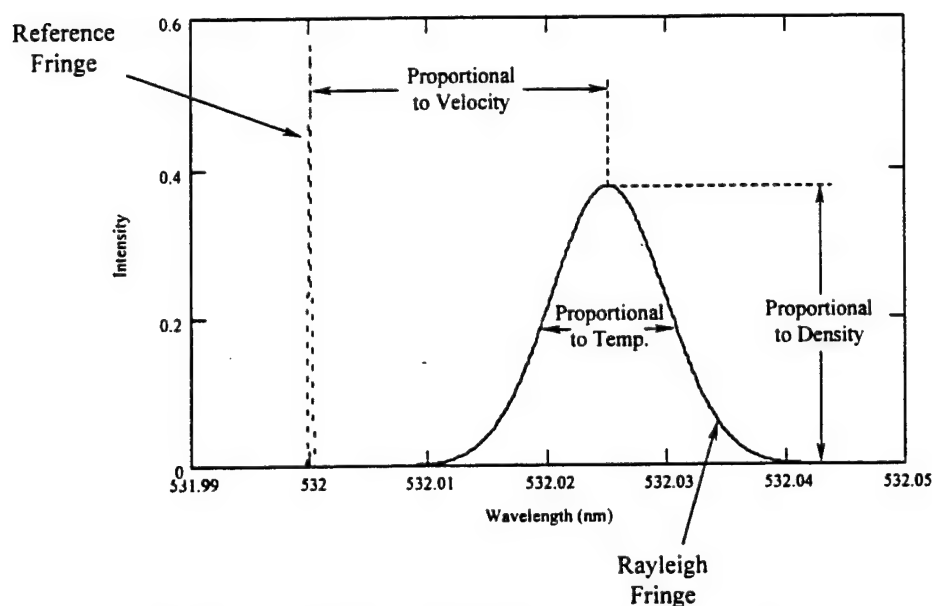
Molecule	$(d\sigma/d\Omega) \times 10^{32}, \text{m}^2 \text{sr}^{-1}$
Ar	5.44
CO <sub>2</sub>	13.65
He	0.08
H <sub>2</sub> O	4.36
N <sub>2</sub>	6.13

Although there are many exceptions, it is useful to note that, in general, denser materials have higher refractive indices than less dense media; thus, a higher Rayleigh scattering cross-section.

### C. Principles of Rayleigh Scattering

Figure 2.2 shows the relationship between the incident or reference laser line and the Rayleigh scattered spectrum, where the shape of the Rayleigh spectrum is a function of the scattering angle and gas density. The velocity of the flow is determined by the phase shift between the reference laser line and the Doppler shifted Rayleigh scattered signal. Velocity measurements are not sensitive to aperture broadening since only the frequency of the spectral

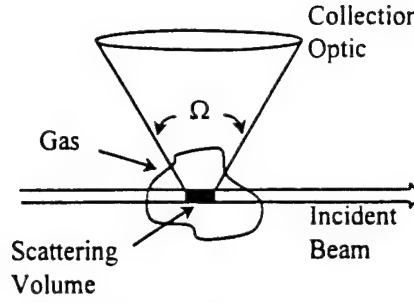
peak is used and the spectrum is symmetrically broadened. The temperature is given by the broadening of the Rayleigh scattered laser light. For a single component gas, the full width at half maximum of the Rayleigh scattering spectrum is proportional to the square root of the gas temperature. The density can be obtained from the intensity of the signal; however, calibration is required for each unique system [13].



**Figure 2.2** Reference Laser Line and Rayleigh Scattered Spectrum

At the low pressures expected in our experiments, the velocity distribution is expected to be Maxwellian. At higher gas densities the molecular motions become correlated and appropriate models must be used to describe the Rayleigh scattered spectrum. Tenti's S6 model [21] is used where needed in this work.

Figure 2.3 shows the solid collection angle,  $\Omega$ , and the scattering volume used for the following calculations.



**Figure 2.3** Solid Collection Angle Illustration

The energy scattering into the solid angle  $d\Omega$  can be found by Equation 2.4.

$$E_s = E_o n L_x \left( \frac{d\sigma}{d\Omega} \right) \sin^2 \chi d\Omega \quad (2.4)$$

Having the electric field perpendicular to the scattering plane (i.e., 's' type), it is noticeable that  $\chi = 90^\circ$  produces the strongest scattered signal from Equation 2.4.

It is critical to have a sufficient number of scattered photons from the Rayleigh scattering interaction. Rewriting Equation 2.4 in the form presented below, Equation 2.5, determines the number of photons scattered through a solid collection angle of  $\Omega$ .

$$N_R = \frac{\epsilon E_o n L_x \lambda \Omega}{hc} \left( \frac{d\sigma}{d\Omega} \right) \sin^2 \chi \quad (2.5)$$

The number density can be found from the ideal gas law [22] presented in Equation 2.6.

$$n = \frac{P}{\kappa T} \quad (2.6)$$

Consider as an example an f/4 optical system with a collection angle of 0.05 [3], having a collection efficiency of 1% used to study a 1 mm long probe volume of nitrogen irradiated by a 1 J, 532 nm laser pulse. This provides for a Rayleigh scattering cross-section of 6.13E-32 m<sup>2</sup>/sr. Making  $\chi = 90^\circ$ , we can find the number of photons scattered through a solid collection angle of  $\Omega$ . Table 2.2 shows a few results pertinent to this project. Note that as the temperature increases and the pressure decreases, the method becomes more difficult as the

number of photoelectrons decreases rapidly with density. As a result, the Rayleigh signal gets buried in the noise.

**Table 2.2 Photoelectron Calculations**

Pressure	Temperature	Number Density	Photoelectrons
1 atm	300 K	$2.446297\text{E}25 \text{ m}^{-3}$	20,080,346
1 torr (0.0013158 atm)	300 K	$3.218811\text{E}22 \text{ m}^{-3}$	26,422
1 torr (0.0013158 atm)	2000 K	$4.828216\text{E}21 \text{ m}^{-3}$	3,963

The Rayleigh scattering spectrum is usually expressed as a function of a non-dimensional optical frequency  $x$  and a non-dimensional collision frequency  $y$  expressed below.

The optical frequency shift  $x$  can be found by Equation 2.7.

$$x = \frac{2\pi(f - f_0)}{Ka} \quad (2.7)$$

where  $f - f_0$  is the frequency shift of the scattered light relative to the frequency of the incident light.

The collision frequency can be found by Equation 2.8.

$$y = \frac{P}{\eta Ka} \quad (2.8)$$

where  $a$ , the most probable molecular speed, can be found through Equation 2.9.

$$a = \left( \frac{2\kappa T}{m} \right)^{\frac{1}{2}} \quad (2.9)$$

The temperature of the gas enters into the Rayleigh scattered profile through the most probable molecular speed as will be shown in Equation 2.14. Temperature is a direct measure of the spectral width as was shown in Figure 2.2. Alternatively, the most probable molecular speed ( $a$ ) can be written as Equation 2.10.

$$a = c_s \left( \frac{2}{\gamma} \right)^{\frac{1}{2}} \quad (2.10)$$

The acoustic wavelength can be found using Equation 2.11.

$$\Lambda_s = \frac{2\pi}{K} \quad (2.11)$$

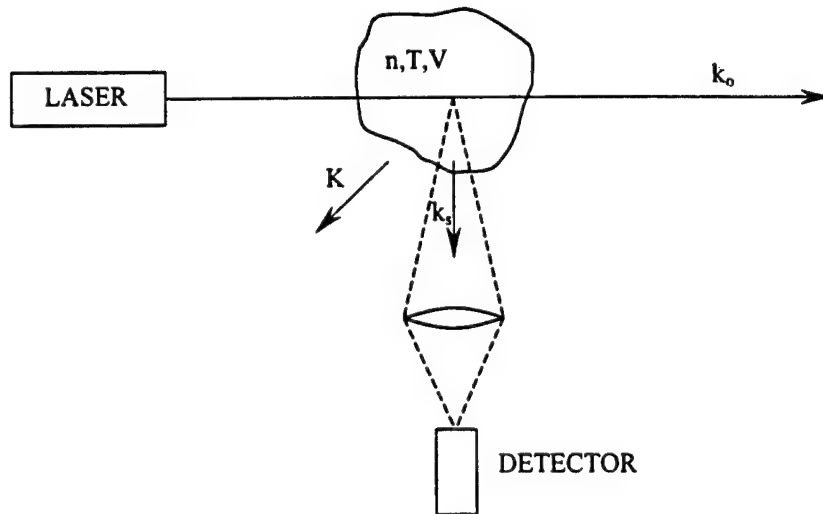
The ratio of scattering acoustic wavelength to molecular mean free path is also  $y$ .

Equation 2.12 shows how the magnitude of the interaction wave vector can be found by knowing merely the wavelength and scattering angle.

$$K = |\mathbf{K}| = 2k_o \sin\left(\frac{\theta_s}{2}\right) = \left(\frac{4\pi}{\lambda}\right) \sin\left(\frac{\theta_s}{2}\right) \quad (2.12)$$

Equation 2.13 demonstrates the relationship between the interaction wave vector and the incident and scattered wave vectors. Figure 2.4 shows the incident wave vector traveling with the laser beam, along with the scattering wave vector traveling in the direction of the detector.

$$\mathbf{K} = \mathbf{k}_s - \mathbf{k}_o \quad (2.13)$$



**Figure 2.4** Interaction Wave Vector as Associated to Scattering Medium

For the conditions expected in these experiments, the normalized spectrum of the Rayleigh scattered light is given by the Gaussian below, which is an equation for a single-component, low density gas, where  $y < 1$ .

$$S(f - f_0)df = \frac{1}{\sqrt{\pi}ak} \exp\left\{-\left[\frac{2\pi(f - f_0) - \mathbf{K} \cdot \mathbf{u}}{aK}\right]^2\right\} df \quad (2.14)$$

Note that the spectral peak is shifted by a frequency proportional to the component of the bulk velocity in the  $\mathbf{K}$  direction.

By introducing the velocity component  $u_K$  in Equation 2.15,

$$u_K = \frac{\mathbf{K} \cdot \mathbf{u}}{K} \quad (2.15)$$

the Gaussian equation can be rewritten as a function of  $x$  along with  $u_K$ , Equation 2.16.

$$S(x)dx = \frac{1}{\sqrt{\pi}} \exp\left[-\left(x - \frac{u_K}{a}\right)^2\right] dx \quad (2.16)$$

#### D. Fabry-Perot Interferometers

There is a need for a very high spectral resolution instrument to resolve the Rayleigh linewidth, which is on the order of 1 GHz. A Fabry-Perot interferometer is the instrument chosen. The Fabry-Perot, unlike other instruments such as the spectrometer, not only allows for the high spectral resolution but it also allows for imaging data to be taken of the flow. The imaging data corresponds directly to specific areas within the plume, providing for point properties to be obtained. The Fabry-Perot was operated in a static imaging mode where light scattered by the measurement region was imaged through the Fabry-Perot causing interference fringes that were recorded using an ICCD camera. The Fabry-Perot interferometer consists of two partially transmitting planar mirrors, Figure 2.5. The instrument relies on multiple beam interference that occurs when light enters the region between the mirrors [23,24]. Thus, the



interferometer transmits a comb of frequencies, separated by the free spectral range. Successive beams have increasing delays, plus a small reduction in amplitude, and the fringes approach a series of spikes. Their shape is described by the Airy function and their sharpness by the finesse, the fringe spacing divided by their width. The finesse depends on the reflectance of the coatings and the flatness of the surfaces. For narrower bandwidths, Fabry-Perot interferometers with larger spacings are used.

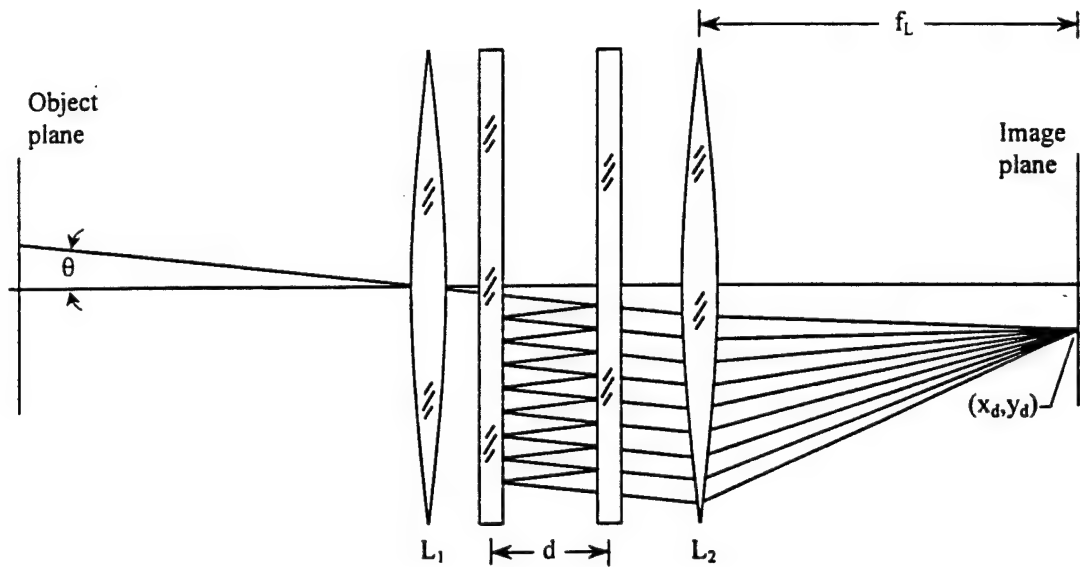


Figure 2.5 Fabry-Perot Interferometer [13]

For an ideal interferometer the finesse could be found by merely calculating it from the reflectivity of the mirrors located within the Fabry-Perot itself,  $F = 4R/(1-R)^2$ . Since these measurements involve losses and calibration errors, we used a slight variation on the original equation presented in Equation 2.17.

$$F = \frac{1}{\sin^2\left(\frac{\pi}{2N_E}\right)} \quad (2.17)$$

$N_E$  is the effective finesse to which the coefficient  $F$  is related. This equation now involves the finesse of the entire system instead of only the Fabry-Perot. One option is to physically measure the finesse during the testing procedure, which would be a good verification of theoretical values. For this work though, the finesse is a fit parameter within the least squares fitting routine used to reduce the data.

The phase change,  $\psi$ , of the light between successive reflections (neglecting any phase change on reflection) may be calculated from Equation 2.18.

$$\psi(f, \theta_r) = \frac{4\pi f \mu d \cos(\theta_r)}{c} \quad (2.18)$$

Note that  $\psi$  changes by  $2\pi$  for a change of mirror spacing of  $\lambda/2$ , which corresponds to the free spectral range of the interferometer.

For an infinite number of reflections and assuming no losses, the transmittance is given by the Airy function presented in Equation 2.19.

$$I_{FP}(\psi) = \left[ 1 + F \sin^2 \left( \frac{\psi(f, \theta_r)}{2} \right) \right]^{-1} \quad (2.19)$$

The total light detected by the  $q_{th}$  pixel of a CCD array can be obtained by evaluating Equation 2.20. This important equation allows you to determine whether or not the camera will obtain enough light coming from the scattering region, which will allow resolution of the Rayleigh image.

$$\langle N_{Dq} \rangle = \int_{\Omega} \int_{\Delta A} \int_{-\infty}^{\infty} [A_R S_R(f, \Omega) + A_w \delta(f - f_0)] I_{FP}(f, \theta_r) df dA d\Omega + B_q \quad (2.20)$$

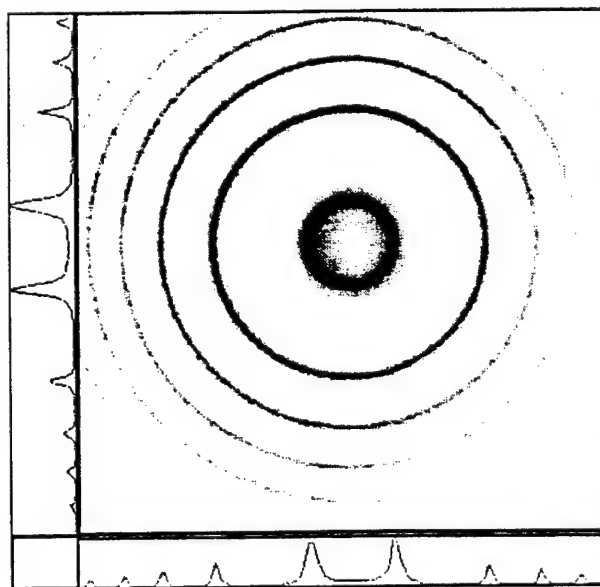
The angle  $\theta$  is the angle of the ray in the interferometer measured from the optical axis, as was shown in Figure 2.5. Theta can be expressed in terms of the position of the ray at the aperture  $(x_d, y_d)$ , Equation 2.21.

$$\theta = \tan^{-1} \left( \frac{\sqrt{x_d^2 + y_d^2}}{f_L} \right) \quad (2.21)$$

When  $\theta$  is small a low photon detection rate occurs, resulting in a low signal-to-noise ratio. Seasholtz wrote, "In practice one selects an aperture size that gives as large a photon collection rate as possible without seriously reducing the instrument resolution. (Detailed calculations have been done by Hernandez [25] to determine the optimum Fabry-Perot finesse and detector aperture size for measurements of gas temperature and velocity for an extended source.)" [11].

### 1. Fringe Pattern

Figure 2.6 is a typical reference image produced from our apparatus by scattering a small portion of light of given wavelength through a fixed mirror Fabry-Perot. The spectrum can only be measured over a spatial region that includes part of an interference fringe. But as the figure shows, there are many fringes located in one image that result in a lot of data being gathered from each individual image. If the Fabry-Perot mirror spacing is decreased, these fringes move toward the axis and disappear. The fringes move outward as the frequency of the laser light entering the Fabry-Perot is increased.



**Figure 2.6** Reference Image for Injection Seeded Nd: YAG Laser at 532 nm

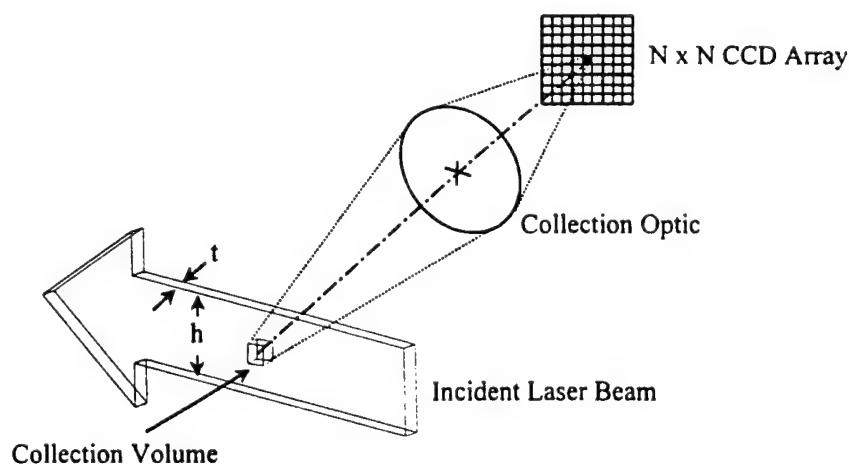
Narrowing the innermost fringe so that it is located on the optical axis, Equation 2.22, may be used to find the other fringe radii where  $n = 1, 2, 3, \dots$

$$r_n = f_L \left( \frac{n\lambda_o}{d} \right)^{\frac{1}{2}} \quad (2.22)$$

Note that although the fringes are unequally spaced, their frequency separations are all equal to the free spectral range Equation 2.23.

$$\text{FSR} = \frac{c}{2d} \quad (2.23)$$

Figure 2.7 shows the relationship between the measurement volume and the CCD array. It is noticeable that there would physically be a one to one relationship between an array pixel and a geometric point of the flow. Therefore a single Rayleigh scattering image could provide thermodynamic information at a number of locations in the flow. The least squares fitting routine used throughout this work was mainly dependent on only the first and second fringe. This provided results at a point in the flow.



**Figure 2.7** One to One Correspondence of Measurement Region to CCD Array

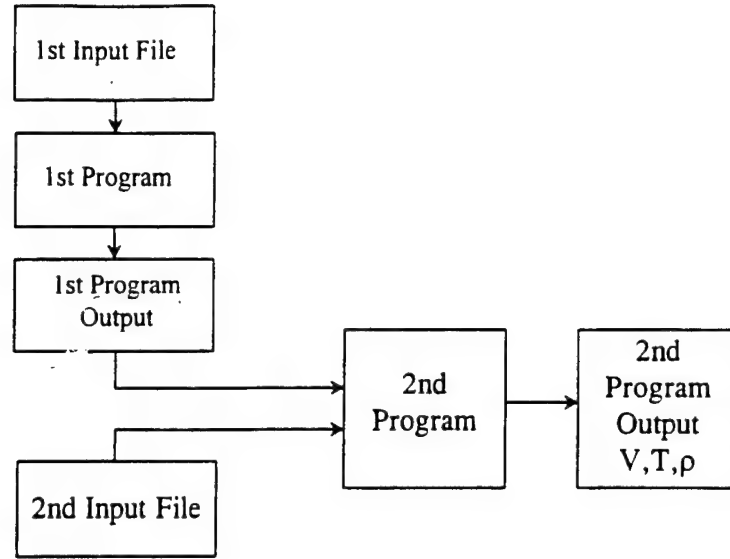
Two large sources of error that can be associated with the Fabry-Perot are acoustic noise or vibrational effects, and temperature drifts. Vibrations of the mirrors within the Fabry-Perot will result in shot-to-shot variation in the phase of the reference image. This will prevent the determination of velocity that is dependent upon the phase shift between subsequent reference and Rayleigh images. Since the temperature is dependent on the Rayleigh broadening instead of the position of the spectral peaks, it is still possible to obtain the temperature data. For the study presented here, vibrational effects were not a problem as the majority of optics were located on air tables. The other source of error, temperature drift, did prove to be a concern for this work. The rods that hold the mirrors in place on a Fabry-Perot proved to be extremely sensitive to rapid temperature changes. Thermally induced length changes will occur in the rods. Therefore, a thermal enclosure was built to hold the temperature of the Fabry-Perot constant and will be discussed further later in this work.

#### E. Fortran Codes

Many different Fortran codes were used throughout this work. They ranged from complicated least squares fitting routines to simplistic batch files that were used to perform easy tasks. The three main codes that were utilized for this work are described below.

##### 1. Seasholtz Code

The Seasholtz code was made up of two main codes which each had many individual parts. Figure 2.8 shows a simplistic breakdown of Seasholtz's two programs. The first program analyzes the reference image and applies a least squares fit to the image. It requires input parameters such as the center point of the fringes, the wavelength, the finesse, the diameter of the first two fringes and a few others.

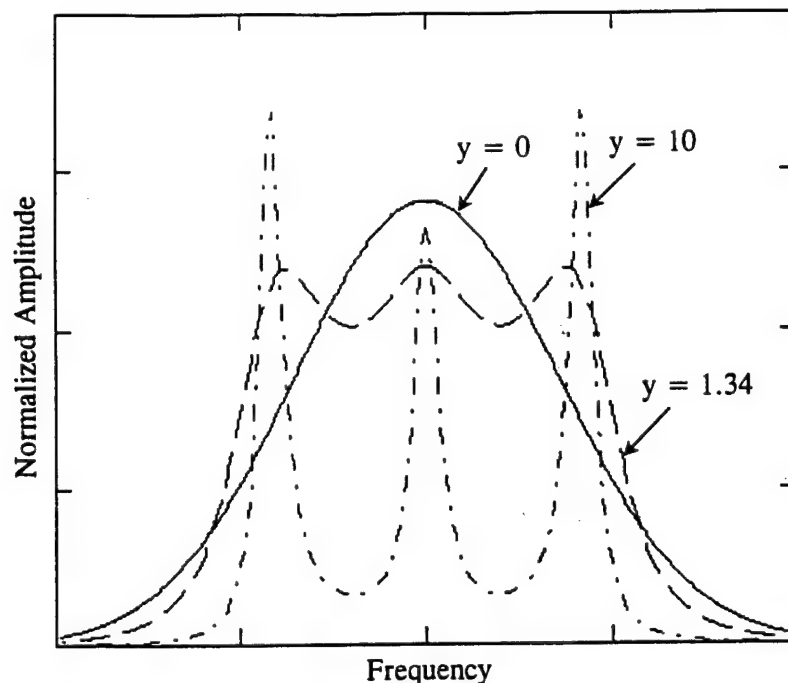


**Figure 2.8** Rayleigh Scattering Program Schematic

These values are used in conjunction with the image itself and a dark current image as inputs to the first program. This program then outputs the fit image along with the parameters to the fit. This output file along with a second input file, associated with the Rayleigh image, are then used as inputs into the second program. This program fits the Rayleigh image, analyzes the two fits and outputs velocity, temperature, and density (if it has been calibrated) [13].

## 2. Tenti Model

As stated earlier, a Gaussian assumption for the Rayleigh scattering signal is not accurate for various density regimes. Therefore a kinetic theory code, in this case Tenti's S6 Model [21], was utilized to predict the profiles in these other regimes. This model requires the shear viscosity, the thermal conductivity, and the internal specific heat of the gas. These values are obtained from the Fluid program [26] that is part of the Seasholtz code. For the low density gas case where  $y < 1$ , a Gaussian profile may be assumed. But as  $y$  approaches one or becomes greater than one, which corresponds to higher density gases, collective effects influence the scattering spectrum. These collective effects become apparent as sidebands that are located about the central peak as shown in Figure 2.9.



**Figure 2.9** Rayleigh Scattering Spectra for Three Different Regimes

Scattering coming from thermally excited random acoustic waves causes the sidebands, referred to as the Brillouin-Mandelstam doublet. The spectrum shape within these sidebands is only a function of the  $y$  parameter and may be modeled using a continuum theory [27]. A more detailed kinetic theory is needed in the transition regime, where  $y \approx 1$ . "In all cases, the Rayleigh scattering spectral shape is a function of the gas thermodynamic properties, which forms the basis for a diagnostic to measure gas density, temperature and velocity [28]."

### 3. Forkey Code

The Forkey code [29] is a code that aids in the design and study of iodine absorption cells. This code is also made up of two programs. The first generates an output file, which contains information about the transitions in the wavenumber region specified. This output file is then used as an input to the second program which requires information about the cell temperature, pressure, and length and generates an output file with cell transmission as a function of wavenumber, over the wavenumber range specified. The output of these programs was compared to experimental data for the Nd:YAG by Forkey et al. to verify the code's

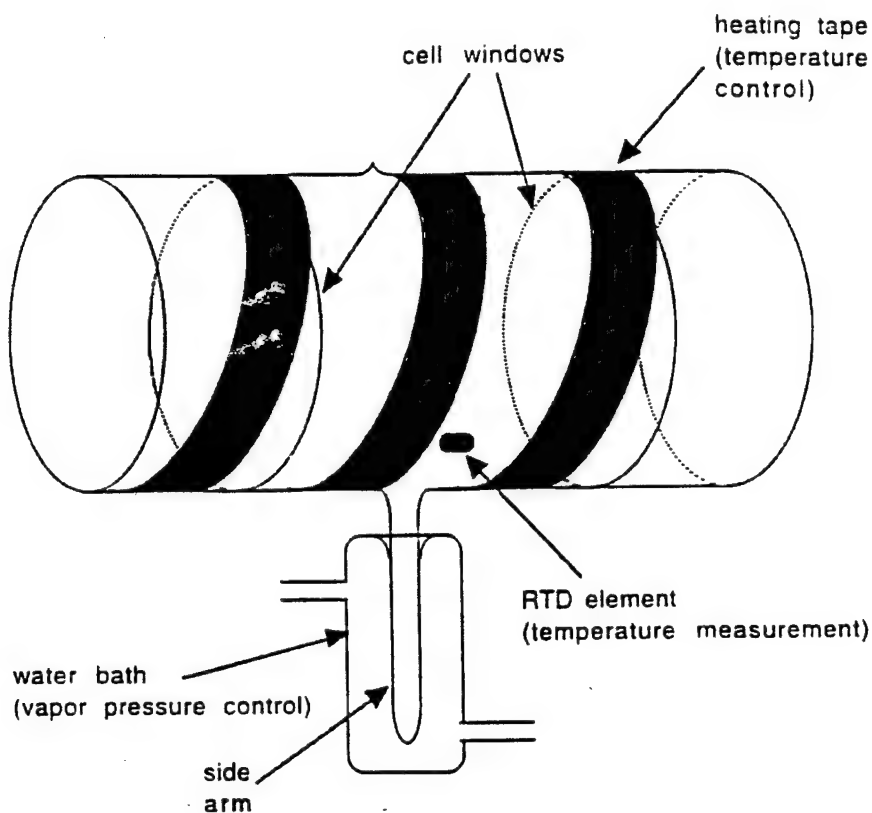
lookup tables utilizing parameters taken at the 532 nm range [29]. They used theoretical equations to describe other wavelengths but found that in real practice the values they obtained in the lab were more accurate than these equations, so they created a lookup table for the Nd:YAG that corrected for these discrepancies.

#### F. Iodine Absorption Filter

Unfortunately, broadband background light is not the only source of interference that affects this method. Stray light produced from windows and solid metal surfaces can dominate a Rayleigh signal. This is especially true when the Rayleigh signal is not shifted far from the incident wavelength. The stray light that comes through the system is at the same wavelength as the original beam because there is no velocity to shift it. Therefore if the stray light is a strong signal and the measurement to be taken is in a low-density environment, thus a weak Rayleigh signal, experience tells us this will end up with a blurred image or no image at all.

Thus the appropriate apparatus to use to eliminate this problem would be an iodine cell, Figure 2.10. Though other gases have been utilized for this work, an iodine vapor cell has been shown to work best by Forkey et al. [29]. The iodine absorption cell is merely made up of two optical flats on either end of a glass tube. The diameter chosen for this work was 3". The stem as seen in the figure holds the iodine crystals. The purpose of the temperature controls is to hold the pressure of the iodine vapor at a constant value so that the filter cut-off will not shift during the course of a test.

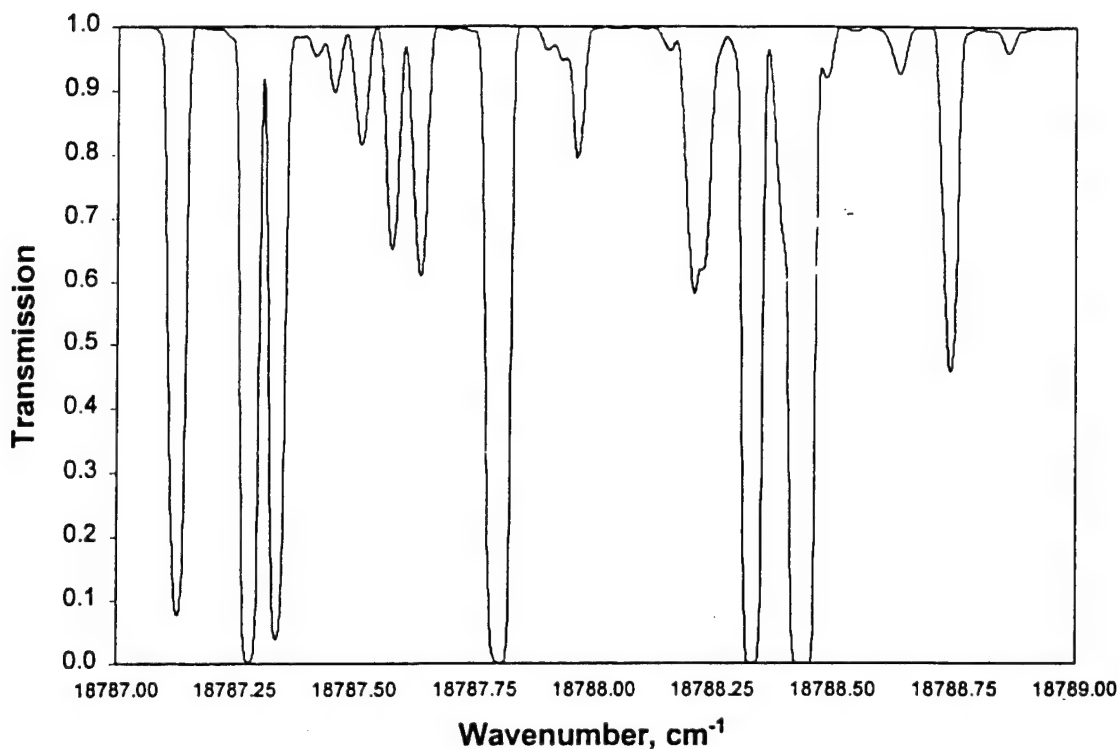




**Figure 2.10** Iodine Absorption Cell

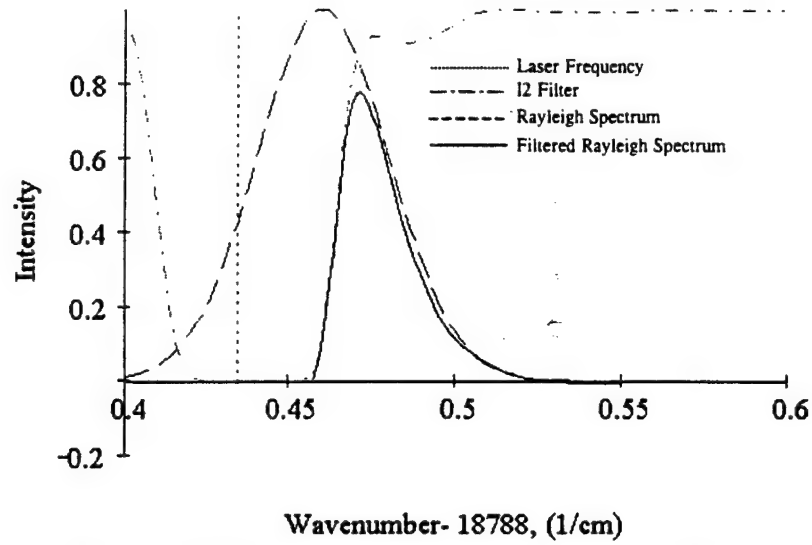
The iodine absorption cell is placed in front of the Fabry-Perot. It lets the Doppler shifted Rayleigh scattered light through and it blocks the stray light at the initial laser frequency. This is done by tuning the laser to the absorption line of the species in the filter. The Nd:YAG laser has an analog voltage supply input that varies the temperature of the seeder and thus slightly shifts the frequency of the output beam. Because the YAG frequency is an important parameter utilized in the data reduction procedure, it must be recorded for each test. Previous work used a HeNe, as a reference, in conjunction with the YAG to determine the exact frequency the YAG was operating at.

Ideally a narrow notch filter centered at the initial frequency of the laser beam is needed. Many of the iodine absorption lines behave like this at the 532 nm wavelength as seen in Figure 2.11. For example it would be wise to select the line near  $18787.50 \text{ cm}^{-1}$  (532.26 nm) because of its relatively sharp edge on the high frequency side, as well as its not having another close adjacent line on the high frequency side.



**Figure 2.11** Iodine Absorption Spectrum for 200 mm Path Length; Pressure=0.46 torr, Temperature = 303 K (calculated using code supplied by Forkey [30])

Figure 2.12 shows the initial frequency of the laser beam that would be entering the measurement volume as a dotted line. This is the frequency on which all of the excess scatter would be localized. The iodine cell will filter these frequencies out of the final signal that reaches the detector. The solid line is the only portion of the Rayleigh signal that would make it through the Fabry-Perot. The idea behind this method is to center half the Rayleigh Gaussian profile exactly on the sharp cutoff. This will block the maximum amount of light while still letting through the signal to be detected.



**Figure 2.12** Iodine Cell Effect on Rayleigh Scattering Spectrum

Equation 2.20 now has to be modified to include the iodine cell term,  $I_{I_2}(f)$ . The expected number of detected photons for the  $q^{\text{th}}$  pixel with area,  $\Delta A$ , can be seen in Equation 2.24.

$$\langle N_{Dq} \rangle = \int_{\Omega} \int_{\Delta A} \int_{-\infty}^{\infty} [A_R S_R(f, \Omega) + A_W \delta(f - f_0)] I_{FP}(f, \theta_r) I_{I_2}(f) df dA d\Omega + B_q \quad (2.24)$$

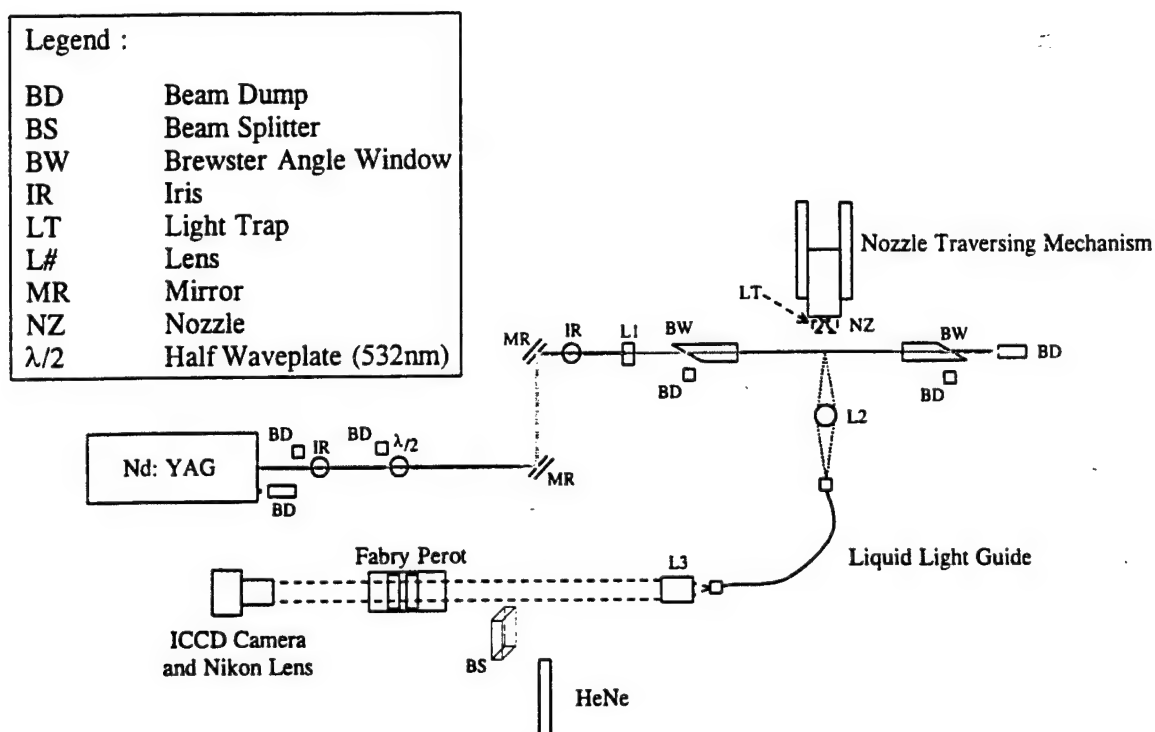
## Chapter III

### EXPERIMENTAL SETUP

The second harmonic of a Spectra Physics GCR-290 pulsed Nd: YAG Laser operating at 10 Hz was used to probe the plume of a microwave plasma thruster. An injection seeder narrowed the linewidth of the laser to less than  $0.002 \text{ cm}^{-1}$ , which is necessary for the Rayleigh scattering technique [31]. A 0-6 kW variable power microwave generator supplied a  $\text{TM}_{011}$  resonant mode cavity. Filtered gas enters the resonant cavity through three tangential ports forming a vortex, which stabilizes the plasma discharge. The filters on the gas supply system remove particles with diameters larger than  $0.2 \text{ }\mu\text{m}$ . Gas heated by the plasma discharge is accelerated through a converging-diverging nozzle into a 18" x 28.5" cylindrical vacuum cavity. A traversing mechanism allows movement of the nozzle exit plane over a range of six inches. The nozzles studied were carbon and boron nitrate based. They were chosen to evaluate the effect of conductive and non-conductive nozzles. The area ratios used ranged from 14 down to 1.8.

The beam path is shown in Figure 3.1. Light leaves the laser and passes through a half wave plate allowing for adjustment to the polarization of the beam within the measurement volume. The polarization was adjusted so that the electric field vector was perpendicular to the collection optics. The beam height is then adjusted through a telescoping mirror assembly. A 700 mm focal length cylindrical lens focuses the light to a 0.1 mm sheet in the measurement region. The light enters and exits the vacuum chamber through Brewster angle windows. Any power being supplied to the measurement region by the laser is negligible. This is because the Rayleigh technique is an elastic scattering process where the internal energy of the molecule does not change. If the molecule being studied were to absorb energy at the 532 nm wavelength used for this work, then breakdown could occur resulting in inaccurate results. But we know, for example, that  $\text{N}_2$  doesn't absorb light at the 532 nm wavelength or the color of

the sky would not be blue. A series of irises before and after the measurement volume minimized scattered light. Appropriate baffles were used in strategic places to minimize the scattered light that could reach the detector.



**Figure 3.1 Optical Setup for Measuring Axial Properties**

The Rayleigh scattered light is focused with a 250 mm spherical lens into a 5 mm core diameter liquid light guide. The lens is positioned such that it is perpendicular to the electric field vector and  $45^\circ$  to the axial velocity vector of the plume. The light exits the liquid light guide and is collimated by a Nikon® 135 mm f/2.8 lens. The collimated light passes through a Burleigh RC-170 Fabry-Perot interferometer. The interferometer is mounted in a temperature controlled enclosure to reduce thermally induced changes in the mirror spacing and parallelism. Finally the light is focused with a Nikon® 180 mm f/2.8 lens onto a Princeton Instruments® ITE/CCD 1024x256 EMLDG-1 cooled intensified camera with a quantum efficiency of 0.1. The pixels on the camera are  $26 \mu\text{m} \times 26 \mu\text{m}$ .

The intensified CCD camera is equipped with a Princeton Instruments® PG-200 Programmable Gate Pulser Generator. This allows gating with widths down to 5 nanoseconds. The Pulse Generator was triggered by the Advanced Q-Switch from the laser and gated to capture only the 10 nanosecond laser pulse. The gain on the intensifier could be adjusted to optimize the image. The images were digitized with a 14 bit A/D converter and transferred to a laboratory computer for storage and analysis.

A stepper motor traversing mechanism carried physical probes such as pitot tubes, thermocouples and langmuir probes through the measurement volume.

#### A. Microwave Model

The microwave thruster used for this work is based upon a design that was originally developed by Micci and coworkers [32,33]. The thruster was rebuilt and modified to fit the needs of this work by removing the viewport window, moving the placement of the gas inlet ports, along with modifying the waveguide coupling section to fit a different type of microwave source. The resonant cavity still utilized tangential inlets for gas flow. These enabled the flow to be stabilized by a vortex pattern of gas. The gas inlets were adjusted to accept gas from a manifold allowing for the rapid change of gases being studied.

#### B. Vacuum Chamber

The vacuum chamber shown in Figure 3.2 enabled testing over a range of pressures from 1 atm down to 1 torr.

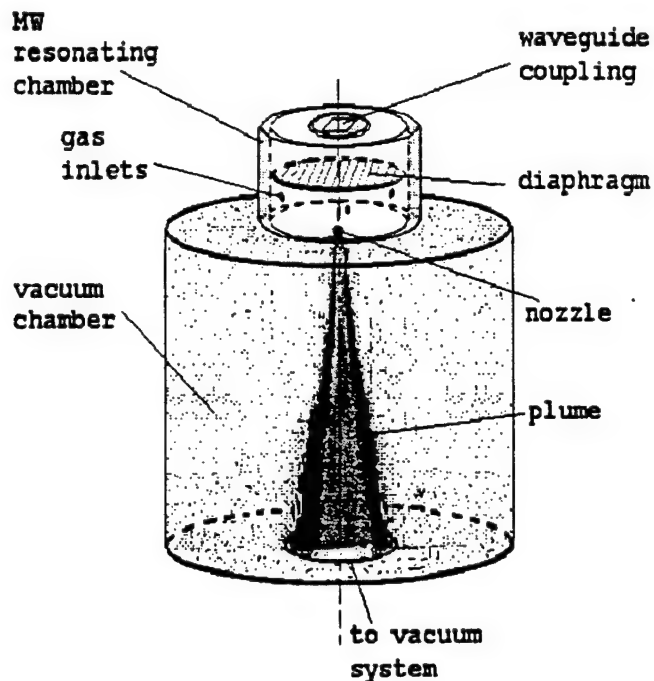


Figure 3.2 Vacuum Chamber and Resonant Cavity

#### 1. Optical Access

Brewster Angle windows were utilized to allow the laser beam to penetrate the side walls of the vacuum chamber. They also helped a great deal to diminish the reflected scattered light that is caused by shooting a beam of light through a medium such as quartz.

#### 2. Baffle System

Figure 3.3 demonstrates how the light would be baffled so that the minimum amount of stray light would be obtained in the measurement region. The technique utilized for this group was to custom cut each iris separately. It proved to be very tedious and time consuming but well worth it in the end to improve the signal to noise ratio. Each iris, merely made from a black rigid paper, would be placed in its appropriate holder then hit with enough of the Nd:YAG light so that it would ablate away the segment where the beam was most intense. A utility knife would then be used to precisely cut out the oval associated with the burn. The final product allowed for the main portion of the beam to travel through the system without ever hitting any iris, thus reducing scatter. Each iris would block any forward or reverse halo associated with the beam. This halo would come from the divergence of the beam, mirrors,

and windows. Point A in Figure 3.3 is the closest distance that the rocket nozzle could be placed to the laser without being lit up by some of the halo.

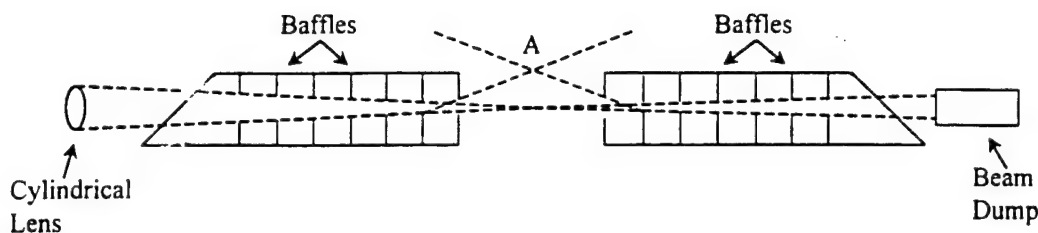


Figure 3.3 Baffle System

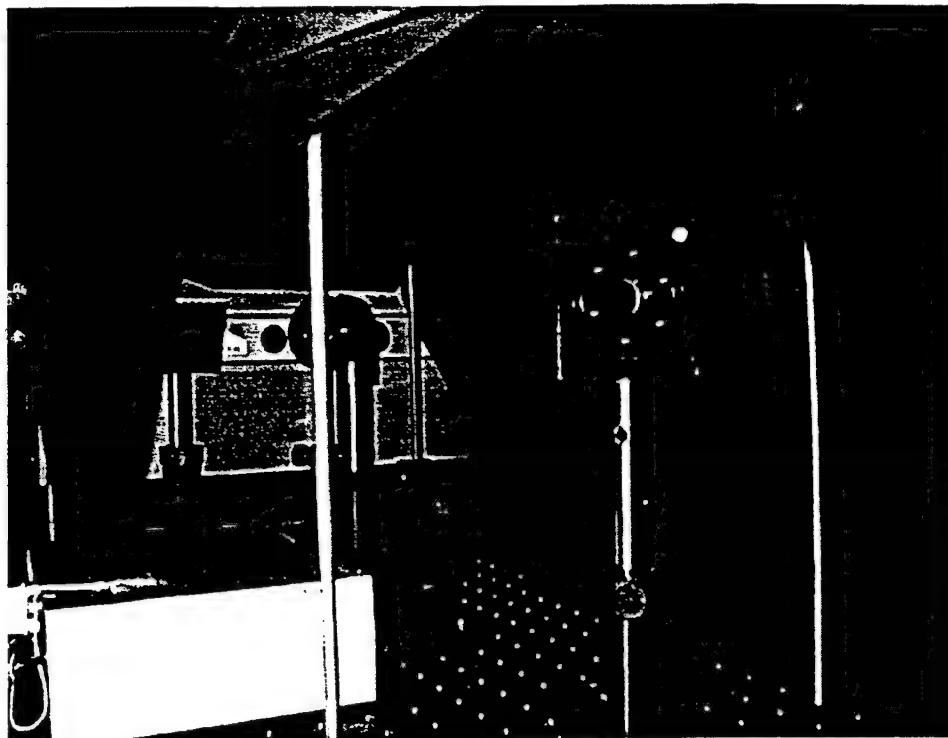
### C. Scattered Light

Stray laser light has the same frequency as the incident laser light. Therefore, for small Doppler shifted flows where the Rayleigh signal is at or near the incident frequency, it is important to use appropriate light traps, apertures and baffles. Otherwise, the signal-to-noise ratio will diminish along with the measurement accuracy. This proved to be very difficult to accomplish in confined measurement locations where the laser beam is near internal surfaces. The technique described by Miles et al. of using an iodine vapor cell [29] works for high velocity flows where the frequency of the Rayleigh scattered light is shifted well away from the laser frequency (which is again the case for the work presented here.) If the signal were not shifted a given amount, which depends on the iodine cell setup, the Rayleigh signal itself would be filtered out. Should the measurement region be a confined space along with a very low speed flow, Rayleigh scattering may not be a feasible technique to use.

#### 1. Stray Light Baffle System

Light tight dark room cloth was setup up on an extended rod assembly that could surround the entire beam path and vacuum chamber assembly to minimize stray light bouncing around the room (Figure 3.4). The end result was that the laser beam traveled down an enclosed path. This helped to eliminate stray light reaching the camera system.





**Figure 3.4 Light Tight Cloth Assembly**

## 2. Background Light

Aside from the broadband background light, there is a certain amount of light that is gathered with each shot whether it is pulsed or not. This background light can be determined by taking an image triggered off the laser set at its lowest power level (not emitting any light). Another background light source that is within each image is any excess charge left on the charge coupled array itself providing for a slight variance in the base image light. This can be determined by taking an image with the lens cover cap on. We refer to this image as a dark current image. By accounting for these backgrounds they can be subtracted from the final images.

## D. Mode Locking and Seeding

A photomultiplier tube can be used to check to see if the laser is mode locking. The modes can be seen by aiming the photomultiplier tube at a portion of the beam and plugging the response into an oscilloscope triggering off the laser. If the seeder is working properly, there should be a single Gaussian profile. If the seeder is malfunctioning or not turned on at all, the

profile will look random and shaky. The maximum height of the malfunctioning profile will not be anywhere near the truly mode locked signal. It is this mode locking that allows the Fabry-Perot to obtain a very crisp image. If multiple modes, as are in the original laser beam, were viewed through the Fabry-Perot, the final result would end up with a bright blurred image.

## Chapter IV

### PROCEDURE

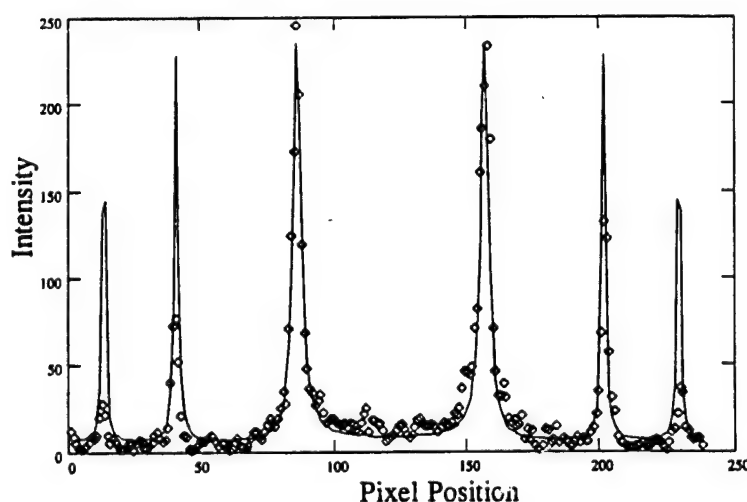
The procedure to operate this Rayleigh scattering system was as follows. A calculation was done to determine the proper mirror spacing that would produce the number of rings needed for each experiment. The Fabry-Perot mirrors would then be set at this distance. A HeNe laser would then be used to align the entire optical system. The HeNe would first be leveled with respect to the optics table. The height of the beam would then be adjusted to match that of the Nd:YAG beam. Preliminary optics could then be quickly aligned with the aid of the existing grid on the optics table itself as another reference point. The more complex part of the alignment procedure involved the fiber optic, Fabry-Perot, and camera. Meticulous care had to be taken to see that these three items were all operating at the exact same physical level and orientation. This would be the key to producing a centered fringe pattern on the ICCD array. The first step was to check that the first lens in the system, on the receiving side, was focused to a point centered on the fiber optic, thus producing collimated light that would enter the Fabry-Perot. This collimated beam also could not be askew in any way. To accomplish this, the HeNe was shot down the viewing axis over the top of two pins, offset in height to each other but partially in the beam. This allowed for the shadow of the first pin to be seen on the second pin along with the combined shadow then on the center of the optic that was being aligned. This procedure checked not only the height of the optics but the centeredness of each optic as well. This would be done for each of the three items one-by-one. The beamsplitter used to guide the HeNe beam down this path would then be used to send the beam down the entire path. Proper alignment was achieved when all of the back reflections went back directly into the HeNe. The reflections coming from the Fabry-Perot which appear on a diagonal would all be tuned into the HeNe using the manual adjustments on the base of the Fabry-Perot. When

all of the reflections virtually traced the incoming beam, the HeNe would start to twinkle a slight amount. The HeNe beam that made it to the camera face would then be examined.

The Fabry-Perot would be turned on and a piece of paper would be placed on the outside of the camera lens cap allowing for the user to see the fringe pattern produced. Initially the image coming through the Fabry-Perot would have fringes cutting across the image that would not be centered. By adjusting the three main knobs on the Faory-Perot that alter the mirrors axes, these interference fringes could be centered on the centerline. This was done by turning one knob at a time in a direction that spaced the fringes farther apart. Depending on which way the knob was turned, the fringes would either get closer together or further apart. Just at the moment the fringes changed direction of movement, i.e., coming in from the right hand side but then start to come in from the top, the user would move to the next knob. After following this procedure on all three knobs, the final result was a very bright spot of light that with a slight adjustment of any knob brought an interference fringe over it. The ramp located on the piezoelectric controller to the Fabry-Perot was turned on to test to see how good the alignment was. This would vary all three knobs in a ramp fashion. A dot would appear centered on the viewing axis blinking on and off. This then meant that the system was aligned. Once the mirror spacing appropriate for the tests is determined, this alignment procedure didn't have to be done again unless something was bumped. The tuning for later tests might require a slight adjustment, but generally were corrected by using the Faury-Perot controller, which provided a more precise control of the three axes.

Four images were taken for a typical measurement. First, a dark current image was taken to characterize the CCD array. Second, a reference image was taken by scattering light off a pin placed near the measurement volume. Third, a Rayleigh scattered image was taken and finally a second reference image was taken. A 200 x 200 pixel image region centered on the fringe pattern was used for all images. The reference images before and after were used to determine the finesse and initial phase of the interferometer and the coordinates of the center of the fringe pattern. This was accomplished by fitting the theoretical Fabry-Perot instrument function to the measured reference image with a least squares fitting routine developed by Seasholtz [13]. The fit parameters from the reference image were taken as inputs in a second

routine which varied temperature and velocity in a nonlinear least squares routine to fit the theoretical Rayleigh scattered spectrum as imaged through the Fabry-Perot. In both the reference image and the Rayleigh image the amplitudes of the broadband background light, laser light scattered from the walls and Rayleigh scattered light were allowed to vary to obtain optimal convergence. The dark current image was subtracted from the reference and Rayleigh images before processing. Figure 4.1 shows the typical least squares fit to a cross-section of a Fabry-Perot image. The data points indicated by diamonds are the intensities of individual pixels. The solid line is the least squares curve fit to these points.



**Figure 4.1** Least Squares Fit to Reference Image

#### A. Fortran Codes Developed

Many different Fortran codes were created to breakdown large data acquisition data sets to be analyzed in manageable sets using a graphing package like Excel®, Matlab®, or Mathcad®. These programs allowed for subset sections to be analyzed instead of the entire array because the array could be thousands of data points long. Programs were then written to recombine these subsets back to their original form. Other programs that were developed enabled the easy manipulation of the ICCD images. They involved reading headers, copying files, breaking off different parts of data, and analyzing the results.

### B. Daily Burns

The laser tuning was checked prior to each test series. A piece of Polaroid® 667 B&W film that had already been developed, therefore black, would be placed within a plastic bag and then placed in front of the laser beam. By firing a fairly high amount of power at the strip, the ring pattern of the beam could be seen along with the relative intensity. These burns could then enable the user to tune the laser to the desired operative laser focus and intensity levels.

### C. System Check

The Rayleigh system would be periodically checked for accuracy using a series of pitot tubes, thermocouples and high-speed data acquisition boards. These intrusive devices provided reference points that could be compared to the Rayleigh scattering results to determine whether there was drift or any other fluctuations in the system.

### D. Data Acquisition

Labview™ was used in conjunction with the high-speed data acquisition boards. The programs created for this project involved running many different devices at any one time. The final result was a nearly complete automated system. The only devices that could not be fully controlled by the board were the large voltage switches on the lab wall that sent electricity to the microwave power supply along with the power supply for the vacuum system. Everything else was on stepper motors, solenoid valves, and other electric switches and monitors.

### E. Data Analysis

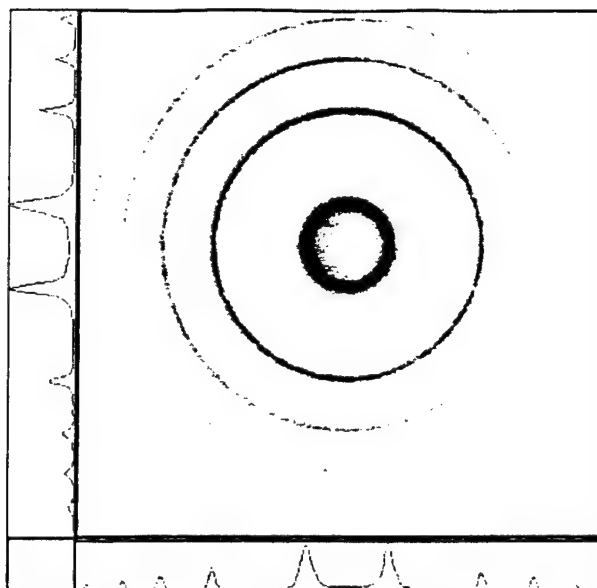
The three main images would be brought up with Winspec™ and visually analyzed to determine key parameters needed in the data reduction. These parameters involved intensity levels, diameters, positions, and some others. They would then be run through two codes which would analyze them and then compare them. This provided for final thermodynamic properties to be found.

## Chapter V

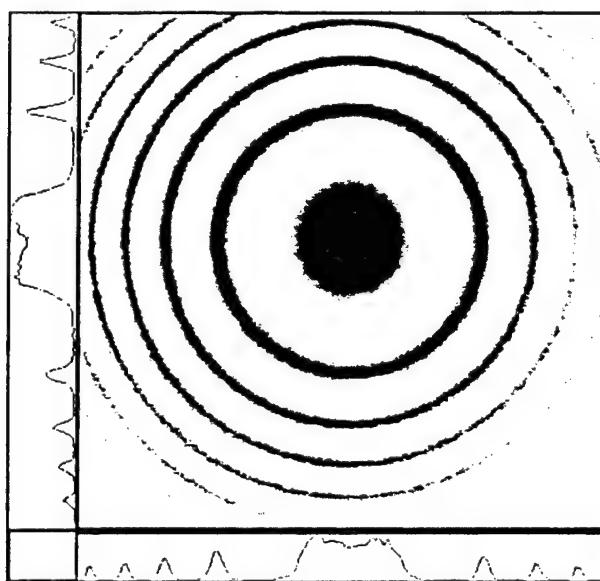
### RESULTS

Two series of tests were run using the Rayleigh scattering method. The first test was run with nitrogen in the vacuum chamber. The chamber was purged with filtered nitrogen several times to remove all particulates. It was then filled to atmospheric pressure with filtered nitrogen, allowing for a pure Rayleigh signal. It was hoped that Rayleigh scattered signals could be taken as the pressure in the vacuum chamber was decreased; however, movement of the vacuum chamber due to pulling the vacuum caused misalignment in the optics, thus eliminating that possibility. Rayleigh scattering successfully measured the temperature of the gas in the purged vacuum chamber after accounting for drift of the interferometer as will be discussed in the following paragraphs. This experiment was repeated for argon and air.

Figures 5.1 and 5.2 show a reference and corresponding Rayleigh image respectively. This Rayleigh image is for nitrogen at atmospheric temperature and pressure. The least squares curve calculated a temperature of 345 K and a velocity of 270 m/s. These results were very disappointing, as we anticipated a temperature of 293 K and a velocity of 0 m/s. A second reference image revealed that both the finesse and initial phase of the interferometer had drifted considerably from the initial reference image.



**Figure 5.1** Reference Image for Injection Seeded Nd: YAG Laser at 532 nm



**Figure 5.2** Rayleigh Scattered Image of Nitrogen at Atmospheric Temperature and Pressure

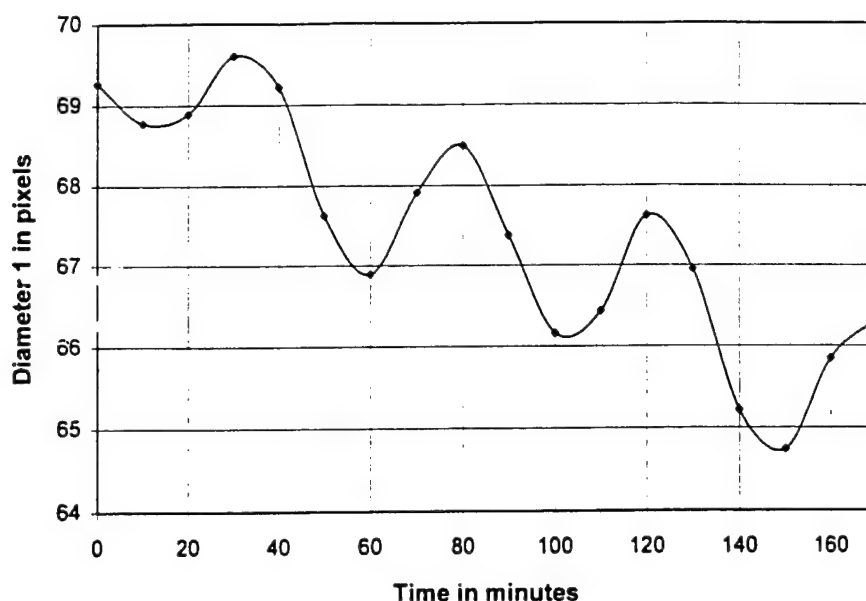
#### A. Thermal Drift

Subsequent tests to determine the source of this drift revealed two major sources. First, variations were noticed during warm up of the laser, interferometer, and camera. A warm up time of at least two hours was required to stabilize the system. Second, even after the warm up period, thermal drifts in the room temperature caused substantial drifts in the interferometer.



This drift is due to thermal expansion and contraction of the metal within the interferometer, specifically the rods holding the mirrors parallel. A thermal enclosure for the interferometer was constructed with optical windows. This enclosure was controlled with a constant temperature water bath. This greatly reduced the drift, but Figure 5.3 shows significant drift still existed. The 30 to 45 minute cycle noticed in the drift can be attributed to the on/off cycle of the air-conditioner and the constant temperature bath. The longer cycle, which is visible in the entire twelve hour run [34], is due to overnight cooling. The drift tests presented in this paper were all run the same way and they are all presented on a three-hour time scale so direct comparisons can be made.

The same optical setup was utilized as it was discussed in Chapter 3, but instead of the light entering the system from the measurement region, the fiber optic was brought back on the original optics table and focused at the HeNe. This allowed for the HeNe beam to travel down the entire path, which would create a crisp reference image on the ICCD array. The assumption that was made for these tests was that the HeNe wavelength was stable. Should it fluctuate, causing the fringes to move, instead of the thermal expansion of the Fabry-Perot, the tests would be inconclusive. The tests were all run at night after an extended warm-up period during the day. After the warm-up period, the device would be aligned and focused one last time before the test was run. These tests were set up in a way that they could be run for hours on end. To reduce the data, Fortran codes were developed that accomplished many different tasks, such as breaking of frames, reading headers, copying files pixel by pixel, and many different bundle programs that could bring the final data all together for analysis. A discussion on the manipulation of \*.spe files can be found in Appendix C.

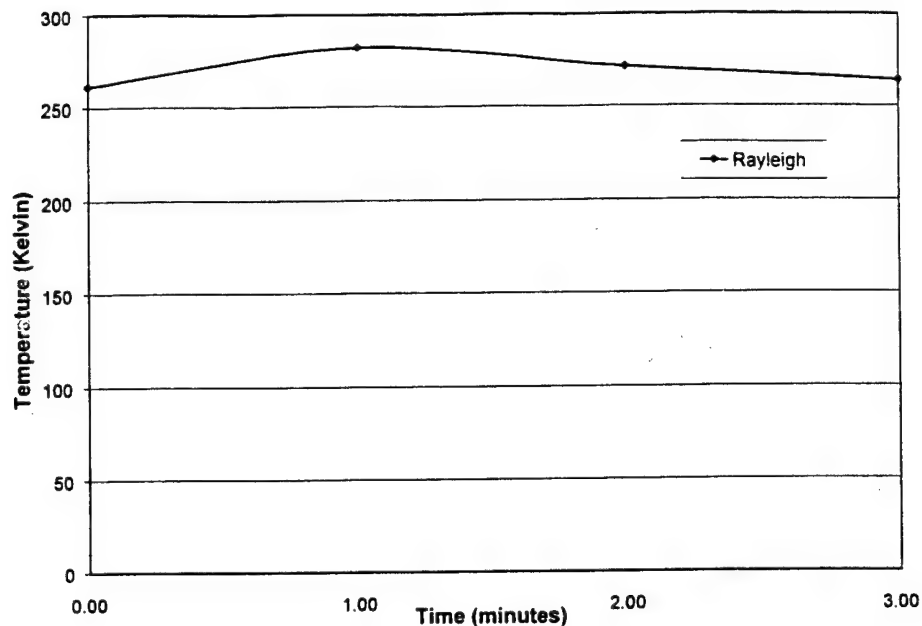


**Figure 5.3 Thermal Drift of the Fabry-Perot Interferometer Over 3 Hours**

The errors found in the earlier tests were attributed to the drift of the Fabry-Perot. This is because the phase of the system is dependent on the diameter of the innermost fringe as well as the distance between the Fabry-Perot mirrors and the frequency of the laser light. Should either of these change during the course of a test then the data will be inaccurate.

#### B. Temperature Measurements

Utilizing the UAH version of the thermal enclosure, Rayleigh scattering measurements were again taken. The results shown in Figure 5.4 show the attempt to measure room temperature, approximately 297 K. As seen in this figure the results fall below this value. It was believed that the results fell within the uncertainty of the code itself. This was proven to be true later. Having obtained velocity and temperature data at atmospheric conditions, further tests were tried at lower density levels.

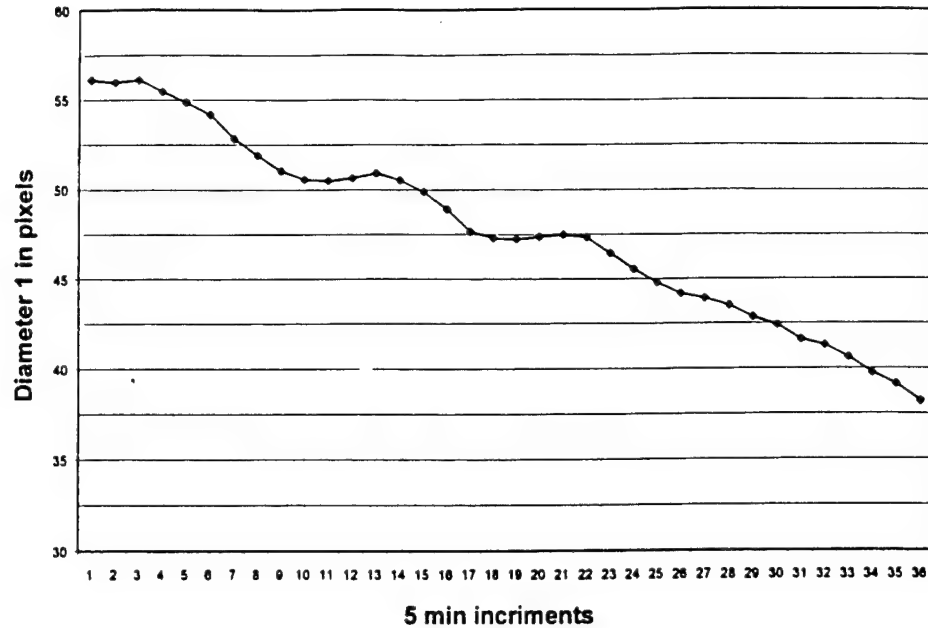


**Figure 5.4 Rayleigh Scatter Room Temperature Measurements**

Obtaining a sufficient signal to noise ratio at vacuum pressures proved to be much more difficult. The scattered laser light coming from the walls of the vacuum chamber was greater than the Rayleigh scattered signal. This prohibited effective evaluation of the Rayleigh image at pressures of 1 to 2 torr with the current setup. The iodine cell was concluded as being necessary to achieve the desired measurements at these lower pressures, but was not evaluated in this program.

#### C. Burleigh Thermal Isolation Box

The significant drift still present promoted the decision to purchase a more precise, commercially available thermal enclosure. The thermal enclosure was ordered from the Burleigh Company. Another series of drift tests was conducted to check the performance of the thermal isolation box. The new thermal isolation box had two temperature settings (low and high) where the low setting corresponded to 29°C and the high setting corresponded to 33°C. Figure 5.5 shows the results for the low setting. This illustrates that the Fabry-Perot still basically has a gradual drift that would inhibit data collection.



**Figure 5.5 Low Setting Night Drift Test**

Figure 5.6 shows the results of a drift test with the high setting. We noticed many different plateau points. This is very good because it means that at these plateaus the finesse is not fluctuating at all; therefore, the phase will not shift. This enabled accurate measurements to be taken without any corrections due to drift. This was done by merely taking a reference image before a test and one after and then comparing the two images' fringe diameters. If they had changed then the test data was inconclusive. Note that the y-axis between Figures 5.3, 5.5, and 5.6 are not the same. This was to enable detailed resolution of the data. As we can see in Figure 5.6, the Fabry-Perot can hold its stability for time periods up to one-half an hour and the overall drift of the Fabry-Perot is very low for a three-hour time frame. The time to take one data set may only be 20 ns; this means that many different data sets can be obtained within one plateau. Obviously the longer the Fabry-Perot is let to warm up along with the rest of the system, the more stable the whole system will be. Note that these longer drift tests were conducted using the HeNe laser instead of the Nd:YAG for safety reasons.

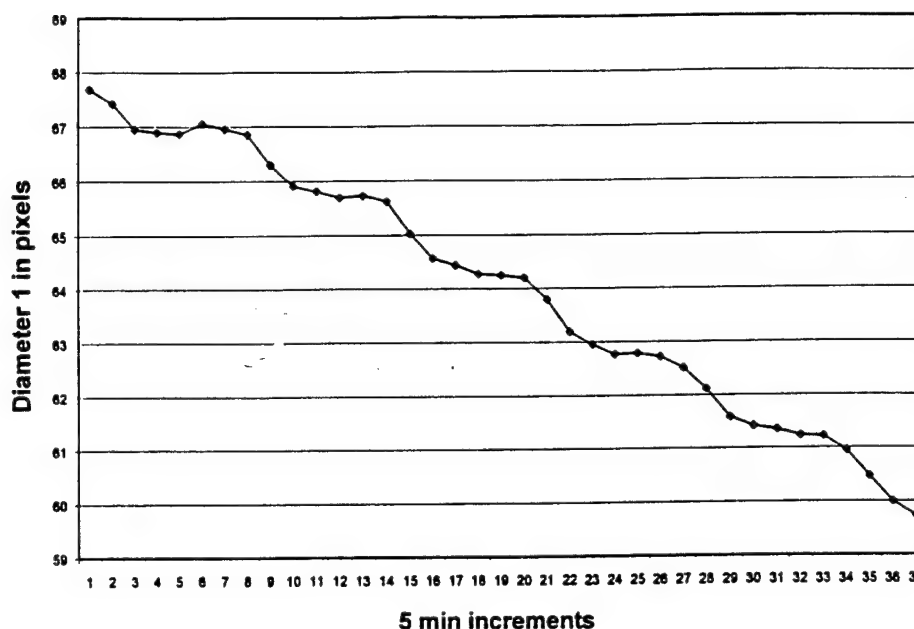


Figure 5.6 High Setting Night Drift Test

Conclusions that were drawn after running all of the tests were that the first box we designed was a lot more robust. It heated everything around itself, thus partially counter-reacting any quick drifts in the room temperature, but it was not as accurate as the Burleigh box. The Burleigh box was not built to work against the room temperature fluctuations; instead it was built to hold only the interior of the box from thermal drifts. Burleigh guaranteed its box down to  $\pm 0.1^\circ\text{C}$  off of the given set point for up to a  $6^\circ\text{C}$  room temperature change. The new box had a very good reaction time and satisfied the requirements of the experiment. Another conclusion that was drawn by inspecting the figures was that as the room cooled, the diameter of the fringe would decrease and vice versa. Thus if the temperature remained a problem for a given setup, its effect could perhaps be subtracted by accurately tracking the room temperature along with all the many parameters associated with the method itself. The best way of completely getting around the problem is to take both the reference and Rayleigh image simultaneously as shown by Seasholtz et al. [13]. This doesn't allow for any change in the parameters at all.

#### D. Uncertainty Analysis

The uncertainty associated with the values of temperature and velocity determined by Seasholtz's code was found using the Monte Carlo simulation technique. This proved to be the best approach to analyzing the non-linear code that was hundreds of lines long. Coleman and Steele [35] have shown the accuracy of the Monte Carlo method to be exceptionally good. It is often seen as being more accurate than the normal analytical data reduction approach.

The uncertainty analysis was performed by analyzing the second program (see Figure 2.8) which does the computing of velocity, temperature, and density (if calibrated for), and by treating the outputs from the first code as inputs (with uncertainties) to the second code.

To set up the program, a reference or true data set had to be generated. Both programs were run in their entirety on a reference set of data that was taken at atmospheric pressure, zero velocity, and room temperature. This provided two fit images along with all of the dependent variables to these images. The Rayleigh program was then modified to accept inputs without the first program running. The inputs that were sent to the program next were the fit images along with the fit parameters. This provided for final reference values coming from the least squares fitting routine for temperature and pressure. A reference had then been found. Using these "true" values along with the fit images as the reference, the program was ready to start. The next step was to estimate the uncertainty associated with each of the input parameters. The six that were examined for this study were the  $x_0$  coordinate of the center of the fringe, the  $y_0$  coordinate of the center of the fringe, the Fabry-Perot finesse, the focal length of the fringe forming lens, the diameter of the first fringe and the second fringe diameter. The true values for these parameters can be seen in Table 5.1, along with the best estimates of uncertainty this author could make.

**Table 5.1** Input Parameters with Associated Uncertainty

Parameter	True Value	Uncertainty
$x_0$	108.607 pixels	$\pm 0.49$ pixels
$y_0$	96.635 pixels	$\pm 0.49$ pixels
finesse	14.436	$\pm 1.96$
focal length of L1	180.00 mm	$\pm 1.96$ mm
diameter 1	38.027 pixels	$\pm 0.98$ pixels
diameter 2	103.528 pixels	$\pm 0.98$ pixels

The images used for the simulation ended up yielding a negative answer for the resultant velocity. Due to the way the test was set up, this did not inhibit the Monte Carlo process in any way. The Monte Carlo process does not depend on what the final result may physically be, it is merely a way of finding the uncertainty about that final value. Therefore with that, the final results that were found using the fit images and “true” input values are shown in Table 5.2.

**Table 5.2** Final Reference Values

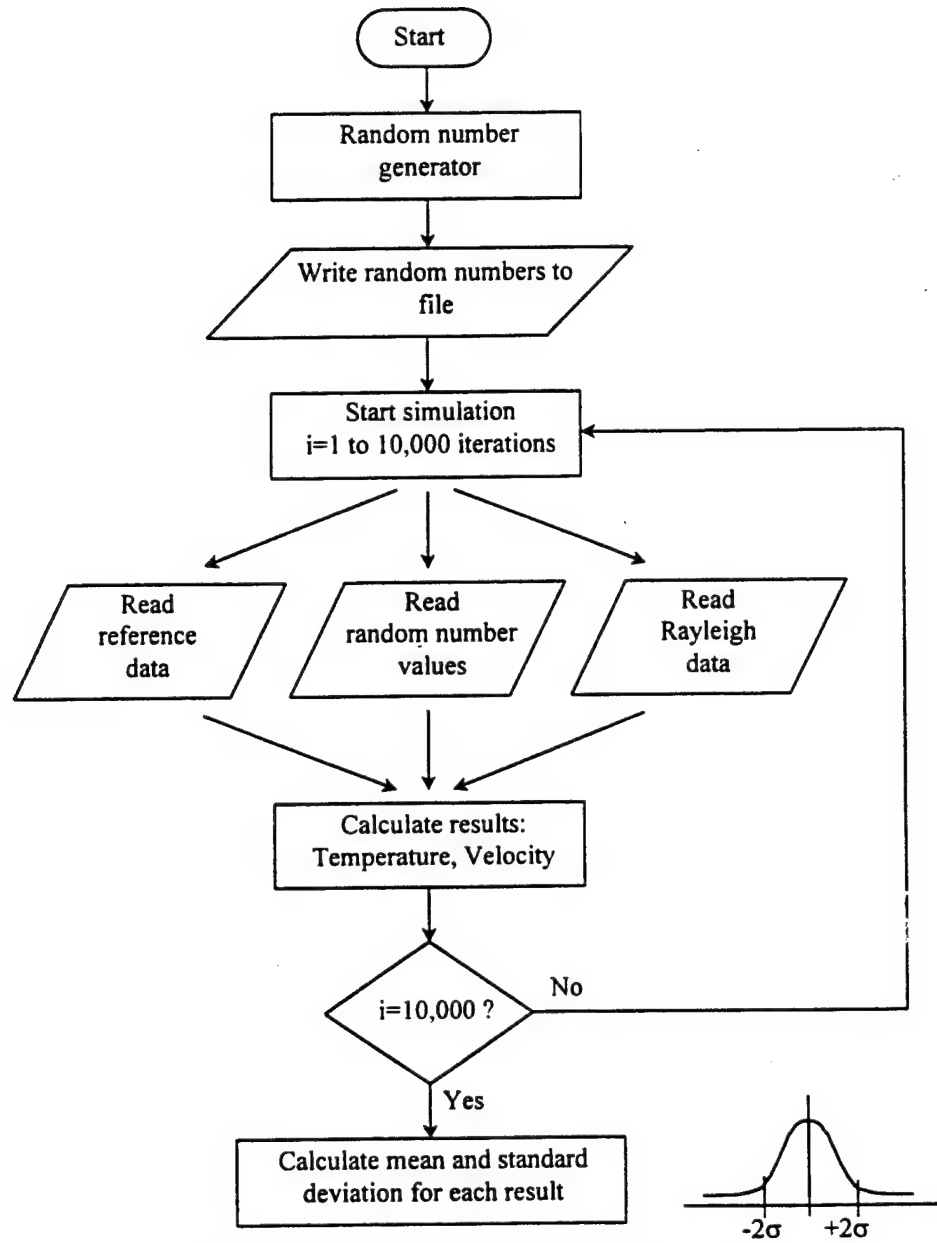
Velocity	-84.0 m/s
Temperature	287.0 K

The center of the image was initially found by a visual technique using Winspec™. It would later be fit by the program, which is why an uncertainty of 0.49 pixels was placed on  $x_0$  and  $y_0$ , which is equivalent to  $1.96 \cdot \sigma$  or 95% of the values. The finesse was fairly well set by the position of the mirrors, but we still placed a fairly large uncertainty band on it due to the low accuracy of the measurement device supplied with the Fabry-Perot for determining the exact mirror distance. The focal length of the fringe forming lens was a set parameter, but to account for user error and possible mechanical inefficiencies, a 1.96 mm uncertainty band was

placed on it. The diameters were visually fit using the Winspec™ program. The best estimate of their uncertainty was  $\pm 0.98$  pixels.

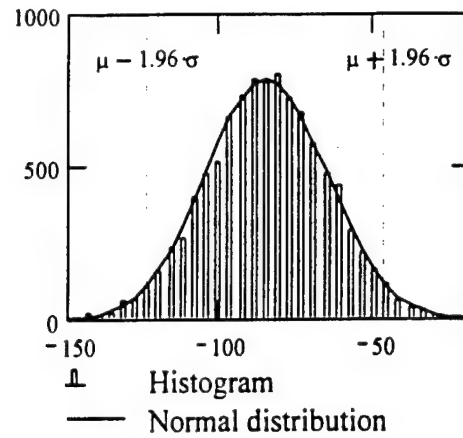
The Monte Carlo technique has been shown to be very accurate at 10,000 iterations [35]. Therefore that is what was used here. A file containing 10,000 normally (Gaussian) distributed random numbers was generated for each variable using the standard deviation and mean of each variable as inputs to the random number program. Therefore a matrix of 10,000 rows by 6 columns was generated. The random number program was the Normal (Gaussian) Deviates, or gasdev, program from Numerical Recipes [36] modified to fit this situation. The gasdev program requires a seed value to generate the random numbers. To ensure that the seed value never came up the same for any of the variables, the program was run using the 100th second of the internal clock of the computer as the seed value. Correlated errors between the six parameters were not examined in this study. This was due to the difficulty of claiming the connection of one variable to another through the non-linear least squares fit. It would be very hard to determine these effects and to then determine a guess on their uncertainty. So as a first cut these tests looked at only uncertainties that were uncorrelated. Figure 5.7 shows a flowchart schematic of the Monte Carlo process used for this work.





**Figure 5.7** Flowchart of Monte Carlo Simulation

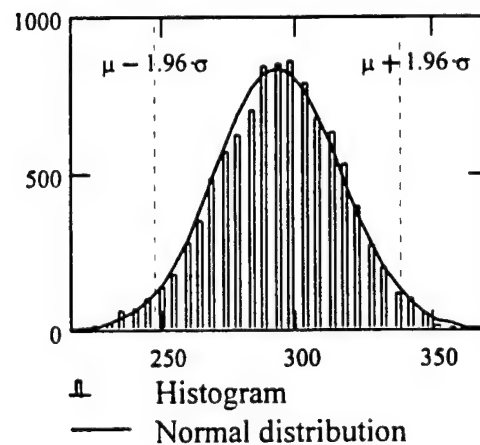
The results of the test are illustrated below in Figures 5.8 & 5.9 and their respective Tables 5.3 & 5.4.



**Figure 5.8** Uncertainty Velocity Distribution

**Table 5.3** Velocity Uncertainty Data

Size	10,000
Mean	-84.5 m/s
Standard Deviation	19.8 m/s
$U_v = 1.96 * \sigma$	38.8 m/s



**Figure 5.9** Uncertainty Temperature Distribution

**Table 5.4 Temperature Uncertainty Data**

Size	10,000
Mean	292.7 K
Standard Deviation	23.2 K
$U_T = 1.96 * \sigma$	45.5 K

It is noticeable that the mean has shifted slightly on both values from the original reference value. This was attributed to the non-linearity of the program. Looking back at Figure 5.4, where the lowest value was 261 K, and applying the temperature uncertainty results, we do now see that the room temperature is taken up in the uncertainty of the code. Although, looking at the final reference values presented in Table 5.2 we notice that the velocity value combined with its respective uncertainty from the code still does not provide a stagnant value. This is attributed to other uncertainties in the system. The largest of which seems to be the thermal drift of the Fabry-Perot interferometer.

#### E. Uncertainty Percentage Contribution

Another important parameter to look at when it comes to uncertainty is the uncertainty percentage contribution (or UPC) of each input variable. This yields a very good idea of how strongly the uncertainty in each variable is affecting the uncertainty in the final result. The relative uncertainty for a result that is a function of J measured variables X is given by Equation 5.1.

$$\frac{U_r^2}{r^2} = \left( \frac{X_1}{r} \frac{\partial r}{\partial X_1} \right)^2 \left( \frac{U_{x_1}}{X_1} \right)^2 + \left( \frac{X_2}{r} \frac{\partial r}{\partial X_2} \right)^2 \left( \frac{U_{x_2}}{X_2} \right)^2 + \dots + \left( \frac{X_J}{r} \frac{\partial r}{\partial X_J} \right)^2 \left( \frac{U_{x_J}}{X_J} \right)^2 \quad (5.1)$$

Dividing by the LHS, each term in the equation is the UPC (in fractional form) for a given variable. Equation 5.2 is the UPCs in percentage form.

$$UPC_i = \frac{[(X_i/r)(\partial r/\partial X_i)]^2 (U_{x_i}/X_i)^2}{(U_r/r)^2} \times 100 \quad (5.2)$$

So what was found was two sets of UPCs for each input variable since there were two results actually being found in the end: temperature and pressure. Both results had to be studied separately to find the effects of the input variables on each. Tables 5.5 & 5.6 show these results.

**Table 5.5** UPCs Calculated for Velocity Output

Input Parameter	UPC
$x_o$	0.1%
$y_o$	0.1%
finesse	0.0%
focal length of L1	0.3%
diameter 1	99.5%
diameter 2	0.0%
Total	100.0%

**Table 5.6** UPCs Calculated for Temperature Output

Input Parameter	UPC
$x_o$	11.5%
$y_o$	10.1%
finesse	62.3%
focal length of L1	15.8%
diameter 1	0.3%
diameter 2	0.0%
Total	100.0%

The UPCs do provide us now with a good understanding of which parameters affect the results the most. We see that for the velocity result, the diameter 1 is the most critical. This makes sense because it is the reference that the Rayleigh shifted image is measured from to find the velocity value. We see for temperature that the majority of parameters may affect it, aside from the diameters. This again is a good agreement to the true data because the temperature result is not dependent on the shift of the signal, rather it is dependent on the broadening of the signal. Finesse has the dominant role in this measurement.

## Chapter VI

### CONCLUSIONS AND RECOMMENDATIONS

The utilization of a Fabry-Perot interferometer to make Rayleigh scattering measurements has been investigated. It was determined that there are two primary sources of error associated with the instrument as used in this experiment. The first, vibrational fluctuations, did not prove to be of concern for this work. It may be removed by either dampening the system or by using a fiber optic and locating the Fabry-Perot in another room. The second, temperature fluctuations with the Fabry-Perot, have been shown to adversely impact the Rayleigh scattered signal resulting in inaccurate readings. Detailed thermal drift tests were performed on two thermal enclosures to highlight the temperature effects on the Fabry-Perot. The enclosure that presented the optimum qualities of a fast reaction time and an accurate temperature setting was a commercially available product by Burleigh. The temperature setting that presented the longest stable duration was determined to be 33°C, which provided for a half hour steady state window during which tests could be run.

Rayleigh scattering measurements were taken at atmospheric pressures using gas emanating from rocket nozzles, a heat gun assembly, and at stagnant conditions. The results obtained appeared to correlate well with thermocouple and pitot tube data. The feasibility of conducting Rayleigh scattering measurements in low density regimes was determined to work if light scattering can be removed from the signal, thus providing for a Rayleigh image that has a strong signal-to-noise ratio. An iodine cell, a thermal isolation box and possibly a dual line detection system are recommended as the means to achieve valid measurements in low density regimes. A baffle system proved to eliminate 70% of the scattered light in the system.

A detailed Monte Carlo uncertainty analysis was performed (assuming uncertainties in six input variables) to find the uncertainty of the velocity and temperature determined using the general Rayleigh scattering code used for these experiments. The uncertainties were found to

be  $\pm 38.8$  m/s for the velocity and  $\pm 45.5$  K for the temperature. An Uncertainty Percentage Contribution calculation was performed to find how the uncertainties in the center of the fringe pattern, the finesse, the focal length of the fringe forming lens and the diameters of the first two fringes affected the uncertainty of the results. The critical parameter impacting the velocity measurement was determined to be the uncertainty in the diameter of the first fringe. Uncertainty in the temperature is seen to depend greatly on the uncertainty in the finesse of the system more than any other parameter. This is because temperature is dependent on the broadening of the signal, which is profoundly affected by the finesse.

## **APPENDICES**



## APPENDIX A: USEFUL FORMULAS AND CONVERSIONS

### Constants

Name	Symbol	Value
Speed of light	c	$2.9979458 \times 10^8 \text{ m/s} \approx 3 \times 10^8 \text{ m/s}$
Permittivity of free space	$\epsilon_0$	$8.8542 \times 10^{-12} \text{ F/m}$
Permeability of free space	$\mu_0$	$4\pi \times 10^{-7} \text{ H/m}$
Planck's constant	h	$6.626076 \times 10^{-34} \text{ J-sec}$
Electronic charge	e	$1.60218 \times 10^{-19} \text{ C}$
Electronic mass	m	$9.1094 \times 10^{-31} \text{ kg}$
Proton mass	$M_p$	$1.67262 \times 10^{-27} \text{ kg}$
Boltzmann constant	k	$1.38066 \times 10^{-23} \text{ J/K}$
Avogadro's constant	$N_A$	$6.02213 \times 10^{23} \text{ atoms/mole}$
Loschmidt's number	$L_0$	$2.687 \times 10^{19} \text{ molecules/cm}^3 \text{ at } 0^\circ \text{ C}$

### Conversions & Equations

Wavelength:  $\lambda = c/\nu$

Frequency:  $\nu = c/\lambda \text{ (Hz)}$

Wave Number:  $\bar{\nu} = \frac{1}{\lambda} \text{ (cm}^{-1}\text{)}$

Energy:  $E = h\nu \text{ (J)}$

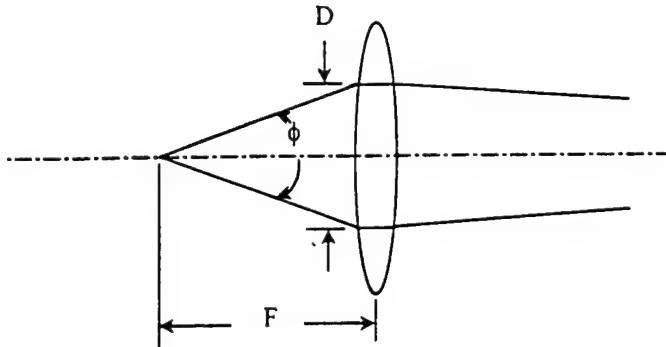
1 electron volt eV =  $1.602 \times 10^{-19} \text{ J}$

1 W =  $1 \text{ J/s}$

1 nm = 10 Angstroms ( $\text{\AA}$ ) =  $10^{-9} \text{ m} = 10^{-7} \text{ cm} = 10^{-3} \mu\text{m}$

Factor	Prefix	Symbol	Factor	Prefix	Symbol
$10^{24}$	yotta	Y	$10^{-1}$	deci	d
$10^{21}$	zetta	Z	$10^{-2}$	centi	c
$10^{18}$	exa	E	$10^{-3}$	milli	m
$10^{15}$	peta	P	$10^{-6}$	micro	$\mu$
$10^{12}$	tera	T	$10^{-9}$	nano	n
$10^9$	giga	G	$10^{-12}$	pico	p
$10^6$	mega	M	$10^{-15}$	femto	f
$10^3$	kilo	k	$10^{-18}$	atto	a
$10^2$	hecto	h	$10^{-21}$	zepto	z
$10^1$	deka	da	$10^{-24}$	yocto	y

### Lens properties



$$\text{f-number: } f/\# = \frac{F}{D} \approx \frac{1}{2 \cdot \text{NA}}$$

where  $F$  is the lens focal length,  $D$  is the collimated beam diameter or diameter illuminated on the lens, and  $\text{NA}$  is the numerical aperture.

$$\text{Depth of Focus: } \text{DOF} = \frac{8\lambda}{\pi} (f/\#)^2$$

$$\text{Beam Spread: } \theta = (f/\#)^{-1}$$

$$\text{lens maker equation: } \frac{1}{f} = (n - 1) \left( \frac{1}{R_1} - \frac{1}{R_2} \right)$$

$$\text{Effective focal length for two lenses: } \frac{1}{f} = \frac{1}{f_1} + \frac{1}{f_2} - \frac{d}{f_1 f_2}$$

where  $d$  is the distance between the two lenses.

$$\text{Solid angle for an on-axis image point: } \Omega = 2\pi(1 - \cos \theta) = 4\pi \sin^2 \left( \frac{\theta}{2} \right)$$

where  $\theta = \phi/2$ . The solution is in steradians. To convert from steradians to the more intuitive "sphere" units, simply divide  $\Omega$  by  $4\pi$ .

### Snell's Law

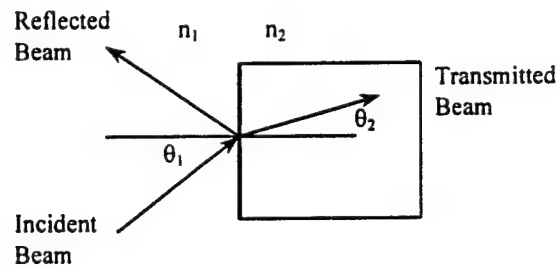
Snell's law tells how a light ray changes direction at a single surface between two media with different refractive indices. The angle of incidence,  $\theta$ , is measured from the normal to the surface. A ray passing from low to high index is bent toward the normal; passing from high to low index it is bent away from the normal.

$$n_1 \sin \theta_1 = n_2 \sin \theta_2$$

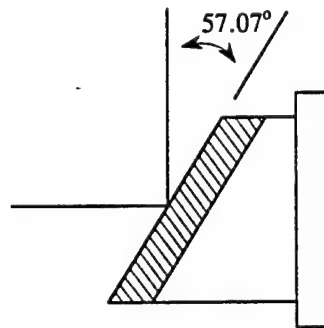
Brewster's Angle:  $\tan \theta_1 = \frac{n_2}{n_1}$

$n_1$  being the index of refraction for air = 1.00

$\theta_1$  being the angle between the horizontal axis and the incident light.



An example using quartz with the approximate index of refraction of 1.544.



### Fluid properties

Mass flow rate:  $\dot{m} = \rho VA$

Pitot-static tube subsonic equation:  $\frac{1}{2} \rho V^2 = P_o - P$

### Isentropic relations

$$\frac{T_o}{T} = 1 + \frac{\gamma - 1}{2} M^2$$

$$\frac{P_o}{P} = \left( 1 + \frac{\gamma - 1}{2} M^2 \right)^{\frac{\gamma}{\gamma - 1}}$$

$$\frac{\rho_o}{\rho} = \left( 1 + \frac{\gamma - 1}{2} M^2 \right)^{\frac{1}{\gamma - 1}}$$

Supersonic flow

Mach number:  $M = \frac{V}{a}$

Speed of Sound:  $a = \sqrt{\gamma R T}$

Area Mach number relation:  $\left(\frac{A}{A^*}\right)^2 = \frac{1}{M^2} \left[ \frac{2}{\gamma+1} \left( 1 + \frac{\gamma-1}{2} M^2 \right) \right]^{\frac{\gamma+1}{\gamma-1}}$

Rayleigh Pitot tube formula:  $\frac{P_{o,2}}{P_1} = \left( \frac{(\gamma+1)^2 M_1^2}{4\gamma M_1^2 - 2(\gamma-1)} \right)^{\frac{\gamma}{\gamma-1}} \frac{1-\gamma+2\gamma M_1^2}{\gamma+1}$

## APPENDIX B: RAYLEIGH DIFFERENTIAL CROSS SECTION CALCULATION

**N<sub>2</sub> at 1 atm and 300K with 532 nm beam**

$$R_L := 4.484 \quad P := 1 \cdot \text{atm} \quad T := 300 \cdot \text{K} \quad \lambda := 532.0 \cdot 10^{-9} \cdot \text{m} \quad R := 8.31451 \frac{\text{J}}{\text{mol} \cdot \text{K}}$$

$$Pv = nRT \quad \kappa := 1.38065810^{-23} \frac{\text{joule}}{\text{K}} \quad \text{This is a Mathcad worksheet used to calculate the Rayleigh scattering cross-section for Nitrogen.}$$

$$\rho := \frac{P}{R \cdot T} \quad \rho = 0.0000406 \frac{\text{mol}}{\text{cm}^3}$$

$n := 1.0$  where  $R_L$  is the molar refractivity of Nitrogen in mol/cm<sup>3</sup> found in a published table.

Given

$$R_L \frac{\text{cm}^3}{\text{mol}} = \frac{n^2 - 1}{n^2 + 2} \cdot \frac{1}{\rho}$$

This is a Mathcad solve block used to find the index of refraction from the Lorenz-Lorentz equation.

$$\mu := \text{Find}(n) \quad \mu = 1.0002732 \quad \text{Notice the change back to } \mu \text{ for the index of refraction from } n \text{ the variable used in the tables.}$$

$$n := \frac{P}{\kappa \cdot T} \quad n = 2.4462973 \cdot 10^{25} \cdot \text{m}^{-3} \quad \text{This is the calculation of the number density.}$$

Realize that depending on how many decimal places are carried out along with whether or not any rounding is done, can have profound impacts on the result.

$$d\sigma_{\text{overd}\Omega} := \frac{4 \cdot \pi^2 \cdot (\mu - 1)^2}{\lambda^4 \cdot n^2} \quad d\sigma_{\text{overd}\Omega} \cdot 10^{32} = 6.148 \cdot \text{m}^2$$

## APPENDIX C: FORTRAN REMARKS

The data that was taken throughout this work, mainly \*.spe files, was backed up on cd-roms. When removing a file from a cd-rom, the file attribute will be in a read only state. Because the breakdown programs had to not only read the files but also write back to them in some cases the file attributes became a problem. Instead of changing hundreds at a time by hand, a quick and easy way of correcting the problem was thought of. By placing the following line of code into a batch file that was copied into the same directory as the \*.spe files and then run, we were able to change all of the file attributes within that specific directory to have read and write privileges. This wasn't a tough problem, more of an inconvenience, but batch files were utilized to do many more tasks for the lab, such as calling the Rayleigh scattering code for multiple data sets and sending pertinent parameters into the program. This enabled the user to work on other things while the code ran instead of constantly inputting parameters.

```
attrib -r *.*
```

As stated earlier the header of these Winspec™ files holds a lot of information. In the case of version 2.2.1.10, there was on the order of 200 items physically written within the header. This group mainly worked with the number of frames, the number of columns, and the number of rows listed in the header. These parameters allowed for the program to understand what size an image it would be processing along with how many images it would look at. The following lines of Fortran code illustrate how these values can be obtained from the binary file.

character*4100 h4100	Declaration of header variable with proper array size of header
integer*2 i2head(0:2048)	Declaration of integer variable with proper array size of header
equivalence(h4100,i2head)	The trick to get the binary character into a readable integer
open(unit=1,file=inpfile,err=898,access='sequential',status='old',form='binary')	
read(1) h4100	Reads the entire header at one time and writes it to an array
ncols = i2head(42/2)	Finds the number of columns within the file
nrows = i2head(656/2)	Finds the number of rows within the file
nframe = i2head(1446/2)	Finds the number of frames within the file
close(unit=1)	Closes the file

Once the header was able to be read, the frame-break-off program could be written. It is important to note when breaking off individual frames from a multiple framed image that when each individual frame is written to a separate file, the frame parameter within the header is changed to one. This did present itself as an interesting problem because it gets at the heart of entering an integer value to a binary file in a specific place in a header. The partial code below shows how it was done.

<code>character*4100 h4100</code>	Declaration of header variable with proper array size of header
<code>integer*2 i2head(0:2048)</code>	Declaration of integer variable with proper array size of header
<code>equivalence(h4100,i2head)</code>	The trick to get the binary character into a readable integer
<code>character*2 frameone</code>	Declaration of variable to be inserted into header
<code>integer*4 value/1/</code>	Declaration of integer value to be inserted into header
<code>equivalence (value,frameone)</code>	The trick to get the integer value into a binary file
<code>open(unit=1,file=inpfile,err=898,access='sequental',status='old',form='binary')</code>	
<code>open(unit=2,file=outfile,err=898,access='sequental',status='old',form='binary')</code>	
<code>read(1) h4100</code>	Reads the entire header at one time and writes it to an array
<code>write(2) h4100(1:1446)</code>	Writes the portion of the header file before frame parameter
<code>write(2) frameone</code>	Writes the new frame value to the header
<code>write(2) h4100(1449:4100)</code>	Writes the remaining portion of the header to the new file
<code>close(unit=1)</code>	Closes the file unit 1
<code>close(unit=2)</code>	Closes the file unit 2

## REFERENCES

- [1] de Groot, W.A., and Zupanc, F.J., "Laser Rayleigh and Raman Diagnostics for Small Hydrogen/Oxygen Rockets," *SPIE*, Vol. 1862, 1993, pp. 98-112.
- [2] Bergmann, V., Meier, W., Wolff, D., and Stricker, W., "Application of Spontaneous Raman Rayleigh Scattering and 2D-LIF for the Characterization of a Turbulent  $\text{CH}_4/\text{H}_2/\text{N}_2$  Jet Diffusion Flame," *Applied Physics B*, Vol. 66, No. 4, 1998, pp. 489-502.
- [3] Eckbreth, A.C., *Laser Diagnostics for Combustion Temperature and Species*. Massachusetts: Abacus Press, 1988.
- [4] Panda, J., and Seasholtz, R. G., "Density measurement in Underexpanded Supersonic Jets Using Rayleigh Scattering," *ALAA Paper 98-0281*, 1998.
- [5] Seasholtz, R.G., Buggele, A.E., and Reeder, M.F., "Instantaneous Flow Measurements in a Supersonic Wind Tunnel using Spectrally Resolved Rayleigh Scattering," *SPIE*, Vol. 2546, 1995, pp. 2-15 [also NASA TM 107042].
- [6] Espey, C., Dec, J.E., Litzinger, T.A., and Santavicca, D.A., "Planar Laser Rayleigh Scattering for Quantitative Vapor-Fuel Imaging in a Diesel Jet," *Combustion and Flame*, Vol. 109, No. 1-2, 1997, pp. 65-86.
- [7] Seasholtz, R.G., and Greer, L.C. III, "Rayleigh Scattering Diagnostic for Measurement of Temperature and Velocity in Harsh Environments," *ALAA Paper 98-0206*, 1998.
- [8] Seasholtz, R.G., and Buggele, A.E., "Study of Injection of Helium into Supersonic Air Flow Using Rayleigh Scattering," *ALAA paper 97-0155*, 1997.
- [9] Elliott, G.S., Samimy, M., and Arnette, S.A., "Molecular Filter-Based Diagnostics in High Speed Flows," *ALAA paper 93-0512*, 1993.
- [10] Seasholtz, R.G., "Fiber Optic Coupled Rayleigh Scattering Diagnostic for Point Measurement of Gas Density, Velocity and Temperature," *ALAA paper 98-3454*, 1998.
- [11] Seasholtz, R.G., Zupanc, F.J., and Schneider, S.J., "Spectrally Resolved Rayleigh Scattering Diagnostic for Hydrogen-Oxygen Rocket Plume Studies," *Journal of Propulsion and Power*, Vol. 8, No. 5, 1992, pp. 935-942.
- [12] Lewis, J. W. L., "Optical Diagnostics of Low-Density Flowfields," *Rarefied Gas Dynamics: Physical Phenomena*, Vol. 117, 1989, pp. 107-132.
- [13] Seasholtz, R.G., Buggele, A.E., and Reeder, M.F., "Flow Measurements Based on Rayleigh Scattering and Fabry-Perot Interferometer," *Optics and Lasers in Engineering*, Vol. 27, 1997, pp. 543-570.



- [14] Verdeyen, J.T., *Laser Electronics, Third Edition*. New Jersey: Prentice-Hall, Inc., 1995.
- [15] Dam, N. J., Rodenburg, M., Tolboom, R.A.L., Stoffels, G.G.M., Huisman-Kleinherenbrink, P.M., and ter Meulen, J.J., "Imaging of an Underexpanded Nozzle Flow by UV Laser Rayleigh Scattering," *Experiments in Fluids*, Vol. 24, No. 2, 1998, pp. 93-101.
- [16] Seasholtz, R.G., "Single-Shot Spectrally Resolved UV Rayleigh Scattering Measurements in High Speed Flow," *NASA Technical Memorandum 107323*, 1996.
- [17] Longhurst, R.S., *Geometrical And Physical Optics, Third Edition*. London: Longman Group Limited, 1973.
- [18] Buckingham, A.D., and Graham, C., "The Density Dependence of the Refractivity of Gases." *Proceedings of the Royal Society of London, Series B, Biological Sciences*, Vol. A337, 1974, pp. 275-291.
- [19] Gardiner, W.C. Jr, Hidaka, Y., and Tanzawa, T., "Refractivity of Combustion Gases," *Combustion and Flame*, Vol. 40, 1981, pp. 213-219.
- [20] Watson, H.E., and Ramaswamy, K.L., "The Refractive Index Dispersion and Polarization of Gases," *Proceedings of the Royal Society of London, Series B, Biological Sciences*, Vol. A156, 1936, pp. 144-157.
- [21] Boley, C.D., Desai, R.C., and Tenti, G., "Kinetic Models and Brillouin Scattering in a Molecular Gas," *Canadian Journal of Physics*, Vol. 50, 1972, pp. 2158-2173.
- [22] Anderson, J.D. Jr., *Modern Compressible Flow, With Historical Perspective*. New York: McGraw-Hill, Inc., 1990.
- [23] Gornall, W.S., "The World of Fabry-Perots, These Elegant Instruments are Versatile, High-Resolution Tunable Wavelength Filters," *Lasers & Applications*, 1983, pp. 47-52.
- [24] Hariharan, P., *Basics of Interferometry* New York: Academic Press, Inc., 1992.
- [25] Hernandez, G., *Fabry-Perot Interferometers*. New York: Cambridge University Press, 1986.
- [26] Fessler, T. E., "Fluid: A Numerical Interpolation Procedure for Obtaining Thermodynamic and Transport Properties of Fluids," *NASA TM X-3572*, 1977.
- [27] Clark, N.A., "Inelastic Light Scattering from Density Fluctuations in Dilute Gases. The Kinetic Hydrodynamic Transition in Monatomic Gas," *Physical Review A*, Vol. 12, No. 1, 1975, pp. 232-244.

- [28] Seasholtz, R. G., "Instantaneous 2D Velocity and Temperature Measurements in High Speed Flows Based on Spectrally Resolved Rayleigh Scattering," *AIAA paper 95-0300*, 1995.
- [29] Forkey, J. N., Lempert, W. R., and Miles, R. B., "Accuracy Limits for Planar Measurements of Flow Field Velocity, Temperature and Pressure using Filtered Rayleigh Scattering," *Experiments in Fluids*, Vol. 24, No. 2, 1998, pp. 151-162.
- [30] Forkey, J.N., Finkelstein, N.D., Lempert, W.R., and Miles, R.B., "Control of Experimental Uncertainties in Filtered Rayleigh Scattering Measurements," *AIAA Paper 95-0298*, 1995.
- [31] Spectra-Physics, *Pulsed Nd: YAG Laser: User's Manual, GCR Series*. Part Number 0000-227A, Revision D, 1997.
- [32] Sullivan, D.J., and Micci, M.M., "Performance Testing and Exhaust Plume Characterization of the Microwave Arcjet Thruster," *AIAA Paper 94-3127*, 1994.
- [33] Sullivan, D.J., Kline, J., Philippe, C., and Micci, M.M., "Current Status of the Microwave Arcjet Thruster," *AIAA Paper 95-3065*, 1995.
- [34] Culley, M.J., Jones, J.E., and Hawk, C.W., "Rayleigh Doppler Velocimetry Measurements of a Microwave Thruster," *AIAA Paper 99-3717*, 1999.
- [35] Coleman, H.W., and Steele, G.W. Jr., *Experimentation and Uncertainty Analysis for Engineers, Second Edition*. New York: John Wiley & Sons, Inc., 1999.
- [36] Press, W.H., Teukolsky, S.A., Vetterling, W.T., and Flannery, B.P., *Numerical Recipes in Fortran; The Art of Scientific Computing, Second Edition*. New York: Cambridge University Press, 1992.

## BIBLIOGRAPHY

1. Boley, C.D., and Yip, S., "Kinetic Theory of Time-Dependent Correlation Functions in a Binary Gas Mixture," *The Physics of Fluids*, Vol. 15, No. 8, 1972, pp. 1433-1446.
2. Buggele, A.E., and Seasholtz, R.G., "Improved Optical Techniques for Studying Sonic and Supersonic Injection into Mach 3 Flow," *SP/E*, Vol. 3172, 1997, pp. 504-517.
3. Buuron, A.J.M., Dudeck, M., and Leprince, P., "Plasma Jets Departing from a Microwave Plasma Source," *AIAA Paper 95-1958*, 1995.
4. Cattolica, R., Robben, F., and Talbot, L., "The Interpretation of the Spectral Structure of Rayleigh Scattered Light from Combustion Gases," *AIAA Paper 76-31*, 1976.
5. Chu, B., *Laser Light Scattering*. New York: Academic Press, 1974.
6. Clark, N.A., "Inelastic Light Scattering from Density Fluctuations in Dilute Gases. II. Nonhydrodynamic Behavior of a Binary Gas Mixture," *Physical Review A*, Vol. 12, No. 5, 1975, pp. 2092-2105.
7. Crowder, M.J., Kimber, A.C., Smith, R.L., and Sweeting, T.J., *Statistical Analysis of Reliability Data*. New York: Chapman & Hall, 1991.
8. Demtröder, W., *Laser Spectroscopy: Basic Concepts and Instrumentation*. New York: Springer-Verlag Berlin Heidelberg, 1981.
9. Elliot, G.S., and Samimy, M., "Rayleigh Scattering Technique for Simultaneous Measurements of Velocity and Thermodynamic Properties," *AIAA Journal*, Vol. 34, No. 11, 1996, pp. 2346-2352.
10. Etter, D.M., *Structured Fortran 77 For Engineers And Scientists, Fourth Edition*. California: The Benjamin/Cummings Publishing Company, Inc., 1993.
11. Folks, J.L., *Ideas of Statistics*. New York: John Wiley & Sons, 1981.
12. Forkey, J. N., Finkelstein, N.D., Lempert, W.R., and Miles, R.B., "Demonstration and Characterization of Filtered Rayleigh Scattering for Planar Velocity Measurements," *AIAA Journal*, Vol. 34, No. 3, 1996, pp. 442-448.
13. Freeman, S.K., *Applications of Laser Raman spectroscopy*. New York: John Wiley & Sons, 1974.
14. Freund, J.E., *Mathematical Statistics, Fifth Edition*. New Jersey: Prentice Hall, 1992.
15. Gornall, W.S., "Interferometry Determines Wavelengths Precisely," *Laser Focus World*, 1997, pp. 123-127.

16. Grinstead, J.H., Finkelstein, N.D., Miles, R.B., Lempert, W.R., and Lavid, M., "Doppler Velocimetry in a Supersonic Jet using Frequency-Modulated Filtered Light Scattering," *AIAA Paper 97-0499*, 1997.
17. Hara, E.H., May, A.D., and Knaap, H.F.P., "Rayleigh-Brillouin Scattering in Compressed H<sub>2</sub>, D<sub>2</sub>, and HD," *Canadian Journal of Physics*, Vol. 49, 1971, pp. 420-431.
18. Harnett, D.L., *Statistical Methods, Third Edition*. Massachusetts: Addison-Wesley Publishing Company, 1982.
19. Hubert, M., and May, A.D., "The Rayleigh-Brillouin Spectrum of Normal and Parahydrogen: A Test of Model Solutions of the Wang-Chang Uhlenbeck Equation," *Canadian Journal of Physics*, Vol. 53, 1975, pp. 343-350.
20. Koningstein, J.A., *Introduction to the theory of the Raman effect*. Holland: D. Reidel Publishing Company, 1972.
21. Kourous, H.E., and Seasholtz, R.G., "Fabry-Perot Interferometer Measurement of Static Temperature and Velocity for ASTOVL Model Tests," *NASA Technical Memorandum 107014*, 1994.
22. Lalanne, J. R., Ducasse, A., and Kielich, S., *Laser-Molecule Interaction: Laser Physics and Molecular Nonlinear Optics*. New York: John Wiley & Sons, Inc., 1996.
23. Laserna, J.J., *Modern Techniques in Raman Spectroscopy*. New York: John Wiley & Sons, Inc., 1996.
24. Laufer, G., *Introduction to Optics and Lasers in Engineering*. New York: Cambridge University Press, 1996.
25. Lempert, W.R., Wu, P-F., and Miles, R.B., "Filtered Rayleigh Scattering Measurements Using a MHz Rate Pulse-Burst Laser System," *AIAA Paper 97-0500*, 1997.
26. Letamendia, L., Chabrat, J.P., Nouchi, G., Rouch, J., Vaucamps, C., and Chen, S.-H., "Light-Scattering Studies of Moderately Dense Gas Mixtures: Hydrodynamic Regime," *Physical Review A*, Vol. 24, No. 3, 1981, pp. 1574-1590.
27. Lock, J.A., Seasholtz, R.G., and John, W.T., "Rayleigh-Brillouin Scattering to Determine One-Dimensional Temperature and Number Density Profiles of a Gas Flow Field," *Applied Optics*, Vol. 31, No. 15, 1992, pp. 2839-2848.
28. Miles, R. B., Lempert, W. R., and Forkey, J., "Instantaneous Velocity Fields and Background Suppression by Filtered Rayleigh Scattering," *AIAA Paper 91-0357*, 1991.
29. Nussbaum, A., and Phillips, R.A., *Contemporary Optics for Scientists and Engineers*. New Jersey: Prentice-Hall, Inc., 1976.

30. Ötügen, M. V., Kim, J., and Popović, S., "Nd: YAG Laser-Based Dual-Line Rayleigh Scattering System," *AIAA Journal*, Vol. 35, No. 5, 1997, pp. 776-781.
31. Ötügen, M.V., Annen, K.D., and Seasholtz, R.G., "Gas Temperature Measurements Using a Dual-Line Detection Rayleigh Scattering Technique," *AIAA Journal*, Vol. 31, No. 11, 1993, pp. 2098-2104.
32. Schawlow, A.L., *Lasers and Light*. San Francisco: W. H. Freeman and Company, 1969.
33. Schwer, D.A., Venkateswaran, S., and Merkle, C.L., "Analysis of Microwave-Heated Rocket Engines for Space Propulsion," *AIAA Paper 93-2105*, 1993.
34. Seasholtz, R.G., "High-Speed Laser Anemometry Based on Spectrally Resolved Rayleigh Scattering," *NASA Technical Memorandum 104522*, 1991.
35. Seasholtz, R.G., "2D Velocity and Temperature Measurements in High Speed Flows Based on Spectrally Resolved Rayleigh Scattering," *NASA Technical Memorandum 105784*, 1992.
36. Seasholtz, R., and Lesco, D., "Rayleigh Scattering Diagnostics Workshop," *NASA Conference Publication 10186*, 1996.
37. Seasholtz, R.G., and Buggele, A.E., "Improvement in Suppression of Pulsed Nd: YAG Laser Light with Iodine Absorption Cells for Filtered Rayleigh Scattering Measurements," *SPIE*, Vol. 3172, 1997, pp. 625-635.
38. Shapiro, A.H., *The Dynamics and Thermodynamics of Compressible Fluid Flow*. New York: The Donald Press Company, Volume I, 1953.
39. Shapiro, A.H., *The Dynamics and Thermodynamics of Compressible Fluid Flow*. New York: The Donald Press Company, Volume II, 1954.
40. Shirley, J. A., and Winter, M., "Air-Mass Flux Measurement System Using Doppler-Shifted Filtered Rayleigh Scattering," *AIAA paper 93-0513*, 1993.
41. Sugawara, A., and Yip, S., "Kinetic Model Analysis of Light Scattering by Molecular Gases," *The Physics of Fluids*, Vol. 10, No. 9, 1967, pp. 1911-1921.
42. Sullivan, P.J., "Interferometer Bandwidth Expanded by Software," *Laser Focus World*, 1995, pp. s5-s7.
43. Tenti, G., Boley, C.D., and Desai, R.C., "On the Kinetic Model Description of Rayleigh-Brillouin Scattering from Molecular Gases," *Canadian Journal of Physics*, Vol. 52, No. 4, 1974, pp. 285-290.
44. Thomson, J.H., *Optics, Second Edition*. New York: John Wiley & Sons Ltd., 1988.

45. Triola, M.F., *Elementary Statistics, Fifth Edition*. New York: Addison-Wesley Publishing Company, 1992.
46. Yalin, A.P., Finkelstein, N.D., Lempert, W.R., and Miles, R.B., "UltraViolet Rotational Raman Spectroscopy with an Atomic Resonance Filter," *AIAA Paper 98-0311*, 1998.
47. Zwillinger, D., *CRC: Standard Mathematical Tables and Formulae, 30<sup>th</sup> Edition*. New York: CRC Press, 1996.

## THESIS APPROVAL FORM

Submitted by Matthew J. Culley in partial fulfillment of the requirements for the degree of Master of Science in Engineering with a major in Mechanical Engineering.

Accepted on behalf of the Faculty of the School of Graduate Studies by the thesis committee:

 8/3/99 Committee Chair  
(Date)

HW Coleman 8/3/99

James C. Wessling 8-3-99

James C. Wessling 8-3-99 Department Chair

J. Cannon Riddle 8/4/99 College Dean

A. C. Smith 8-3-99 Graduate Dean

# **Experimental Study of Plasma Energization at Magnetic Neutral Points**

by

**Stelu Deaconu**

**2002**



## **Abstract**

A new experiment of magnetic field diffusion through plasma was performed with static, time varying, quadrupole magnetic fields created by a dual coil device. The experiment was designed to answer some of the questions raised by the process of plasma energization at magnetic neutral points, in a hydrostatic configuration. In this configuration, the variation of the magnetic field provides the only source of plasma energization, and is the process of engineering interest. The goals of the investigation were to evaluate the effectiveness of plasma energization (heating and acceleration) when starting from a hydrostatic initial condition, and to discuss the possibility that the energy transfer process involves magnetic field line reconnection.

Parallel to the experimental work, an analytic fluid model was proposed to describe the possibility of plasma acceleration at the magnetic neutral line. The model also discussed the case of weakly ionized plasma from a particle – kinetic viewpoint. Experimentally, the investigation was limited to the case of weakly ionized plasma. The limitation was imposed by the low ionization levels obtained with a thermionic arc-discharge plasma source. The experimental data showed good agreement with the model.

The new experiment demonstrated that the diffusion of two opposite, variable magnetic field through plasma toward a dissipation region leads to plasma ionization, plasma waves and bulk plasma motion. In terms of energy transfer, the experiment showed that the weak coupling between the magnetic field and the low conductivity plasma is directly responsible for the small energy conversion efficiency. The data also showed that, in the configuration tested, magnetic field line reconnection is an unlikely mechanism for plasma energization.

## TABLE OF CONTENTS

List of Symbols .....	i
Chapter	
I. INTRODUCTION AND BACKGROUND	
I. Introduction .....	1
II. Theoretical Background .....	3
III. The Criticism of Reconnection .....	9
IV. Magnetic Reconnection Experiments .....	11
V. Objective of the Dissertation .....	14
VI. The Denver Model .....	18
II. THE MDE EXPERIMENT	
I. Experimental Apparatus .....	21
II. Diagnostics and Data Acquisition .....	27
III. Testing Procedure .....	32
IV. Experimental Results .....	34
III. ANALYSIS OF EXPERIMENTAL DATA	
I. Discharge Power and Efficiency .....	39
II. MDE Magnetic and Electric Fields .....	43
III. Plasma Conductivity .....	56
IV. Ion Acoustic Waves and Bulk Plasma Motion .....	65
IV. CONCLUSIONS .....	75
APPENDIX: Plasma Study on the Ionization of Flowing Gases by DC Thermionic Arc Discharge	
I. Introduction .....	79
II. TDID Diagnostics .....	81

III. TDID Ionization .....	83
IV. TDID Flow .....	86
V. Experimental Results .....	90
VI. Discharge Stability and Electron Density in the Plume .....	98
VII. Conclusions .....	102
REFERENCES .....	104

## LIST OF SYMBOLS

$b, \bar{B}$	magnetic field induction
$c$	sound speed $(\gamma RT)^{1/2}$
$c_e$	electron mean thermal speed $(8k_b T_e / \pi m_e)^{1/2}$
$c_p$	heat capacity
$C_{cb}$	capacitance of capacitor bank
$e$	electron charge
$\bar{E}$	vector electric field
$I, i$	current
$j$	current density
$k_b$	Boltzman's constant
$L_h$	coil impedance
$m_e$	electron mass
$m_i$	ion mass
$M$	Mach number ( $M = u/c$ )
$m_s$	mass of gas particle
$n_e$	electron density
$n_s$	gas density
$p$	pressure
$Q_{es}$	electron collision cross-section
$R$	gas constant
$T, T_i$	gas/ion temperature
$T_e$	electron temperature

$u$	gas speed
$\bar{v}, v$	particle velocity
$V, U_0$	voltage
$V_{cb}$	capacitor bank voltage
$V_L$	coil voltage
$V_R$	voltage drop on ohmic resistance
$W$	electric power
$\alpha$	Townsend ionization coefficient
$\chi$	compression ratio
$\epsilon_0$	electrical permittivity of vacuum
$\phi$	electric potential
$\gamma$	gas specific heat ratio
$\lambda_D$	Debye shielding length
$\mu_e, \mu_i$	electron/ion mobility
$\nu$	collision frequency
$\rho$	charge density
$\rho_1, \rho_2$	gas density
$\xi$	geometrical ratio TDID

## **CHAPTER I**

### **INTRODUCTION AND BACKGROUND**

#### **I. Introduction**

Of all ideas put forward in the physics of plasmas of the twentieth century, magnetic reconnection is undoubtedly the most controversial. Magnetic field line reconnection or magnetic line merging is regarded as a local topological rearrangement of the magnetic field within a conductive gaseous environment, in a region containing magnetic neutral points. Initially rejected and viewed as entertaining fiction rather than serious science, the concept of magnetic reconnection rode since its inception a sinuous borderline between heresy and enlightenment. Even today, after five decades of theoretical and experimental work and more than two decades of formal acceptance by the scientific community, magnetic field line reconnection is the object of open debate and subjective interpretation. Nevertheless, the large spectrum of phenomena associated with reconnection: solar flares, acceleration of particles at magnetopause, tearing mode instabilities in tokamak, sheet pinch and reverse field configurations, has fuelled the interest on the subject and has propelled the concept in the mainstream plasma research. The result is an astounding amount of analytical and experimental work devoted to reconnection over the years. It was with all these in mind that this thesis, yet another experimental investigation on the subject, was begun with the specific goal to uncover some of the engineering uses of the physical process that takes place at magnetic neutral points, in a hydrostatic configuration.

On a historical note, the origin of the concept is attributed to Giovanelli<sup>1</sup> who was attempting to explain the solar flare phenomena in terms of the interplay between the

chromospheric plasma and the magnetic field of sunspots. Hoyle<sup>2</sup> and Dungey<sup>3</sup> crystallized the main ideas behind magnetic field line reconnection: the acceleration of particles at neutral points and the existence of a singular line at the intersection of anti-parallel magnetic fields, and described the applicability of the concept to the theory of what was to be called magnetosphere. During the same period, Sweet<sup>4</sup> gave his view of Dungey's x-point magnetic field structure<sup>5</sup> by considering opposite magnetic fields diffusing steadily into a neutral sheet and annihilating, an interpretation which had become the classic picture of magnetic reconnection. Although appealing, Sweet's process of field annihilation seemed an unlikely mechanism for solar flares, since the predicted reconnection rates were much too slow to account for the energy release, see monograph by Parker.<sup>6</sup> The deficiencies in Sweet's model prompted Petschek<sup>7</sup> to consider a similar model that included a field component normal to the neutral line and a system of slow shockwaves bounding two outflowing, super-Alfvénic plasma jets. Petschek's model seemed to have solved the problem of the energy dissipation rate in solar flares, and led many to conclude that the entire reconnection problem was elucidated. However, the Sweet-Parker and the Petschek reconnection models are steady state and therefore unable to correctly model the impulsive behavior of solar flares. Thus, by the mid sixties the stage was set for a debate which has continued to this date, and raised the question of the legitimacy of magnetic field-line reconnection as a valid physical process, see for instance Alfvén<sup>8</sup> and Heikkila.<sup>9</sup> A decade later the balance was tipped in favor of reconnection by new experimental evidence that indirectly supported the idea of reconnecting magnetic field lines, see review by Baum and Bratenahl.<sup>10</sup> Nevertheless, the exotic nature of the reconnection mechanism and the lack of direct experimental proof leave the reconnection problem open for debate and unquestionably, a subject to be approached open-mindedly.

Aside from the pure theoretical exercise, reconnection is believed to play an important role in the onset and development of some tearing-mode and disruptive MHD instabilities in astrophysical plasmas,<sup>11</sup> and plasma confinement experiments: pinches,<sup>12, 13, 14</sup> reverse field

configurations,<sup>15, 16</sup> and tokamaks.<sup>17</sup> However, the engineering potential of the process resides primarily with an exceptional ability to energize ionized particles. It is well known that solar flares and prominences release coronal mass at velocities of hundreds of kilometers per second, see study by Parker<sup>18</sup> or the monograph by Tandberg-Hanssen.<sup>19</sup> Likewise, ionized particles are highly energized during magnetic substorms in magnetosphere, see for instance Heikkila et al.<sup>20</sup> or Axford.<sup>21</sup> Evidently, a space propulsion engine based on the same mechanism would have a remarkable specific impulse.

The new experiment is designed around a static, time varying, quadrupole magnetic field created by a dual coil device. In this configuration, the variation of the magnetic field provides the only source of plasma energization, and is the process of engineering interest. The goals of the investigation are to evaluate the effectiveness of plasma energization (heating and acceleration) at neutral points starting from a hydrostatic initial condition, and to discuss the possibility that the energy transfer process involves reconnection.

## II. Theoretical Background

In its essence, the concept of magnetic reconnection is an attempt to model a multi-scale, multi-phenomena plasma-field interaction process from a macroscopic, magnetohydrodynamic (MHD) viewpoint. The classic MHD formalism pertaining to reconnection starts with Ohm's law, written for a simply conducting fluid

$$\vec{j} = \sigma(\vec{E} + \vec{v} \times \vec{B}) \quad (1.1)$$

where the symbols have their usual meaning:  $\vec{j}$  is the electric current density,  $\vec{E}$  is the electric field,  $\vec{B}$  is the magnetic induction,  $\vec{v}$  is the velocity of the fluid and  $\sigma$  is the conductivity of the fluid. Taking the curl of Equation 1.1 and adding the simplified differential form of Maxwell's equations



$$\frac{\partial \bar{\mathbf{B}}}{\partial t} = -\nabla \times \bar{\mathbf{E}} \quad (1.2)$$

$$\bar{\mathbf{j}} = \frac{1}{\mu} \cdot \nabla \times \bar{\mathbf{B}} \quad (1.3)$$

$$\nabla \cdot \bar{\mathbf{B}} = 0 \quad (1.4)$$

one obtains the magnetic induction equation after a few algebraic manipulations

$$\frac{\partial \bar{\mathbf{B}}}{\partial t} = \nabla \times (\bar{\mathbf{v}} \times \bar{\mathbf{B}}) + \frac{1}{\mu \sigma} \nabla^2 \bar{\mathbf{B}} \quad (1.5)$$

where  $\mu$  is the magnetic permeability of the fluid. Variations of this result can be obtained by considering a generalized Ohm's law equation instead of Equation 1.1, see for instance the review by Vasyliunas.<sup>22</sup> The important aspect of Equation 1.5 is that it describes the coupling established between the conductive medium and the magnetic field, and introduces the concept<sup>23</sup> of "frozen in flux." If the fluid conductivity is large,  $\sigma \rightarrow \infty$  the diffusion term in the right hand side is small and can be neglected

$$\frac{\partial \bar{\mathbf{B}}}{\partial t} - \nabla \times (\bar{\mathbf{v}} \times \bar{\mathbf{B}}) = 0 \quad (1.6)$$

The rate of change of the magnetic flux  $d\Phi/dt$  through a surface  $S$  bounded by a closed curve  $\Gamma$  is

$$\begin{aligned} \frac{d\Phi}{dt} &= \iint_S \frac{\partial \bar{\mathbf{B}}}{\partial t} \cdot \bar{\mathbf{n}} dA + \oint_{\Gamma} (\bar{\mathbf{v}} \times d\bar{\mathbf{l}}) \cdot \bar{\mathbf{B}} \\ &= \iint_S \left[ \frac{\partial \bar{\mathbf{B}}}{\partial t} - \nabla \times (\bar{\mathbf{v}} \times \bar{\mathbf{B}}) \right] \cdot \bar{\mathbf{n}} dA \end{aligned} \quad (1.7)$$

Obviously if Equation 1.6 is true then  $d\Phi/dt = 0$  and the magnetic flux bounded by  $\Gamma$  is constant. In limit of  $S \rightarrow 0$  this situation can be seen as the fluid moving with the magnetic field lines or equivalently the flux of magnetic field is frozen into the fluid. In case of finite conductivity (or otherwise if  $\nabla^2 \bar{\mathbf{B}} \rightarrow \infty$ ) the magnetic diffusion term can be of the same order as the frozen in term, and leads to the conclusion that in certain circumstances the frozen in theorem may break

down locally, Axford<sup>21</sup>. More precisely reconnection is thought as the process in which “fluid elements” entering a diffusion dominated region get disconnected from their initial magnetic field lines and connect afterward with different field lines. Thus, the process is also interpreted as field lines breaking and reconnecting to different partners. The result is a local change in the topology of the magnetic field, accompanied by energy release into the plasma. This idea is the essential ingredient of magnetic reconnection, and the basis of the plasma energization mechanism.

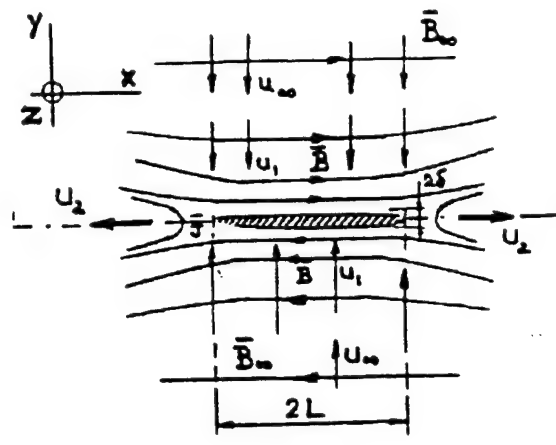
The classic reconnection picture is of anti-parallel magnetic field lines merging steadily and reconnecting in the vicinity of a neutral line (current sheet). In this case, rapid conversion of magnetic energy to plasma enthalpy depends on maintaining a strong field gradient at the neutral line<sup>21</sup>. The three models of, Sweet-Parker, Petschek, and Sonnerup-Priest are consistent with this configuration and are recalled here, see Figure 1.1. It is noted that these models are simplified (i.e. two-dimensional and incompressible) analytic MHD solutions and that they differ in the conditions imposed just outside the current sheet in the inflow region. The resultant outflow conditions and the rates of magnetic energy conversion (reconnection rates) in these models are discussed next.

In the Sweet-Parker model<sup>4,24</sup> (Figure 1.1.a), the uniform plasma inflow keeps a high rate of magnetic field diffusion, thus maintaining a large field gradient. The incoming magnetic flux produces an electric field (here in  $z$  direction), which can be expressed from Ohm's law (Equation 1.1)

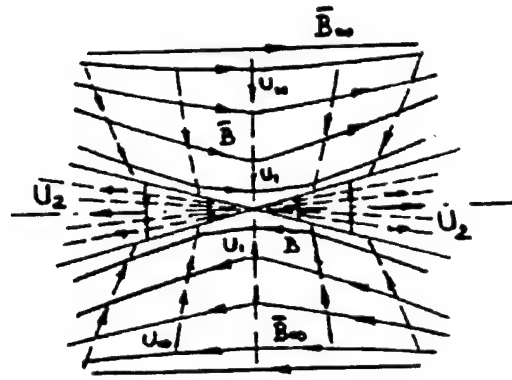
$$\vec{E} = \vec{j}/\sigma - \vec{v} \times \vec{B} \quad (1.8)$$

Close to the neutral sheet (i.e. in the diffusion region) the velocity and the magnetic field vanish and Equation 1.8 becomes  $E \cong j/\sigma$ . In the upstream region the current is negligible and  $E \cong u_1 B$ . Assuming a spatially uniform electric field and approximating the neutral sheet current from Ampere's law (Equation 1.3),  $j \cong B/\mu\delta$ , one obtains the inflow speed

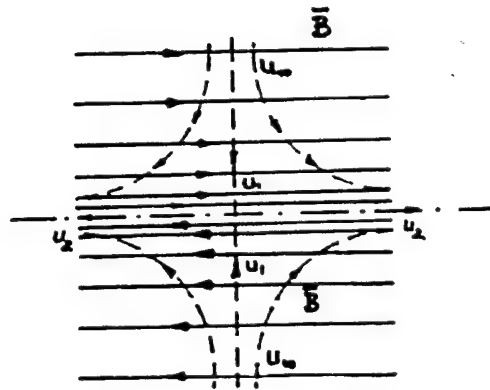
$$u_1 = 1/\mu\delta\sigma \quad (1.9)$$



(a)



(b)



(c)

**Figure 1.1** Magnetic field configuration and plasma flow in (a) Sweet-Parker model, (b) Petschek model, and (c) Sonnerup-Priest model ( $\bar{j}$ ,  $z$  out of page)

This condition can be also obtained directly from Equation 1.5 by equating the magnetic field advection and diffusion terms  $-\nabla \times (\bar{v} \times \bar{B}) = (1/\mu\sigma)\nabla^2 \bar{B}$ . Clearly, this expression (Equation 1.9) is only an approximation of the flow speed near the reconnection region, and cannot provide the far-field flow velocity. A simple pressure balance along and across the diffusion region  $p_0 + B^2/2\mu = p_0 + (1/2)\rho u_2^2$  gives the necessary outflow velocity  $u_2 = (B^2/\mu\rho)^{1/2} = v_A$ , where  $v_A$  (Alfvén speed) is the speed of a hydromagnetic disturbance in the inflow region close to the neutral sheet. Phenomenologically, the acceleration of the outflow particles is sometimes explained in terms of the tendency of curved magnetic field lines to act like rubber bands or elastic strings<sup>21</sup>. The tensile component of the Maxwell stress tensor (i.e. magnetic pressure) associated with the reconnected field lines (Figure 1.1.a) acts such as to straighten the bent magnetic field lines, thus removing (the frozen in) fluid from the reconnection region.

Finally, the conservation of mass requires that the inflow and outflow velocities satisfy the following relationship

$$u_1 \cdot L = u_2 \cdot \delta \quad (1.10)$$

Eliminating  $\delta$  between (1.9) and (1.10) one obtains

$$u_1 = v_A \cdot \sqrt{\frac{1}{\mu\sigma L v_A}} = Re_m^{-1/2} \cdot v_A \quad (1.11)$$

where  $Re_m = \mu\sigma L \cdot v_A$  is the magnetic Reynolds number. The reconnection rate  $M_A$  is expressed<sup>22</sup> as the ratio of the plasma inflow speed to the Alfvén speed  $u_1/v_A$ . From Equation 1.11 the reconnection rate is  $M_A = Re_m^{-1/2}$ . Further use of this result requires an estimate of the size of the system. In the Sweet-Parker configuration it is reasonable to assume that  $L$  is at least of the same order of magnitude as the scale of the system. Parker<sup>6</sup> applied this result to solar flares and found that the predicted reconnection rates are orders of magnitude smaller than the observed rates of energy release. An apparently easy fix to this problem was suggested by Axford<sup>25, 21</sup> who

considered that  $L$  may have any value, as long as it is larger than  $\delta$  and thus the reconnection rates could, theoretically, be as high as unity.

Petschek's model<sup>7</sup> (Figure 1.1.b) is based on the assumption that a convergent inflow is carrying the magnetic flux toward the neutral sheet. This solution involves a system of slow shockwaves and a super-Alfvénic plasma outflow ( $u_2 > v_A$ ). The conditions near the diffusion region are  $u_1 > u_\infty$ ,  $B_1 < B_\infty$ , and  $v_{A1} < v_{A\infty}$ , and the reconnection rate is controlled by the rate of fluid inflow. Clearly, the acceleration of the flow as it approaches the neutral sheet favors higher reconnection rates. The upper limit of Petschek's reconnection rate is of the order 0.1 and, in principle, is large enough to account for solar flares.

The third model recalled here is the exact stagnation-point flow solution of Sonnerup and Priest,<sup>26</sup> see Figure 1.1.c. This solution corresponds to a divergent inflow model. The divergent flow brings the magnetic flux toward the neutral line and is the source of the field gradient build-up. The inflow conditions near the diffusion region are  $u_1 < u_\infty$ ,  $B_1 > B_\infty$ . An interesting conclusion to this solution is that the magnetic field annihilates in the diffusion region at an arbitrary rate, which is not affected by the conductivity of the medium.

Simultaneous with the MHD analytical effort, steps were taken toward the development of an alternative kinetic – single particle description of the process, see for instance Dessler,<sup>27, 28</sup> Alfvén,<sup>29</sup> and Heikkilä et al.<sup>20</sup> More recently the researchers have turned their attention toward numerical modeling of reconnection. Two-fluid collisionless reconnection models were proposed and simulated numerically by Biskamp et al.,<sup>30</sup> Drake et al.,<sup>31</sup> and Shay et al.<sup>32</sup> Numerical simulations of the nonlinear evolution of the collisional tearing mode instability at magnetotail were performed by Forbes and Priest<sup>33</sup> and their conclusion was that the simulation is consistent with the proposed reconnection models of the magnetospheric substorms. Similarly, a numerical study of a resistive MHD reconnection model in a global scale coronal magnetic field was performed by Wu et al.<sup>34</sup>

### III. The Criticism of Reconnection

A significant part of the reconnection literature presents a critical view. Based on the level of disagreement the critique of reconnection can be divided into two distinct categories: (I) the criticism of some individual features of the theoretical reconnection models and analytic solutions, and (II) the rejection of reconnection and the dismissal of all related theoretical work altogether. The first level of criticism is a result of (a) discrepancies between theoretical predictions and some of the experimental data and (b) serious inconsistencies between models. The second level of criticism dismisses the entire reconnection problem on grounds of physical impossibility. These issues are reviewed in this section.

I. Parker<sup>6</sup> was the first to question the applicability of Sweet's model to solar flares and expressed doubts that magnetic fields have anything to do with flares, since it seemed impossible to him to get the reconnection rates to go fast enough. This deficiency of the Sweet-Parker model led to the emergence of new points of view: the Petschek model and some other "exact," time-dependent, incompressible solutions, see for instance Uberoi<sup>35</sup> and Chapman and Kendall.<sup>36</sup> Exact solutions for incompressible flows in configurations similar to Petschek's were also discussed in terms of dimensional analysis by Sonnerup<sup>37</sup> and Yeh and Axford.<sup>38</sup> The latter authors divided the problem into two parts by considering an outer flow describing the far field and an inner flow characterizing a dissipative x-type magnetic field configuration. Although the two flow solutions have been obtained independently, one conclusion was that "in principle" a complete solution could be "patched together" despite the lack of a rigorous formalism. These authors pointed out that the previous analytical efforts of Chapman-Kendall and Uberoi are not valid reconnection solutions since they do not involve plasma flow across the neutral line, and consequently connection is maintained at all times. Another result of these studies was that a MHD shock solution as presented by Petschek is actually impossible to obtain in the configuration shown, and that Petschek's model was "less convincing than it seemed originally." This conclusion was somewhat reinforced by a numerical analysis performed by Stevenson.<sup>39</sup>

However, the superficial examination of the governing equations and the summary treatment of the diffusion region in the Sonnerup and Yeh-Axford solutions have led some (notably Cowley<sup>40</sup>) to claim that the premises of these results are erroneous and thus they should be discarded entirely. Parker<sup>41</sup> re-visits these solutions and finds that the smoothing of the magnetic field prior to the arrival at the neutral point slows the reconnection rate in the Petschek model. Thus, he theorizes that the problem could be overcome if the effective diffusion coefficient is much higher in the dissipation region than outside it. This is a peculiar conclusion considering the higher energy density levels in the dissipation region. Another conclusion of Parker's study was that the similarity solutions of Sonnerup and Yeh-Axford are "mathematically elegant" but not physically realizable. Amid these conflicting views, Vasyliunas<sup>22</sup> reconciled the puzzling differences between Petschek's model and the Sonnerup and Yeh-Axford solutions by concluding that "subtle differences" in the initial physical assumptions could account for the different results. Nevertheless, the dimensional analysis arguments of Sonnerup and Yeh-Axford were deemed somewhat artificial. As a closing remark, it is worth noting that two decades from the initial appearance of Sweet's model, Giovanelli<sup>42</sup> expressed his doubts about the reconnection solution to the solar flare problem, and suggested that reconnection is more likely to be related to solar prominences.

II. A more severe attitude toward reconnection was taken by other physicists, most notably Alfvén and Heikkilä, who proposed the dismissal of the reconnection theory on grounds of physical impossibility. Alfvén<sup>8</sup> points out that reconnection is the result of the misuse of the concept of "frozen-in flux," which he first introduced<sup>23</sup> as a visualization aid to some cases of the plasma-field interaction in astrophysics. Thus he argues that (a) one can speak of particles moving within the constraints of a magnetic field but cannot speak of magnetic field lines being moved by the fluid, and (b) "to ask whether a field line moves or not has no sense," since the field line is only a concept having the Maxwellian meaning of a line which everywhere has the direction of the magnetic field. In view of these arguments, the magnetic field of a stationary

source remains static at all times and magnetic field lines neither disconnect nor reconnect. On a similar note, Heikkilä<sup>9</sup> discusses the magnetosphere and points out that (a) there is no direct indication that the reconnection process does actually take place, (b) reconnection fails to account for the energy dissipation by the magnetopause current, and (c) the conversion of magnetic energy into particle kinetic energy must involve an induced (rotational) electric field at the neutral line (separatrix). The third conclusion is in direct disagreement with all steady state theories of reconnection since  $\nabla \times \mathbf{E} = -\partial \mathbf{B} / \partial t = 0$ . On a different occasion Heikkilä<sup>43</sup> made a plea for a "common sense" approach to magnetospheric and auroral problems and argued for the use of kinetic models instead of the MHD/reconnection theory. Aside from some discrediting reactions (see for instance Axford<sup>21</sup>), these arguments prompted some attempts to a formal redefinition of reconnection as the plasma dynamic process in which there is plasma flow across a separatrix<sup>10,22</sup>, or as the plasma process in which there is an electric field along the separator.<sup>21</sup> Another interesting result of the criticism was the apparently impartial review by Baum and Bratenahl.<sup>10</sup> There the authors start by acknowledging Alfvén's point of view, and then conclude with a discussion about the role of reconnection in further enhancing human understanding of laboratory and astrophysical magnetoplasmas.

#### **IV. Magnetic Reconnection Experiments**

At the time of its inception, magnetic reconnection was a theoretical exercise designed to describe two extreme cases of interaction between magnetic fields and plasmas: the solar flares and the magnetospheric substorms. Since then reconnection has grown into a multi-faceted theory encompassing all phenomena (waves, hydromagnetic shocks, particle heating etc.) conceivably related to a neutral point magnetic field configuration. Gradually reconnection became also the answer to some energetic phenomena (tearing mode instabilities, current sheet disruptions etc.) observed during the magnetic confinement of plasma in fusion experiments. Thus, the first experimental cases of magnetic reconnection were observed in the pinches and



tokamaks of nuclear fusion research. Nevertheless, the magnetic reconnection data collected in most of these experiments was a byproduct of the main experimental effort. Early magnetic reconnection experiments were attempted with pinch devices in the early sixties, see review by Baum and Bratenahl.<sup>10</sup> While the literature of experimental reconnection is extensive, only four efforts to design and run repeatable, magnetic reconnection experiments are recalled here. These experiments were chosen since, to a certain extent, they are similar to the new experiment.

Ohyabu et al.<sup>44, 45</sup> studied the magnetic neutral point configuration created by currents flowing into four pairs of conductive rods. Plasma was produced and injected in the diffusion region by a plasma gun and a quadrupole magnetic field was created by the slow discharge of a capacitor bank through the rods. One important feature of these experiments was the excitation of a current sheet by the fast discharge of another capacitor bank through the plasma. In this configuration, the current sheet was assumed to closely model the magnetotail current. Two notable results of these experiments were strong ion heating and current disruptions. The authors attributed the disruption of the current sheet to an anomalous resistivity in the diffusion region. Similar observations were made by Stenzel and Gekelman,<sup>46, 47, 48, 49, 50</sup> who carried out a series of experiments in a linear glow-discharge stationary plasma. The neutral point magnetic field configuration was established by time varying currents flowing along two parallel plates. Added to this was an axial field component (along the plates) produced by an external coil. The plasma obtained in their experiments was in an electron-MHD regime, i.e. a regime in which only the electrons are magnetized while the ions are slow to respond to the changes in the applied magnetic field. Detailed measurements of the field strength and plasma properties were made but a quantitative validation of the analytical models available at the time has not been done. These authors noted strong ion heating and calculated an anomalously high resistivity value (in the dissipation region) by using Ohm's law and measured field quantities. This result seemed to support the idea (theorized by Parker<sup>41</sup>) that the Petschek mechanism requires a much higher diffusion coefficient inside the dissipation region than outside it.

Baum and Bratenahl<sup>12, 13, 14, 51</sup> and Bratenahl and Yeates<sup>52</sup> undertook a series of reconnection experiments with a double linear pinch discharge. The double, inverse pinch was constructed with two rods covered by insulation and terminated at the ends with flat, circular electrodes. In this device, the simultaneous discharge of two capacitor banks creates two outward-expanding cylindrical current sheets and a x-type neutral point. This series of experiments showed that (a) the ions are heated and accelerated, and (b) a system of large amplitude fast-mode waves is generated. The results led the authors to conclude that the experiment was in fact validating Petschek's model of wave-assisted diffusion, despite some obvious topological differences.

The largest magnetic reconnection experimental work to date was begun by Yamada<sup>53</sup> with the merging of two spheromaks in the TS-3 device at the University of Tokyo, and has continued with the MRX experiments at the Princeton Plasma Physics Laboratory.<sup>54, 55</sup> The MRX experiments were designed to answer a broad range of questions about the magnetic field topology, reconnection rates, ion and electron acceleration mechanisms, and the validity of the appropriate analytical models. In the MRX, highly conductive plasmas and large variable magnetic fields are created by the discharge of a capacitor bank through a series of toroidal (and poloidal) coils. The reconnection rates calculated from these experiments were somewhat similar to the predictions of a generalized Sweet-Parker (i.e. considering finite compressibility and anomalous resistivity) model.

The immediate conclusions from this review are that (a) any reconnection experiment must be limited to a restricted set of physical conditions and (b) due to inconsistencies between models, the experimental results may at best show agreement with one theoretical model. A second observation is that all experiments are necessarily transient due to energetic requirements. Thus, there is an unavoidable discrepancy between any experiment and all steady-state theoretical models. The problem is compounded by certain difficulties in scaling the experiments in a laboratory environment, a fact which limits their usefulness when trying to validate theoretical

models of astrophysical phenomena<sup>22</sup>. The summary of these arguments leads to the paradigm of experimental reconnection: one cannot design the definitive reconnection experiment.

## V. Objective of the Dissertation

The objective of this thesis is to experimentally investigate the engineering potential of phenomena associated with a hydrostatic x-type magnetic field configuration. Specifically, the goals are (a) to argue the possibility of plasma energization from a conceptual (single fluid MHD) viewpoint, and (b) to evaluate experimentally the effectiveness and the efficiency of the energy transfer from the magnetic field to the plasma.

One important observation must be made beforehand concerning the interpretation of the commonly used concept of “frozen-in flux” in the MHD theory of plasma. As pointed out by Alfvén<sup>8</sup> the topology of any magnetic field is completely determined by its source. Thus a magnetic field line will not move (or do anything) even if the magnetic field is embedded into a moving conductive medium (here plasma). Henceforth the terms of “frozen in flux” or “magnetic field advection” will be used only to represent a situation where ionized particles move within the ~~constraints~~<sup>58</sup> of a spatially or time changing magnetic field. This observation applies equally to the concept of magnetic flux diffusion. In view of the same arguments, the diffusion of the magnetic field must be understood as a gradual penetration of the plasma through a region permeated by a magnetic field. The particle motion of interest (i.e. diffusion) is across magnetic field lines and is due to electric fields and collisional processes within the plasma, see also Chen.<sup>56</sup>

It was noted previously that all MHD models of reconnection account for the rapid conversion of magnetic energy to plasma enthalpy by imposing an “advection of magnetic flux” toward the neutral line (see Figure 1.1). This process (despite its nonphysical nature) requires opposite plasma flows bringing the magnetic field into a dissipation region, and is not particularly useful from an engineering point of view. Instead, a situation where time varying magnetic fields energize the plasma must be considered. This is the case of hydrostatic, time dependent diffusion

of the magnetic field studied analytically by Yeh and Axford and experimentally by Stenzel and Gekelman.

Yeh and Axford<sup>38</sup> solved the magnetic induction equation (Equation 1.5) for a simple unidimensional case where the velocity of the flow is zero ( $\bar{v} = 0$ )

$$\frac{\partial B}{\partial t} = \frac{1}{\mu\sigma} \cdot \frac{\partial^2 B}{\partial y^2} \quad (1.12)$$

The authors considered also that the fluid has constant conductivity, and the magnetic field has only a component along the neutral line (x axis),  $B_x = B_x(y, t)$ . The magnetic field diffuses in y direction (similar to Figure 1.1.a) and the initial boundary condition is a step function  $B_x(y, 0) = \pm B_0$  for any  $y \neq 0$ . Assuming that the magnetic diffusion time  $t_d = \mu\sigma L^2$  is large compared to the Alfvén time  $t_A = L/v_A$  one obtains an error function solution of Equation 1.12

$$B_x(y, t) = \frac{4}{\pi} B_0 \cdot \int_0^{\sqrt{\frac{\mu\sigma}{t}} \frac{y}{2}} e^{-u^2} du = \frac{2}{\sqrt{\pi}} B_0 \cdot \text{erf}\left(\frac{y}{2 \cdot \delta}\right) \quad (1.13)$$

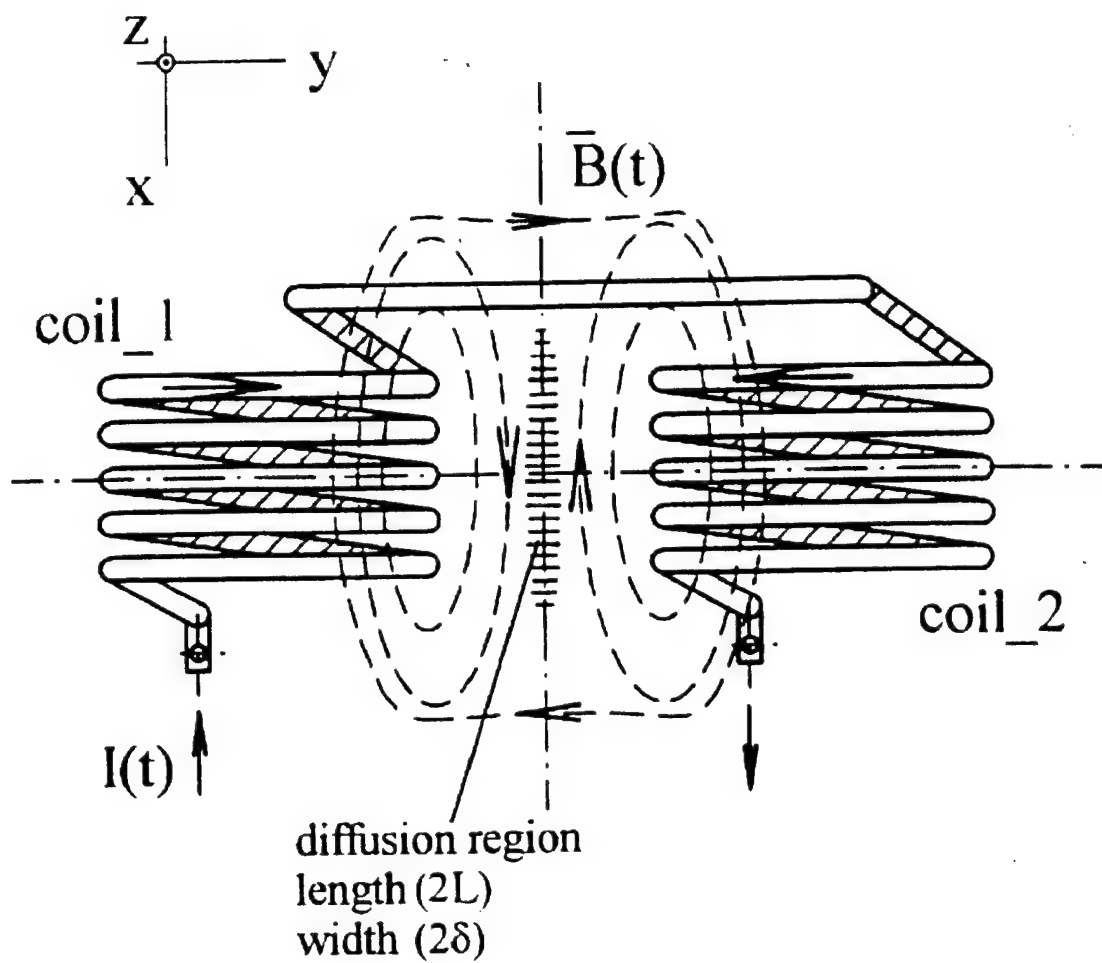
$$\delta \equiv \sqrt{\frac{t}{\mu\sigma}}$$

This similarity solution shows that the only characteristic length of the system is the instantaneous thickness of the current sheet  $\delta$ . It is noted that in this situation, the magnetic field lines do not reconnect and the magnetic field is annihilated at the neutral line. Thus, the energy of the magnetic field is being converted directly into heat. Another important observation is that the rate of magnetic field diffusion and annihilation is proportional to  $1/\delta$ . Yeh and Axford noted that  $\delta$  increases with time and concluded that the hydrostatic, time-dependent diffusion of magnetic fields is a “self-defeating process” as far as the rapid conversion of magnetic energy into plasma enthalpy is concerned.

Some of the conclusions of this theoretical study were partially corroborated by the Stenzel-Gekelman experiment (see previous subsection). However, the same experiment has

shown that time dependent diffusion is a more complex process, involving ion acceleration ( $\bar{v} \neq 0$ ), generation of waves, current sheet instabilities, and changes in plasma conductivity. It is concluded that there is enough evidence to question the universal applicability of this model (Equation 1.13), and there are grounds for designing a new time-dependent magnetic field diffusion experiment.

The apparatus considered for this investigation consists of two opposing coils. The neutral line magnetic field configuration is created in the inter-coil space by the discharge of a high-capacity, low-voltage capacitor bank. The new experiment is similar in principle to the Stenzel-Gekelman flat-plate experiments, while the new device resembles the multiple rod arrangement of Ohyabu. A schematic view of the magnetic fields is shown in Figure 1.2. Several differences from the Stenzel-Gekelman experiments are noted: (1) the relaxed boundary conditions near the coils (the flow is allowed to pass through), (2) the inter-coil plasma is free from electric fields prior to the discharge of the capacitor bank, and (3) the time constant of the discharge is an order of magnitude higher than that of Stenzel-Gekelman. The new experiment is also dissimilar from the Ohyabu experiments in that all external energy is supplied to the field coils. The first account of the new experiment and an analytical single fluid model were presented by Deaconu et al.<sup>57</sup> The same model (hereafter referred to as the Denver model) is recalled here and constitutes the starting point of this investigation.



**Figure 1.2** Field-coils and magnetic field configuration in the new experiment

## VI. The Denver Model

In the new model plasma is considered quasi-neutral, highly conductive, and is allowed to move ( $\bar{v} \neq 0$ ) under the effects of the magnetic pressure toward the neutral sheet, preventing the theoretically less favorable case of pure diffusion ( $\bar{v} = 0$ ) described by Yeh-Axford. The opposing magnetic fields are generated by the discharge of a capacitor bank through the coils, and the rise of the fields compresses and energizes the plasma sandwiched in-between the coils. Consider the variable magnetic field produced at the onset of the discharge in an average sense

$$B_{avg} \equiv \frac{1}{\tau} \cdot \int_0^{\tau} (\partial \bar{B} / \partial t) dt, \text{ where } \tau \text{ can be taken as the rise time of the magnetic field and let the}$$

system be infinite in the  $z$  direction (2-D model). The plasma is pushed toward the neutral line by the magnetic pressure  $p_m = B_{avg}^2 / 2\mu$ . Let  $p$  be the thermodynamic pressure building inside the compressed plasma due to the magnetic field pressure. The average force acting upon the incoming plasma is proportional to the pressure difference and area  $2Lp_m(1-p/p_m)$ . The momentum equation yields the acceleration of the plasma (taking a unit length on  $z$ )

$$a_{avg} \sim \frac{F_{avg}}{m} \sim \frac{p_m \left(1 - \frac{p}{p_m}\right)}{\rho \delta_{avg}} \quad (1.14)$$

Introducing plasma beta ( $\beta = p/p_m < 1$ ), and the Alfvén velocity  $v_A = B_{avg} / (\mu \rho)^{1/2}$  and integrating over a time  $\tau_{event}$ , an estimate of the inflow plasma speed is obtained (let  $u_1(t_0) = 0$ )

$$u_1 \sim \frac{B_{avg}^2}{2\mu\rho\delta} (1-\beta)\tau_{event} \sim \frac{v_A^2}{2\delta} (1-\beta)\tau_{event} \quad (1.15)$$

The plasma diffuses a distance  $\delta$  through the magnetic field in  $\tau_D \sim \delta^2 \mu \sigma$ , the diffusion time. It is noted that here the diffusion time can be defined in terms of  $\delta$  rather than in terms of  $L$ . In the case of interest here, the diffusion time  $\tau_D \ll \tau_{discharge}$ . In these conditions the “event” time  $\tau_{event}$  is of the order of  $\tau_D$ . Dropping the average (avg) indices the inflow speed becomes  $u_1 \sim v_A(1-$

$\beta) \text{Re}_m(\delta/L)$ . Mass conservation yields the outflow plasma speed  $u_2 = (L/\delta)u_1$ . Using Equation 1.15 the outflow speed is

$$u_2 \sim v_A (1 - \beta) \cdot \text{Re}_m \quad (1.16)$$

where  $\text{Re}_m$  is the magnetic Reynolds number defined in a previous section as  $\text{Re}_m = \mu \sigma v_A L$ . It is evident from Equation 1.16 that the outflow could involve a magnetodynamic shock solution, given the right combination of dimensionless parameters. For instance, a fast increase of the magnetic field may generate a magnetic shock ( $\beta \ll 1$ ) and lead to a super-Alfvénic outflow ( $u_2 > v_A$ ), in a somewhat similar manner to Petschek's model.

The efficiency of the energy conversion process is defined as the ratio of the rate of kinetic energy outflow to the rate of electromagnetic energy inflow. Using (1.15) and (1.16), the rate of reconnection is  $M_A = u_1/v_A = (1 - \beta)\text{Re}_m(\delta/L)$ , and the ratio  $R$  of the rate of kinetic energy outflow  $(\rho u_2^2/2)u_2\delta$  to the rate of inflow of magnetic energy<sup>20</sup>, here taken as

$$\iiint_{\Omega} \frac{\partial}{\partial t} \left( \frac{B^2}{2\mu} \right) \cdot d\Omega \approx L\delta \cdot \frac{B^2}{2\mu\tau}, \text{ with } \tau \equiv \tau_D \text{ is given by}$$

$$R \sim (1 - \beta)^3 \text{Re}_m^3 \cdot \left( \frac{\delta}{L} \right)^2 \quad (1.17)$$

Equation 1.17 indicates that the efficiency of the energy transfer from the magnetic field to the plasma scales with the cube of the magnetic Reynolds number, and the square of the aspect ratio of the diffusion region. According to this simplified model, plasma particles could be energized by the magnetic field, at least during the period of high field gradient at the onset of the discharge.

Two important remarks must be made regarding this model. First, the model is obtained from a phenomenological description of the process and is not derived from the magnetic induction equation (Equation 1.5). Thus, the model does not imply that the predicted acceleration



of particles is necessarily the result of a reconnection event. Second, the acceleration of plasma particles at the rate predicted by Equation 1.17 is based on the assumption of high plasma conductivity  $\sigma \geq 1000 \text{ } (\Omega^{-1} \cdot \text{m}^{-1})$ , or with the current experimental configuration  $\text{Re}_m \gg 1$ . This condition is equivalent to imposing that a large number of ionized particles is interacting with the magnetic field. The deterioration of the efficiency of this process in case of low plasma conductivity is evident from Equation 1.17, where the rate of energy transfer is indeed proportional to the cube of the magnetic Reynolds number.

The case of low conductivity plasma is also of interest since the ionization rates attainable in the new experiment are relatively low  $\sigma \cong 1 \dots 100 \text{ } (\Omega^{-1} \cdot \text{m}^{-1})$ . Qualitatively, the case of low plasma conductivity can be understood from a particle-kinetic point of view. At the onset of the capacitor bank discharge, the few ionized particles are accelerated by the rising magnetic pressure and gain energy. The electrons will travel along the magnetic field lines and eventually lose some of the energy gained by collisions with slow neutral particles. The ions are slower to respond to the magnetic field change due to their larger mass and will transfer the acquired energy to neutrals within a few mean free paths. Thus, one could expect (a) a quick thermalization of the ions to gas temperature and (b) a dampening of the initial magnetic shock to weak ion acoustic waves. Mathematically the process can be modeled by treating the initial rise of the magnetic field as a step function input. The rapid increase of the magnetic field induces a large variation of the electric field (delta function). Clearly, the result of this input is a broadband frequency excitation of the system. The highly collisional regime of the weakly ionized plasma will then favor those perturbations that travel with the mean thermal speed i.e. acoustic waves. Nonetheless, additional energization (and movement) of the ionized particles is also possible during the slow decay of the magnetic field (i.e. betatron acceleration) following the initial spike of the induced electric field. These premises suggest that plasma energization could be detected by tracking the motion of the ionized particles with conductivity probes.

## CHAPTER II

### THE MDE EXPERIMENT

#### I. Experimental Apparatus

The new magnetic diffusion experiment (MDE) was carried out at the University of Alabama in Huntsville, Advanced Propulsion Laboratory in a cylindrical glass vacuum chamber, see Figure 2.1. In this chamber, vacuum levels as low as 0.02Torr can be achieved with a variety of gases: nitrogen, argon, and helium. During steady state pumping with gas flow the vacuum pressures attainable are in the 0.2 – 1Torr range. The MDE experimental apparatus consists of two opposing coils, an energy storage and delivery system (capacitor bank and triggered spark gap), a plasma source, and diagnostics.

The dual-coil arrangement is presented in Figure 2.2. The coils are made of 9AWG enameled copper wire of  $\phi_w = 2.92\text{mm}$  diameter, and have five turns each. The turning radius of the coils is  $R_c = 35\text{mm}$  and the least separation distance is  $a = 14.5\text{mm}$ . The combined inductance of the two coils has been estimated analytically and measured experimentally and is  $3.2 \pm 0.5\mu\text{H}$ . The coils are held in place by a copper supporting ring at the top and an aluminum plate at the bottom. The copper ring and the aluminum plate are grounded to the main ground line of the laboratory and are electrically insulated from the coil windings. The plate serves as the base for the device and holds all electrical connections for power wires and for electric and magnetic probes.

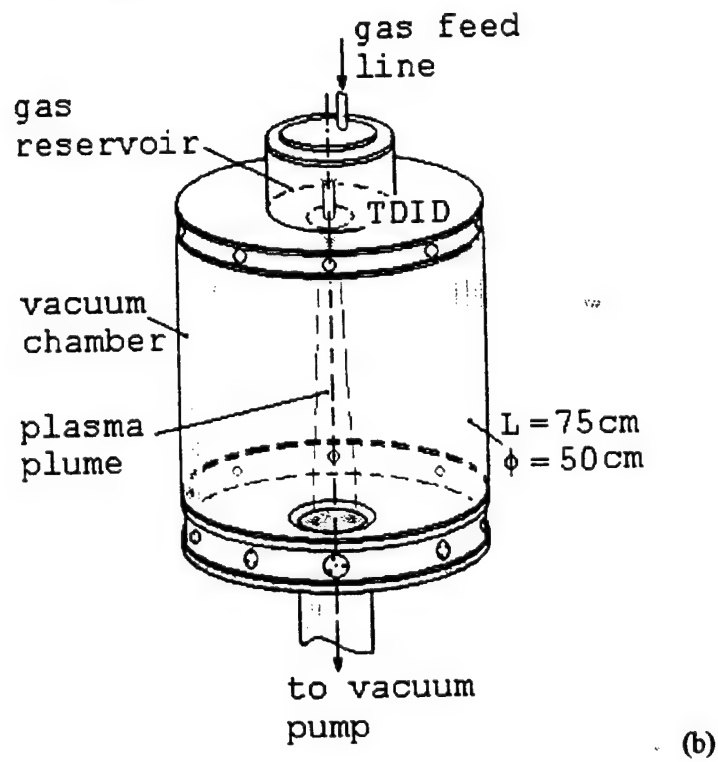
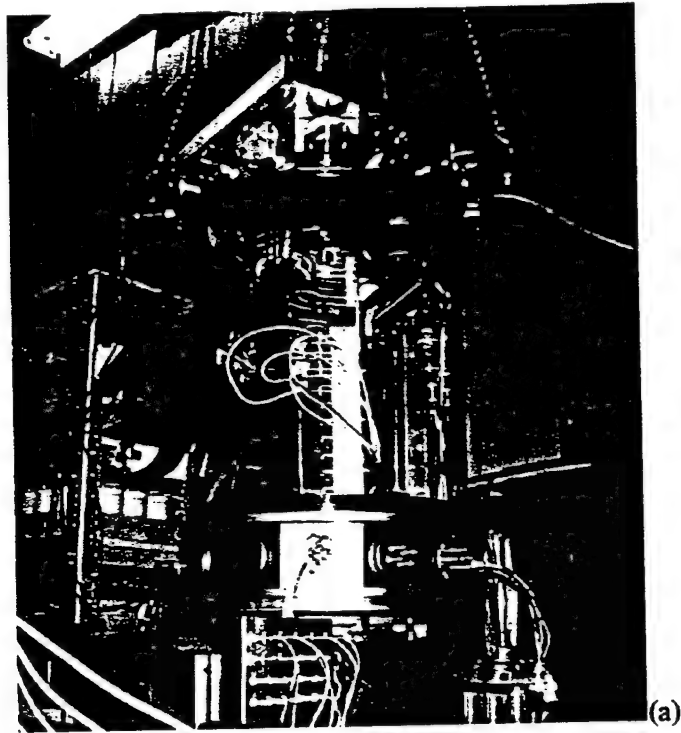
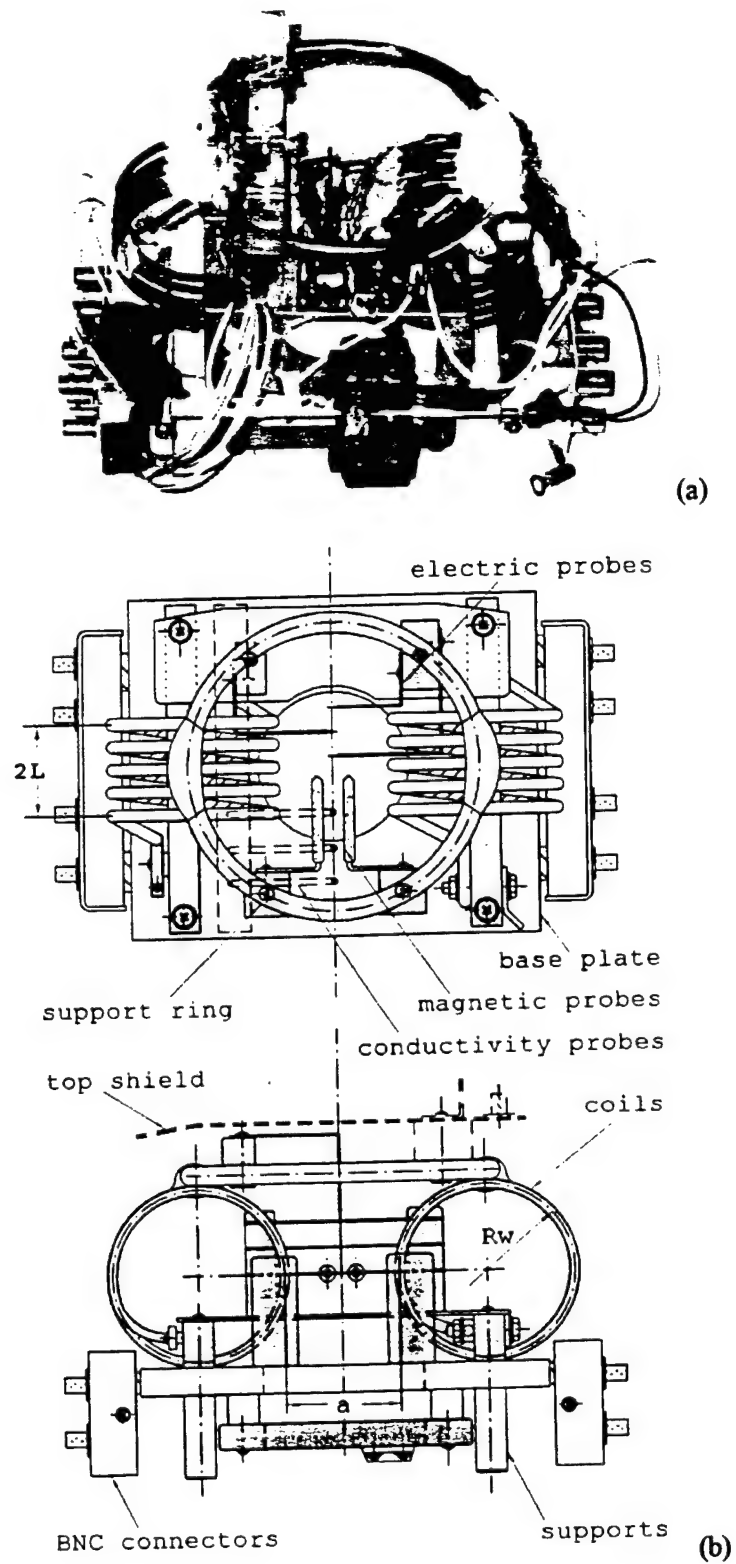


Figure 2.1 Vacuum chamber photo (a) and sketch (b)



**Figure 2.2** The dual coil arrangement photo (a) and sketch (b) ( $2L = 28\text{mm}$ ,  $R_w = 35\text{mm}$ ,  $a = 14.5\text{mm}$ )

The magnetic neutral line is created in the inter-coil space by the discharge of the capacitor bank through the coils. The capacitor bank is rated at 86mF/350V and provides a maximum of 5.26kJ of energy. The charging circuit of the capacitor bank is composed of a 0-350Vdc controllable power supply and a 125 $\Omega$ /50W power resistor mounted on a heat sink. The current in the dual-coil circuit is switched by a low voltage, triggered spark gap positioned inside the vacuum chamber (see Figure 2.3.a). The spark gap was specifically designed for this application and features three electrodes: the anode, the cathode, and the trigger, see Figure 2.3.b. The anode and the cathode are two similar electrodes made of cylindrical brass rod of 6.4mm diameter. These electrodes are separated by a distance of about 7mm. At any vacuum pressure, this distance is sufficiently large to prevent gap breakdown for voltages up to 350Vdc. The trigger electrode is connected to a separate high voltage (2000V) pulsed dc power supply (see Figure 2.3.a). When the high voltage is applied to the trigger electrode, a small spark occurs between the trigger and the cathode leading to an increase in the conductivity of the inter-electrode gap and subsequently to gap breakdown.

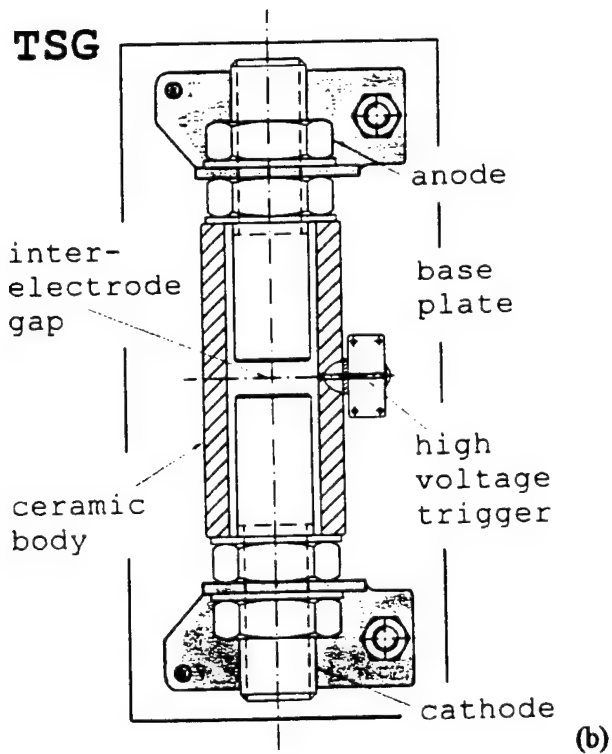
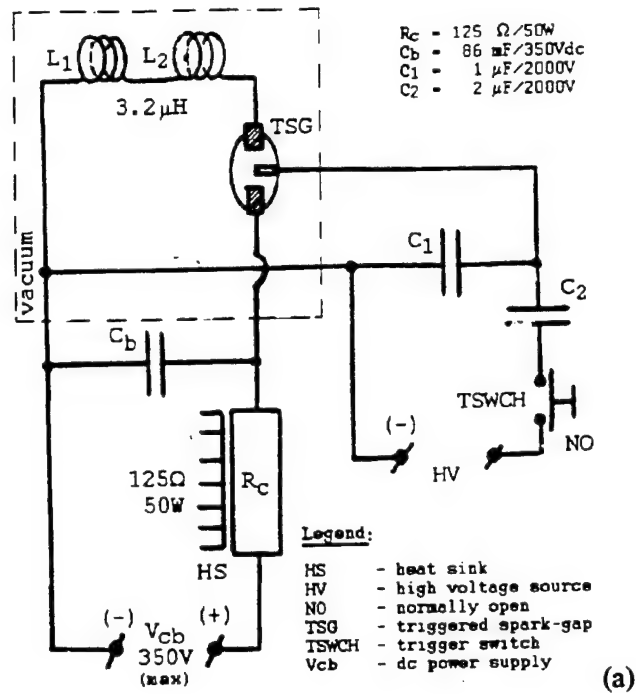


Figure 2.3 Charging circuit (a) and triggered spark-gap (b)

The second important aspect of the experiment is the generation of stable, conductive plasmas. The plasma source in this experiment was a newly designed dc thermionic-arc discharge ionization device<sup>38</sup> (TDID), see Figure 2.4.

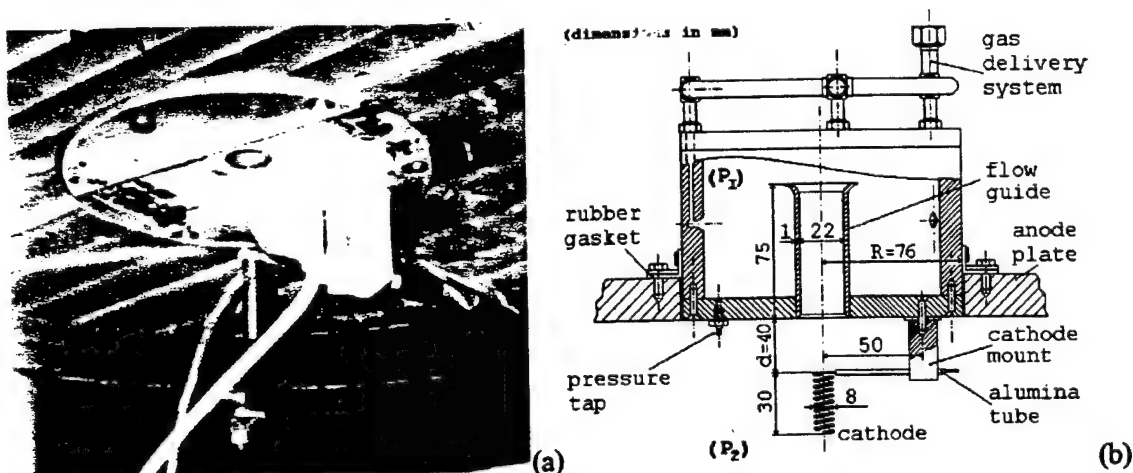


Figure 2.4 TDID photo (a) and sketch (b)

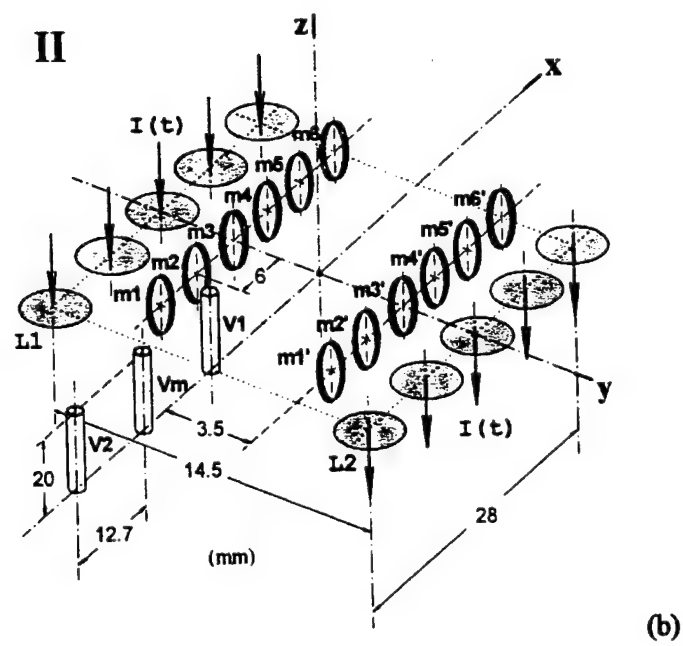
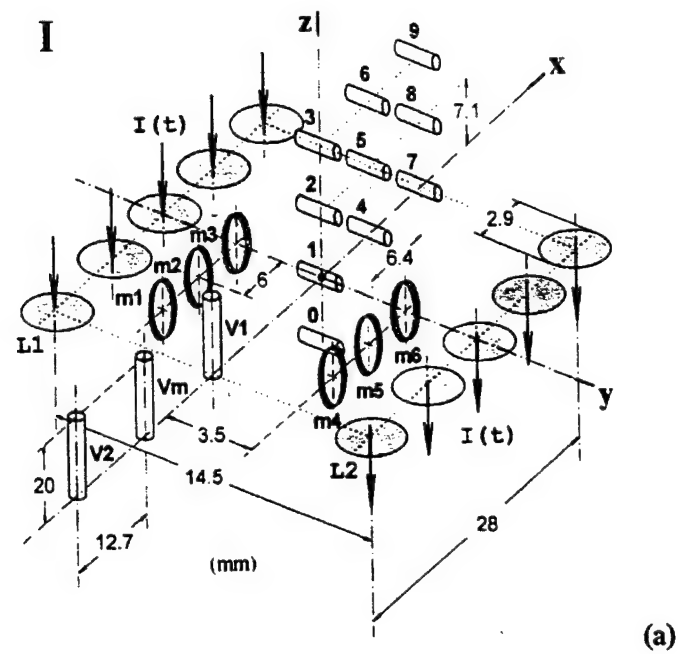
The ionization device was grafted onto the bottom of the top plate of the vacuum chamber, see Figure 2.4.a. This plate holds a gas reservoir at the top and serves as the anode of the ionization device. An opening was machined in the center of the anode plate and the upper side was fitted a smooth stainless steel tube, as illustrated in Figure 2.4.b. The tube is flared at the top and acts as a flow guide for the gas exiting the reservoir. The TDID features a self-heated cathode made of tungsten-rhenium wire spiraled as a filament. Under typical operating conditions, the ionization device produces a steady, field-free, nonequilibrium plasma plume ( $T_e > T_{gas}$ ) by ionizing a flowing gas column. The ionization device input power levels are in the 1 - 1.4kW range and the electron densities in the plume are  $10^{17} \text{ m}^{-3}$  in nitrogen,  $10^{18} \text{ m}^{-3}$  in argon and  $10^{15} \text{ m}^{-3}$  in helium. The dual-coil is situated below the cathode filament with the upper supporting ring approximately 30mm below the TDID cathode filament.

## II. Diagnostics and Data Acquisition

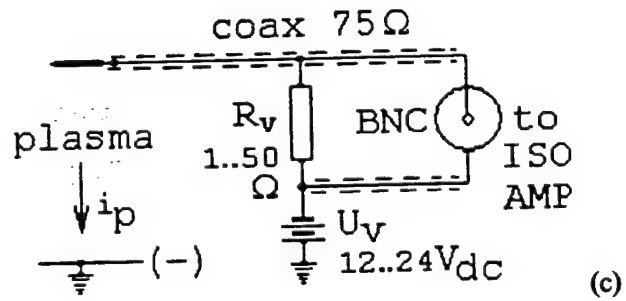
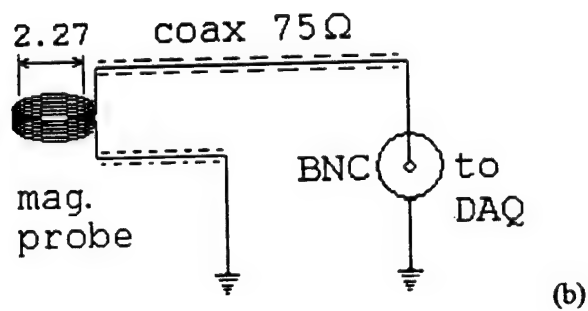
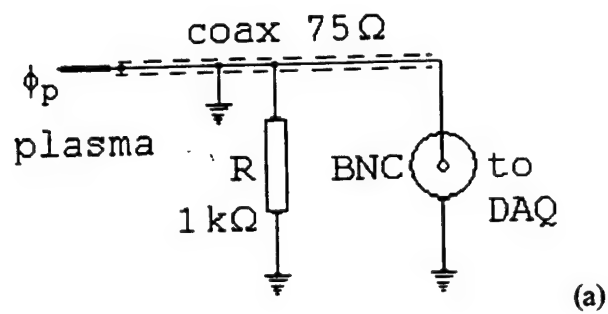
The diagnostics employed in the experiment consist of measurements of the power-input, plasma properties, and electric and magnetic fields. These data were automatically recorded for the entire duration of the capacitor bank discharge by a computerized data acquisition system. The input power is estimated from measurements of the capacitor bank charging voltage and the ohmic resistance of the coil circuit. Plasma properties of interest are the electron temperature, electron density, and gas temperature and pressure. The measurements of plasma properties were performed separately from the MDE and the procedure is documented in Appendix A. The study performed on the TDID showed that for each gas the ionization levels in the plume are proportional to the power input and to the pressure of the gas (see Appendix A). Hence, during the MDE tests only the input power to the TDID and the vacuum chamber pressure were monitored and recorded. This procedure reduced the number of recorded channels on the data acquisition and allowed for a higher sampling rate.

Plasma motion, and electric and magnetic fields in the inter-coil gap were monitored by electric and magnetic probes mounted on the dual coil device. Two configurations were used: (I) an array of ten electric probes, two conductivity probes and six magnetic probes, see Figure 2.5, and (II) twelve magnetic probes and three conductivity probes. In configuration (I) the electric probes span one quadrant of the neutral sheet and monitor the changes of the electric field in the plasma. In the second configuration (II) the electric probes were removed and replaced with six additional magnetic probes. The electric probes are made of 0.5mm tungsten-rhenium wire and have an active length of 4 mm. Each probe is connected to the system ground through a  $1\text{k}\Omega$  resistor. The probe signal is collected as the potential drop on the resistor and is proportional to the local plasma potential at the tip of the probe (see Figure 2.6.a).





**Figure 2.5** MDE probes configurations I (a) and II (b)



**Figure 2.6** Electric circuit for electric (a), magnetic (b), and conductivity probes (c)

In the first configuration the six magnetic probes  $m_1, \dots, m_6$  are positioned in the inter-coil gap and monitor the axial component of the magnetic field ( $B_x$ ). Each coil is 1.8mm long and has 30 turns of 36AWG enameled copper wire, wound on 1.6mm alumina ( $Al_2O_3$ ) cylindrical core. In configuration II these probes were replaced with twelve new probes of 2.3mm length and 40 turns each. The size of the probes limited both configurations to monitoring only the x component of the magnetic field. All probes have a mean cross-sectional area of  $4mm^2$ . The magnetic probes are covered with a protective, high-temperature ceramic compound, which also acts as supplementary electrical insulation. These probes have very low impedance ( $< 0.1\Omega$ ) and are connected directly to BNC connectors through coaxial cables, see Figure 2.6.b. The signals from the magnetic probes are proportional to the time variation of the magnetic field<sup>59</sup>

$$V = N_c A_c \frac{dB_x}{dt} \quad (2.1)$$

Here  $V$  is the coil induced voltage,  $N_c$  is the number of turns, and  $A_c$  is the mean cross-sectional area of the coil. The values of the magnetic induction were found by numerically integrating the probe signals.

Three conductivity (velocity) probes  $v_1, v_m$  and  $v_2$  were also provided in both diagnostic configurations. These probes are vertical tungsten wires of 0.7mm diameter and 20mm active length, and respond to changes in plasma conductivity. The electrical circuit of a conductivity probe consists of a 12/24Vdc battery, a resistor placed in series with the probes, and the plasma, see Figure 2.6.c. The current in the circuit is proportional to the local conductivity of the plasma, and changes only if there is a change in the plasma ionization fraction at that location. Generally, a local variation of the plasma ionization fraction (i.e. electron density) can occur if (a) there is an electric field in the plasma and (b) there is plasma movement. Two or more conductivity probes are able to monitor any low frequency ( $f < f_{\text{sampling}}/2$ ) plasma motion along the x-neutral line. The first test configuration employed only the  $v_1$  and  $v_2$  probes since the large number of recorded channels reduced the sampling rate.

Three remarks must be made about the operation of the conductivity probes:

- (1) The voltages recorded by the probes are in the mV range and are not suitable for direct recording with the data acquisition. Thus, the signals from the probes are preamplified and decoupled from the chamber ground by wideband, constant gain ( $\times 100$ ) isolation amplifiers prior to being recorded by the data acquisition. This procedure ensures that the signals are not lost in the digitization error of the data acquisition board, and the battery in the circuit is not short-circuited, see Figure 2.6.c.
- (2) The interference of the probe itself with the plasma property it measures (conductivity) is minimal, since the current flowing through each probe is at most of the order of hundreds of microamperes.

The entire test sequence and data acquisition were performed with two Pentium II computers equipped with National Instruments™ e-series, multifunction 12 bit analog I/O data acquisition boards. The signals from all probes and the capacitor bank voltage were recorded at high sampling rate (65-83ksample/sec-channel) by a PCI-6071E board. At these sampling rates, the array of conductivity probes can pick up plasma motion of frequencies up to 32-41kHz, or considering the maximum probe separation of 0.025m, any plasma movement of velocities up to 800-1000m/sec. The PCI board was also the master controller of the experiment. The second (slave) board was a slower (20-25ksample/sec-channel) AT-MIO-16E-10 and was used to record the chamber pressure, the TDID gas reservoir pressure, and TDID power input. This board was also employed in the separate study of the TDID plasma. The digitization resolution of these boards is  $\pm 2\text{mV}$ . The acquisition programs for both boards were programmed in National Instrument's LabView™ software.

### III. Testing Procedure

Three types of tests were run. I) Base line tests run with no plasma and at low chamber pressure 0.05Torr. II) No plasma tests – Capacitor bank discharge with gas flowing and chamber pressure at test values, (0.2 – 0.6Torr) and TDID turned off. These two types of tests provided information about (a) noise and interference levels in the system and (b) plasma formation due to the induced electric field created by the rapidly varying magnetic field. III) The complete tests: discharge of the capacitor bank through the coil under a steady plasma flow.

The test matrix of the experiment was designed such that (a) all three types of tests are performed with nitrogen, argon and helium and (b) the tests are replicated at least once. Aside from calibration runs of the probes and data acquisition, a total of ninety-two MDE tests were performed. However, a large number (thirty-six) of these tests were unsuccessful or only partially successful. The four main causes for test failure were: (a) unsuccessful synchronization of the data acquisition with the discharge, (b) the failure of the spark-gap to trigger the discharge, and (c) failure of the TDID to produce a stable plasma, leading to automated system shut-down before the end of the test. Some of the failed tests could not be reproduced due to time and financial constraints. The successful test runs are tabulated in Table 2.1.

**Table 2.1** Summary of successful tests

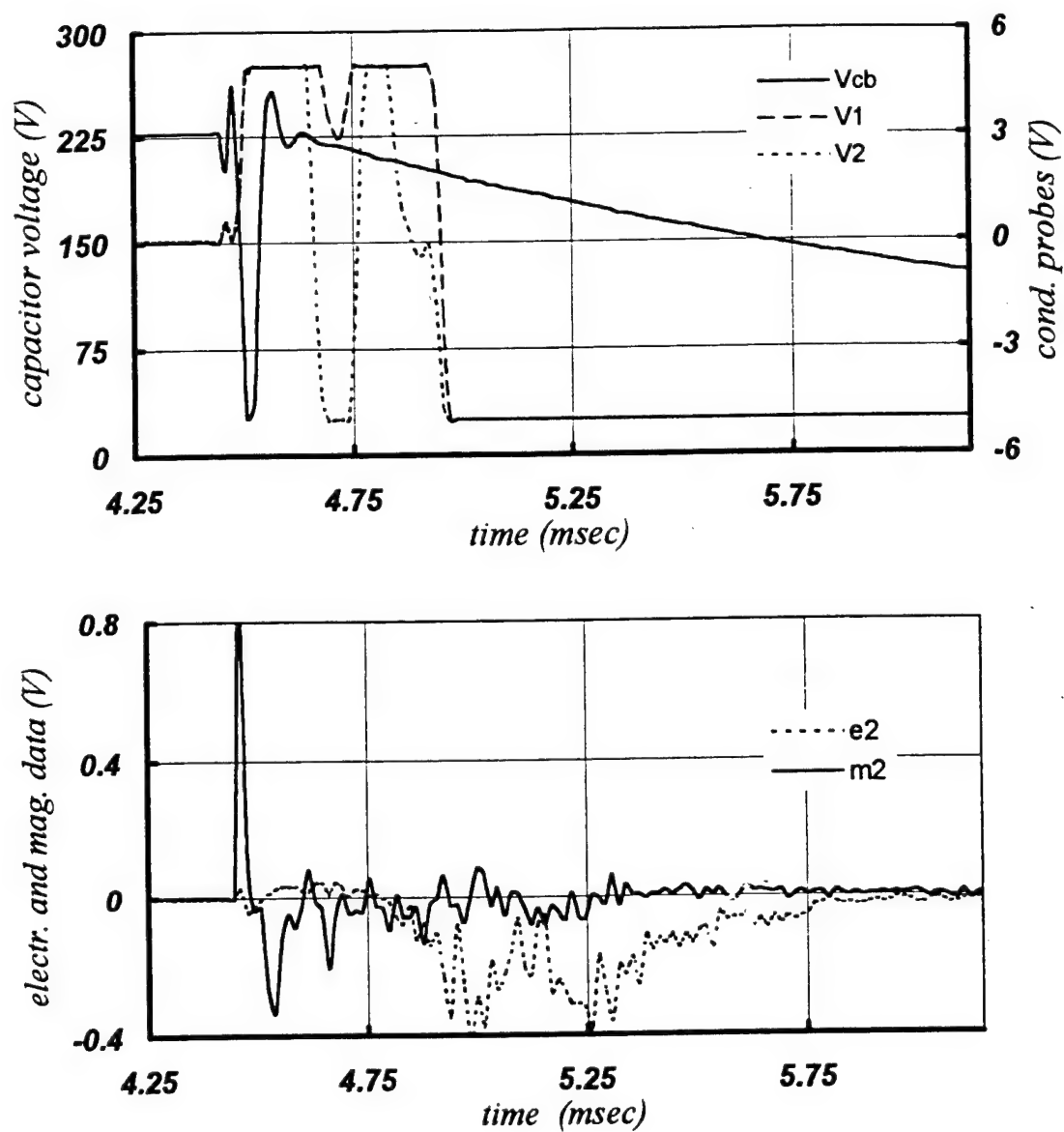
Test Type	Gas	No. tests	Pressure (Torr)	Scan rate (kHz/channel)	Recorded data
(I) Base line	N <sub>2</sub>	3	0.05	65 and 135	All probes (config. I) Pressures Discharge power
(II) No plasma	Ar	1	0.3	65 and 78	All probes (configs. I, II) Pressures Discharge power
		1	0.4		
	He	1	0.3		
		1	0.5		
	N <sub>2</sub>	1	0.6		
		1	0.2		
		1	0.3		
		3	0.4		
		6	0.5		
		2	0.6		
(III) Complete	Ar	2	0.3	65, 78 and 83	All probes (configs. I, II) Pressures Discharge power TDID power
		1	0.4		
	He	1	0.3		
		1	0.5		
	N <sub>2</sub>	3	0.6		
		2	0.2		
		4	0.3		
		3	0.4		
		13	0.5		
		5	0.6		

#### IV. Experimental Results

The experimental data set from each test run contains the time variation of the capacitor bank voltage, electric field, magnetic field and plasma properties in the inter-coil gap. The capacitor bank voltage is the essential information needed to calculate the discharge power level, the intensity of the magnetic field and the energy transferred to the plasma. The capacitor voltage was used to determine the data recording time for all acquisition channels, and to synchronize the two data acquisition platforms. The electric probe data (probes configuration I) is a time history of the plasma to chamber ground potential. The location of the electric probes (see Figure 2.5) permits the evaluation of the  $E_x$  and  $E_z$  components of the electric field in the neutral sheet. The magnetic and the conductivity probe data were taken in both probe configurations.

Sample data from a base line test performed in nitrogen at a pressure of 0.05Torr is presented in Figure 2.7. The conductivity probes show the formation of plasma immediately after the discharge onset. The response of the plasma to the magnetic field is significant in the first three milliseconds of the discharge. A somewhat similar behavior was recorded in the no plasma tests, see Figure 2.8. The test shown was run with nitrogen at a pressure of 0.5Torr and with the TDID turned off. Typically, the occurrence of the plasma in the no plasma tests is somewhat delayed (0.9-1 msec) from the discharge onset.

Figure 2.9 and Figure 2.10 show sample data from two complete tests in nitrogen. The first test was run with probes configuration I, while the second was run with probes configuration II. The presence of plasma prior to discharge onset changes the plasma potential, see electric data in Figure 2.9. The conductivity probes show that plasma conductivity is small prior to the capacitor bank discharge and increases dramatically after 0.7-1.2 msec from discharge onset.



**Figure 2.7** Sample data from base line test ( $N_2$ , 0.05Torr,  $W_{\Delta t} = 0.84\text{MW}$ ,  $U_v = 12\text{V}$ ,  $R_v = 25\Omega$ , sampling rate 65kHz)



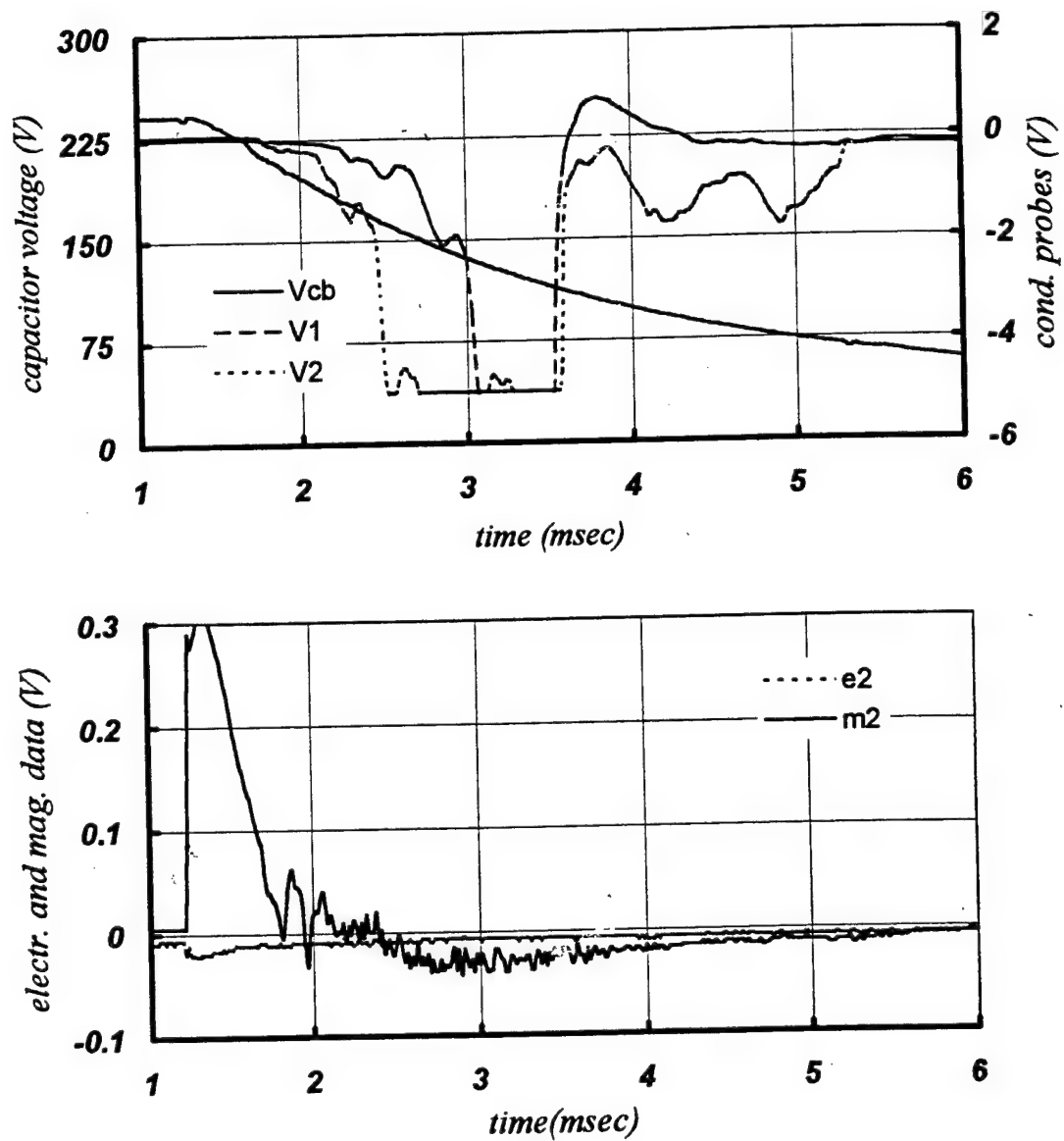


Figure 2.8 Sample data from no plasma test ( $N_2$ , 0.5Torr,  $W_{\Delta t} = 0.69\text{MW}$ ,  $U_v = 12\text{V}$ ,  $R_v = 16.6\Omega$ , sampling rate 65kHz)

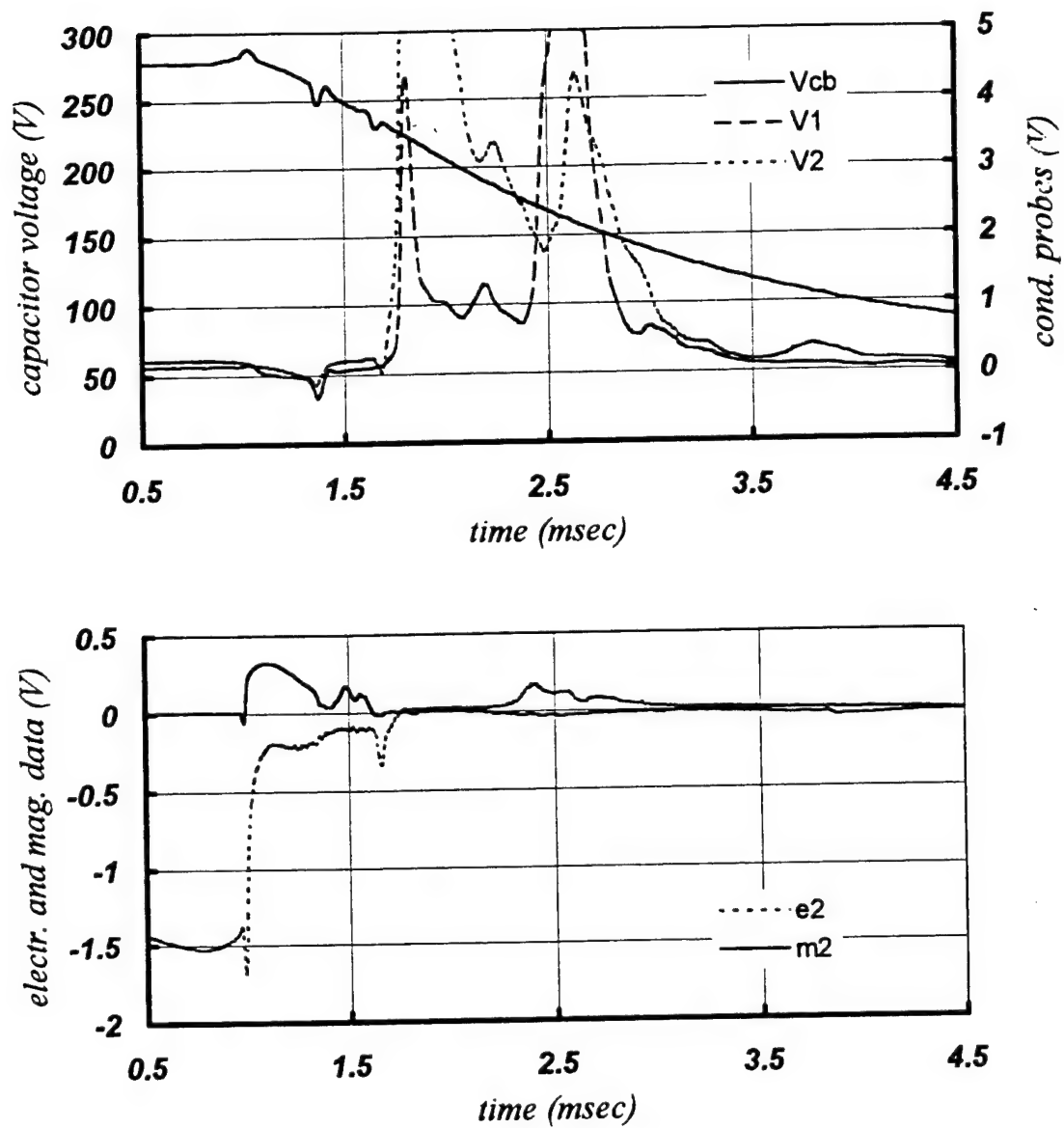


Figure 2.9 Sample data from complete test ( $N_2$ , 0.5Torr,  $W_{\Delta t} = 0.96\text{MW}$ ,  $U_v = 24\text{V}$ ,  $R_v = 16.6\Omega$ , sampling 65kHz,  $P_{TDID} = 1\text{kW}$ , probes config. I)

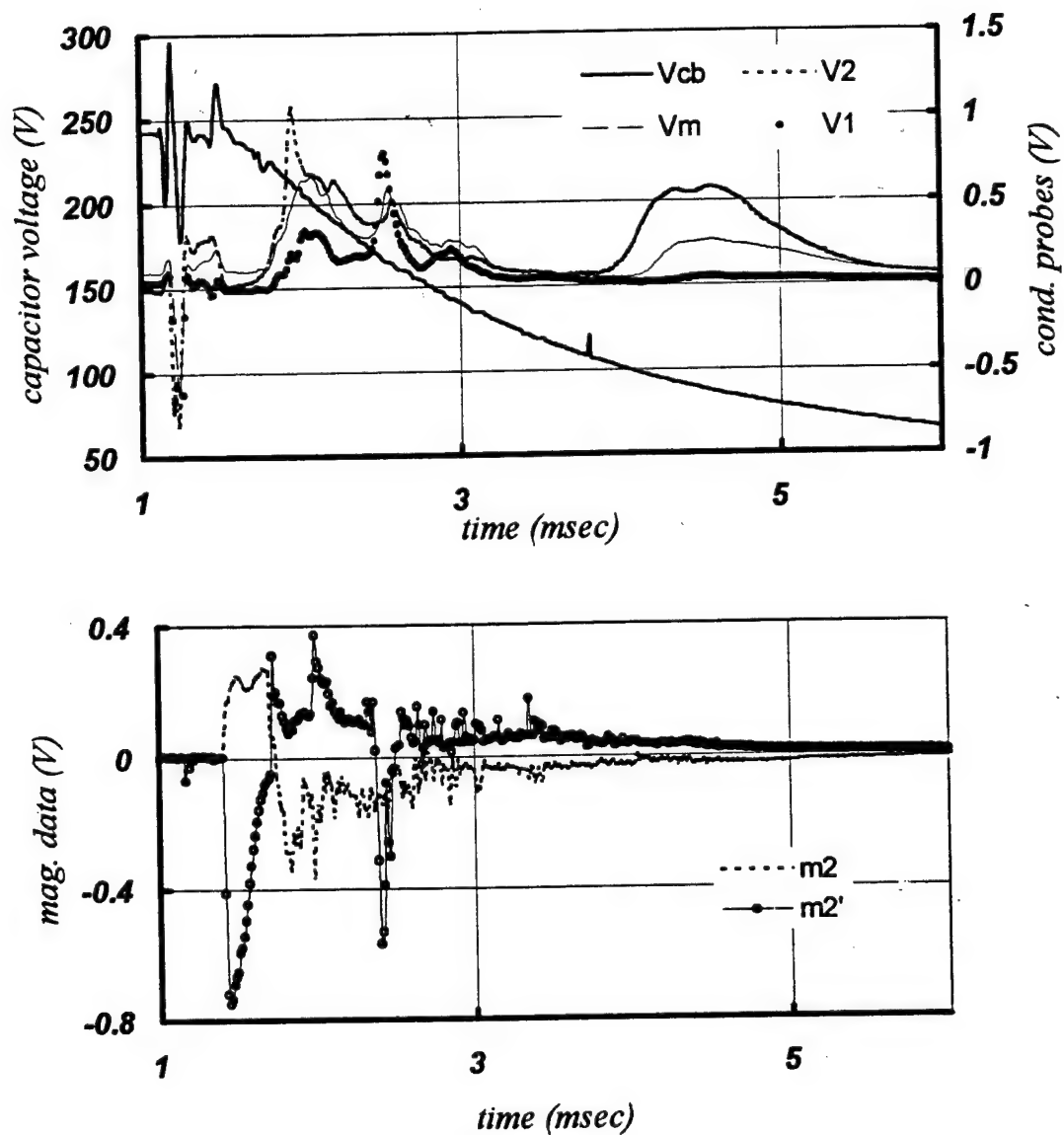


Figure 2.10 Sample data from complete test ( $N_2$ , 0.3Torr,  $W_{\Delta t} = 0.62\text{MW}$ ,  $U_v = 24\text{V}$ ,  $R_v = 2\Omega$ , sampling 78kHz,  $P_{TDID} = 1.48\text{kW}$ , probes config. II)

## CHAPTER III

### ANALYSIS OF EXPERIMENTAL DATA

#### I. Discharge Power and Efficiency

The MDE circuit is a variable resistance RLC discharge described by the following differential equation

$$R_c(t) \cdot i(t) + L_b \frac{di(t)}{dt} + \frac{q(t)}{C_{cb}} = 0 \quad (3.1)$$

Here  $R_c$  is the resistance of the circuit,  $i(t)$  is the current,  $L_b = 3.2\mu\text{H}$  is the combined impedance of the coils,  $C_{cb} = 86\text{mF}$  is the capacitance of the capacitor bank, and  $q = \int i(t)dt$  is the electric charge. The initial conditions are

$$\begin{aligned} i(t=0) &= 0 \\ q(t=0) &= q_0 \end{aligned} \quad (3.2)$$

where  $q_0 = U_0 C_{cb}$ , and  $U_0$  is the capacitor bank charging voltage. At the onset of the discharge, the spark gap is fully ionized and has a low resistance. This resistance increases as the amount of energy supplied by the capacitor bank diminishes. The discharge stops when there is not enough energy left to maintain gap breakdown. Typically, the total discharge time is 12-15msec. Experimental data show that plasma responds to the magnetic field created by the coils in the first three milliseconds of the discharge,  $\Delta t \cong 3\text{msec}$ . Assuming that the resistance of the circuit is constant  $R_c(t \in \Delta t) = R$  during this period, Equation (3.1) can be solved analytically for the current

in the circuit. Taking the derivative of Equation (3.1) and applying the initial conditions (Equation 3.2) the following solution is obtained

$$i(t) = \frac{U_0}{L_h(r_2 - r_1)} \cdot [\exp(r_1 t) - \exp(r_2 t)] \quad (3.3)$$

where  $r_{1,2} = -(R/2L_h) \mp (1/2)\sqrt{(R/L_h)^2 - 4/(L_h C_{cb})}$ . The capacitor bank voltage drops according to

$$V_{cb}(t) = U_0 + \frac{U_0}{C_{cb} L_h} \left[ \frac{\exp(r_1 t) - 1}{r_1} - \frac{\exp(r_2 t) - 1}{r_2} \right] \quad (3.4)$$

The resistance of the circuit (for the initial 3msec of the discharge),  $R$  was found by fitting expression (3.4) to the experimental data. The typical value of this resistance was in the 0.029 - 0.031 $\Omega$  range for the nitrogen tests, 0.026 - 0.028 $\Omega$  range for the argon tests, and 0.036 - 0.038 $\Omega$  range for the helium tests, depending on the vacuum chamber pressure (spark gap pressure). Figure 3.1 shows the current  $i(t)$ , the resistor voltage  $VR(t)$ , the coil voltage  $VL(t)$ , the experimental capacitor voltage  $V_{cb}(\text{exp})$ , and the voltage predicted by Equation 3.4  $V_{cb}(t)$ , in the dual coil circuit during a nitrogen discharge at 0.5 Torr.

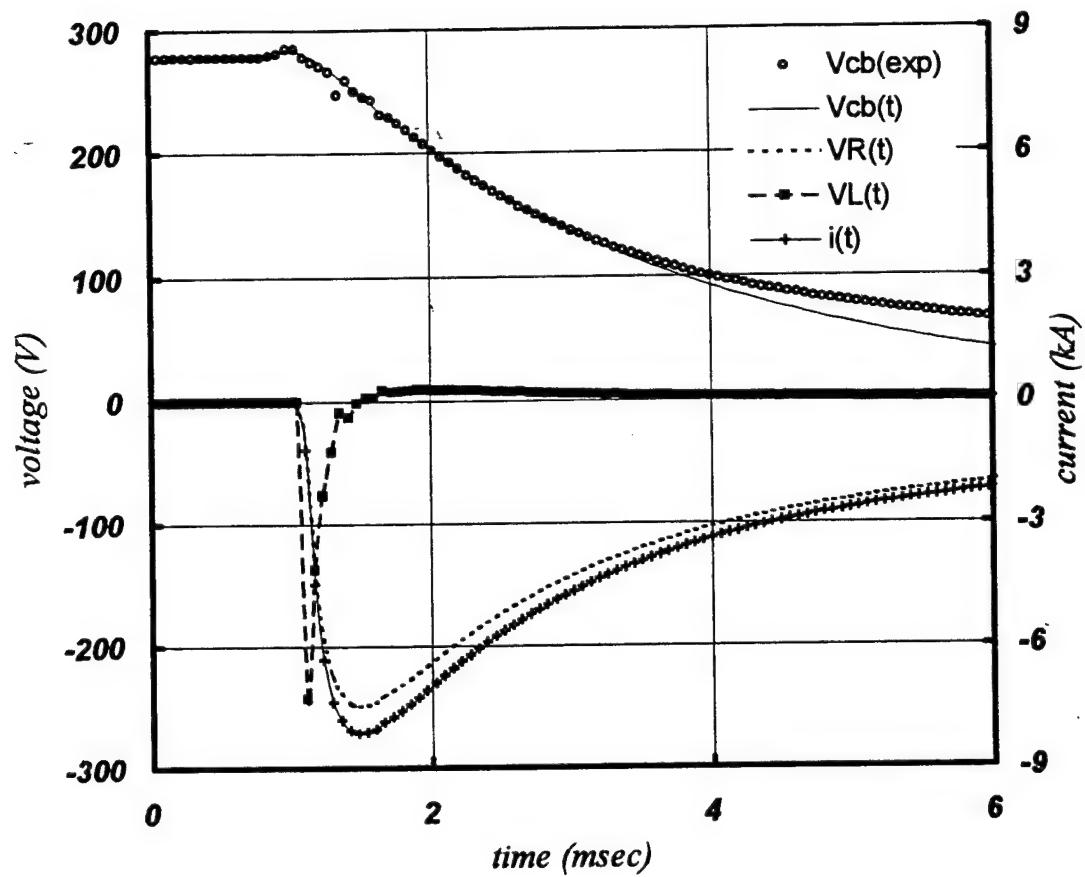


Figure 3.1 Voltages and current in the MDE circuit ( $N_2$ , 0.5Torr,  $R = 0.03\Omega$ .)

It is observed that the theoretical solution (Equation 3.4) approximates well the experimental capacitor voltage drop,  $V_{cb}$  for the initial 3msec of the discharge, thus justifying the constant resistance assumption. As the discharge progresses the spark gap resistance increases and the rate at which  $V_{cb}$  decreases is lower than the rate predicted by Equation 3.4 (i.e.  $V_{cb}(t) < V_{cb}(\text{exp})$ , for  $t > \Delta t$ ), see Figure 3.1.

The conservation of energy in the circuit requires that the rate of change of the stored electric and magnetic energy in the inductance and capacitance is equal to the rate of energy dissipation in the resistance by Joule heating.

$$\frac{L_h}{2} i(t)^2 + \frac{C_{cb}}{2} V_{cb}(t)^2 = R \int i(t)^2 dt \quad (3.5)$$

Equation (3.5) gives the instantaneous power on the coils. In the absence of plasma and any other external dissipation mechanism, the energy consumed during the  $\Delta t$  period of the discharge is equal to the Joule heating

$$E_{\Delta t} = \frac{1}{2} C_{cb} [U_0^2 - (V_{cb}(\Delta t_0))^2] = R \int_{t=0}^{t=\Delta t} i(\tau)^2 d\tau \quad (3.6)$$

In the test shown (see Figure 3.1)  $\Delta t = 2.52\text{msec}$ , the energy spent was  $E_{\Delta t} = 2.89\text{kJ}$  and the heat generated was  $E_h \cong 2.83\text{kJ}$ . The difference (60J) was dissipated by the induced plasma currents. The average discharge power in this test was  $W_{\Delta t} = 1.04\text{MW}$ . The maximum instantaneous power of the magnetic field was achieved immediately after the current onset (0.63MW), and the average power transmitted to the plasma over the entire  $\Delta t$  period was approximately 24kW. Overall, the efficiency of energy transfer from the magnetic field to the plasma,  $(E_{\Delta t} - E_h)/E_{\Delta t}$  was about 2.3%, and is typical for all nitrogen tests. Typical values of the energy conversion efficiency in the argon and helium runs were 3.5% and 1% respectively. The poorer performance of helium is attributed mainly to its low ionization fraction.

## II. MDE Magnetic and Electric Fields

The magnetic field of the coils  $\overline{B}_c$  is related to the discharge current by Ampere's law (Equation 1.3). The current generating this field is spatially limited to the volume occupied by the wires of the coils. Thus, the  $\overline{B}_c$  field must have a zero curl anywhere in the plasma

$$\nabla \times \overline{B}_c = 0 \quad (3.7)$$

The Laplacian of the magnetic field of the coils is given by the following algebraic equation

$$\nabla^2 \overline{B}_c = \nabla(\nabla \cdot \overline{B}_c) - \nabla \times \nabla \times \overline{B}_c \quad (3.8)$$

Combining Equation 3.8 with Equations 1.4 and 3.7 one obtains that the magnetic field of the coils must be potential at all times

$$\nabla^2 \overline{B}_c = 0 \quad (3.9)$$

Thus, the presence of the plasma does not lead to diffusion or dissipation of the magnetic flux of the  $\overline{B}_c$  field, in the manner suggested by Equation 1.5. The situation can be visualized by plotting the  $\overline{B}_c$  vector magnetic field.

Considering each current carrying wire (coil turn) as long compared to the inter-coil distance, the magnetic field (in the median plane xOy) can be calculated as the sum of the individual fields of all turns

$$\overline{B}_c = \left( \sum_{k=1}^{N_c} B_{x_k} \right) \cdot \vec{i} + \left( \sum_{k=1}^{N_c} B_{y_k} \right) \cdot \vec{j} \quad (3.10)$$

The magnitude of the magnetic induction falls off inversely as the first power of the distance from the wire<sup>61</sup>

$$\begin{aligned} B_x(x, y, t) &= \frac{\mu \cdot i(t)}{2\pi \cdot r(x, y)} \cdot \sin(\alpha) \\ B_y(x, y, t) &= \frac{-\mu \cdot i(t)}{2\pi \cdot r(x, y)} \cdot \cos(\alpha) \end{aligned} \quad (3.11)$$



where  $r(x,y)$  is the magnitude of the position vector of the current carrying wire and  $\alpha$  is the angle this vector makes with the x-axis. Topologically the  $\vec{B}_c$  vector field remains unchanged, (regardless of field intensity), see Figure 3.2.

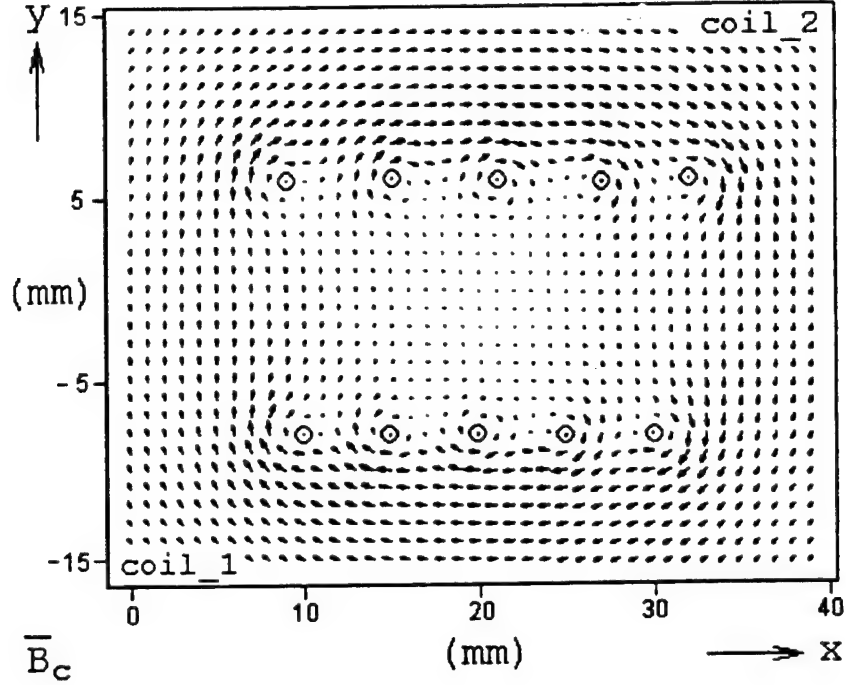


Figure 3.2  $\vec{B}_c$  vector magnetic field in the inter-coil space

The magnetic field in the inter-coil space features a neutral line for each field component (quadrupole field), as illustrated in Figure 3.3. Moreover, Figure 3.3 shows that the spatial field gradients are equal everywhere, except at the wires locations

$$\frac{\partial B_x}{\partial y} = \frac{\partial B_y}{\partial x} \quad (3.12)$$

This condition can be also obtained directly by taking the derivatives  $\partial B_x/\partial y$  and  $\partial B_y/\partial x$  of Equation 3.10, and is the two-dimensional expression of Equation 3.7. Considering also that the

divergence of the field is null, ( $\partial B_x/\partial x + \partial B_y/\partial y = 0$ ) the consequence is that both field components must be potential in the plasma

$$\begin{aligned}\frac{\partial^2 B_x}{\partial x^2} + \frac{\partial^2 B_x}{\partial y^2} &= 0 \\ \frac{\partial^2 B_y}{\partial x^2} + \frac{\partial^2 B_y}{\partial y^2} &= 0\end{aligned}\tag{3.13}$$

and thus non-dissipative.

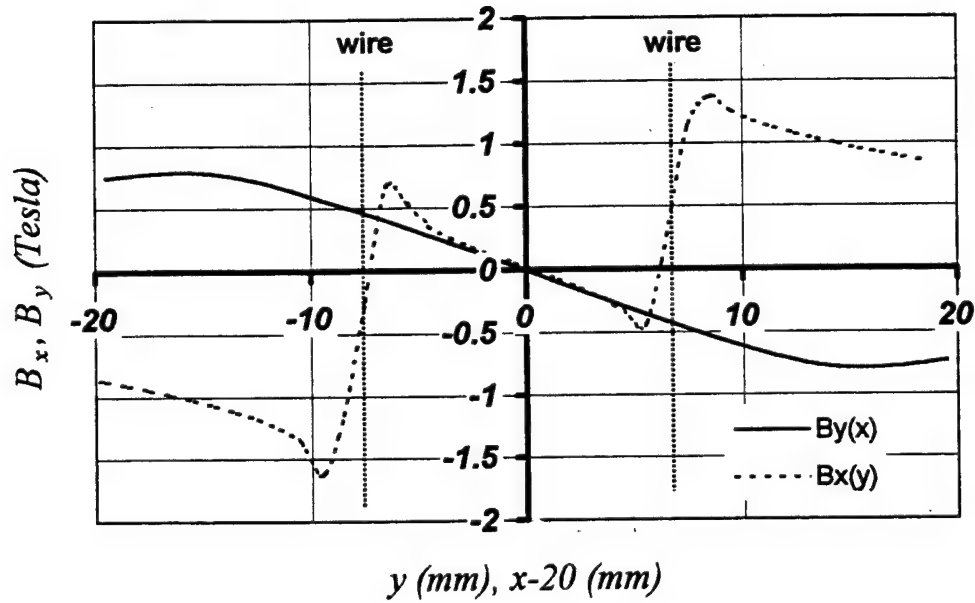


Figure 3.3 Spatial variation of the  $B_x$  and  $B_y$  field components (x axis translated 20mm)

Since  $\bar{B}_c$  is topologically unchanging, the energy transfer from the magnetic field to the plasma must be intermediated by an electric field. This field is generated by the variation of the magnetic field (Faraday's induction law, see Equation 1.2). During the first 50 -100 $\mu$ s from discharge onset the interaction of the weakly ionized TDID plasma with the induced electric field

can be neglected. Hence, the electric field is found by solving Equation 1.2 (here the field has only one component,  $E_z$ )

$$\frac{\partial E_z}{\partial y} = -\frac{\partial B_x}{\partial t}, \quad \frac{\partial E_z}{\partial x} = \frac{\partial B_y}{\partial t} \quad (3.14)$$

The initial conditions are that the electric field of each coil-turn becomes zero at the surface of its corresponding current wire. Integrating Equations 3.14 with the induction values given by Equation 3.10 and applying the initial conditions, the solution obtained is logarithmic

$$E_z(x, y, t) = \sum_{k=1}^{N_c} \left[ \frac{-\mu}{4\pi} \cdot \frac{di(t)}{dt} \ln \left( \frac{(x - a_k)^2 + (y - b_k)^2}{r_0^2} \right) \right] \quad (3.15)$$

where  $(a_k, b_k)$  is the position of each coil turn (wire) and  $r_0$  is the radius of the wires. Figure 3.4 shows the electric field in the inter-coil space for the nitrogen test presented in Figure 3.1.

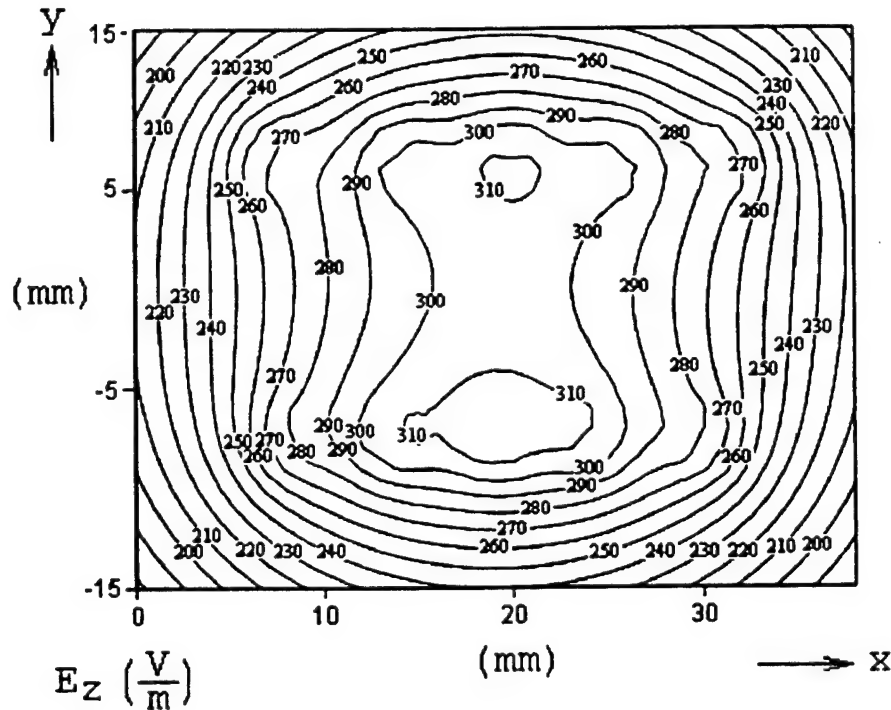
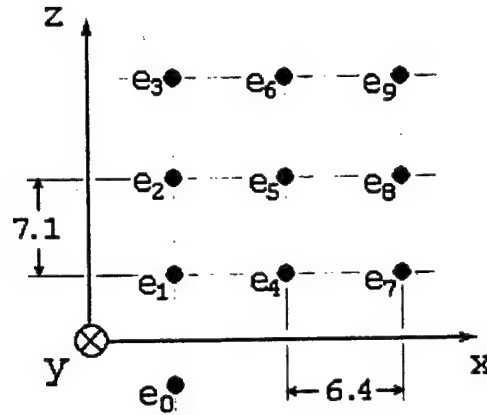


Figure 3.4 Peak electric field  $E_z$  in V/m ( $N_2$ , 0.5Torr,  $R = 0.03\Omega$ ,  $t = 15\mu s$ )

Experimentally, the existence of this field was confirmed by the electric probe data. The spatial positioning of the array of electric probes (see Figure 3.5) enables the calculation of the  $E_z$  electric field along the neutral line,  $x \in (19 - 32)$  mm and  $y = 0$  mm. The vertical separation of the electric probes is  $z = 14.2$  mm.



**Figure 3.5** Arrangement of the electric probes (dimensions in mm)

The variation of the electric field in the plasma at the three  $x$  probe locations  $x_{123}$ ,  $x_{456}$ , and  $x_{789}$  is illustrated in Figure 3.6. It is noticed that when the spark gap is triggered, (at  $t_0$ ) the initial electric field in the plasma (TDID level) changes with the amount  $E_z(t_0)$  as predicted by Equation 3.15. In other words, the initial plasma potential changes at  $t_0$  with the  $E_z(t_0) \cdot z$ . The experimental data shows also that plasma potential remains perturbed for the duration of the discharge and then returns slowly to its initial (TDID) value.

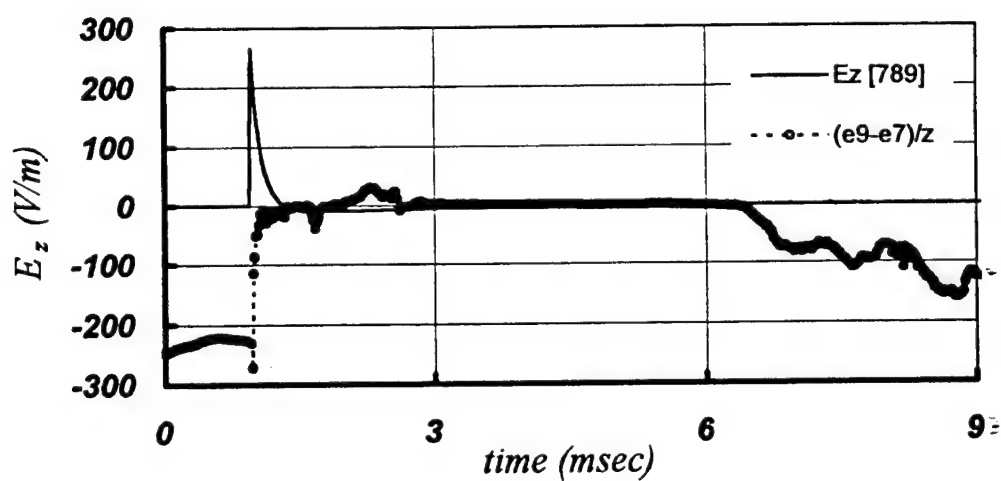
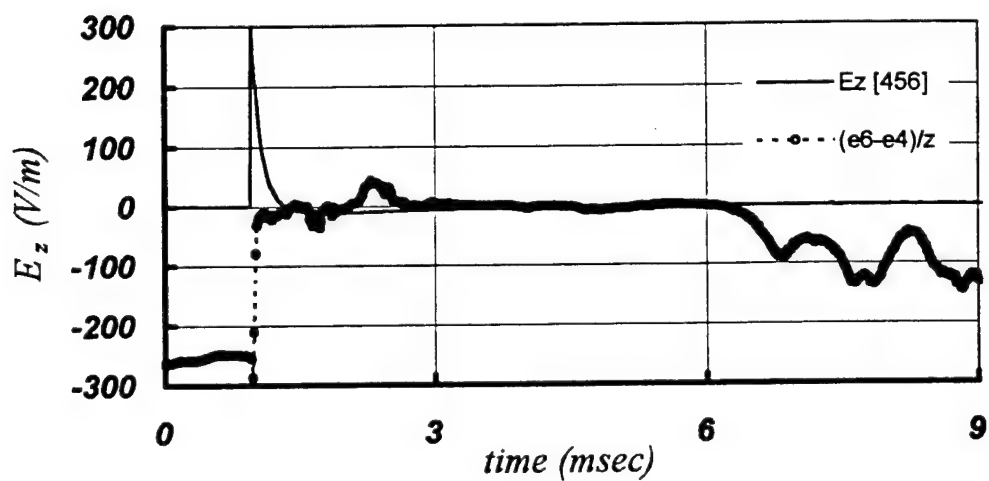
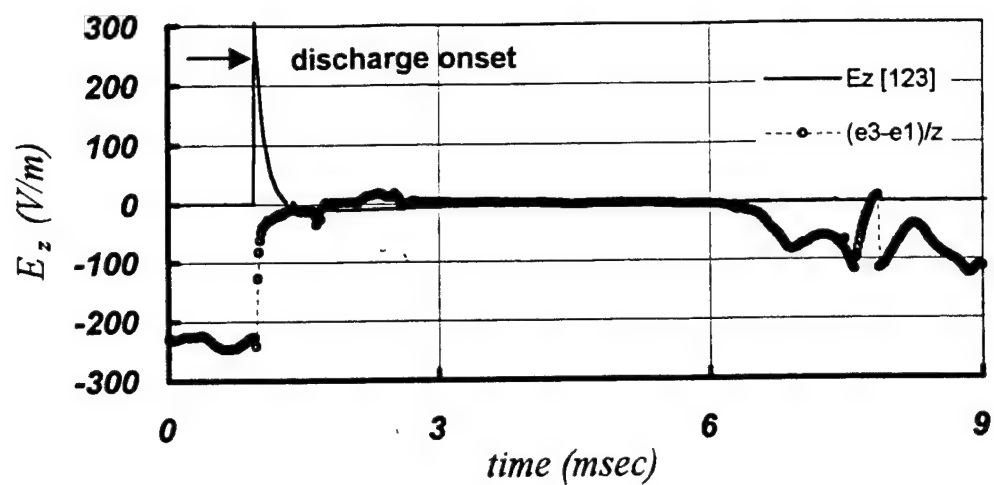


Figure 3.5 Experimental evidence of the  $E_z$  field ( $N_2$ , 0.5Torr,  $W_{\Delta t} = 1\text{MW}$ ,  $P_{\text{TDD}} = 1\text{kW}$ )

There are two facets to the interaction of the  $E_z$  field with the plasma:

(1) Gas Ionization. The electric field is created mainly by the time variation of the vector potential (at least initially)  $-\partial\bar{A}/\partial t$ , ( $\bar{A} = \nabla \times \bar{B}$ ), and to a less extent by the space charge contributions  $-\nabla\phi$ . Although these two field components are coupled to the plasma dynamics in different ways<sup>10</sup>, the effect of  $-\partial\bar{A}/\partial t$  in this instance is to create spatial gradients of the plasma potential. The variation of the plasma potential can be calculated by integrating the electric field over the coil space

$$E_z = -\left(\frac{\partial\phi}{\partial x} + \frac{\partial\phi}{\partial y}\right) \quad (3.16)$$

For simplicity, the integration of (3.16) is done only in the y direction and the boundary condition is chosen such that the potential at the centerline is null,  $\phi(x, 0) = 0V$ . The integration was performed for three different moments from the current onset ( $t_0 = 0\mu s$ ,  $t_1 = 15.38\mu s$ ,  $t_2 = 30.76\mu s$ ) and the results are presented in Figure 3.7.

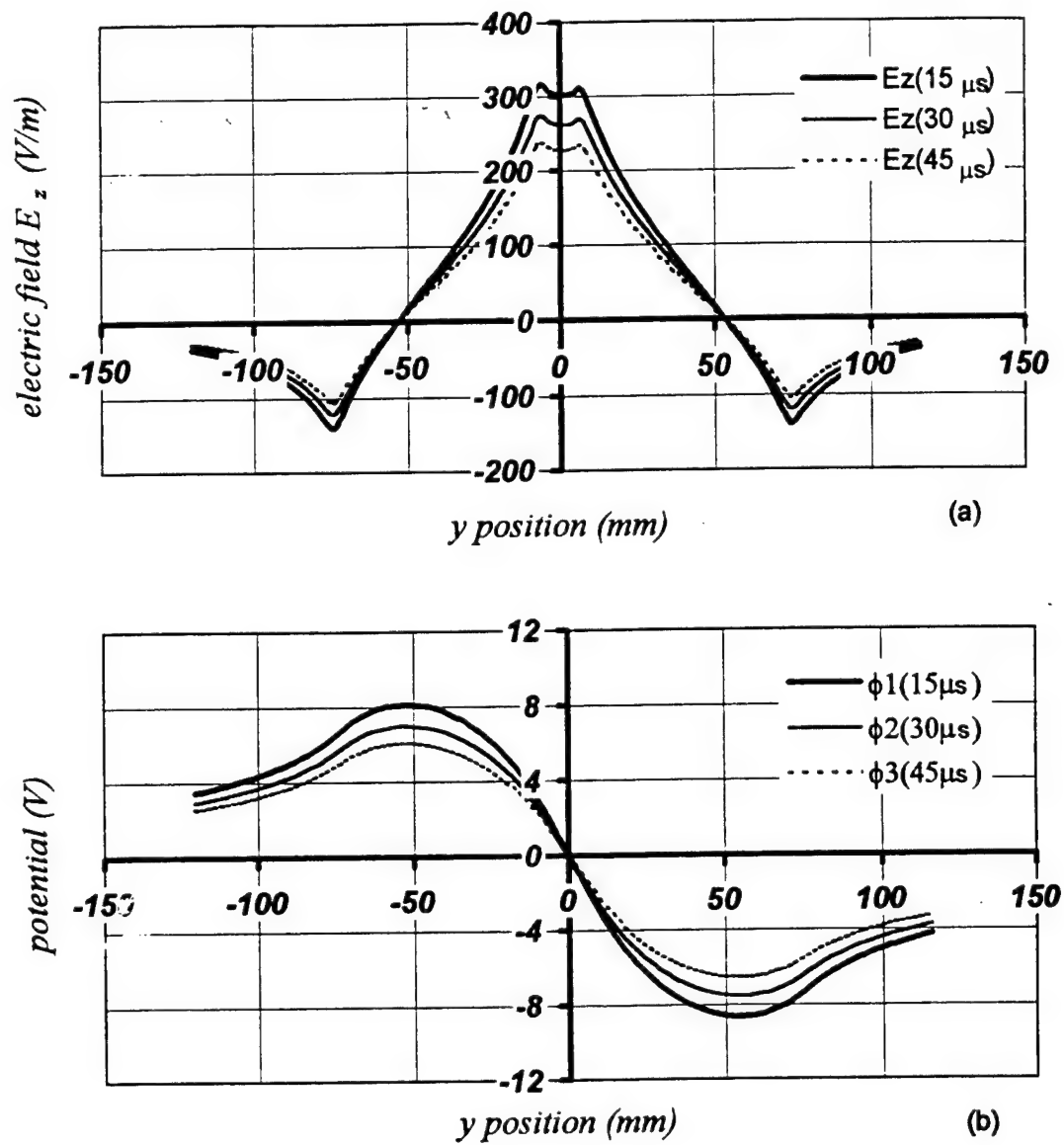


Figure 3.7 Time change of the  $E_z$  electric field (a) and double layer potential (b) ( $N_2$ , 0.5 Torr, time step  $\Delta t = 1/f_s = 15.38 \mu s$ )

The potential curves show the characteristics of a double layer. The largest potential difference in the test shown ( $N_2$ , 0.5Torr, same as in Figure 3.1) is approximately 17V and the maximum and minimum values are located roughly at the center of the two coils. The immediate conclusions are that the electric field is large enough to produce extra ionization of both argon (ionization potential 15.75V) and nitrogen (ionization potential 14.53V), and the double layer lasts long enough ( $30 - 45\mu s \gg \tau_{\text{collisions}} \cong 0.3\text{nsec}$ ) to effectively energize the plasma particles.

(2) Generation of Plasma Currents. If the inter-coil space is filled with plasma of finite, nonzero conductivity the electric field generates a current according to generalized Ohm's law (see Equation 1.1). This current,  $\bar{j}_p$  according to Ampere's law must create a local (plasma) magnetic field  $\bar{b}$

$$\bar{j}_p = \frac{1}{\mu} \cdot \nabla \times \bar{b} \quad (3.17)$$

The total magnetic field,  $\bar{B}$  is the sum of the field produced by the coils,  $\bar{B}_c$  and the locally induced magnetic field  $\bar{b}$ . Thus, the induced current provides the necessary mechanism for transferring the magnetic energy from the coil to the plasma. In effect the energy transfer is accomplished much like in the case of a transformer having the coil as a primary and the plasma current as the secondary winding. In this situation, the topology of the total magnetic field may change only because of the plasma-induced magnetic field (effectively because of the changes in  $j_p$ ).

The variation of the  $B_x$  component of the total magnetic field was traced by the magnetic probes (see Equation 2.1). Generally, the numerical integration of the signals from the probes must be performed with an explicit, forward in time routine since the only initial condition available is  $B_x(t_0 = 0s) = 0T$ . However, this method performs poorly when the voltage measured by the probe is corrupted by electrical noise. Figure 3.8 shows that the voltages of the probes become noisier as the test progresses and  $dB_x/dt$  decreases (i.e. the signal to noise ratio decreases)



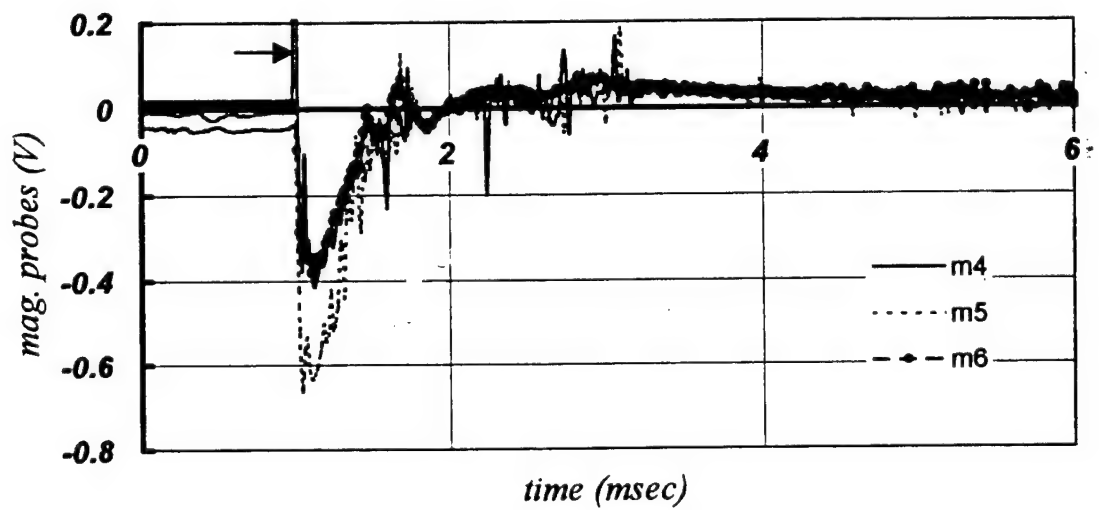
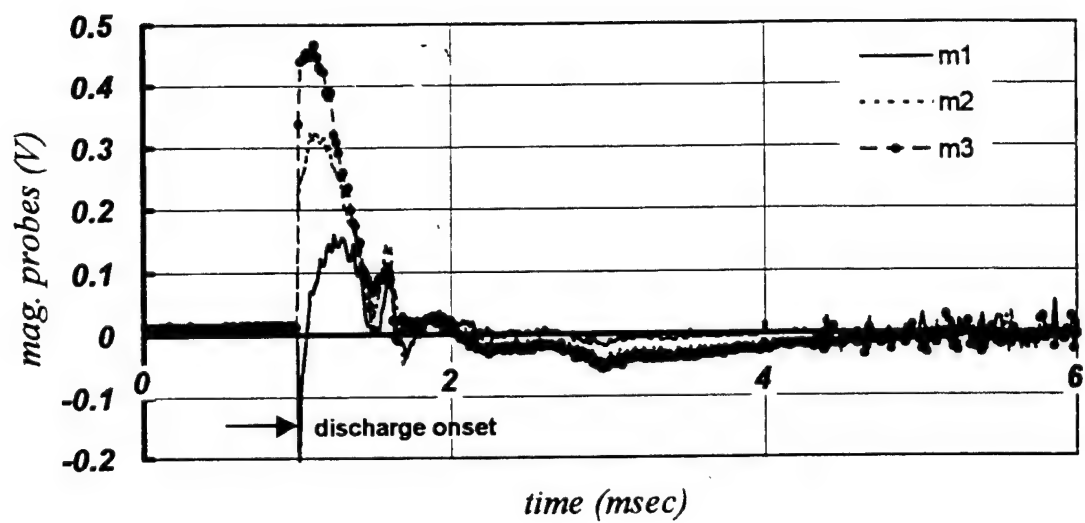


Figure 3.8 Magnetic probes voltages ( $N_2$ , 0.5Torr, probes config. I)

Practically, after 2-3msec from discharge onset the signals recorded by the probes have the same magnitude as the noise.

To alleviate the problem, the voltages of the probes were integrated numerically using an implicit method. The approach involves the differentiation of Equation 2.1

$$\frac{dV}{dt} = N_c A_c \frac{d^2 B_x}{dt^2} \quad (3.18)$$

and requires an additional boundary condition at the end of the test. The differentiation in Equation 3.18 removes any constant voltage (dc bias) that may be added to the signals by the data acquisition, and the implicit (centered in time) numerical routine averages out the random noise component of  $dV/dt$ . The end boundary condition,  $B(t > t_{\text{end}}) = 0T$  is found by noting that the current in the circuit stops abruptly (step function) when the spark-gap breakdown can no longer be maintained. Thus, at  $t_{\text{end}}$  the voltage on the coil  $L_A(di/dt)$  is necessarily a jump (delta function), which is recorded by the data acquisition as a spike of the capacitor voltage, see Figure 3.9.

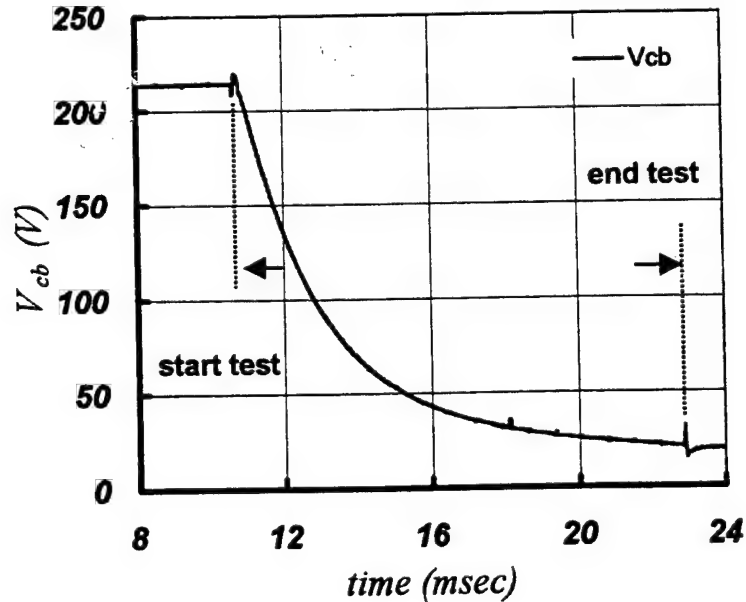


Figure 3.9 Test duration from  $V_{cb}$  data (Ar, 0.4Torr)

A no plasma test ( $N_2$ , 0.5 Torr,  $j_p \approx 0$ ), see Figure 3.10, shows the expected distribution of the  $B_x$  field component at probes locations along the x-axis, and was used for the calibration of the magnetic probes. The calibration is simply done by comparing the highest/lowest measured field values (in the test chosen) with the maximum/minimum values in Figure 3.10. The two probe arrays have, as expected, the same calibration constant despite the slight asymmetry of the dual-coil device.

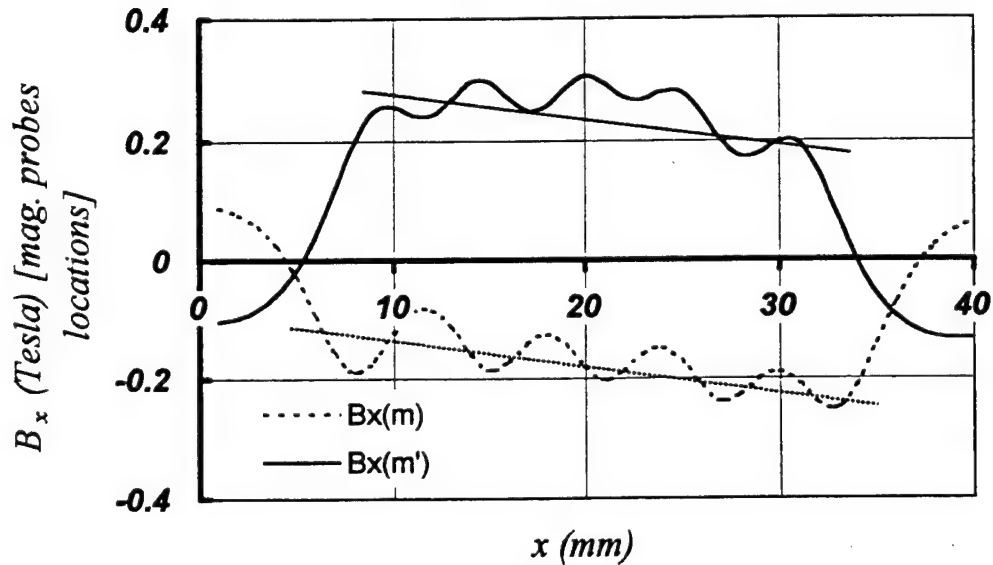


Figure 3.10  $B_x$  magnetic field values at ( $\pm y$ ) magnetic probes locations

Figure 3.11 illustrates the  $B_x$  component of the (total) magnetic field in the inter-coil space. The magnetic induction levels measured by the magnetic probes show agreement with the trend illustrated in Figure 3.10. The time differential between shots is  $390\mu s$ . The slight change of the topology is evidence of the local magnetic field, and implicitly of the induced plasma current. Unfortunately, the large size of these probes with respect to the device size did not permit measurements of the  $B_y$  field component and a more detailed survey of the magnetic field.

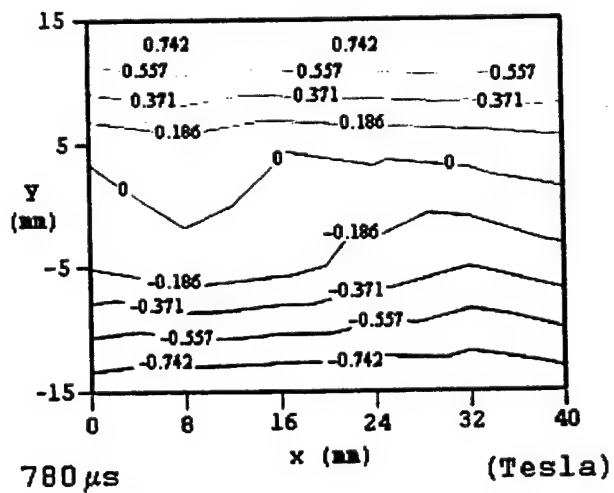
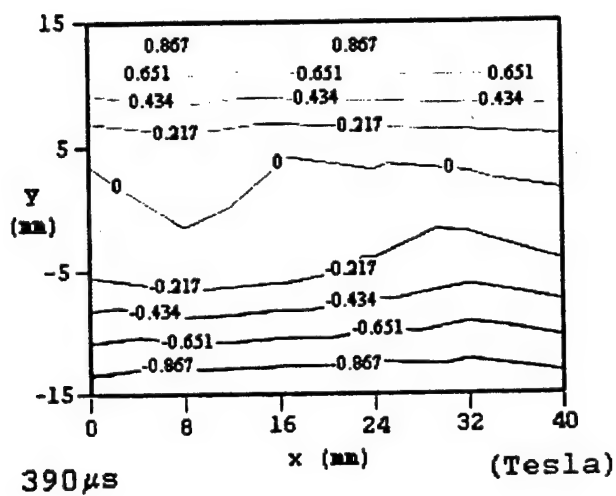
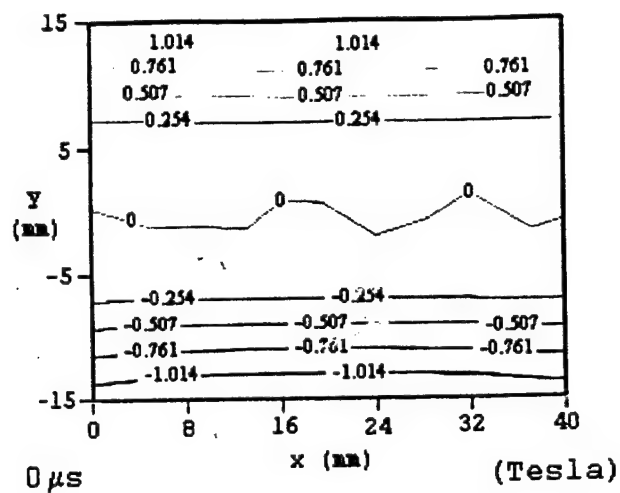


Figure 3.11 Time history of  $B_x$  from magnetic probe data ( $N_2$ , 0.5 Torr, probes config. II)

### III. Plasma Conductivity

The efficiency of the energy transfer from the magnetic field to the plasma is primarily determined by the conductivity of the plasma. Electrical conductivity of weakly ionized plasmas<sup>60</sup> is a function of the ionization fraction,  $n_e$  (electron density), electron-neutrals collision cross-section, and electron temperature,  $T_e$

$$\sigma = \frac{n_e \cdot e^2}{m_e \cdot c_e} \left[ \frac{1}{n_n Q_{en} + \frac{\pi^3 \ln \Lambda}{16} \left( \frac{e^2}{4\pi\epsilon_0} \right)^2 \frac{n_i}{(k_b T_e)^2}} \right] \quad (3.19)$$

where  $c_e = (8k_b T_e / \pi m_e)^{1/2}$  is the electron mean thermal speed,  $n_n$  is the density of neutral particles,  $Q_{en} \sim 10^{-15} \text{cm}^2$  is the electron-neutrals collision cross-section,  $\ln \Lambda \cong 10$  is a small angle collision effect<sup>56</sup> and the rest of the symbols have their usual meaning:  $e$  electron charge,  $m_e$  electron mass,  $n_i$  ion density, and  $k_b$  Boltzman's constant.

Prior to the capacitor bank discharge the inter-coils space is filled with the TDID plasma plume. The TDID plasma is field free and therefore quasi-neutral  $n_i = n_e$ . For a nitrogen plume at an average TDID power of 1kW the electron density is in the  $10^{17} \text{m}^{-3}$  range and the electron temperature 0.7-0.9eV (see Appendix A). With these values, Equation 3.19 yields conductivity values of approximately  $4\text{-}20 \Omega^{-1} \text{m}^{-1}$ . The same procedure applied to the argon plasma ( $n_e \sim 10^{18} \text{m}^{-3}$ ,  $T_e \sim 0.3\text{-}0.4 \text{eV}$ ) yields a conductivity of approximately  $45\text{-}60 \Omega^{-1} \text{m}^{-1}$ . As noted in the previous subsection, further ionization of the gas takes place during the discharge. The effect of the larger ionization fraction is an increase of plasma conductivity, and is measured by the conductivity probes (see Figures 2.7 – 2.10). For a certain electron temperature, the highest plasma conductivity<sup>56, 60</sup> (the Spitzer conductivity) for a singly ionized gas is

$$\sigma(T_e) = \frac{(4\pi\epsilon_0)^2 \cdot (k_b T_e)^{3/2}}{\pi \cdot e^2 m_e^{1/2} \cdot \ln \Lambda} \quad (3.20)$$

The TDID and Spitzer conductivity are the lower and upper bounds of the plasma conductivity in the MDE tests.

The actual variation of plasma conductivity is obtained by analyzing the signals from the conductivity probes. Consider the conductivity probe circuit sketched in Figure 2.6.c. The voltage drop on the resistor,  $U_p$  is given by Ohm's law

$$U_p = I \cdot R_v \quad (3.21)$$

where  $I$  is the current in the probe circuit. The current density at the probe surface is inversely proportional to the active area of the probe  $A_p$

$$j = \frac{I}{A_p} \quad (3.22)$$

The generalized Ohm's law (Equation 1.1) written for the plasma portion of the conductivity probe circuit is

$$j = \sigma E \quad (3.23)$$

Here the  $\sigma(\bar{v} \times \bar{B})$  current component can be neglected since the conductivity probes are mounted on the  $B_x$  magnetic neutral line ( $B_x = 0$ ) and  $\bar{v} \times \bar{B}_y \cong 0$ . The electric field,  $E$  is created between the probe and the MDE device ground by the potential difference  $U_v$  of the 12/24V battery, see Figure 2.6.c. Thus the average electric field produced at the tip of the probe is

$$E = \frac{U_v - U_p}{d_{avg}} \quad (3.24)$$

where  $d_{avg}$  is some average distance from the probe to plasma ground. Eliminating the current density between Equations 3.22 and 3.23 and using Equations 3.21 and 3.24 the conductivity is

$$\sigma = \frac{U_p}{U_v - U_p} \cdot \left( \frac{1}{R_v} \right) \cdot \left( \frac{d_{avg}}{A_p} \right) \quad (3.25)$$

Equation 3.25 relates plasma conductivity to the voltage measured by the probe.

Rough estimates of the distance,  $d_{avg}$  and probe area,  $A_p$  can be obtained from geometrical considerations. The complex geometry of the MDE device makes this evaluation difficult and the values obtained questionable. However, a better estimate of the  $(d_{avg}/A_p)$  ratio can be obtained from known conductivity values at the beginning of the complete tests. This approach involves (a) the calculation of the electron density,  $n_e$  and temperature,  $T_e$  as functions of the TDID power (see Appendix A) and (b) the use of  $n_e$ ,  $T_e$  and Equation 3.19 to estimate plasma conductivity. It is noted that the method has the disadvantage of not being able to provide the individual  $(d_{avg}/A_p)$  values for each probe. Consequently, the conductivity value at the location of each probe is somewhat averaged. The results of the conductivity analysis are presented next starting with a nitrogen test.

The TDID plasma was the most stable in the pre-discharge phase of the nitrogen tests, and thus, these tests are the best suited for the estimation of the average  $(d_{avg}/A_p)$  ratio of the probes. The test chosen to illustrate the conductivity analysis is a 0.6Torr nitrogen test run with  $W_{\Delta t} = 1\text{MW}$ , see Figure 3.12. The TDID power level is 1.22kW ( $V_{TDID} = 943\text{V}$ ,  $I_{TDID} = 1.3\text{A}$ ) and the corresponding electron density and temperature levels in the plume are  $n_e \cong 5 \cdot 10^{17}\text{m}^{-3}$  and  $T_e \cong 0.7\text{eV}$ . The highest pre-discharge voltage level recorded by the conductivity probes is 1.35mV and corresponds to a conductivity level of  $16\Omega^{-1}\text{m}^{-1}$ . The resultant  $(d_{avg}/A_p)$  ratio is  $5.68 \cdot 10^5 \text{ m}^{-1}$ . The analysis of the other nitrogen tests showed that this is a good estimate of the  $(d_{avg}/A_p)$  ratio in both probe configurations. The maximum conductivity in the test shown is  $590\Omega^{-1}\text{m}^{-1}$ , and is reached at the location of probe  $v_2$ , see Figure 3.12. Assuming for now (an argument will be provided later in this subsection) that the electric field heats the electrons to about the same levels as the TDID ( $T_e \sim 1\text{-}1.5\text{eV}$ ), the Spitzer conductivity of the nitrogen plasma is approximately  $1000\text{-}2000\Omega^{-1}\text{m}^{-1}$ .

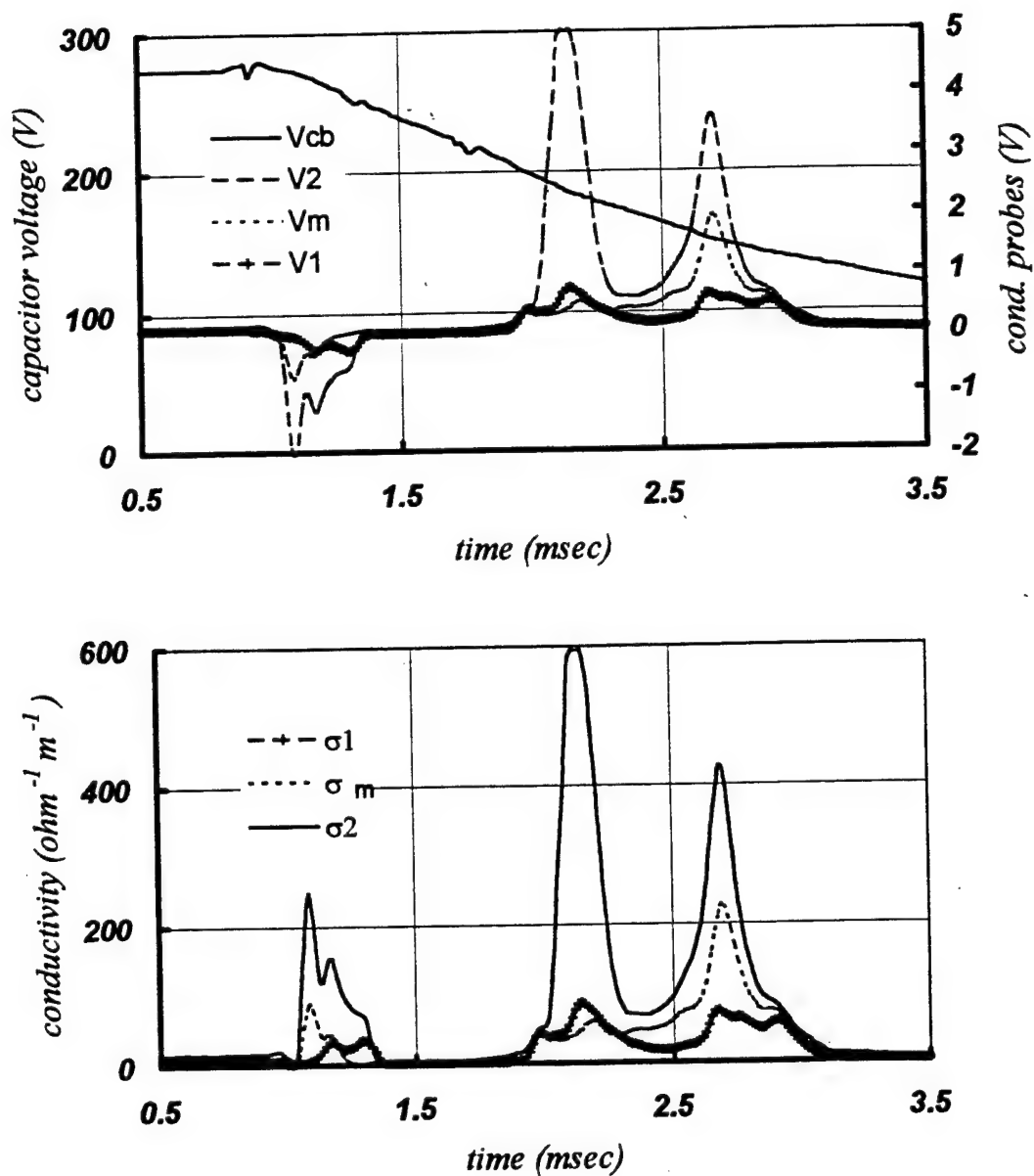


Figure 3.12 Plasma conductivity ( $\text{N}_2$ , 0.6Torr,  $W_{\Delta t} = 1\text{MW}$ ,  $U_v = 24\text{V}$ ,  $R_v = 2\Omega$ , sampling rate 78kHz,  $P_{\text{TDD}} = 1.22\text{kW}$ , probes config. II)



Equation 3.19 shows that an average conductivity of  $500\Omega^{-1}\text{m}^{-1}$  in nitrogen with electron temperature of 1-1.5eV necessitates an electron density of approximately  $(2.2 - 2.5)\times 10^{19}\text{m}^{-3}$ . The discharge had increased the ionization fraction of the plasma ( $n_e/n_n$ ) by two orders of magnitude from 0.002% to 0.2%. In terms of plasma conductivity the MDE coils transfer to the nitrogen plasma an average of 25kW for 3msec, and increase its conductivity 30-35 times over the TDID level.

Similar results were noted in the argon tests. A 0.3Torr test was chosen to illustrate the conductivity increase in argon, see Figure 3.13. It is observed that at a third of the TDID power input the argon plasma has an ionization fraction about one order of magnitude higher than the nitrogen plasma. However, the electron temperature in the TDID argon plasma is lower 0.3-0.4eV. Figure 3.13 shows that conductivity levels in excess of  $600\Omega^{-1}\text{m}^{-1}$  are attainable at half-megawatt discharge power levels. The electron temperature in the argon plasma is increased by the discharge (at least temporarily) to similar levels as in the nitrogen plasma, and the ionization fraction of argon is increased about one order of magnitude to 0.4%.

The most remarkable behavior is noted in the helium tests. As noted previously, the strong ionization of the nitrogen and argon TDID plasma is attributed to the double layer potential. The largest potential difference in the double layer is 17-18V and depends on the initial capacitor voltage. Thus, the double layer potential was not expected to produce helium ionization since the first ionization potential for helium is 24.58eV. Figure 3.14 shows a puzzling jump in helium conductivity, despite the insufficient potential difference of the double layer.

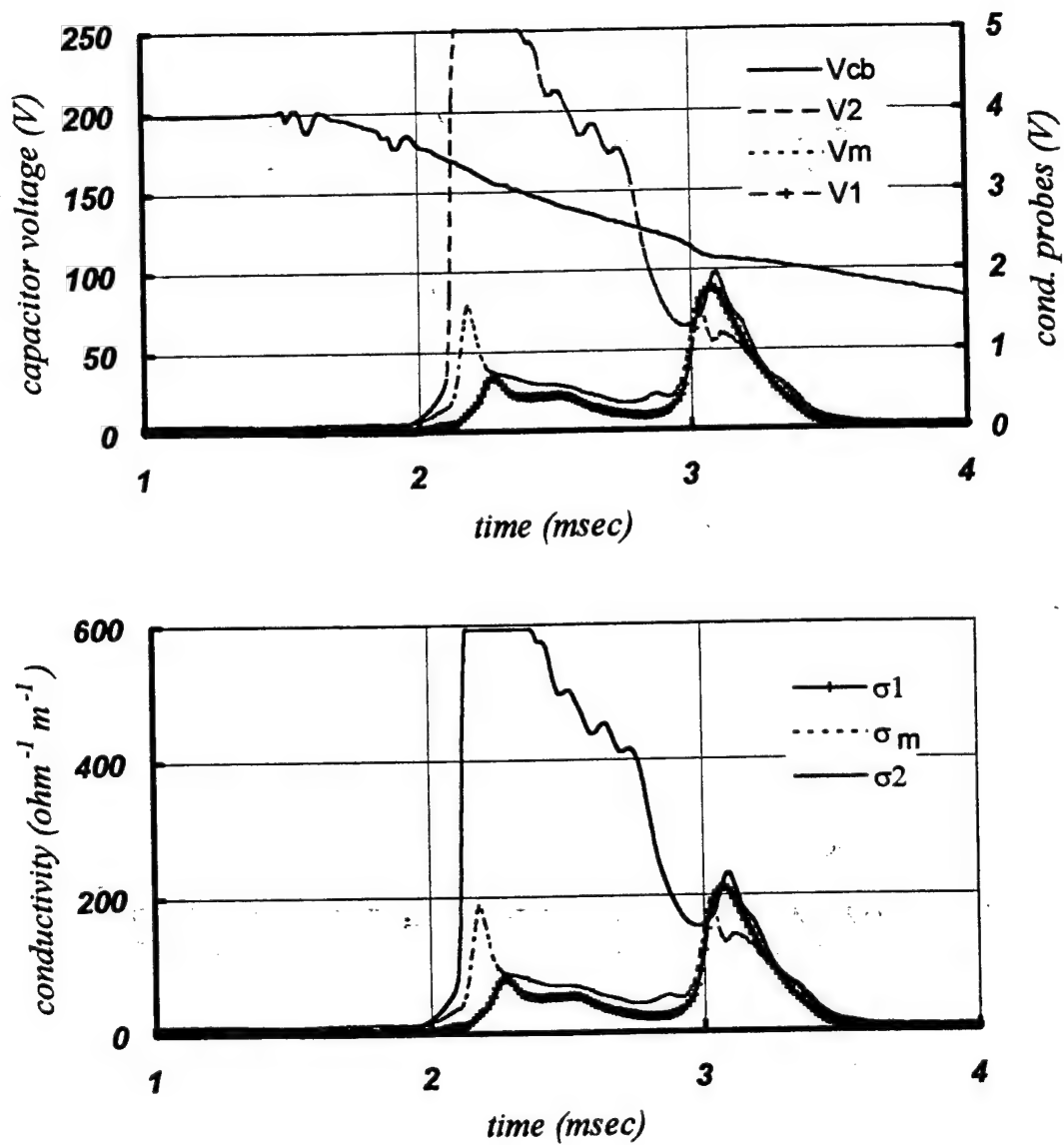


Figure 3.13 Plasma conductivity (Ar, 0.3Torr,  $W_{\Delta t} = 0.57\text{MW}$ ,  $U_v = 24\text{V}$ ,  $R_v = 2\Omega$ , sampling rate 78kHz,  $P_{\text{TDD}} = 0.44\text{kW}$ , probes config. II)

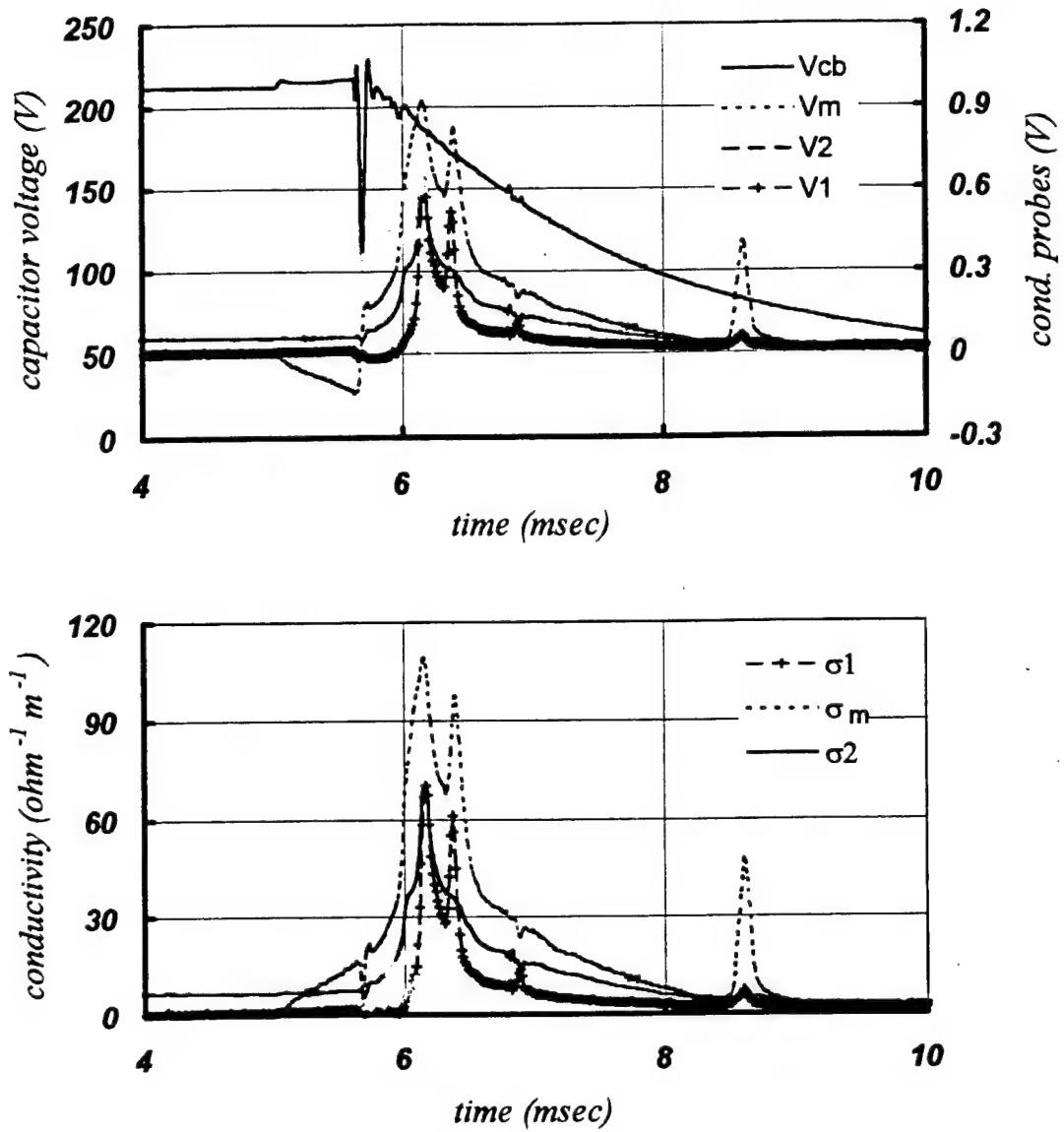


Figure 3.14 Plasma conductivity (He, 0.5 Torr,  $W_{\Delta t} = 0.65 \text{ MW}$ ,  $U_v = 24 \text{ V}$ ,  $R_v = 2 \Omega$ , sampling rate 78 kHz,  $P_{\text{TID}} = 0.7 \text{ kW}$ , probes config. II)

The clues for resolving the apparent paradox of helium ionization lie with the no plasma tests. Figure 3.15 shows maximum conductivity levels attained in three no plasma tests ( $P_{TDID} = 0W$ ) performed in argon, nitrogen and helium. These tests were run at a pressure of 0.3Torr and initial capacitor voltage in the range 210-270V. The nitrogen and argon tests show conductivity levels three to seven times greater than the helium tests. The explanation is that the double layer potential difference is sufficiently large to partially ionize the nitrogen and argon atoms, but not the helium atoms. However, a certain amount of ionization is produced in all gases due to the energization of the few free electrons (for instance electrons produced by cosmic rays) which must be present in the low-pressure gas. These electrons gain enough energy to ionize some of the neutral particles of the gas and free some other bound electrons. The net result is a small but finite conductivity, even in helium.

During a complete helium test, the TDID plasma contains a much larger number of free electrons (approx.  $10^{15} \text{ m}^{-3}$ ), at an average temperature<sup>58</sup> of 4-5eV. The double layer potential energizes the free electrons by increasing their temperature with the potential difference. Thus, the average temperature of the electrons in the helium plasma is increased to 21-22eV. Clearly, "hotter" electrons in the high-end tail of the energy distribution ( $T_e > 24.58\text{eV}$ ) are capable of producing additional ionization of neutral helium atoms.

The situation is somewhat similar in nitrogen and argon, with the exception that at discharge onset these gases are already ionized by the TDID to  $10^{17} - 10^{18} \text{ m}^{-3}$ . The initial temperature of the free electrons is 0.8 - 1eV in nitrogen and 0.3-0.4eV in argon. Once the discharge is triggered, the double layer energizes the electrons to average temperature of 17-18eV thus enabling bulk ionization of the gas. However, at an average collision time of 0.3nsec the electrons may undergo several thousand collisions in the first millisecond of the discharge alone and thus thermalize quickly to TDID temperature levels (1-1.5eV in nitrogen and 0.4-0.6eV in argon). This argument justifies the temperature assumption made previously in the calculation of the Spitzer conductivity.

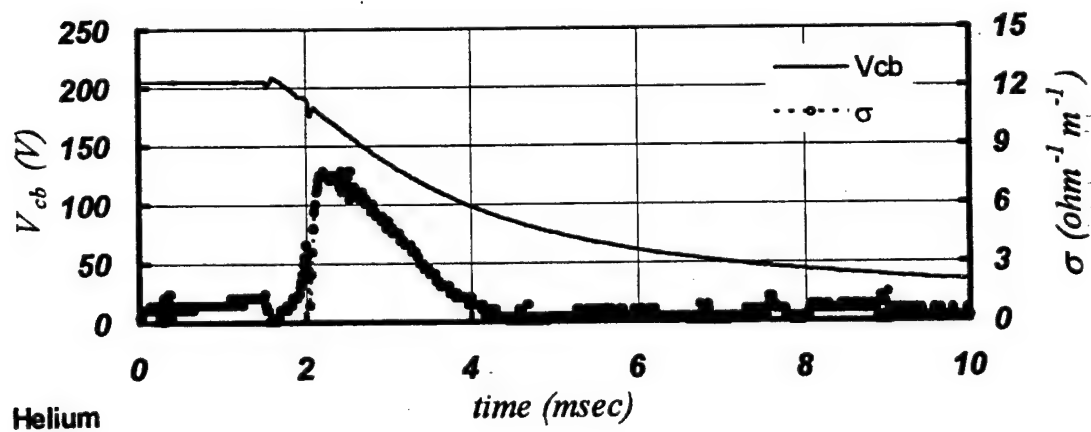
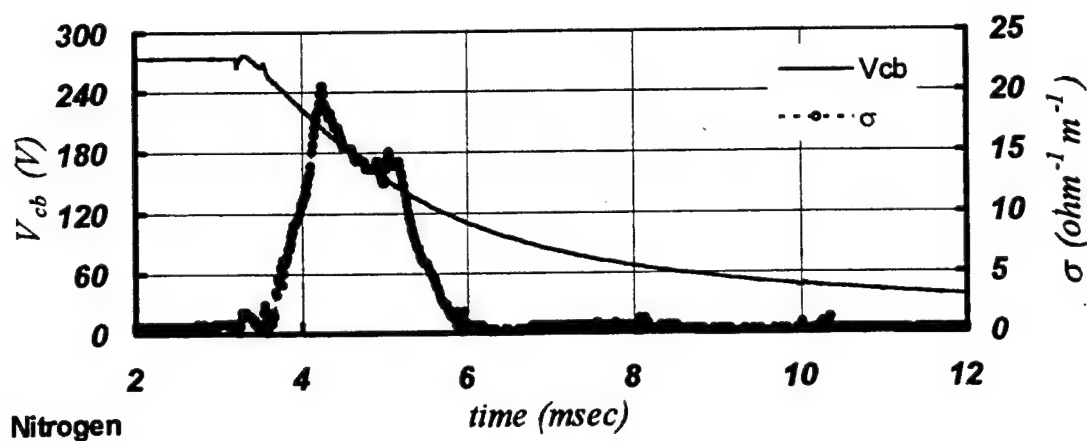
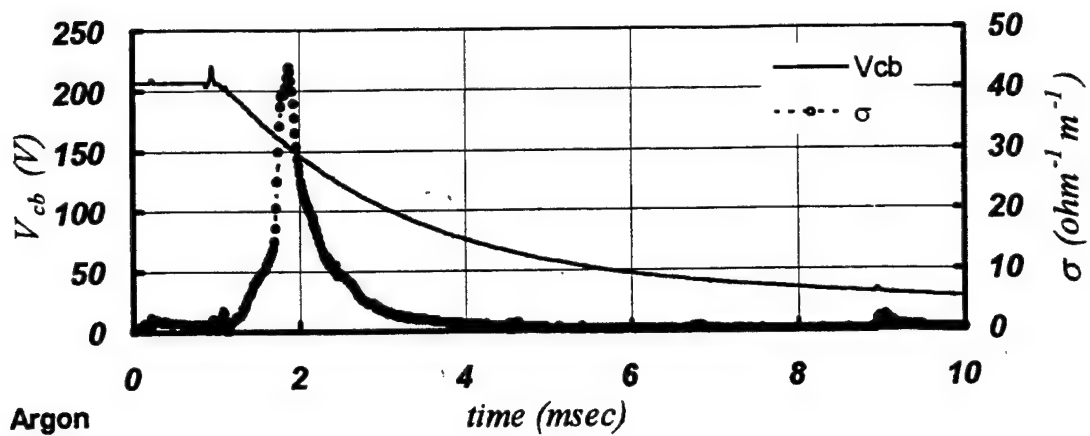


Figure 3.15 Gas conductivity (Ar, N<sub>2</sub>, He, 0.3Torr, no plasma tests  $P_{TDD} = 0W$ )

#### IV. Ion Acoustic Waves and Bulk Plasma Motion

The Denver model suggests that plasma outflow from the magnetic neutral region is proportional to the local magnetic Reynolds number (Equation 1.16)

$$u_2 \sim v_A (1 - \beta) \cdot \text{Re}_m \quad (3.26)$$

The only condition necessary for the derivation of Equation 3.26 is that ionized plasma particles act like a fluid. This is equivalent to imposing that (a) there is a large number of ionized particles which respond to the rapid change in the magnetic field, and (b) meaningful bulk properties (pressure, density) can be defined for the ionized particles. The TDID plasma at the beginning of the MDE tests is weakly ionized (about 0.002% ionization fraction) and thus few particles interact with the magnetic field. In this case, the quantities in Equation 3.26 cannot be defined, and a kinetic treatment of the plasma motion is appropriate.

Consider the ionized particles (electrons or ions) located in the inter-coil space or near it. Once the magnetic field starts to rise, the particles are accelerated by the induced electric field. The motion is in the same direction for both electrons and ions and is given by their corresponding momentum equations

$$m_{e,i} \frac{d\bar{v}_{e,i}}{dt} = \mp e \cdot (\bar{E} + \bar{v}_{e,i} \times \bar{B}) + m_{e,i} (\bar{v}_{e,i} - \bar{v}_n) \nu_{en,in} \quad (3.27)$$

Here the indices  $e, i, n$  stand for electrons, ions, and neutrals, and  $\nu_{en}, \nu_{in}$  are the collision frequencies of electron neutrals and ion neutrals respectively. It is noted that due to the small number of ionized particles the thermodynamic pressure terms in the right hand side of Equation 3.27 were ignored ( $-\nabla p_{e,i} = 0$ ). In principle, analytic solutions  $\bar{v}_{e,i}$  of these equations could be found by introducing the current and field quantities in Equations 3.3, 3.10, and 3.15 and some average collision frequencies<sup>60</sup>. However, for the purpose of this discussion it is sufficient to notice that particles experience some complex  $\bar{E} \times \bar{B}$  drift in spatially and time varying fields. The directions of motion are sketched in Figure 3.16. Ionized particles that are pushed out of the

inter-coil space are trapped by the slowly varying magnetic field and will continue to drift, and accelerate along field lines with  $\bar{v} \parallel \bar{B}$  (betatron acceleration).

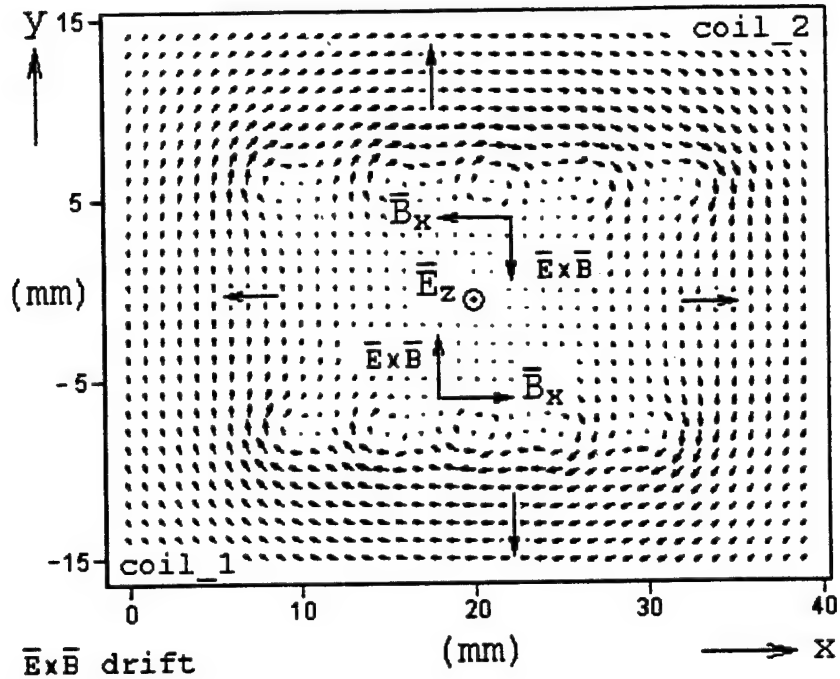


Figure 3.16  $\bar{E} \times \bar{B}$  drift

A simple, order of magnitude calculation of the electric drift ( $E_z/B_x$ ) shows that the initial particle drift velocities are in excess of 1km/sec. Considering the much larger time scale of the discharge, the surge in ionized particle velocity at the onset of the test can be described as a magneto-kinetic shock. The energy gained by the particles is then quickly lost in the first microseconds of the discharge by collisions with neutral particles. The result is that the initial magnetic shock is damped to weak plasma oscillations (i.e. waves).

A theoretical study of the problem of wave generation by an induction coil of finite length was presented by Stix<sup>62</sup> and involves a Bessel-function solution of the dispersion equation.

The study showed that (a) plasma waves are generated, and (b) they propagate and exit the induction coil along the magnetic field lines.

Wave generation is most efficient if the axial frequency of the coil is matched by the frequency of one of the oscillation modes of the plasma system. This condition is the equivalent of impedance matching for resonant RLC circuits, and is referred to as coupling resonance. Based on these arguments it is concluded that the dual coil will favor the particular plasma frequency that match its own impedance. Additionally, lower amplitude harmonics of the basic plasma frequency may be observed. Assuming that the dual-coil behaves as a classic quarter-wavelength resonator, the basic frequency of plasma oscillations is

$$f_p = \frac{v_w}{\lambda_c} \quad (3.27)$$

where  $v_w$  is the wave velocity, and  $\lambda_c = 4 \cdot L_{\text{coil\_wire}}$  is the coil wavelength. The total length of the coil wires is approximately  $16\pi R_w = 1.74\text{m}$  (see Figure 2.2).

Experimentally, the wave dissipation in the MDE plasma was detected by the conductivity probes. The detection of plasma wave motion by a conductivity probe can be explained in terms of conductivity changes at probe location. Waves and plasma motion in general, set up fluctuations in local plasma density and temperature, thus influencing plasma conductivity. In the external circuit of the probe, these fluctuations were recorded as variations in the probe current. Due to speed limitation, the conductivity probes were able to trace all plasma waves of frequencies below half the scanning frequency. Effectively, the probes were able to pick up all low frequency (ion) waves in the acoustic range (up to 32-41kHz).

The probe signals were converted to the frequency domain by Fourier analysis. The results are the power spectra of the signals, see Figure 3.17. The tests shown are at different pressures and best exemplify the waves produced in argon, nitrogen and helium.



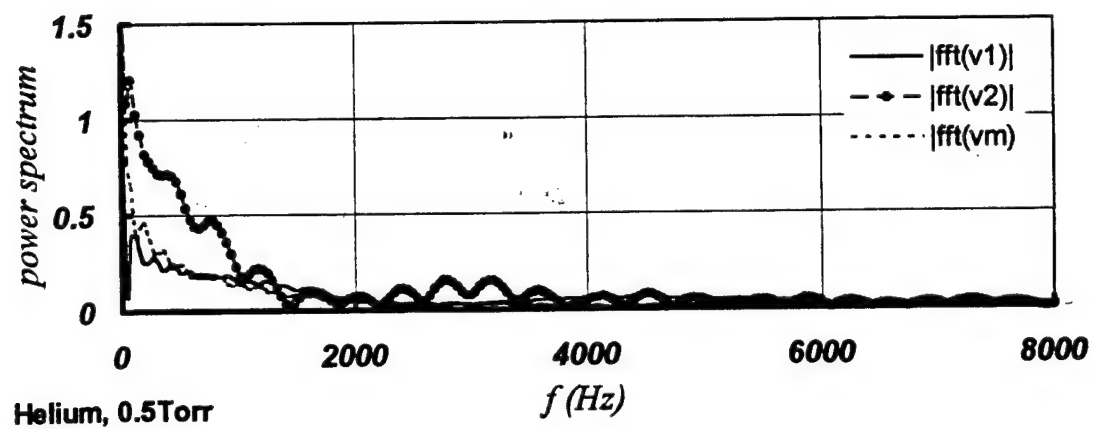
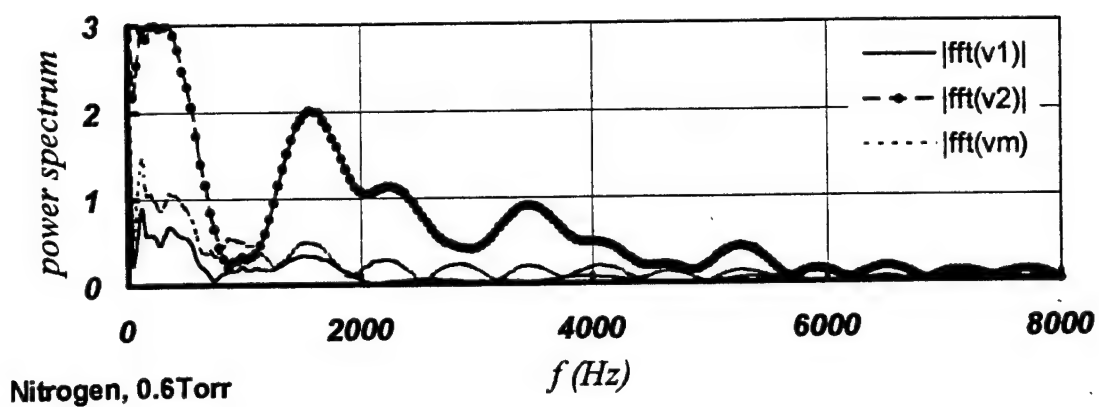
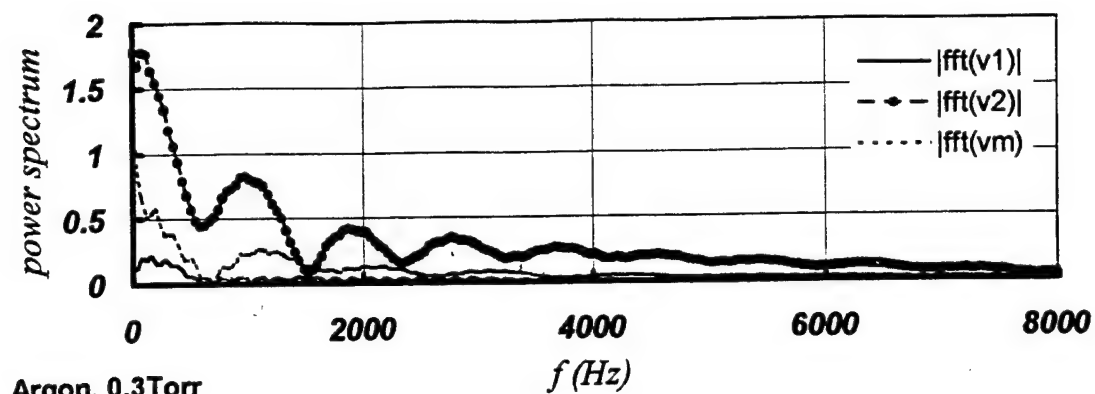


Figure 3.17 Power spectra of the signals from conductivity probes

The largest amplitude of the wave motion was detected (consistently) by the  $v_2$  conductivity probe, and is typical for all gases and both probe configurations. Figure 3.17 shows that the amplitude of the waves diminishes gradually toward the center of the dual-coil device. Two conclusions are drawn: (a) the initial magneto-kinetic shock dampens and weak ion acoustic waves are generated, and (b) wave motion is along field lines (i.e. ion density compression or rarefaction) and away from the inter-coil region.

The phase velocity of the waves is found (considering the wavelength discussion above) from the frequency data. Thus, the first frequency peak for argon and nitrogen is 975Hz and 1600Hz respectively, and the corresponding wave velocities are 1670m/sec in argon and 2780m/sec in nitrogen. Helium shows smaller amplitude waves and the excitation of some high frequency modes, suggesting much higher velocities.

The possibility for the propagation of ion acoustic waves along the magnetic field lines can be demonstrated if we consider the ion momentum equation with  $\bar{v} \parallel \bar{B}$ , ( $\bar{v} \times \bar{B} = 0$ ) for a conductive gas

$$m_i \frac{d\bar{v}_i}{dt} = e \cdot \bar{E} - \nabla p_i \quad (3.28)$$

Clearly, the magnetic field does not influence the motion of the ions (and electrons) along the magnetic field lines, and the linearization of this equation leads to the ion-wave dispersion equation<sup>56</sup>

$$v_w = \frac{\omega}{k} = \left( \frac{k_b T_e + 3k_b T_i}{m_i} \right)^{1/2} \quad (3.29)$$

where  $\omega$  is the angular velocity of the wave,  $k = 2\pi/\lambda$  is the wave number,  $m_i$  is the ion mass, and  $T_i$  is the ion (gas) temperature. Table 3.1 lists the ion acoustic speeds for the tests shown in Figure 3.17 for average ion (gas) and electron temperatures (see Appendix A).

**Table 3.1** Gas properties and ion acoustic speeds

Gas	Pressure (torr)	$T_i = T_{\text{gas}}$ (K)	$T_e$ (eV)	$v_w$ (m/sec)	$v_{\text{exp}}$ (m/sec)
Ar	0.3	400	0.5	1210	1670
N <sub>2</sub>	0.6	450	1.2	2120	2780
He	0.5	320	4	9800	> 3400

Considering the approximate nature of the temperature estimates, the agreement shown by the theoretical predictions  $v_w$ , and the experimental results  $v_{\text{exp}}$  is satisfactory.

The conductivity probe data shows also evidence of bulk plasma motion along the magnetic field lines as discussed above. Figure 3.18 shows typical conductivity probe traces from argon and nitrogen tests. The response of the conductivity probe has a delay of 0.7 – 0.8msec from the discharge onset. The explanation is that although the ion acoustic waves propagates rapidly even through weakly ionized plasma, the conductivity probes will only detect significant signals if plasma of high conductivity reaches their location. Considering that the position of the  $v_2$  probe is remote from the inter-coil space, and the electric field (double layer potential) is much weaker there, it is concluded that high conductivity plasma must arrive at that location. The mean distance that an ionized particle has to travel along field lines to reach probe  $v_2$  is a quarter of a circular arc of length  $\pi(a/2 + R_w)/2 \cong 67\text{mm}$ . Hence, the average speed,  $v_p$  of these particles must be about 100m/sec in argon and 80m/sec in nitrogen. These low speed values are explainable if one considers the large number of collisions that an ionized particle undergoes along its path.

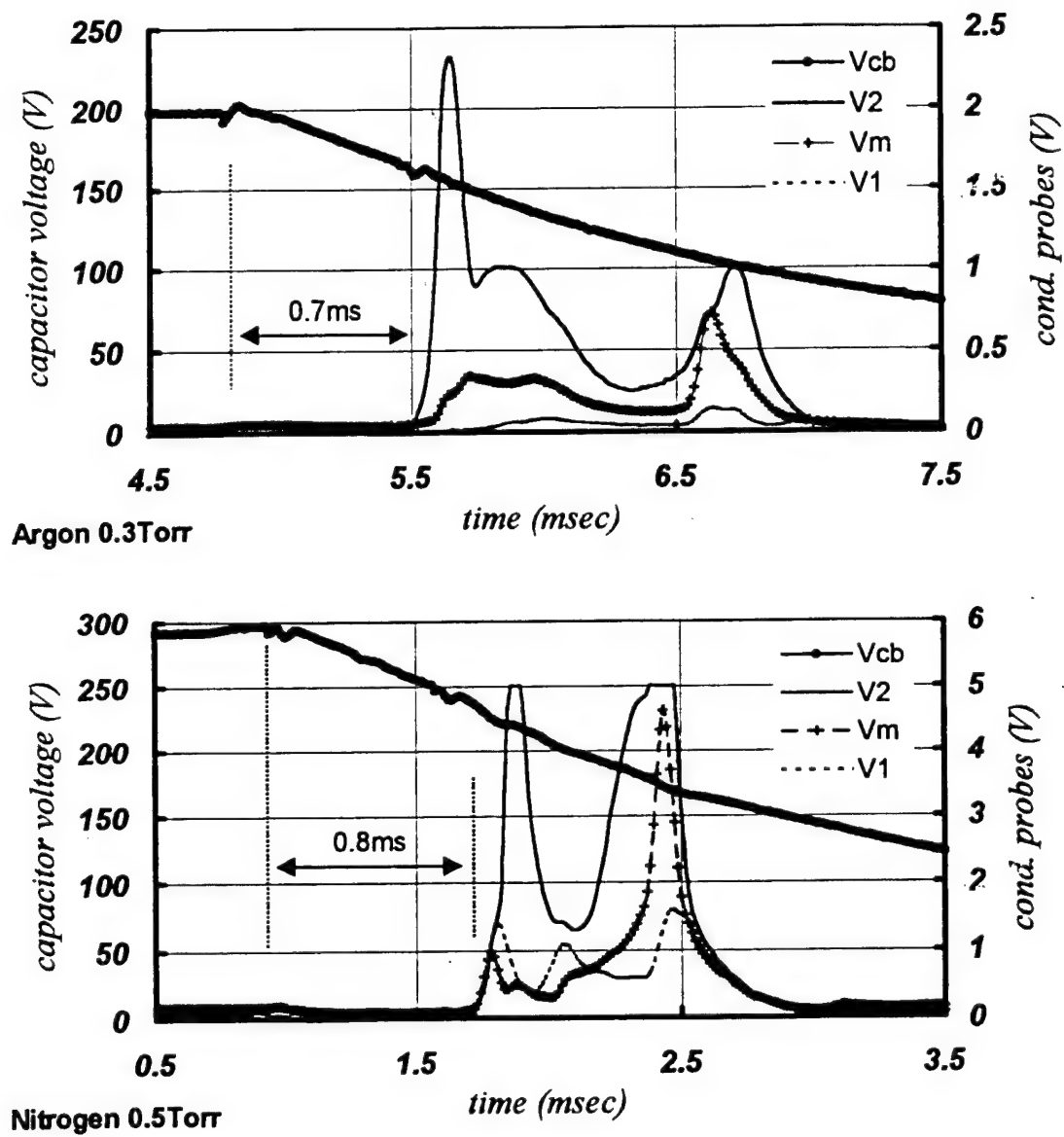


Figure 3.18 Response lag of the conductivity probes, indicative of  $\bar{v} \parallel \bar{B}$  plasma motion

In terms of energy, the power transformed into plasma enthalpy is proportional to the gas density and particles velocity

$$P_{v||B} \cong m_g n_n A_h \frac{v_p^3}{2} \quad (3.30)$$

Here  $P_{v||B}$  is plasma enthalpy (for  $\vec{v} \parallel \vec{B}$ ),  $m_g$  is the mass of the gas particle,  $A_h$  is an average cross section of the energized plasma volume, and  $v_p$  is the speed of the particles. Assuming that the cross-section of the volume of energized plasma is of the same order as the coil area,  $A_h \cong \pi R_w^2 = 0.004\text{m}^2$ , the power used to accelerate the gas particles is approximately 0.6W in nitrogen and 1.5W in argon.

A cross-correlation analysis of the conductivity probes signals was performed in order to detect any plasma motion along the x-neutral line. The analysis showed that no consistent plasma motion is detectable, within the limitations of the array of conductivity probes. However, this result does not preclude the possibility of ionized particles moving along the x-neutral line at velocities higher than the pick-up threshold of the conductivity probes ( $v_p > 1\text{km/sec}$ ). One indication of this fact is the detection of a nonzero electric field component  $E_x$  along the x-neutral line, see Figure 3.19. The  $E_x$  electric field is calculated from differences in plasma potential at the locations of the electric probes (see also Figure 3.5 for nomenclature). Figure 3.19 shows the occurrence of electric field spikes that coincides with the surge in plasma conductivity at the locations of the conductivity probes. At this time, the gradients of the magnetic field are too small to be able to generate an electric field  $E_x \cdot \vec{i} + E_z \cdot \vec{k}$  of the magnitude shown in this test. Moreover, Faraday's law states that there is no rotational part to  $E_x$  in the MDE configuration, since the  $B_z$  component of the magnetic field in the inter-coil space is null. Hence, it must be concluded that  $E_x$  is a result of charge separation (i.e. plasma motion) and plasma wave interaction.

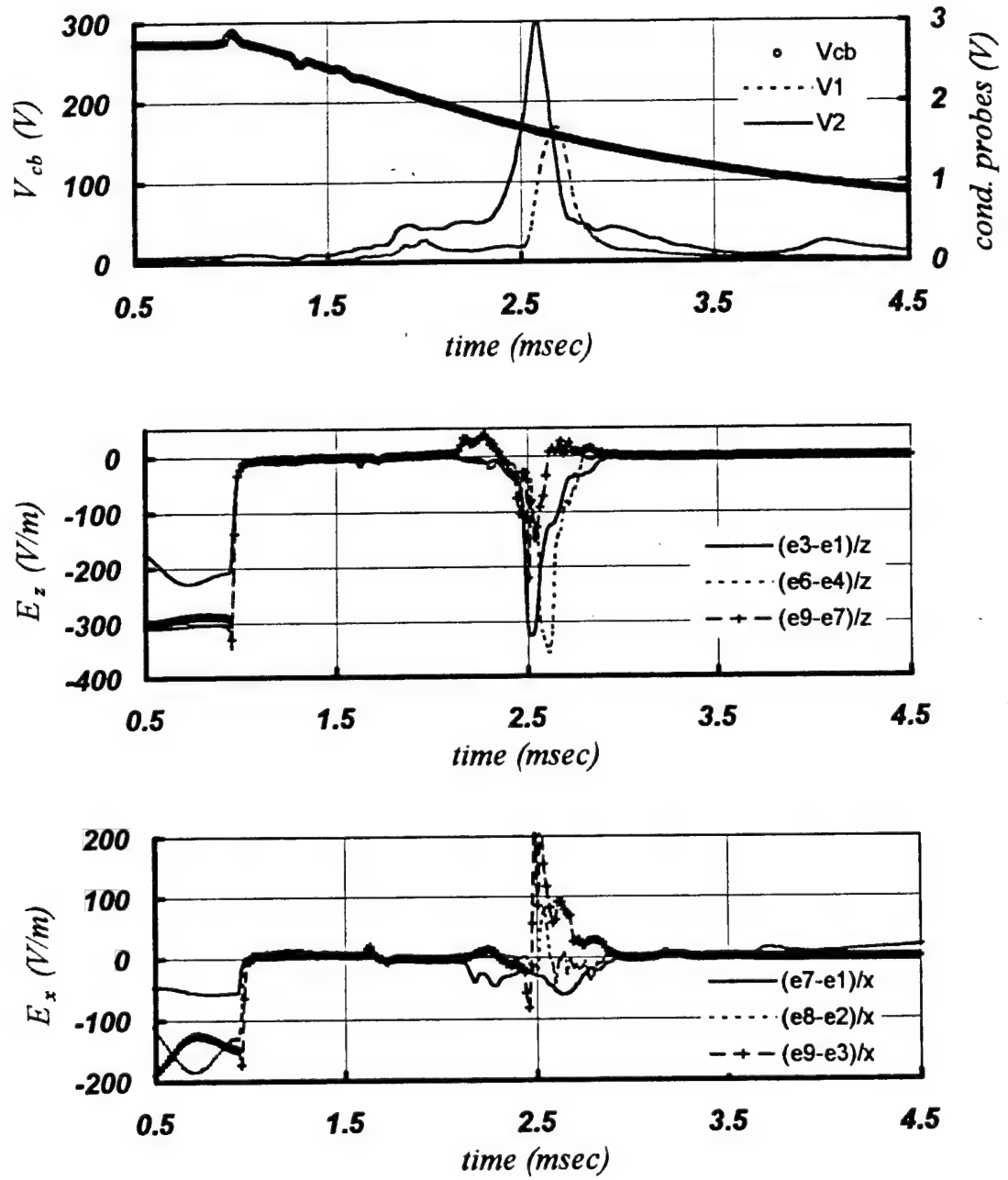


Figure 3.19 Conductivity probes signals and electric field components ( $N_2$ , 0.5Torr,  $W_{\Delta} = 1.2\text{MW}$ ,  $P_{\text{TDD}} = 950\text{W}$ )

In the test shown, the average  $E_x$  electric field is 50V/m for a period of 0.5msec. Given an average conductivity of the nitrogen plasma of  $500\Omega^{-1}\text{m}^{-1}$ , the power associated with this motion is

$$P_{vx} = \sigma E_x^2 \cong 1.25\text{MW/m}^3 \quad (3.31)$$

Estimating the effective volume of plasma motion, in both sides of the x-neutral line, at about  $2\text{-}3\text{cm}^3$ , the power spent for the acceleration of plasma particles along the x-axis is 2.5-4W.

The conclusion of this analysis is that only a small quantity ( $\sim 0.02\%$ ) of the energy transferred to the plasma is actually converted to plasma enthalpy.

## CHAPTER IV

### CONCLUSIONS

The interest in the problem of plasma energization at magnetic neutral points was triggered by astrophysical phenomena such as solar flares and magnetospheric substorms, and had as the result the development of the theory of magnetic reconnection. The magnetic reconnection theory predicts the energization of plasma at neutral points if large gradients of the magnetic field are maintained by plasma motion. This situation is not particularly useful in engineering applications where the goal is to transfer the magnetic field energy to plasma enthalpy. The MDE experiment was designed to answer some of the questions raised by the process of plasma energization at magnetic neutral points, in a hydrostatic configuration. More specifically, the experiment was to provide the means for the evaluation of the potential for plasma heating and acceleration, of a stationary, time varying magnetic field in engineering applications.

The classic MHD model of the problem is a simplified form of the magnetic induction equation (Equation 1.12) which leads to magnetic field diffusion and annihilation.<sup>21, 38</sup> This model shows that the magnetic energy is converted directly to heat and dissipated into the plasma. Prior experimental work<sup>44, 46, 52</sup> showed that the actual process involves not only heating but also strong ionization, waves and bulk plasma motion. However, those experiments were mainly designed to validate reconnection models rather than to investigate the potential uses of the process. Indeed, one conclusion of those experiments was that the data seemed to validate the wave assisted magnetic diffusion (reconnection) model of Petschek<sup>7</sup>, despite the initially static plasma.



The analytical modeling of the new experiment (the Denver model) was performed for different plasma conditions: (a) a fluid model describing the case of fully ionized plasma, and (b) a particle/wave model appropriate for the case of weakly ionized plasma. The Denver model suggests that a fully ionized plasma sandwiched between two opposing, time varying magnetic fields may be accelerated, and the efficiency of the process is dependent of the magnetic Reynolds number (i.e. plasma ionization fraction).

Experimentally, the investigation was limited to the case of weakly ionized plasma. The experimental results show agreement with the model and with some of the conclusions drawn from the Stenzel-Gekelman experiment. Thus, the MDE experiment demonstrated that the diffusion of variable magnetic field through (weakly ionized) plasma leads to one or two orders of magnitude increase in the ionization fraction, plasma waves and bulk plasma motion. Another similar result of the two experiments is a larger increase in plasma ionization just outside the dissipation region, along the neutral line. In the MDE experiment, this is the location of the  $v_2$  conductivity probe.

In terms of energy transfer, the experiment showed that the weak coupling between the magnetic field and the low conductivity plasma leads to a small efficiency of the energy transfer. Table 4.1 shows the distribution and the dissipation of power into the plasma. Ultimately, after the damping of the ion acoustic waves the entire amount of power transferred to the plasma is converted to heat.

**Table 4.1** Average power distribution

Gas	Discharge Power (MW)	Power Dissipated in Plasma $P_d$ (kW)	Plasma Enthalpy $P_h$ (W)	$P_h/P_d$ (%)
Ar	0.6	21	8 - 10	0.03 - 0.05
N <sub>2</sub>	1	25	3 - 6	0.01 - 0.02
He	0.65	6.5	—	—

The experiment showed also that reconnection process is an unlikely mechanism of the plasma energization process observed in experiment. The observations leading to this conclusion are: (1) even after the discharge, plasma is not sufficiently ionized to strongly influence the magnetic field of the coils, (2) the onset of plasma motion along the x-neutral line shows a significant time delay from the onset of the discharge, and (3) the electric field  $E_x$  that appears along the separator is only a result of wave motion and charge separation. The second observation is in direct disagreement with all reconnection models, since it does not show streams of particles leaving the inter-coil space at Alfvén velocity. This velocity is directly proportional to the magnetic field intensity and would be large enough to make these streams of ionized particles appear immediately after discharge onset. Moreover, the motion of ionized particles in the plasma is described by a large number of collisions with the neutrals, and thus cannot be adequately described by Alfvén velocity, which is a parameter defined in terms of gas density.

The existence of the  $E_x$  field component seems to indicate a reconnection process, as stated by some alternative definitions of the reconnection process.<sup>10</sup> However, it is clear from the experimental data that this field cannot be due to a topological change of the magnetic field, since

at the time of its occurrence any change of field topology would not be able to produce an electric field of that magnitude.

The conclusion of the MDE experiment is that direct magnetic field plasma heating, and more importantly, plasma acceleration at hydrostatic magnetic neutral points is possible. The energy transfer is mediated by the electric fields and currents induced in the plasma. However, the effectiveness of the process is small if the plasma is not sufficiently conductive to efficiently couple with the magnetic field.

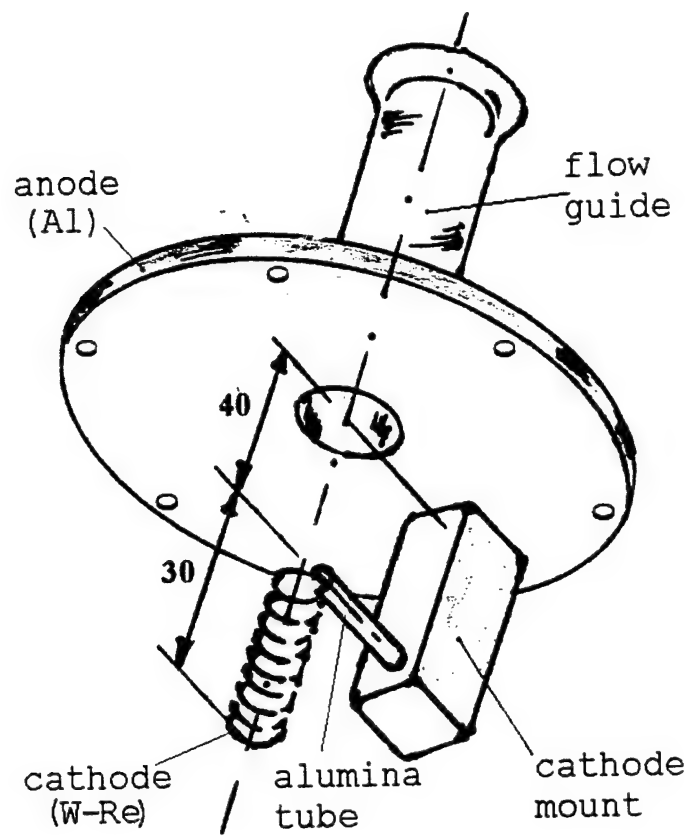
## **APPENDIX**

### **Plasma Study on the Ionization of Flowing Gases by DC Thermionic Arc Discharge**

#### **I. Introduction**

The study presents the working characteristics of a new DC-field thermionic-arc discharge ionization device (TDID), and an approximate electron density model scaled with the TDID power input. The TDID was used as plasma source in the MDE experiments.

The tests were carried out in a 0.75m long by 0.5m diameter cylindrical glass vacuum chamber at pressures ranging from 200 mTorr to 700 mTorr. At the top the vacuum chamber has an aluminum plate which holds a gas reservoir. The TDID was grafted onto the bottom of the vacuum chamber top plate, see Figure A.1. The device has a radial-axial symmetry and consists of two electrodes. The aluminum end plate of the vacuum chamber forms the anode of the ionization device. The cathode is made of a 0.8 mm tungsten-rhenium (95%W-5%Re) wire spiraled in the shape of a filament with an exterior diameter of 8 mm and having 20 turns. The cathode is 30 mm long and is mounted 40 mm below the anode plate on the axis of symmetry.



**Figure A.1. TDID sketch**

An opening of 24 mm was machined in the center of the anode plate and the upper side was fitted with a 75 mm long, smooth stainless steel pipe, as illustrated in Figure A.1 (see also Figure 2.4). The pipe is flared at the top and acts as a flow guide for the gas exiting the gas reservoir.

## II. TDID Diagnostics

The diagnostics involved in the study consist of measurements of (I) electrical discharge parameters (voltage, current), (II) flow parameters (pressure, temperature), and (III) plasma electron density and electron temperature.

(I) Electrically, the TDID discharge is fed from a constant-voltage power supply. The discharge current is determined by the local plasma parameters through Ohm's law. Figure A.2 illustrates the electrical circuit. The BC\_1 power supply is an "in-house" designed, variable high-voltage rectifier capable of supplying a sustained power level of 1.5kW. Two voltage-divider circuits ( $R_3 - R_5$  and  $R_4 - R_6$ ) are connected to the cathode line. They provide the cathode voltage and the current in the circuit.  $R_1$  and  $R_2$  are placed in series with the discharge and they prevent the short-circuiting of the power supply in case of discharge breakdown.

(II) The pressures measured are the reservoir,  $p_1$  and the vacuum chamber pressure  $p_2$ . The measurements were performed with two Omega PX-305 series vacuum-pressure transducers. The calibration of the pressure transducers was performed using a NRC 521 thermocouple vacuum gauge. The uncertainty associated with pressure measurements is estimated as  $\pm 5\%$  of reading, and its main component is the bias introduced by the calibration procedure. The gas and cathode temperature was measured by thermocouple and by infrared pyrometry. The temperature sensors used were: (1) an Omega K-type miniature probe thermocouple, which provided point measurements in the plasma, and (2) a Mikron 9000 infrared (IR) pyrometer, which rendered the cathode temperature. The uncertainty associated with the thermocouple reading is estimated to be about  $\pm 15\%$  of reading (in K) and was caused mainly by the thermal inertia of the probe during the tests.

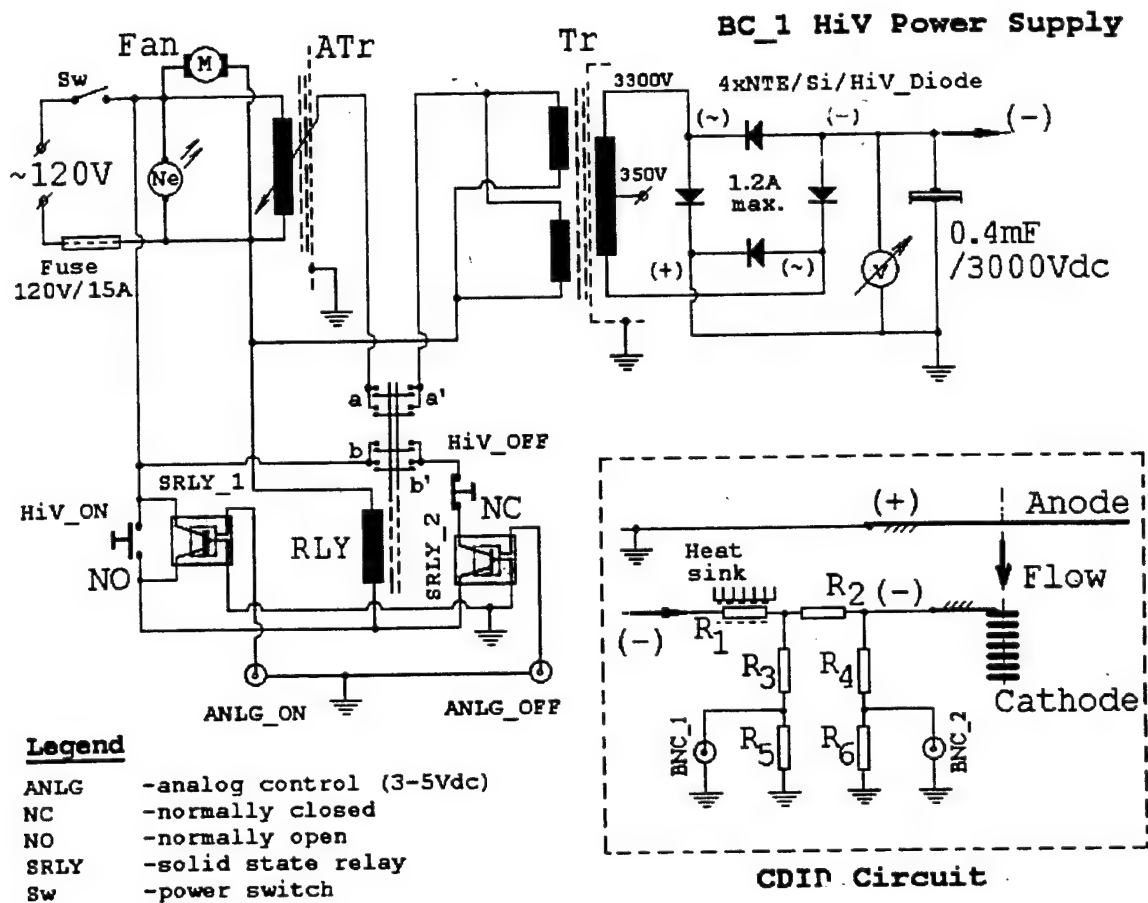


Figure A.2 BC\_1 power supply and CDID electrical circuit ( $R_1 = 80\Omega/125W$ ,  $R_2 = 50\Omega/50W$ ,  $R_3 = R_4 = 8M\Omega/5W$ ,  $R_5 = R_6 = 5k\Omega/1W$ ). BNC\_1 and BNC\_2 are high voltage probes

The infrared pyrometer was calibrated for tungsten emissivity and transmission through glass. The estimated uncertainty associated with the IR temperature measurements is  $\pm 2 - 5\%$  of reading (in K), with the higher values pertaining to the higher temperature range.

(III) Electron density and electron temperature radial distributions were obtained in a diametral plane of the plume, at a location approximately 30 mm below the cathode filament. These measurements were performed with a four-prong electric probe. For a more detailed description of the experimental procedures the reader is referred to Ref. 58.

### **III. TDID Ionization**

At relatively low voltages 100 – 400V the TDID cathode is not sufficiently hot to produce thermionic emission. The primary ionization processes in the discharge take place in a region of concentrated electric field near the cathode – the ionization region. In this operating regime the TDID discharge closely resembles a point to plane, pulseless negative corona<sup>63</sup>. As the inter-electrode potential is increased the discharge current increases leading to a rapid rise of cathode temperature. In the nominal operational regime the TDID discharge departs from the corona behavior and becomes a thermionic-arc. From this perspective the TDID is similar to a hollow cathode ion source, although the flow is in the opposite direction (i.e. from the low field to the high field electrode). This similarity warrants a quick review of the hollow cathode discharges. Hollow cathode discharges (arcs) are efficient high-current plasma sources<sup>64</sup>, and are good candidates for neutral beam injection<sup>65, 66</sup>. Ferreira and Delcroix<sup>64</sup>, present the physical mechanism of operation of the hollow cathode arc (HCA) discharge and the general theoretical framework. A typical HCA ion source features a cylindrical cathode and a flat anode plate/grid downstream, see Figure A.3.



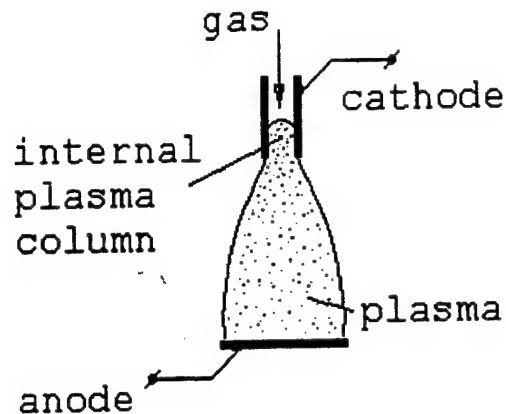


Figure A.3 Typical electrode arrangement of a hollow cathode arc

The primary HCA ionization processes are taking place inside the cathode space, the resulting plasma being referred to as the internal plasma column. The gas flow carries the plasma downstream in the inter-electrode space, where further ionization takes place, mainly due to impact of high-energy electrons. Three important differences between the hollow cathode arc and the TDID discharge are noted (1) the hollow cathode discharge is typically a collapsed-arc discharge, and operates near local thermal equilibrium, (2) the HCA plasma is not field-free and (3) the TDID cathode filament was designed to reduce the number of high-energy electrons in the downstream plasma. However, the basic theory of the HCA applies equally well to the TDID. The effect of the dissimilarities will be discussed in a subsequent section.

The physics of the TDID ionization region is somewhat complicated, as this is the volume where most of the energy transfer takes place. Only a short qualitative description is given here. Ions drifting along the field lines that enter the sheath surrounding the cathode must have velocities greater than the Bohm velocity<sup>36</sup>  $v_i \geq (k_b T_e / m_i)^{1/2}$ . The discharge is a non-LTE process with an electron temperature about one order of magnitude higher than ion (gas) temperature. As a result a large amount of energy is transferred from ions to the cathode surface through collisions. There are two relevant consequences: (1) the cathode reaches temperatures

that cannot be attained solely by ohmic heating, and (2) free electrons are produced by ion impact and thermionic emission at the cathode. The equilibrium thermionic current in the presence of an accelerating field is exponentially dependent on the cathode temperature<sup>60, 64, 67</sup> and is given by the Richardson Dushman equation

$$j_{th} = A_M T^2 \cdot \exp\left(-\frac{\chi_M - 2ea \cdot E_w^{1/2}}{k_b T}\right), \quad (A.1)$$

where  $a = 1.89 \cdot 10^{-5} \text{ (volt} \cdot \text{m)}^{1/2}$  and  $E_w$  is the electric field at the cathode. The two coefficients  $A_M$  and  $\chi_M$  are specific to the cathode material and can be found in literature, see for instance Refs. 60, 68. For the tungsten filament we take  $A_M = 70 \text{ A/(cm}^2 \text{ K}^2)$  and  $\chi_M = 4.5 \text{ eV}$ . Additional ionization in this region is generated by electron avalanche (Townsend mechanism) due to impact by energetic primary (thermionic) electrons. Other processes taking place within the ionization region are reattachment, recombination and the excitation of molecular vibrational modes and metastable states. The de-excitation of these metastable states results in emission of quanta and is partially responsible for the bright appearance of the ionization region. The maximum electron density in the discharge is found in the ionization region and can be estimated from the equality of ion and electron fluxes at the edge of the cathode sheath  $n_e \cdot v_i = \alpha \cdot l_e \cdot (j_{th}/e)$ . The term in parenthesis is the flux of primary (thermionic) electrons in the cathode sheath, and  $l_e$  is some characteristic length of the ionization region. Recalling that the average ion velocity in the sheath is  $(k_b T_e / m_i)^{1/2}$  the density of the plasma in the ionization region is

$$n_e = \left(\frac{m_i}{k_b T_e}\right)^{1/2} \cdot (\alpha \cdot l_e) \cdot \frac{j_{th}}{e}. \quad (A.2)$$

Clearly Equation A.2 is derived assuming that the electric field is high enough to maintain an ionization coefficient greater than the attachment coefficient. It is also noted that the charge density in the ionization region is exponentially dependent of the cathode temperature through  $j_{th}$ .

Therefore Equation A.2 is at best an average estimate of the overall electron density in the ionization region.

Finally, the plume is the region of interest for the experimenters and is formed by the flowing gas, which sweeps the ionized particles downstream of the ionization region. The field intensity in the plume is minimal and little additional energy is added to the plasma. Thus the ionization fraction in the plume is determined mainly by the recombination rate.

#### IV. TDID Flow

An important aspect of the TDID operation is the gas flow. The solution to the TDID flow is obtained from the basic conservation laws, mass momentum and energy, written such that the only unknowns are the experimentally measured parameters. For simplicity consider the plume quasi-one-dimensional. Written with the standard notation between two successive states, the one-dimensional mass, momentum, and energy conservation equations<sup>69</sup> for flow with heat addition are

$$\begin{aligned}\rho_1 u_1 &= \rho_2 u_2 \\ p_1 + \rho_1 u_1^2 &= p_2 + \rho_2 u_2^2 \\ c_p T_1 + \frac{u_1^2}{2} + q &= c_p T_2 + \frac{u_2^2}{2}\end{aligned}\quad , \quad (A.3)$$

where  $q$  is the added heat per unit mass,  $p_1$  is the total (stagnation) upstream pressure, and  $T_1$  is the total upstream temperature. Additionally we can write the ideal equation of state,  $p = \rho RT$  and the isentropic pressure, and the adiabatic temperature relations

$$\begin{aligned}p_t &= p_1 \left( 1 + \frac{\gamma-1}{2} M_1^2 \right)^{\frac{\gamma}{\gamma-1}} \\ T_t &= T_1 \left( 1 + \frac{\gamma-1}{2} M_1^2 \right)\end{aligned}\quad (A.4)$$

Heat addition to the flow is the primary effect of the discharge. A secondary effect of the ionization process is the decrease<sup>70</sup> of the effective adiabatic coefficient  $\gamma$  of the gas. A noticeable  $\gamma$  change in the TDID flow can only be expected in regions with a significant ionization fraction, i.e. the immediate neighborhood of the cathode, and thus  $\gamma$  is assumed constant throughout the flow.

In a quasi-one-dimensional isentropic flow approximation the velocity of the jet at the reservoir exit is a function of the  $p_2/p_1$  pressure ratio. The experimental pressure data indicate that argon and nitrogen reach sonic speed in the flow-guide, while helium flow remains subsonic. The two situations corresponding to the downstream flow are (I) supersonic expansion – normal shock at cathode (Ar, N<sub>2</sub>), and (II) subsonic recompression (He). The supersonic solution is the case of interest and is discussed further.

Even with the simplifying assumptions an exact one-dimensional shock solution of Equation A.3 is difficult to obtain. The difficulty stems from (a) inability to properly model the shock – heat interaction with only the available data, and (b) the downstream flow is not adiabatic. Specifically, the stagnation pressure and temperature ahead of the shock, and the aft shock pressure cannot be estimated, and thus the location of the shock cannot be anchored. To circumvent this difficulty we disregard the shock and assume that the heat is added to the entire downstream region, see Figure A.4.

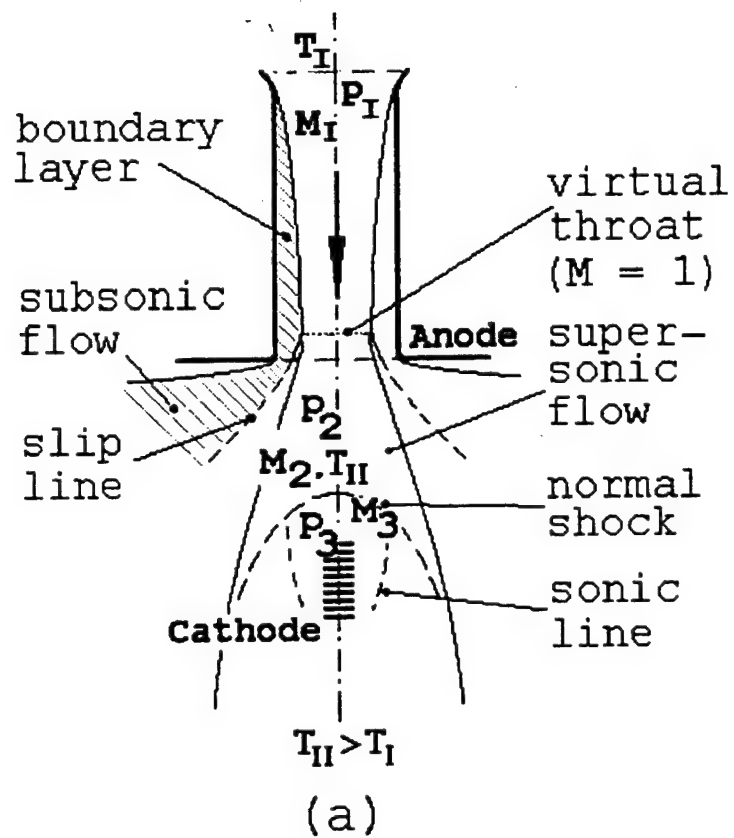


Figure 4. TDID flow pattern

Solving Equations A.3 and A.4 for upstream (flow-guide) and downstream (inter-electrode space) Mach numbers one obtains

$$\frac{M_1^2 \left(1 + \frac{\gamma-1}{2} M_2^2\right)}{M_2^2 \left(1 + \frac{\gamma-1}{2} M_1^2\right)^{\frac{\gamma+1}{\gamma-1}}} = \frac{\left(\frac{p_2}{p_1}\right)^2}{\frac{T_{II}}{T_I}} \quad (\text{A.5})$$

$$\frac{1 + \gamma \cdot M_1^2}{1 + \gamma \cdot M_2^2} \cdot \frac{1}{\left(1 + \frac{\gamma-1}{2} M_1^2\right)^{\frac{\gamma}{\gamma-1}}} = \frac{p_2}{p_1}$$

In obtaining Equation A.5 the temperature downstream,  $T_2$  was approximated using the adiabatic stagnation temperature,  $T_{II}$  although the adiabatic condition is violated. In doing this it is assumed that the error introduced is acceptable for this approximate one-dimensional model. It is also noted that a shock solution of (7) with  $p_{II} = p_I$ ,  $T_{II} = T_I$  and  $p_3 = \chi \cdot p_2$ ,  $T_{III} = T_I + q/c_p$  (i.e. heat addition only aft shock) is not mathematically possible for any compression ratio  $\chi > 1$ . This substantiates the assumption that heat is actually added in the entire downstream region, and therefore justifies the use of Equation A.5. The solution of Equation A.5 yields the flow Mach number ahead of the shock,  $M_2$  and consequently the shock strength.

## V. Experimental Results

Nineteen successful experimental runs were performed. The test names are given by the attempted test pressure  $p_2$  in the vacuum chamber, and the test matrix is given in Table A.1.

**Table A.1.** TDID test matrix

Test Pressure (Torr)	Ar	He No. tests	N <sub>2</sub>
0.2	N/A	N/A	1
0.3	2	2	2
0.4	2	N/A	2
0.5	N/A	1	3
0.6	N/A	1	3

The TDID testing was performed in two phases: (a) plasma flow and electric property measurements and (b) pyrometric temperature measurements with similar test conditions. In order to increase the lifetime of the cathode the power levels in these tests were kept below 1kW. The relevant test results for argon and nitrogen are displayed in Table A.2.  $W_0$  is the total power supplied to the TDID and  $T$  is the average gas temperature in the ionization region. We note that the actual pressure in the vacuum chamber does not exactly match the test name pressure (see Table A.2, col.2).

**Table A.2 Argon and nitrogen data**

Test	P <sub>2</sub> (mTorr)	P <sub>1</sub> (mTorr)	V <sub>0</sub> (volt)	I (amp)	W <sub>0</sub> (Watt)	n <sub>e</sub> x10 <sup>-17</sup> avg.(m <sup>-3</sup> )	n <sub>e</sub> x10 <sup>-18</sup> max.(m <sup>-3</sup> )	T (K)	T <sub>e</sub> (eV)
<b>Ar</b>									
300_1	247	668	857	0.65	530	2.4	1.0	604	0.39
300_2	255	670	888	1.07	906	8.1	2.1	773	0.31
400_1	355	1360	657	0.78	493	4.2	2.0	673	0.27
400_2	350	1350	634	1.03	600	7.0	2.9	763	0.23
<b>N<sub>2</sub></b>									
200_1	200	406	1489	0.557	830	0.45	0.10	873	1.04
300_1	274	639	1369	0.560	768	0.30	0.08	860	1.00
300_2	237	609	1337	0.663	887	0.52	0.13	961	0.80
400_1	368	887	1239	0.710	884	0.25	0.10	1016	1.08
400_2	376	929	1183	0.719	850	0.44	0.12	1009	1.09
500_2	515	1214	1032	0.808	834	0.80	0.20	811	0.74
500_3	575	1192	1057	0.556	589	0.47	0.14	800	0.89
500_5	602	1105	1097	0.760	834	0.86	0.24	827	1.28
600_2	699	1519	959	0.813	777	0.88	0.25	895	0.73
600_3	699	1519	952	0.776	739	0.86	0.24	884	0.69
600_4	692	1526	950	0.774	736	0.83	0.26	883	0.70

Plasma parameters are characteristic to the plume region downstream of the cathode. Characteristic to both argon and nitrogen plumes is the exponential decay of the electron density with radius. Results from a typical four-prong probe scan are presented in Figure A.5. Electron temperature profiles in these tests show little radial change, a fact that suggests rapid thermalization of the electrons leaving the ionization region.



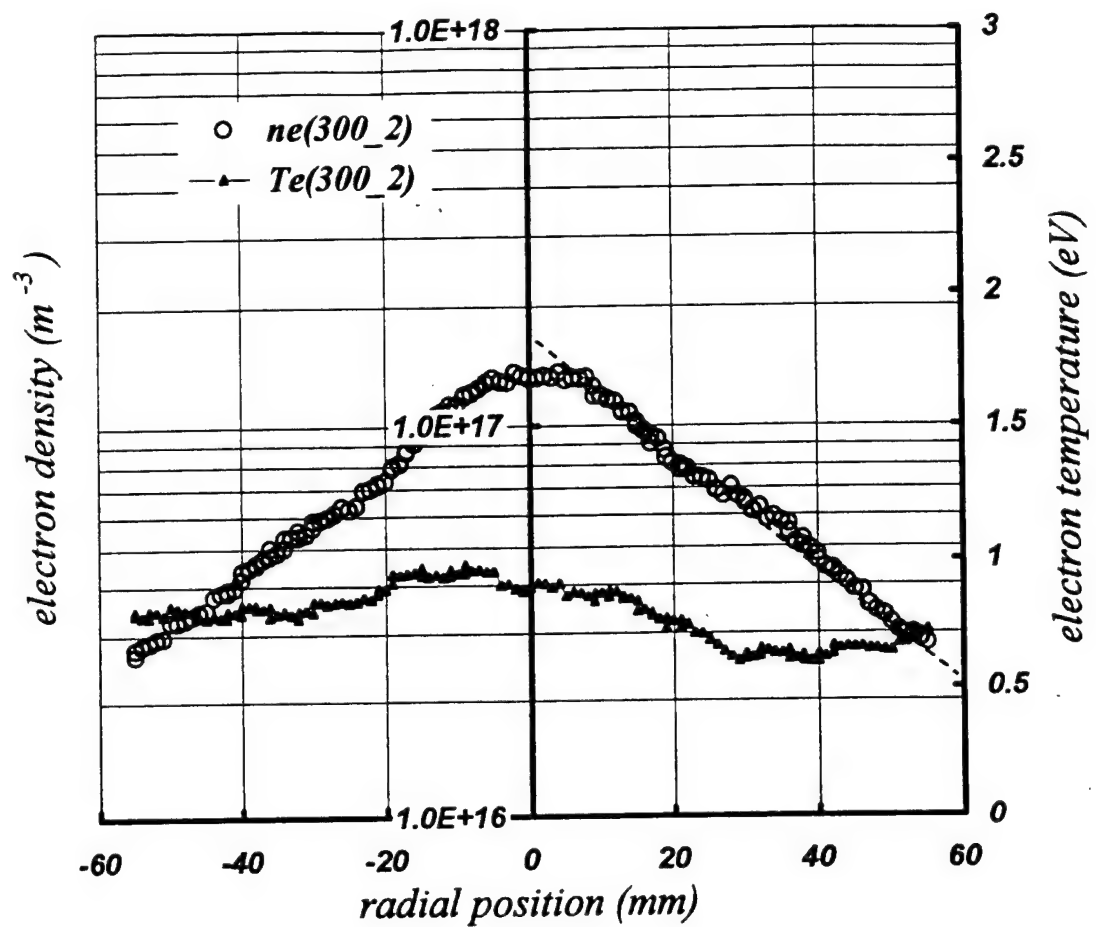
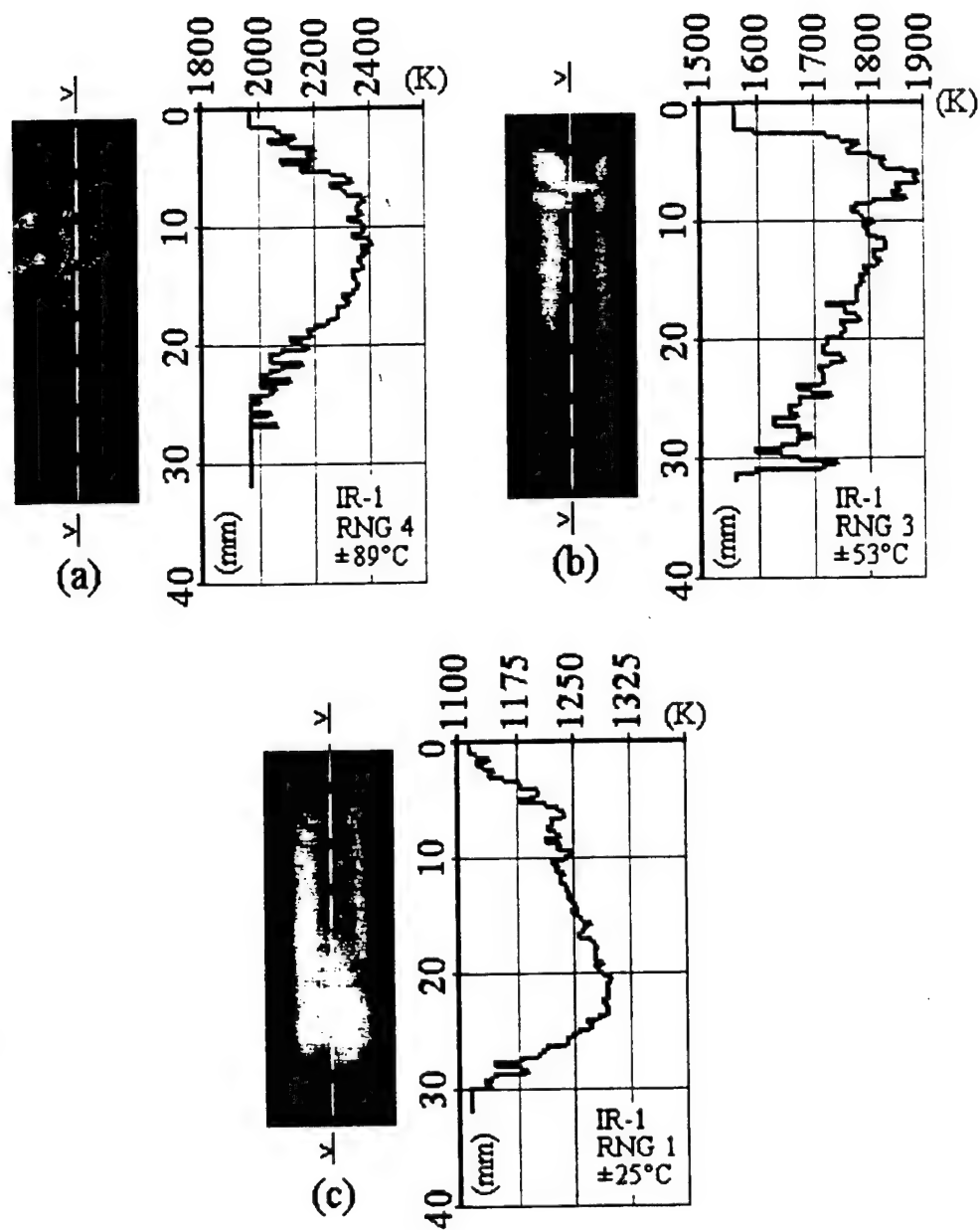


Figure A.5 Electron density and temperature (test  $N_2$ , 300\_2)

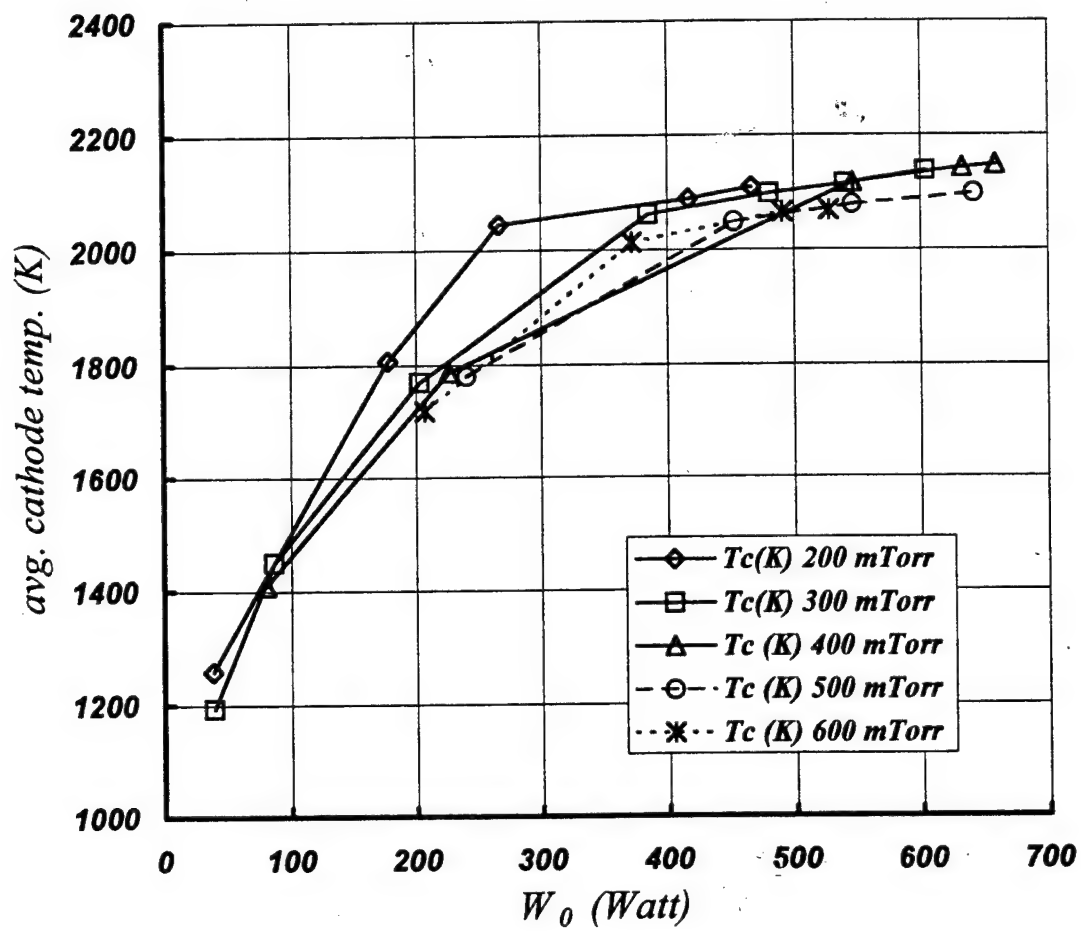
The nitrogen discharge exhibited good stability as illustrated by the data in Figure A.5, which shows little scattering. A more significant amount of scatter was observed in the argon density profiles and it was attributed to the occasional spark breakdown in the discharge gap during the four-prong probe scan.

In terms of electron density helium yielded the poorest results. Densities measured are in the mid  $10^{15} \text{ m}^{-3}$  range and the average electron temperature is  $4 - 4.5 \text{ eV}$ . This situation was due to constant onset of breakdown instabilities. Although the helium plasma is of little practical use, the helium tests provided insight into the stabilization mechanism of the TDID discharge.

A large portion of the experimental data consists of cathode and gas temperature measurements. In the TDID the cathode is the main source of ion heating, while heating by electron collision is only secondary or marginal. Cathode radiation/convection is responsible for dissipating more than 60% of the total power input. Generally the cathode heating is nonuniform due to field concentration and convection cooling, see Figure A.6. The infrared camera shows regions of the filament being heated to temperatures 10 – 15% higher than the average. The cooling patterns in Figure A.6 are consistent with the convective properties of the three gases used. In argon ( $c_p = 0.51 \text{ kJ/kgK}$ ) the cathode exhibits a hot spot near the top (Figure A.6.b) while in helium ( $c_p = 5.2 \text{ kJ/kgK}$ ) the cathode is cooled most at the top (Figure A.6.c). Figure A.7 illustrates the overall effect of convection and radiation on the average cathode temperature. Two regions are distinguishable in Figure A.7, a convection region for power levels lower than 300W and a saturation region above 400W where the radiation loss is significant. The higher temperature gradient in the low power region is a direct consequence of an inadequate dissipation mechanism (radiation is less effective). An increased cooling effect due to convection is evident in the high-pressure tests.

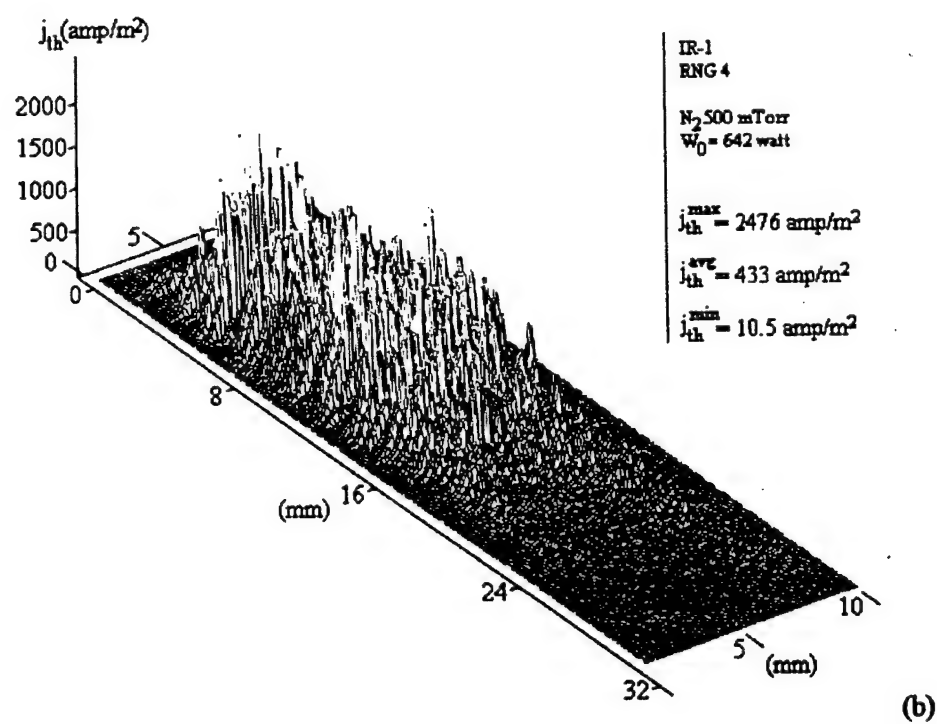
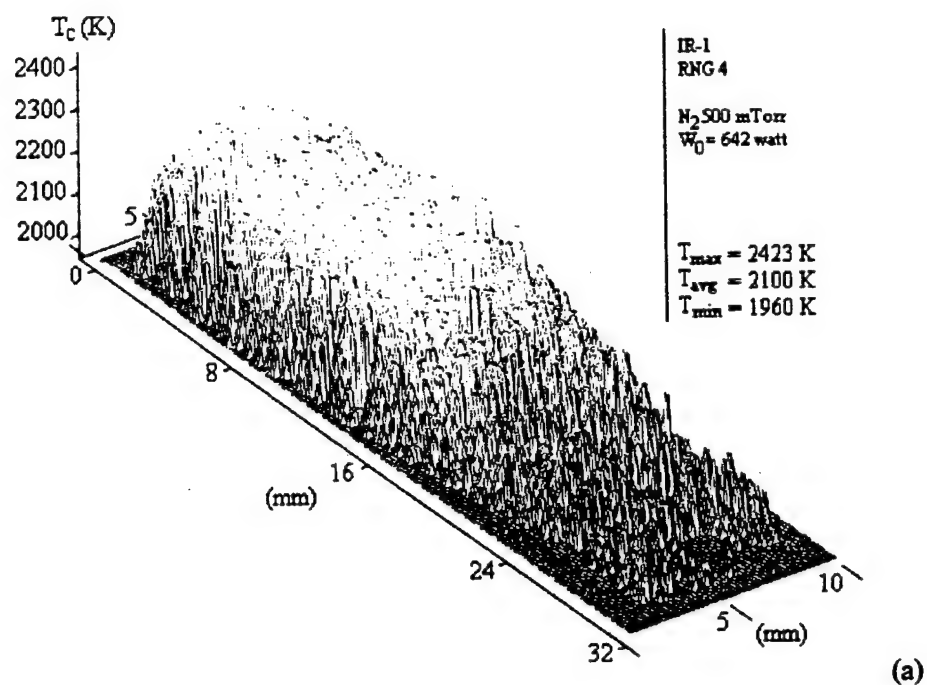


**Figure A.6** Convection effects on cathode temperature: nitrogen (a), argon (b), and (c) helium



**Figure A.7** Average cathode temperature ( $N_2$  tests)

The exact distribution of the thermionic current density along the cathode is inferred from the spatially resolved cathode temperature profile. Figure A.8.a presents the graph of the cathode temperature profile in a 500 mTorr/642 W nitrogen temperature test (not included in Table A.2). The current density is given by Equation A.1. The electric field at the cathode is  $E_w \cong \phi_w/\lambda_D$  where the cathode fall  $\phi_w$  is estimated from the equality of the electron and ion fluxes at the edge of the cathode sheath<sup>71</sup> as  $\phi_w \cong (k_b T_e/2e) \cdot \ln(\pi \cdot m_e/8 \cdot m_i) = 12.6$  volt. Figure A.8.b shows the calculated thermionic current density. Summing over the entire cathode surface the average thermionic current is 433 A/m<sup>2</sup>. The difference from the current density measured in the external circuit,  $j_{exp} = 505$  A/m<sup>2</sup> is about 15%. Clearly thermionic emission is the principal mechanism of sustaining the discharge current at the cathode.



**Figure 8.** Cathode temperature (a), and current distribution (b) ( $N_2$ , 500mTorr,  $W_0 = 642$  Watt)

## VI. Discharge Stability and Electron Density in the Plume

The gas flow plays a significant role in the discharge as a stabilizing factor. The stabilizing mechanism is two-sided (I) the shock recompresses the gas in the ionization region and (II) the flow removes heat and charge from the ionization region. These two flow effects are discussed further.

(I). The stabilizing effect of the shock recompression lies with the operating values of the field to gas density ratio  $E/n_s$ . In general the discharge tends to destabilize in regions of high  $E/n_s$ . The shock recompression reduces the local value of this ratio by increasing the gas density. To exemplify the recompression effect numerically we choose test 400\_2 ( $p_1 = 929\text{mTorr} - (123.5\text{Pa})$ ,  $p_2 = 376\text{mTorr} - (50\text{Pa})$ ,  $T_1 = 300\text{K}$ ,  $T_{II} = 1009\text{K}$ ). Solving Eqs. 9 we obtain  $M_1 = 0.21$  in the flow guide and  $M_2 = 1.05$  ahead of the shock. The aft shock static pressure is  $p_3 \cong 1.12 \cdot p_2$  while at the cathode the pressure is increased to the stagnation value  $p_{III} \cong 2 \cdot p_2$ . The density of the gas in the ionization region reaches stagnation values  $\rho_{III} \cong 1.65 \rho_2$ . The density increase is sufficient to compensate the increase in the  $E/n_s$  ratio due to field concentration at the cathode. In effect the shock is a stabilizing boundary. This mechanism suggests that a higher Mach number flow would be a more efficient stabilizing factor due to a higher degree of aft shock recompression. It also explains the unstable behavior of the helium discharge. The helium flow is subsonic and the gas density in the ionization region is low. Consequently the  $E/n_s$  ratio is high and the discharge collapses frequently.

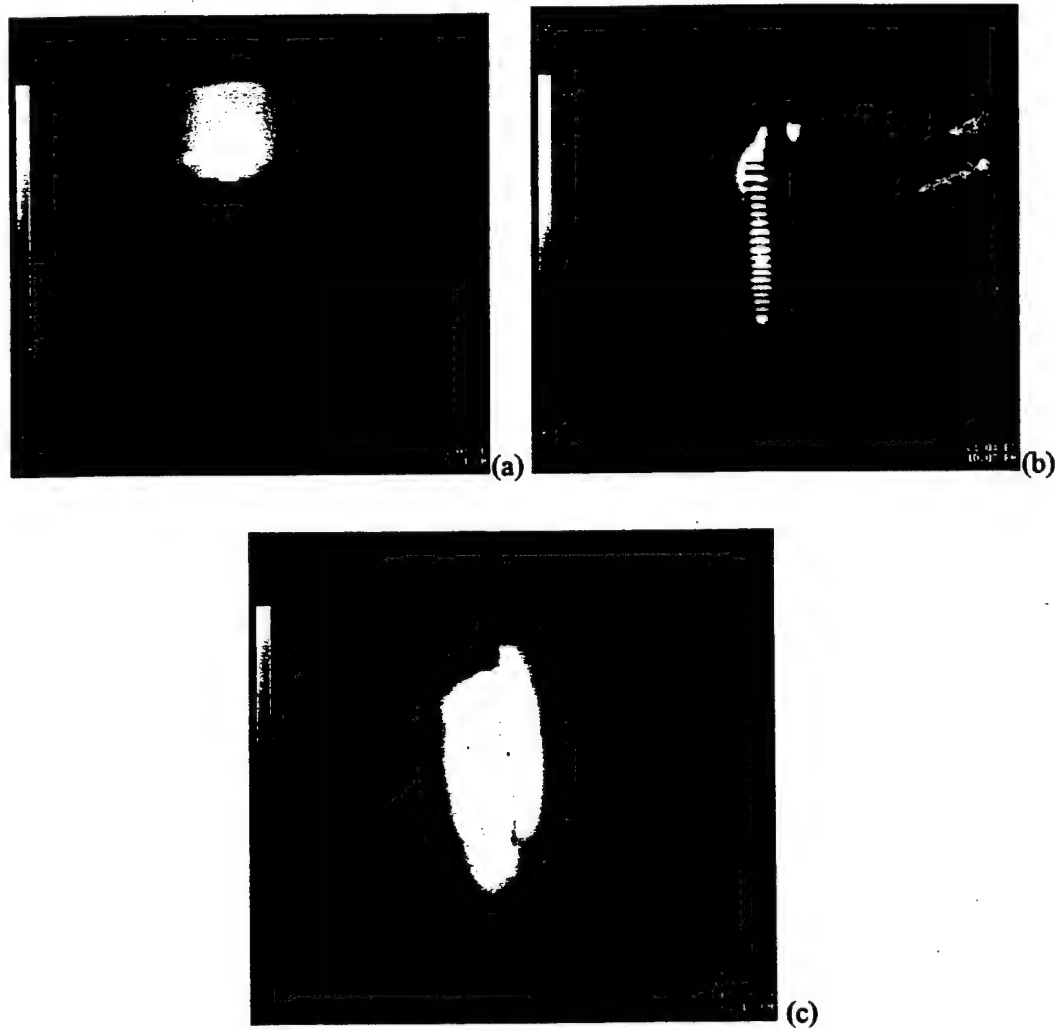
(II). A local increase in gas temperature triggers a destabilizing energy exchange feedback loop between the discharge and the flow called thermal instability<sup>68</sup>. The second flow stabilization mechanism is the convective heat removal from the ionization region, see Figure A.6. Generally the flow cools the region of high electric field at the top of the cathode, inhibiting the onset of thermal instabilities. A secondary stabilizing effect of the cooling process is a reduction of the cathode thermionic emission. The number of primary electrons emitted into the

ionization region is reduced and thus the local energy density is low. As a result the feedback temperature increase loop is removed and the discharge is stabilized. Argon has the poorest cooling properties and the cathode forms a hot spot at the top, Figure A.6.b while the nitrogen realizes a more uniform cooling along the cathode length. Figure A.6.a shows that in nitrogen the maximum cathode temperature does not coincide with the region of highest field strength at the cathode top. This stabilizing effect of the flow explains the better stability of the nitrogen over the argon discharge.

The instabilities developed in the three gases are, as illustrated in Figure A.10, dissimilar. Helium instabilities are explosive, symmetric and involve a large volume of the inter-electrode (drift) region, Figure A.10.a. Nitrogen instabilities show asymmetry, Figure A.10.c and are also caused by gap breakdown in the drift region, while in argon the discharge breakdown was at random to the lower vacuum chamber walls, Figure A.10.b. The exact breakdown mechanism is unknown. The patterns of light recorded by the camera suggest the development of anode-directed streamer channels<sup>68</sup>. A probable breakdown mechanism in argon is the development of streamer channels triggered by run-away electrons, which are accelerated along field lines parallel to the cathode surface.

The electron density distribution along the cathode is similar to the thermionic current distribution profile, see Figure A.8.b, and its maximum (Equation A.2) is attained in the ionization region. The ionization coefficient  $\alpha$  for various gases and  $E/p$  conditions is tabulated in Ref. 68. With the average TDID test conditions the ionization coefficients are  $\alpha \cong 0.7\text{cm}^{-1}$  for nitrogen and  $\alpha \cong 1.1\text{cm}^{-1}$  for argon. Assuming the characteristic length of the ionization region of the order of electron mean free path  $1/n_e \cdot Q_{es} \cong 1\text{cm}$  the maximum electron density is in the mid  $10^{18}\text{ m}^{-3}$  range in nitrogen and low  $10^{19}\text{ m}^{-3}$  range in argon.





**Figure A.10** TDID instabilities: helium (a), argon (b), and nitrogen (c)

More useful is to predict plasma density in the plume based on electrical parameters measured in the discharge circuit. An exact relationship between the electron density in the plume and power, current or applied voltage is difficult to find on theoretical grounds due to discharge complexity. Instead, the author has tried for a simple approximation starting from Equation A.2. Rewriting the current density in terms of electron mobility we have

$$\begin{aligned} n_e &= \left( \frac{m_i}{k_b T_e} \right)^{1/2} \cdot \frac{\alpha \cdot I}{e \cdot A_c} \cdot \frac{1}{n_s Q_{es}} \\ &= \left( \frac{m_i}{k_b T_e} \right)^{1/2} \cdot \frac{\alpha \cdot I}{e^2 \cdot A_c} \cdot \mu_e m_e c_e \end{aligned} \quad (A.6)$$

where  $A_c$  is the cathode emission surface area. Assuming that the current density distribution in the drift region is given by the empirical Warburg distribution<sup>63, 72</sup>, the total current in the TDID circuit is

$$\frac{I}{V_0} = \xi \frac{\mu \cdot \epsilon_0}{d} V_0, \quad (A.7)$$

where  $\xi$  is some constant depending on geometry, and  $d$  is the average distance between the electrodes. Using  $c_e = (8k_b T_e / \pi \cdot m_e)^{1/2}$  the electron density in the ionization region becomes

$$n_e = \left( \frac{8}{\pi} m_i m_e \right)^{1/2} \cdot \frac{\alpha \cdot d}{\xi \cdot \epsilon_0 e^2 A_c} \cdot \left( \frac{I}{V_0} \right)^2. \quad (A.8)$$

The electron density in the plume is dependent mainly on the recombination rate. Recombination describes the process of electron density decay in time, and can only affect the magnitude of the density profile downstream but not its shape. Some distortion of the electron density profile can be expected due to the radial expansion of the plume as it travels downstream. Accordingly, it is estimated that the maximum electron density in the plume follows an approximate profile given by

$$n_e \sim (I/V_0)^2. \quad (A.9)$$

The  $n_{e(max)}$  data in Table 2 scaled with Equation A.9 produces the following results

$$n_e \times 10^{-18} = 0.09 \cdot (I/V_0)^2 \times 10^7 + 0.634, \quad (A.10)$$

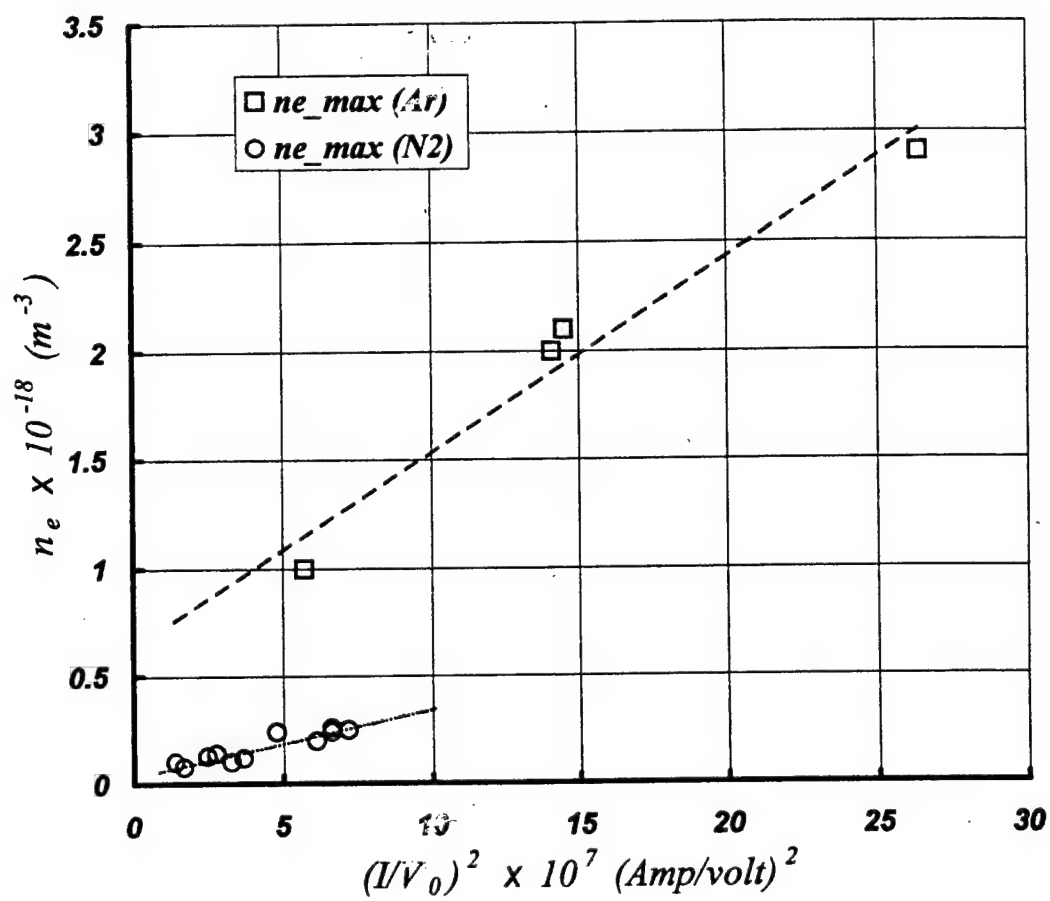
for argon and

$$n_e \times 10^{-18} = 0.03 \cdot (I/V_0)^2 \times 10^7 + 0.042 \quad (A.11)$$

for nitrogen, where  $n_e$  is in ( $m^{-3}$ ) and  $(I/V_0)^2$  is in (amp/volt)<sup>2</sup>. Graphically the electron density vs.  $(I/V_0)^2$  is depicted in Figure A.11. Equations A.10 and A.11 can be used to estimate electron densities in the plume of the discharge by measuring only two external electrical parameters, voltage and current.

## VII. Conclusions

Experiments with a DC thermionic-arc discharge ionization device have shown that steady electron densities of  $10^{17} - 10^{18}$  part/ $m^3$  can be obtained in nitrogen and argon flows. The experiments suggests that the development of a weak normal shock in front of the cathode is an effective stabilization boundary for the discharge. A plume electron density model based on the electrical parameters of the discharge was obtained. Based on this model plasma density can be calculated in the MDE experiments only from the voltage, and current input of the TDID.



**Figure 11.** Electron density scaling in the plume

## REFERENCES

- [1] Giovanelli, R. G., A theory of chromospheric flares, *Nature*, Vol. 158, pp. 81, 1946
- [2] Hoyle, F., Some recent researches in solar physics, Cambridge University Press, London, 1949
- [3] Dungey, J. W., Interplanetary magnetic field and the auroral zones, *Phys. Rev. Lett.*, 6, 47, 1961
- [4] Sweet, P. A., The neutral point theory of solar flares, in "Electromagnetic phenomena in cosmical physics," (B. Lehnert, ed.), IAU Symp. No. 6, pp. 123-134, Cambridge University Press, London and NY., 1958
- [5] Dungey, J. W., Conditions for the occurrence of electrical discharges in astrophysical systems, *Philos. Mag.* 7, 44, pp. 725-738, 1953
- [6] Parker, E. N., The solar flare phenomenon and the theory of reconnection and annihilation of magnetic fields, *Ap. J. Suppl. Ser.* 8, 177, 1963
- [7] Petschek, H. E., Magnetic field annihilation, NASA SP-50, p. 425, US. Gov. Printing Office, Washington, DC., 1964
- [8] Alfvén, H., On Frozen-In Field Lines and Field-Line Reconnection, *J. Geophys. Res.*, Vol. 81, No. 22, pp. 4019-4021, 1976
- [9] Heikkila, W. J., Criticism of Reconnection Models of the Magnetosphere, *Planet. Space. Sci.*, Vol. 26, pp. 121-129, 1978
- [10] Baum, P. J., and Bratenahl, A., Magnetic Reconnection Experiments, *Adv. In Electronics and Electron Phys.*, Vol. 54, pp. 1-67, Academic Press, 1980
- [11] Syrovatskii S. I., Pinch sheets and reconnection in astrophysics, *Ann. Rev. Astron. Astrophys.*, Vol. 19, pp.163-229, 1981

- [12] Baum P. J., Bratenahl A., et al., Plasma instability at an X-type Magnetic Neutral Point, *Physics of Fluids*, Vol. 16, pp. 1501, 1973
- [13] Baum P. J., Bratenahl A., "Laboratory Solar Flare Experiments", *Solar Physics*, Vol. 47, pp. 331, 1976
- [14] Baum P. J., Bratenahl A., "On Reconnection Experiments and their Interpretation", *Journal of Plasma Physics*, Vol. 18, pp. 257, 1977
- [15] Sevillano E., Ribe F. L., "Driven Magnetic Reconnection During the Formation of a Two-Cell Field Reversed Configuration", *Geophys. Monograph 30*, pp 313-318, American Geophys. Union, 1984
- [16] Baker D. A., "The Role of Magnetic Reconnection Phenomena in the Reversal Field Pinch", *Geophys. Monograph 30*, pp 323-340, American Geophys. Union, 1984
- [17] Pare V. K., "Reconnection in Tokamaks", *Geophys. Monograph 30*, pp 341-346, American Geophys. Union, 1984
- [18] Parker E. N., Interaction of the solar wind with the geomagnetic field, *Phys. Fluids*, Vol. 1, No. 3, pp. 171-187, 1958
- [19] Tandberg-Hanssen, E., Solar prominences, in *Geophys. and Astrophys. Monographs*, Vol. 12, D. Reidel Pub. Co., 1974
- [20] Heikkila W. J., Pellinen R. J., Falthammar C. G., and Block L. P., Potential and Inductive Electric Fields in the Magnetosphere During Auroras, *Planet. Space Sci.*, Vol. 27, pp.1383-1389, 1979
- [21] Axford, W. I., Magnetic Field Reconnection, *Geophys. Monograph 30*, pp. 1-8, American Geophys. Union, 1984
- [22] Vasyliunas V. M., Theoretical Models of Magnetic Field Line Merging 1, *Rev. Geophys. Space. Phys.*, Vol. 13, pp. 303-336, 1975
- [23] Alfvén, H., and Fälthammar, C. G., *Cosmical Electrodynamics*, Oxford Clarendon Press, 1963

- [24] Parker E. N., Sweet's Mechanism for Merging Magnetic Fields in Conducting Fluids, *J. Geophys. Res.*, Vol. 62, No. 4, pp. 509-520, 1957)
- [25] Axford, W. I., Magnetic storm effects in the tail of the magnetosphere, *Space Sci. Rev.*, Vol. 7, pp.149, 1967)
- [26] Sonnerup B. U. O., and Priest E. R., Resistive MHD stagnation-point flows at a current sheet, *J. Plasma Phys.*, Vol. 14, pp. 161, 1970)
- [27] Dessler A. J., Magnetic merging in the magnetospheric tail, *J. Geophys. Res.*, Vol. 73, pp. 209-214, 1968
- [28] Dessler, A. J., Vacuum merging: A possible source of the magnetospheric cross-tail electric field, *J. Geophys. Res.*, Vol. 76, pp. 3174-3176, 1971
- [29] Alfvén H., Some properties of magnetospheric neutral surfaces, *J. Geophys. Res. Space Phys.*, Vol. 73, No. 13, pp. 4379-4381, 1968
- [30] Biskamp D., Schwarz E., and Drake J. F., Two-fluid theory of collisionless magnetic reconnection, *Phys. Plasmas*, Vol. 4, No. 4, pp. 1002-1009, 1997
- [31] Drake J. F., Biskamp D., and Zeiler A., Breakup of the electron current layer during 3-D collisionless magnetic reconnection, *Geophys. Res. Lett.*, Vol. 24, No. 22, pp. 2921-2924, 1997
- [32] Shay M. A., and Drake J. F., The role of electron dissipation on the rate of collisionless magnetic reconnection, *Geophys. Res. Lett.*, Vol. 25, No. 20, pp. 3759-3762, 1998
- [33] Forbes T. G., and Priest E. R., On reconnection and plasmoids in the geomagnetic tail, *J. Geophys. Res.*, Vol. 88, No. A2, pp. 863-870, 1983
- [34] Wu S. T., Wang A. H., Plunkett S. P., and Michels D. J., Evolution of global-scale coronal magnetic field due to magnetic reconnection: The formation of the observed blob motion in the coronal streamer belt, *Astrophys. J.* Vol. 545, No. 2, pp. 1101-1115, 2000
- [35] Uberoi M. S., Some exact solutions of magnetohydrodynamics, *Phys. Fluids*, Vol. 6, No. 10, pp. 1379-1381, 1963

- [36] Chapman S., and Kendall P.C., Liquid instability and energy transformation near a magnetic neutral line: a soluble non-linear hydromagnetic problem, *Proc. Royal Soc., series A*, Vol. 271, pp. 435-448, 1963
- [37] Sonnerup B. U. O., Magnetic-field line re-connexion in a highly conducting fluid, *J. Plasma Phys.*, Vol. 4, pp. 161-174, 1970
- [38] Yeh T., and Axford W. I., On the re-connexion of magnetic field lines in conducting fluids, *J. Plasma Phys.* Vol. 4, part 2, pp. 207-229, 1970
- [39] Stevenson J. C., Numerical studies of magnetic field annihilation, *J. Plasma Phys.*, Vol. 7, part 2, pp. 293-311, 1972
- [40] Cowley S. W. H., Magnetic field-line reconnection in a highly-conducting incompressible fluid: properties of the diffusion region, *J. Plasma Phys.*, Vol. 14, part. 3, pp. 475-490, 1975
- [41] Parker E. N., Comments on the reconnexion rate of magnetic fields, *J. Plasma Phys.*, Vol. 9, part 1, pp. 49-63, 1973
- [42] Giovanelli R. G., Some comments on solar reconnection problems, *Geophys. Monograph* 30, pp. 357-359, American Geophys. Union, 1984
- [43] Heikkila, W. J., Critique of fluid theory of magnetospheric phenomena, *Astrophys. Space Sci.*, Vol. 23, pp. 261-268, 1973
- [44] Ohya N., Okamura S., and Kawashima N., Strong ion heating in a magnetic neutral point discharge, *Phys. Fluids*, Vol. 17, No. 11, pp. 2009-2013, 1974
- [45] Ohya N., Okamura S., and Kawashima N., Simulation experiment of the current disruption and plasma acceleration in the neutral sheet, *J. Geophys. Res.*, Vol. 79, No. 13, pp. 1977-1979, 1974
- [46] Stenzel R. L., and Gekelman W., Magnetic field line reconnection experiments 1. Field Topologies, *J. Geophys. Res.*, Vol. 86, No. A2, pp. 649-658, 1981
- [47] Gekelman W., and Stenzel R. L., Magnetic field line reconnection experiments 2. Plasma Parameters, *J. Geophys. Res.*, Vol. 86, No. A2, pp. 659-666, 1981



- [48] Gekelman W., Stenzel R. L., and Wild N., Magnetic field line reconnection experiments 3. Ion acceleration, Flows, and Anomalous scattering, *J. Geophys. Res.*, Vol. 87, No. A1, pp. 101-110, 1982
- [49] Stenzel R. L., Gekelman W., and Wild N., Magnetic field line reconnection experiments 4. Resistivity, Heating, and Energy flow, *J. Geophys. Res.*, Vol. 87, No. A1, pp. 111-117, 1982
- [50] Stenzel R. L., Gekelman W., and Wild N., Magnetic field line reconnection experiments 5. Current disruptions and double layers, *J. Geophys. Res.*, Vol. 88, No. A6, pp. 4793-4804, 1983
- [51] Bratenahl A., and Baum P. J., A plasmoid release mechanism that could explain the sub-storm's impulse earthward diversion of cross-tail current, *Geophys. Monograph* 30, pp. 347-354, American Geophys. Union, 1984
- [52] Bratenahl A., and Yeates C. M., Experimental study of magnetic flux transfer at the hyperbolic neutral point, *Phys. of Fluids*, Vol. 13, No. 11, pp. 2696-2709, 1970
- [53] Yamada M., Ono Y., Hayakawa A., Katsurai M., and Perkins F. W., Magnetic Reconnection of Plasma Toroids with Cohelicity and Counterhelicity", *Phys. Rev. Letters*, Vol. 65, No. 6, pp. 721-724, 1990
- [54] Yamada M., Ji H., Hsu S., Carter T., Kulsrud R., Bretz N., Jobs F., Ono Y., and Perkins F., Study of driven magnetic reconnection in a laboratory plasma. *Phys. Plasmas*, Vol. 4, No. 5, pp. 1936-1944, 1997
- [55] Ji H., Yamada M., Hsu S., and Kulsrud R., Experimental test of the Sweet-Parker model of magnetic reconnection, *Physical Rev. Lett.*, Vol. 80, No. 15, pp. 3256-3259, 1998
- [56] Chen F. F., *Introduction to Plasma Physics and Controlled Fusion*, Vol. I: Plasma Physics, second. ed., Plenum Press, NY, 1984
- [57] Deaconu S., Coleman H. W., and Wu S. T., Assessment of the magnetic field reconnection potential for space propulsion applications, *AIAA 2000-2270*, 31-st Plasma Dynamics and Lasers Conference, Denver, Co., 2000

- [58] Deaconu S., Coleman H. W., and Wu S. T., "Experimental Characterization of a Thermionic-Arc Discharge Ionization Device for Flowing Gases," *Rev. Sci. Instrum.*, Vol. 73, No. 1, pp. 91-97, January 2002
- [59] Lovberg, R. H., Magnetic probes, in *Plasma diagnostic techniques*, edited by Huddleston, H. R., and Leonard, L. S., Academic Press, New York, 1965
- [60] Sutton, G. W., and Sherman, A., *Engineering magnetohydrodynamics*, McGraw-Hill Book Co., NY, 1965
- [61] Lorrain, P., and Corson, D., R., *Electromagnetic fields and waves*, sec. ed., W.H. Freeman and Co., San Francisco, 1970
- [62] Stix, T., H., *The theory of plasma waves*, Advanced Monograph Series, McGraw-Hill, NY, 1962
- [63] Sigmond R. S., and Goldman M., "Corona Discharge Physics and Applications," in *NATO Adv. Sci. Inst. Series - Electrical Breakdown and Discharges of Gases*, Plenum Press, 1981, Vol. 89B, pp. 1-65, (edited by Kunhardt E. E., and Luessen L. H.)
- [64] Ferreira C. M., and Delcroix J. L., *J. Appl. Phys.* Vol. 49, No.4, pp. 2380-2395, April 1978
- [65] S. Tanaka, M. Akiba, H. Horiike, Y. Okumura, and Y. Ohara, *Rev. Sci. Instrum.*, Vol. 54, No. 9, pp.1104-1112, September 1983
- [66] D. M. Goebel and A. T. Forester, *Rev. Sci. Instrum.*, Vol. 53, No. 6, pp. 810-815, June 1982
- [67] Melissinos A. C., "Experiments in Modern Physics," Academic Press, 1966, pp. 65-70
- [68] Raizer Y. P., "Gas Discharge Physics," Springer Verlag, Berlin 1991
- [69] Anderson J. D., "Fundamentals of Aerodynamics," McGraw-Hill, New York 1984
- [70] Y. B. Zel'dovich, Y. P. Raizer, "Physics of Shock Waves and High Temperature Hydrodynamic Phenomena," edited by W. D. Hayes and R. F. Probstein, Vol. 1, Academic Press, New York 1966

[71] Vriens L., Smeets A. H. M., and Cornelissen H. J., "Modeling of a Glow Discharge," NATO ASI Series. Series B, Physics, Vol. 89B, 1981, pp. 65-117

[72] Sigmond R. S., "Simple Approximate Treatment of Unipolar Space-Charge-Dominated Coronas: The Warburg Law and the Saturation Current," J. Appl. Phys. 53(2), Feb. 1982, pp. 891-898

# **MHD Accelerator Technology Research at the UAH Propulsion Research Center**

## **INTRODUCTION**

Magnetohydrodynamics (MHD) has been extensively studied for the past several decades for the potential application in power generation, space propulsion, hypersonic wind tunnel facilities and onboard flow control systems, etc. MHD accelerators are critical for most of these applications. MHD technologies are based on the principles of electromagnetic induction in conducting plasma fluids. In a MHD accelerator or thruster, the thrust is produced through electro-magnetic body forces (Lorentz force) created from the interaction between the current carried by the plasma and the applied or self-induced magnetic field. It uses direct electro-magnetic body force to accelerate the plasma fluids, so it doesn't like the chemical rockets, which is limited by the available chemical reaction energy. A propulsion system driven by MHD accelerators can achieve very high specific impulse, so it is suitable for long duration space missions.

The objective of this research project is to evaluate and develop MHD accelerator technology for application to advanced propulsion system. The experimental investigations of several MHD accelerator configurations coupled with a microwave thruster are underway at our Advance Propulsion Lab in the University of Alabama in Huntsville Propulsion Research Center (UAH PRC). All kind of accelerator configurations can be tested in this Lab includes Faraday type current accelerators Hall type thrusters and MPD thrusters, etc. The microwave-generated plasma, which is in highly non-equilibrium, is expanded through a thermodynamic nozzle to MHD plasma accelerators. A 2-inche long Faraday type continuous electrode crossed-field accelerator has been tested for further acceleration and ionization of the microwave plasma. A linear laboratory type rectangular Hall current accelerator has been constructed, and the testing of this thruster coupled with the plasma generated by the microwave plasma, and/or the Faraday type continuous electrode crossed-field accelerator is underway.

**The Advanced Propulsion Laboratory** is the major facility in UAH Propulsion Research Center for advanced electric and MHD propulsion, and plasma physics research. The research activities conducted in this Lab include plasma generation, performance studies of electromagnetic plasma thrusters, testing and development of advanced MHD technology, and basic research in plasma physics problems relevant to plasma propulsion, and development of electrostatic probes and optical diagnostics.

A 6kW microwave generator coupled to a propellant and steam feed system and a thruster can be used to produce plasma. A vacuum system consisted of an 18-inch diameter by 24-inch length glass cylinder, and is capable of maintaining pressures down to  $10 \times 10^{-3}$  torr. Figure 1 shows the vacuum chamber with a plasma thruster operating inside it. A 300KW DC power sources provides the electrical power for the plasma thrusters. The maximum output of the DC power source is 60V/1000A, or 500V/600A. A much larger vacuum facility, as shown in Figure 2, is being installed in UAH.



Figure 1 the picture of the vacuum chamber with a plasma thruster operating inside it.

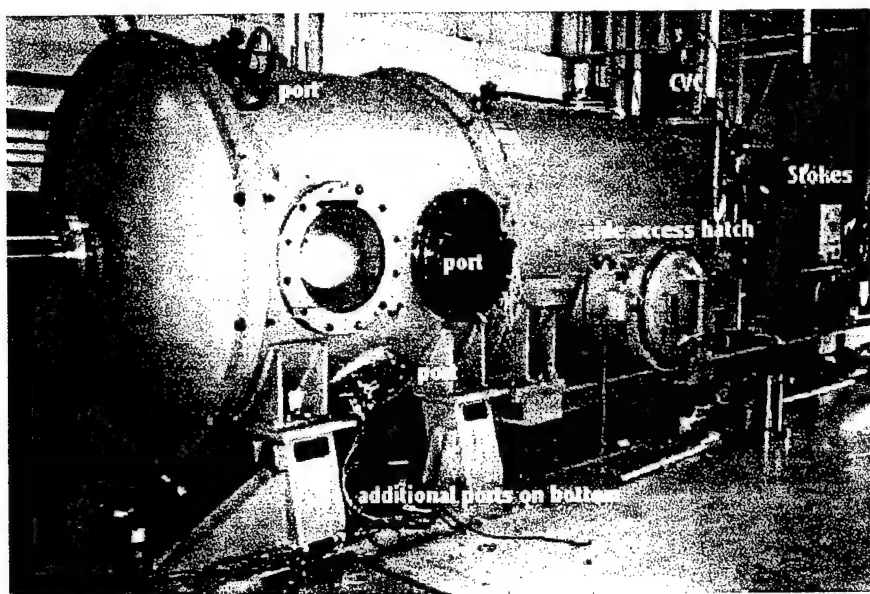


Figure 2 the picture of the UAH PRC new vacuum facility.

The laboratory is well equipped with diagnostic equipments. Single, double, and multi Langmuir probes and other electrostatic probes along with a high-speed step motor position system are used to measure plasma properties. An ultraviolet vacuum spectrometer, a SPEX 1-m double spectrometer, a mass spectrometer, and a goniometry are available in the laboratory for use on research projects. A Spectra-Physics Nd: YAG laser and a Princeton Instruments ICCD camera with related optics are also currently in use for optical diagnostics. A 500MHz, 1Gsa/s HP Infinium Oscilloscopes and a high-speed computer data acquisition system allow real-time measurements.

**MHD Accelerators** can be divided into two categories. One is the Faraday type crossed-field accelerator, and another one is Hall current accelerator. As shown in Figure 3, the crossed-field accelerators utilize the Lorentz force that is  $\mathbf{J} \times \mathbf{B}$  to accelerate the plasma flow. The schematic of a typical Faraday type crossed-field accelerator is shown in Figure 3(a).

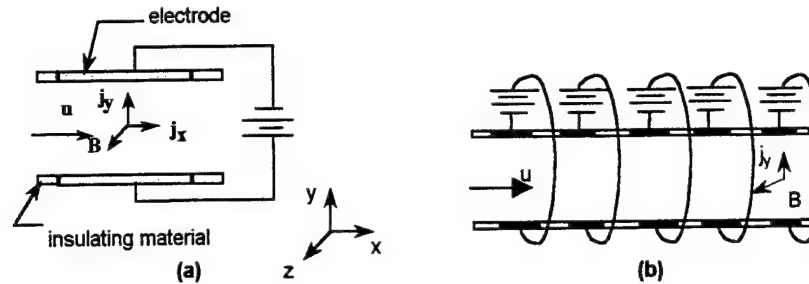


Figure 3 Crossed-field Faraday accelerator configurations. (a) Continuous-electrode, (b) Segmented-electrode.

Due to the Hall effect, current component perpendicular to the applied electrical field direction are produced. This current component is so called Hall current. In this configuration,  $j_y$  is the regular current and  $j_x$  is the Hall current. The conductivity along the  $\mathbf{E}$  field direction has been reduced due to the Hall effect. As shown in Figure 3(b), the segmented-electrode accelerator, in which several pairs of segmented electrodes are used, and each pair of electrodes are connected separately to an external power supply, are proposed to avoid the Hall effect. In both of the two Faraday accelerators, the acceleration force is  $\mathbf{j}_y \times \mathbf{B}$ .

However, an alternative approach is to use the Hall current directly to produce an axial acceleration instead of suppressing it. Figure 4 shows a Hall current accelerator with constant cross section area channel<sup>9</sup>. In this configuration, an axial electrical field is applied. The resulting current flow interacts with the transverse  $\mathbf{B}$  field inducing a Hall current across the accelerator. The segmented electrodes are short-circuited to encourage this Hall current. The Hall current  $j_y$  interacts with the  $\mathbf{B}$  field and produces an accelerating force along the fluid flow direction. A Figure 5 shows two kinds of coaxial Hall current accelerator configurations. In both the cases, the azimuthally Hall current interacting with the applied radial magnetic field component produces an axial Lorentz force  $j_\theta B_r$  that acts upon and accelerates the plasma. Hall current accelerator needs only one power supply, and has performance advantages in cases with large Hall parameters.

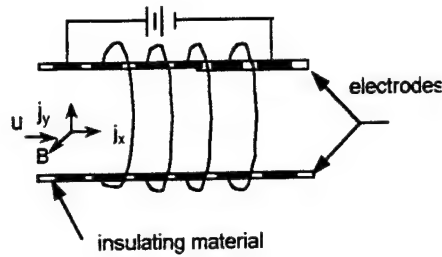


Figure 4 Linear Hall current accelerators.

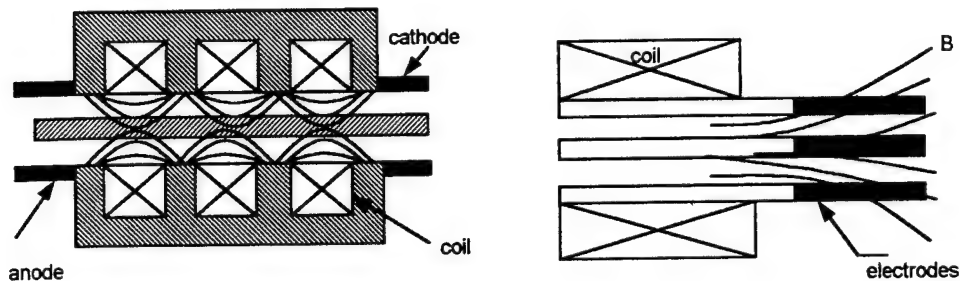


Figure 5 Coaxial Hall current accelerator configurations. Left: utilizing an axial electric field and radial magnetic field. Right: utilizing a radial electric field and a slanted magnetic field with segmented electrodes.

In the past decade, the electric propulsion community has conducted a lot of research on Hall thrusters and MPD thrusters. The Hall thruster actually is a variation of the Hall current accelerator in Figure 5 left. They claim that it works as an electrostatic acceleration device, and has demonstrated good performance at low power levels (<15 KW). The MPD thruster, which has a coaxial configuration with a cathode core, produces thrust by the interaction of a self-induced magnetic field with the radial current. The MPD thruster operates at very high power levels (induces an adequate B field) to achieve a high efficiency. In this research, we are looking for some MHD plasma accelerator configurations, which may work in the power range between the Hall and MPD thrusters, and with acceptable efficiency.

### EXPERIMENTAL SETUP

The experimental setup for testing microwave plasma MHD accelerators includes a microwave plasma generation system, propellant and steam feed system, a vacuum system, microwave thruster, MHD accelerators, power supplies, and plasma diagnostic and data acquisition system.

Figure 6 shows the schematic diagrams of the vacuum chamber, and the microwave thruster. Microwaves generated by a 0~6 kW variable power microwave generator are

delivered to a 4-inch diameter by 8-inch long  $TM_{011}$  mode resonant cavity operating at 2.45GHz by several components of WR 284 wave-guide. A propellant and steam feed system is also mounted to the cavity to supply propellant gases (Argon, helium, nitrogen, carbon dioxide and steam). The plasma is expanded to the vacuum chamber from the cavity through a converging-diverging nozzle after it is heated in the microwave field. In the tests presented in this paper, a large nozzle with a throat diameter 3.81mm and area ratio 7.11 was used.

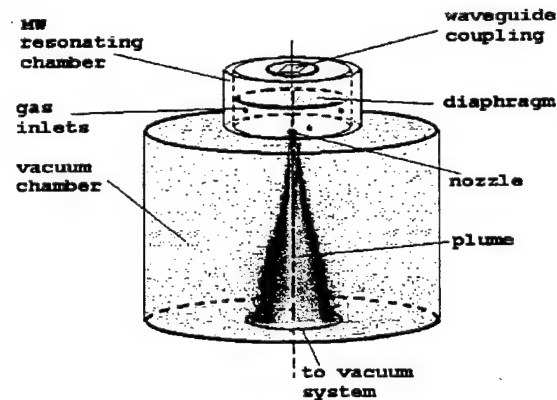


Figure 6 Schematic diagrams of the vacuum chamber and microwave thruster.

### Faraday type crossed-field MHD accelerator

The picture of a laboratory type continuous electrode crossed-field MHD accelerator constructed in UAH PRC is shown schematically in Figure 7. The channel body was made with Boron Nitride. The channel length is 2.4 inches. The cross section is approximately 0.55 inch wide by 0.60 inch high. The anode and cathode are 1.9 inch long and were made using copper. The electrodes are not water-cooled, which puts limits on the operating current and the time duration of the tests. A permanent magnet is used to apply a magnetic field to the channel, and the distance between the two magnetic poles is 1.2 inches. A maximum magnetic field of 0.3 Tesla has been measured. A 300KW DC power supply provides the electrical power for the plasma accelerator. The maximum output of the DC is 60V/1000A, or 500V/600A.



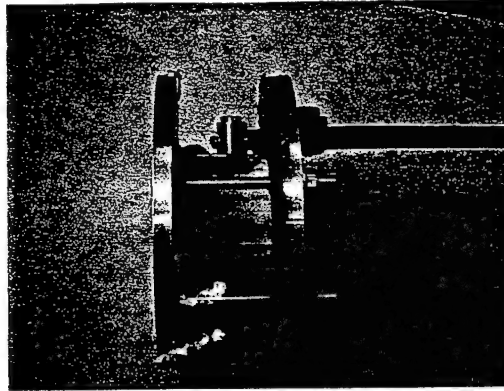


Figure 7 the picture of the crossed-field plasma accelerator assembly (without magnet).

### Rectangular type Hall current accelerator

A laboratory type Hall current accelerator has been constructed, and is under test in UAH PRC Advanced Propulsion Lab. As shown in Figure 8, there are five pairs of copper electrodes cast inside the accelerator. Each pair of electrodes, which are installed facing each other in the two opposite walls, is connected together. The two pairs of electrodes in the front and the end of the channel will be connected to the 300KW power supply afore mentioned in this paper. The channel body is cast using castable high temperature alumina base ceramics. The ceramic materials can withstand up to 3200°F, and the dielectric strength is 200 volts/mm. The actual channel length is 3.8 inches. The cross section is 0.8 inch by 0.8 inch. Each electrode is 3/8-inch in thickness, and the internal distance between two-neighboring electrodes is 0.25 inch. The same kind of permanent magnet used in the Faraday type accelerator is used here to provide the magnetic field. Also, the electrodes are not water-cooled. Current transducers (shunts) are integrated in the circuits of the channel to measure the Hall current.

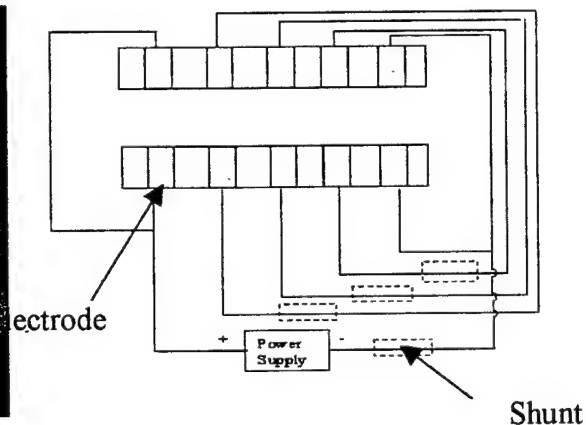
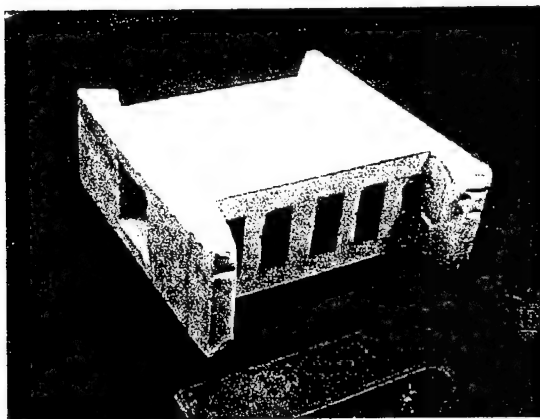


Figure 8 the picture and circuits of the laboratory type Hall current accelerator.

## DIAGNOSTICS

An open-circuit diagnostic MHD channel has been constructed to measure the open-circuits voltage of the plasma from the accelerators. As shown in Figure, the two electrodes are disconnected from the power supply, and are in 'open' status to. Due to the existence of the magnetic field and a plasma flow velocity that is not parallel to the magnetic field, an induced Faraday electric field  $V \times B$  is created. The velocity is estimated using the following formula:

$$E_y = \frac{V_{open-cir}}{L} = \alpha U B$$

Where,  $E_y$  is the average electrical field,  $L$  is the distance across the electrodes,  $V_{open-cir}$  is the measured total voltage, and  $U$  is velocity.  $B$  is calculated as the average of the whole magnetic field. The  $\alpha$  is called the efficient factor ( $<1$ ).

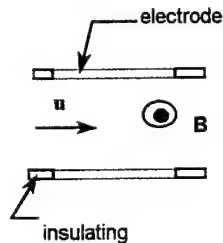


Figure 9 Schematic diagrams of the Open-circuit diagnostic channel.

**Emissive probes**<sup>12, 13, 14</sup> were constructed to measure the plasma potential and E field of the accelerator plume. As shown in Figure 10, the probe is heated by a floating DC power source to continually emitting electrons from the heating surface. If the electron emissions exceeds the electron-saturation current, the probe will tend to float at a potential close to the plasma potential<sup>12</sup>.

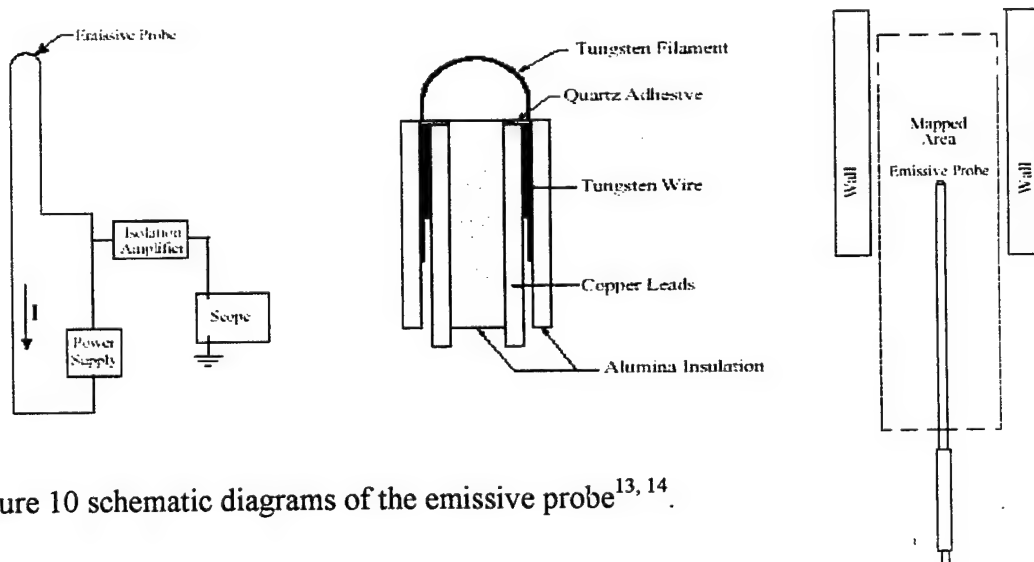


Figure 10 schematic diagrams of the emissive probe<sup>13, 14</sup>.

The single, double, triple, and quadruple Langmuir probes are used to measure plasma properties. A **triple probes**, as shown in Figure 11, is used to map the plasma field of the Hall current accelerator.

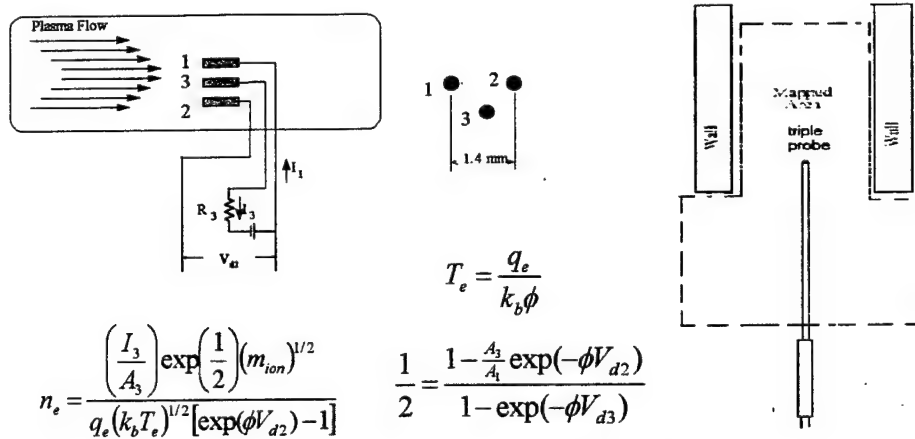


Figure 11 Schematic diagrams of the triple probes.

A **Faraday probes**<sup>6</sup> are constructed to measure the ion current distribution across the accelerator exit plane. The probe, as shown in Figure 12, is biases to collect the ion current. By dividing the surface area, we can get the local ion current density. This is important for us to know the actually acceleration directions.

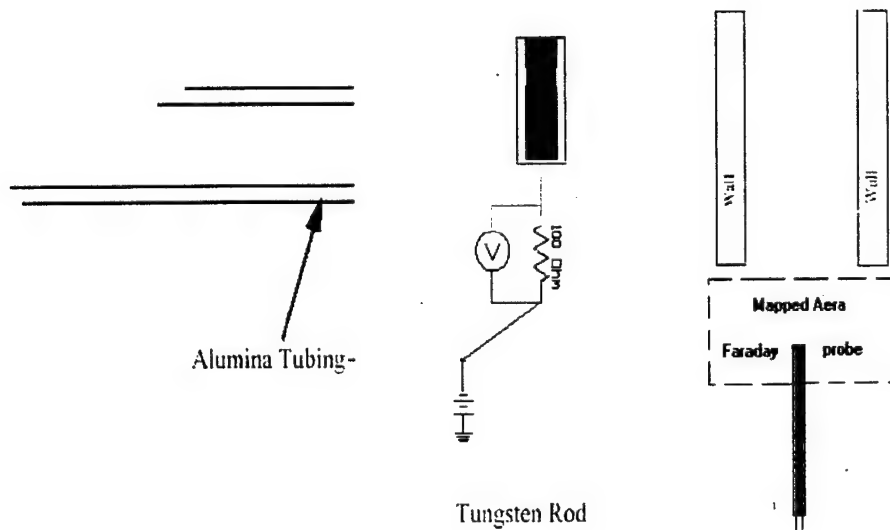


Figure 12 Schematic diagrams of the Faraday probes<sup>6</sup>.

We do have the ability and equipments to do optical **non-intrusive diagnostics**. Due to the small available space of the current vacuum chamber, the optical diagnostics will be postponed to when the larger vacuum tank available.

## RESULTS

The testing of both the Faraday type cross-field accelerator, and the rectangular type Hall current accelerator are underway. A lot of data have been collected waiting to be analyses. The following two Figures show some of the partial results of the testing.

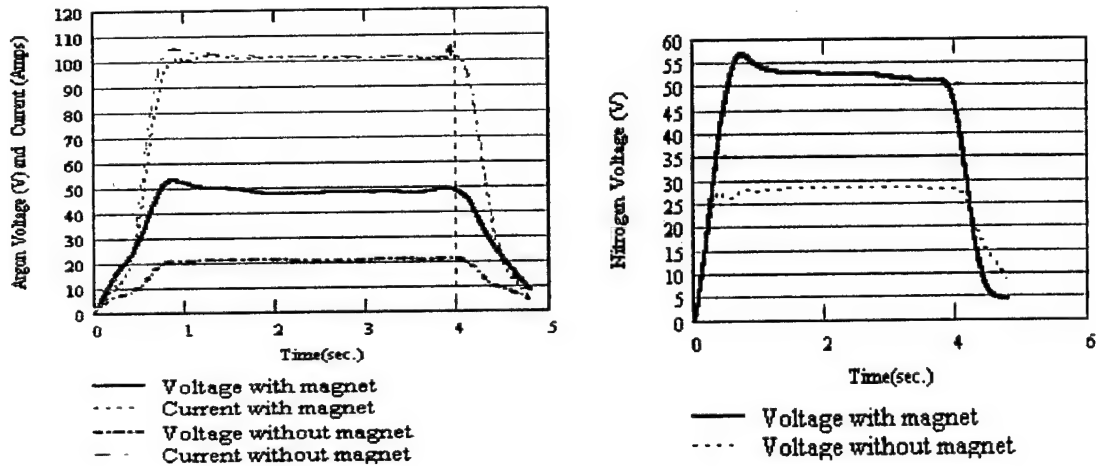


Figure 12 Discharge voltages and current for the **Faraday type cross-field accelerator** (DC power is turned off after 4 seconds). Left: use argon gas. Right: use nitrogen gas.

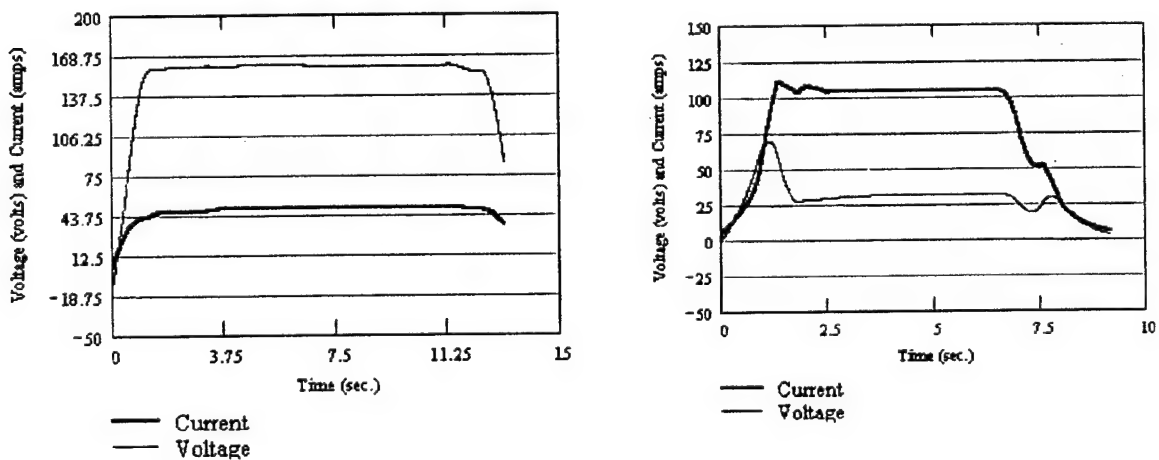


Figure 14 rectangular types Hall current accelerator discharge voltage and current (without magnet). Left: Nitrogen. Right: Argon.

## REFERENCE

<sup>1</sup>Li, Zhongmin, Jones, J.E., Hawk, W.C., "Experimental Study of Microwave Plasma MHD Accelerators," AIAA-2000-3882, July 2000.

<sup>2</sup>Li, Zhongmin, Hawk, W.C., Jones, J.E., "Experimental Study of A Crossed-Field MHD Accelerator Coupling with Microwave Plasma," AIAA-2001-3495, July 2001.

<sup>3</sup>Jones, J. E., "An Assessment of Microwave Generated Plasma for Use in Magnetohydrodynamic Accelerators," PhD dissertation, MAE department, Univ. of Alabama in Huntsville.

<sup>4</sup>Li, Zhongmin, Hawk, W.C., Jones, J.E., "Experimental Investigation of MHD Plasma Accelerators for In-Space Propulsion Application," Pennsylvania State University Propulsion Engineering Research Center 13<sup>th</sup> Annual Symposium on Propulsion, 22-23 October 2001, Huntsville, AL.

<sup>5</sup>Macheret, S.O., Miles, R.B., and Nelson, G.L., "MHD Acceleration of Supersonic Air Flows Using Electron Beam – Enhanced Conductivity," AIAA 98-2922, June 1992.

<sup>6</sup>Kim, S.-W., *Experimental Investigations of Plasma Parameters and Species-Dependent Ion Energy Distribution in the Plasma Exhaust Plume of a Hall Thruster*, Ph.D. Thesis, University of Michigan Department of Aerospace Engineering, University Microfilms International, 1999.

<sup>7</sup>Bajovic, Valentina S, "A Reliable Tool for the Design of Shape and Size of Faraday Segmented MHD Generator Channel," *Energy Conversion and Management*, Vol.37, No.12, pp.1753-1764, 1996.

<sup>8</sup>Simmons, G.A., Nelson, G.L., and Lee, Y.M. "Analysis of An unseeded, Non-equilibrium MHD Accelerator Concept For Hypersonic Propulsion Ground Testing applications," AIAA 92-3994, July 1992.

<sup>9</sup>Sutton, George W, Sherman, Arthur, *Engineering Magnetohydrodynamics*, McGraw-Hill, Inc, New York, 1965.

<sup>10</sup>Rosa, R.J., George, *Magnetohydrodynamics, Energy Conversion*, revised printing, Hemisphere Publishing Corp., Washington, 1987.

<sup>11</sup>Burton, R.L., Bufton, S.A., Tiliakos, N.T., and Krier, H., "Application of Multiple Electrostatic Probes to a Low Power Arc jet," *Journal of Propulsion and Power*, 1994.

<sup>12</sup>Hutchinson, I., *Principles of Plasma Diagnostics*, Cambridge University Press, New York, 1987.

<sup>13</sup>Hershkowitz, N., Cho, M., "Measurement of Plasma Potential Using Collecting and Emitting Probes," *Journal of Vacuum Science & Technology A*, Vol. 6, No. 3, May 1988, p.2054.

<sup>14</sup>J.M. Haas, A.D. Gallimore, "Considerations on the Role of the Hall current in a Laboratory-Model Thruster," AIAA 2001-3507, Salt Lake City, UT, 2001.

# **Electrical Transport Properties of Pulsed Microwave Plasmas**

Jonathan E. Jones and Clark W. Hawk  
Propulsion Research Center  
The University of Huntsville in Alabama

## **Abstract**

The determination of electrical transport properties of microwave generated plasmas is of interest for applications ranging from under water, vapor deposition to advanced magnetohydrodynamic propulsion. It is of particular interest to investigate the onset and decay of the microwave discharge. Transport properties of a 60 Hz pulsed microwave plasma generator are being studied via Langmuir Probes, spectroscopic line reversal, and Thompson/Rayleigh Scattering. The properties are being measured in the microwave resonant cavity as well as in plumes injected under water and in vacuum. Properties have been measured in plasmas generated from argon, nitrogen, and air. In addition, the microwave plasma generator has been operated with steam. In the near term, the measurements are being used to determine appropriate operating parameters of a MHD accelerator.

For both the MHD accelerator and under water, vapor deposition it is desirable to obtain real time feed back of the electrical transport properties to allow control of vital parameters. While Langmuir probes can provide real time feed back, they are intrusive in nature and require long processing times to interpret the data. Spectroscopic and scattering techniques are non-intrusive, but require optical access to the plasma and long processing times. To aid in providing real time property evaluations, Neural Networks can be trained to interpret both Langmuir probe characteristics and Rayleigh/Thompson scattered spectrums. If successful, real time diagnostic techniques would allow optimization of MHD accelerator performance, as well as, providing an invaluable tool for studying plasmas in proposed fusion, antimatter, and laser based rockets.

## **Introduction**

The Advanced Propulsion Laboratory at UAH's Propulsion Research Center was established in 1996 to investigate the performance of H<sub>2</sub>OTSTUF (H<sub>2</sub>O Thermionic Solar Thermal Upperstage Flight). A resonant cavity microwave plasma generator (MPG) produces plasma to feed a magnetohydrodynamic (MHD) accelerator. The MPG has been operated with nitrogen, air, argon, and steam. Past work on the MPG has focused on its use as a plasma thruster. Tests and theoretical studies have shown that the MPG thruster is an attractive alternative to arcjets by measuring its thrust and specific impulse. In order to use the MPG as the front end for a MHD accelerator, the electrical transport properties of the generated plasma need to be characterized.

The microwave plasma generator currently being used is powered with a power supply out of a Panasonic 1 kW microwave oven. The power supply is half wave rectified; thus the microwave power is not continuous but pulses on and off sixty times a second. Unfortunately this was not realized in early experiments resulting in considerable confusion in trying to determine were the

60 Hz noise was coming from. Even with the realization that the microwave was pulsing on and off, a considerable effort has been required to appropriately measure the unsteady properties of the plasma.

A 6 kW continuous microwave generator is currently on order to provide a steady state plasma. This will aid in verifying results in of diagnostic techniques used in the pulsed plasma, as well as, providing continuous plasma for the MHD accelerator.

## Experimental Setup

### General

The layout of the lab is shown in Figure 1. A 300-CFM roughing pump can maintain pressures from 1 to 10 Torr. A Spectra Physics GCR-290 Nd-YAG laser provides 1 J per pulse at 532 nm operating at 10 Hz. The Nd-YAG is also seed injected, which narrows the line width to  $0.002 \text{ cm}^{-1}$  allowing discrimination of the Doppler shifted component in scattering experiments. The Burleigh 170 mm aperture Fabry-Perot Interferometer has a variable free spectral range and resolution of 1.4 – 1,500 GHz and 20 MHz – 750 GHz respectively. The Princeton Instruments ICCD camera has a 1024 X 256 pixel intensified array. The ICCD camera can be gated to 5 ns effectively eliminating background room light. Also, available for data acquisition are a 32 channel 1.25 MS/second National Instruments board, and a 2 channel 5 MS/second Hewlett Packard Infinium oscilloscope.

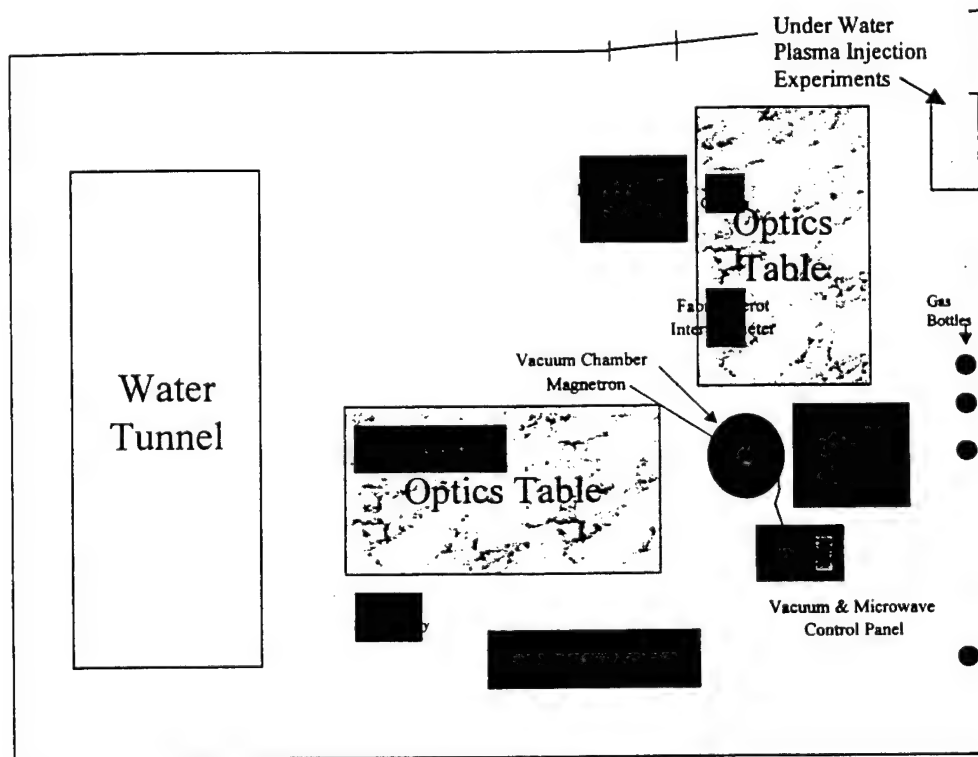


Figure 1 shows the layout of the Advanced Propulsion Laboratory.

## Langmuir Probes

Both single and multiple probe Langmuir or electrostatic probes have been used to measure electron density and temperature. For single and double wire probes a floating probe voltage ramp is applied to obtain the probe characteristic. The theory of Langmuir probes has been described extensively in the literature and for brevity will not be repeated here. The layout of a four wire electrostatic probe is given in Figure 2. The four-wire probe measures electron temperature and density and the ratio of the mean flow speed to the ion velocity.

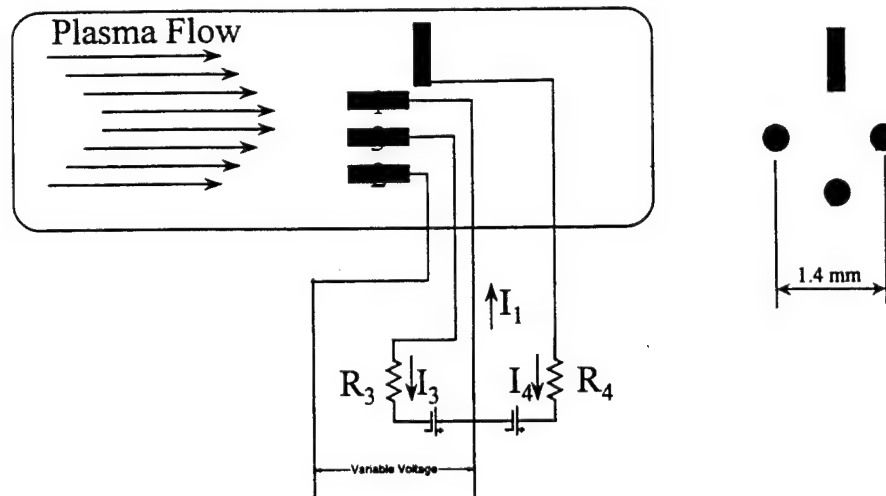


Figure 2 shows the schematic of the four wire, Langmuir probe.

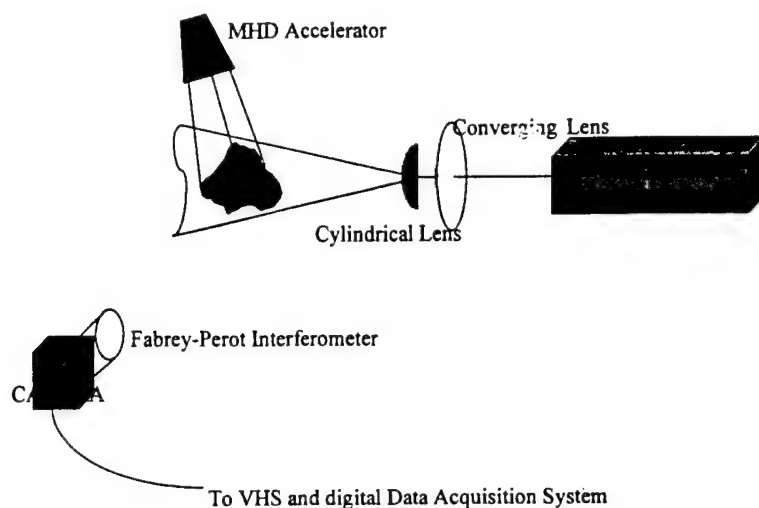
## Rayleigh/Thompson Scattering

Rayleigh scattering is the inelastic scattering of light off of molecules through induction of a dipole on the electron cloud of the molecule. Thompson scattering is the scattering of light from free electrons. Figure 3 shows the optical layout for both Thompson and Rayleigh scattering experiments. The Doppler broadening of the Thompson scattered signal is generally much wider than the Rayleigh scattered signal, thus the free spectral range of the Fabrey-Perot interferometer must be set differently for each signal. The use of an iodine filter can block stray light from the laser and/or the Rayleigh scattered signal when the much weaker Thompson scattered signal is of interest.

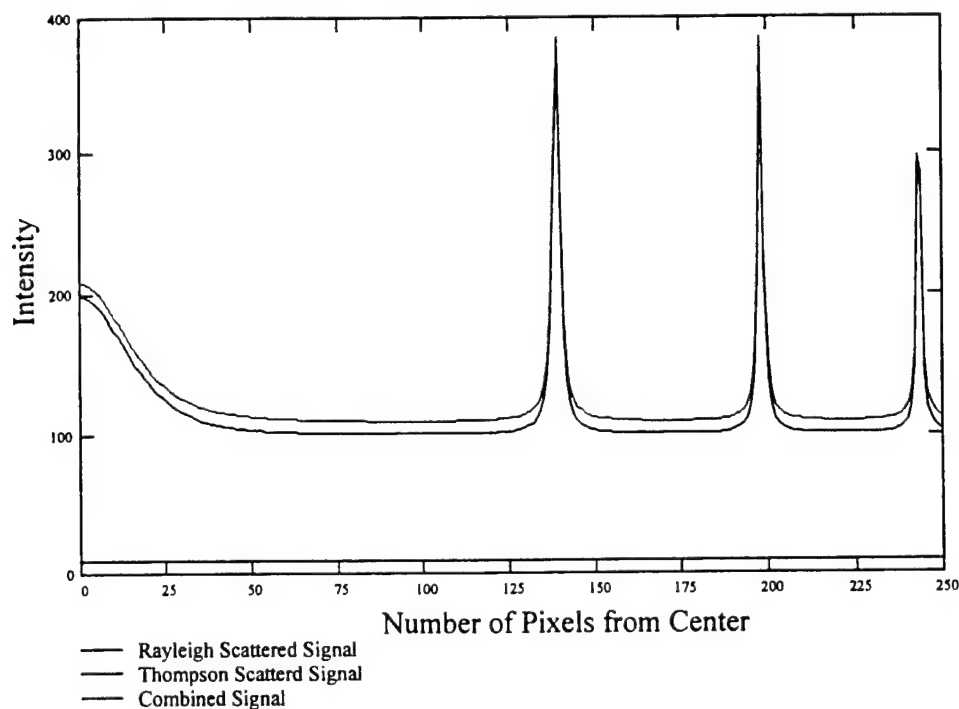
When using Rayleigh Scattering to determine neutral density, it must be remembered that the electrons will add to the intensity of the signal. Figure 4 shows the Rayleigh Scattered spectrum, along with the Thompson scattered signal. Notice that because of the low mass of the electron and high temperature, their Doppler broadened signal is greater than the free spectral range setting of the interferometer; thus the electron signal appears as if it were a component of the broadband background signal. While this gives us information about the electron density, it is impossible to decipher the electron temperature from this measurement. This can be improved by decreasing the distance between the mirrors, increasing the free spectral range. However, for



electron temperature in the range of interest this requires separation distances of less than 0.1 mm. Great care must be taken when using separation distances this small to avoid damaging the interferometer mirrors. A spectrometer can be used to determine temperature from the Thompson scattered spectrum, but the photon detector must be sensitive enough to record the small Thompson scattered signal.



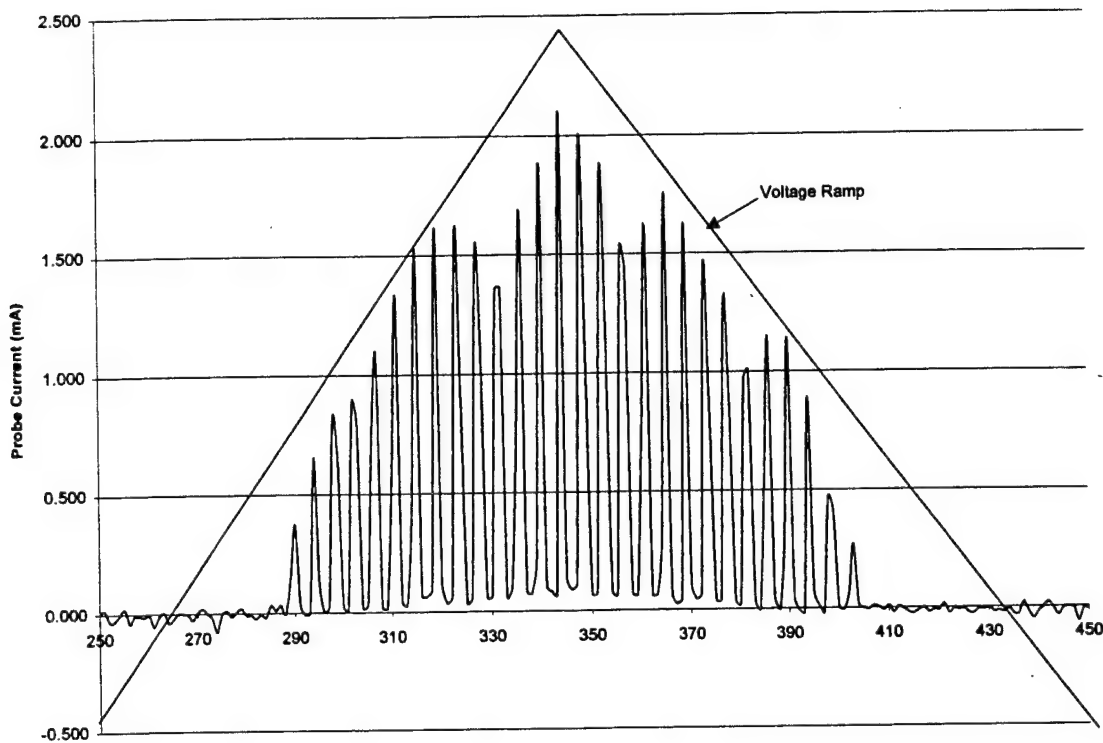
**Figure 3** shows the optical setup of the Rayleigh scattering measurement system.



**Figure 4** shows the Rayleigh Scattered Spectrum from the gas molecules, the Thompson Scattered Spectrum from the electrons, and the combined spectrum.

## Results and Discussion

Most of the work to date has been done with a single wire Langmuir probe. The first attempts were made in the plume of a nozzle with a 40:1 expansion ratio. Due to the cooling during expansion recombination lowered the electron density below the sensitivity of the probe electronics. A screen replaced the nozzle on the resonant microwave cavity. The screen contained the microwaves while allowing the plasma to exit without expanding through the nozzle. This resulted in a detectable signal from the Langmuir probe. Figure 5 shows the current from a single wire Langmuir probe immersed in a Nitrogen plasma with a vacuum chamber pressure of 1 Torr.



**Figure 5** shows the single probe current for a 60 Hz pulsed microwave plasma.

In order to estimate the properties corresponding to when the microwave is on the probe characteristic was taken to be the envelope of the peaks of the signal in Figure 5. Using this method an electron temperature of greater than 30,000 K was calculated, which is much higher than expected. Previous spectroscopic line reversal measurements of the electron density within the microwave cavity gave electron temperature of 7,000 to 10,000 K. However, electron temperatures of 30,000 K are reasonable for low-pressure microwave discharges.

## Conclusions

The Advanced Propulsion Laboratory has the capability of characterizing pulsed microwave discharges. Preliminary results show that at lower pressures electron temperature may be much higher than expected. Utilizing the equipment in the lab and theoretical predictions Neural Networks can be trained to give real time feedback of electrical transport properties.

# **Experimental Investigation of MHD Plasma Accelerators for In-Space Propulsion Application**

Zhongmin Li, Clark W. Hawk  
Propulsion Research Center  
University of Alabama in Huntsville  
Huntsville, Alabama 35899

Jonathan E. Jones  
NASA Marshall Space Flight Center  
Propulsion Research Center  
Huntsville, AL 35812

**Pennsylvania State University**  
**Propulsion Engineering Research Center 13<sup>th</sup> Annual Symposium on**  
**Propulsion**  
22-23 October 2001 / Huntsville, AL

# Experimental Investigation of MHD Plasma Accelerators For In-Space Propulsion Application

Zhongmin Li<sup>\*</sup>, Clark W. Hawk<sup>†</sup>  
*Propulsion Research Center*  
*The University of Alabama in Huntsville*  
*Huntsville, AL 35899*

Jonathan E. Jones<sup>‡</sup>  
*NASA Marshall Space Flight Center*  
*Propulsion Research Center*  
*Huntsville, AL 35812*

## ABSTRACT

Magnetohydrodynamic (MHD) plasma propulsion belongs to the electric propulsion category. MHD plasma accelerators use direct electro-magnetic body force to accelerate the plasma flow. The experimental investigations of MHD accelerators coupled with a microwave thruster for potential in-space propulsion applications are underway at the UAH Propulsion Research Center. The microwave-generated plasma, which is in highly non-equilibrium, is expanded through a thermodynamic nozzle to MHD plasma accelerators. A 2-inche long Faraday type continuous electrode crossed-field accelerator is tested for further acceleration and ionization of the microwave plasma. The test results of the crossed-field accelerator with a 100 amps discharge current are presented. The detailed measurements of electron temperature and density at the entrance and the exit of the MHD channel were obtained by using quadruple Langmuir probes. A linear rectangular type Hall current accelerator has been constructed, and the testing of this thruster coupled with the plasma generated by the microwave plasma, and/or the Faraday type continuous electrode crossed-field accelerator is underway.

## NOMENCLATURE

$B$	Magnetic field strength	$Q_{en}$	Average collision cross section for electrons with all neutral species
$c_e$	Mean thermal speed of electrons	$Q_{el}$	Average collision cross section for electrons with ions
$E$	Local electric field	$q_e$	Electron charge
$\epsilon_0$	Permittivity of vacuum (constant)	$T_e$	Electron temperature
$J$	Current density	$T_g$	Gas temperature
$k_b$	Boltzmann's constant	$V$	Velocity
$m_e$	Electron rest mass	$\beta$	Hall constant ( $1/q_e n_e$ )
$n_e$	Electron number density	$\eta$	Efficiency
$n_n$	Neutral gas number density	$\rho$	Density
$n_s$	Number density of species s	$\sigma$	Electrical conductivity
$Q$	Average collision cross section	$\omega$	Electron cyclotron frequency
$Q_{es}$	Collision cross section for electrons with species s		

<sup>\*</sup> PhD Candidate, liz@email.uah.edu

<sup>†</sup> Director & Professor, hawkc@email.uah.edu

<sup>‡</sup> Aerospace Engineer, MSFC/NASA

$\tau$  Mean time interval between collisions for electrons with ions and neutrals

$\omega\tau$  Hall parameter

## INTRODUCTION

Electric propulsion has been extensively studied for the past several decades with a goal of producing high specific impulses for long duration space missions. Such a system relies on the acceleration of propellants for propulsion through electrical heating, electric body forces, and/or magnetic body forces. So, correspondingly, the various electric propulsion devices can be categorized into three categories, electro-thermal, electro-static, and electro-magnetic propulsion. In electro-magnetic propulsion, the thrust is produced through electro-magnetic body forces (Lorentz force) created from the interaction between the current carried by the plasma and the applied or self-induced magnetic field. The MHD plasma accelerators presented in this paper belongs to this category.

In the past decade, a lot of research has been conducted on Hall thrusters and MPD thrusters. The Hall thruster actually works as an electrostatic acceleration device, and has demonstrated good performance at low power levels (<15 KW). The MPD thruster, which has a coaxial configuration with a cathode core, produces thrust by the interaction of a self-induced magnetic field with the radial current. The MPD thruster operates at very high power levels (induces an adequate B field) to achieve a high efficiency. In this research, we are looking for some MHD plasma accelerator configurations, which may work in the power range between the Hall and MPD thrusters, and with acceptable efficiency.

This research focuses on the investigation of MHD plasma accelerators coupling with non-equilibrium microwave plasma for in-space propulsion applications. The proposed propulsion system includes a microwave thruster, a crossed-field MHD plasma accelerator, and a linear rectangular type Hall current accelerator (or thruster). The microwave thruster is used to produce non-equilibrium plasma for the plasma accelerators, and also preliminarily accelerate the plasma flow. The Faraday type crossed-field accelerator is put in the system for further ionization and acceleration of the plasma. The linear Hall current thruster is the major device for plasma acceleration in this system.

In the microwave thruster, the microwave is guided into a resonating cavity to heat the propellant gas. By adding energy to the electrons using microwave radiation inside the microwave thruster, non-equilibrium plasma can be created where the temperature of the electrons is higher than the temperature of the gas<sup>1</sup>. The resulting free electron density can then be several orders of magnitude higher than electron densities at thermodynamic equilibrium. The non-equilibrium plasmas with an electron temperature much higher than the gas temperature can improve the efficiency of the MHD accelerator by reducing the heat transfer to channel walls, and lowering the thermal energy remaining in flow, while increasing the electrical conductivity of the flow<sup>2</sup>.

Crossed-field plasma accelerators have been the subjects of many theoretical and some experimental studies for possible applications for propulsion devices and wind-tunnel gas accelerators<sup>4, 5, 6, 7</sup>. Due to the boundary layer voltage drop and Hall current effect, it is hard to get high specific impulse at acceptable efficiency (>50%). However, in this research, the crossed-field accelerator is considered as a secondary ionization device to further ionize the gas, and also as one of the three stages of acceleration.

In the rectangular type Hall current accelerator, shown in figure 2, the plasma acceleration is conducted by the Lorentz force produced by the interaction of the Hall current with the applied magnetic field. A Hall current accelerator needs only one power supply, and has performance advantages in cases with large Hall parameters.

## THEORY

### The Generalized Ohm's law

The Generalized Ohm's law governs the interaction of electrically conducting plasma with applied electric and magnetic fields. For partially ionized plasma and neglecting ion-slip, the Generalized Ohm's law may be written in the form of Equation (1)<sup>8</sup>.

$$\mathbf{j} = \sigma [\mathbf{E} + \mathbf{V} \times \mathbf{B} - \beta (\mathbf{j} \times \mathbf{B})] \quad (1)$$

### The Faraday type crossed-field accelerator

The crossed-field accelerators utilize the Lorentz force that is  $\mathbf{j} \times \mathbf{B}$  to accelerate the plasma flow. The schematic of a typical Faraday type crossed-field accelerator is shown in Figure 1(a).

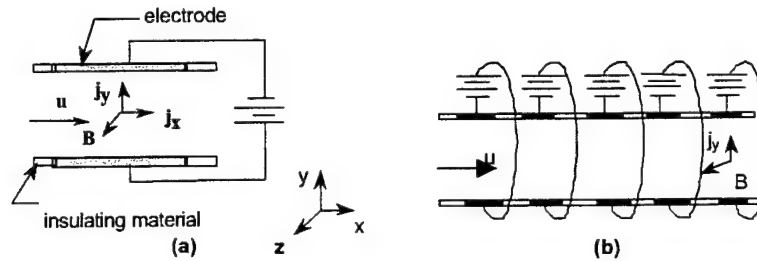


Figure 1 Crossed-field Faraday accelerator configurations. (a) Continuous-electrode, (b) Segmented-electrode.

For the Faraday type continuous electrode accelerator,  $E_x = B_y = B_z = v = w = j_z = 0$ . Thus, expand Equations (1) and rearrange in a Cartesian coordinates system, we get

$$j_x = -\frac{\omega\tau(E_y - uB)}{1 + (\omega\tau)^2} = -\omega\tau j_y \quad (2)$$

$$j_y = \frac{\sigma(E_y - uB)}{1 + (\omega\tau)^2} \quad (3)$$

Where,  $\omega\tau$  is the Hall parameter and can be calculated with the following equation:

$$\omega\tau = \sigma\beta B = \frac{q_e B_0}{m_e c_e \sum_{k,s} n_{k,s} Q_{k,s}} \quad (4)$$

Due to the Hall effect, currents perpendicular to the applied electrical field direction are produced. These currents are so called Hall currents. In this configuration,  $j_y$  is the regular current and  $j_x$  is the Hall current, and the Hall parameter can be interpreted as the ratio of the Hall current to the current parallel to the electric field<sup>8</sup>.

From equation (3), we can consider the conductivity to have been reduced by the factor  $1+\omega\tau^2$  due to the Hall effect. As shown in Figure 1(b), the segmented-electrode accelerator<sup>8</sup>, in which several pairs of segmented electrodes are used, and each pair of electrodes are connected separately to an external power supply, are proposed to avoid the Hall effect.

In the segmented electrode Faraday configuration as shown in Figure 1(b),  $j_x = 0$ . Thus,

$$j_y = \sigma(E_y - uB) \quad (5)$$

The ideal efficiency for this segmented Faraday accelerator is given by

$$\eta_f = \frac{j_y u B}{E_y j_y} = \frac{1}{K_f} \quad (6)$$

Where the loading factor,  $K$  for the Faraday type channel equals

$$K_f = \frac{E_y}{uB_z} \quad (7)$$

The thrust of segmented Faraday accelerator is given by

$$F_x = j_y B = \sigma u B_z^2 [K_f - 1] \quad (8)$$

### Rectangular type Hall current accelerator

However, an alternative approach is to use the Hall current directly to produce an axial acceleration instead of suppressing it. Figure 2 shows a Hall current accelerator with constant cross section area channel. In this configuration, an axial electrical field is applied. The resulting current flow interacts with the transverse B field inducing a Hall current across the accelerator. The segmented electrodes are short-circuited to encourage this Hall current. The Hall current  $j_y$  interacts with the B field and produces an accelerating force along the fluid flow direction.

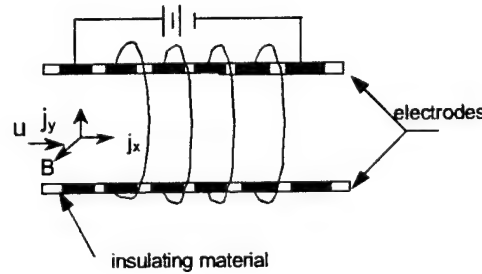


Figure 2 Linear Hall current accelerator.

For the configuration shown in Figure 2,  $E_y = B_y = B_x = v = w = 0$ , which upon substitution into Equations (1), yield

$$j_x = -\frac{\sigma u B_z (\omega\tau)}{1 + (\omega\tau)^2} (1 + K) \quad (9)$$

$$j_y = \frac{\sigma u B_z}{1 + (\omega\tau)^2} [(\omega\tau)^2 K - 1] \quad (10)$$

Where the loading factor  $K$  is defined by

$$K = \frac{E_x}{(\omega\tau)\mu B_z} \quad (11)$$

The ideal efficiency for Hall current accelerator<sup>8</sup> with this configuration is:

$$\eta = \frac{F_x u}{j_x E_x} = \frac{(\omega\tau)^2 K - 1}{(\omega\tau)^2 K(K+1)} \quad (12)$$

The Hall current channel thrust is given by

$$F_x = \frac{\sigma_0 u B_z^2}{1 + (\omega\tau)^2} [(\omega\tau)^2 K - 1] \quad (13)$$

Figure 3 shows that the ideal efficiency of Hall current accelerator can be comparable to that of a segmented Faraday accelerator for a Hall parameter greater than 2. Figure 4 plots the thrust for the Hall and Faraday channels divided by  $\sigma_0 u B_z^2$ . For optimum loading factor the thrust of the Hall accelerator is always lower than that of the Faraday accelerator. However, the thrust increases and the efficiency drops off slowly as the loading factor is increased. As the Hall parameter is increased the apparent disadvantage of the Hall channel is minimized.

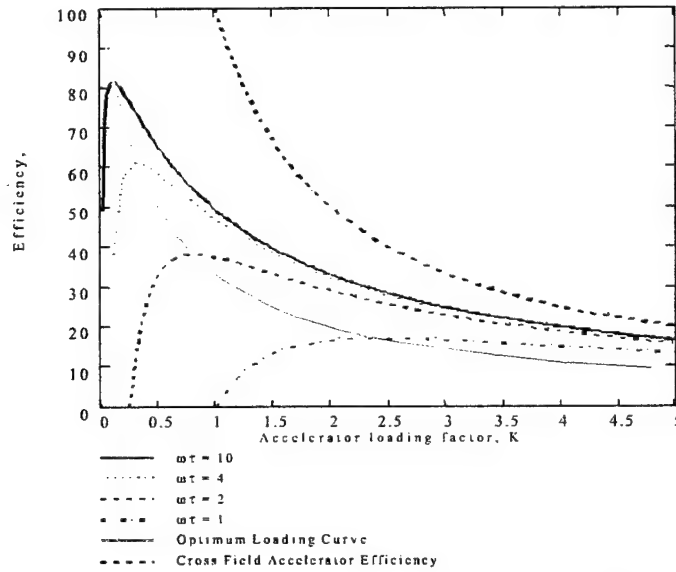


Figure 3 MHD efficiency comparisons for Hall current and Segmented Faraday type accelerators.



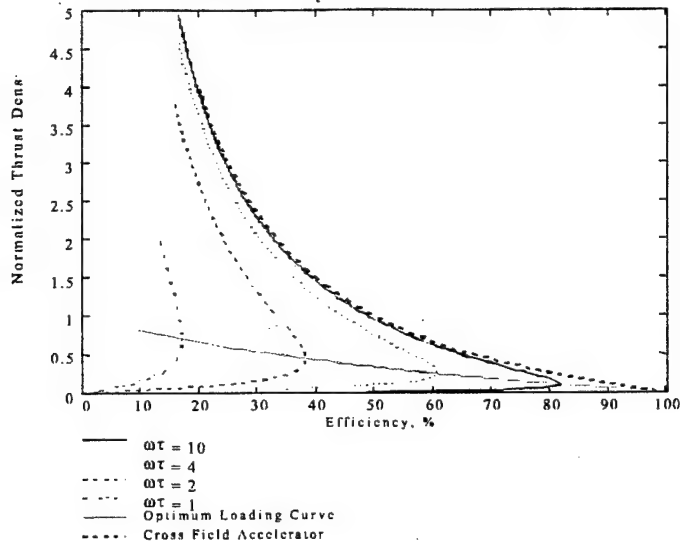


Figure 4 Thrust densities versus efficiency for Hall and segmented Faraday channels.

#### Local electrical conductivity

The scalar electrical conductivity of a mixture of gases can be calculated from the following<sup>8</sup>:

$$\sigma_0 = \frac{n_e q_e^2}{m_e \langle c_e \rangle (n_n \langle Q_{en} \rangle + n_e Q_{el}^*)} \quad (14)$$

Where

$$Q_{en} = \sum_{s \neq e, I} \frac{n_s}{n_n} \langle Q_{es} \rangle \quad (15)$$

Most of the collision cross section values were found experimentally and are tabulated. And Rosa<sup>9</sup> gives the mean electron speed by

$$c_e = \sqrt{\frac{8k_b T_e}{\pi m_e}} \quad (16)$$

Rosa<sup>9</sup> also gives the collision cross section for electrons with ions:

$$Q_{el}^* = 3.9 \left[ \frac{q_e^2}{8\pi\epsilon_0 k_b T_e} \right]^2 \ln \Lambda \quad (17)$$

Where

$$\Lambda = \frac{12\pi}{\sqrt{n_e}} \left[ \frac{\epsilon_0 k_b T}{q_e^2} \right]^{3/2} \quad (18)$$

The total neutral number density can be calculated from

$$n_n = \frac{P}{k_b T_g} \quad (19)$$

## EXPERIMENTAL SETUP AND DIAGNOSTICS

The experimental setup for testing microwave plasma MHD accelerators includes a microwave plasma generation system, propellant and steam feed system, a vacuum system, microwave thruster, MHD accelerators, power supplies, and plasma diagnostic and data acquisition system.

Figure 5 shows the schematic diagrams of the vacuum chamber, and the microwave thruster. Microwaves generated by a 0~6 kW variable power microwave generator are delivered to a 4-inch diameter by 8-inch long  $TM_{011}$  mode resonant cavity operating at 2.45GHz by several components of WR 284 wave-guide. A propellant and steam feed system is also mounted to the cavity to supply propellant gases (Argon, helium, nitrogen, carbon dioxide and steam). The plasma is expanded to the vacuum chamber from the cavity through a converging-diverging nozzle after it is heated in the microwave field. In the tests presented in this paper, a large nozzle with a throat diameter 3.81mm and area ratio 7.11 was used.

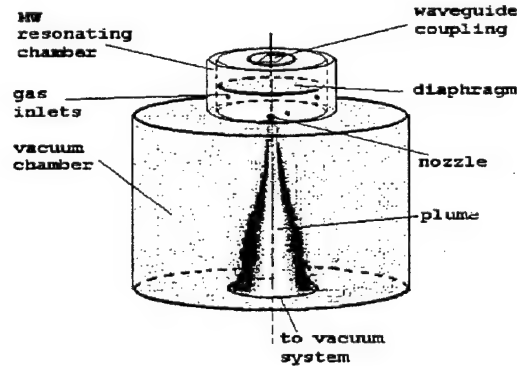


Figure 5 Schematic diagrams of the vacuum chamber and microwave thruster.

The vacuum system consisted of an 18-inch diameter by 24-inch length glass cylinder with 18-inch Varian port rings on the top and bottom. Twelve ports were available in both the top and the bottom port rings for optical and electrical feeds. The microwave cavity was mounted to the top of the tank with an aluminum adapter plate. The adapter plate was connected to a pulley system and hand crank, which was used to gain access to the chamber. A Stokes, Model 412H-H, 300 CFM roughing pump provided base pressures down to 10 mTorr. Vacuum pressures between 0.5 – 2.0 Torr were maintained, while operating the microwave cavity. Vacuum pressure was measured with a Varian 801, thermocouple vacuum gauge with a range of 0 to 2,000 mTorr.

### Faraday type crossed-field MHD accelerator

The actual configuration and the picture of the laboratory type continuous electrode crossed-field MHD accelerator is shown schematically in Figure 6. The channel body was made with Boron Nitride. The channel length is 2.4 inches. The cross section is approximately 0.55 inch wide by 0.60 inch high. The anode and cathode are 1.9 inch long and were made using copper. The electrodes are not water-cooled, which puts limits on the operating current and the time duration of the tests. To make sure the electrode temperature does not get too high, they are made of as one-inch tall copper blocks, and large electric cables are used to connect them with the power supply. To prevent arcing to other surfaces, the two electrodes and leads are painted with a layer of high temperature insulation ceramic. An aluminum plate is used at each end of the accelerator to hold the channel together, and to couple the channel to the microwave thruster.

A permanent magnet is used to apply a magnetic field to the channel, and the distance between the two magnetic poles is 1.2 inches. The magnetic field along the centerline of the channel is shown in Figure 7. A maximum magnetic field of 0.3 Tesla has been measured. A 300KW DC power supply provides the electrical power for the plasma accelerator. The maximum output of the DC is 60V/1000A, or 500V/600A.

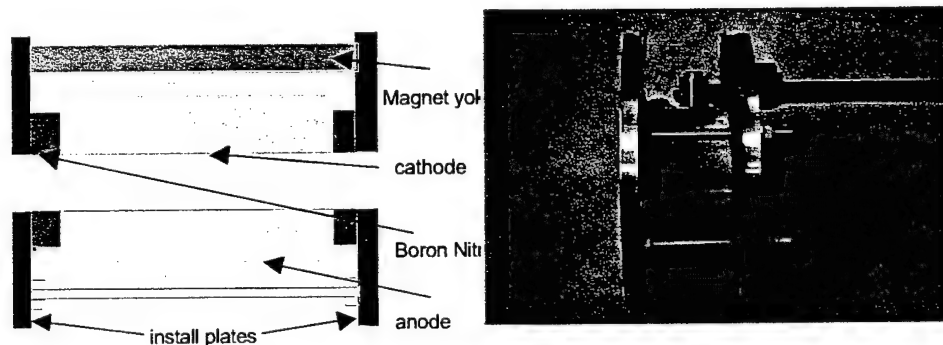


Figure 6 Left: Schematic of the MHD accelerator. Right: The picture of the crossed-field plasma accelerator assembly (without magnet)

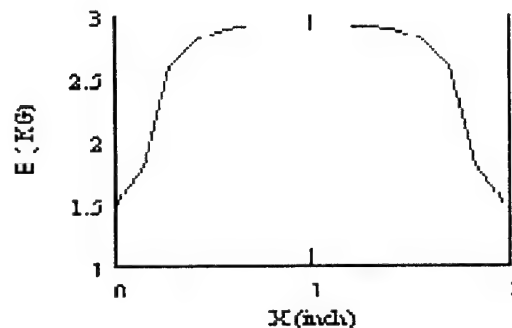


Figure 7 Magnetic field curve

### Rectangular type Hall current accelerator

A laboratory type Hall current accelerator has been constructed, and is ready for testing. As shown in Figure 8, there are five pairs of copper electrodes cast inside the accelerator. Each pair of electrodes, which are installed facing each other in the two opposite walls, is connected together. The two pairs of electrodes in the front and the end of the channel will be connected to the 300KW power supply afore mentioned in this paper. The channel body is cast using castable high temperature alumina base ceramics. The ceramic materials can withstand up to 3200°F, and the dielectric strength is 200 volts/mm. The actual channel length is 3.8 inches. The cross section is 0.8 inch by 0.8 inch. Each electrode is 3/8-inch in thickness, and the internal distance between two-neighboring electrodes is 0.25 inch. The same kind of permanent magnet used in the Faraday type accelerator is used here to provide the magnetic field. Also, the electrodes are not water-cooled.

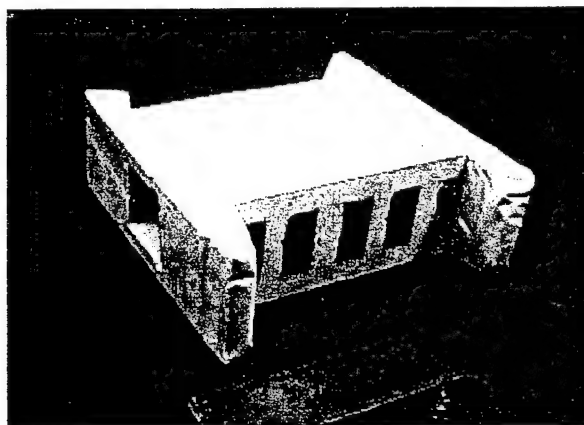


Figure 8 The picture of the laboratory type Hall current accelerator.

### Diagnostics

The single, double, and triple Langmuir probes are used to measure plasma properties. Quadruple Langmuir probes<sup>10</sup> are also constructed to measure electrical transport properties, of which the configuration<sup>10</sup> is shown in Figure 9. Tungsten wires make up the probe's 4 electrodes, and four-hole alumina tubing is used to insulate the wires and probe electrodes. The alumina tubing was supported with stainless steel tubing that is coupled to a shielded connecting block providing support for the probe. Two twelve-volt batteries were used in the experiments to supply a floating electric potential between probes 1 and 3, and probes 1 and 4. Probe 2 is allowed to float; and measurements are made of the voltage between probe 1 and 2, and the current flow between probes 1 and 3, and probes 1 and 4.

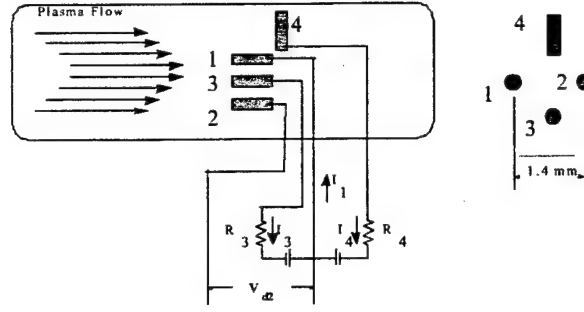


Figure 9 Quadruple Langmuir probes setup.

Burton and Bufton<sup>10</sup> gave the derivation of the quadruple probe response.

$$1 = \frac{1 + \exp(\phi V_{d3}) - 2 \exp[\phi(V_{d3} - V_{d2})]}{(I_4 / I_3) \{ \exp[\phi(V_{d3} - V_{d2})] - 1 \}} \quad (20)$$

The quantities  $V_{d2}$ ,  $I_3$ , and  $I_4$  are measured quantities, and  $V_{d3}$  is the battery voltage. The electron temperature is found by solving for  $\phi$  through iteration, and use

$$T_e = q_e / k_b \phi \quad (21)$$

The electron density is given by

$$n_e = \frac{\kappa \left( \frac{I_3}{A_3} \right) \left( 1 + \frac{I_4}{I_3} \right) \exp\left(\frac{1}{2}\right) (m_{ion})^{1/2}}{q_e (k_b T_e)^{1/2} [\exp(\phi V_{d2}) - 1]} \quad (22)$$

## RESULTS AND ANALYSIS

### Microwave thruster and the Faraday type continuous electrode cross-field accelerator

The characterization of microwave thruster plasma has been conducted in our previous research<sup>1, 2</sup>. The results show that non-equilibrium plasma with electron temperatures an order of magnitude higher than the gas temperature could be created with the microwave thruster. For the monatomic gases argon and helium, electron densities slightly higher than the critical plasma density for 2.45 GHz microwaves ( $10^{17}$  e/m<sup>3</sup>) were obtained. For diatomic and polyatomic molecules, electron densities were one to two orders of magnitude below the critical density.

In this research, only argon and nitrogen gas was tested so far, and a nozzle with 7.11 area ratio is used for microwave thruster in all the tests. Table 1 gives some measured or calculated plasma properties in the exit of the microwave thruster, which is also the inlet of the MHD plasma accelerators. The electron density and temperature is measured using quadruple Langmuir probes and calculated from Equations (20) ~ (22). The local electrical conductivity is calculated from Equation (14) ~ (19). The mass flow rates are estimated from measurements in previous test under similar conditions. Gas temperatures are measured using thermal couples, and the values are adjusted considering flow conditions.

Table 1 Parameters in the exit of microwave thruster and the inlet of MHD plasma accelerator.

	Argon	Nitrogen
Electron density $n_e$ (/m <sup>3</sup> )	$1 \times 10^{17}$	$2 \times 10^{16}$
Electron temperature $T_e$ (eV)	6.2	3
Electrical conductivity $\sigma$ (mho/m)	28.92	0.53
Gas temperature T (K)	750	680
Gas pressure (Torr)	0.85	1
Mass flow rate (mg/s)	160	150
Gas velocity (m/s)	1200	505

The velocities in Table 1 were obtained by running the crossed-field MHD accelerator in the MHD generator model. In this case, the two electrodes are disconnected from the power supply, and are in 'open' status to the microwave plasma. Due to the existence of the magnetic field and a plasma flow velocity that is not parallel to the magnetic field, an induced Faraday electric field  $\mathbf{V} \times \mathbf{B}$  is created. Figure 10 shows the measured induced electrical field, which is the so-called open-circuit voltage. The velocity is estimated using the following formula:

$$E_y = \frac{V_{open - cir}}{L} = \alpha UB \quad (23)$$

Where,  $E_y$  is the average electrical field,  $L$  is the distance across the electrodes,  $V_{open-cir}$  is the measured total voltage, and  $U$  is velocity.  $B$  is calculated as the average of the whole magnetic field, and is given a value of 0.22 Tesla,  $\alpha$  is called the efficient factor ( $<1$ ), and is chosen as 0.85 at this case. A large uncertainty exists at the velocity estimation using this method because the flow velocity is not constant along the electrode length, and also the flow is retarded due to the  $B$  field. New techniques to directly measure the gas velocity are under development. And, a much smaller diagnostic MHD channel is also being built, so that a better understanding of the gas velocity can be obtained.

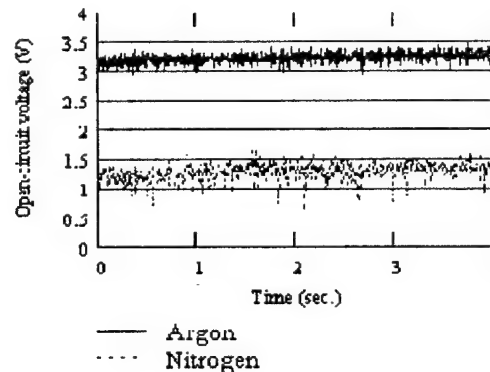


Figure 10 Open-circuit voltage traces of microwave plasma between accelerator electrodes.

The Faraday type cross-field MHD accelerator discharge voltage and current for Argon and Nitrogen gas are shown in Figure 11. The data are smoothed and curve fitted. Figure 12 shows the traces of voltage for argon gas without the data smoothing. In the accelerator tests presented here, the discharge current limits were set to 100 Amps. Tests that run different discharge currents will be conducted later.

Comparing the data of the Faraday type cross-field MHD accelerator with and without the magnet in Figure 11, we can see the discharge voltages increase substantially to keep the same current flowing across the channel with a magnet. This is mainly due to the  $V \times B$  induced field, and the Hall effect by applying a perpendicular magnetic field to the electrical field. When a very large magnetic field is applied, and the gas velocity is very high, the induced electric field becomes very significant. This could cause a substantial loss of the applied electrical power.

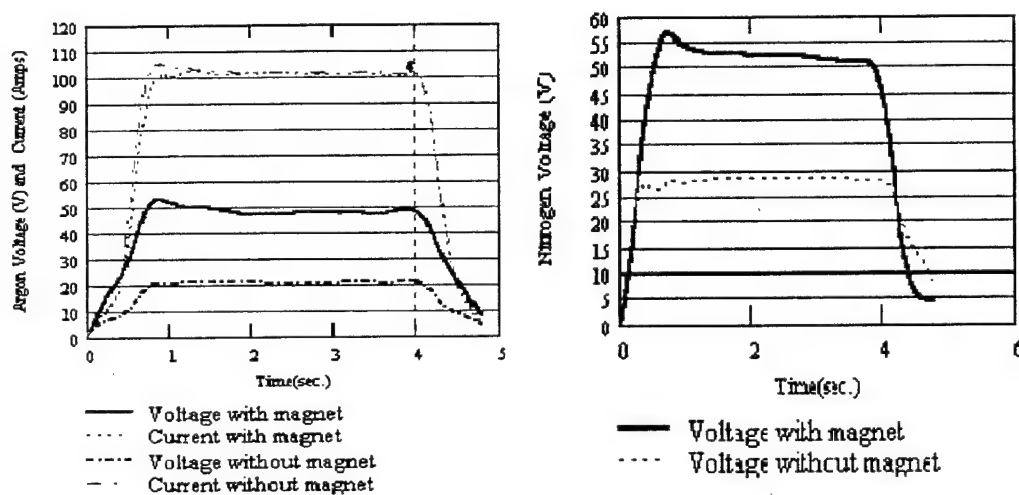


Figure 11 Discharge voltage and current for the Faraday type cross-field accelerator (DC power is turned off after 4 seconds). Left. use argon gas. Right: use nitrogen gas.

The local electron temperature and density of MHD plasma are also measured, and are shown in Figure 13. Because of the erosion of the copper electrodes, sections of the plume that lie near the electrodes are contaminated by green copper vapor. So, instead of measuring the radial electron density and temperature profile, only the properties at the core of the plume are measured, otherwise copper will coat the probes. Although, the quadrupole probes are cleaned thoroughly before each run, we find that the probes are covered with a layer of non-conductive black colored material very quickly. And, a layer of conductive materials covers the support insulation ceramic tube. These could change the probe current and voltage measurements. Also, we find that the large plasma potential gradient close to the electrodes affects the measuring results dramatically. So, the probes are sited about one inch below the plasma accelerator exit. The actual electron density and temperature at the exit of the plasma are estimated one order of magnitude bigger than the measured results. The overall uncertainty of the electron density and temperature measurements could be one order of magnitude of the actual values.

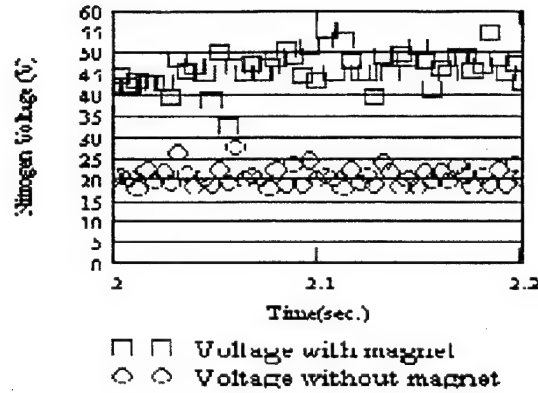


Figure 12 Discharge voltage traces for argon gas in the Faraday type cross-field accelerator.

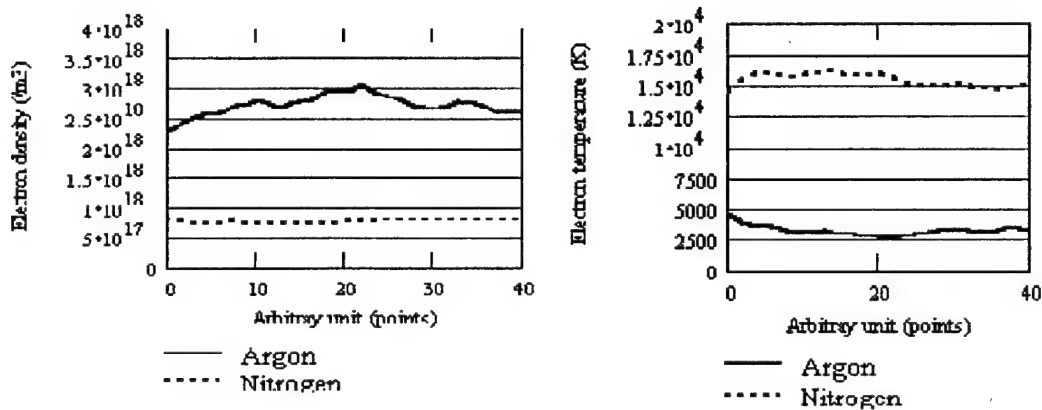


Figure 13 Plasma properties of the plume core measured at one inch below the Faraday type cross-field MHD accelerator exit. Left: Electron Density. Right: Electron temperature.

Table 2 gives a summary of some measurements and calculated results. The electrical conductivities for argon and nitrogen are calculated from Equation (14). The Hall parameters are obtained from Equation (4).

A reasonable gas velocity cannot be obtained from Equation (3) when using the Hall parameter and conductivity values shown in Table 2. Rosa suggested that when the Hall parameter  $\omega\tau$  has exceeded a value of 10, the ion-slip factor must be considered. Also, non-equilibrium ionization instability can occur when the Hall parameter is large<sup>7</sup>. And, this will cause a reduction of the Hall parameter and conductivity in the region where the non-equilibrium ionization instability occurs. Simmons<sup>7</sup> suggested that the Hall parameter value should be limited to a maximum value, and a limit of 5 is chosen in their case.



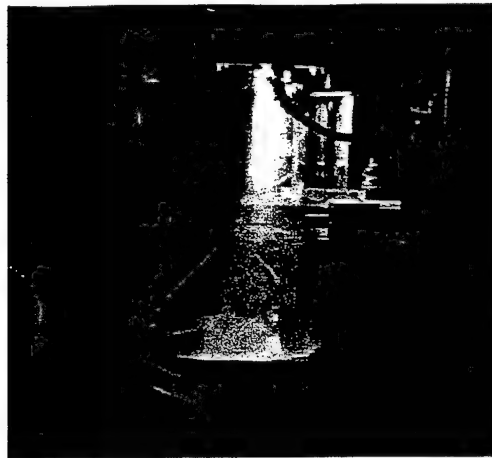


Figure 14 The picture of the plasma plume during the crossed-field accelerator testing.

Table 2 Parameters in the exit of the Faraday type cross-field accelerator.

	Argon	Nitrogen
Discharge voltage (volts)	47	53
Discharge current (amps)	100	100
Current Density (amps/m <sup>2</sup> )	$1.36 \times 10^5$	$1.36 \times 10^5$
Electron density $n_e$ (/m <sup>3</sup> )	$3.0 \times 10^{18}$	$8.02 \times 10^{17}$
Electron temperature $T_e$ (K)	5000	15000
Electrical conductivity $\sigma$ (mho/m)	1802	52
B field (T)	0.22	0.22
Hall parameter $\omega\tau$	825	88
Gas temperature T (K)	1300	1100
Gas pressure (Torr)	0.85	1
Mass flow rate (mg/s)	160	150
Total power putted in (KW) (includes about 3 KW microwave power)	7.7	8.3

#### Rectangular type Hall current accelerator

The testing of the rectangular type Hall current accelerator is underway. It will be tested coupling with the microwave plasma generator, or/and the crossed-field accelerator. The results will be reported later.

## CONCLUSION

The current test results of a laboratory type crossed-field MHD plasma accelerator with microwave thruster were presented. The accelerator increases the electrical conductivity of the plasma substantially, and the plasma still remains non-equilibrium. Further detailed and accurate measurements are necessary to better understand the velocity, the efficiency, and the Hall and ion-slip effects. The testing of a laboratory type rectangular Hall current accelerator is under way in the lab, and it will be tested coupled with the microwave plasma thruster and/or the crossed-field accelerator.

## ACKNOWLEDGEMENTS

The authors appreciate the support of Mr. Tony Robertson with magnet design and characterization. Also, thanks are given to Mr. George Olden and Paul Vaughan for their support in the set up and execution of the experiment. This research was supported by a grant from the Air Force Office of Scientific Research under contract number F49620-98-0-0083. Additional support and equipment has been provided by NASA's Marshall Space Flight Center.

## REFERENCE

- <sup>1</sup>Li, Zhongmin, Jones, J.E., Hawk, W.C., "Experimental Study of Microwave Plasma MHD Accelerators," AIAA-2000-3882, July 2000.
- <sup>2</sup>Jones, J. E., "An Assessment of Microwave Generated Plasma for Use in Magnetohydrodynamic Accelerators," PhD dissertation, MAE department, Univ. of Alabama in Huntsville.
- <sup>3</sup>Macheret, S.O., Miles, R.B., and Nelson, G.L., "MHD Acceleration of Supersonic Air Flows Using Electron Beam - Enhanced Conductivity," AIAA 98-2922, June 1992.
- <sup>4</sup>Rosa, Richard J, "Magnetohydrodynamic Generators and Nuclear Propulsion," *ARS Journal*, Aug. 1962.
- <sup>5</sup>Bajovic, Valentina S, "A Reliable Tool for the Design of Shape and Size of Faraday Segmented MHD Generator Channel," *Energy Conversion and Management*, Vol.37, No.12, pp.1753-1764, 1996.
- <sup>6</sup>Demetriades, Sterge T., "Experiments with a High Specific Impulse Crossed-field Accelerator," 3<sup>rd</sup> Symposium on Engineering Aspects of Magnetohydrodynamics, 1963.
- <sup>7</sup>Simmons, G.A., Nelson, G.L., and Lee, Y.M. "Analysis of An unseeded, Non-equilibrium MHD Accelerator Concept For Hypersonic Propulsion Ground Testing applications," AIAA 92-3994, July 1992.
- <sup>8</sup>Sutton, George W, Sherman, Arthur, *Engineering Magnetohydrodynamics*, McGraw-Hill, Inc, New York, 1965.
- <sup>9</sup>Rosa, R.J., George, *Magnetohydrodynamics, Energy Conversion*, revised printing, Hemisphere Publishing Corp., Washington, 1987.
- <sup>10</sup>Burton, R.L., Bufton, S.A., Tiliakos, N.T., and Krier, H., "Application of Multiple Electrostatic Probes to a Low Power Arc jet," *Journal of Propulsion and Power*, 1994.
- <sup>11</sup>Li, Zhongmin, Hawk, W.C., Jones, J.E., "Experimental Study of A Crossed-Field MHD Accelerator Coupling with Microwave Plasma," AIAA-2001-3495, July 2001.



**AIAA 2001-3495**

**Experimental Study of A Crossed-Field MHD  
Accelerator Coupling with Microwave Plasma**

**Zhongmin Li, Clark W. Hawk**  
Propulsion Research Center  
University of Alabama in Huntsville  
Huntsville, Alabama 35899

**Jonathan E. Jones**  
NASA Marshall Space Flight Center  
Propulsion Research Center  
Huntsville, AL 35812

**37th AIAA/ASME/SAE/ASEE Joint Propulsion Conference &  
Exhibit**  
7-11 July 2001 / Salt Lake City, UT

For permission to copy or republish, contact the American Institute of Aeronautics and Astronautics,  
1801 Alexander Bell Drive, Suite 500, Reston, VA 20191-4344

# Experimental Study of A Crossed-Field MHD Accelerator Coupling with Microwave Plasma

Zhongmin Li\*, Clark W. Hawk\*\*  
*Propulsion Research Center*  
*The University of Alabama in Huntsville*  
*Huntsville, AL 35899*

Jonathan E. Jones\*\*\*  
*NASA Marshall Space Flight Center*  
*Propulsion Research Center*  
*Huntsville, AL 35812*

## Abstract

MHD accelerators use direct electromagnetic body force for acceleration. The experimental investigations of MHD accelerators coupled with a microwave thruster for potential in-space propulsion applications are underway at the UAH Propulsion Research Center. The microwave-generated plasma, which is in highly non-equilibrium, is expanded through a thermodynamic nozzle to a 2 inches long continuous electrode crossed-field accelerator for further acceleration and ionization. The test results of the crossed-field accelerator with a 100 amps discharge current are presented. The detailed measurements of electron temperature and density at the entrance and the exit of the MHD channel were obtained by using quadrupole Langmuir probes. The construction of a laboratory type applied-field MPD thruster is underway for testing coupling with the microwave plasma.

## Nomenclature

$B$	Magnetic field strength
$c_e$	Mean thermal speed of electrons
$E$	Local electric field
$\epsilon_0$	Permittivity of vacuum (constant)
$J$	Current density
$k_b$	Boltzmann's constant
$m_e$	Electron rest mass

$n_e$	Electron number density
$n_n$	Neutral gas number density
$n_s$	Number density of species $s$
$Q$	Average collision cross section
$Q_{es}$	Collision cross section for electrons with species $s$
$Q_{en}$	Average collision cross section for electrons with all neutral species
$Q_{ei}$	Average collision cross section for electrons with ions
$q_e$	Electron charge
$T_e$	Electron temperature
$T_g$	Gas temperature
$V$	Velocity
$\beta$	Hall constant ( $1/q_en_e$ )
$\eta$	Efficiency
$\rho$	Density
$\sigma$	Electrical conductivity
$\omega$	Electron cyclotron frequency
$\tau$	Mean time interval between collisions for electrons with ions and neutrals
$\omega\tau$	Hall parameter

## Introduction

Electric propulsion has been extensively studied for the past several decades for promising of producing high specific impulse for long duration space missions. Such a system relies on the acceleration of propellants for propulsion by electrical heating, electric body forces, and/or magnetic body forces. So, correspondingly, electric propulsion is divided in three categories, electro-thermal, electro-static, electro-magnetic propulsion. In electro-thermal propulsion, such as

\*Graduate Research Assistant, Member AIAA

\*\*Director and Professor, Fellow AIAA

\*\*\*Aerospace Engineer, Member AIAA

arcjets, the propellant is heated electrically then isentropically expanded through a nozzle. In electro-static propulsion, e.g. ion thruster, ionized propellant is accelerated through the direct application of electric fields. In electro-magnetic propulsion, the thrust is produced through electric and magnetic body forces (Lorentz Force) interacting with highly ionized gases. All the MHD accelerators and Magnetoplasma dynamic (MPD) thrusters belong to this category.

This research focuses on non-equilibrium microwave plasma MHD accelerators for in-space propulsion applications. The proposed propulsion system includes a microwave thruster, a crossed-field MHD plasma accelerator, and a coaxial applied-field MPD thruster. The microwave thruster is used to produce non-equilibrium plasma for the plasma accelerators, and also preliminarily accelerate the plasma flow. The Faraday type crossed-field accelerator is put in the system for further ionization and acceleration of the plasma. The MPD thruster is the major propulsion device in this system.

In the microwave thruster, the microwave is guided into a resonating cavity to heat the propellant gas. By adding energy to the electrons using microwave radiation inside the microwave thruster, non-equilibrium plasma can be created where the temperature of the electrons is higher than the temperature of the gas<sup>1</sup>. The resulting free electron density can then be several orders of magnitude higher than electron densities at thermodynamic equilibrium. The non-equilibrium plasmas with electron temperature much higher than gas temperature can improve the efficiency of the MHD accelerator by reducing the heat transfer to channel walls, and lowering the thermal energy remaining in flow, while increasing the electrical conductivity of the flow<sup>2</sup>.

In traditional MHD devices such as generators and hypersonic wind tunnels, non-equilibrium conditions are hard to maintain due to operation at pressures from 10 to 100atm<sup>3</sup>. At these pressures collision rates are high, and a large amount of energy must be added to the flow to depart from equilibrium conditions. However, because in-space propulsion systems do not require operation at high pressures, the energy required maintaining non-equilibrium ionization is reduced, thus it is advantageous to examine non-

equilibrium ionization for in-space MHD accelerators.

Crossed-field plasma accelerators have been the subjects of many theoretical and some experimental studies for possible applications for propulsion devices and wind-tunnel gas accelerators<sup>4, 5, 6, 7</sup>. Due to the boundary layer voltage drop and Hall current effect, it is hard to get high specific impulse at acceptable efficiency (>50%). However, in this research, the crossed-field accelerator is considered as a secondary ionization device to further ionize the gas, and also as one of the three stages of acceleration. The crossed-field accelerator is not a sole source of acceleration, and only operates at moderate current. When accelerating the flow by several devices in a chain, it avoids putting too much power on the MPD thruster. This is desirable because arching makes it difficult to put high power into a MPD thruster. When operate at lower power levels MPD thruster has relative higher efficiency.

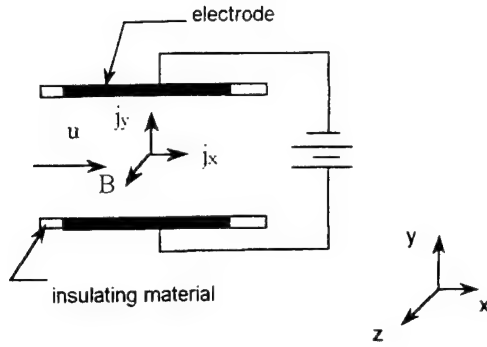
### Some Equations and Plasma Parameters

The Generalized Ohm's law governs the interaction of electrically conducting plasma with applied electric and magnetic fields. For partially ionized plasma the Generalized Ohm's law may be written in the form of Equation (1)<sup>9</sup>.

$$\mathbf{j} = \sigma(\mathbf{E} + \mathbf{V} \times \mathbf{B}) - \frac{\omega_e \tau_e}{B} \mathbf{j} \times \mathbf{B} + \frac{\omega_e \tau_e \omega_i \tau_i}{B^2} (\mathbf{j} \times \mathbf{B}) \times \mathbf{B} \quad (1)$$

Where the first term is the sum of all electric fields and motional emf's, the second term on the right is the Hall effect term, and the third term introduces ion-slip. In this case, the ion-slip term is neglected.

The crossed-field accelerators utilize the Lorentz force that is  $\mathbf{J} \times \mathbf{B}$  to accelerate the plasma flow. The schematic of a typical Faraday type crossed-field accelerator is shown in Figure 1.



**Figure 1. Faraday type Crossed-field accelerator configuration.**

For the Faraday type continuous electrode accelerator,  $E_x = B_y = B_z = v = w = j_z = 0$ . If the ion-slip is neglected, expand Equations (1) and rearrange in a Cartesian coordinates system, we get

$$j_x = -\frac{\sigma\omega\tau(E_y - uB)}{1 + (\omega\tau)^2} = -\omega\tau j_y \quad (2)$$

$$j_y = \frac{\sigma(E_y - uB)}{1 + (\omega\tau)^2} \quad (3)$$

where,  $\omega\tau$  is the Hall parameter and can be calculated with the following equation:

$$\omega\tau = \sigma\beta B = \frac{q_e B_0}{m_e c_e \sum_{k,s} n_{k,s} Q_{k,s}} \quad (4)$$

Due to the Hall effect, currents perpendicular to the applied electrical field direction are produced. These currents are so called Hall currents. In this configuration,  $j_y$  is the regular current and  $j_x$  is the Hall current, and the Hall parameter can be interpreted as the ratio of the Hall current to the current parallel to the electric field<sup>8</sup>.

#### Local electrical conductivity

The scalar electrical conductivity of a mixture of gases can be calculated from the following<sup>8</sup>:

$$\sigma_0 = \frac{n_e q_e^2}{m_e \langle c_e \rangle (n_n \langle Q_{en} \rangle + n_e Q_{ei}^*)} \quad (5)$$

where

$$Q_{en} = \sum_{s=c,i} \frac{n_s}{n_n} \langle Q_{es} \rangle \quad (6)$$

Most of the collision cross section values were found experimentally and are tabulated. And Rosa<sup>9</sup> gives the mean electron speed by

$$c_e = \sqrt{\frac{8k_b T_e}{\pi m_e}} \quad (7)$$

Rosa<sup>9</sup> also gives the collision cross section for electrons with ions

$$Q_{ei}^* = 3.9 \left[ \frac{q_e^2}{8\pi\epsilon_0 k_b T_e} \right]^2 \ln \Lambda \quad (8)$$

where

$$\Lambda = \frac{12\pi}{\sqrt{n_e}} \left[ \frac{\epsilon_0 k_b T}{q_e^2} \right]^{3/2} \quad (9)$$

The total neutral number density can be calculated from

$$n_n = \frac{P}{k_b T_g} \quad (10)$$

#### Experimental Setup and Diagnostics

The experimental setup for testing microwave plasma MHD accelerators includes a microwave plasma generation system, propellant and steam feed system, a vacuum system, microwave thruster, MHD accelerators, power supplies, and plasma diagnostic and data acquisition system.

Figure 2 shows the schematic diagrams of the vacuum chamber, and the microwave thruster. Microwaves generated by a 0~6 kW variable power microwave generator are delivered to a 4-inch diameter by 8-inch long TM<sub>011</sub> mode resonant cavity operating at 2.45GHz by several

components of WR 284 wave-guide. A propellant and steam feed system is also mounted to the cavity to supply propellant gases (Argon, helium, nitrogen, carbon dioxide and steam). The plasma is expanded to the vacuum chamber from the cavity through a converging-diverging nozzle after it is heated in the microwave field. In the tests presented in this paper, a large nozzle with a throat diameter 3.81mm and area ratio 7.11 was used.

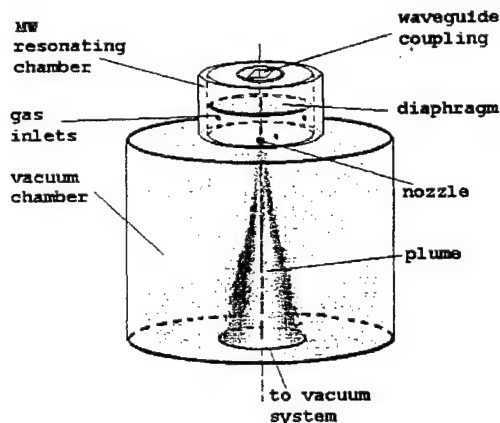


Figure 2. Schematic diagrams of the vacuum chamber and microwave thruster.

The vacuum system consisted of an 18-inch diameter by 24-inch length glass cylinder with 18-inch Varian port rings on the top and bottom. Twelve ports were available in both the top and the bottom port rings for optical and electrical feeds. The microwave cavity was mounted to the top of the tank with an aluminum adapter plate. The adapter plate was connected to a pulley system and hand crank, which was used to gain access to the chamber. A Stokes, Model 412H-H, 300 CFM roughing pump provided base pressures down to 10 mTorr. Vacuum pressures between 0.5 – 2.0 Torr were maintained, while operating the microwave cavity. Vacuum pressure was measured with a Varian 801, thermocouple vacuum gauge with a range of 0 to 2,000 mTorr.

A 300KW DC power supply provides the electrical power for the plasma accelerator. The maximum output of the DC is 60V/1000A, or 500V/600A.

The actual configuration of the laboratory type continuous electrode crossed-field MHD accelerator is shown schematically in Fig. 3, and the picture is shown in figure 4. The channel body

was made with Boron Nitride. The actual channel length is 2.4 inches. The cross section is approximately 0.55 inch wide by 0.60 inch high. The anode and cathode are 1.9 inch long and were made using copper. The electrodes are not water-cooled, which puts limits on the operating current and time during the tests. To make sure the electrode temperature does not get too high, they are made as one-inch high copper blocks, and large electric cables used to connect them with the power supply. To prevent arcing to other surfaces, the two electrodes and leads are painted with a layer of high temperature insulation ceramics. An aluminum plate is used at the each end of the accelerator to hold the channel together, and couple the channel to the microwave thruster.

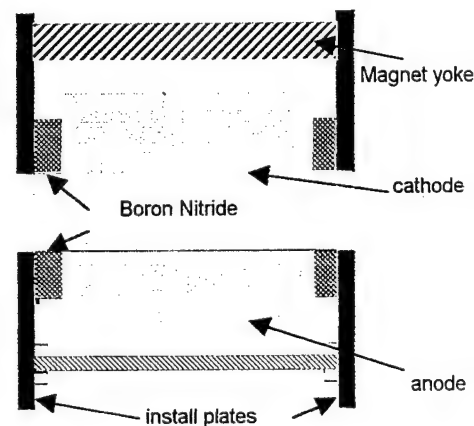


Figure 3. Schematic of the MHD accelerator.

A permanent magnet is used to apply a magnetic field to the channel, and the distance between the two magnetic poles is 1.2 inches. The magnetic field along the centerline of the channel is shown in Figure 5. A maximum magnetic field of 0.3 Tesla has been measured.

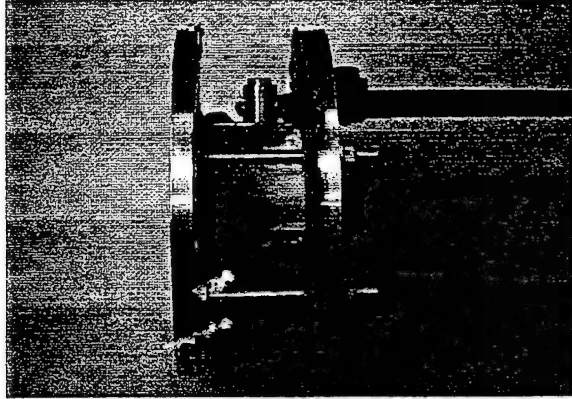


Figure 4. The crossed-field plasma accelerator assembly (without magnet).

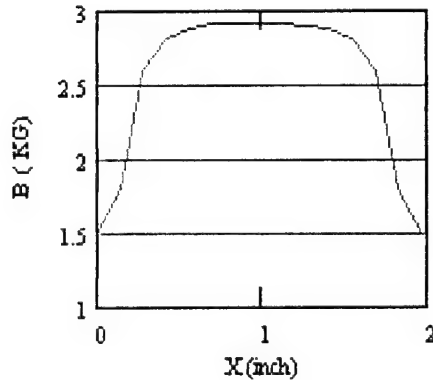


Figure 5. Magnetic field curve

Quadruple Langmuir probes<sup>10</sup> are constructed to measure electrical transport properties. Tungsten wires make the probe's 4 electrodes, and four-hole alumina tubing is used to insulate the wires or probe electrodes. The alumina tubing was supported with stainless steel tubing that was connected to a shielded connecting block providing support for the probe. BNC connectors were attached to the shielded box to provide electrical connection for the probe circuitry.

The four-probe configuration<sup>10</sup> is shown in Figure 6. Two twelve-volt batteries were used in these experiments to supply a floating electric potential between probes 1 and 3, and probes 1 and 4. Probe 2 is allowed to float; and measurements are made of the voltage between probe 1 and 2, and the current flow between probes 1 and 3, and probes 1 and 4.

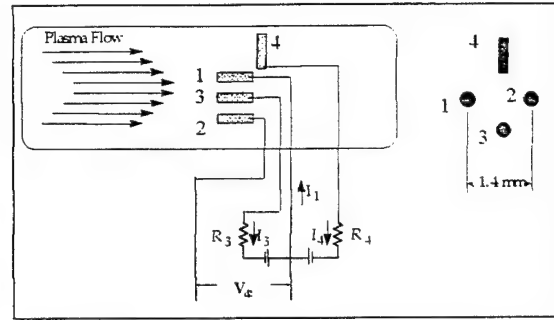


Figure 6. Quadruple Langmuir probes setup.

Burton and Bufton<sup>10</sup> gave the derivation of the quadruple probe response.

$$I = \frac{1 + \exp(\phi V_{d3}) - 2 \exp[\phi(V_{d3} - V_{d2})]}{(I_4 / I_3) \{ \exp[\phi(V_{d3} - V_{d2})] - 1 \}} \quad (11)$$

The quantities  $V_{d2}$ ,  $I_3$ , and  $I_4$  are measured quantities, and  $V_{d3}$  is the battery voltage. The electron temperature is found by solving for  $\phi$  through iteration, and use

$$T_e = q_e / k_b \phi \quad (12)$$

The electron density is given by

$$n_e = \frac{\kappa \left( \frac{I_3}{A_3} \right) \left( 1 + \frac{I_4}{I_3} \right) \exp\left( \frac{1}{2} \right) (m_{ion})^{1/2}}{q_e (k_b T_e)^{1/2} [\exp(\phi V_{d2}) - 1]} \quad (13)$$

### Results and Analysis

The characterization of microwave thruster plasma has been conducted in our previous research<sup>1,2</sup>. The results show that non-equilibrium plasma with electron temperatures an order of magnitude higher than the gas temperature could be created with the microwave thruster. For the monatomic gases argon and helium, electron densities slightly higher than the critical plasma density for 2.45 GHz microwaves ( $10^{17}$  e/m<sup>3</sup>) were obtained. For diatomic and polyatomic molecules, electron densities were one to two orders of magnitude below the critical density.



In this research, only argon and nitrogen gas was tested so far, and a nozzle with 7.11 area ratio is used for microwave thruster in all the tests. Table 1 gives some measured or calculated plasma properties in the exit of the microwave thruster, which is also the inlet of the MHD plasma accelerator. The electron density and temperature are measured using quadruple Langmuir probes and calculated from Equations (11) ~ (13). The local electrical conductivity is calculated from Equation (5) ~ (10). The mass flow rates are estimated from measurements in previous test with the similar conditions. Gas temperatures are measured using thermal couples, and the values are adjusted considering flow conditions.

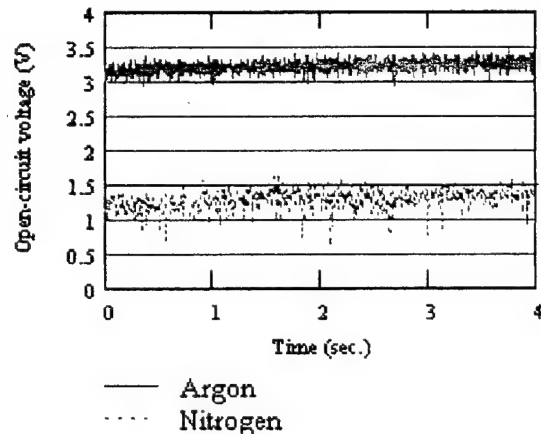
**Table 1 Parameters in the exit of microwave thruster and inlet of MHD accelerator.**

	Argon	Nitrogen
Electron density $n_e$ (/m <sup>3</sup> )	$1 \times 10^{17}$	$2 \times 10^{16}$
Electron temperature $T_e$ (eV)	6.2	3
Electrical conductivity $\sigma$ (mho/m)	28.92	0.53
Gas temperature T (K)	750	680
Gas pressure (Torr)	0.85	1
Mass flow rate (mg/s)	160	150
Gas velocity (m/s)	1200	505

The velocities in Table 1 were obtained by running the crossed-field MHD accelerator in the MHD generator model. At this case, the two electrodes are disconnected from the power supply, and are in 'open' status to the microwave plasma. Due to the existence of the magnetic field and a plasma flow velocity that is not parallel to the magnetic field, an induced Faraday electric field  $V \times B$  is created. Figure 7 shows the measured induced electrical field, which is the so-called open-circuit voltage. The open-circuit condition implies that  $j_y = 0$ ; thus from Equation (3), the open-circuit electric field should be equal  $UB^8$ . The velocity is estimated using the flowing formula:

$$E_y = \frac{V_{open-cir}}{L} = KUB \quad (16)$$

Where,  $E_y$  is the average electrical field,  $L$  is the distance across the electrodes,  $V_{open-cir}$  is the measured total voltage, and  $U$  is velocity.  $B$  is calculated as the average of the whole magnetic field, and is given a value of 0.22 Tesla,  $K$  is called the efficient factor ( $<1$ ), and is chosen as 0.85 at this case. A big uncertainty exists at the velocity estimation using this method because the flow velocity is not constant along the electrode length, and also there are voltage drop along electrode boundaries. New techniques to directly measure the gas velocity are under development. And, a much shorter diagnostic MHD channel is also been building. A better understanding of the gas velocity could be obtained after that.



**Figure 7. Open-circuit voltage traces of microwave plasma in accelerator electrodes.**

The MHD accelerator discharge voltage and current for Argon and Nitrogen gas are shown in Figure 8, Figure 9, which the data are smoothed and curve fitted. Figure 10 shows the traces of voltage for argon gas without smoothing the data. In the accelerator tests presented here, the discharge current limits are set to 100 Amps. Tests that run different discharge current will also be conducted later.

Comparing the data with and without magnet in Figure 8 and 9, we can see the discharge voltages increase substantially to keep the same current flowing across the channel with a magnet. This is mainly due to the  $V \times B$  induced field and the Hall effect. When a very large magnetic field is applied, and the gas velocity is very high, the

induced electric field becomes very significant. This could cause a big lose of the applied electrical power.

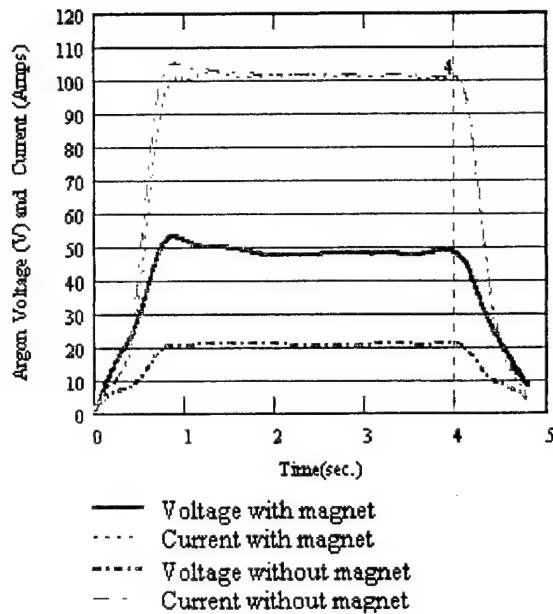


Figure 8. MHD accelerator discharge voltage and current for argon gas. (DC power is turned off after 4 seconds).

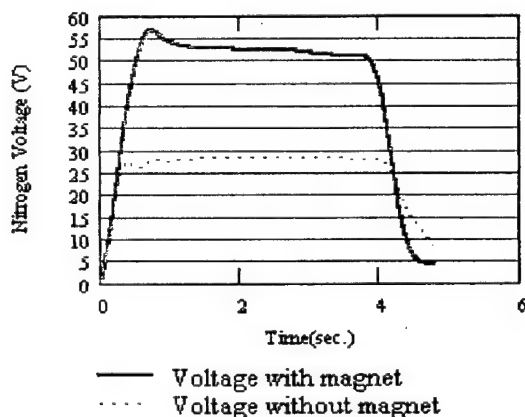


Figure 9. MHD accelerator discharge voltage (The current is limited to 100 Amps, and DC power is turned off after about 4 seconds) with nitrogen.

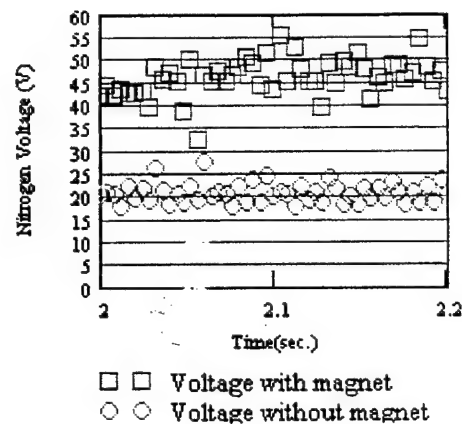


Figure 10. Discharge voltage traces for argon gas.

The local electron temperature and density of MHD plasma are also measured, and are shown in Figure 11 and 12. Because the erosion of the copper electrodes, sections of the plume that lie near the electrodes is contaminated by green copper vapor. So, instead of measuring the radial electron density and temperature profile, only the properties at the core of the plume are measured. Otherwise, copper will coat the probes if they are scanned across the plume. Although, the quadrupole probes are cleaned thoroughly before each run, we find that the probes are covered a layer of non-conductive black color material very quickly. And, a layer of conductive materials covers the support insulation ceramic tube. These could change the probe current and voltage measurements. Also, we find that the big plasma potential gradient closed to the electrodes affects the measuring results dramatically. So, the probes are sited about one inch below the plasma accelerator exit. The actual electron density and temperature at the exit of the plasma accelerator are estimated one order of magnitude bigger than the measured results. The overall uncertainty of the electron density and temperature measurements could be as big as one order of magnitude more or less than that of the actual values.

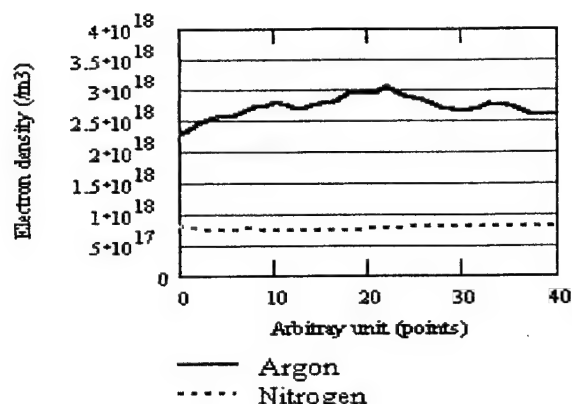


Figure 11. Electron density of the plume core at one inch below the MHD accelerator exit.

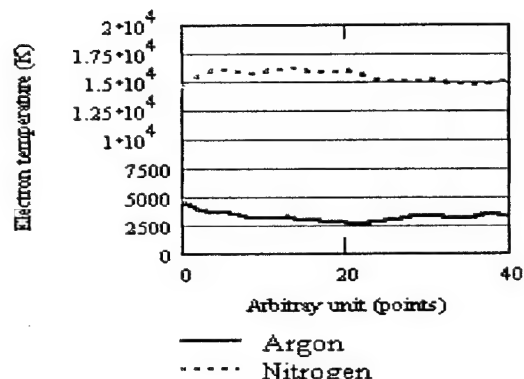


Figure 12 Electron temperature of the plume core at one inch below the MHD accelerator exit.

Table 2 gives a summary of some measurements and calculated results. The electrical conductivities for argon and nitrogen are calculated from Equation (5). The Hall parameters are obtained from Equation (4).

The reasonable gas velocity cannot be obtained from Equation (3) by using the Hall parameter and conductivity values that shown in table 2. Rosa<sup>9</sup> suggested that when Hall parameter  $\omega\tau$  become very large (exceeds a value of 10), the ion-slip factor must be considered. Also, non-equilibrium ionization instability can occur when the Hall parameter is large<sup>7</sup>. And, this will cause a reduction of Hall parameter and conductivity in the region where the non-equilibrium ionization instability occurs. Simmons<sup>7</sup> suggested that the Hall parameter value should be limited to a

maximum value, and a limit of 5 is chosen in their case.

If we assume the Hall effect could be neglected, and the discharge voltage difference with and without magnet is only due to the UB term, a velocity of about 8500 m/s at the accelerator exit is obtained. The actual velocity should be less than this value.

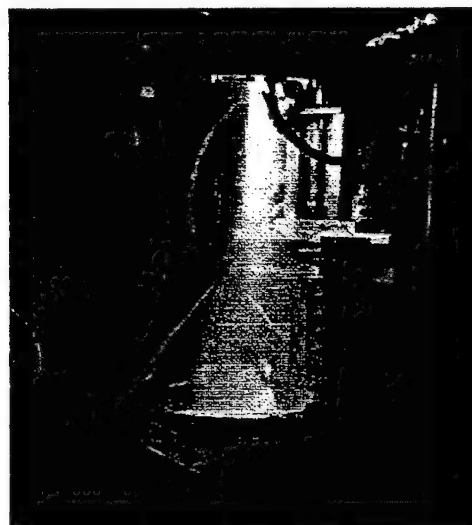


Figure 13. Plasma plume during the crossed-field MHD accelerator testing.

Table 2. Parameters in the exit of the MHD accelerator.

	Argon	Nitrogen
Discharge voltage with magnet (volts)	47	53
Discharge voltage without magnet (volts)	21	28
Discharge current (amps)	100	100
Current Density (amps/m <sup>2</sup> )	$1.36 \times 10^5$	$1.36 \times 10^5$
Electron density $n_e$ (/m <sup>3</sup> )	$3.0 \times 10^{18}$	$8.02 \times 10^{17}$
Electron temperature $T_e$ (K)	5000	15000
Electrical conductivity $\sigma$ (mho/m)	1802	52
B field (T)	0.22	0.22
Hall parameter $\omega\tau$	825	88
Gas temperature T (K)	1300	1100
Gas pressure (Torr)	0.85	1
Mass flow rate (mg/s)	160	150
Total power putted in (KW) (includes about 3 KW microwave power)	7.7	8.3

### Conclusion

The current available test results of a laboratory type crossed-field MHD plasma accelerator with microwave thruster were presented. The accelerator increases the electrical conductivity of the plasma substantially, and the plasma still remains non-equilibrium. Further detailed and accurate measurements are necessary to better understand of the velocity, the efficiency, and the Hall and ion-slip effects. The construction of a laboratory type applied-field MPD thruster is under way in the lab, and it will be tested coupling with the microwave plasma and the crossed-field accelerator.

### Acknowledgements

The authors appreciate the support of Mr. Tony Robertson with magnet design and characterization. Also, thanks are given to Mr. George Olden for his support in the set up and execution of the experiment. This research was supported by a grant from the Air Force Office of Scientific Research under contract number F49620-98-0-0083. Additional support and equipment has been provided by NASA's Marshall Space Flight Center.

### Reference

- <sup>1</sup>Li, Zhongmin, Jones, J.E., Hawk, W. H., "Experimental Study of Microwave Plasma MHD Accelerators," AIAA-2000-3882, July 2000.
- <sup>2</sup>Jones, J. E., "An Assessment of Microwave Generated Plasma for Use in Magnetohydrodynamic Accelerators," PhD dissertation, MAE department, Univ. of Alabama in Huntsville.
- <sup>3</sup>Macheret, S.O., Miles, R.B., and Nelson, G.L., "MHD Acceleration of Supersonic Air Flows Using Electron Beam - Enhanced Conductivity," AIAA 98-2922, June 1992.
- <sup>4</sup>Rosa, Richard J, "Magnetohydrodynamic Generators and Nuclear Propulsion," *ARS Journal*, Aug. 1962.
- <sup>5</sup>Bajovic, Valentina S, "A Reliable Tool for the Design of Shape and Size of Faraday Segmented MHD Generator Channel," *Energy Conversion and Management*, Vol.37, No.12, pp.1753-1764, 1996.
- <sup>6</sup>Demetriades, Sterge T., "Experiments with a High Specific Impulse Crossed-field Accelerator," 3<sup>rd</sup> Symposium on Engineering Aspects of Magnetohydrodynamics, 1963.
- <sup>7</sup>Simmons, G.A., Nelson, G.L., and Lee, Y.M. "Analysis of An unseeded, Non-equilibrium MHD Accelerator Concept For Hypersonic Propulsion Ground Testing applications," AIAA 92-3994, July 1992.
- <sup>8</sup>Sutton, George W, Sherman, Arthur, *Engineering Magnetohydrodynamics*, McGraw-Hill, Inc, New York, 1965.
- <sup>9</sup>Rosa, R.J., George, *Magnetohydrodynamics, Energy Conversion*, revised printing, Hemisphere Publishing Corp., Washington, 1987.
- <sup>10</sup>Burton, R.L., Bufton, S.A., Tiliakos, N.T., and Krier, H., "Application of Multiple Electrostatic Probes to a Low Power Arc jet," *Journal of Propulsion and Power*, 1994.



**AIAA 2000-3757**

**Evaluation of the Ionization Performance of a  
Stable DC Glow-Discharge in Flowing Plasmas**

**Stelu Deaconu, Clark W. Hawk**

**University of Alabama in Huntsville  
Huntsville, Alabama 35899**

**36th AIAA/ASME/SAE/ASEE Joint Propulsion Conference & Exhibit**  
**17-19 July 2000 / Huntsville, AL**

For permission to copy or republish, contact the American Institute of Aeronautics and Astronautics,  
1801 Alexander Bell Drive, Suite 500, Reston, VA 20191-4344

# Evaluation of the Ionization Performance of a Stable DC Glow-Discharge in Flowing Plasmas

Stelu Deaconu<sup>1</sup> and C.W. Hawk<sup>2</sup>

*The University of Alabama in Huntsville  
Propulsion Research Center, AL 35899*

## Abstract

The renewed interest in MHD propulsion raises the problem of generating steady state plasma flows with high conductivity levels. Several alternative solutions to steady ionization of plasma columns are available: microwave and RF breakdown, laser illumination, electric field breakdown etc. We are evaluating a DC glow discharge ionization device (GDID) with cylindrical symmetry. The plasma is generated by breakdown of the gas in a stable, radial DC electrical field. The ionization device is composed of a cylindrical, open-ended anode and an inner, coaxial cathode. The device is powered by a high voltage DC power supply. The GDID has been tested with nitrogen. Plasma electron temperature and electron density are measured with an array of single Langmuir probes. Local plasma conductivity is inferred from these measurements, by using a collisional model. The GDID shows improvement in the ionization level over microwave breakdown.

## Nomenclature

$c_e$	electron mean thermal speed
$e$	electron charge
$E$	electric field
$i$	current
$j_e$	electron current density
$k_b$	Boltzman's constant
$m_e$	electron mass
$m_i$	ion mass
$m_s$	mass gas particle
$n_e$	electron density

$n_x$	density species $x$
$p_x$	partial pressure species $x$
$Q$	collision cross-section
$T_e$	electron temperature
$T_i$	ion temperature
$W$	power
$\alpha$	$(T_e/T_i)$ temperature ratio
$\beta$	$(p/p_0)$ pressure ratio
$\delta$	collision loss factor
$\epsilon_0$	electrical permittivity of free space
$\phi$	electric potential
$\nu$	collision frequency
$\sigma$	plasma conductivity
$\xi$	$(W/p_0)$ scaling factor
$\Omega$	volume GDID

## Introduction

The development of efficient electric and magneto-electric propulsion systems is conditioned by the ability to produce and diagnose highly conductive plasma. Some of the recent plasma thruster<sup>1</sup> and MHD accelerator research<sup>2</sup> dealt with the problem of generating columns of flowing plasma. These experiments focused on ionization by microwave induced breakdown of the working gas. The plasma obtained was only weakly ionized and had a low electric conductivity. Current magnetic reconnection experiments<sup>3</sup> have raised the necessity of producing steady plasma columns of higher conductivity. A DC (direct current) glow discharge ionization device (GDID) was designed to augment the ionization level of the microwave plasma column. In this paper we describe the construction features as well as the working characteristics of this device, working as the single ionization source in the system. In this case an unbiased description of the ionization performance of the GDID is obtained.

- 
1. Graduate Research Assistant
  2. Professor MAE, Fellow AIAA

Arc and glow discharges are produced when an electric field is established between conducting electrodes in a rarefied gas. Glow discharge ionization is a well-documented process. The theoretical modeling of discharge ionization is to a large extent based on empirical formulae, and often inferred from experimental data<sup>4,5</sup>. Most of the literature on glow discharges presents experimental results from stationary plasma. Plasma guns and ion thrusters are examples of discharge systems producing flowing plasmas. Pulsed or steady plasma flows of low density, high conductivity and extreme velocity (hundreds of km/sec) are customary in these devices. Unlike these, the GDID is intended to produce a steady plasma, in a slow flowing gas column (10 – 100 m/sec).

In this paper the analysis of the operating mode of the ionization device is viewed from a magnetohydrodynamic (macroscopic) point of view. However, plasma electron density as a function of gas thermodynamic properties and power input are predicted using a collisional (kinetic theory) energy transfer model. The experimental work presented consists of electric probes, pressure and electric power measurements. Plasma properties and the performance of the device are inferred, and the experimental results are compared with the analytical predictions.

### Glow Discharge Ionization Device

The experiments were carried out in the UAH Advanced Propulsion Lab facility. Various ( $N_2$ , Ar, He,  $CO_2$ ) plasmas are created in a 0.75m long by 0.5m diameter cylindrical, glass vacuum chamber, see Figure 1. Vacuum levels as low as of 20 – 30 mTorr can be achieved with the attached mechanical vacuum pump. During steady state plasma generation the vacuum pressure attainable with low gas flow-rates is in the 0.1 – 0.5 Torr range. In the initial laboratory setup, plasma was generated by microwave (MW) breakdown of the working gas. A cylindrical, two volume MW  $TM_{011}$  resonating chamber is fitted at the top of the vacuum chamber. Commercial standard, 2.45GHz, microwaves are produced by a remote magnetron and brought to the chamber by

a three-meter long WR284 wave-guide. The coupling to the resonating chamber is accomplished with a metallic diaphragm. Typically a weakly ionized plasma column ( $10^{-4}$  ionization fraction,  $n_e \sim 10^{16} \text{ m}^{-3}$ ) is obtained for most of the gases used. The ionization fraction of the plasma is limited to a critical density given by the frequency of the microwaves.

The glow discharge ionization device (GDID) has been added to the system to perform subsequent ionization of the weak MW plasma.

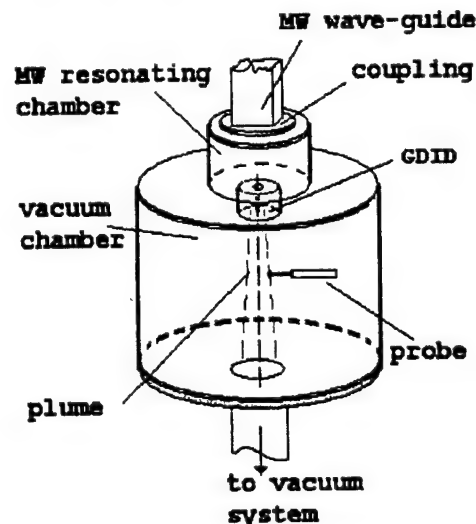


Figure 1. Plasma Generator and Vacuum System

The GDID has a cylindrical symmetry and consists of two electrodes. The anode is an aluminum cylinder of 86 mm diameter and 82 mm length with a smooth finish of its inside surface. The cathode is made of a stainless steel tube of 8.2 mm diameter and 36 mm length. The cathode is mounted in the center of the anode cylinder. The stainless steel tube is plugged at both ends with ceramic insulators and has a smooth exterior surface finish. A sketch of the device is shown in Figure 2. At the bottom an aluminum mesh closes the anode. This screen is part of the anode and has the role of confining the electric field inside the device. The anode has mounting brackets at the upper part and fastens the GDID to the bottom plate of the MW resonating chamber (see Figure 1). The distances from the cathode to the upper chamber wall and screen are roughly the same.



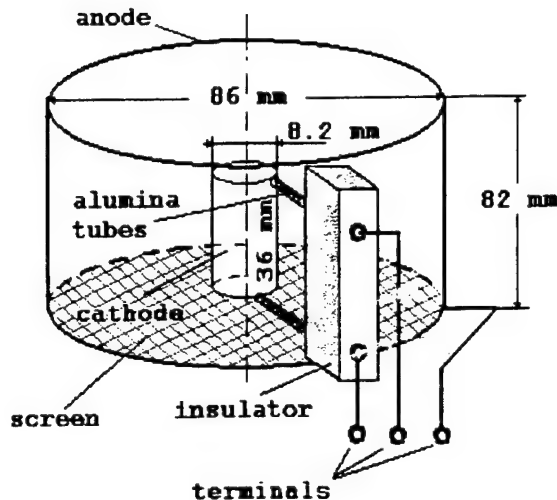


Figure 2. Glow Discharge Ionization Device

The GDID is powered by a variable 0 – 1.4kW, high voltage DC power supply. The power supply is a full wave rectifier, and is built with the positive terminal to ground. The voltage can be continuously varied from 0 – 2200V and is internally filtered by a 2.7 $\mu$ F capacitor bank.

The degree of plasma ionization obtained with a glow discharge is to some degree dependent on the cathode material. In the initial, "trial and error" stage a Nickel-Chromium (commercial heating element wire) filament cathode was used. The filament is a desirable geometry for the cathode, since most of the electric field lines seem to close inside the device. However the nickel-chrome wire did not withstand the heat generated during steady state operation. A second try was done with the current configuration: a continuous stainless steel tube. An open, continuous tube is a poor geometry for the cathode. The electric field lines inside the tube are parallel to the walls and stretch to all the metallic surfaces inside the vacuum chamber (which act as the anode). Consequently, the electrons emitted inside the tube are accelerated along these lines of field and eventually gain enough energy to become runaway electrons. The effect is an inefficient operation mode of the ionization device. The whole vacuum chamber glows faintly in this case, as these electrons hit the neutralizing surfaces. To prevent this effect the ends of the cathode were plugged with high temperature ceramics and the aluminum screen was added at the bottom of the device. A

disadvantage of the closed tube is a more intrusive presence in the flow at higher pressures and velocities. Future plans are to replace the stainless steel tube with a rhenium-tungsten (Re-W) cathode filament. A Re-W cathode has the advantages of being able to withstand the intense heat generated during the discharge and also of providing a higher thermionic electron emission rate from the surface. Due to the high cost of the rhenium wire, the trial runs of the device were made in the configurations mentioned.

### Ionization by Electron Collisions in the GDID

Electron collision ionization is possible if the free electrons in the gas are heated to a temperature higher than the gas temperature. In the GDID the electrons receive energy from the electric field and increase their kinetic energy in a direction parallel to the field. Collisions with heavy particles randomize this energy and the result is an increase in electron temperature. These hot electrons are then causing additional ionization. Since the electrons are much hotter than the ions or neutrals the process leads to nonequilibrium ionization. Thermal nonequilibrium lends a very desirable feature to the DC glow discharges plasmas: the gas remains relatively cold while highly conductive.

In the GDID the neutral gas enters from the top, ionizes as it passes through the intense field region and exits as plasma at the bottom. Spatially, the ionization process can be separated into two distinct regions: I) an active ionization region within the enclosed volume of the device, and II) a plasma relaxation-decay region downstream of the anode screen. This space free of the electric field is the region of interest, and is mapped by an array of electric probes.

I. The active ionization region is the space between the outer anode shell and the inner cathode tube. The top (chamber wall) and the bottom (anode screen) of the GDID are connected to the ground (anode) potential, and therefore the ionization volume is approximately equal to the volume of the device  $9 \sim 4.5 \cdot 10^5 \text{ mm}^3$ .

II. The plasma relaxation region is the space below the GDID in the vacuum chamber. If reasonably far from the anode screen, it can be



assumed that the electric field leakage outside the anode cylinder is small. In this region plasma does not receive extra energy from the field and starts decaying.

Qualitatively, a glow discharge is composed of a multitude of phenomena (discharge regions): dark spaces, a cathode and a negative glow, the positive column etc., although not all of them need be observed in the same time. Analytical descriptions for each of these phenomena can be found in the literature, see for instance Fowler<sup>6</sup>. Our goal is to describe the total behavior of the ionization device, without entering into the details of each of these phenomena.

Inside region I the relation between the electric field and the space charge density is given by Poisson's equation

$$\epsilon_0 \nabla E = n_i e - n_e e \quad (1)$$

Generally the Poisson equation (1) cannot be used to solve for the potential<sup>7</sup> but could eventually yield the charge density, once the potential distribution is known. Although the externally applied electric field gives the boundary conditions for equation (1), there is little hope that it can be easily integrated in case of a glow discharge. To make the problem mathematically tractable, in the following we make use of the plasma approximation:  $n_i = n_e$  while maintaining the condition  $\nabla E \neq 0$ .

Another possible approach to finding electron density is to relate the ionization rate to the electrical power supplied from the external circuit and to the gas properties. Due to their higher mobility the electrons are heated more in the electric field than the ions. Plasma conductivity is therefore due mainly to the electrons. The motion of the electrons creates an electron current of density  $j_e$ . The electric field energy absorbed by the electrons per unit volume is  $E \cdot j_e$ . This electron energy is lost by collisions with the heavy particles. The conservation of energy and momentum for an elastic collision yields the average energy loss per electron<sup>8</sup>  $(2m_e/m_s)(3/2)k_b(T_e - T_s)$ . The total energy loss to all species of heavy particles is

$$E \cdot j_e = 3n_e k_b \sum_s v_{es} \frac{m_e}{m_s} \delta_{es} (T_e - T_s) \quad (2)$$

where  $s$  sums over all species of heavy particles,  $v_{es}$  is the electron-particle collision frequency and  $\delta_{es}$  is the energy loss factor due to inelastic electron-particle collisions. It is fair to assume that the temperatures of all heavy species (ions and neutral particles) are equal  $T_i = T_n = T_s$ , and that the inelastic-collision loss factors  $\delta_{es}$  are also approximately the same. With these assumptions Equation (2) becomes

$$E \cdot j_e = 3n_e \frac{m_e}{m_s} k_b (T_e - T) \delta_{es} (v_{ei} + v_{en}) \quad (3)$$

In Equation (3) the mass of the neutrals was assumed equal to the ion mass  $m_n = m_i = m_s$  and the dot product  $E \cdot j_e$  was changed to its magnitude  $E j_e$  since both vectors have the same direction. The collisions of like particles (e.g. electron-electron) were ignored in (3) since they do not lead to significant net momentum and energy transfer. However, electron-electron collisions are important because they provide the means for the electrons to acquire a maxwellian distribution. The left-hand side in Equation (3) is the power per unit volume supplied to the gas from the external circuit.

From (3) an estimate for the electron density can be obtained if radiation, attachment, recombination and other electron loss mechanisms are ignored. The collision frequency<sup>7</sup> of an electron with a heavier particle is  $v_{es} = Q_{es} n_s c_e$  where  $Q_{es}$  is the collision cross section of electron-particle and  $c_e = (8k_b T_e / \pi m_e)^{1/2}$  is the mean thermal speed of the electrons (if maxwellian distribution). Replacing these in Equation (3) and multiplying by the volume of the GDID we obtain

$$E \cdot j_e \mathcal{V} = 3n_e \frac{m_e}{m_s} k_b (T_e - T) \delta_{es} c_e \mathcal{V} (n_i Q_{ei} + n_n Q_{en}) \quad (4)$$

The left-hand side in Equation (4) is the electric power,  $W$  supplied to the device. The density of the neutral particles can be written in terms of the total particle density  $n$  in the gas  $n_n = n - n_i - n_e$ .

Using plasma approximation ( $n_i = n_e$ ) Equation (4) becomes

$W =$

$$3n_e \frac{m_e}{m_s} k_b (T_e - T) \delta_{es} c_e g \cdot [n_e Q_{ei} + (n - 2n_e) Q_{en}] \quad (5)$$

Thermodynamically the total particle density is related to the gas pressure  $n = p_0/k_b T$ . Let the ratio of electron pressure to gas pressure be  $\beta = p_e/p_0$  and the ratio of electron temperature to gas temperature be  $\alpha = T_e/T$ . Evidently, from the previous arguments  $\alpha > 1$  and  $\beta < 1$ . Factoring out the electron density and grouping terms Equation (5) becomes

$$\frac{W}{P_0} = 3n_e \left( \frac{m_e}{m_s} \right) \cdot (\alpha - 1) \delta_{es} c_e g \cdot \left[ \frac{\beta}{\alpha} (Q_{ei} - 2Q_{en}) + Q_{en} \right] \quad (6)$$

Generally, the collision cross-sections are complicated functions of electron energy and gas properties. Most of the collision cross section values were found experimentally and are tabulated. Further simplification of Equation (6) is possible if we consider an approximate analytical formula for the electron-ion collision cross-section as presented in Sutton<sup>8</sup>. The average electron-ion collision cross-section can be calculated with the following formula

$$\langle Q_{ei} \rangle = \frac{\pi^3 \ln \Lambda}{16} \left( \frac{e^2 Z_i}{4\pi\epsilon_0} \right)^2 \frac{1}{(k_b T_e)^2} \quad (7)$$

where  $Z_i$  is the number of charges per ion. Due to lack of information the  $Z_i$  is assumed equal to unity – singly ionized ions. Equation (7) is a good approximation if the electron-electron collision frequency is smaller than the collision frequency of the electrons with heavy particles. The results obtained with (7) are only approximate and are generally higher than the actual collision cross-

section values. The factor  $\ln \Lambda$  is a small angle collision effect<sup>7</sup> and a sufficiently accurate value for most plasmas is 10. Sutton<sup>8</sup>, citing other references, provides also experimental electron-neutrals collision cross sections  $Q_{en}$  and energy loss factors  $\delta_{en}$  for nitrogen, as functions of electron energy. Denoting  $W/p_0 = \xi$  the electron density is

$$n_e(\xi) = \frac{\xi \left( \frac{m_s}{m_e} \right) \cdot \left[ \frac{\beta}{\alpha} (Q_{ei}(T_e) - 2Q_{en}) + Q_{en} \right]^{-1}}{3(\alpha - 1) \delta_{es}(T_e) c_e(T_e) g} \quad (8)$$

Some quantities in (8) are functions of only electron temperature. Therefore, the electron density will be scaled with  $\xi$  and having  $T_e$  as a parameter. Equation (8) estimates the electron density in the plasma based on the electric power input, with the assumptions made.

The conductivity of the plasma is calculated with a collisional model<sup>8,9</sup>. According to the kinetic theory, the conductivity of an ionized gas is dependent on the collision cross sections of electrons with neutral atoms and ions:  $\sigma = n_e e^2 / (m_e c_e (n_n Q_{en} + n_i Q_{ei}))$ . Using expression (7) the conductivity is

$$\sigma = \frac{n_e e^2}{m_e c_e} \left[ \frac{1}{n_n Q_{en} + \frac{\pi^3 \ln \Lambda}{16} \left( \frac{e^2}{4\pi\epsilon_0} \right)^2 \frac{n_i}{(k_b T_e)^2}} \right] \quad (9)$$

### Experimental Setup

Figure 3 presents a sketch of the GDID and the array of Langmuir probes. Six electric probes are mounted on a slide with two degrees of freedom actuated by stepper motors (not shown in Figure 3 for simplicity). The arrangement provides reproducible probe positioning, single

point measurements and also the possibility for rapid scans across the plasma.

The flowing plasma provides a path for the flow of electric current between the probes and ground. The probes are made of a Re-(5%)/W-(95%) wire with a diameter of 0.5 mm and active length of 5 mm. The first probe is located about 25 mm below the aluminum screen. A distance of 12 mm separates each of the following probes. The probes are positioned to scan a mid-section of the plume.

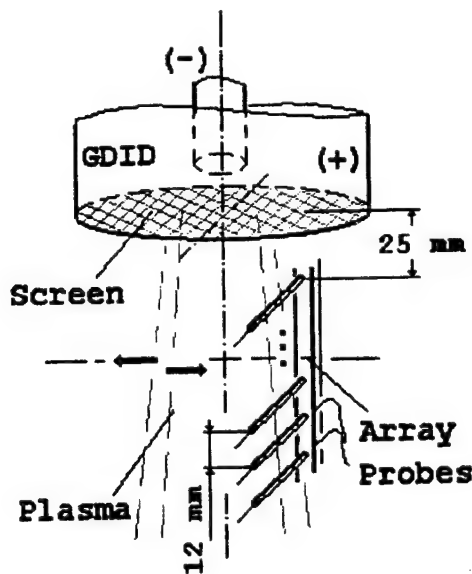


Figure 3. GDID and Probe Array

A detailed description of the electrical circuitry for single Langmuir probe measurements was described in reference [2]. A signal generator produces a ramp signal with a frequency in the range 10 - 20 Hz and a voltage typically in the  $\pm 10$  V<sub>pp</sub> range. The signal is amplified (and DC offset) by a programmable power supply (voltage amplifier). The voltage amplifier supplies to the probes the amplified saw-tooth signal with an amplitude of -90V...+10V. The currents flowing through the probes are found through voltage drop measurements across 100Ω resistors inserted in the circuit of the probes. The data acquisition and GDID power control was directed from two Pentium II class computers equipped with the National Instruments' LabView 5.0 software. A third computer was used to control

the actuators of the stepper motors positioning the probe.

## Results

Four experimental runs have been completed with nitrogen. With few exceptions, the tests showed that during steady operation the device can produce stable plasma columns. Two tests were attempted with argon but the device failed and no reliable data could be obtained. The chamber (plasma) pressure during the nitrogen tests was set to three values 300 - 400 - 500 mTorr. The power supplied to the ionization device was in the 75 - 130 watt range. Attempts to raise the power level in the argon runs led to the failure of the alumina insulating tubes. Analysis of the probe data showed that the electric field leakage affected the probes closest to the screen. Analysis of the data from the other probes yielded estimates of the electron temperature density and electron density. The six-probe array is capable of yielding spatially resolved electron density maps in the plume. In this presentation only the average values of these measurements are considered.

The electron temperature in the nitrogen runs was about 1 - 2eV. Gas temperature measurements have not been made for these initial runs. Prior experiments with nitrogen have shown the gas temperature to be roughly one order of magnitude smaller than the electron temperature,  $\alpha \sim 10$ . An upper limit to the pressure ratio  $\beta$  can be estimated from the equation of state of an ideal gas written independently for each partial pressure:  $\beta = p/p_0 = n_e k_b T_e / (n_i K_b T + n_e k_b T + n_e k_b T_e)$ . Let  $n_i = n_e$  from plasma approximation and assume the limit case of  $n_n = 0$  (fully ionized gas). In these conditions  $\beta \sim T_e / (T_e + T_i) = \alpha / (\alpha + 1) = 0.9$ . The N<sub>2</sub> experimental results are plotted on the same graph with the analytical predictions ( $\alpha = 10$ ,  $\beta = 0.9$ ) in Figure 4. It is to be noted that the model prediction (Equation (8)) is deduced for region I while the measurements are made in region II. Therefore, it can be stated with certitude that the model predicts an upper bound for the electron density in the downstream plasma.

The failure of the alumina insulating tubes in the argon runs allowed part of the electrical power to be dissipated directly into heat in the electrodes. Visibly the argon plasma was much weaker in terms of light emission and to some extent more unstable.

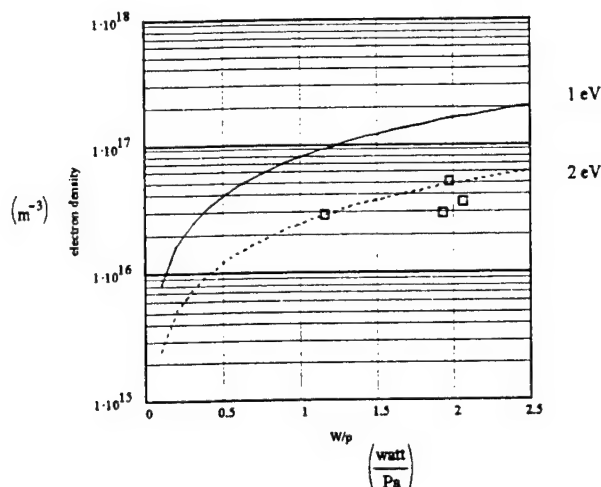


Figure 4. Nitrogen Analytical Predictions (*lines*) and Experimental Data ( $\square$ )

With an average electron temperature of 1.5 eV and an electron density of  $3.5 \cdot 10^{16} \text{ m}^{-3}$ , the conductivity of the nitrogen plasma (using Equation (9)) is about  $10 \text{ ohm}^{-1} \text{ m}^{-1}$ .

### Conclusions and Discussion

The construction features of a cylindrical glow discharge ionization device were presented. Several construction issues were identified during this phase: cathode geometry and material, the resistance of the insulating materials and the necessity for a better confinement of the electric field inside the device. The paper also presented a simple analytical model for the electron density of the plasma. The model shows that the mode of operation of this type of device can be characterized by an intensive property: the ratio of power in to gas pressure  $W/p_0$ . Tests were run with nitrogen at different power levels and different pressures and the experimental data seem to validate the model prediction. More tests at higher power levels and in different gases are necessary for a full device characterization.

The power levels supplied to the gas were modest  $\sim 130 \text{ Watt}$ . The electron density in the plasma generated was in the  $10^{16} \text{ particles/m}^3$  range. Comparison with MW breakdown<sup>2</sup> shows that the GDID produces plasma with a density about one order of magnitude higher, while the power consumed is one order of magnitude smaller.

The glow discharge ionization device showed potential for ionization of flowing gas columns. Future efforts in improving the performance of the GDID are necessary. A new cathode (Re-W) and a better power supply are in the construction phase in the lab. Future tests will also include gas temperature and upstream pressure measurements. Independent spectrometric measurements of the electron temperature are planned, and will help calibrate electrical probe data.

### Acknowledgements

The authors wish to thank Mr. Paul Vaughan and Mr. Sam Brockington for their assistance in setting up the experimental apparatus. This research program was sponsored in part by NASA Marshall Space Flight Center and by the Air Force Office of Scientific Research under the contract number F 49620-98-0-0083.

### References

- <sup>1</sup>Sullivan, D. J., et al., "Current Status of the Microwave Arcjet Thruster", AIAA-95-3065, 31<sup>st</sup> AIAA/ASME/SAE/ASEE Joint Propulsion Conference, San Diego, CA, July 10-12, 1995
- <sup>2</sup>Deaconu, S., et al., "Diagnostics of Electric Properties of Flowing Microwave Plasmas for MHD Applications", AIAA-99-2715, 35<sup>th</sup> AIAA/ASME/SAE/ASEE Joint Propulsion Conference, Los Angeles, CA, June 20-24, 1999
- <sup>3</sup>Deaconu, S., et al., "Assessment of the Magnetic Field Reconnection Potential for Space Propulsion Applications", AIAA-2000-2270, 31<sup>st</sup> AIAA

Plasmadynamics and Lasers Conference, Denver, CO, July 19-22, 2000

<sup>4</sup>Meek, J. M., and Craggs, J. D., (*editors*) "Electrical Breakdown of Gases", J. Wiley and Sons, 1978

<sup>5</sup>Raizer, Y. P., "Gas Discharge Physics", Springer-Verlag, Berlin, 1991

<sup>6</sup>Fowler, R. G., "Structure of the Glow Discharge", Chapter 15, pp. 217, in "An Introduction to Discharge and Plasma Physics", edited by S. C. Haydon, Department of University Extension, The University of New England, N.S.W. Australia 1964

<sup>7</sup>Chen, F. F., "Introduction to Plasma Physics and Controlled Fusion, Volume I: Plasma Physics", Plenum Press, NY, 1984

<sup>8</sup>Sutton, G. W., and Sherman, A., "Engineering Magnetohydrodynamics", McGraw-Hill Book Co., NY, 1965

<sup>9</sup> Magnetohydrodynamic Accelerator Research Into Advanced Hypersonics (MARIAH), Final Report, NASA/CR-97-206242, 1997



**AIAA 2000-3882**

**Experimental Study of Microwave Plasma  
MHD Accelerators**

Zhongmin Li, Jonathan E. Jones, Clark W. Hawk

Propulsion Research Center  
University of Alabama in Huntsville  
Huntsville, Alabama 35899

**36th AIAA/ASME/SAE/ASEE Joint Propulsion Conference &  
Exhibit**

16-19 July 2000 / Huntsville, AL

# Experimental Study of Microwave Plasma MHD Accelerators

Zhongmin Li<sup>†</sup>, Jonathan E. Jones<sup>‡</sup>, Clark W. Hawk<sup>\*</sup>

*Propulsion Research Center*

*The University of Alabama in Huntsville*

*Huntsville, AL 35899*

## Abstract

Experimental investigations of MHD accelerators coupled with microwave generated non-equilibrium plasma are underway at the UAH Advanced Propulsion Laboratory. A 0~6 kW microwave plasma generator utilizing a TM<sub>011</sub> microwave plasma resonant cavity operating at 2.45 GHz was used to breakdown various working gases. A 2 inches continuous electrode cross-field accelerator configuration was chosen for this phase of our research. The detailed measurements of electron temperature and density at the exit of the microwave generator and at the entrance of the MHD channel were obtained by using a quadruple Langmuir probe. The gases temperature and pressure were also obtained. The results showed that an electron temperature an order of magnitude higher than the gas temperature can be obtained in both diatomic and monatomic gases. Detailed measurements of the electrical, thermal and kinetic properties of the plasma in the accelerator channel will be conducted. Based on these, the efficiency of the channel will be calculated.

## Nomenclature

$B$	Magnetic field strength
$c_e$	Mean thermal speed of electrons
$E$	Local electric field
$J$	Current density
$m_e$	Electron rest mass
$n_e$	Electron number density
$n_n$	Neutral gas number density
$n_s$	Number density of species $s$
$Q$	Average collision cross section

$Q_{es}$	Collision cross section for electrons with species $s$
$Q_{en}$	Average collision cross section for electrons with all neutral species
$Q_{ei}$	Average collision cross section for electrons with ion $i$
$q_e$	Electron charge
$T_e$	Electron temperature
$V$	Velocity
$\beta$	Hall constant ( $1/q_en_e$ )
$\eta$	Efficiency
$\rho$	Density
$\sigma$	Electrical conductivity
$\omega$	Electron cyclotron frequency
$\tau$	Mean time interval between collisions for electrons with ions and neutrals
$\omega\tau$	Hall parameter

## Introduction

Magnetohydrodynamics has been studied for the past fifty years for power generation<sup>1, 2</sup>, hypersonic wind tunnel<sup>3</sup>, and propulsion applications<sup>4</sup>. This work focuses on non-equilibrium plasma MHD accelerators for in-space propulsion applications. The non-equilibrium plasmas with electron temperature much higher than gas temperature can improve the efficiency of the MHD accelerator by reducing the heat transfer to channel walls, and lowering the thermal energy remaining in flow, while increasing the electrical conductivity of the flow<sup>5</sup>.

Of particular interest was the use of water, carbon dioxide, or other non-conventional propellants as the working fluid for the MHD accelerator. Both water and carbon dioxide are plentiful throughout the solar system, enabling in-situ propellant utilization. However, because of the relatively large electron collision cross section and electron energy loss factors for water and

<sup>†</sup>Graduate Research Assistant, Member AIAA

<sup>‡</sup>Research Associate, Member AIAA

<sup>\*</sup>Director and Professor, Fellow AIAA

carbon dioxide, it has been assumed previous to this work that non-equilibrium ionization would be unable to produce adequate conductivity for MHD acceleration<sup>6</sup>.

However, a unique combination of microwave generated plasma and a low pressure (<10 Torr) Hall current MHD accelerator offers significant performance gains for MHD accelerators operating with water or carbon dioxide. This combination is enabled by preferentially adding energy to the electrons in the flow enhancing the conductivity of the working fluid<sup>5</sup>. One method to accomplish this is to excite the plasma with radio or microwave frequency radiation. By adding energy to the electrons, non-equilibrium plasma can be created where the temperature of the electrons is higher than the temperature of the gas. The resulting free electron density can then be several orders of magnitude higher than electron densities at thermodynamic equilibrium. Thus, the operation of an MHD accelerator with non-equilibrium plasma can: reduce thermal losses, extend electrode life, and improve overall efficiency<sup>7</sup>.

In traditional MHD devices such as generators and hypersonic wind tunnels, non-equilibrium conditions are hard to maintain due to operation at pressures from 10 to 100atm<sup>5</sup>. At these pressures collision rates are high, and a large amount of energy must be added to the flow to depart from equilibrium conditions. However, because in-space propulsion systems do not require operation at high pressures, the energy required to maintain non-equilibrium ionization is reduced, thus it is advantageous to examine non-equilibrium ionization for in-space MHD accelerators.

### MHD Accelerators

The interaction of electrically conducting plasma with applied electric and magnetic fields is given by the Generalized Ohm's law. For partially ionized plasma and neglecting ion-slip, the Generalized Ohm's law may be written in the form of equation (1)<sup>6</sup>.

$$\mathbf{j} = \sigma [\mathbf{E} + \mathbf{V} \times \mathbf{B} - \beta (\mathbf{j} \times \mathbf{B})] \quad (1)$$

In Cartesian coordinates system, it has the following forms:

$$j_x = \sigma [E_x + vB_z - wB_y - \beta(j_y B_z - j_z B_y)] \quad (2)$$

$$j_y = \sigma [E_y + wB_x - uB_z - \beta(j_z B_x - j_x B_z)] \quad (3)$$

$$j_z = \sigma [E_z + uB_y - vB_x - \beta(j_x B_y - j_y B_x)] \quad (4)$$

The MHD accelerators utilize the Lorentz force that is  $\mathbf{J} \times \mathbf{B}$  to accelerate the plasma flow. Generally speaking, there are two categories of MHD plasma accelerator configurations: the crossed-field Faraday accelerators as shown in Figure 1 and the Hall current accelerators as shown Figure 2.

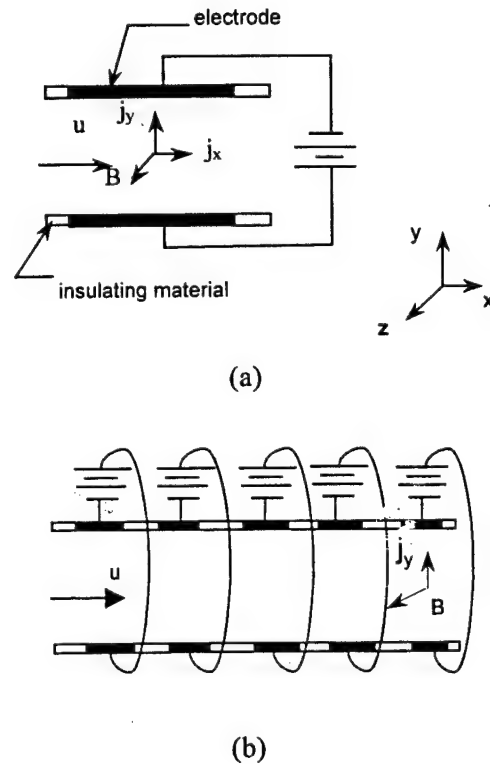


Figure 1 Crossed-field Faraday accelerator configurations. (a) Continuous electrodes (b) Segmented electrodes

For the continuous electrode Faraday accelerator shown in Figure 1(a),  $E_x = B_y = B_x = v = w = j_z = 0$ . Thus, from Equations (2)–(4) we can obtain:



$$j_x = -\frac{\sigma\omega\tau(E_y - uB)}{1 + (\omega\tau)^2} = -\omega\tau j_y \quad (5)$$

$$j_y = \frac{\sigma(E_y - uB)}{1 + (\omega\tau)^2} \quad (6)$$

Where,  $\omega\tau$  is the Hall parameter and can be calculated with the following equation:

$$\omega\tau = \sigma\beta B = \frac{q_e B_0}{m_e c_e \sum_{k,s} n_{k,s} Q_{k,s}} \quad (7)$$

Due to the Hall effect, currents perpendicular to the applied electrical field direction are produced. These currents are so called Hall currents. In a continuous electrode crossed-field accelerator configuration,  $j_y$  is the regular current and  $j_x$  is the Hall current. The Hall parameter can be interpreted as the ratio of the Hall current to the current parallel to the electric field<sup>6</sup>.

For the configuration shown in Figure 1(a), the acceleration force  $\mathbf{J} \times \mathbf{B}$  is produced by the interaction of cross direction current,  $j_y$ , with  $\mathbf{B}$  field because only  $j_y \times \mathbf{B}$  lie in the direction of the plasma flow. The Hall current does not contribute to the useful acceleration, and when  $\omega\tau > 1$ , this current will be larger than the parallel current. Because of large magnetic fields and/or low particle densities, axial Hall current can become significant. These interact with the applied magnetic field, produce undesirable transverse forces and reduce performance<sup>8</sup>.

In the segmented electrode Faraday configuration as shown in Figure 1(b), each pair of electrodes is connected separately to an external power supply, so that no Hall current can flow axially. In this case  $j_x = 0$ . Thus,

$$j_y = \sigma(E_y - uB) \quad (8)$$

The ideal efficiency for a MHD accelerator is obtained by

$$\eta = \frac{\text{Push Work}}{\text{Input Power}} \quad (9)$$

Thus, the ideal efficiency for this segmented Faraday accelerator is given by

$$\eta_f = \frac{j_y u B}{E_y j_y} = \frac{1}{K_F} \quad (10)$$

Where the loading factor,  $K$  for the Faraday channel equals

$$K_F = \frac{E_y}{uB_z} \quad (11)$$

The thrust of segmented Faraday accelerator is given by

$$F_x = j_y B = \sigma u B_z^2 [K_F - 1] \quad (12)$$

However, an alternative approach is to use the Hall current directly to produce an axial acceleration instead of suppressing it. Figure 2 shows a Hall current accelerator with constant area channel. In this configuration, an axial electrical field is applied. The resulting current flow interacts with the transverse  $\mathbf{B}$  field inducing a Hall current across the accelerator. The segmented electrodes are short-circuited to encourage this Hall current. The Hall current  $j_y$  interacts with the  $\mathbf{B}$  field and produces an accelerating force along the fluid flow direction.

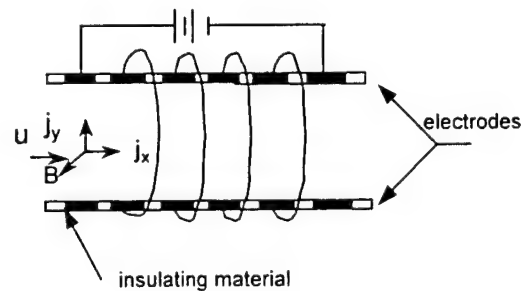


Figure 2 Hall current accelerator with constant area channel.

For the configuration shown in Figure 2,  $E_x = B_y = B_x = v = w = 0$ , which upon substitution into Equations (2)~(4), yield

$$j_x = -\frac{\sigma u B_z (\omega \tau)}{1 + (\omega \tau)^2} (1 + K) \quad (13)$$

$$j_y = \frac{\sigma u B_z}{1 + (\omega \tau)^2} [(\omega \tau)^2 K - 1] \quad (14)$$

Where the loading factor  $K$  is defined by

$$K = \frac{E_x}{(\omega \tau) u B_z} \quad (15)$$

The ideal efficiency for Hall current accelerator with this configuration is:

$$\eta = \frac{F_x u}{j_x E_x} = \frac{(\omega \tau)^2 K - 1}{(\omega \tau)^2 K(K + 1)} \quad (16)$$

The Hall current channel thrust is given by

$$F_x = \frac{\sigma_0 u B_z^2}{1 + (\omega \tau)^2} [(\omega \tau)^2 K - 1] \quad (17)$$

Using Equations (10) and (16), the relationships for the ideal thrust efficiency for the cross-field and Hall current MHD accelerators are shown in Figure 3 as a function of loading factor. While the cross-field accelerator has been experimentally tested more thoroughly, the Hall current accelerator has comparable performance for large Hall parameter. In addition, the Hall current accelerator requires only a single power supply, substantially reducing the power conditioning equipment required for in space propulsion vehicles.

Figure 3 shows that the efficiency of Hall current accelerator can be comparable to that of a Faraday accelerator for a Hall parameter greater than 2. The next question that must be asked is if the thrust of the Hall current accelerator is competitive with that of a Faraday channel. The thrust for Hall and Faraday channels is given in Equations (12) and (17), respectively. Figure 4 plots the thrust for the Hall and Faraday channels divided by  $\sigma_0 u B_z^2$ . For optimum loading the thrust of the Hall accelerator is always lower than

that of the Faraday accelerator. However, the thrust increases and the efficiency drops off slowly as the loading factor is increased. As the Hall parameter is increased the apparent disadvantage of the Hall channel is minimized.

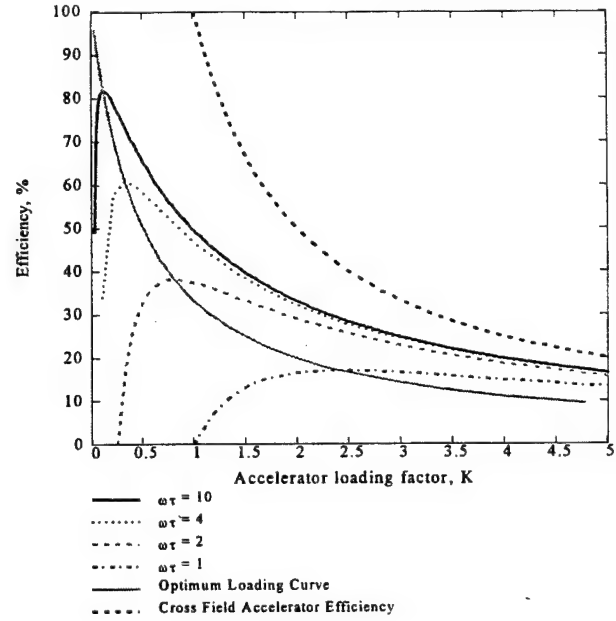


Figure 3 MHD efficiency comparison for Hall and Faraday accelerators.

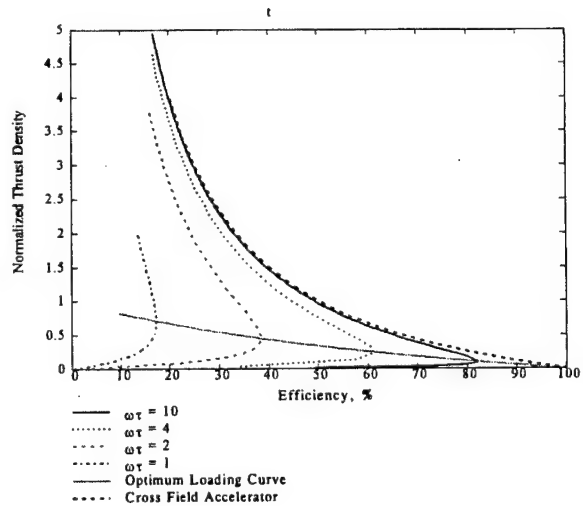


Figure 4 Thrust densities versus efficiency for Hall and Faraday channels.

Figure 2 shows a two-dimensional rectangular cross section Hall current accelerator configuration. In past decades, a few Hall configuration experiments were conducted<sup>8, 9, 10, 11</sup>.

However, most of them have utilized the coaxial Hall current accelerator configurations shown in Figure 5.

In this configuration, as shown in Fig. 5(a), an axial electrical field is applied along the channel; thus, the ordinary current is the axial current  $j_x$ , and the Hall current is the azimuthal current  $j_\theta$ . In configuration 5(b), a radial electric field is applied, and the ordinary current is  $j_r$ , the segmented electrodes are used to limited  $j_x$ . The Hall current is  $j_\theta$ .

In both Figure 5(a) and (b), the azimuthal Hall current interacting with the applied radial magnetic field component produces an axial Lorentz force  $j_\theta B$ , that acts upon and accelerates the plasma.

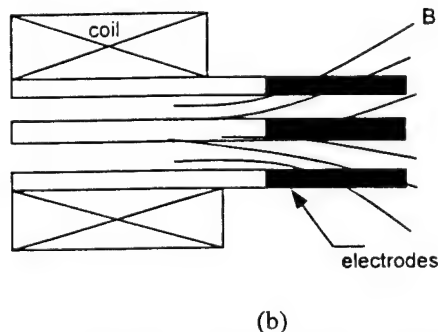
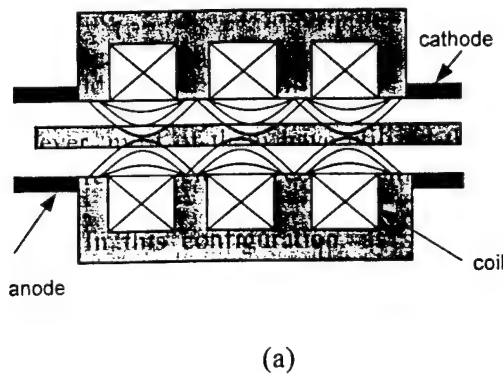


Figure 5 Coaxial Hall current accelerator configurations (a) utilizing an axial electric field and radial magnetic field, and (b) utilizing a radial electric field and a slanted magnetic field with segmented electrodes<sup>9</sup>.

### Experimental Setup

The experimental setup for testing microwave plasma MHD accelerators includes a

microwave plasma generation system, propellant and steam feed system, a vacuum system, MHD accelerators, power supplies, and plasma diagnostic and data acquisition system. The vacuum chamber, microwave resonant cavity and MHD accelerator assembly is shown in Figure 6.

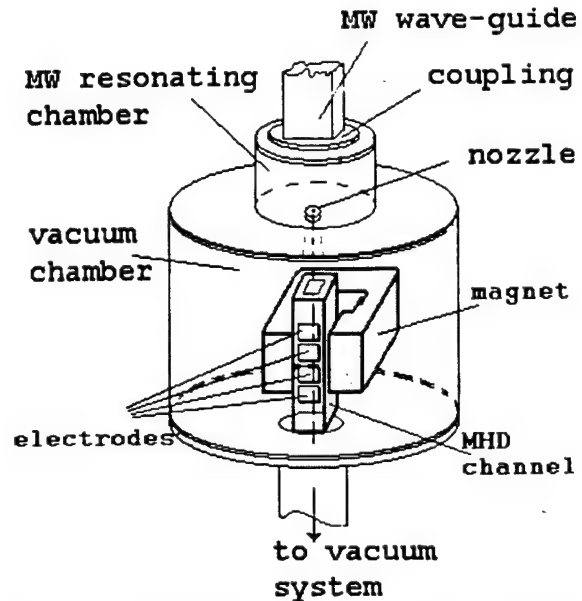


Figure 6 Schematic diagrams of the vacuum, microwave resonant cavity and MHD accelerator assemblies

The microwave plasma generation system generates the plasma to drive the MHD channel. Microwaves generated by a 0-6 kW variable power microwave generator, are delivered to a 4-inch diameter by 8-inch long  $TM_{011}$  mode resonant cavity operating at 2.45GHz by several components of WR 284 wave-guide. A propellant and steam feed system is also mounted to the cavity to supply propellant gases (Argon, helium, nitrogen, carbon dioxide and steam). The plasma is expanded to the vacuum chamber from the cavity through a one-inch hole or converging-diverging nozzle after it is heated in the microwave field.

The vacuum system consisted of an 18-inch diameter by 24-inch length glass cylinder with 18-inch Varian port rings on the top and bottom. Twelve ports were available in both the top and the bottom port rings for optical and electrical feeds. The microwave cavity was mounted to the top of the tank with an aluminum

adapter plate. The adapter plate was connected to a pulley system and hand crank, which was used to gain access to the chamber. A Stokes, Model 412H-H, 300 CFM roughing pump provided base pressures down to 10 mTorr. Vacuum pressures between 0.5 – 2.0 Torr were maintained, while operating the microwave cavity. Vacuum pressure was measured with a Varian 801, thermocouple vacuum gauge with a range of 0 to 2,000 mTorr. A 300KW DC power supply has been purchased. The maximum output of the DC is 60V/1000A, or 500V/600A.

At this phase, a continuous electrode cross-field MHD accelerator has been made to study the behaviors of microwave generated non-equilibrium plasmas in the simple cross-field channel. The actual configuration is shown schematically in Fig. 7.

In Fig 7, the channel body was made with Boron Nitride. The actual channel length is 2.4 inches. The cross section is approximately 0.6 inch wide by 0.65 inch high. The anode and cathode are 2 inch long and were made using copper. There are two aluminum plates at the two ends used to hold the channel and couple the channel to the microwave cavity.

A permanent magnetic was purchased to provide a magnetic field for the channel. The distance between the two magnetic poles is 1.2 inches. The magnetic field along the centerline of the channel is shown in Figure 8. A maximum magnetic field of 0.3 Tesla has been measured.

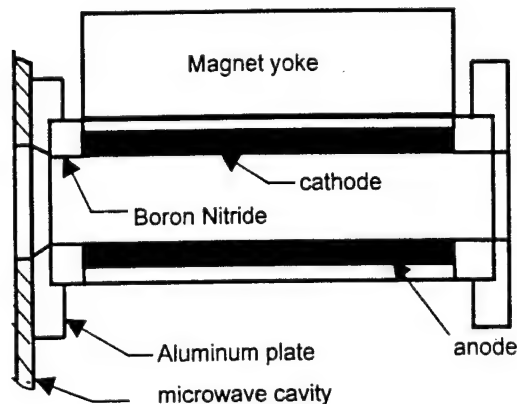


Figure 7 Schematic of the MHD accelerator

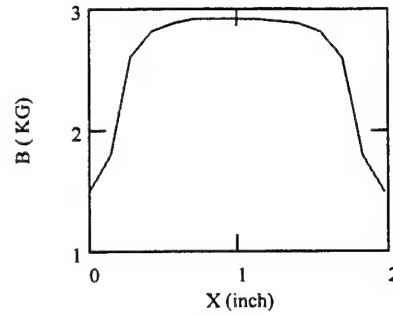


Figure 8. Magnetic field curve

Quadruple Langmuir probes were constructed to measure electrical transport properties. Tungsten wire was used for the electrodes. Four-hole alumina tubing was used to insulate the wire or probe electrodes. The alumina tubing was supported with stainless steel tubing that was connected to a shielded connecting block providing support for the probe. BNC connectors were attached to the shielded box to provide electrical connection for the probe circuitry.

The four-probe configuration is shown in Figure 9. Two twelve-volt batteries were used in these experiments to supply a floating electric potential between probes 1 and 3, and probes 1 and 4. Probe 2 is allowed to float; and measurements are made of the voltage between probe 1 and 2, and the current flow between probes 1 and 3, and probes 1 and 4.

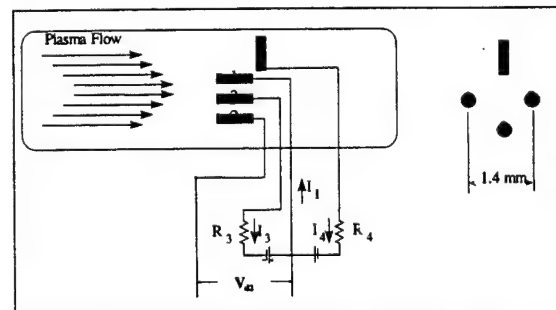


Figure 9 Quadruple Langmuir probes setup.

The derivation of the quadruple probe response is presented by Burton and Bufton<sup>12</sup>. The electron temperature can be obtained from

$$1 = \frac{1 + \exp(\phi V_{d3}) - 2 \exp[\phi(V_{d3} - V_{d2})]}{(I_4 / I_3) \{ \exp[\phi(V_{d3} - V_{d2})] - 1 \}} \quad (18)$$

The quantities  $V_{d2}$ ,  $I_3$ , and  $I_4$  are measured quantities, and  $V_{d3}$  is the battery voltage. The electron temperature is found by solving for  $\phi$  through iteration and noting that  $T_e = q_e/k_b\phi$ .

The electron density is given by

$$n_e = \frac{\kappa \left( \frac{I_3}{A_3} \right) \left( 1 + \frac{I_4}{I_3} \right) \exp\left(\frac{1}{2}\right) (m_{ion})^{1/2}}{q_e (k_b T_e)^{1/2} [\exp(\phi V_{d2}) - 1]} \quad (19)$$

### Results

The objective of this phase is to experimentally study a continuous electrode cross-field MHD accelerator and characterize the plumes of a 2.45 GHz microwave-generated plasma with various working fluids. Tests to date have focused on measurement of electron density and electron temperature of microwave generated plasma plumes at the inlet of the MHD accelerator. The tests to measure the plume properties at the exit of the MHD accelerator, and thus, investigate the accelerator behavior, have not yet been conducted.

To provide supersonic flow at the inlet of the accelerator, plasmas were expanded through a nozzle. Tests were conducted to determine the electron density and temperature at the nozzle exit for various expansion ratios. Figure 10 and 11 show the electron density and temperature profile for nitrogen with a 7.11 area ratio nozzle at a flow rate 155mg/sec.

The open cavity tests were conducted with the nozzle removed from the microwave resonant cavity, allowing the flow to expand freely through a 1-inch diameter hole. Electron density and temperature profiles at a chamber pressure of 600mTorr and a flow rate of 393mg/sec are shown in Figure 12 and 13, respectively. Axial profiles of electron temperature and density and gas temperature are shown respectively in Figures 14, 15 and 16 for argon, helium, carbon dioxide, nitrogen and steam.

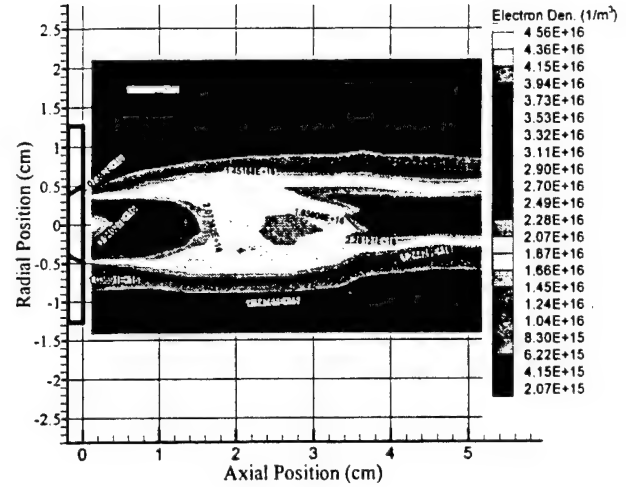


Figure 10 Electron density profile for nitrogen with large nozzle

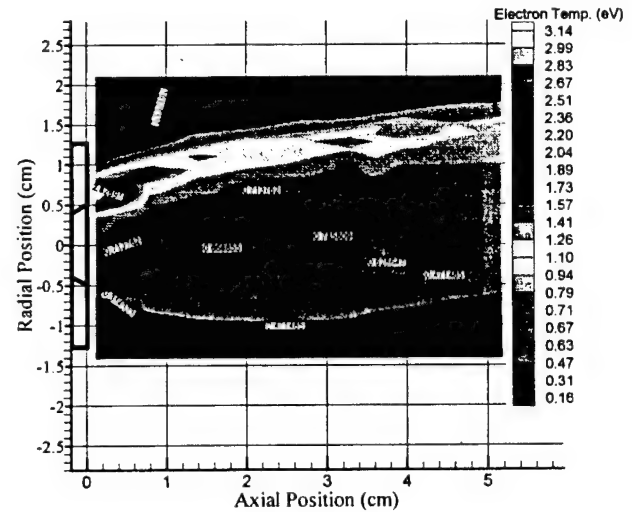


Figure 11 Electron temperature profile for nitrogen with large nozzle.

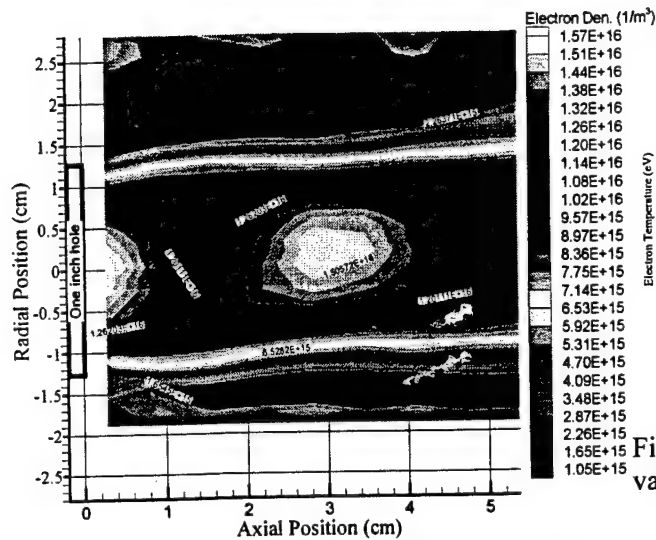


Figure 12 Electron density profile for carbon dioxide with no nozzle

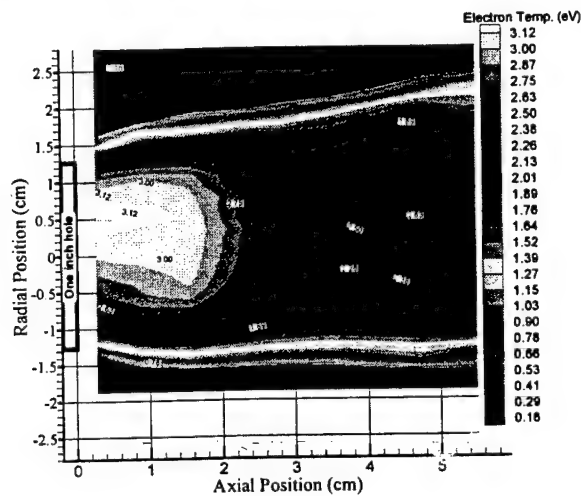


Figure 13 Electron temperature profiles for carbon dioxide with no nozzle

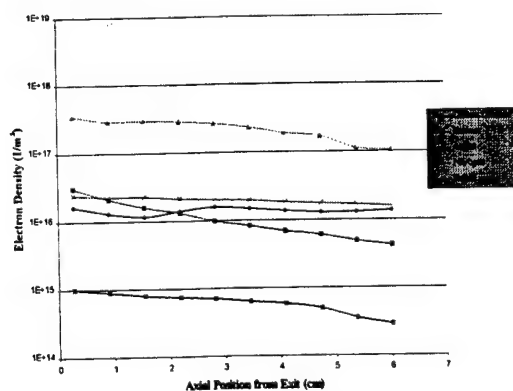


Figure 14. Axial scan of electron density for various gases.

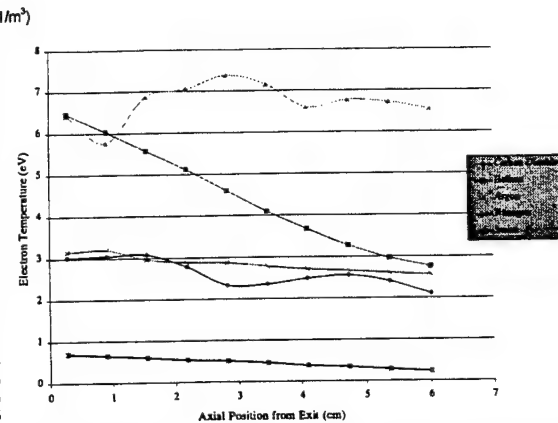


Figure 15. Axial scan of electron temperature for various gases.

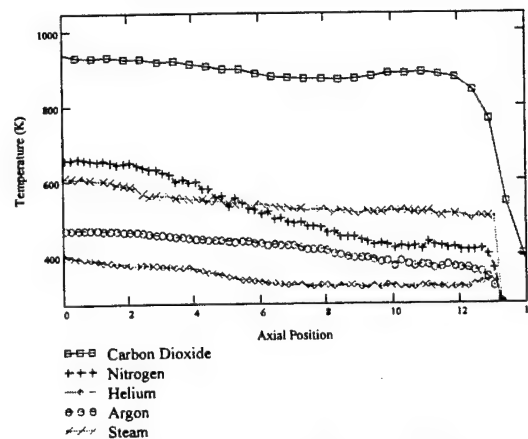


Figure 16 Axial gas temperature profiles

### Conclusion and Discussion

The results showed that non-equilibrium plasmas with electron temperatures an order of magnitude higher than the gas temperature can be created with the microwave plasma generator. For the monatomic gases argon and helium, electron densities slightly higher than the critical plasma density for 2.45 GHz microwaves ( $10^{17} \text{ e/m}^3$ ) were obtained. For diatomic and polyatomic molecules, electron densities were one to two orders of magnitude below the critical density.

This leads to the conclusion that microwave resonant cavities may be used directly for the MHD accelerator tests using argon as working fluid, but it cannot be used as the sole source of ionization for MHD accelerators; however, the high electron temperatures obtained suggest the possibility of driving the non-equilibrium ionization to acceptable levels within

the MHD channel itself. In addition, the gas temperatures were well below the temperatures required for thermal ionization; therefore, heat transfer to the walls and thermal losses at the accelerator exit should be reduced proportionally.

The current Faraday type MHD accelerator will be tested utilizing the microwave plasma source. The detailed measurements of the electrical, thermal and kinetic properties of the plasma within the accelerator channel and at its exit will be conducted under various operating conditions.

Based on the current measurement, the Hall parameters for various plasmas were estimated using Equation (7). The results show the Hall parameters for current test conditions are 10-100. This coupled with the fact that a Hall channel can be operated with a single power supply makes it the configuration of choice for our next phase experiments. The present accelerator is not water-cooled. Because the large power input into the accelerator electrodes, the run times for each test have to be limited within several seconds. A water-cooled coaxial Hall current configuration is under considering for our next phase.

### Acknowledgements

The authors appreciate the support of Mr. Tony Robertson with magnet design and characterization. Mr. James Kodrowski has provided significant support through the fabrication of critical test articles. This research was supported by a grant from the Air Force Office of Scientific Research under contract number F49620-98-0-0083. Additional support and equipment has been provided by NASA's Marshall Space Flight Center.

### Reference

- <sup>1</sup> Rosa, Richard J, " Magnetohydrodynamic Generators and Nuclear Propulsion," *ARS Journal*, Aug. 1962.
- <sup>2</sup> Bajovic, Valentina S, " A Reliable Tool for the Design of Shape and Size of Faraday Segmented MHD Generator Channel," *Energy Conversion and Management*, Vol.37, No.12, pp.1753-1764, 1996.

- <sup>3</sup> Crawford, R.A., Chapman, J.N., and Rhodes, R.P., "Performance Potential and Technology Issues of MHD Augmented Hypersonic Simulation Facilities," AIAA Paper 90-1380, June 1990.
- <sup>4</sup> Demetriades, Sterge T., "Experiments with a High Specific Impulse Crossed-field Accelerator," 3<sup>rd</sup> Symposium on Engineering Aspects of Magnetohydrodynamics, , 1963.
- <sup>5</sup> Macheret, S.O., Miles, R.B., and Nelson, G.L., " MHD Acceleration of Supersonic Air Flows Using Electron Beam - Enhanced Conductivity," AIAA 98-2922, June 1992.
- <sup>6</sup> Sutton, George W, Sherman, Arthur, *Engineering Magnetohydrodynamics*, McGraw-Hill, Inc, New York, 1965.
- <sup>7</sup> Argyropoulos, G. S., Demetriades, S. T., Doss, E. D., and Olivers, D. A., " Electron Non-equilibrium in Open-Cycle MHD Generators," AIAA Journal, Vol. 12, No. 5, pp. 669-671, May 1974.
- <sup>8</sup> Brandmaier,, H. E., Durand, J. L., Gouridine, M. C., and Rubel, A., " An Investigation of Hall Propulsor Characteristics," AIAA Journal, Vol. 2, No. 4, pp. 674-681, April 1964.
- <sup>9</sup> Henry, R. P, " Lorentz Force Maximization in Continous Flow Hall Current Plasma Accelerators," AIAA Journal, Vol. 4, No. 3, pp. 165-166, January 1966.
- <sup>10</sup> Cann, G. L., Marlotte, G. L., " Hall Current Plasma Accelerator," AIAA Journal, Vol. 2, No. 7, pp. 1234-1241, July 1964.
- <sup>11</sup> Klepeis, J, Rosa, R. J., " Experimental Studies of Strong Hall Effects and UxB Induced Ionization," AIAA Journal, Vol. 3, No. 9, pp. 1659-1665, September 1965.
- <sup>12</sup> Burton, R.L., Bufton, S.A., Tiliakos, N.T., and Krier, H., "Application of Multiple Electrostatic Probes to a Low Power Arc jet," *Journal of Propulsion and Power*, 1994.



**AIAA 99-3717**

**Rayleigh Doppler Velocimetry Measurements  
of a Microwave Thruster**

M.J. Culley, J.E. Jones, and C.W. Hawk  
Propulsion Research Center  
University of Alabama in Huntsville  
Huntsville, Alabama 35899

**30th Plasmadynamics and Lasers Conference**  
**28 June – 1 July, 1999 / Norfolk, VA**

For permission to copy or republish, contact the American Institute of Aeronautics and Astronautics  
1801 Alexander Bell Drive, Suite 500, Reston, VA 20191-4344



# Rayleigh Doppler Velocimetry Measurements of a Microwave Thruster

Matthew J. Culley\*

Jonathan E. Jones†

Clark W. Hawk‡

Propulsion Research Center  
University of Alabama in Huntsville  
Huntsville, Alabama 35899

## ABSTRACT

The performance of a microwave plasma thruster augmented with a magnetohydrodynamic accelerator is being evaluated. Both electrical conductivity and flow velocity are needed to determine the efficiency at the inlet to a magnetohydrodynamic accelerator. This work focuses on the measurement of velocity and temperature in the plumes of a microwave plasma thruster. Tests were conducted at pressures from atmospheric down to 1 torr. Rayleigh scattered light from an injection-seeded, frequency doubled Nd:YAG laser is analyzed using a planar mirror Fabry-Perot interferometer operating in the static imaging mode. Images were taken with an ICCD camera and digitally stored for later evaluation using a least squares curve fit. Good agreement is seen between thermocouple data and the Rayleigh scattering technique at atmospheric conditions. Preliminary data taken at 1 torr shows the Rayleigh signal dominated by scattered laser light coming from windows and metal surfaces. Methods of reducing this scatter along with the theory of Rayleigh scattering are discussed.

## NOMENCLATURE

$a$	= Most probable molecular speed (m/s)
$A_R$	= Amplitude of the Rayleigh scattered signal
$A_w$	= Amplitude of the laser light scattered from walls and windows
$B_q$	= Amplitude of broadband background light
$c$	= Velocity of light (m/s)

$d$	= Fabry-Perot mirror spacing (mm)
$E_o$	= Laser energy
$f$	= Frequency of scattered light (Hz)
$f_o$	= Frequency of incident light (Hz)
$h$	= Planck's constant (J-s)
$I_{FP}(\psi)$	= Transmission function
$k_o$	= Incident wave vector
$k_s$	= Scattered light wave vector
$K$	= Magnitude of wave vector
$K$	= Interaction wave vector
$L_x$	= Length along beam of the scattering volume
$m$	= Molecular mass (kg)
$n$	= Number density (particles/m <sup>3</sup> )
$N_E$	= Effective finesse
$N_R$	= Number of detected photoelectrons collected by an optical system with solid angle $\Omega$
$\langle N_{Dq} \rangle$	= Expected number of detected photons for the $q$ th pixel
$T$	= Gas temperature (K)
$u$	= Mean gas velocity (m/s)
$\chi$	= Angle between the electric field vector of the incident light and the direction of scattered light.
$\epsilon$	= Overall collection efficiency
$\kappa$	= Boltzmann's constant (J/K)
$\lambda$	= Wavelength (nm)
$\lambda_o$	= Incident wavelength (nm)
$\mu$	= Refractive index
$d\sigma/d\Omega$	= Rayleigh differential scattering cross-section (m <sup>2</sup> /sr)
$\theta_s$	= Scattering Angle (deg or rad)
$\theta_r$	= Angle between ray and the optical axis
$\Omega$	= Solid collection angle
$\psi$	= Phase change

\* Graduate Research Assistant, Student Member AIAA

† Graduate Research Assistant

‡ Professor of Mechanical and Aerospace Engineering  
Director, Propulsion Research Center  
Fellow, AIAA

## INTRODUCTION

of magnetohydrodynamics (MHD) has been used extensively for the last fifty years. As 1960 it was noted that the efficiency of an MHD engine could be greatly enhanced "when the entropy or enthalpy of the fluid is divorced from the energy, i.e., when the main thermal energy used to drive the fluid and an other-than-thermal energy source is used to produce the high ionization"<sup>1</sup>. Despite this, little experimental work has been done to investigate the performance of MHD engines driven by a non-thermal ionization source.

work with a non-equilibrium plasma generated in a microwave resonant cavity drives an MHD engine. This combination has the potential to increase efficiency as well as reduce thermal losses and erosion. To assess the feasibility of this option, aerodynamic and electrical transport properties were measured in the plumes of a microwave engine developed by Michael Micci at Pennsylvania State University<sup>2</sup>.

This paper reports current efforts to measure temperature, and pressure using Rayleigh scattering.

These measurements when coupled with transport properties being reported at the Joint MHD Conference allow the performance at the MHD accelerator to be evaluated<sup>3</sup>.

Rayleigh scattering allows planar measurement and seeding. The scattered signal allows for the determination of flow properties. Richard G. Seasholtz has led pioneering of the Rayleigh scattering at the Glenn Research Center. The technique used by Seasholtz et al. to measure velocity, temperature, and pressure profiles of Hydrogen-Oxygen at low pressure<sup>4</sup>. Their results agree well with calculations and comparisons to other techniques.

## RAYLEIGH SCATTERING

The development of the Rayleigh scattering technique and use of a Fabry-Perot interferometer has recently been reported by Seasholtz<sup>5</sup>. The pertinent theory and experiment are presented here for reference.

Rayleigh scattering is an elastic scattering process, where the internal energy of the molecule is not changed, therefore the frequency of the scattered light is the same as the frequency of the incident light altered by the Doppler effect due to the motion of the

molecules. Figure 1 shows the relationship between the incident or reference laser line and the Rayleigh scattered spectrum. The velocity of the flow is determined by the phase shift between the reference laser line and the Doppler shifted Rayleigh scattered signal. The temperature is given by the broadening of the Rayleigh scattered laser light. The density can be obtained from the intensity of the signal however calibration is required for each unique system.

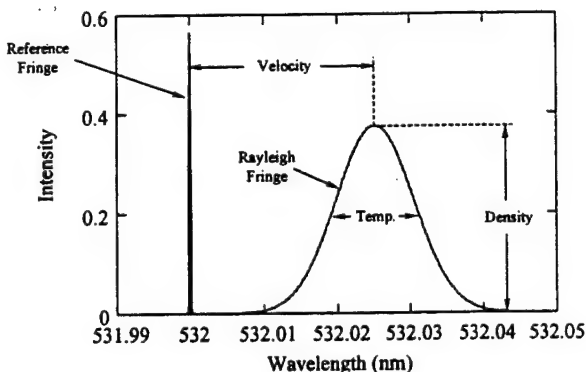


Figure 1. Reference laser line and Rayleigh scattered spectrum.

At the low pressures expected in our experiments the velocity distribution is expected to be Maxwellian. At higher gas densities the molecular motions become correlated and appropriate models must be used to describe the Rayleigh scattered spectrum. Tenti's S6 model<sup>6</sup> is used where needed in our work.

It is critical to have a sufficient number of scattered photons from the Rayleigh interaction. Equation 1 determines the number of photons scattered through a solid collection angle of  $\Omega$ .

$$N_R = \frac{\epsilon E_o n L_x \lambda \Omega}{hc} \left( \frac{d\sigma}{d\Omega} \right) \sin^2 \chi \quad (1)$$

Where  $\epsilon$  is the overall collection efficiency,  $E_o$  is the incident laser energy,  $\lambda$  is the wavelength of the incident light,  $\chi$  is the angle between the electric field vector of the incident light and the direction of the scattered light,  $n$  is the number density of the gas,  $h$  is Planck's constant, and  $c$  is the velocity of light.

The Rayleigh scattering differential cross-section,  $d\sigma/d\Omega$ , shown in Equation 2 is directly dependent on the index of refraction of the gas to be studied.

$$\left( \frac{d\sigma}{d\Omega} \right) = \frac{4\pi^2}{\lambda^4 n^2} (\mu - 1)^2 \quad (2)$$

The total light detected by the  $q_{th}$  pixel of a CCD array can be obtained by evaluating Equation 11.

$$\langle N_{Dq} \rangle = \int_{\Omega} \int_{\Delta\lambda} \int_{-\infty}^{\infty} \left\{ \frac{[A_R S_R(f, \Omega) + A_w \delta(f - f_0)]}{I_{FP}(f, \theta_i)} df d\lambda d\Omega \right\} + B_q \quad (11)$$

Where  $A_R$  is the amplitude of the Rayleigh scattered signal in the absence of the Fabry-Perot interferometer,  $A_w$  is the amplitude of the laser light scattered from the walls and windows,  $B_q$  is the amplitude of broadband background light. Further detail on the evaluation of Equation 11 can be obtained from Seasholtz's work<sup>8</sup>.

### EXPERIMENTAL SETUP

A pulsed Nd:YAG laser was used to probe the plume of a microwave plasma thruster. A 0-6 kW variable power microwave generator supplied a  $TM_{011}$  resonant mode cavity. Filtered gas enters the resonant cavity through three tangential ports forming a vortex which stabilizes the plasma discharge. The filters on the gas supply system remove particles with diameters larger than  $0.2 \mu m$ . Gas heated by the plasma discharge is accelerated through a converging-diverging nozzle into a  $18'' \times 28.5''$  cylindrical vacuum cavity. A traversing mechanism allows movement of the exit plane of the nozzle over a range of six inches.

The second harmonic of a Spectra Physics GCR-290 pulsed Nd: YAG Laser operating at 10 Hz was

used. The second harmonic was chosen so that operation could be performed in the visible region. It is realized that stronger Rayleigh scattering can be obtained from the third and fourth harmonics, however the additional cost of UV optics and lower power levels justified the use of the second harmonic. An injection seeder narrowed the linewidth of the laser to less than  $0.002 \text{ cm}^{-1}$  which is necessary for the Rayleigh scattering technique.

The beam path is shown in Figure 3. Light leaves the laser and passes through a half wave plate allowing for adjustment to the polarization of the beam within the measurement volume. The polarization was adjusted so that the electric field vector was perpendicular to the collection optics. The beam height is then adjusted through a telescoping mirror assembly. A 700 mm focal length cylindrical lens focuses the light to a 0.1 mm sheet in the measurement region. The light enters and exits the vacuum chamber through Brewster angle windows. A series of irises before and after the measurement volume minimized scattered light.

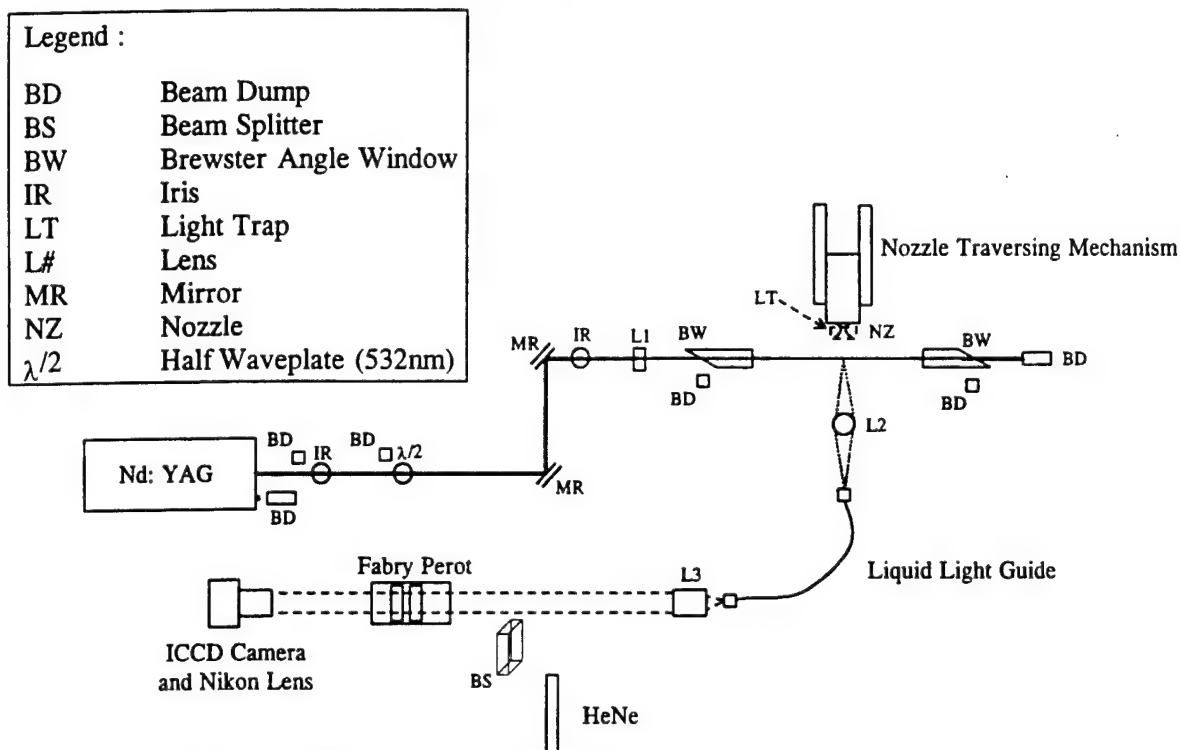


Figure 3. Optical Setup For Measuring Axial Properties.

atter technique can be used to image cross-section of the flow. Initially made to image the flow, instead light is focused with a 250 mm a 5 mm core diameter liquid light is positioned such that it is electric field vector and  $45^\circ$  to the of the plume. The light exits the d is collimated by a Nikon 135 mm collimated light passes through a abry-Perot interferometer. Finally with a Nikon 180 mm f/2.8 lens Instruments ITE/CCD 1024x256 intensified camera. The pixels on n x 26  $\mu\text{m}$ .

CCD camera is equipped with a nts PG-200 Programmable Gate his allows gating with widths down The Pulse Generator was triggered -Switch from the laser and gated to .0 nanosecond laser pulse. This adband background light, including from the plume. The gain on the adjusted to optimize the image.

## FA REDUCTION

be taken for a typical measurement. image was taken to characterize the d, a reference image was taken by a pin placed near the measurement Rayleigh scattered image was taken l-reference image was taken. A 200 egion centered on the fringe pattern ages. The reference images before to determine the finesse and initial rometer and the coordinates of the pattern. This was accomplished by al Fabry-Perot instrument function ference image with a least squares veloped by Seasholtz. The fit ie reference image were taken as routine which varied temperature, least squares routine to fit the h scattered spectrum as imaged Perot. In both the reference image i image the amplitudes of the und light, laser light scattered from igh scattered light were allowed to nal convergence. The dark current ed from the reference and Rayleigh essing. Figure 4 shows the typical o a cross-section of a Fabry-Perot ints indicated by diamonds are the

intensities of individual pixels. The solid line is the least squares curve fit to these points.

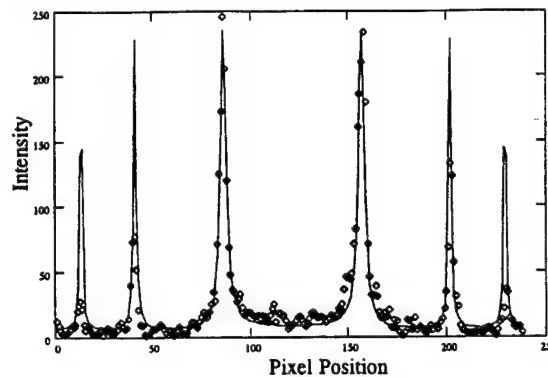


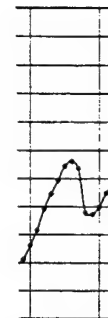
Figure 4. Least squares fit to reference image.

## RESULTS

Initial tests have been conducted with the vacuum off. Two series of tests were run. First the vacuum chamber was purged with filtered nitrogen several times to remove all particulates. It was then filled to atmospheric pressure with filtered nitrogen allowing a pure Rayleigh signal. It was hoped that Rayleigh scattered signals could be taken as the pressure in the vacuum chamber was decreased, however movement of the vacuum chamber due to pulling the vacuum caused misalignment in the optics eliminating the possibility. Rayleigh scattering successfully measured the temperature of the gas in the purged vacuum chamber after accounting for drift of the interferometer as discussed in the following paragraphs. This experiment was repeated for argon and air.

Figure 5 and 6 show a reference and corresponding Rayleigh image respectively. This Rayleigh image is for nitrogen at atmospheric temperature and pressure. The least squares curve calculated a temperature of 345 K and a velocity of 270 m/s. These results were very disappointing, as we anticipated a temperature of 293 K and a velocity of 0 m/s. A second reference image revealed that both the finesse and initial phase of the interferometer had changed considerably from the initial reference image.

exists. A Burleigh to minute cycle on/off cycle rate bath.



600 700

ge, as well ors and the ase of the riations in bserved. nt for the ent.

enclosure ain taken. ed air was shows the parison to couple as employees est and the ced in the ults agree rferometer eference asured at

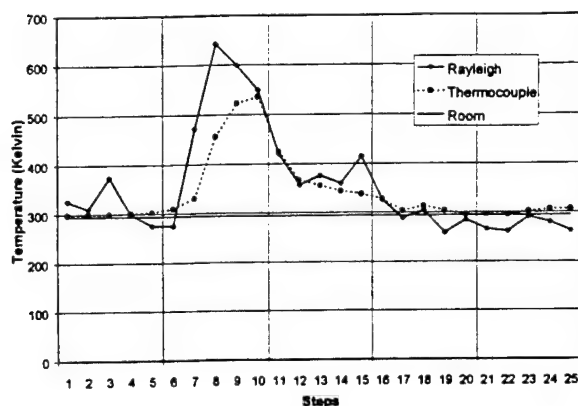


Figure 8. Comparison of Rayleigh scatter and thermocouple measurements of atmospheric air.

Obtaining a sufficient signal to noise ratio at vacuum pressures proved to be much more difficult. The scattered laser light coming from the walls of the vacuum chamber was greater than the Rayleigh scattered signal. This prohibited affective evaluation of the Rayleigh image.

### DISCUSSION

Despite the difficulties experienced in using Rayleigh scattering to measure thermodynamic properties at low pressure, the benefits are promising. J. Lewis at UTSI showed the relative difficulties between five of the methods and the regimes where they are found to be optimum, Figure 9. The five methods he compares are vibrational Raman scattering (VRS), rotational Raman scattering (RRS), Rayleigh scattering, electron beam fluorescence technique (EBFT), and laser-induced fluorescence (LIF)<sup>9</sup>. Raman scattering has the advantage of being shifted from the incident laser light, however the signal is an order of magnitude lower than the already weak Rayleigh signal. EBFT could not be used due to the lack of availability of an electron beam source. LIF is an attractive option but is dependent upon the propellant used and a general diagnostic technique is desired.

At a pressure of 1 torr and a temperature of 300 K the ideal gas law gives a number density of  $3.2 \times 10^{16} \text{ cc}^{-1}$ , which puts us in the optimum range for Rayleigh scattering according to Lewis's chart. At higher operating temperatures the number density decreases and the technique becomes more difficult.

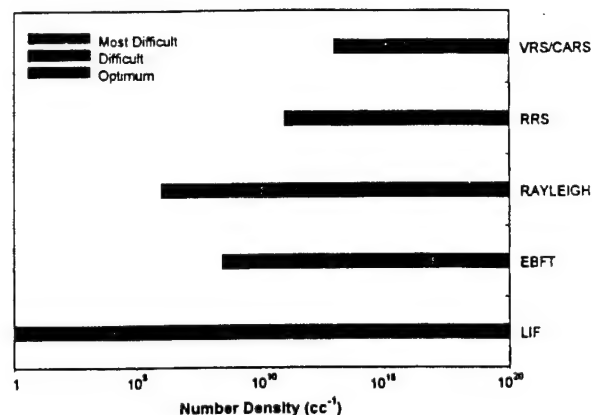


Figure 9. Diagnostics Application Regimes<sup>9</sup>

Several adjustments can be made to the current system to enable Rayleigh scattering at pressures from 1 to 10 torr. First, an upgrade of the vacuum chamber will provide adequate space for beam dumping and control of scattered laser light.

Second, a molecular iodine filter placed in front of the Fabry-Perot will provide the capability of filtering out any remaining scattered laser light. Joseph N. Forkey et al. at Princeton University have developed models and successfully used iodine filters in Rayleigh scatter measurements. They have presented results that include "two-dimensional, spatially resolved measurements of velocity, temperature, and pressure derived from time-averaged spectra."<sup>10</sup>

Figure 10 shows the relationship between a Rayleigh scattered signal, iodine cell absorption, and the filtered output. The beauty of the iodine cell is the narrow notch filters near 532 nm. The frequency of the Nd: YAG can be centered on one of these notches by varying the temperature of the seed injection laser. Thus the troubling scattered light can be filtered while still allowing transmission of a sufficient portion of the Rayleigh scattered signal.

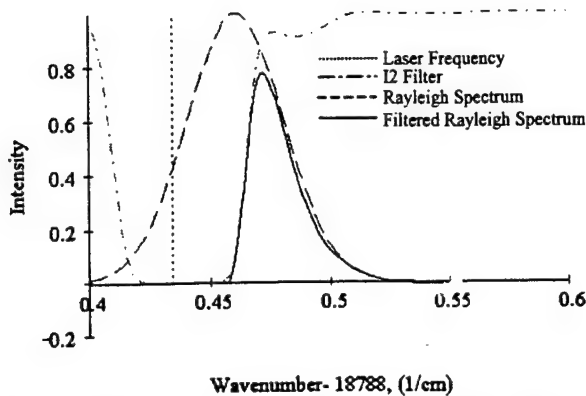


Figure 10. Relationships between incident laser light, Rayleigh scattered signal, and iodine absorption cut-off.

In order to evaluate the filtered Rayleigh scattered spectrum the transmission function of the iodine cell must be added to Equation 11.

### CONCLUSIONS

Rayleigh scattering was used to successfully measure the temperature of room air. Additionally agreement between thermocouple and Rayleigh measurements was obtained for filtered air from a hot air gun. While the task of controlling stray laser light is formidable, additional space in the anticipated vacuum chamber upgrade and filtering provided by the iodine cell should facilitate successful Rayleigh scattering measurements at low pressures. The ability to measure temperature, and pressure in the plume of the microwave plasma thruster will help to characterize and optimize this device. In addition, this information will aid in the design of a MHD accelerator which can utilize the non-equilibrium plasma created by the microwave plasma generator.

### ACKNOWLEDGEMENTS

The authors wish to thank Dr. Richard Seasholtz for providing us with his Rayleigh scattering code along with the many hours of help he provided our group. We thank Dr. J. Forkey and Dr. G. Tenti for graciously allowing us to use their Fortran codes on iodine absorption cells and kinetic theory respectively. We also wish to thank Eric Tuck, Gary Hicks, and Doug Parkinson for the many hours of work devoted to the lab. This research program was sponsored in part by NASA Marshall Space Flight Center and by the Air Force Office of Scientific Research under the grant number F49620-98-0-0083.

### REFERENCES

- <sup>1</sup> Demetriades, Sterge T., "Experimental Magnetogasdynamic Engine for Argon, Nitrogen and Air." ASRL-TM-60-23, Norair Division, Northrop Corporation, Hawthorne, California; presented at the Second Symposium on Engineering Aspects of Magnetohydrodynamics, March 9-10, 1961.
- <sup>2</sup> Sullivan, D.J., Kline, J., Philippe, C., and Micci, M.M., "Current Status of the Microwave Arcjet Thruster," AIAA Paper 95-3065, July 1995.
- <sup>3</sup> Deaconu, S., Jones, J.E., Hawk, C.W., "Diagnostics of Electric Properties of Flowing Microwave Plasmas for MHD Applications." AIAA 99-2715, June 1999.
- <sup>4</sup> Seasholtz, R.G., Zupanc, F.J., and Schneider, S.J., "Spectrally Resolved Rayleigh Scattering Diagnostic for Hydrogen-Oxygen Rocket Plume Studies," *Journal of Propulsion and Power*, Vol. 8, No. 5, 1992, pp. 935-942.
- <sup>5</sup> Seasholtz, Richard G., "Fiber Optic coupled Rayleigh Scattering diagnostic for Point Measurement of Gas Density, Velocity and Temperature." AIAA 34<sup>th</sup> Joint Propulsion conference & Exhibit, Cleveland, AIAA paper 98-3454, 1998.
- <sup>6</sup> Boley, C. D., Desai, Rashmi C. and Tenti, G., "Kinetic Models and Brillouin Scattering in a Molecular Gas," *Can. J. Phys.*, Vol. 50, 1972, pp. 2158-2173.
- <sup>7</sup> Gardiner, W. C. Jr, Hidaka, Y. & Tanzawa, T., "Refractivity of combustion gases," *Comb. Flame*, Vol. 40, 1981, pp. 213-219.
- <sup>8</sup> Seasholtz, Richard G., Buggele, Alvin E., and Reeder, Mark F., "Flow Measurements Based on Rayleigh Scattering and Fabry-Perot Interferometer," *Optics and Lasers in Engineering*, Vol. 27, pp. 543-570.
- <sup>9</sup> Lewis, J. W. L., "Optical Diagnostics of Low-Density Flowfields," *Rarefied Gas Dynamics: Physical Phenomena*, Vol. 117, 1989, pp. 107-132.
- <sup>10</sup> Forkey, J. N., Finkelstein, N.D., Lempert, W.R., and Miles, R.B., "Demonstration and Characterization of Filtered Rayleigh Scattering for Planar Velocity Measurements," *AIAA Journal*, Vol. 34, No. 3, 1996, pp. 442-448.



**AIAA 99-2715**

**Diagnostics of Electric Properties of Flowing  
Microwave Plasmas for MHD Applications**

Stelu Deaconu, J.E. Jones, and C.W. Hawk

Propulsion Research Center  
University of Alabama in Huntsville  
Huntsville, Alabama 35899

**35th AIAA/ASME/SAE/ASEE Joint Propulsion Conference & Exhibit  
20-24 June, Los Angeles CA**

For permission to copy or republish, contact the American Institute of Aeronautics and Astronautics,  
1801 Alexander Bell Drive, Suite 500, Reston, VA 20191-4344



# DIAGNOSTICS OF ELECTRIC PROPERTIES OF FLOWING MICROWAVE PLASMAS FOR MHD APPLICATIONS

Stelu Deaconu, J. E. Jones, C. W. Hawk

*Propulsion Research Center*

*University of Alabama in Huntsville, Huntsville, AL 35899*

## Abstract

Tests of a magnetohydrodynamic (MHD) accelerator coupled with a microwave (MW) generated plasma are underway at the UAH Advanced Propulsion Laboratory. The plasma is generated by microwave breakdown of the working gas in the MW resonant chamber. The gas exits the resonant chamber and is expanded through a supersonic nozzle in order to attain a reasonable velocity at the inlet of the MHD channel. This plasma is at a relatively high pressure even after expansion through the nozzle, and it is only weakly ionized. The efficiency of the MHD accelerator is tightly connected to the electrical properties of the plasma entering the channel. Single Langmuir probes provide information about the electron temperature, and electron number density. Local plasma conductivity is inferred from these measurements by using a model based on particle collision. These quantities constitute the basis for the preliminary MHD channel design and flow seeding requirements. The results of the measurements are presented together with the estimated theoretical performance of the MHD channel.

## Nomenclature

$A_e$	electron collection area
$A_i$	ion collection area
$B$	magnetic field intensity
$c_e$	thermal speed of electrons $\sim (8kT_e/\pi m_e)^{1/2}$
$e$	electron charge
$I$	current
$i_e, i_+$	electron/ion current
$i_e$	emitted electron current
$J$	current density
$j_e$	random electron current density
$k$	Boltzman's constant
$m_e, m_i$	electron/ion mass
$n_0, n_e$	plasma/electron number density
$Q_{en}$	electron-neutrals collision cross-section
$T_e$	electron temperature

$u$	flow speed
$v_0$	initial velocity of emitted electrons
$V$	probe voltage
$V_f$	floating potential
$V_p$	plasma potential
$V_{pp}$	voltage peak to peak
$\epsilon_0$	electric permittivity of air
$\eta_{MHD}$	MHD channel efficiency
$\lambda_{mfp}$	mean free path between collisions
$\nu$	collision frequency
$\sigma$	plasma conductivity
$\tau$	mean time between collisions

## Introduction

Intensive work has been done in the past<sup>1</sup> on plasma MHD electric energy generation. The potential of the MHD channel in propulsion received little attention due to inherent shortcomings of the system (low efficiency, heavy magnets etc.). Most of the work<sup>1, 2</sup>, encompassed a detailed analysis of basic aspects of MHD plasma flow acceleration. New permanent and superconducting magnet technologies and plasma generation techniques (MW) can make the MHD channel competitive for a space propulsion application. A more in depth analysis of the MW plasma is necessary in order to maximize the efficiency of such a propulsion system.

The main parameter in describing the performance of the system is the energy conversion efficiency. The efficiency of a segmented MHD channel is approximately<sup>1</sup>

$$\eta_{MHD} = \frac{uB}{uB + \left(\frac{1}{\sigma}\right)J} \quad (1)$$

where  $u$  is the speed of the flow entering the channel,  $B$  is the intensity of the magnetic field in the channel, and  $J$  is the applied current density between channel



electrodes. The quantities in the above equation are average values across the channel area. Equation (1) quantifies the amount of energy that goes into accelerating the flow as a percentage of total energy supplied to the MHD channel. Ohmic heating of the plasma accounts for the rest of the supplied energy. Expression (1) indicates that the efficiency is increased as the resistivity ( $1/\sigma$ ) of the plasma decreases. In this experimental study the efficiency of the channel is inferred from plasma properties measured by electric (Langmuir) probes.

Langmuir probe measurements are common in diagnostic of quiescent or flowing plasmas. The analysis of probe data is quite intricate and no general theory has been developed to date. Generally the information obtained from Langmuir probes depends on several factors (gas composition, the way the plasma is generated, degree of ionization, pressure, gas velocity etc.). A well-developed single probe theory is available for fully ionized low-pressure plasmas<sup>3</sup>. Previous work indicates that the MW plasma is only weakly ionized at an input energy level of ~2kW. In essence, the plasma is a very hot gas. Hot ions and neutral particles hit the probe heating it to elevated temperatures. Thermocouple measurements have shown that even during short time sweeps the probe temperature reaches up to 2000 K. Heating causes thermionic emission of electrons from the probe surface. Complications, introduced by excessive heating of the probes in the flowing MW generated plasma, required the development of a slightly modified theory, which accounts for the flow and for the electron emission from the hot probe. Additionally, four prong probe measurements were run for comparison with single probe data.

### Review of Single Probe Theory

A single probe is commonly a wire, made of high temperature metals, inserted in the plasma. A ramp voltage is supplied to the probe and a voltage - current (V-I) characteristic is traced. The arrangement necessitates the existence of a large electrode in contact with the plasma, in order to close the circuit. The typical V-I characteristic of a single probe is shown in Figure 1. The characteristic of the probe can be analyzed in different ways by making appropriate approximations<sup>3</sup>. One method is reviewed here. With uncalibrated probes, this approach yields approximate estimates of the electron temperature and electron number density.

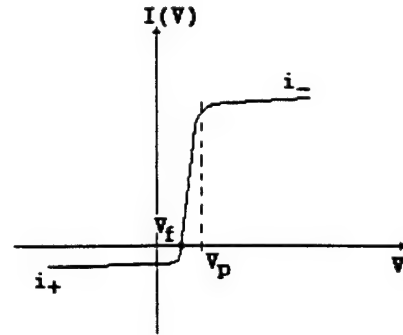


Figure 1. Single Non-Emitting Probe V-I Trace

Assuming fully ionized plasma, and in conformity with Figure 1, the current flowing to the probe is given by the sum of electron and ion currents

$$I = i_- - i_+ \quad (2)$$

Consider the case of electrons having a Maxwellian velocity distribution function. The distribution function is not altered by the presence of the probe<sup>3</sup>. Without entering the details of the potential distribution around the probe we shall assume that the potential drop  $V - V_p$  occurs in a finite region around the probe called "the sheath". The sheath dimension is usually on the order of the Debye length in the plasma. For a collisionless plasma and  $V - V_p < 0$  the momentum equation for the electrons entering the sheath reduces to the Boltzman relation<sup>5</sup>,  $n_e = n_0 \exp(e(V - V_p)/kT_e)$ . In this region of  $V - V_p < 0$  the probe potential is negative with respect to the plasma potential, and the probe is repelling the electrons. This region of probe bias is called "the electron retarding region". The electron current to a retarding probe<sup>3</sup> is then given by

$$i_- = A_e j_e \exp\left(\frac{e(V - V_p)}{kT_e}\right) \quad (3)$$

where  $j_e$  is the electron random current density, and  $A_e$  is the electron collection area of the probe. For a cylindrical probe of diameter  $d$ , and length  $l$ , the collection area for electrons in a cross flow arrangement is approximately  $A_e = \pi dl/2$ . The random electron current density is calculated by integrating the electron flux over the velocities for which the electrons can overcome the retarding potential ( $m_e v^2/2 > e(V - V_p)$ )

$$j_e = n_0 e c_e / 4 \quad (4)$$

When the probe is biased at a potential  $V = V_f$  the total current drawn by the probe is zero. If only the region of potential with  $V - V_f < 0$  is considered, the ion current

can, to a fair approximation, be replaced by the ion saturation current  $i_+ = i_{sat}$ . This is equivalent to saying that the ions enter the sheath with a drift velocity, which has a weak dependence on the potential drop  $V - V_p$ . Combining equations (2) and (3) with the condition  $I = 0$  at  $V = V_f$  one gets the classical formula that relates the probe current to the applied bias voltage

$$I(V) = i_{sat} \left[ \exp \left( \frac{e(V - V_f)}{kT_e} \right) - 1 \right] \quad (5)$$

Rearranging terms in equation (5) and taking the logarithm, the electron temperature is proportional to the inverse of the slope of  $\ln(I/i_{sat} + 1)$  vs.  $V - V_f$ . The electron number density can be approximated from the saturation ion current (the Bohm sheath analysis)

$$i_{sat} = \frac{1}{2} n_0 e A_i (kT_e/m_i)^{1/2} \quad (6)$$

where  $A_i$  is the ion collection area. An approximate value of this area<sup>4</sup> for a flowing plasma is  $A_i = ld$ . More accurate electron density determination procedures for this case are presented elsewhere<sup>3, 7</sup>. This theoretical treatment, Equation (5), has been unable to model the behavior of the MW heated plasma and forms only the starting point for the following analysis.

A characteristic of the weak ionization is a collision-dominated plasma. Fortunately the collision effect becomes negligible when the sheath radius is smaller than the collision mean free path. In other words there are hardly any collisions taking place in the sheath, and all the charged particles entering the sheath reach the probe. In the following we shall assume that the sheath thickness is smaller than the collision mean free path and also smaller than the probe diameter. A justification of this assumption is given in the Appendix. The approach employed for data analysis follows the guidelines presented in works done on plasmas previously<sup>3, 4, 6, 8</sup>. The emission effect due to probe heating is treated in a global sense i.e. we did not solve for spatial variation of the potential around the probe.

A typical V-I trace for a single probe, (see Figure 4.b) in the MW generated plasmas shows a remarkable difference when compared to Figure 1 - the region of negative bias does not exhibit saturation of the ion current. Additionally, there are superimposed current oscillations due to plasma instabilities and MW power supply ripple. The downward sloping of the retarding region of the V-I characteristic can be explained by thermionic electron emission from the

probe. In the region of retarding potential the emitted electrons are accelerated into the plasma, contributing to the current flowing through the probe as an apparent ion current. The emission current is denoted as  $i_e$ , and the total current to the probe is

$$I = i_+ - i_e \quad (7)$$

The effect of electron emission is treated in an average sense by making several assumptions on the motion of the emitted electrons: (a) - the electrons are emitted in the radial direction with a mean velocity  $v_0$ , (b) - the initial energy of the electrons is supplied by the thermal heating of the probe and is proportional to the probe temperature, and (c) the average velocity of these electrons as they reach the edge of the sheath is increased by the energy amount supplied by the accelerating field  $V - V_p$ . If  $n_e$  is the emitted electron density then the emitted current density is

$$j_e = en_e v_e = en_e v_0 \left[ 1 - \frac{2e}{m_e v_0^2} (V - V_p) \right]^{1/2} \quad (8)$$

Making use of (3) and (7), using the condition  $I = 0$  at  $V_f$  setting  $i_+ = i_{sat}$ , and  $i_e(V_f) = i_{ef}$  the current is

$$I(V) = i_{sat} \left[ \exp \left( \frac{e(V - V_f)}{kT_e} \right) - 1 \right] + i_{ef} \left[ \exp \left( \frac{e(V - V_f)}{kT_e} \right) - \left( \frac{m_e v_0^2 - 2e(V - V_p)}{m_e v_0^2 - 2e(V_f - V_p)} \right)^{1/2} \right] \quad (9)$$

The second term in Equation (9) is the contribution of the emitted electrons to the current drawn by the probe from the plasma. The model, Equation (9), complicates the analysis by introducing two unknown parameters,  $v_0$  and  $V_p$ . An attempt to simplify the model is necessary. The square root in the emission term can be linearized to a good approximation by using a binomial expansion if  $|V - V_f| < V_p - V_f$

$$I(V) = (i_{sat} + i_{ef}) \left[ \exp \left( \frac{e(V - V_f)}{kT_e} \right) - 1 \right] + i_{ef} \frac{e(V - V_f)}{m_e v_0^2 - 2e(V_f - V_p)} \quad (10)$$

Neglecting the initial velocity term compared to the effect of the field and compressing  $i_{sat} + i_{ef}$  to  $J_0$ , and  $i_{ef}/2(V_p - V_f)$  to  $A$ , one obtains

$$I(V) \cong J_0 \left[ \exp \left( \frac{e(V - V_f)}{kT_e} \right) - 1 \right] + A(V - V_f) \quad (11)$$

Equation (11) can be used to predict the current from the probe for all probe voltages below  $V_f$  and slightly above it. Assuming subsonic flow around the probe, Equation (6) is still valid for the flowing plasma since the directed velocity of the flow around the probe is smaller than the average thermal speed (sonic velocity) in the flow. The approximations made in obtaining Equation (6), and the value of ion collection area give only an order of magnitude estimate for electron number density.

### Local Plasma Conductivity Estimate

The conductivity of the plasma has been calculated with the model provided by a collisional theory<sup>1,9</sup>. According to this theory, the conductivity of weakly ionized plasma is dependent on the collision cross section of the charged particles with neutral atoms. The conductivity also has a weaker dependence on the collisions between charged particles. The conductivity is due mostly to electron motion, and therefore its expression<sup>1</sup> is

$$\sigma = \frac{n_0 e^2}{m_e c_e} \left[ \frac{1}{n_n Q_{en} + 3.9 n_i \left( \frac{e^2}{8\pi\epsilon_0 kT_e} \right)^2 \ln \Lambda} \right] \quad (12)$$

where  $Q_{en}$  is the collision cross section between electrons and neutral particles, and  $c_e$  is the average thermal speed of the electrons. Reference [9], citing others gives estimates for this parameter for different gases as a function of electron temperature. For a nitrogen plasma with electron temperature of 0.4 – 0.8 eV, the collision cross section is  $(5 - 3.5) \times 10^{-15} \text{ cm}^2$ . The factor,  $\ln \Lambda$ , is a small angle collision effect<sup>5</sup>, and a sufficiently accurate value is 10.

### Experimental Setup

Figure 2 presents a global sketch of the MW plasma generator and the vacuum chamber. The gas enters the MW resonant cavity where it is heated and ionized. The plasma expands through a supersonic nozzle into the vacuum chamber. The electric probes are mounted on a slide with two degrees of freedom actuated by stepper motors (not shown in Figure 2 for simplicity). The arrangement provides reproducible probe positioning, single point measurements and also the possibility for rapid scans across the plasma.

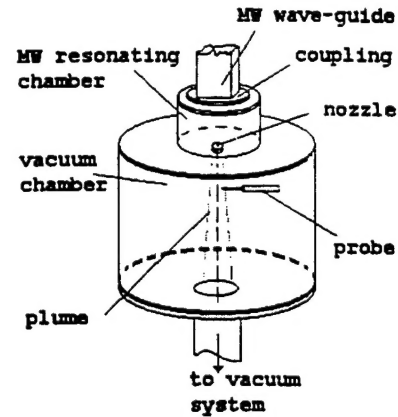


Figure 2. MW Plasma Generator and Vacuum System

The electrical equipment for a single Langmuir probe is shown schematically in Figure 3. The flowing plasma provides a path for the flow of electric current between electrode (1) and (2 - GND). The probe is made of a Re-(5%)/Tu-(95%) wire with a diameter of 0.5 mm and a length of 0.75 mm. The probe is supported by an alumina insulator and shielded by stainless steel tubing. BNC connectors and coaxial cables are used in order to provide a good common noise rejection in electrical connections.

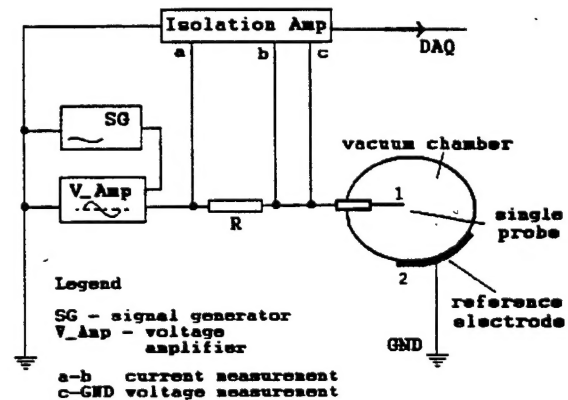


Figure 3. Probes Electric Circuitry

The signal generator produces a ramp signal with a frequency in the range 10 - 100 Hz and a voltage typically in the  $\pm 5 \text{ V}_{pp}$  range. The signal is amplified (and DC offset when necessary) by a programmable power supply (voltage amplifier). The currents flowing through the circuits are found through voltage drop measurements across the resistor (R) inserted in the circuit of the probe. The data acquisition and MW control was directed from two Pentium class computers equipped with the National Instruments' Labview 5.0

software. A third computer was used to control the actuators of the stepper motors positioning the probe.

### Results

The probe data consists of two mid-scans across a nitrogen plume, at a location two inches below the nozzle. The names, North/South, identify the direction of probe movement as it entered the plume. Figure 4.a presents a sample, time history plot from one of the scans.

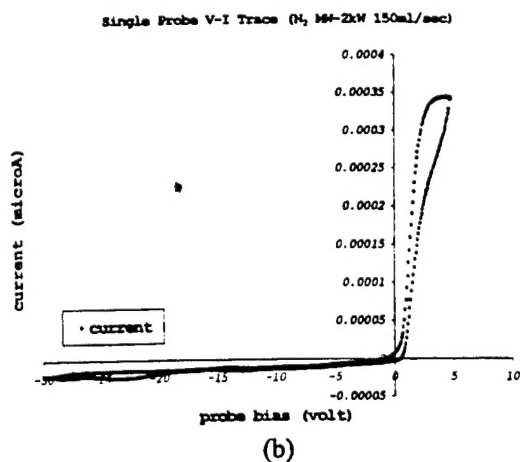
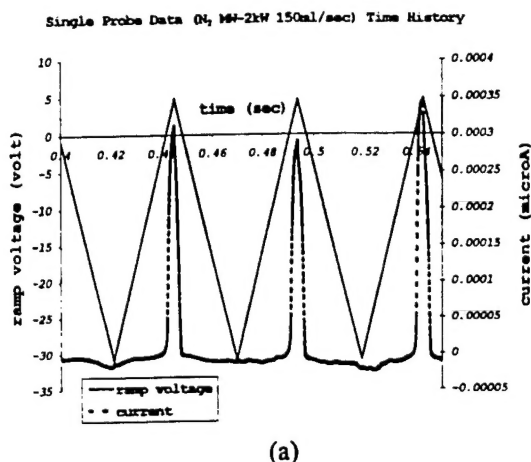


Figure 4. Single Probe Data, ( $N_2$ ) a) time history b) V-I characteristic

The voltage amplifier supplied to the probe a 20 Hz saw-tooth signal with  $V_{pp}$  of  $-30/+5V$ . The data acquisition board was set to 20kHz sampling frequency. These settings provide an average of 500 data points for each ramp. Software manipulation of the data rendered the up-going and down-going ramp signals, Figure 4.b. Microwave power was set at 2kW and the volumetric flowrate of nitrogen to 150 ml/sec.

Reflected MW power measurements indicate that more than 90% of the MW energy was absorbed by the gas. The remaining energy was associated with wave guide, wave guide - resonating chamber coupling, and resonant chamber losses. The upper curve in Figure 4.b. is data from the up-going ramp, while the lower one is the down-going ramp. Even at maximum scan rate the spatial difference in plasma properties does not account for the observed discrepancies between these two V-I traces. The smaller slope of the down-going ramp suggests a higher electron temperature. This behavior proved to be consistent throughout the plume. An explanation of this fact may reside in the contamination of the probe surface while at high potential<sup>7</sup>. The results presented in this section have been obtained from the up-going ramps. We assumed that ion bombardment at lowest potential value help clean the probe through sputtering.

Equation (11) allows a distinct separation of the linear (emitting probe) effect from the exponential (plasma) effect. The value of  $A$  in Equation (11) is estimated as the slope of the V-I characteristic for  $V < V_f$ . A general fitting routine provided the least squares values of the electron temperature and  $J_0$  for each ramp. Figure 5 shows a typical data fit with model (11). With  $A$  and  $J_0$  known, the ion saturation current can be easily obtained from the relations given above. The electron number density estimate is given by Equation (6).

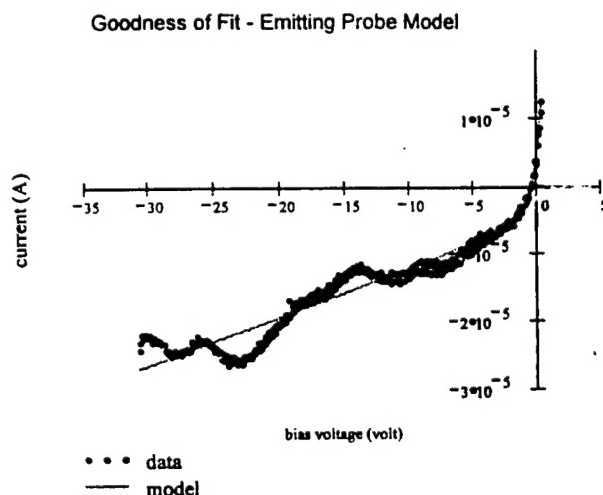


Figure 5. Sample of Single Probe Data in the Region of Retarding Potential, and Goodness of Fit for Emitting Probe Model ( $T_e \approx 0.6 eV$ )

More information about gas temperature and/or changes in probe material work function<sup>9</sup> could be obtained from  $A$  and  $J_0 - i_{sat}$ . Figure 6 presents the results for the two scans. The asymmetry with respect

to plume centerline has not been explained, and it is still under investigation. The floating potential varied slightly about zero, ( $-0.9 \dots 0.1V$ ), as the probe scanned across the plume. Plasma potential was found not to change greatly across the plume and it had the average values of  $\sim 2.9V$  in the North scan and  $\sim 2.6V$  in the South scan. Note that the electron temperature estimate does not depend on the plasma potential. The error introduced by using these average values in the estimation of electron number density is negligible compared to the conceptual error introduced by the approximation in Equation (6).

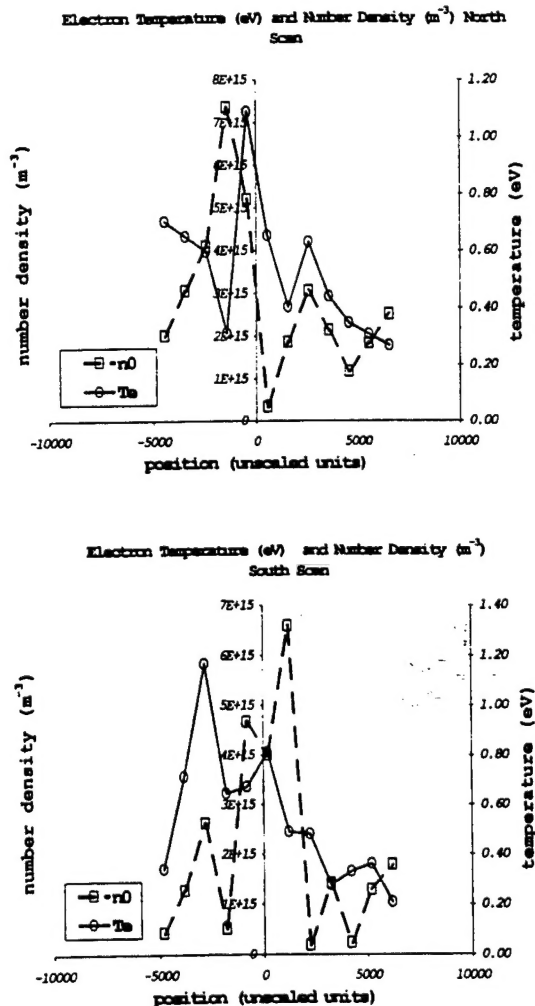


Figure 6. Electron Temperature and Number Density North/South Scans ( $N_2$ , MW-2kW 150ml/s)

The average electron temperature in the two scans is about 0.6 eV ( $\sim 7000$  K), and the average electron density is of the order  $10^{15} \text{ m}^{-3}$ . With these values, Equation (12) predicts an average bulk plume conductivity of about  $0.04 \text{ ohm}^{-1} \cdot \text{m}^{-1}$ .

Additional four-prong probe measurements in nitrogen plasma of similar parameters have been conducted, and they showed good agreement with the results presented. Very fast sweeps with the four-prong probe have been employed in order to reduce the heating of the probe. This was possible since the four-prong probe does not necessitate the ramping of the bias voltage. The data reduction procedure for the four-prong probe is found in the literature<sup>10</sup>.

### Conclusions and Discussion

A simple parametric study on MHD energy conversion efficiency is possible, starting with Equation (1). Considering the limitations on magnetic field strength of permanent magnets we shall give  $B$  a fixed value of 0.5 Tesla. Equipment already existing in the lab allows for MHD current densities of  $10^5 - 10^6 \text{ Amp/m}^2$ . Let the channel inlet flow velocity be the parameter of the study. The necessary plasma conductivity for a MHD energy conversion efficiency of 60 – 80 % is presented in Figure 7. The inlet velocities of the plasma flow are in the range 100 – 2000 m/sec.

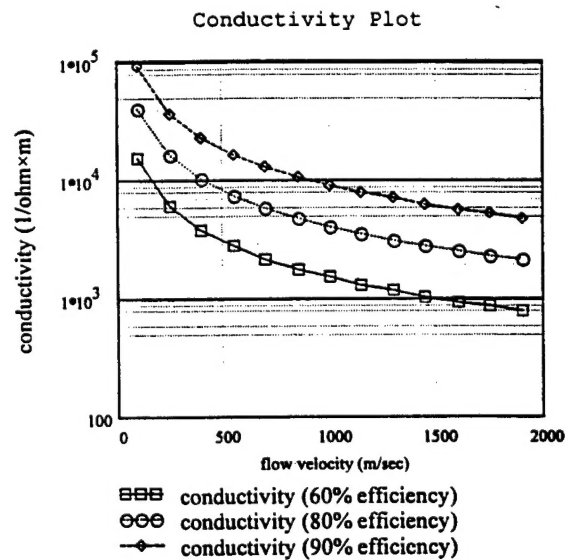


Figure 7. Required MW Plasma Conductivity for Efficient MHD Operation ( $J = 5 \cdot 10^5 \text{ A/m}^2$ )

It is concluded that the MW plasma flow is not suitable for use in a MHD accelerator. With a conductivity of only  $0.04 \text{ ohm}^{-1} \cdot \text{m}^{-1}$  the efficiency of the channel is about 0.005 – 0.01%. The entire amount of energy supplied to the flow would be converted into heat. Conductivity values of four or five orders of magnitude higher than the ones obtained are necessary in order to attain reasonable (60 – 80 %) energy conversion

efficiencies. One solution to this is to seed the flow with small amounts of an easily ionized material (potassium, cesium etc). Work is underway at UAH Advanced Propulsion Lab to finish the assembly of a potassium salt, liquid injection seeder.

Single probes have been successfully employed in diagnostics of MW flowing plasma. Future efforts will concentrate on determining the amount of seed required for obtaining high MHD channel energy conversion efficiency. Tests of different gases at various mass flowrates and microwave power are scheduled in the near future. Measurements with a magnetic field present in the flow will constitute the next step in the diagnostic of the MW plasma. These tests will provide an answer to the possibility of using the MW generated plasma in MHD space propulsion application.

### Appendix

One assumption on which Equation (11) was based is that the sheath thickness around the probe is much smaller than the probe diameter. With the measured  $T_e$  and  $n_0$ , the average Debye length for this plasma,  $\sim(\epsilon_0 k T_e / n_0 e^2)^{1/2}$  is less than 0.1 mm. The thickness of the sheath developed around the probe is usually a few times the Debye length. We concluded that it is safe to assume a sheath dimension smaller than the diameter of the probe.

The mean free path for collision of electrons and neutral particles is proportional to the mean time between collisions  $\tau_e = 1/\nu_e$ . The random thermal speed of neutrals is considerably lower than electron thermal speed. In these conditions the collision frequency for electrons-neutrals,  $\nu_{en}$  is proportional to the collision cross section  $Q_{en}$  and the density of neutrals<sup>9</sup>,  $\nu_{en} = c_e n_n Q_{en}$ . Using  $\tau_{en} = \lambda_{mfp}/c_e$  the mean free path for collision with neutrals is

$$\lambda_{mfp} = 1/n_n Q_{en} \quad (A.1)$$

At a gas pressure of ~500 mTorr and a temperature of ~2000K the mean free path for collision is about 2 mm (one order of magnitude higher than the sheath dimension). These approximate calculations based on expected plasma properties allowed for the assumptions that led to single probe model formulated above.

### Acknowledgements

The authors wish to thank Mr. Matthew Culley and Mr. Douglas Parkinson for their assistance

in setting up the experimental apparatus. This research program was sponsored in part by NASA Marshall Space Flight Center and by the Air Force Office of Scientific Research under the contract number F 49620-98-0-0083.

### References

- <sup>1</sup> Magnetohydrodynamic Accelerator Research Into Advanced Hypersonics (MARIAH), Final Report, NASA/CR-97-206242, 1997
- <sup>2</sup> Kantaratos, A. N., and Demetriade, S. T., "Interaction of a Jet of Plasma with Electric and Magnetic Fields" Applied Science, Sect. B, Vol. 11, 1964
- <sup>3</sup> Huddleston, R. H., and Leonard, S., L., (editors) "Plasma Diagnostic Techniques", Academic Press NY, 1965
- <sup>4</sup> De Boer, P. C. T., "Electric Probe Measurements in the Plume of an Ion Thruster", Journal of Propulsion and Power, Vol. 12, No. 1 pag. 95-103, January-February 1996
- <sup>5</sup> Chen, F. F., "Introduction to Plasma Physics and Controlled Fusion, Volume I: Plasma Physics", Plenum Press, NY, 1984
- <sup>6</sup> Chang, K. W., and Bienkowski, G., K., "Effects of Electron Emission on Electrostatic Probes at Arbitrary Pressures", The Physics of Fluids, Vol. 13, No. 4, pag. 902-920, 1970
- <sup>7</sup> Chung, P. M., et. al., "Electric Probes in Stationary and Flowing Plasmas: Theory and Application", Springer-Verlag, NY, 1975
- <sup>8</sup> Segall, S. B., and Koopman, D. W., "Application of Cylindrical Langmuir Probes to a Streaming Plasma Diagnostics", The Physics of Fluids, Vol 16, No. 7, pp. 1149-1156, July 1973
- <sup>9</sup> Sutton, G. W., and Sherman, A., "Engineering Magnetohydrodynamics", McGraw-Hill Book Co., NY, 1965
- <sup>10</sup> Burton, R. L. and Bufton, S. A., "Exit-Plane Electrostatic Probe Measurements of a Low-Power Arcjet," Journal of Propulsion and Power, Vol. 12, No. 6, pp. 1099-1106, Nov.-Dec., 1996.